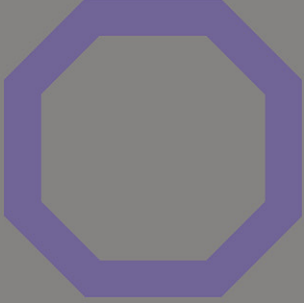
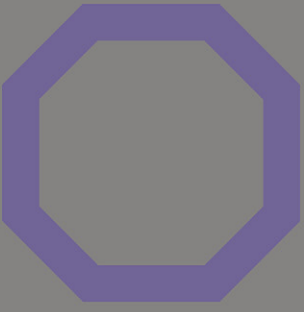


J.-C.G. Bünzli and V.K. Pecharsky
Editors



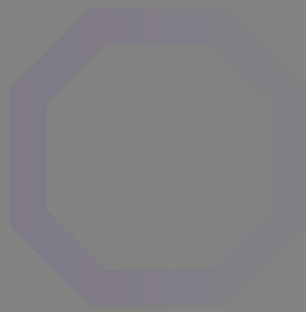
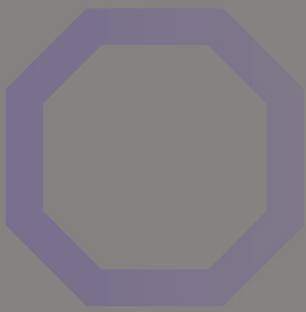
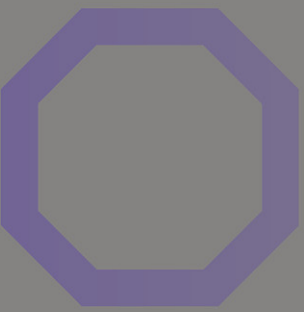
HANDBOOK ON THE
PHYSICS AND CHEMISTRY OF
RARE EARTHS



Volume 48

North-Holland

Including Actinides



Handbook on the Physics and Chemistry of Rare Earths

Volume 48

Including Actinides

HANDBOOK ON THE PHYSICS AND CHEMISTRY
OF RARE EARTHS

Advisory Editorial Board

GIN-YA ADACHI

Kobe, Japan

WILLIAM J. EVANS

Irvine, USA

YURI GRIN

Dresden, Germany

SUZAN M. KAUZLARICH

Davis, USA

MICHAEL F. REID

Canterbury, New Zealand

CHUNHUA YAN

Beijing, P.R. China

Editors Emeritus

KARL A. GSCHNEIDNER, JR

Ames, USA

LEROY EYRING✠

Tempe, USA

✠*Deceased (2005)*

Handbook on the Physics and Chemistry of Rare Earths

Volume 48

Including Actinides

Editors

Jean-Claude Bünzli

Swiss Federal Institute of Technology, Lausanne (EPFL)
Institute of Chemical Sciences and Engineering
BCH 1402
CH-1015 Lausanne
Switzerland

Vitalij K. Pecharsky

The Ames Laboratory, U.S. Department of Energy, and
Department of Materials Science and Engineering
Iowa State University,
Ames, Iowa 50011-3020
USA



Amsterdam • Boston • Heidelberg • London • New York • Oxford
Paris • San Diego • San Francisco • Singapore • Sydney • Tokyo
North-Holland is an imprint of Elsevier



North-Holland is an imprint of Elsevier

Radarweg 29, PO Box 211, 1000 AE Amsterdam, The Netherlands
The Boulevard, Langford Lane, Kidlington, Oxford OX5 1GB, UK

Copyright © 2015 Elsevier B.V. All rights reserved

No part of this publication may be reproduced or transmitted in any form or by any means, electronic or mechanical, including photocopying, recording, or any information storage and retrieval system, without permission in writing from the publisher. Details on how to seek permission, further information about the Publisher's permissions policies and our arrangements with organizations such as the Copyright Clearance Center and the Copyright Licensing Agency, can be found at our website: www.elsevier.com/permissions.

This book and the individual contributions contained in it are protected under copyright by the Publisher (other than as may be noted herein).

Notices

Knowledge and best practice in this field are constantly changing. As new research and experience broaden our understanding, changes in research methods, professional practices, or medical treatment may become necessary.

Practitioners and researchers must always rely on their own experience and knowledge in evaluating and using any information, methods, compounds, or experiments described herein. In using such information or methods they should be mindful of their own safety and the safety of others, including parties for whom they have a professional responsibility.

To the fullest extent of the law, neither the Publisher nor the authors, contributors, or editors, assume any liability for any injury and/or damage to persons or property as a matter of products liability, negligence or otherwise, or from any use or operation of any methods, products, instructions, or ideas contained in the material herein.

ISBN: 978-0-444-63483-2

ISSN: 0168-1273

For information on all North-Holland publications
visit our website at <http://store.elsevier.com/>



Working together
to grow libraries in
developing countries

www.elsevier.com • www.bookaid.org

Contents

Contributors	vii
Preface	ix
Contents of Volumes 1–47	xv
Index of Contents of Volumes 1–48	xxix
274. Persistent Phosphors	1
<i>Philippe F. Smet, Koen Van den Eeckhout, Olivier Q. De Clercq, and Dirk Poelman</i>	
275. Quaternary R_2X_3—PbX—ZX_2 ($X = S, Se$; $Z = Si, Ge, Sn$) Chalcogenides	109
<i>Lubomir D. Gulay, Marek Daszkiewicz, and Oleg V. Marchuk</i>	
276. Hybrid Materials of the f-Elements Part II: The Uranyl Cation	163
<i>Robert G. Surbella III and Christopher L. Cahill</i>	
277. Progress in the Separation Processes for Rare Earth Resources	287
<i>Zhifeng Zhang, Qiong Jia, and Wuping Liao</i>	
Index	377

This page intentionally left blank

Contributors

Numbers in Parentheses indicate the pages on which the author's contributions begin.

Christopher L. Cahill (163), Department of Chemistry, The George Washington University, Washington, District of Columbia, USA

Marek Daszkiewicz (109), Institute of Low Temperature and Structure Research, Polish Academy of Sciences, Wrocław, Poland

Olivier Q. De Clercq (1), LumiLab, Department of Solid State Sciences, Ghent University, Ghent, Belgium

Lubomir D. Gulay (109), Department of Ecology and Protection of Environment, Eastern European National University, Lutsk, Ukraine

Qiong Jia (287), College of Chemistry, Jilin University, Changchun, China

Wuping Liao (287), State Key Laboratory of Rare Earth Resource Utilization, ERC for the Separation and Purification of REs and Thorium, Changchun Institute of Applied Chemistry, Chinese Academy of Sciences, Changchun, China

Oleg V. Marchuk (109), Department of Inorganic and Physical Chemistry, Eastern European National University, Lutsk, Ukraine

Dirk Poelman (1), LumiLab, Department of Solid State Sciences, Ghent University, Ghent, Belgium

Philippe F. Smet (1), LumiLab, Department of Solid State Sciences, Ghent University, Ghent, Belgium

Robert G. Surbella III (163), Department of Chemistry, The George Washington University, Washington, District of Columbia, USA

Koen Van den Eeckhout (1), LumiLab, Department of Solid State Sciences, Ghent University, Ghent, Belgium

Zhifeng Zhang (287), State Key Laboratory of Rare Earth Resource Utilization, ERC for the Separation and Purification of REs and Thorium, Changchun Institute of Applied Chemistry, Chinese Academy of Sciences, Changchun, China

This page intentionally left blank

Preface

These elements perplex us in our reaches [sic], baffle us in our speculations, and haunt us in our very dreams. They stretch like an unknown sea before us—mocking, mystifying, and murmuring strange revelations and possibilities.

Sir William Crookes (February 16, 1887)

Volume 48 of the *Handbook on the Physics and Chemistry of Rare Earths* adds four chapters to the series, covering broadly different, but timely, subjects ranging from luminescent materials to properties of chalcogenides, uranyl hybrid materials, and separation processes. Featured themes include persistent luminescence, a phenomenon used in emerging applications such as signage and bioimaging, the phase diagrams, structure, and physical properties of quaternary rare earth/lead/group IV (Si, Ge, Sn)/sulfur or selenium compounds, structural chemistry of crystalline uranyl-containing compounds obtained via hydrothermal synthesis, as well as description of state-of-the-art in separation and purification processes of rare earths along with the preparation of high-purity rare-earth and thorium metals.

The first chapter (Chapter 274) is devoted to persistent luminescence, a phenomenon whereby a compound keeps emitting light for a long time after excitation is switched off. Ancient civilizations knew about this curious phenomenon, but the first account of it in the Western world dates back to the seventeenth century when the Bologna stone, obtained by calcining barite, was described. The emission of light in such materials depends on traps generated by tiny amounts of impurities; hence, different synthetic conditions lead to widely different emission colors. Studying this fascinating phenomenon is difficult so that it remained a curiosity until the twentieth century when zinc sulfide doped with transition metals (cobalt, copper) started to play an important role in luminous paints. Contributions of lanthanides to the field started at the end of the 1960s when strontium aluminate doped with divalent europium was discovered. A further and decisive impetus occurred in the mid-1990s initiated by the finding that co-doping trivalent dysprosium in this material produced a much brighter persistent phosphor. The chapter reviews all aspects of lanthanide persistent luminescence along with a critical evaluation of potential applications in marking, solar energy conversion, and biosciences.

Quaternary rare-earth chalcogenide systems $R_2X_3-PbX-ZX_2$ ($X=S, Se$; $Z=Si, Ge, Sn$) are the subject of Chapter 275. These compounds are of broad interest in both basic and applied sciences due to their intriguing

thermal, optical, electrical, and magnetic properties. The design of increasingly complex chalcogenide compounds is indeed vital for modern materials science, primarily in reference to the development of nonlinear optical devices. The systems based on lead, sulfur, and selenium are of special importance because substitution of lead with rare earths results in modified optical and magnetic properties that can be modulated while preserving the parent crystal structure. These new phases can also be obtained at the nanoscale, which considerably broadens their potential applications, for instance in catalysis, biotechnology, or medicine. In this review, synthetic conditions are detailed, followed by a systematic presentation of known phase diagrams, structures, and magnetic properties.

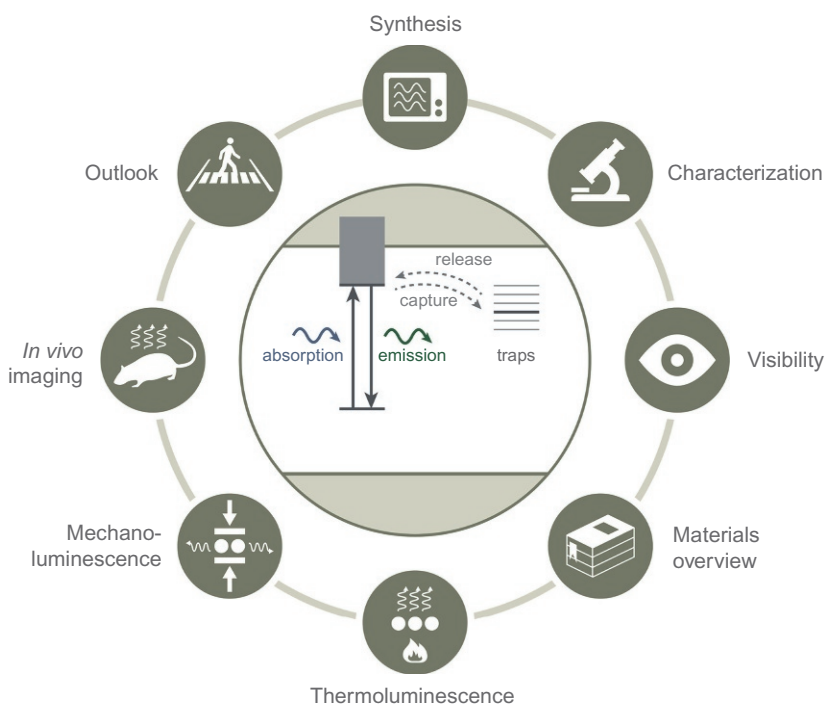
Chapter 276 deals with crystalline hybrid materials of uranyl. These materials combine a substrate (organic or inorganic) with uranyl ion or its complexes that are blended on the molecular scale. Generally speaking, hybrid materials are found in numerous systems and can be broadly divided into sol-gel (glasses, silica, organically modified xerogels), porous (metal-organic frameworks), mesoporous (silicates, zeolites), polymeric, intercalation (layered double hydroxides), and nanocomposite (nanoparticles) materials. Uranyl hydrolysis and complex aqueous speciation are the red thread of the review as they represent drivers for structural diversity. The chapter explores covalent bonding with O- and N-donor ligands before highlighting ways of programming targeted coordination geometries, compositions, and connectivities into the hybrid materials. Purely supramolecular systems, assembled thanks to noncovalent bonds from simple tectons under high concentrations of anions such as chloride, bromide, or isothiocyanate, are also presented. Finally, luminescence properties are described, particularly with respect to structure/property relationships.

The final chapter (Chapter 277) presents a historical insight as well as recent progresses in separation processes of rare earths, with a special focus on Chinese operations. Rare earth ores always contain a blend of several elements, and if some applications rely on mixtures (e.g., the Mischmetal, neodymium/praseodymium/dysprosium mixtures for magnets, or lanthanum/ cerium mixtures for nickel metal hydride batteries or catalysts), many high-technology uses need high-purity individual elements. Separation and purification operations are complex, time consuming, and have negative environmental effects. This points to the importance of developing efficient separation taking into account environmental issues, by making use of “greener” reactants and/or by recycling the chemicals involved. Both fundamental and applied investigations have to be combined to reach this goal. The chapter reviews the various extractants, methods, and equipment that have been developed for achieving efficient methodologies, progresses being sustained by adequate theoretical modeling. It ends by describing technologies for the production of very high-purity rare-earth elements and thorium, a by-product of rare-earth extraction.

CHAPTER 274: PERSISTENT PHOSPHORS

Philippe F. Smet, Koen Van den Eeckout, Olivier Q. De Clercq, and Dirk Poelman

LumiLab, Department of Solid State Sciences, Ghent University, Ghent, Belgium. E-mail: philippe.smet@ugent.be



Persistent luminescence is the phenomenon whereby a material keeps emitting light for seconds to hours after the excitation has stopped. This chapter describes the history of this class of materials and how the discovery of a new family of very efficient persistent phosphors has given a boost to the development of both new materials and applications. Synthesis conditions and analytical techniques specific to persistent luminescent compounds are described, together with ways to evaluate their performance in terms of human eye perception. A state of the art is presented about the materials—hosts and dopants—currently investigated for persistent luminescence, consistently referring to the original literature. Finally, *in vivo* medical imaging is shown to be a promising but challenging application of long-wavelength persistent luminescence and the relation between persistent luminescence and mechanoluminescence are described.

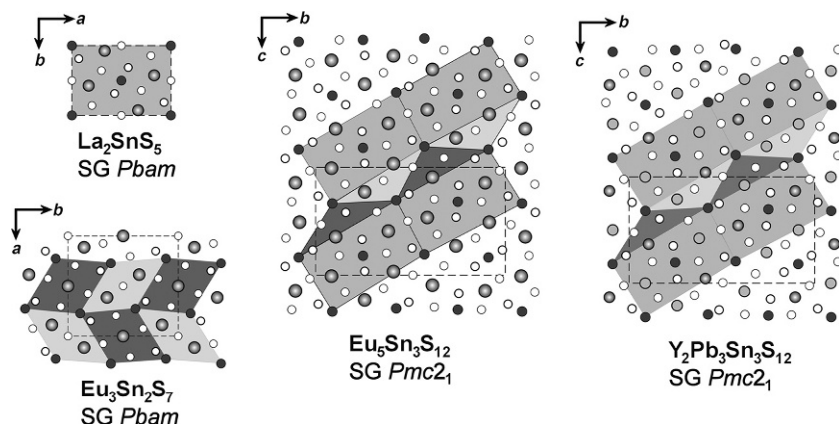
CHAPTER 275: QUATERNARY R_2X_3 — PbX — ZX_2 ($X = S, Se$; $Z = Si, Ge, Sn$) CHALCOGENIDES

Lubomir D. Gulay*, Marek Daszkiewicz†, and Oleg V. Marchuk**

*Department of Ecology and Protection of Environment, Eastern European University, Lutsk, Ukraine

†Institute of Low-Temperature and Structure Research, Polish Academy of Sciences, Wrocław, Poland. E-mail: m.daszkiewicz@int.pan.wroc.pl

**Department of Inorganic and Physical Chemistry, Eastern European National University, Lutsk, Ukraine

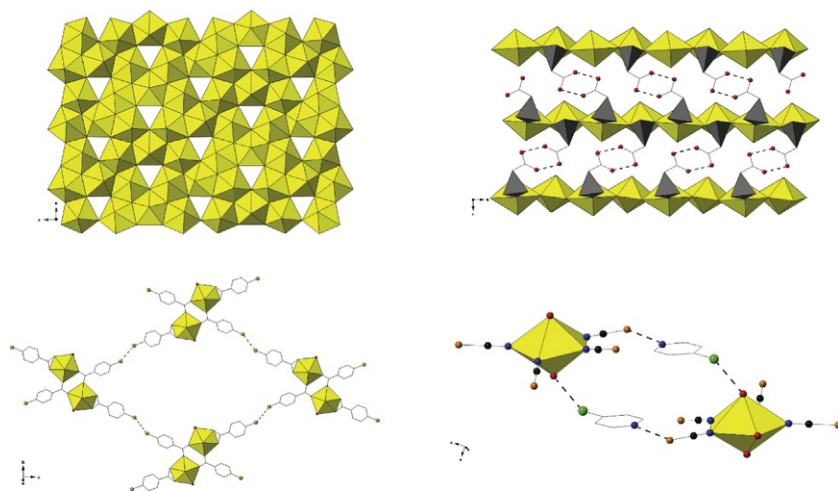


Complex ternary, quaternary, and multicomponent chalcogenides containing rare earths are interesting because of potential applications in the fields of ionic conductivity and nonlinear optics. The current knowledge about experimental investigations of phase diagrams, crystallographic relationships, and magnetic properties of quaternary rare-earth chalcogenides R_2X_3 — PbX — ZX_2 ($X = S, Se$; $Z = Si, Ge, Sn$) is the focus of the chapter. The initial section describes typical preparation of these novel materials in small quantities for studies of their basic physical properties and serves as a guide for those interested in preparing larger quantities in order to explore their potential for practical applications. Then the structure types of ternary Pb — Z — X ($X = S, Se$; $Z = Si, Ge, Sn$) systems are presented, before the review concentrates on the rare-earth-containing quaternary chalcogenides that are discussed according to their structure type. Description of superstructures and known magnetic properties concludes the chapter.

CHAPTER 276: HYBRID MATERIALS OF THE f-ELEMENTS PART II: THE URANYL CATION

Robert G. Surbella III and Christopher L. Cahill

The George Washington University, Washington, DC, USA. E-mail: cahill@gwu.edu



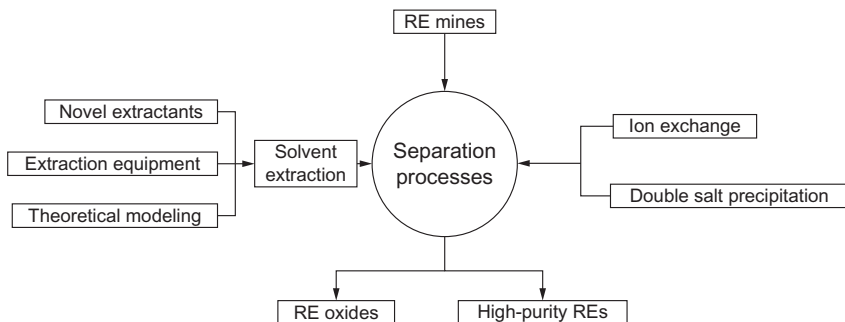
The catalog of uranyl-bearing hybrid materials has expanded considerably over the past 10–15 years. Researchers have drawn inspiration from the rich portfolio of structural topologies found in naturally occurring uranyl mineral phases where uranyl oligomerization stemming from hydrolysis is the norm. With these phenomena as guiding principles, our group in particular has pursued a program of exploring the relationship between synthetic reaction conditions, including ligand geometries and functionalities, with solid-state structure. As the synthetic efforts have flourished, a wide variety of structure types have emerged, yet the ability to fully correlate reaction conditions with resulting topologies remains elusive. As such, this chapter provides an overview of (whenever possible) synthetic “causes and effects” in the hydrothermal synthesis of uranyl hybrid materials. It then progresses to more recent developments wherein milder, high anion conditions are utilized to develop themes of assembly via noncovalent interactions between a more restricted suite of uranyl species.

CHAPTER 277: PROGRESS IN THE SEPARATION PROCESSES FOR RARE EARTH RESOURCES

Zhifeng Zhang¹, Qiong Jia², Wuping Liao^{1,*}

¹State Key Laboratory of Rare Earth Resource Utilization, Changchun Institute of Applied Chemistry, Chinese Academy of Sciences, Changchun. E-mail: wpliao@ciac.ac.cn

²College of Chemistry, Jilin University, Changchun, China



Rare earth elements have widespread applications in materials critical for many high-technology applications, including catalysts, permanent magnets, phosphors, lasers, and rechargeable batteries. Individual rare-earth elements are often needed so that separation and purification of rare-earth concentrates are crucial. Importantly, these operations are suffering from environmental problems and viable utilization of the resources. The chapter gives an overview of the evolution in fundamental research and industrial separation processes for rare earths. First, the progresses in extractants, novel equipment, alternative technologies, and theoretical modeling are summarized. Industrial hydrometallurgy processes are discussed and evaluated with respect to different ores of various origins. The preparation of highly pure rare earths and associated elements such as thorium is then presented. Easily accessible resources and environmentally friendly processes are essential issues to deal with in order to ensure sustainable developments in rare earth metallurgy.

Jean-Claude G. Bünzli
Vitalij K. Pecharsky

Contents of Volumes 1–47

VOLUME 1: Metals

1978, 1st repr. 1982, 2nd repr. 1991; ISBN 0-444-85020-1

1. Z.B. Goldschmidt, *Atomic properties (free atom)* 1
 2. B.J. Beaudry and K.A. Gschneidner Jr, *Preparation and basic properties of the rare earth metals* 173
 3. S.H. Liu, *Electronic structure of rare earth metals* 233
 4. D.C. Koskenmaki and K.A. Gschneidner Jr, *Cerium* 337
 5. L.J. Sundström, *Low temperature heat capacity of the rare earth metals* 379
 6. K.A. McEwen, *Magnetic and transport properties of the rare earths* 411
 7. S.K. Sinha, *Magnetic structures and inelastic neutron scattering: metals, alloys and compounds* 489
 8. T.E. Scott, *Elastic and mechanical properties* 591
 9. A. Jayaraman, *High pressure studies: metals, alloys and compounds* 707
 10. C. Probst and J. Wittig, *Superconductivity: metals, alloys and compounds* 749
 11. M.B. Maple, L.E. DeLong and B.C. Sales, *Kondo effect: alloys and compounds* 797
 12. M.P. Dariel, *Diffusion in rare earth metals* 847
- Subject index 877

VOLUME 2: Alloys and intermetallics

1979, 1st repr. 1982, 2nd repr. 1991; ISBN 0-444-85021-X

13. A. Iandelli and A. Palenzona, *Crystal chemistry of intermetallic compounds* 1
 14. H.R. Kirchmayr and C.A. Poldy, *Magnetic properties of intermetallic compounds of rare earth metals* 55
 15. A.E. Clark, *Magnetostrictive RFe_2 intermetallic compounds* 231
 16. J.J. Rhyne, *Amorphous magnetic rare earth alloys* 259
 17. P. Fulde, *Crystal fields* 295
 18. R.G. Barnes, *NMR, EPR and Mössbauer effect: metals, alloys and compounds* 387
 19. P. Wachter, *Europium chalcogenides: EuO, EuS, EuSe and EuTe* 507
 20. A. Jayaraman, *Valence changes in compounds* 575
- Subject index 613

VOLUME 3: Non-metallic compounds – I

1979, 1st repr. 1984; ISBN 0-444-85215-8

21. L.A. Haskin and T.P. Paster, *Geochemistry and mineralogy of the rare earths* 1
22. J.E. Powell, *Separation chemistry* 81
23. C.K. Jørgensen, *Theoretical chemistry of rare earths* 111
24. W.T. Carnall, *The absorption and fluorescence spectra of rare earth ions in solution* 171
25. L.C. Thompson, *Complexes* 209
26. G.G. Libowitz and A.J. Maeland, *Hydrides* 299
27. L. Eyring, *The binary rare earth oxides* 337
28. D.J.M. Bevan and E. Summerville, *Mixed rare earth oxides* 401

29. C.P. Khattak and F.F.Y. Wang, *Perovskites and garnets* 525
30. L.H. Brixner, J.R. Barkley and W. Jeitschko, *Rare earth molybdates (VI)* 609
Subject index 655

VOLUME 4: Non-metallic compounds – II

1979, 1st repr. 1984; ISBN 0-444-85216-6

31. J. Flahaut, *Sulfides, selenides and tellurides* 1
32. J.M. Haschke, *Halides* 89
33. F. Hulliger, *Rare earth pnictides* 153
34. G. Blasse, *Chemistry and physics of R-activated phosphors* 237
35. M.J. Weber, *Rare earth lasers* 275
36. F.K. Fong, *Nonradiative processes of rare-earth ions in crystals* 317
37A. J.W. O’Laughlin, *Chemical spectrophotometric and polarographic methods* 341
37B. S.R. Taylor, *Trace element analysis of rare earth elements by spark source mass spectroscopy* 359
37C. R.J. Conzemius, *Analysis of rare earth matrices by spark source mass spectrometry* 377
37D. E.L. DeKalb and V.A. Fassel, *Optical atomic emission and absorption methods* 405
37E. A.P. D’Silva and V.A. Fassel, *X-ray excited optical luminescence of the rare earths* 441
37F. F.W.V. Boynton, *Neutron activation analysis* 457
37G. S. Schuhmann and J.A. Philpotts, *Mass-spectrometric stable-isotope dilution analysis for lanthanides in geochemical materials* 471
38. J. Reuben and G.A. Elgavish, *Shift reagents and NMR of paramagnetic lanthanide complexes* 483
39. J. Reuben, *Bioinorganic chemistry: lanthanides as probes in systems of biological interest* 515
40. T.J. Haley, *Toxicity* 553
Subject index 587

VOLUME 5

1982, 1st repr. 1984; ISBN 0-444-86375-3

41. M. Gasgnier, *Rare earth alloys and compounds as thin films* 1
42. E. Gratz and M.J. Zuckermann, *Transport properties (electrical resistivity, thermoelectric power thermal conductivity) of rare earth intermetallic compounds* 117
43. F.P. Netzer and E. Bertel, *Adsorption and catalysis on rare earth surfaces* 217
44. C. Boulesteix, *Defects and phase transformation near room temperature in rare earth sesquioxides* 321
45. O. Greis and J.M. Haschke, *Rare earth fluorides* 387
46. C.A. Morrison and R.P. Leavitt, *Spectroscopic properties of triply ionized lanthanides in transparent host crystals* 461
Subject index 693

VOLUME 6

1984; ISBN 0-444-86592-6

47. K.H.J. Buschow, *Hydrogen absorption in intermetallic compounds* 1
48. E. Parthé and B. Chabot, *Crystal structures and crystal chemistry of ternary rare earth–transition metal borides, silicides and homologues* 113
49. P. Rogl, *Phase equilibria in ternary and higher order systems with rare earth elements and boron* 335

50. H.B. Kagan and J.L. Namy, *Preparation of divalent ytterbium and samarium derivatives and their use in organic chemistry* 525
Subject index 567

VOLUME 7

1984; ISBN 0-444-86851-8

51. P. Rogl, *Phase equilibria in ternary and higher order systems with rare earth elements and silicon* 1
52. K.H.J. Buschow, *Amorphous alloys* 265
53. H. Schumann and W. Genthe, *Organometallic compounds of the rare earths* 446
Subject index 573

VOLUME 8

1986; ISBN 0-444-86971-9

54. K.A. Gschneidner Jr and F.W. Calderwood, *Intra rare earth binary alloys: phase relationships, lattice parameters and systematics* 1
55. X. Gao, *Polarographic analysis of the rare earths* 163
56. M. Leskelä and L. Niinistö, *Inorganic complex compounds I* 203
57. J.R. Long, *Implications in organic synthesis* 335
Errata 375
Subject index 379

VOLUME 9

1987; ISBN 0-444-87045-8

58. R. Reisfeld and C.K. Jørgensen, *Excited state phenomena in vitreous materials* 1
59. L. Niinistö and M. Leskelä, *Inorganic complex compounds II* 91
60. J.-C.G. Bünzli, *Complexes with synthetic ionophores* 321
61. Zhiqian Shen and Jun Ouyang, *Rare earth coordination catalysis in stereospecific polymerization* 395
Errata 429
Subject index 431

VOLUME 10: High energy spectroscopy

1987; ISBN 0-444-87063-6

62. Y. Baer and W.-D. Schneider, *High-energy spectroscopy of lanthanide materials – An overview* 1
63. M. Campagna and F.U. Hillebrecht, *f-electron hybridization and dynamical screening of core holes in intermetallic compounds* 75
64. O. Gunnarsson and K. Schönhammer, *Many-body formulation of spectra of mixed valence systems* 103
65. A.J. Freeman, B.I. Min and M.R. Norman, *Local density supercell theory of photoemission and inverse photoemission spectra* 165
66. D.W. Lynch and J.H. Weaver, *Photoemission of Ce and its compounds* 231
67. S. Hüfner, *Photoemission in chalcogenides* 301
68. J.F. Herbst and J.W. Wilkins, *Calculation of 4f excitation energies in the metals and relevance to mixed valence systems* 321
69. B. Johansson and N. Mårtensson, *Thermodynamic aspects of 4f levels in metals and compounds* 361
70. F.U. Hillebrecht and M. Campagna, *Bremsstrahlung isochromat spectroscopy of alloys and mixed valent compounds* 425

71. J. Röhler, *X-ray absorption and emission spectra* 453
72. F.P. Netzer and J.A.D. Matthew, *Inelastic electron scattering measurements* 547
Subject index 601

VOLUME 11: Two-hundred-year impact of rare earths on science

1988; ISBN 0-444-87080-6

H.J. Svec, *Prologue* 1

73. F. Szabadváry, *The history of the discovery and separation of the rare earths* 33
74. B.R. Judd, *Atomic theory and optical spectroscopy* 81
75. C.K. Jørgensen, *Influence of rare earths on chemical understanding and classification* 197
76. J.J. Rhyne, *Highlights from the exotic phenomena of lanthanide magnetism* 293
77. B. Bleaney, *Magnetic resonance spectroscopy and hyperfine interactions* 323
78. K.A. Gschneidner Jr and A.H. Daane, *Physical metallurgy* 409
79. S.R. Taylor and S.M. McLennan, *The significance of the rare earths in geochemistry and cosmochemistry* 485
Errata 579
Subject index 581

VOLUME 12

1989; ISBN 0-444-87105-5

80. J.S. Abell, *Preparation and crystal growth of rare earth elements and intermetallic compounds* 1
81. Z. Fisk and J.P. Remeika, *Growth of single crystals from molten metal fluxes* 53
82. E. Burzo and H.R. Kirchmayr, *Physical properties of $R_2Fe_{14}B$ -based alloys* 71
83. A. Szytuła and J. Leciejewicz, *Magnetic properties of ternary intermetallic compounds of the RT_2X_2 type* 133
84. H. Maletta and W. Zinn, *Spin glasses* 213
85. J. van Zytveld, *Liquid metals and alloys* 357
86. M.S. Chandrasekharaiah and K.A. Gingerich, *Thermodynamic properties of gaseous species* 409
87. W.M. Yen, *Laser spectroscopy* 433
Subject index 479

VOLUME 13

1990; ISBN 0-444-88547-1

88. E.I. Gladyshevsky, O.I. Bodak and V.K. Pecharsky, *Phase equilibria and crystal chemistry in ternary rare earth systems with metallic elements* 1
89. A.A. Eliseev and G.M. Kuzmichyeva, *Phase equilibrium and crystal chemistry in ternary rare earth systems with chalcogenide elements* 191
90. N. Kimizuka, E. Takayama-Muromachi and K. Siratori, *The systems R_2O_3 – M_2O_3 – $M'O$* 283
91. R.S. Houk, *Elemental analysis by atomic emission and mass spectrometry with inductively coupled plasmas* 385
92. P.H. Brown, A.H. Rathjen, R.D. Graham and D.E. Tribe, *Rare earth elements in biological systems* 423
Errata 453
Subject index 455

VOLUME 14

1991; ISBN 0-444-88743-1

93. R. Osborn, S.W. Lovesey, A.D. Taylor and E. Balcar, *Intermultiplet transitions using neutron spectroscopy* 1
94. E. Dormann, *NMR in intermetallic compounds* 63
95. E. Zirngiebl and G. Güntherodt, *Light scattering in intermetallic compounds* 163
96. P. Thalmeier and B. Lüthi, *The electron–phonon interaction in intermetallic compounds* 225
97. N. Grewe and F. Steglich, *Heavy fermions* 343
- Subject index 475

VOLUME 15

1991; ISBN 0-444-88966-3

98. J.G. Sereni, *Low-temperature behaviour of cerium compounds* 1
99. G.-Y. Adachi, N. Imanaka and Zhang Fuzhong, *Rare earth carbides* 61
100. A. Simon, Hj. Mattausch, G.J. Miller, W. Bauhofer and R.K. Kremer, *Metal-rich halides* 191
101. R.M. Almeida, *Fluoride glasses* 287
102. K.L. Nash and J.C. Sullivan, *Kinetics of complexation and redox reactions of the lanthanides in aqueous solutions* 347
103. E.N. Rizkalla and G.R. Choppin, *Hydration and hydrolysis of lanthanides* 393
104. L.M. Vallarino, *Macrocyclic complexes of the lanthanide(III), yttrium(III), and dioxouranium (VI) ions from metal-templated syntheses* 443
- Errata 513
- Subject index 515

CUMULATIVE INDEX, Vols. 1–15

1993; ISBN 0-444-89965-0

VOLUME 16

1993; ISBN 0-444-89782-8

105. M. Loewenhaupt and K.H. Fischer, *Valence-fluctuation and heavy-fermion 4f systems* 1
106. I.A. Smirnov and V.S. Oskotski, *Thermal conductivity of rare earth compounds* 107
107. M.A. Subramanian and A.W. Sleight, *Rare earth pyrochlores* 225
108. R. Miyawaki and I. Nakai, *Crystal structures of rare earth minerals* 249
109. D.R. Chopra, *Appearance potential spectroscopy of lanthanides and their intermetallics* 519
- Author index 547
- Subject index 579

VOLUME 17: Lanthanides/Actinides: Physics – I

1993; ISBN 0-444-81502-3

110. M.R. Norman and D.D. Koelling, *Electronic structure, Fermi surfaces, and superconductivity in f electron metals* 1
111. S.H. Liu, *Phenomenological approach to heavy-fermion systems* 87
112. B. Johansson and M.S.S. Brooks, *Theory of cohesion in rare earths and actinides* 149
113. U. Benedict and W.B. Holzapfel, *High-pressure studies – Structural aspects* 245

114. O. Vogt and K. Mattenberger, *Magnetic measurements on rare earth and actinide monopycnitides and monochalcogenides* 301
115. J.M. Fournier and E. Gratz, *Transport properties of rare earth and actinide intermetallics* 409
116. W. Potzel, G.M. Kalvius and J. Gal, *Mössbauer studies on electronic structure of intermetallic compounds* 539
117. G.H. Lander, *Neutron elastic scattering from actinides and anomalous lanthanides* 635
 Author index 711
 Subject index 753

VOLUME 18: Lanthanides/Actinides: Chemistry

1994; ISBN 0-444-81724-7

118. G.T. Seaborg, *Origin of the actinide concept* 1
119. K. Balasubramanian, *Relativistic effects and electronic structure of lanthanide and actinide molecules* 29
120. J.V. Beitz, *Similarities and differences in trivalent lanthanide- and actinide-ion solution absorption spectra and luminescence studies* 159
121. K.L. Nash, *Separation chemistry for lanthanides and trivalent actinides* 197
122. L.R. Morss, *Comparative thermochemical and oxidation – reduction properties of lanthanides and actinides* 239
123. J.W. Ward and J.M. Haschke, *Comparison of 4f and 5f element hydride properties* 293
124. H.A. Eick, *Lanthanide and actinide halides* 365
125. R.G. Haire and L. Eyring, *Comparisons of the binary oxides* 413
126. S.A. Kinkad, K.D. Abney and T.A. O'Donnell, *f-Element speciation in strongly acidic media: lanthanide and mid-actinide metals, oxides, fluorides and oxide fluorides in superacids* 507
127. E.N. Rizkalla and G.R. Choppin, *Lanthanides and actinides hydration and hydrolysis* 529
128. G.R. Choppin and E.N. Rizkalla, *Solution chemistry of actinides and lanthanides* 559
129. J.R. Duffield, D.M. Taylor and D.R. Williams, *The biochemistry of the f-elements* 591
 Author index 623
 Subject index 659

VOLUME 19: Lanthanides/Actinides: Physics – II

1994; ISBN 0-444-82015-9

130. E. Holland-Moritz and G.H. Lander, *Neutron inelastic scattering from actinides and anomalous lanthanides* 1
131. G. Aeppli and C. Broholm, *Magnetic correlations in heavy-fermion systems: neutron scattering from single crystals* 123
132. P. Wachter, *Intermediate valence and heavy fermions* 177
133. J.D. Thompson and J.M. Lawrence, *High pressure studies – Physical properties of anomalous Ce, Yb and U compounds* 383
134. C. Colinet and A. Pasturel, *Thermodynamic properties of metallic systems* 479
 Author index 649
 Subject index 693

VOLUME 20

1995; ISBN 0-444-82014-0

135. Y. Ōnuki and A. Hasegawa, *Fermi surfaces of intermetallic compounds* 1
136. M. Gasgnier, *The intricate world of rare earth thin films: metals, alloys, intermetallics, chemical compounds,...* 105
137. P. Vajda, *Hydrogen in rare-earth metals, including RH_{2+x} phases* 207
138. D. Gignoux and D. Schmitt, *Magnetic properties of intermetallic compounds* 293
Author index 425
Subject index 457

VOLUME 21

1995; ISBN 0-444-82178-3

139. R.G. Bautista, *Separation chemistry* 1
140. B.W. Hinton, *Corrosion prevention and control* 29
141. N.E. Ryan, *High-temperature corrosion protection* 93
142. T. Sakai, M. Matsuoka and C. Iwakura, *Rare earth intermetallics for metal–hydrogen batteries* 133
143. G.-y. Adachi and N. Imanaka, *Chemical sensors* 179
144. D. Garcia and M. Faucher, *Crystal field in non-metallic (rare earth) compounds* 263
145. J.-C.G. Bünzli and A. Milicic-Tang, *Solvation and anion interaction in organic solvents* 305
146. V. Bhagavathy, T. Prasada Rao and A.D. Damodaran, *Trace determination of lanthanides in high-purity rare-earth oxides* 367
Author index 385
Subject index 411

VOLUME 22

1996; ISBN 0-444-82288-7

147. C.P. Flynn and M.B. Salamon, *Synthesis and properties of single-crystal nanostructures* 1
148. Z.S. Shan and D.J. Sellmyer, *Nanoscale rare earth–transition metal multilayers: magnetic structure and properties* 81
149. W. Suski, *The $ThMn_{12}$ -type compounds of rare earths and actinides: structure, magnetic and related properties* 143
150. L.K. Aminov, B.Z. Malkin and M.A. Teplov, *Magnetic properties of nonmetallic lanthanide compounds* 295
151. F. Auzel, *Coherent emission in rare-earth materials* 507
152. M. Dolg and H. Stoll, *Electronic structure calculations for molecules containing lanthanide atoms* 607
Author index 731
Subject index 777

VOLUME 23

1996; ISBN 0-444-82507-X

153. J.H. Forsberg, *NMR studies of paramagnetic lanthanide complexes and shift reagents* 1
154. N. Sabbatini, M. Guardigli and I. Manet, *Antenna effect in encapsulation complexes of lanthanide ions* 69
155. C. Görrler-Walrand and K. Binnemans, *Rationalization of crystal-field parameterization* 121
156. Yu. Kuz'ma and S. Chykhrij, *Phosphides* 285

157. S. Boghosian and G.N. Papatheodorou, *Halide vapors and vapor complexes* 435
158. R.H. Byrne and E.R. Sholkovitz, *Marine chemistry and geochemistry of the lanthanides* 497
Author index 595
Subject index 631

VOLUME 24

1997; ISBN 0-444-82607-6

159. P.A. Dowben, D.N. McIlroy and Dongqi Li, *Surface magnetism of the lanthanides* 1
160. P.G. McCormick, *Mechanical alloying and mechanically induced chemical reactions* 47
161. A. Inoue, *Amorphous, quasicrystalline and nanocrystalline alloys in Al- and Mg-based systems* 83
162. B. Elschner and A. Loidl, *Electron-spin resonance on localized magnetic moments in metals* 221
163. N.H. Duc, *Intersublattice exchange coupling in the lanthanide-transition metal intermetallics* 339
164. R.V. Skolozdra, *Stannides of rare-earth and transition metals* 399
Author index 519
Subject index 559

VOLUME 25

1998; ISBN 0-444-82871-0

165. H. Nagai, *Rare earths in steels* 1
166. R. Marchand, *Ternary and higher order nitride materials* 51
167. C. Görrler-Walrand and K. Binnemans, *Spectral intensities of f-f transitions* 101
168. G. Bombieri and G. Paolucci, *Organometallic π complexes of the f-elements* 265
Author index 415
Subject index 459

VOLUME 26

1999; ISBN 0-444-50815-1

169. D.F. McMorrow, D. Gibbs and J. Bohr, *X-ray scattering studies of lanthanide magnetism* 1
170. A.M. Tishin, Yu.I. Spichkin and J. Bohr, *Static and dynamic stresses* 87
171. N.H. Duc and T. Goto, *Itinerant electron metamagnetism of Co sublattice in the lanthanide-cobalt intermetallics* 177
172. A.J. Arko, P.S. Riseborough, A.B. Andrews, J.J. Joyce, A.N. Tahvildar-Zadeh and M. Jarrell, *Photo-electron spectroscopy in heavy fermion systems: Emphasis on single crystals* 265
Author index 383
Subject index 405

VOLUME 27

1999; ISBN 0-444-50342-0

173. P.S. Salamakha, O.L. Sologub and O.I. Bodak, *Ternary rare-earth-germanium systems* 1
174. P.S. Salamakha, *Crystal structures and crystal chemistry of ternary rare-earth germanides* 225
175. B. Ya. Kotur and E. Gratz, *Scandium alloy systems and intermetallics* 339
Author index 535
Subject index 553

VOLUME 28

2000; ISBN 0-444-50346-3

176. J.-P. Connerade and R.C. Karnatak, *Electronic excitation in atomic species* 1
177. G. Meyer and M.S. Wickleder, *Simple and complex halides* 53
178. R.V. Kumar and H. Iwahara, *Solid electrolytes* 131
179. A. Halperin, *Activated thermoluminescence (TL) dosimeters and related radiation detectors* 187
180. K.L. Nash and M.P. Jensen, *Analytical separations of the lanthanides: basic chemistry and methods* 311
Author index 373
Subject index 401

VOLUME 29: The role of rare earths in catalysis

2000; ISBN 0-444-50472-9

P. Maestro, *Foreword* 1

181. V. Paul-Boncour, L. Hilaire and A. Percheron-Guégan, *The metals and alloys in catalysis* 5
182. H. Imamura, *The metals and alloys (prepared utilizing liquid ammonia solutions) in catalysis II* 45
183. M.A. Ulla and E.A. Lombardo, *The mixed oxides* 75
184. J. Kašpar, M. Graziani and P. Fornasiero, *Ceria-containing three-way catalysts* 159
185. A. Corma and J.M. López Nieto, *The use of rare-earth-containing zeolite catalysts* 269
186. S. Kobayashi, *Triflates* 315
Author index 377
Subject index 409

VOLUME 30: High-Temperature Superconductors – I

2000; ISBN 0-444-50528-8

187. M.B. Maple, *High-temperature superconductivity in layered cuprates: overview* 1
188. B. Raveau, C. Michel and M. Hervieu, *Crystal chemistry of superconducting rare-earth cuprates* 31
189. Y. Shiohara and E.A. Goodilin, *Single-crystal growth for science and technology* 67
190. P. Karen and A. Kjekshus, *Phase diagrams and thermodynamic properties* 229
191. B. Elschner and A. Loidl, *Electron paramagnetic resonance in cuprate superconductors and in parent compounds* 375
192. A.A. Manuel, *Positron annihilation in high-temperature superconductors* 417
193. W.E. Pickett and I.I. Mazin, *RBa₂Cu₃O₇ compounds: electronic theory and physical properties* 453
194. U. Staub and L. Soderholm, *Electronic 4f-state splittings in cuprates* 491
Author index 547
Subject index 621

VOLUME 31: High-Temperature Superconductors – II

2001; ISBN 0-444-50719-1

195. E. Kaldis, *Oxygen nonstoichiometry and lattice effects in YBa₂Cu₃O_x. Phase transitions, structural distortions and phase separation* 1
196. H.W. Weber, *Flux pinning* 187
197. C.C. Almasan and M.B. Maple, *Magnetoresistance and Hall effect* 251
198. T.E. Mason, *Neutron scattering studies of spin fluctuations in high-temperature superconductors* 281

199. J.W. Lynn and S. Skanthakumar, *Neutron scattering studies of lanthanide magnetic ordering* 315
200. P.M. Allenspach and M.B. Maple, *Heat capacity* 351
201. M. Schabel and Z.-X. Shen, *Angle-resolved photoemission studies of untwinned yttrium barium copper oxide* 391
202. D.N. Basov and T. Timusk, *Infrared properties of high- T_c superconductors: an experimental overview* 437
203. S.L. Cooper, *Electronic and magnetic Raman scattering studies of the high- T_c cuprates* 509
204. H. Sugawara, T. Hasegawa and K. Kitazawa, *Characterization of cuprate superconductors using tunneling spectra and scanning tunneling microscopy* 563
 Author index 609
 Subject index 677

VOLUME 32

2001; ISBN 0-444-50762-0

205. N.H. Duc, *Giant magnetostriction in lanthanide-transition metal thin films* 1
206. G.M. Kalvius, D.R. Noakes and O. Hartmann, *μ SR studies of rare-earth and actinide magnetic materials* 55
207. Rainer Pötting, Dirk Johrendt and Dirk Kußmann, *Structure–property relations of ternary equiatomic YbTX intermetallics* 453
208. Kurima Kobayashi and Satoshi Hirotsawa, *Permanent magnets* 515
209. I.G. Vasilyeva, *Polysulfides* 567
210. Dennis K.P. Ng, Jianzhuang Jiang, Kuninobu Kasuga and Kenichi Machida, *Half-sandwich tetrapyrrole complexes of rare earths and actinides* 611
 Author index 655
 Subject index 733

VOLUME 33

2003; ISBN 0-444-51323-X

211. Brian C. Sales, *Filled skutterudites* 1
212. Oksana L. Sologub and Petro S. Salamakha, *Rare earth – antimony systems* 35
213. R.J.M. Konings and A. Kovács, *Thermodynamic properties of the lanthanide (III) halides* 147
214. John B. Goodenough, *Rare earth – manganese perovskites* 249
215. Claude Piguet and Carlos F.G.C. Geraldes, *Paramagnetic NMR lanthanide induced shifts for extracting solution structures* 353
216. Isabelle Billard, *Lanthanide and actinide solution chemistry as studied by time-resolved emission spectroscopy* 465
217. Thomas Tröster, *Optical studies of non-metallic compounds under pressure* 515
 Author index 591
 Subject index 637

VOLUME 34

2004; ISBN 0-444-51587-9

218. Yaroslav M. Kalychak, Vasyl' I. Zaremba, Rainer Pötting, Mar'yana Lukachuk and Rolf-Dieter Hoffman, *Rare earth–transition metal–indides* 1
219. P. Thalmeier and G. Zwicknagl, *Unconventional superconductivity and magnetism in lanthanide and actinide intermetallic compounds* 135
220. James P. Riehl and Gilles Muller, *Circularly polarized luminescence spectroscopy from lanthanide systems* 289

221. Oliver Guillou and Carole Daiguebonne, *Lanthanide-containing coordination polymers* 359
222. Makoto Komiyama, *Cutting DNA and RNA* 405
Author index 455
Subject index 493

VOLUME 35

2005; ISBN 0-444-52028-7

223. Natsuko Sakai, Katsuhiko Yamaji, Teruhisa Horita, Yue Ping Xiong and Harumi Yokokawa, *Rare-earth materials for solid oxide fuel cells (SOFC)* 1
224. Mathias S. Wickleder, *Oxo-selenates of rare-earth elements* 45
225. Koen Binnemans, *Rare-earth beta-diketonates* 107
226. Satoshi Shinoda, Hiroyuki Miyake and Hiroshi Tsukube, *Molecular recognition and sensing via rare-earth complexes* 273
Author index 337
Subject index 377

VOLUME 36

2006; ISBN 0-444-52142-9

227. Arthur Mar, *Bismuthides* 1
228. I. Aruna, L.K. Malhotra and B.R. Mehta, *Switchable metal hydride films* 83
229. Koen Binnemans, *Applications of tetravalent cerium compounds* 281
230. Robert A. Flowers II and Edamana Prasad, *Samarium (II) based reductants* 393
Author index 475
Subject index 511

VOLUME 37: Optical Spectroscopy

2007; ISBN 978-0-444-52144-6

231. Kazuyoshi Ogasawara, Shinta Watanabe, Hiroaki Toyoshima and Mikhail G. Brik, *First-principles calculations of $4f^n \rightarrow 4f^{n-1} 5d$ transition spectra* 1
232. Gary W. Burdick and Michael F. Reid, *$4f^n-4f^{n-1} 5d$ transitions* 61
233. Guokui Liu and Xueyuan Chen, *Spectroscopic properties of lanthanides in nanomaterials* 99
234. Takuya Nishioka, Kôichi Fukui and Kazuko Matsumoto, *Lanthanide chelates as luminescent labels in biomedical analyses* 171
235. Steve Comby and Jean-Claude G. Bünzli, *Lanthanide near-infrared luminescence in molecular probes and devices* 217
Author index 471
Subject index 503

VOLUME 38

2008; ISBN 978-0-444-52143-9

236. Z.C. Kang, *Lanthanide higher oxides: The contributions of Leroy Eyring* 1
237. Rainer Pöttgen and Ute Ch. Rodewald, *Rare earth–transition metal–plumbides* 55
238. Takao Mori, *Higher borides* 105
239. K.-H. Müller, M. Schneider, G. Fuchs and S.-L. Drechsler, *Rare-earth nickel borocarbides* 175
240. Michael T. Pope, *Polyoxometalates* 337
Author index 383
Subject index 431

VOLUME 39

2009; ISBN 978-0-444-53221-3

241. W.M. Temmerman, L. Petit, A. Svane, Z. Szotek, M. Lüders, P. Strange, J.B. Staunton, I.D. Hughes, and B.L. Gyorffy, *The dual, localized or band-like, character of the 4f-states* 1
242. L. Vasylechko, A. Senyshyn, and U. Bismayer, *Perovskite-type aluminates and gallates* 113
243. Toshihiro Yamase, *Luminescence of polyoxometallolanthanoates and photochemical nano-ring formation* 297
- Author index 357
- Subject index 381

VOLUME 40

2010; ISBN 978-0-444-53220-6

244. Christiane Görller-Walrand and Linda Fluyt, *Magnetic circular dichroism of lanthanides* 1
245. Z. Zheng, *Cluster compounds of rare-earth elements* 109
246. François Nief, *Molecular chemistry of the rare-earth elements in uncommon low-valent states* 241
247. Claude Piguët and Jean-Claude G. Bünzli, *Self-Assembled lanthanide helicates: From basic thermodynamics to applications* 301
- Author index 555
- Subject index 583

VOLUME 41

2011; ISBN 978-0-444-53590-0

248. Pieter Thyssen and Koen Binnemans, *Accommodation of the rare earths in the periodic table: A historical analysis* 1
249. Hisanori Shinohara and Yahachi Saito, *Metallofullerenes* 95
250. Lubomir D. Gulay and Marek Daszkiewicz, *Ternary and quaternary chalcogenides of Si, Ge, Sn, Pb, and In* 157
251. Chun-Hua Yan, Zheng-Guang Yan, Ya-Ping Du, Jie Shen, Chao Zhang, and Wei Feng, *Controlled synthesis and properties of rare earth nanomaterials* 275
- Author index 473
- Subject index 517

VOLUME 42

2012; ISBN 978-0-444-54316-5

252. Y. Uwatoko, I. Umehara, M. Ohashi, T. Nakano, and G. Oomi, *Thermal and electronic properties of rare earth compounds at high pressure* 1
253. Alexander D. Chervonnyi, *Thermodynamic properties of lanthanide fluorides and chlorides in the gaseous and condensed states* 165
- Author index 485
- Subject index 507

VOLUME 43: Including Actinides

2013; ISBN 978-0-444-59536-2

254. Koen Binnemans, *Lanthanidomesogens* 1
255. Mikiya Tanaka, Tatsuya Oki, Kazuya Koyama, Hirokazu Narita, and Tetsuo Oishi, *Recycling of rare earths from scrap* 159

256. Isabelle Billard, *Ionic liquids: New hopes for efficient lanthanide/actinide extraction and separation?* 213
257. Gopi K. Samudrala and Yogesh K. Vohra, *Structural properties of lanthanides at ultra high pressure* 275
258. John W. Arblaster, *Selected values of the thermodynamic properties of scandium, yttrium, and the lanthanide elements* 321
- Author index 567
- Subject index 591

VOLUME 44: Including Actinides

2014; ISBN 978-0-444-62711-7

259. Sophie M. Guillaume, Laurent Maron, and Peter W. Roesky, *Catalytic behavior of rare-earth borohydride complexes in polymerization of polar monomers* 1
260. Yasuhiko Iwadate, *Structures and properties of rare-earth molten salts* 87
261. Jean-Claude G. Bünzli and Anne-Sophie Chauvin, *Lanthanides in solar energy conversion* 169
262. Yaroslav Mudryk, Vitalij K. Pecharsky, and Karl A. Gschneidner, Jr., *R5T4 Compounds: An extraordinary versatile model system for the solid state science* 283
- Index 451

VOLUME 45: Including Actinides

2014; ISBN 978-0-444-63256-2

263. Joaquim Marçalo and John K. Gibson, *Gas-phase ion chemistry of rare earths and actinides* 1
264. Gerd Meyer, *Symbiosis of intermetallic and salt: Rare-earth metal cluster complexes with endohedral transition metal atoms* 111
265. Markus P. Hehlen, Mansoor Sheik-Bahae, and Richard I. Epstein, *Solid-state optical refrigeration* 179
266. Wenliang Huang and Paula L. Diaconescu, *Rare earth arene-bridged complexes obtained by reduction of organometallic precursors* 261
- Index 331

VOLUME 46

2015; ISBN 978-0-444-63260-9

267. Philippe Goldner, Alban Ferrier, and Olivier Guillot-Noël, *Rare Earth-Doped Crystals for Quantum Information Processing* 1
268. Kentaro Nakamura, Koichiro Fujinaga, Kazutaka Yasukawa, Yutaro Takaya, Junichiro Ohta, Shiki Machida, Satoru Haraguchi, and Yasuhiro Kato, *REY-Rich Mud: A Deep-Sea Mineral Resource for Rare Earths and Yttrium* 79
- Index 129

VOLUME 47

2015; ISBN 978-0-444-63481-8

269. Ignacio Hernández and William P. Gillin, *Organic Chromophores-Based Sensitization of NIR-Emitting Lanthanides: Toward Highly Efficient Halogenated Environments* 1
270. Yasuchika Hasegawa and Takayuki Nakanishi, *Europium Chalcogenide Nanoparticles* 101
271. Corey P. Carter and Christopher L. Cahill, *Hybrid Materials of the f-Elements Part I: The Lanthanides* 147

272. Claude Piguet, *Microscopic Thermodynamic Descriptors for Rationalizing Lanthanide Complexation Processes* 209
273. Diana C. Rodriguez Burbano, Rafik Naccache, and John A. Capobianco, *Near-IR Triggered Photon Upconversion: Imaging, Detection, and Therapy* 273
- Index 349

Index of Contents of Volumes 1–48

4f excitation energies, calculations
of **10**, ch. 68, p. 321
4f levels, thermodynamic aspects
10, ch. 69, p. 361
4f state splittings in cuprates **30**,
ch. 194, p. 491
4f states, character of **39**, ch. 241, p. 1
4fⁿ-4fⁿ⁻¹5d transitions **37**, ch. 231,
p. 1; **37**, ch. 232, p. 61

A

ab-initio calculation of energy
levels **37**, ch. 231, p. 1
absorption spectra of ions in
solution **3**, ch. 24, p. 171; **18**,
ch. 120, p. 159
actinides origin of concept **18**,
ch. 118, p. 1
– extraction of **43**, ch. 256, p. 213
– separation from lanthanides **43**,
ch. 256, p. 213
activated phosphors **4**, ch. 34, p. 237
activated thermoluminescence **28**,
ch. 179, p. 187
activation
– of P₄ by rare earths **45**, ch. 266, p. 261
aluminates **39**, ch. 242, p. 113
amorphous alloys **7**, ch. 52, p. 265
– Al- and Mg-based **24**, ch. 161, p. 83
– magnetic **2**, ch. 16, p. 259
anion interaction in organic solvents **21**,
ch. 145, p. 305
antimony alloy systems **33**,
ch. 212, p. 35
An-Ln separation using ionic liquids **43**,
ch. 256, p. 213
atomic ions
– actinides in gas phase **45**, ch. 263, p. 1
– rare-earth ions in gas phase **45**, ch. 263,
p. 1
arene-bridged complexes **45**, ch. 266, p. 261
atomic properties (free atom) **1**, ch. 1, p. 1
atomic theory **11**, ch. 74, p. 81

B

batteries, recycling of **43**, ch. 255, p. 159
beta-diketonates **35**, ch. 225, p. 107
– mesogenic complexes **43**, ch. 254, p. 1
Belousov-Zhabotinsky reactions **36**,
ch. 229, p. 281
biochemistry **18**, ch. 129, p. 591
bioinorganic chemistry **4**, ch. 39, p. 515
biological systems **13**, ch. 92, p. 423
bioprobes **40**, ch. 247, p. 301; **47**, ch. 273,
p. 273
biphenyl complexes **45**, ch. 266, p. 261
bis(benzimidazole)pyridine
– mesogenic complexes **43**, ch. 254, p. 1
– self-assembled complexes **40**, ch. 247,
p. 303
bismuth alloy systems **36**, ch. 227, p. 1
borides **6**, ch. 48, p. 113; **6**, ch. 49,
p. 335; **38**, ch. 238, p. 105; **38**,
ch. 239, p. 175
borohydride complexes **44**, ch. 259, p. 1

C

carbides **15**, ch. 99, p. 61; **38**, ch. 239, p. 175
Carnall, William T. **37**, dedication, p. xiii
catalysis **29**, foreword, p. 1
– arene-bridged complexes **45**, ch. 266, p. 261
– borohydrides **44**, ch. 259, p. 1
– ceria-containing three-way **29**,
ch. 184, p. 159
– metals and alloys **29**, ch. 181, p. 5
– metals and alloys in liquid ammonia
solutions **29**, ch. 182, p. 45
– stereospecific polymerization **9**, ch. 61,
p. 395; **44**, ch. 262, p. 283
– mixed oxides **29**, ch. 183, p. 75
– zeolites **29**, ch. 185, p. 269
catalysts, recycling of **43**, ch. 255, p. 159
cerimetry **36**, ch. 229, p. 281
cerium **1**, ch. 4, p. 337
cerium compounds
– low-temperature behavior **15**, ch. 98, p. 1
– tetravalent **36**, ch. 229, p. 281

- cerium(IV)
- catalysts **36**, ch. 229, p. 281
 - mediated reactions **36**, ch. 229, p. 281
 - redox properties **36**, ch. 229, p. 281
- chalcogenides,
- europium nanoparticles **47**, ch. 270, p. 101
 - magnetic measurements on mono- **17**, ch. 114, p. 301
 - quaternary **41**, ch. 250, p. 157; **48**, ch. 275, p. 109
 - ternary **41**, ch. 250, p. 157
- chemical analysis by
- atomic emission with inductively coupled plasmas **13**, ch. 91, p. 385
 - mass spectrometry, *see* spectroscopy, mass
 - neutron activation **4**, ch. 37F, p. 457
 - optical absorption **4**, ch. 37D, p. 405
 - optical atomic emission **4**, ch. 37D, p. 405
 - polarography **4**, ch. 37A, p. 341; **8**, ch. 55, p. 163
 - spectrophotometry **4**, ch. 37A, p. 341
 - trace determination in high-purity oxides **21**, ch. 146, p. 367
 - x-ray excited optical luminescence **4**, ch. 37E, p. 441
- chemical sensors **21**, ch. 143, p. 179
- chemical understanding and classification **11**, ch. 75, p. 197
- chirality sensing **35**, ch. 226, p. 273
- chlorides, thermodynamic properties of **42**, ch. 253, p. 165
- cluster compounds **40**, ch. 245, p. 109
- produced from solids and solutions **45**, ch. 263, p. 1
- cluster halides
- structure of **45**, ch. 264, p. 111
 - synthesis of **45**, ch. 264, p. 111
- coherent emission **22**, ch. 151, p. 507
- cohesion, theory of **17**, ch. 112, p. 149
- complexes (also *see* lanthanide chelates) **3**, ch. 25, p. 209
- antenna effect **23**, ch. 154, p. 69
 - arene-bridged **45**, ch. 266, p. 261
 - beta-diketonates **35**, ch. 225, p. 107
 - biphenyl **45**, ch. 266, p. 261
 - borohydrides in catalysis **44**, ch. 259, p. 1
 - encapsulation **23**, ch. 154, p. 69
 - group 3 stilbene **45**, ch. 266, p. 261
 - half-sandwich tetrapyrrole **32**, ch. 210, p. 611
 - inorganic **8**, ch. 56, p. 203; **9**, ch. 59, p. 91
 - low-valent state **40**, ch. 246, p. 241
 - macrocycles **15**, ch. 104, p. 443
 - molecular recognition in **35**, ch. 226, p. 273
 - organometallic π type **25**, ch. 168, p. 265
 - polyoxometalates **38**, ch. 240, p. 337
 - sensing in **35**, ch. 226, p. 273
 - with synthetic ionophores **9**, ch. 60, p. 321
- cooperativity, in complex formation **47**, ch. 272, p. 209
- coordination chemistry **47**, ch. 272, p. 209
- coordination in organic solvents **21**, ch. 145, p. 305
- coordination polymers **34**, ch. 221, p. 359; **47**, ch. 271, p. 147
- core-shell nanoparticles **41**, ch. 251, p. 275; **47**, ch. 273, p. 273
- corrosion
- prevention and control **21**, ch. 140, p. 29
 - protection **21**, ch. 141, p. 93
- cosmochemistry **11**, ch. 79, p. 485
- crystal chemistry
- of aluminates **39**, ch. 242, p. 113
 - of elements at ultra high pressure **43**, ch. 257, p. 275
 - of gallates **39**, ch. 242, p. 113
 - of higher borides **38**, ch. 238, p. 105
 - of hybrid materials of lanthanides **47**, ch. 271, p. 147
 - of hybrid materials with uranyl cation **48**, ch. 275, p. 163
 - of intermetallic compounds **2**, ch. 13, p. 1
 - of quaternary systems with chalcogenides **41**, ch. 250, p. 157; **48**, ch. 275, p. 109
 - of R_5T_4 intermetallic compound **44**, ch. 262, p. 283
 - of ternary germanides **27**, ch. 174, p. 225
 - of ternary systems with chalcogenides **13**, ch. 89, p. 191; **41**, ch. 250, p. 157
 - of ternary systems with metallic elements **13**, ch. 88, p. 1
 - of ternary transition metal borides **6**, ch. 48, p. 113
 - of ternary transition metal plumbides **38**, ch. 237, p. 55
 - of ternary transition metal silicides **6**, ch. 48, p. 113
 - of $ThMn_{12}$ -type compounds **22**, ch. 149, p. 143
- crystal field **2**, ch. 17, p. 295
- in non-metallic compounds **21**, ch. 144, p. 263

- parametrization, rationalization of **23**,
ch. 155, p. 121
- crystal structures, *see* crystal chemistry
- cuprates
 - 4f state splittings **30**, ch. 194, p. 491
 - crystal chemistry **30**, ch. 188, p. 31
 - electron paramagnetic resonance (EPR)
30, ch. 191, p. 375
 - electronic theory **30**, ch. 193, p. 453
 - flux pinning **31**, ch. 196, p. 187
 - Hall effect **31**, ch. 197, p. 251
 - heat capacity **31**, ch. 200, p. 351
 - infrared properties **31**, ch. 202, p. 437
 - magnetoresistance **31**, ch. 197, p. 251
 - neutron scattering
 - – magnetic ordering **31**, ch. 199, p. 315
 - – spin fluctuations **31**, ch. 198, p. 281
 - overview **30**, ch. 187, p. 1
 - oxygen nonstoichiometry and lattice effect
31, ch. 195, p. 1
 - phase equilibria **30**, ch. 190, p. 229
 - – of R_5T_4 intermetallic compounds **44**,
ch. 262, p. 283
 - phase transitions, structural distortions and
phase separation **31**, ch. 195, p. 1
 - – in R_5T_4 intermetallic compounds **44**,
ch. 262, p. 283
 - photoemission, angle-resolved studies **31**,
ch. 201, p. 391
 - physical properties **30**, ch. 193, p. 453
 - – of R_5T_4 intermetallic compounds **44**,
ch. 262, p. 283
 - positron annihilation **30**, ch. 192, p. 417
 - Raman scattering **31**, ch. 203, p. 509
 - scanning tunneling microscopy **31**,
ch. 204, p. 563
 - single crystals, growth of **30**, ch. 189, p. 67
 - superconductivity **30**; **31**
 - thermochemical properties **30**, ch. 190, p. 229
 - tunneling spectra **31**, ch. 204, p. 563

D

- dedications
 - F. H. Spedding **11**, p. 1
 - Friedrich Hund **14**, p. ix
 - LeRoy Eyring **36**, p. xi
 - William T. Carnall **37**, p. xiii
- diffraction techniques
 - at high pressure **42**, ch. 242, p. 4
 - for molten salts structure determination
- diketonates, *see* beta-diketonates
- diffusion in metals **1**, ch. 12, p. 847

- divalent samarium in organic
chemistry **6**, ch. 50, p. 525; **36**,
ch. 230, p. 393
- divalent ytterbium in organic chemistry **6**,
ch. 50, p. 525
- DNA, cutting of **34**, ch. 222, p. 405
- drug delivery **47**, ch. 273, p. 273
- dye-sensitized solar cells, lanthanides in **44**,
ch. 261, p. 169
- dynamical screening of core holes in
intermetallic compounds **10**, ch. 63, p. 75

E

- elastic and mechanical properties of
metals **1**, ch. 8, p. 591
- electron paramagnetic resonance (EPR) **2**,
ch. 18, p. 387; **24**, ch. 162, p. 221
- in cuprate superconductors **30**, ch. 191,
p. 375
- electronic excitation in atomic species **28**,
ch. 176, p. 1
- electronic properties of compounds at high
pressure **42**, ch. 252, p. 1
- electronic structure
 - of actinide atomic ions in gas phase **45**,
ch. 263, p. 1
 - calculations for molecules **22**, ch. 152,
p. 607
 - of chalcogenides **39**, ch. 241, p. 1
 - of metals **1**, ch. 3, p. 233; **17**,
ch. 110, p. 1; **39**, ch. 241, p. 1
 - of oxides **39**, ch. 241, p. 1
 - of rare-earth atomic ions in gas phase **45**,
ch. 263, p. 1
 - of pnictides **39**, ch. 241, p. 1
- electronic theory of cuprates **30**, ch. 193,
p. 453
- electron-phonon interaction in intermetallic
compounds **14**, ch. 96, p. 225
- electron-spin resonance, *see* electron
paramagnetic resonance
- emission spectra (also *see* fluorescence and
luminescence)
 - in solution **3**, ch. 24, 172
 - X-ray excited **10**, ch. 71, p. 453
- energetics
 - of actinide ions in gas phase **45**,
ch. 263, p. 1
 - of rare-earth ions in gas phase **45**,
ch. 263, p. 1
- energy transfer, in NIR-emitting complexes
47, ch. 269, p. 1

- enthalpy of atomization
- of fluorides **42**, ch. 253, p. 429
 - of monochlorides **42**, ch. 253, p. 412
 - of RX^+ ions **42**, ch. 253, p. 436
- enthalpy of formation
- calculation with Born-Haber cycle **42**, ch. 253, p. 324
 - of crystalline dichlorides **42**, ch. 253, p. 318
 - of crystalline trichlorides **42**, ch. 253, p. 271
 - of trichlorides, from mass spectra **42**, ch. 253, p. 306
 - of trichlorides, from saturated vapor data **42**, ch. 253, p. 306
- enthalpy-entropy correlation, in complex formation **47**, ch. 272, p. 209
- enthalpy of phase transition
- of crystalline trichlorides **42**, ch. 253, p. 256
- enthalpy of reaction involving RF , RF_2 , and RCl **42**, ch. 253, p. 403
- enthalpy of sublimation
- of dichlorides **42**, ch. 253, p. 354
 - of elements **43**, ch. 258, p. 321
 - of trichlorides **42**, ch. 253, p. 274
- enthalpy, standard of the elements **43**, ch. 258, p. 321
- entropy, standard, of the elements **43**, ch. 258, p. 321
- equilibrium constant
- calculation for trichlorides **42**, ch. 253, p. 290
 - calculation for RF , RF_2 , and RCl **42**, ch. 253, p. 403
- europium chalcogenides **2**, ch. 19, p. 507; **47**, ch. 270, p. 101
- europium semiconductors **47**, ch. 270, p. 101
- exchange coupling in transition metal intermetallics **24**, ch. 163, p. 339
- excited state phenomena in vitreous materials **9**, ch. 58, p. 1
- extraction, of rare earths and actinides **43**, ch. 256, p. 213
- Eyring, L.
- dedication **36**, p. xi
 - contributions of, higher oxides **38**, ch. 236, p. 1
- ## F
- f-electron hybridization **39**, ch. 241, p. 1
- in intermetallic compounds **10**, ch. 63, p. 75
- f-element speciation in strongly acidic media (superacids) **18**, ch. 126, p. 507
- f-f transitions, spectral intensities **25**, ch. 167, p. 101
- f-states: dual, localized, band-like character **39**, ch. 241, p. 1
- fast-atom bombardment mass spectrometry **45**, ch. 263, p. 1
- Fermi surfaces
- of intermetallic compounds **20**, ch. 135, p. 1
 - of metals **17**, ch. 110, p. 1
- ferrocene-based ligands **45**, ch. 266, p. 261
- fluorescence spectra of ions in solution **3**, ch. 24, p. 171
- fluorescence, anti-Stokes **45**, ch. 265, p. 179
- fluoride glasses **15**, ch. 101, p. 287; **45**, ch. 265, p. 179
- fluorides
- properties **5**, ch. 45, p. 387
 - thermodynamic properties **42**, ch. 253, p. 165
- flux pinning in cuprates **31**, ch. 196, p. 187
- fullerenes **41**, ch. 249, p. 95
- ## G
- gallates **39**, ch. 242, p. 113
- garnets **3**, ch. 29, p. 525
- gas-phase ion chemistry **45**, ch. 263, p. 1
- geochemistry **3**, ch. 21, p. 1; **11**, ch. 79, p. 485; **23**, ch. 158, p. 497
- of rare-earth-rich muds **46**, ch. 268, p. 79
- germanium, ternary systems **27**, ch. 173, p. 1
- glow-discharge mass spectrometry **45**, ch. 263, p. 1
- giant magnetocaloric effect, see magnetocaloric effect
- guided ion beam mass spectrometry **45**, ch. 263, p. 1
- ## H
- halides **4**, ch. 32, p. 89; **18**, ch. 124, p. 365
- metal-rich **15**, ch. 100, p. 191
 - Molten salts **44**, ch. 260, p. 87
 - simple and complex **28**, ch. 177, p. 53
 - thermodynamic properties **18**, ch. 122, p. 239; **33**, ch. 213, p. 147
 - vapors and vapor complexes **23**, ch. 157, p. 435
- Hall effect in cuprates **31**, ch. 197, p. 251

- heat capacity
- of cuprates **31**, ch. 200, p. 351
 - of metals **1**, ch. 5, p. 379; **43**, ch. 258, p. 321
- heavy fermions **14**, ch. 97, p. 343; **16**, ch. 105, p. 1; **19**, ch. 132, p. 177
- phenomenological approach **17**, ch. 111, p. 87
 - photoelectron spectroscopy **26**, ch. 172, p. 265
- helicates **40**, ch. 247, p. 301; **47**, ch. 272, p. 209
- high pressure studies **1**, ch. 9, p. 707
- anomalous Ce, Yb and U compounds **19**, ch. 133, p. 383
 - diffraction techniques **42**, ch. 252, p. 4
 - electronic properties **42**, ch. 252, p. 82
 - heat capacity **42**, ch. 252, p. 45
 - mass spectra **42**, ch. 252, p. 18
 - magnetic properties **42**, ch. 252, p. 44
 - optical studies of non-metallic compounds **33**, ch. 217, p. 515
 - physical properties **42**, ch. 252, p. 4
 - structural aspects **17**, ch. 113, p. 245; **42**, ch. 252, p. 4
 - thermal expansion **42**, ch. 252, p. 33
- high temperature superconductors **30**; **31**
- history
- of the discovery and separation of rare earths **11**, ch. 73, p. 33
 - of the positioning of rare earths in the periodic table **41**, ch. 248, p. 1
- Hund, F. **14**, dedication, p. ix
- hybrid materials
- of lanthanides **47**, ch. 271, p. 147
 - with uranyl cation **48**, ch. 276, p. 163
- hydration **15**, ch. 103, p. 393; **18**, ch. 127, p. 529; **45**, ch. 263, p. 1
- hydrides **3**, ch. 26, p. 299; **18**, ch. 123, p. 293
- borohydrides **44**, ch. 259, p. 1
 - switchable films **36**, ch. 228, p. 83
- hydrogen absorption in intermetallic compounds **6**, ch. 47, p. 1
- hydrogen in metals, including RH_{2+x} phases **20**, ch. 137, p. 207
- hydrolysis **15**, ch. 103, p. 393; **18**, ch. 127, p. 529; **40**, ch. 245, p. 109; **45**, ch. 263, p. 1; **47**, ch. 272, p. 209
- hyperfine interactions **11**, ch. 77, p. 323
- I**
- inelastic electron scattering **10**, ch. 72, p. 547
- information storage
- high fidelity **46**, ch. 267, p. 1
- infrared properties
- of cuprates **31**, ch. 202, p. 437
 - of molten salts **44**, ch. 260, p. 87
- inorganic complex compounds **8**, ch. 56 p. 203; **9**, ch. 59, p. 91
- intermetallic compounds
- amorphous magnetic alloys **2**, ch. 16, p. 259
 - binary and pseudo-binary R_5T_4 compounds **44**, ch. 262, p. 283
 - chalcogenides **2**, ch. 19, p. 507
 - crystal chemistry **2**, ch. 13, p. 1
 - crystal fields in **2**, ch. 17, p. 295
 - dynamical screening of core holes **10**, ch. 63, p. 75
 - electron-phonon interaction **14**, ch. 96, p. 225
 - exchange coupling **24**, ch. 163, p. 339
 - f-electron hybridization **10**, ch. 63, p. 75
 - Fermi surfaces **20**, ch. 135, p. 1
 - growth of **12**, ch. 80, p. 1
 - hydrogen absorption **6**, ch. 47, p. 1
 - itinerant electron metamagnetism in cobalt compounds **26**, ch. 171, p. 177
 - light scattering **14**, ch. 95, p. 163
 - magnetic properties **2**, ch. 14, p. 55; **12**, ch. 83, p. 133; **20**, ch. 138, p. 293
 - magnetocaloric effect in R_5T_4 compounds **44**, ch. 262, p. 283
 - magnetostriction - in RFe_2 compounds **2**, ch. 15, p. 231
 - in R_5T_4 compounds **44**, ch. 262, p. 283
 - Mössbauer effect in **17**, ch. 116, p. 539
 - nuclear magnetic resonance in **2**, ch. 18, p. 387; **14**, ch. 94, p. 63
 - scandium alloy systems **27**, ch. 175, p. 339
 - ternary RT_2X_2 type compounds **12**, ch. 83, p. 133
 - ternary equiatomic YbTX **32**, ch. 207, 453
 - transport properties **5**, ch. 42, p. 117; **17**, ch. 115, p. 409
 - valence changes in **2**, ch. 20, p. 575
 - intermediate valence **19**, ch. 132, p. 177
- ion cyclotron resonance
- mass spectrometry **45**, ch. 263, p. 1
- ionic liquids (also see molten salts), in An-Ln extraction and separation **43**, ch. 256, p. 213
- itinerant electron metamagnetism in cobalt intermetallics **26**, ch. 171, p. 177

J

Judd-Ofelt theory, NIR-emitting complexes
47, ch. 269, p. 1

K

kinetics of complexation in aqueous solutions
15, ch. 102, p. 347
 Kondo effect **1**, ch. 11, p. 797

L

lanthanide-induced shifts **4**, ch. 38, p. 483;
23, ch. 153, p. 1; **33**, ch. 215, p. 353
 lanthanide chelates (also see complexes)
 – for sensitizing NIR luminescence **37**,
 ch. 234, p. 171; **47**, ch. 270, p. 101
 – in biomedical analyses **37**, ch. 235, p. 217
 lanthanidomesogens **43**, ch. 254, p. 1
 laser-ablation mass spectrometry **45**, ch. 263,
 p. 1
 laser cooling cycle **45**, ch. 265, p. 179
 laser spectroscopy **12**, ch. 87, p. 433
 lasers **4**, ch. 35, p. 275
 leaching
 – of rare-earth-rich muds **46**, ch. 268, p. 79
 light-emitting diodes, NIR **47**, ch. 269, p. 1
 light scattering in intermetallic
 compounds **14**, ch. 95, p. 163
 linkers, in hybrid materials **47**, ch. 271,
 p. 147; **48**, ch. 276, p. 163
 liquid crystalline complexes **43**, ch. 254, p. 1
 liquid salts **44**, ch. 260, p. 87
 liquid metals and alloys **12**, ch. 85, p. 357
 LIS, *see* lanthanide-induced shifts
 lithology
 – of rare-earth-rich muds **46**, ch. 268, p. 79
 luminescence
 – antenna effect **23**, ch. 154, p. 69
 – in biomedical analyses **37**, ch. 234,
 p. 171; **40**, ch. 247, p. 301
 – of europium chalcogenides **47**, ch. 270,
 p. 101
 – NIR-emitting complexes **47**, ch. 269, p. 1
 – in NIR molecular probes and devices **37**,
 ch. 235, p. 217
 – NIR-triggered upconversion **47**, ch. 273,
 p. 273
 – persistent **48**, ch. 274, p. 1
 – polyoxometalates **39**, ch. 243, p. 297
 – sensitization of NIR luminescence **47**,
 ch. 269, p. 1
 – studies of ions **18**, ch. 120, p. 159

– spectra of ions in solution **3**, ch. 24,
 p. 171
 – thermometry **45**, ch. 265, p. 179
 luminescent solar concentrators, lanthanides
 in **44**, ch. 261, p. 169

M

μ SR studies of magnetic materials **32**,
 ch. 206, p. 55
 magnetic circular dichroism **40**, ch. 244, p. 1
 magnetic and transport properties of metals **1**,
 ch. 6, p. 411
 magnetic correlations in heavy-fermion
 systems **19**, ch. 131, p. 123
 magnetic properties (also see physical
 properties)
 – at high pressure **42**, ch. 252, p. 1
 – of borides **38**, ch. 238, p. 105
 – of europium chalcogenide nanoparticles **47**,
 ch. 270, p. 101
 – of intermetallic compounds **2**,
 ch. 14, p. 55; **20**, ch. 138, p. 293
 – of nickel borocarbides **38**, ch. 239, p. 175
 – of nonmetallic compounds **22**, ch. 150,
 p. 295
 – photo-induced, in europium chalcogenides
47, ch. 270, p. 101
 – of R_5T_4 pseudobinary intermetallic
 compounds **44**, ch. 262, p. 283
 – of ternary RT_2X_2 type intermetallic
 compounds **12**, ch. 83, p. 133
 – of $ThMn_{12}$ -type compounds **22**, ch. 149,
 p. 143
 magnetic structures **1**, ch. 7, p. 489
 magnetism **34**, ch. 219, p. 135
 – exotic phenomena **11**, ch. 76, p. 293
 – surface **24**, ch. 159, p. 1
 magnetocaloric effect, in R_5T_4
 compounds **44**, ch. 262, p. 283
 magneto-optical properties, of europium
 chalcogenides **47**, ch. 270, p. 101
 magnetoresistance
 – in cuprates **31**, ch. 197, p. 251
 – negative **42**, ch. 252, p. 145
 – pressure dependent **42**, ch. 252, p. 128
 magnetostriiction
 – in R_5T_4 intermetallic compounds **44**,
 ch. 262, p. 283
 – RFe_2 **2**, ch. 15, p. 231
 – transition metal thin films **32**, ch. 205, p. 1
 marine chemistry **23**, ch. 158, p. 497

- mass spectra
- of actinide ions in gas phase **45**, ch. 263, p. 1
 - calculation of enthalpy of formation from **42**, ch. 253, p. 299
 - of EuCl_3 and Eu_2Cl_6 **42**, ch. 253, p. 313
 - of rare-earth ions in gas phase **45**, ch. 263, p. 1
- mechanical alloying **24**, ch. 160, p. 47
- mechanically induced chemical reactions **24**, ch. 160, p. 47
- metal cluster complexes **45**, ch. 264, p. 111
- metal-hydrogen batteries **21**, ch. 142, p. 133
- metallofullerenes **41**, ch. 249, p. 95
- metallo-supramolecular chemistry **47**, ch. 272, p. 209
- mineral resource
- rare earths in deep-sea mud **46**, ch. 268, p. 79
- mineralogy **3**, ch. 21, p. 1
- minerals, crystal structures **16**, ch. 108, p. 249
- mining
- of rare-earth-rich muds **46**, ch. 268, p. 79
- mixed valence systems
- bremsstrahlung isochromat spectroscopy **10**, ch. 70, p. 425
 - calculation of $4f$ excitation energies **10**, ch. 68, p. 321
 - many-body formulation of spectra **10**, ch. 64, p. 103
- molecular recognition **35**, ch. 226, p. 273
- molten salts
- electrolysis **43**, ch. 255, p. 159
- structure of halides **44**, ch. 260, p. 87
- molybdates (VI) **3**, ch. 30, p. 609
- mud
- rare-earth rich **46**, ch. 268, p. 79
- multilayers
- negative magnetoresistance in Fe/Tb **42**, ch. 252, p. 145
 - transition metals **42**, ch. 148, p. 81
- Mössbauer effect **2**, ch. 18, p. 387
- of intermetallic compounds **17**, ch. 116, p. 539
 - ceria **41**, ch. 249, p. 95
 - europium chalcogenides **47**, ch. 270, p. 101
 - halides **41**, ch. 249, p. 95
 - hydroxides **41**, ch. 249, p. 95
 - metallofullerenes **41**, ch. 249, p. 95
 - oxides **41**, ch. 249, p. 95
 - oxysalts **41**, ch. 249, p. 95
 - properties **22**, ch. 147, p. 1; **41**, ch. 251, p. 275
 - photochemical ring formation **39**, ch. 243, 297
 - synthesis **22**, ch. 147, p. 1; **41**, ch. 251, p. 275
 - spectroscopic properties **37**, ch. 233, p. 99
 - sulfates **41**, ch. 249, p. 95
 - transition metal multilayers **22**, ch. 148, p. 81
- negative magnetoresistance in multilayer Fe/Tb **42**, ch. 252, p. 145
- neutron scattering
- elastic **17**, ch. 117, p. 635
 - inelastic **1**, ch. 7, p. 489
 - intermultiple transitions **14**, ch. 93, p. 1
 - inelastic of anomalous lanthanides **19**, ch. 130, p. 1
 - in heavy-fermion systems **19**, ch. 131, p. 123
 - of magnetic ordering in cuprates **31**, ch. 199, p. 315
 - of molten salts **44**, ch. 260, p. 87
 - of spin fluctuations in cuprates **31**, ch. 198, p. 281
- near-infrared luminescence
- complexes with halogenated chromophores **47**, ch. 269, p. 1
 - in molecular probes and devices **37**, ch. 235, p. 217
 - organic light emitting diodes **47**, ch. 269, p. 1
 - upconversion **47**, ch. 273, p. 273
- nitride materials, ternary and higher order **25**, ch. 166, p. 51
- NMR **2**, ch. 18, p. 387
- in intermetallic compounds **14**, ch. 94, p. 63
 - lanthanide induced shifts for extracting solution structures **33**, ch. 215, p. 353
 - of complexes **23**, ch. 153, p. 1
 - of paramagnetic complexes **4**, ch. 38, p. 483
- N**
- nanostructures and nanomaterials
- Al- and Mg-based systems **24**, ch. 161, p. 83
 - bioimaging and therapy **47**, ch. 273, p. 273

- solution structure by paramagnetic NMR analysis **33**, ch. 215, p. 353
- nonradiative processes
- in crystals **4**, ch. 36, p. 317
- in NIR-emitting complexes **47**, ch. 269, p. 1
- nuclear magnetic resonance, *see* NMR

O

- optical glasses, recycling of **43**, ch. 255, p. 159
- optical refrigeration **45**, ch. 265, p. 179
- organic synthesis **8**, ch. 57, p. 335
- organometallic compounds **7**, ch. 53, p. 446
 - arene-bridged compounds **45**, ch. 266, p. 261
 - divalent samarium, in **6**, ch. 50, p. 525; **36**, ch. 230, p. 393
 - divalent ytterbium, in **6**, ch. 50, p. 525
 - low valent **40**, ch. 246, p. 241
 - tetravalent cerium, in **36**, ch. 229, p. 281
- oxidation – reduction properties **18**, ch. 122, p. 239
- oxides
 - aluminates **39**, ch. 242, p. 113
 - binary **3**, ch. 27, p. 337; **18**, ch. 125, p. 413
 - gallates **39**, ch. 242, p. 113
 - higher **38**, ch. 236, p. 1
 - mixed **3**, ch. 28, p. 401
 - sesqui, defects in **5**, ch. 44, p. 321
 - sesqui, phase transformation in **5**, ch. 44, p. 321
 - ternary systems, R_2O_3 - M_2O_3 - $M'O$ **13**, ch. 90, p. 283
- oxo-selenates **35**, ch. 224, p. 45
- oxygen nonstoichiometry and lattice effect in $YBa_2Cu_3O_x$ **31**, ch. 195, p. 1

P

- permanent magnets **12**, ch. 82, p. 71; **32**, ch. 208, p. 515
 - recycling of **43**, ch. 255, p. 159
- periodic table
 - influence of rare earths on **11**, ch. 75, p. 197
 - position of rare earths in **41**, ch. 248, p. 1
- perovskites **3**, ch. 29, p. 525
 - aluminates **39**, ch. 242, p. 113
 - gallates **39**, ch. 242, p. 113
 - manganese **33**, ch. 214, p. 249
- persistent phosphors **48**, ch. 274, p. 1

- phase equilibria
 - in binary R_5T_4 intermetallic compounds **44**, ch. 262, p. 283
 - in cuprates **30**, ch. 190, p. 229
 - in quaternary R_2X_3 - PbX - ZX_2 chalcogenides **48**, ch. 275, p. 109
 - in ternary systems with boron **6**, ch. 49, p. 335; **38**, ch. 238, p. 105
 - in ternary systems with chalcogenides **13**, ch. 89, p. 191
 - in ternary systems with metallic elements **13**, ch. 88, p. 1
 - in ternary systems with lead **38**, ch. 237, p. 55
 - in ternary systems with silicon **7**, ch. 51, p. 1
 - in rare earth binary alloys **8**, ch. 54, p. 1
- phase transitions
 - structural distortions and phase separation in $YBa_2Cu_3O_x$ **31**, ch. 195, p. 1
 - in the elements at ultra high pressure **43**, ch. 257, p. 275
 - in R_5T_4 intermetallic compounds **44**, ch. 262, p. 283
- phosphides **23**, ch. 156, p. 285
- phosphors
 - persistent **48**, ch. 274, p. 1
 - recycling of **43**, ch. 255, p. 159
- photochemical, nano-ring formations in polyoxometalates **39**, ch. 243, p. 297
- photodynamic treatment of cancer **47**, ch. 273, p. 273
- photoemission
 - angle-resolved studies of untwinned $YBa_2Cu_3O_x$ **31**, ch. 201, p. 391
 - in chalcogenides **10**, ch. 67, p. 301
 - inverse spectra, local density supercell theory **10**, ch. 65, p. 165
 - of Ce and its compounds **10**, ch. 66, p. 231
 - spectra, local density supercell theory **10**, ch. 65, p. 165
 - theory of **39**, ch. 241, p. 1
- photothermal treatment of cancer **47**, ch. 273, p. 273
- photovoltaics, lanthanides in **44**, ch. 261, p. 169
- physical metallurgy **11**, ch. 78, p. 409
- physical properties (also *see* magnetic properties)
 - at high pressure **42**, ch. 252, p. 1
 - of cuprates **30**, ch. 193, p. 453
 - of metals **1**, ch. 2, p. 173

- of metals at ultra high pressure **43**, ch. 257, p. 275
- of $R_2Fe_{14}B$ -based alloys **12**, ch. 82, p. 71
- of R_5T_4 intermetallic compounds **44**, ch. 262, p. 283
- pnictides **4**, ch. 33, p. 153
- magnetic measurements on mono- **17**, ch. 114, p. 301
- polishing powders, recycling of **43**, ch. 255, p. 159
- polymerization, stereospecific catalysis
 - with borohydride complexes **44**, ch. 259, p. 1
 - with coordination complexes **9**, ch. 61, p. 395
- polyoxometalates **38**, ch. 240, p. 337
- luminescence of **39**, ch. 243, p. 297
- positron annihilation in high-temperature superconductors **30**, ch. 192, p. 417
- preparation and purification of metals **1**, ch. 2, p. 173
- pressure-induced
 - cross-over **42**, ch. 252, p. 83
 - electronic transitions **42**, ch. 252, p. 82
 - magnetic order **42**, ch. 252, p. 129
 - structural transitions **43**, ch. 257, p. 275; **44**, ch. 262, p. 283
 - superconductivity **42**, ch. 252, p. 96
- pyrochlores **16**, ch. 107, p. 225
- pyrometallurgy, in rare-earth recycling **43**, ch. 255, p. 159

Q

- quantum computing **46**, ch. 267, p. 1
- quantum information processing (QIP) **46**, ch. 267, p. 1
- quantum memory **46**, ch. 267, p. 1
- quasicrystalline, Al- and Mg-based systems **24**, ch. 161, p. 83
- qubit **46**, ch. 267, p. 1

R

- radiative process, in NIR-emitting complexes **47**, ch. 269, p. 1
- Raman scattering of cuprates **31**, ch. 203, p. 509
- rare-earth doped crystals
 - spectroscopy **46**, ch. 267, p. 1
- recycling of rare earths **43**, ch. 255, p. 159
- redox reactions
 - arene-bridged complexes **45**, ch. 266, p. 261
 - in aqueous solutions **15**, ch. 102, p. 347
 - Ce(IV)/Ce(III) **36**, ch. 229, p. 347
 - Sm(III)/Sm(II) **36**, ch. 230, p. 393

- relativistic effects and electronic structure **18**, ch. 119, p. 29
- ring opening polymerization (ROP) **44**, ch. 259, p. 1
- RNA, cutting of **34**, ch. 222, p. 405, **36**, ch. 229, p. 392

S

- samarium(II) reductants **36**, ch. 230, p. 393
- scandium
 - alloy systems and intermetallics **27**, ch. 175, p. 339
 - arene complexes **45**, ch. 266, 261
- scanning tunneling microscopy of cuprates **31**, ch. 204, p. 563
- Schiff's base complexes **43**, ch. 254, p. 1
- selenates **35**, ch. 224, p. 45
- selenides **4**, ch. 31, p. 1
- selenites **35**, ch. 224, p. 45
- self-assembly of helicates **40**, ch. 247, p. 301
- separation chemistry **3**, ch. 22, p. 81; **18**, ch. 121, p. 197; **21**, ch. 139, p. 1; **43**, ch. 256, p. 213; **48**, ch. 277, p. 287
- analytical, basic chemistry and methods **28**, ch. 180, p. 311
- silicon solar cells, lanthanides in **44**, ch. 261, p. 169
- separation equipment **48**, ch. 277, p. 287
- shift reagents **4**, ch. 38, p. 483; **23**, ch. 153, p. 1; **33**, ch. 215, p. 353; **35**, ch. 225, p. 107
- single crystals
 - growth from molten metal fluxes **12**, ch. 81, p. 53
 - growth of cuprates **30**, ch. 189, p. 67
 - growth of metals and intermetallic compounds **12**, ch. 80, p. 1
- skutterudites, filled **33**, ch. 211, p. 1
- single-source precursor **47**, ch. 270, p. 101
- single energy conversion, lanthanides in **44**, ch. 261, p. 169
- solid electrolytes **28**, ch. 178, p. 131; **35**, ch. 223, p. 1
- solid oxide fuel cells (SOFC) **35**, ch. 223, p. 1
- solution chemistry **15**, ch. 103, p. 393; **18**, ch. 127, p. 529; **18**, ch. 128, p. 559; **21**, ch. 145, 305
- solvation
 - in organic solvents **21**, ch. 145, p. 305
 - thermodynamic model **47**, ch. 272, p. 209

- spectroscopic properties
- in solution **3**, ch. 24, p. 172
 - in transparent crystals **5**, ch. 46, p. 461
 - nanomaterials **37**, ch. 233, p. 99
- spectroscopy
- absorption and fluorescence of R ions **3**, ch. 22, p. 172
 - appearance potential **16**, ch. 109, p. 519
 - bremsstrahlung isochromat **10**, ch. 70, p. 425
 - circularly polarized luminescence **34**, ch. 220, p. 289
 - high-energy **10**, ch. 62, p. 1
 - magnetic circular dichroism **40**, ch. 244, p. 1
 - magnetic resonance **11**, ch. 77, p. 323
 - mass
 - spark source matrices **4**, ch. 37C, p. 377
 - spark source trace element analysis **4**, ch. 37B, p. 359
 - stable-isotope dilution analysis **4**, ch. 37G, p. 471
 - with inductively coupled plasmas analysis **13**, ch. 91, p. 385
 - of rare-earth doped crystals **46**, ch. 267, p. 1
 - optical **3**, ch. 24, p. 172; **5**, ch. 46, p. 461; **11**, ch. 74, p. 81; **33**, ch. 216, p. 465; **37**, ch. 233, p. 99; ch. 234, p. 171; **37**, ch. 235, p. 217; **39**, ch. 243, p. 297
 - photoelectron in heavy fermion systems **26**, ch. 172, p. 265
 - time-resolved emission in solution chemistry **33**, ch. 216, p. 465
- Spedding, F. H., **11**, prologue, p. 1
- spin glasses **12**, ch. 84, p. 213
- stannides, transition metal ternary systems **24**, ch. 164, p. 399
- steels **25**, ch. 165, p. 1
- Stokes shift **45**, ch. 265, p. 179
- stresses, static and dynamic **26**, ch. 170, p. 87
- structural properties
- hybrid materials of lanthanides **47**, ch. 271, p. 147
- hybrid materials with uranyl cation **48**, ch. 276, p. 163
- lanthanides at high pressure **43**, ch. 257, p. 275
- sublimation enthalpy
- of metals **43**, ch. 258, p. 321
 - of trichlorides **42**, ch. 253, p. 274
 - of trifluorides **42**, ch. 253, p. 235
- sulfides **4**, ch. 31, p. 1
- poly **32**, ch. 209, 567
- superconductivity **1**, ch. 10, p. 749; **34**, ch. 219, p. 135
- at high pressure **42**, ch. 252, p. 96
 - crystal chemistry of cuprates **30**, ch. 188, p. 31
 - in metals **17**, ch. 110, p. 1
 - high-temperature layered cuprates:
 - overview **30**, ch. 187, p. 1
 - nickel borocarbides **38**, ch. 239, p. 175
 - unconventional and magnetism **34**, ch. 219, p. 135
- supramolecular chemistry, of lanthanides **40**, ch. 247, p. 301; **47**, ch. 272, p. 209
- surfaces
- adsorption on **5**, ch. 43, p. 217
 - catalysis on **5**, ch. 43, p. 217
- switchable metal hydride films **36**, ch. 228, p. 83
- synthesis of cluster halides
- comproportionation **45**, ch. 264, p. 111
 - metallothermic reduction **45**, ch. 264, p. 111
- systematics, intra rare earth binary alloys **8**, ch. 54, p. 1
- ## T
- telecommunications, optical **47**, ch. 269, p. 1
- tellurides **4**, ch. 31, p. 1
- ternary equiatomic YbTX intermetallics **32**, ch. 207, p. 453
- tetravalent cerium compounds **36**, ch. 229, p. 281
- theoretical chemistry **3**, ch. 23, p. 111
- thermal conductivity of compounds **16**, ch. 106, p. 107
- thermal properties of compounds at high pressure **42**, ch. 252, p. 1
- thermodynamic functions
- of complexation processes **47**, ch. 272, p. 209
 - of dichlorides **42**, ch. 253, p. 198
 - of difluorides **42**, ch. 253, p. 207
 - of dimeric trichlorides **42**, ch. 253, p. 296
 - of metals **43**, ch. 258, p. 321
 - microscopic descriptors **47**, ch. 272, p. 209
 - of monochlorides **42**, ch. 253, p. 381
 - of monofluorides **42**, ch. 253, p. 381
 - of trichlorides **42**, ch. 253, p. 176
 - of trifluorides **42**, ch. 253, p. 196
- thermochemical properties **18**, ch. 122, p. 239
- of chlorides **42**, ch. 253, p. 165

- of cuprates **30**, ch. 190, p. 229
- of dimeric trichlorides **42**, ch. 253, p. 214
- of fluorides **42**, ch. 253, p. 165
- of gaseous species **12**, ch. 86, p. 409
- of metallic systems **19**, ch. 134, p. 479
- of metals **43**, ch. 258, p. 321
- of trichlorides **42**, ch. 253, p. 176
- of trifluorides **42**, ch. 253, p. 196
- thin films **5**, ch. 41, p. 1; **20**, ch. 136, p. 105
- switchable metal hydrides **36**, ch. 228, p. 83
- thorium, high purity **48**, ch. 277, p. 287
- time-of-flight mass spectrometry **45**, ch. 263, p. 1
- toxicity **4**, ch. 40, p. 553
- transition metal-iodides **34**, ch. 218, p. 1
- transport properties
 - at high pressure **42**, ch. 252, p. 68
 - of intermetallics **5**, ch. 42, p. 117; **17**, ch. 115, p. 409
- triflates **29**, ch. 186, p. 315
- tunneling spectra of cuprates **31**, ch. 204, p. 563

U

- upconverting nanoparticles **47**, ch. 273, p. 273
- ultra high pressure (also see high pressure studies)
 - elements at **43**, ch. 258, p. 321
 - structural properties at **43**, ch. 257, p. 275
- uranyl, hybrid materials **48**, ch. 277, p. 287

V

- valence fluctuations **2**, ch. 20, p. 575; **16**, ch. 105, p. 1; **39**, ch. 241, p. 1
- vapor pressure of halides **42**, ch. 253, p. 441

X

- x-ray absorption and emission spectra **10**, ch. 71, p. 453
- x-ray scattering **26**, ch. 169, p. 1

This page intentionally left blank

Chapter 274

Persistent Phosphors

Philippe F. Smet¹, Koen Van den Eeckhout, Olivier Q. De Clercq and Dirk Poelman

LumiLab, Department of Solid State Sciences, Ghent University, Ghent, Belgium

¹Corresponding author: e-mail: philippe.smet@ugent.be

Chapter Outline

1 Introduction	2	7.3 Silicates	35
2 History of Persistent Luminescence	3	7.4 Aluminates	36
2.1 The Early Days	3	7.5 Other Oxides	36
2.2 ZnS:Cu,Co	4	7.6 Nonoxide Hosts	36
2.3 SrAl ₂ O ₄ :Eu,(Dy)	5	7.7 Glasses	58
3 Terminology and Publication Analysis	7	8 TL and Afterglow Curves	58
3.1 Terminology	7	8.1 Thermoluminescence	58
3.2 Publication Analysis	8	8.2 Afterglow Curves	64
4 Experimental Methods	9	9 Applications	66
4.1 Introduction	9	9.1 Safety Signage	66
4.2 Synthesis	9	9.2 Potential Energy Storage Capacity	67
4.3 Optical Characterization	10	9.3 Mechanoluminescence	70
4.4 Structural Characterization	15	10 Persistent Luminescence for In Vivo Imaging	71
5 Measuring Afterglow Intensities	19	10.1 Requirements for <i>In Vivo</i> Imaging	72
5.1 Standards and Classifications	19	10.2 Lanthanide-Based Phosphors	75
5.2 Performance of Persistent Luminescent Emission	20	10.3 Cr ³⁺ -Based Phosphors	77
6 Observation by the Human Eye	22	10.4 Other Phosphors	79
6.1 Introduction	22	11 Outlook	80
6.2 CIE Model for Mesopic Luminance Measurements	25	11.1 Safety Signage	80
6.3 Accounting for Dark Adaptation: Visibility Index	27	11.2 Persistent Phosphors in Outdoor Applications	82
6.4 Conclusions	31	11.3 Solar and Energy Storage Applications	83
7 Persistent Phosphors: Materials	32	11.4 <i>In Vivo</i> Imaging	83
7.1 Introduction: Host and Dopants	32	11.5 Final Remarks	83
7.2 Literature Overview: Notes	35	References	84

1 INTRODUCTION

Persistent luminescence, the phenomenon whereby a luminescent materials keeps emitting light after the excitation has stopped, has intrigued people since centuries. Often, it has been associated with radioactive compounds and therefore was, and maybe sometimes still is, treated with some suspicion. Nevertheless, persistent luminescent materials have found numerous applications in safety signage and toys, especially since the discovery of a new class of very efficient compounds in the mid-1990s.

In *standard* impurity-doped (photo)luminescent materials, commonly called phosphors, absorption of light brings the luminescent impurity into an excited state, which has typically a lifetime of nanoseconds up to a few milliseconds, depending on the specific electronic transition and the host–dopant interactions. A persistent phosphor is a specific modification of such a photoluminescent material, where energy is stored in the so-called traps (Fig. 1). To release the trapped charge carriers, thermal energy is required, after which the delayed light emission at the luminescent impurity occurs. The thermal barrier, or depth, associated to the trap is such that for persistent phosphors room temperature (RT) is sufficient to release the charge carrier within an average

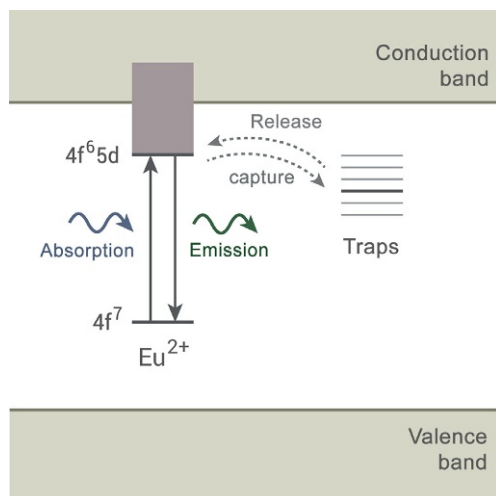


FIGURE 1 Schematic view of persistent luminescence in a Eu^{2+} -doped persistent phosphor. Absorption of a photon by an Eu^{2+} impurity transfers an electron from the $4f$ to the $5d$ orbital. Typically, a return to the ground state occurs within microseconds and results in the emission of a photon (i.e., common photoluminescence). Alternatively, the excited electron can be captured at a defect (a so-called trap). The associated energy levels are characterized by a certain trap depth (or a distribution of trap depths). For a certain range of trap depths, sufficient thermal energy is available at RT to lead to a release of the trapped charge carrier within seconds up to hours, after which recombination and delayed emission occur at the europium centre. Persistent phosphors are thus photoluminescent materials with a high density of traps, where trapping and detrapping are playing a dominant role.

time frame of seconds to hours. Thermoluminescence (TL)—measuring the light output as a function of increasing temperature—is often used as a diagnostic method for determining trap depths.

The report on the bright green persistent luminescence in strontium aluminate doped with europium and dysprosium ($\text{SrAl}_2\text{O}_4:\text{Eu,Dy}$) in 1994 (Matsuzawa et al., 1996), triggered a renewed interest in this class of compounds, yielding both new materials and new applications. Quite remarkably, most research has been based on a trial-and-error approach, trying small variations on existing phosphors. This stems from the fact that, despite their long history, there is still no strong theoretical basis for the description—let alone prediction—of the behavior of many persistent luminescent materials.

While there are a number of review papers compiling materials and properties of different classes of persistent phosphors, a complete overview of this particular field of luminescence research is still lacking. This chapter aims at filling this gap and tries to cover all aspects of persistent phosphors from history, synthesis, models, and analysis to applications. Special attention is given to a number of analytical techniques that are ideally suited for characterization and to some new applications—mechanoluminescence (ML) and medical imaging—that directly result from this emerging field of research.

This review is far from exhaustive in terms of a description of all existing persistent luminescent materials and their properties. However, it should suffice as a starting point for the reader, who is referred to the original literature for the very details.

2 HISTORY OF PERSISTENT LUMINESCENCE

2.1 The Early Days

According to Harvey, the first accounts of glow-in-the-dark paint date back more than 1000 years (Harvey, 1957). The persistent phosphor was presumably made from seashells or volcanic material, with little information available on the synthesis conditions or the composition. The first account in the Western world on persistent luminescence is the so-called Bologna Stone, described at the beginning of the seventeenth century (Zomer et al., 2011). This persistent phosphor was prepared by calcining a barite containing rock found at Monte Paderno near Bologna, Italy. A detailed historical account on the wide interest this discovery created in the seventeenth century, can be found in Zomer et al. (2011). At that time, the energy storage capability was compared to a sponge retaining water. The process behind the (calcined) Bologna Stone received strong attention in the scientific world in the seventeenth century. Remarkably, different emission colors could be obtained depending on the synthesis conditions. The first excitation experiments were performed in the eighteenth century to study the storage mechanism, showing that both blue and red light could induce the same (red) afterglow, which led to abandoning the “sponge” idea (Zomer et al., 2011).

Recently, Lastusaari et al. were successful in recreating and studying the persistent luminescence in the Bologna Stone, by starting from a similar (barite) stone found at Monte Paderno (Lastusaari et al., 2012). First, they convincingly showed that the persistent luminescence is due to doped BaS, not the original BaSO₄, showing the need for a reducing heating step to get the reddish persistent luminescence as described in the old literature. The afterglow spectrum peaks at 610 nm (with a FWHM of about 100 nm). Given the presence of Cu⁺ in the Bologna Stone and by elimination of other suspected impurities on spectroscopic grounds, BaS:Cu⁺ is presumably the basic composition of the reduced Bologna Stone. The hypothesis was raised that sulfur vacancies are responsible for the trapping. Although the afterglow intensity was not quantified in absolute numbers, afterglow could be observed for about 30 min, which is relatively long for persistent luminescence in this wavelength region. Note that this was achieved without further optimizing the naturally occurring starting material, e.g., by codoping. Nevertheless, barite is known to contain many naturally occurring impurities, so certain trace elements might have played already a beneficial role in the trapping. Note that also europium-doped BaS shows near-IR (NIR) persistent luminescence upon excitation with blue light (Smet et al., 2006). Unfortunately, the poor chemical stability of BaS is hampering applications of this particular phosphor system, which has limited the research into this historical phosphor host (Lastusaari et al., 2012).

2.2 ZnS:Cu,Co

ZnS doped with transition metals played an important role in the twentieth century, not only for its persistent luminescence but also for its efficient electroluminescent and cathodoluminescent emission. According to the *Phosphor Handbook*, ZnS:Cu can be produced by adding 10⁻² wt% Cu to ZnS, mixing with a flux (such as NaCl, KCl, or NH₄Cl), and subsequent heating to 1250 °C for 2 h in air. If, in addition to Cu, several ppm of Co are added to ZnS, the afterglow persistence can be nearly doubled, but its initial brightness is decreased (Yen et al., 2007).

In the first half of the twentieth century, ZnS:Cu was often used in combination with the radioactive decay of ²²⁶Ra, giving a luminous paint which did not require optical excitation. It was used in watch dials and clocks, where the reduction in emission intensity over the course of tens of years was not due to the decreasing activity of the radioactive source, but due to the radiation damage in the phosphor.

Clabau et al. elaborated on the role of Co²⁺, which was believed to concentrate and stabilize the trapping centers, presumed to be sulfur vacancies, sufficiently far away from the Cu⁺ recombination centers (Clabau et al., 2006). Without Co, the TL glow curve peaks below RT, while the addition of Co shifts the peak above RT (Hoogenstraaten and Klasens, 1953), due to

the larger average distance between the trap and the recombination center. As such, only a limited amount of Co^{2+} is needed as a codopant, relative to the Cu concentration. If trapping would occur by the cobalt codopant, then the overall trapping capacity would be very low.

Using TL excitation spectroscopy (Section 4.3.4), Bos et al. showed that the trap filling is strongly dependent on the excitation wavelength. Filling of traps with visible light is limited in efficiency, compared to excitation with photon energy above or close to the band gap (Bos et al., 2011).

Considering the relative ease by which ZnS can be made in nanometer-sized particles, it recently gained renewed interest in the framework of biological labeling, imaging, and photodynamic therapy (Ma and Chen, 2010, 2011; Ma et al., 2014).

2.3 $\text{SrAl}_2\text{O}_4:\text{Eu}(\text{Dy})$

2.3.1 $\text{SrAl}_2\text{O}_4:\text{Eu}$ —The 1970s

The luminescence properties of $\text{SrAl}_2\text{O}_4:\text{Eu}$ were described in 1968 by Pallila et al. in a paper on the luminescence of divalent europium in MAl_2O_4 hosts (Palilla et al., 1968). On $\text{SrAl}_2\text{O}_4:\text{Eu}$, they wrote “*The phosphors are further characterized by a rapid initial decay followed by a long persistence at a very low light level. Thus, the $\text{SrAl}_2\text{O}_4:\text{Eu}$ phosphor decays to 1/10 of initial brightness in 10 μs but has a low-level persistence which lasts many seconds.*”

The persistent luminescence of $\text{SrAl}_2\text{O}_4:\text{Eu}$ was studied in more detail by Abbruscato (1971). Using an excess amount of Al_2O_3 in the synthesis was beneficial for the afterglow intensity, compared to a stoichiometric reaction or when an excess of strontium was used. This is an interesting example of how synthesis conditions are used to steer the trapping capacity of a persistent phosphor, while keeping the (steady-state) luminescence properties unaffected. Based on the Hall effect measurements, which were only briefly described in Abbruscato (1971), it was concluded by Abbruscato that holes were the conducting species under UV excitation. Given that the photoconductivity and the afterglow intensity followed a similar decay profile (at least during the first seconds after stopping the excitation) led to the conclusion that the same charge type (i.e., holes) was involved in the trapping process. It was suggested that a hole was created in the valence band upon UV excitation, which is subsequently trapped in a lattice defect, supposed to be a Sr^{2+} vacancy. Note that it was not suggested that the hole originates from Eu^{2+} , nor that Eu^{2+} would be the hole trapping center (which was inferred from the absence of Eu^{3+} emission lines in fully “charged” $\text{SrAl}_2\text{O}_4:\text{Eu}$ at low temperature). The work of Abbruscato received little attention in the following two decades, presumably due to the relatively weak persistent luminescence of the material (compared to $\text{ZnS}:\text{Cu},\text{Co}$). In addition, the persistence was rather seen as a disadvantage considering the initially envisioned cathode ray applications.

2.3.2 $\text{SrAl}_2\text{O}_4:\text{Eu},\text{Dy}$ —The 1990s

In 1994, a patent was filed on the $\text{SrAl}_2\text{O}_4:\text{Eu},\text{Dy}$ phosphor by Murayam, Takeuchi, Aoki, and Matsuzawa from Nemoto Co, Tokyo, Japan (Murayam et al., 1994). The famous publication in the *Journal of the Electrochemical Society* followed in 1996, entitled “New long phosphorescent phosphor with high brightness, $\text{SrAl}_2\text{O}_4:\text{Eu}^{2+},\text{Dy}^{3+}$ ” (Matsuzawa et al., 1996). From Fig. 2, it is immediately clear that the addition of Dy^{3+} to $\text{SrAl}_2\text{O}_4:\text{Eu},\text{Dy}$ created a much brighter persistent phosphor, when compared to $\text{ZnS}:\text{Cu},\text{Co}$.

TL glow curves of $\text{SrAl}_2\text{O}_4:\text{Eu}$ revealed a rather broad trap distribution, with several clearly distinguishable glow peaks, which explains why for $\text{SrAl}_2\text{O}_4:\text{Eu}$ the slope of the afterglow decay is not very steep and the associated afterglow duration is rather long (Fig. 2). The addition of Nd^{3+} or Dy^{3+} leads to the formation of additional traps, which translates into a glow peak at 333 or 348 K, respectively (for a heating rate of 2 K/s). This results in a relatively longer persistent luminescence for Dy^{3+} codoping. Based on the Hoogenstraaten’s heating rate method (Furetta, 2003; Hoogenstraaten, 1958), an associated trap depth of 0.65 eV was found (Matsuzawa et al., 1996). In later years, several literature sources have been citing this trap depth value as “ideal.” Based on the earlier work by Abruscato (1971) and photocurrent measurements under local illumination near both electrodes, it was concluded that holes were the charge carriers involved in the trapping. Based on these conclusions, a mechanism involving a $\text{Eu}^{2+}-\text{Dy}^{3+}/\text{Eu}^{+}-\text{Dy}^{4+}$ redox couple was proposed. The model involving Eu^{+} was however rejected several years later in 2001, by Lastusaari et al. in the case of $\text{CaAl}_2\text{O}_4:\text{Eu},\text{Nd}$ (Hölsä et al., 2001). In 2005, Dorenbos proposed a $\text{Eu}^{2+}-\text{Dy}^{3+}/\text{Eu}^{3+}-\text{Dy}^{2+}$ redox couple, explicitly involving electrons as the relevant charge carriers

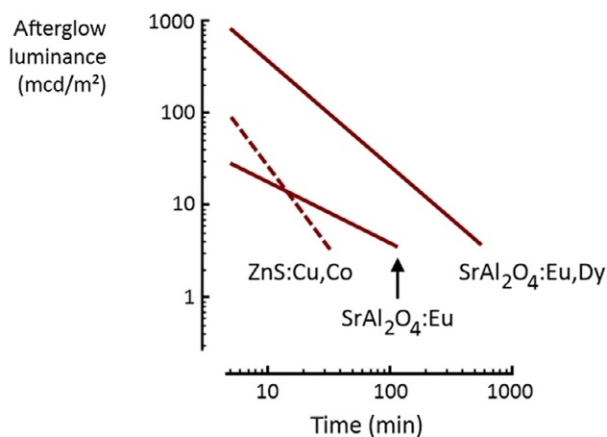


FIGURE 2 Comparison of afterglow characteristics measured after a 10 min exposure to 200 lux of D65 light for $\text{ZnS}:\text{Cu},\text{Co}$, $\text{SrAl}_2\text{O}_4:\text{Eu}^{2+}$, and $\text{SrAl}_2\text{O}_4:\text{Eu}^{2+},\text{Dy}^{3+}$. Adapted from Matsuzawa et al. (1996) by permission of The Electrochemical Society.

(Dorenbos, 2005). The trapping of the electron at the trivalent codopant is still contested (Section 4.4.2). Finally, also the high-performance $\text{CaAl}_2\text{O}_4:\text{Eu},\text{Nd}$ persistent phosphor, emitting at 440 nm, was described in the original paper by Matsuzawa et al. (1996).

3 TERMINOLOGY AND PUBLICATION ANALYSIS

3.1 Terminology

Several names and abbreviations are currently in use to denote the phenomenon of persistent luminescence and the corresponding luminescent materials. To gain some insight into the usage of certain names, the papers (in the *Web of Science Core Collection*) that are citing the $\text{SrAl}_2\text{O}_4:\text{Eu},\text{Dy}$ paper by Matsuzawa et al. (1996), or one of the two recent reviews by Van den Eeckhout et al. (2010, 2013b) were classified according to the most common terms used to describe the phenomenon. This yields a set of almost 1000 papers in the period 1997–2014 which are representative to the field, although not fully covering the total scientific output. Nevertheless, it is sufficient to study the prevalence and the evolution of the terminology.

There is clearly no unique term to designate the process (Fig. 3). On average, papers contain two of the following common strings in title, abstract, or keywords: *persistent*, *LLP*, *phosphorescence* (or *phosphorescent*), *afterglow*, and *long lasting*.

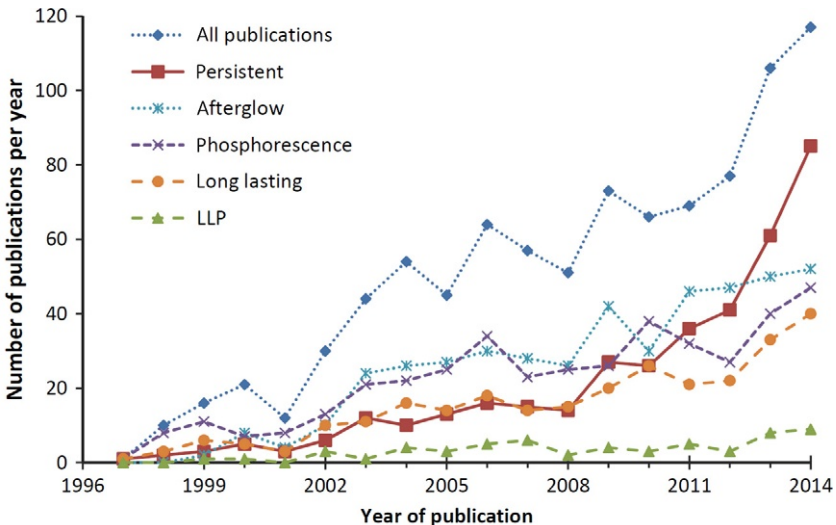


FIGURE 3 Evolution of the number of publications on persistent luminescence since 1997, within the data set studied. Note that most of the papers contain two or more of the mentioned keywords.

In the first years after the discovery of $\text{SrAl}_2\text{O}_4:\text{Eu,Dy}$, *phosphorescence* was the preferred name for the process, rather than *persistent luminescence*. Although the delayed emission in $\text{SrAl}_2\text{O}_4:\text{Eu,Dy}$ is strictly spoken not the result of an excited state with a longer lifetime, as in the triplet state of an exciton in organic molecules, this term is relatively common. Interestingly, “*the persistence of the phosphorescence*” was used in the 1996 paper by Matsuzawa et al. (1996). *Phosphorescence* is now often complemented with *long lasting*, leading to the abbreviation long-lasting phosphorescence (LLP). The same abbreviation can also be used for the material itself, as it is also encountered as *long-lasting phosphor*. It is only in the past 5 years that *persistent luminescence* gained popularity. Unfortunately, its obvious abbreviation is *PL*, which is normally used for *photoluminescence* and thus would lead to confusion. The abbreviation *PLUM* has been suggested, but it is not frequently used. To denote the material itself, *persistent phosphor* is commonly used.

A key aspect of persistent luminescence is of course the intensity during the decay when the excitation ends, which is often referred to as the *afterglow*. This term is commonly used, and can be combined to denote several aspects, such as the *afterglow decay* and the *afterglow intensity*. Within this chapter, we have chosen to denote the general phenomenon as *persistent luminescence*, the materials as *persistent phosphors* and to use *afterglow* to describe the “decay of the persistent luminescence.”

During the first International Workshop on Persistent Luminescence (Ghent, Belgium, 2011), a poll was held on what terminology to prefer (Smet et al., 2012b) with a majority favoring “persistent luminescence” over “long-lasting phosphorescence (LLP).” One could argue that whether there is a need for a standard terminology. Although this would be convenient when searching papers, proper use of (multiple) keywords, and reference to reviews or Matsuzawa’s paper seems sufficient.

3.2 Publication Analysis

Figure 3 might give the impression that the field of persistent luminescence has strongly expanded during the past 20 years. Figure 4 puts the publication output into perspective by comparing to all publications with “luminesce*” in the title, abstract, or keywords. Within the 2003–2012 timeframe, the output on persistent luminescence roughly follows the increase in the number of general luminescence papers, when ignoring the year-by-year fluctuations. In the years 2013–2014, there appears to be a relatively faster increase in papers on persistent luminescence, a trend which is yet to be confirmed in the coming years. At least, Fig. 4 confirms that the research into luminescent materials is still active and growing.

From a geographical point of view, 42% of papers contain an affiliation situated in the People’s Republic of China, while European countries

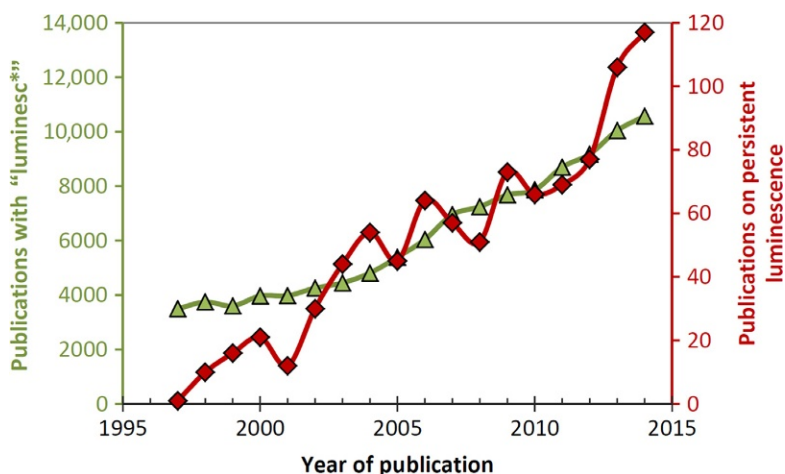


FIGURE 4 Evolution of the annual number of publications on persistent luminescence in the *Web of Science*, in comparison to the publications mentioning “luminesc*.”

contribute to 18% of the analyzed papers, followed by Japan (14%), India (7%), and the United States of America (6%).

4 EXPERIMENTAL METHODS

4.1 Introduction

The composition, and therefore, also the optical and structural properties of persistent luminescent materials are quite similar to that of the ordinary luminescent compounds. Therefore, most synthetic and analytical methods used in luminescence research can be transferred directly to the investigation of persistent luminescence. Nevertheless, there are some subtle (and less subtle) differences in approach needed, which makes it useful to review the experimental methods suited for studying the persistent luminescent materials. Some techniques which are specific to persistent luminescence—TL and afterglow characteristics—will be treated separately in more detail in [Section 8](#).

4.2 Synthesis

Based on the overview of the hundreds of different compositions featuring persistent luminescence ([Section 7](#)), it is clear that a wide range of synthesis techniques are applied for these materials. In general, solid-state reactions at elevated temperature constitute the main synthesis approach, although wet-chemical techniques, such as sol–gel, hydrothermal, or precipitation reactions are also applied, motivated by the anticipated homogeneous distribution of the

constituent ions. Less controllable synthesis techniques are used as well, such as combustion. In the case of bottom-up nanoparticle synthesis, other approaches have to be used.

Irrespective of the chosen synthesis method, one should obviously try to arrive at the desired composition without minority phases. These secondary phases can dramatically obscure the optical and luminescent properties of the intended phase and lead to false conclusions. Consequently, a thorough (micro)structural characterization at the start of the investigation (Section 4.4.1) is a prerequisite.

The wide range of synthesis techniques is indicative of the importance of the precise synthesis conditions on the persistent luminescence. It often does not suffice to obtain the right crystallographic phase, as the valence state of the dopant ions, the purity of the starting compounds, and the introduction of (lattice) defects are equally important.

To control the valence state, which is especially relevant for the Eu^{2+} -based persistent phosphors, a postsynthesis treatment in reducing conditions (whether under vacuum or in so-called forming gas, which is a mixture of a few percent of hydrogen in an inert gas) is often required on the already formed host compound. Most often, the synthesis starts with a solid-state reaction in air, leaving the Eu ions in a trivalent state, and a subsequent reduction step for the Eu ions is necessary. In other methods, such as the combustion synthesis, the experimental conditions are such that an appropriate reduction of the europium ions can already occur during the synthesis. This postsynthesis treatment is not only relevant to the dopant ion but also for the control of the lattice defects held responsible in many materials for a significant role in the trapping. The conditions of this treatment are often optimized in terms of the luminescent properties of the final phosphor, rather than by deliberate control of the defects, as their exact chemical nature is often unknown.

4.3 Optical Characterization

4.3.1 Steady-State Luminescence

A persistent phosphor is also a (standard) photoluminescent material. Similar characterization techniques can be used, such as emission and excitation spectroscopy, to determine the basic properties and to assess the influence of codoping on the “intrinsic” luminescence properties. Some cautions are needed, especially when measuring persistent phosphors with the elevated trapping capacity.

Excitation spectra are typically measured going from short to long wavelength. Starting the measurement of an excitation spectrum on a persistent phosphor with empty traps—because it was kept in the dark for some time prior to the measurement or was heated to empty the traps—will first lead to a filling of traps, without yielding emission. Hence, in the short wavelength

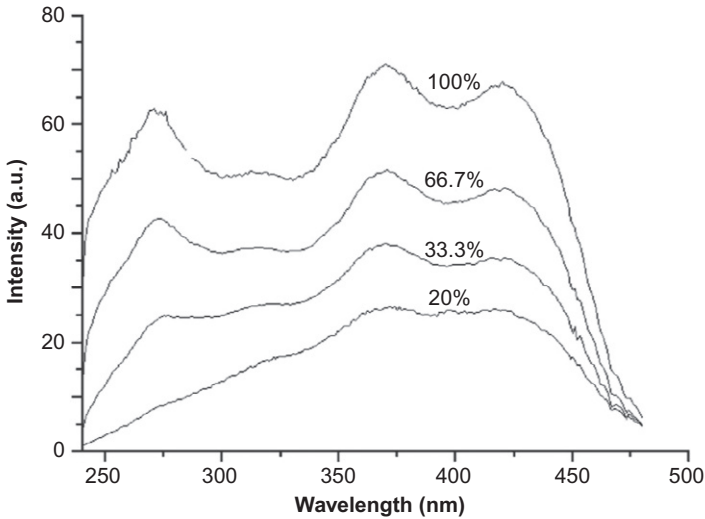


FIGURE 5 Excitation spectra for $\text{SrAl}_2\text{O}_4:\text{Eu,Dy}$ measured upon monitoring the emission at 520 nm as a function of excitation intensity (normalized to maximum intensity). Adapted from Jia (2003).

range, one can obtain a lower value in the excitation spectrum (Fig. 5). Similarly, afterglow at the end of the excitation scan, where the phosphor is not excited anymore, can lead to an appreciable emission intensity, which is being altogether reflected in a red shift of the “true” excitation bands (Jia, 2003).

To overcome these problems when characterizing the steady-state photoluminescence, excitation spectra can be measured at low temperature to avoid afterglow or by using a sufficiently high intensity of the excitation light in combination with slow scanning at RT, to reduce the impact of the dynamic trapping and detrapping on the shape of the excitation spectrum.

Similarly, when measuring emission spectra by means of a scanning emission monochromator, one should make sure to be in an excitation regime where the global emission intensity has stabilized.

4.3.2 Afterglow

The afterglow can be characterized in different ways. First, the emission spectrum during the afterglow can be collected, and compared to the steady-state emission spectrum. To collect such an afterglow emission spectrum, one has to resort to non-scanning detection, for instance by means of a charge-coupled device (CCD)-based spectrometer, as the rapidly declining emission intensity does not allow sequential scanning methods, at least not in the initial part of the afterglow decay curve.

The afterglow intensity is typically measured for the entire emission, i.e., by integration over all emission wavelengths. Preferably, this is performed by means of a calibrated photometer, yielding intensities in cd/m^2 (for phosphors emitting in the visible) or in W/sr/m^2 (for other phosphors). Alternatively, afterglow decay curves can also be measured in a standard luminescence spectrometer, by monitoring the emission intensity at a particular emission wavelength as a function of time after ending the excitation, typically in arbitrary units.

The excitation conditions (type of excitation source, spectral distribution, duration, and intensity) are of course influencing the afterglow intensity. This aspect is commented in detail in [Sections 5.1 and 8.2.1](#).

4.3.3 Standard TL

Afterglow measurements can take a very long time, especially if deep traps are present in the material. Measuring the TL is then often an ideal way to speed up the thermal emptying of traps, by applying a linear heating rate, and thus accelerating the thermal release. Plotting the emission intensity of a previously excited persistent phosphor as a function of temperature allows one to extract information on the trap depth (or often, on the trap depth *distribution*) and on the possibility of retrapping. Specific guidelines on interpreting TL glow curves are given in [Section 8.1.2](#).

4.3.4 TL Emission and Excitation

In general, the *wavelength integrated* emission intensity is measured in a TL experiment, after excitation of the phosphor with a typically broad emission spectrum (unfiltered light from a Xe-arc lamp), by commonly accessible excitation lines (e.g., the mercury 254 nm emission line) or occasionally by ionizing radiation. However, two extensions to this standard method have proven valuable for the study of persistent phosphors.

First, the full emission spectrum can be monitored during the heating, instead of only the emission intensity (whether integrated or at a fixed emission wavelength). To do this, a CCD-based setup is required, where the entire emission spectrum is available at any moment, without the need to scan through the emission range. If certain traps would be coupled to distinct emission centers, then the emission spectrum could be different, depending on the position in the afterglow curve. This is helpful to determine different contributions in the TL glow curve. In case persistent luminescent impurity phases are present in a synthesized persistent phosphor, then this type of analysis is highly informative, as it will quickly allow discriminating between the different contributions.

The second extension to standard TL spectroscopy has a greater beneficial impact on the understanding of trapping and detrapping processes in persistent phosphors. With TL excitation spectroscopy, it is possible to identify what

excitation wavelengths are required to fill traps. In these experiments, a monochromatic light source is used to excite the phosphor, after which a TL glow curve is recorded. Consecutive TL glow curves are recorded, by systematically varying the excitation wavelength. In principle, the same information can also be extracted by performing afterglow measurements as function of the excitation wavelength (Lei et al., 2010c), but this leads in general to impractically long measurements. In the paper by Bos et al., the technical aspects of such a TL excitation setup are detailed, as well as its application to a number of benchmark persistent phosphors, including $\text{SrAl}_2\text{O}_4:\text{Eu,Dy}$, $\text{Sr}_4\text{Al}_{14}\text{O}_{25}:\text{Eu,Dy}$, $\text{ZnS}:\text{Cu}$ (Fig. 6), and $\text{CaAl}_2\text{O}_4:\text{Eu,Nd}$ (Bos et al., 2011).

From a technical point of view, these TL excitation measurements almost require a (semi)automated setup, as otherwise it is a tedious job to perform these measurements in a reproducible way. One should take care of an appropriate intensity correction for the wavelength-dependent output of the excitation source. Also, it is important to determine in which regime the setup is operating, as using high excitation intensities might lead to saturation of the available traps for certain excitation wavelengths.

An interesting additional feature of such a TL excitation setup is the possibility to excite below RT, as persistent luminescence is actually TL at RT.

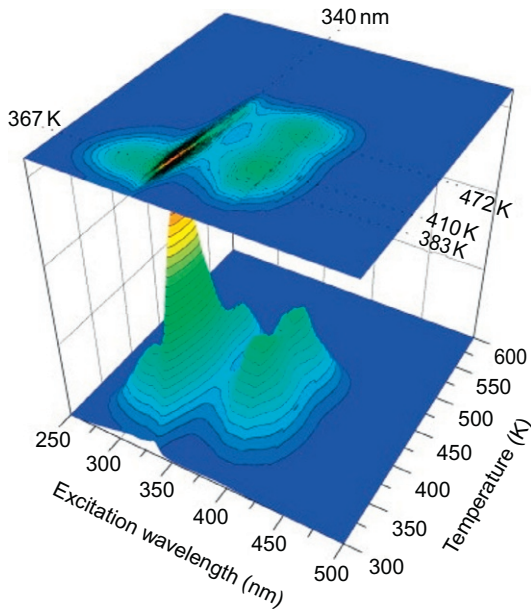


FIGURE 6 TL intensity of $\text{ZnS}:\text{Cu}$ as a function of excitation wavelength and temperature as contour plot (top) and in 3D representation (bottom). Glow curves were recorded at a heating rate of 5 K/s. Note the filling of different traps for excitation wavelengths below and above the band gap (3.66 eV corresponding with 340 nm). *Reproduced from Bos et al. (2011).*

When traps can be filled, but not emptied under the charging conditions, this simplifies the interpretation afterward. Furthermore, thermal barriers for the trapping can be identified.

4.3.5 *Optically Stimulated Luminescence*

In storage phosphors, the trap depths are considerably larger than in the case of persistent phosphors. To empty these traps after excitation, for instance after exposure to ionizing radiation, elevated temperatures are needed to overcome the thermal barrier for detrapping. Therefore, it is common use to empty traps by means of (infra)red light, in a process called optically stimulated luminescence (OSL). The amount of emitted light is then proportional to the number of trapped charges. Unfortunately, limited information can be extracted on the trap depth. Nevertheless, for dosimetry purposes, this is a very useful technique (Yukihara *et al.*, 2014) and the same principle is used in computed radiography (Leblans *et al.*, 2011), where the fast and local read-out by means of OSL is clearly advantageous over a thermal read-out of phosphor plates.

Transferring OSL to persistent phosphors is not so straightforward, as the smaller trap depths do not allow the use of visible light in the read-out. Nevertheless, by means of NIR lasers (typical wavelength of 808 or 980 nm) filled traps can be emptied (Chen *et al.*, 2012). Instead of using a single wavelength for the OSL source, one might consider performing OSL spectroscopy by probing the wavelengths which can induce the detrapping (Fig. 7).

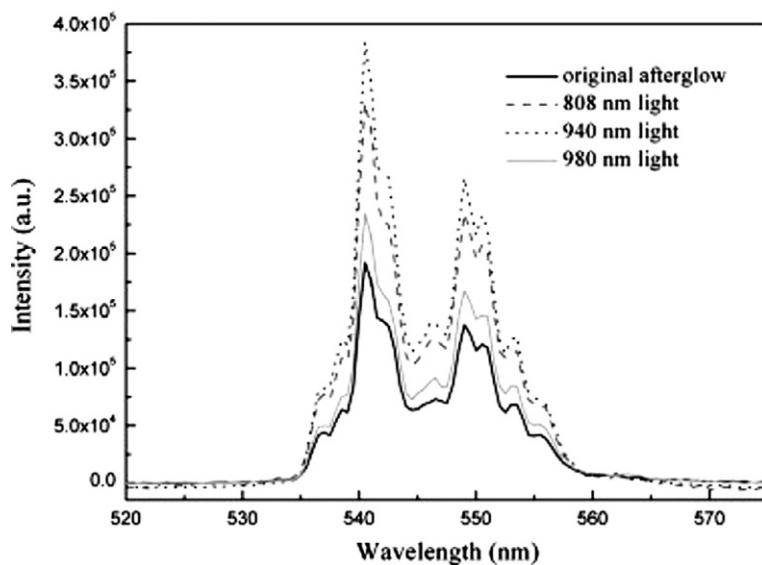


FIGURE 7 Optically stimulated luminescence spectra of green $\text{Lu}_2\text{O}_3:\text{Tb}^{3+}, \text{Sr}^{2+}$ persistent luminescent ceramics, obtained by irradiation at 808, 940, and 980 nm. *Reproduced from Chen et al. (2012).*

4.4 Structural Characterization

4.4.1 Crystallographic Phase and Impurities

Sufficient attention should be given to the structural characterization of persistent phosphors. First of all, when exploring and synthesizing (novel) compounds, there is always a risk that minority phases are formed. Powder X-ray diffraction (XRD) is a straightforward method to assess sample purity. At a next level, the refinement of lattice parameters allows to assess the incorporation of dopant ions if they have a different ionic radius than that of the host ions. Especially, when synthesizing compounds in rather complex compositional classes, such as the Sr–Al–O system, with many compositions and polymorphs (Boutinaud et al., 2015), this structural analysis deserves special attention.

In addition, it should be standard procedure to perform a morphological and chemical analyses at the microscopic level, for instance by scanning electron microscopy (SEM), energy-dispersive X-ray analysis (EDX), or elemental mapping by time-of-flight secondary ion mass spectroscopy (TOF-SIMS). Taking into account that powder XRD does not allow to detect minority phases present in less than about 1 wt%, a microscopic analysis can reveal relevant precipitations which otherwise remain undetected.

Figure 8 shows an elemental mapping for a $\text{SrAl}_2\text{O}_4:\text{Eu},\text{Dy}$ phosphor, where precipitation of a dysprosium rich phase is found inside a phosphor particle. Given the typically low rare earth concentrations (0.5–2% substitution of the cation, which is strontium in this case), these precipitates will

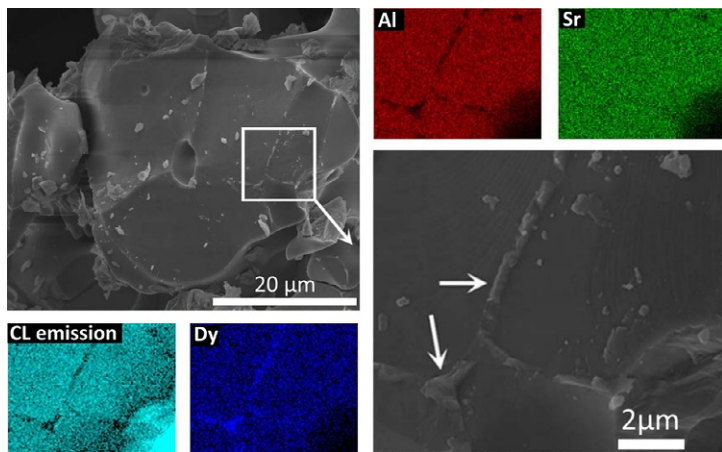


FIGURE 8 SEM cross section of a $\text{SrAl}_2\text{O}_4:\text{Eu},\text{Dy}$ phosphor grain, with elemental maps obtained by EDX for dysprosium, aluminum, and strontium. Notice the precipitation of Dy in the grain boundaries. The cathodoluminescence emission intensity is also much weaker in the grain boundaries. The sample was kindly provided by Jorma Hölsä.

go unnoticed in powder XRD, let alone if they are not crystalline. When interpreting results from a compositional variation, it is important to know what fraction of the dopants is actually incorporated into the persistent phosphor.

4.4.2 Valence States

Determining the valence state of dopant ions is of critical nature in the study of persistent phosphors. Although one cannot make statements for all types of persistent phosphors, electrons are often the charge carriers being trapped. At least for the Eu^{2+} - and Ce^{3+} -doped phosphors, it seems that these electrons are originating from the dopant ions. A further complication in the case of europium-doped phosphors is the simultaneous presence of both 2+ and 3+ valence states, with the relative abundance depending on the synthesis conditions, including the heat treatment, the atmosphere, and the codoping.

It turns out that optical spectroscopy is unsuitable to detect the fraction of each valence state, despite the fact that Eu^{2+} and Eu^{3+} have strongly different spectral characteristics (Avcı et al., 2012). A few analytical techniques are at hand, but they should be handled with sufficient care.

X-ray photoelectron spectroscopy is in principle ideally suited to make distinction between valence states. It is, however, a surface sensitive technique and to obtain information of the bulk of a phosphor particle, one needs to sputter away the top layers (e.g., by ion bombardment). Consequently, the probed region is always forming a surface, and it has been shown that in the case of Eu^{2+} , this leads to a quick oxidation to Eu^{3+} even in high vacuum, allowing only a short measurement time (Vercaemst et al., 1995a,b). As such, the detected fraction of Eu^{3+} should be considered an upper limit.

X-ray absorption spectroscopy (XAS) has gained more interest in recent years as an analytical technique to study persistent phosphors. X-ray absorption near-edge spectroscopy (XANES) probes the onset of an X-ray absorption edge. In the case of europium, this is often the L-III edge, for which the valence states of interest (Eu^{2+} and Eu^{3+}) show an 8 eV difference in the onset of the 2p–5d absorption, also called the white lines. Appropriate analysis of the contribution in the XANES spectrum allows to estimate the fraction of both valence states. It turns out that most Eu^{2+} -doped persistent phosphors also have a considerable fraction of Eu^{3+} (Avcı et al., 2012; Korthout et al., 2011; Lastusaari et al., 2014). One should take care about the disturbing influence of the incident X-ray beam, as it can irreversibly damage the persistent phosphor if the flux is too high. The fact that the X-ray beam, can not only induce radioluminescence but also afterglow, was used to show that a valence state change occurs from Eu^{2+} to Eu^{3+} upon filling the traps in $\text{SrAl}_2\text{O}_4:\text{Eu},\text{Dy}$ (Korthout et al., 2011). Nevertheless,

interpreting XANES data are not trivial, as the fraction of dopant ions participating in the trapping process appears to be limited (Korthout et al., 2011). In addition, also extended X-ray absorption fine structure can be used to probe the coordination of the dopant ions and to determine site occupancy (Rodrigues et al., 2012).

In principle, also TOF-SIMS can be used to make statements about the valence state of dopant ions (Swart et al., 2014), and even map their distribution at the microscopic scale, although the interpretation is not straightforward.

4.4.3 Defects

An improved knowledge of the nature of the defects would be highly beneficial for understanding the processes driving persistent luminescence. Unfortunately, relatively few tools are available to determine the type and concentration of defects, often yielding only indirect information. Electron spin resonance (ESR) or electron paramagnetic resonance is a nonperturbing technique which has proven essential to discriminate between different Cr^{3+} sites in ZnGa_2O_4 (Gourier et al., 2014). It would become especially valuable if combined with *in situ* optical excitation to change the fraction of trapped charges (Ahmad et al., 2011).

Photoconductivity measurements were especially decisive in establishing the first mechanisms on persistent luminescence (Abbruscato, 1971; Matsuzawa et al., 1996), but are unfortunately notoriously difficult on powder-like materials. This technique was recently applied again by Ueda et al. as a function of temperature and excitation wavelength to probe the charge carrier dynamics in $\text{CaAl}_2\text{O}_4:\text{Eu}$ (Ueda et al., 2015). These measurements could also be useful in determining whether trapping occurs locally, i.e., without or with limited involvement of the conduction band states. Obviously, other effects should be carefully taken into account, such as photoionization driven thermal quenching.

Clearly, the structural characterization of defects is lagging behind on the luminescence characterization. Of course, the type of (dominant) trapping center will not be the same for the large range of compositions encountered in persistent luminescence. As such, the purpose of this chapter is not to go into detail of all proposed defect structures and mechanisms, partly because the field is still evolving, partly because the different mechanisms have been reviewed in detail in the past years. The following papers, Clabau et al. (2006, 2007), Dorenbos (2005), Van den Eeckhout et al. (2010), and Brito et al. (2012) provide a good starting point for getting an overview of the competing ideas in the field.

When trivalent ions are substituting for divalent cations like Ca, Sr, or Ba, charge compensation schemes involving cation vacancies, are often proposed. Direct proof is however largely lacking, let alone information on the geometrical configuration of dopants, codopants, and defects is known.

After 20 years of research, there are still two main suspected trapping centers in the case of $\text{Eu}^{2+}, \text{R}^{3+}$ codoped phosphors, which are at the basis of most commercialized phosphors:

- Dorenbos argued, on the basis of empirically derived energy level schemes, that in many persistent phosphors, including $\text{SrAl}_2\text{O}_4:\text{Eu}, \text{Dy}$, the trivalent codopant ions can be suspected as the electron trapping center, thereby reducing to a divalent state (Dorenbos, 2005; Dorenbos et al., 2013). Experimental evidence is mainly found in (storage) phosphors with deeper traps, such as $\text{YPO}_4:\text{Ce}^{3+}, \text{R}^{3+}$, where clear correlation was encountered between the position of the divalent lanthanide's ground state and the trap depth derived from TL spectroscopy (Dorenbos et al., 2013) (see also Fig. 18). Further evidence is mainly coming from optical absorption spectroscopy in charged phosphors (Dorenbos et al., 2013). Doubts on the chemical stability and the lack of observation of these reduced lanthanides in XANES make that this model is still being contested (Holsa et al., 2010; Rodrigues et al., 2014).
- The other main line of thought is centered around intrinsic (lattice) defects as the relevant trapping centers, since several Eu^{2+} -doped persistent phosphors do not require the presence of trivalent ions to show persistent luminescence. Examples included $\text{SrAl}_2\text{O}_4:\text{Eu}$ and $\text{BaSi}_2\text{O}_2\text{N}_2:\text{Eu}$, although it should be noted that these compounds also invariably contain a significant fraction of Eu^{3+} . Adding the appropriate (trivalent) codopant would then alter the number of lattice defects, or the specific location in the lattice with respect to the europium ion, rather than acting as the trapping center itself. In that sense, it was noticed by Hölsä that for Sr-based compounds dysprosium is often the best choice as codopant (Brito et al., 2012). As motivated earlier, direct evidence for these types of defects is lacking and their presence is mostly inferred from chemical considerations.

For persistent phosphors based on the line-emitting $4f^n$ ions, the knowledge on the trapping mechanism is very limited and fragmented. It is clearly different from the trapping in Eu^{2+} and Ce^{3+} phosphors, where excitation into the (higher) 5d states is the main charging mechanism leading to trapping. For the line-emitting $4f^n$ ions, this is not the case as direct excitation does not lead to trapping. Often high energy excitation is needed, well into the UV, in order to induce the persistent luminescence, which is not favorable from an application point of view. $\text{Y}_2\text{O}_2\text{S}:\text{Eu}^{3+}, \text{Ti}, \text{Mg}$ is a notorious exception, with blue light being able to induce trapping. For this red persistent phosphor, hole trapping has been suspected (Brito et al., 2012).

For the recently described persistent phosphors based on the deep-red to NIR emission of Cr^{3+} , remarkable progress has been made in the understanding of the trapping mechanism (Basavaraju et al., 2015; Gourier et al., 2014). By the combination of ESR, XANES, density functional theory calculations,

and optical spectroscopy, the defect structure around the Cr^{3+} has been detailed, leading to a consistent trapping mechanism.

It is expected that the theoretical calculations will get a more prominent role in the study of persistent phosphors, once energy levels of excited states and defects can be calculated with sufficient precision, which is not trivial for, e.g., the lanthanide ions. Given that the process of persistent luminescence is driven by a well-defined trap depth, accuracy in the range of 0.1 eV is required for the calculated energy levels.

5 MEASURING AFTERGLOW INTENSITIES

5.1 Standards and Classifications

The brightness of a persistent luminescent material as a function of time is obviously the most important quantity to specify its performance. Persistent phosphor samples usually consist of a flat-emitting surface which can be considered as a Lambertian emitter. Therefore, the apparent surface brightness of the phosphor can be quantified by the luminance, expressed in cd/m^2 .

Over the last decades, with the number of applications of persistent luminescent materials constantly increasing, standards for exciting, measuring, and classifying them have been developed and published. Some of the benchmark documents in this respect are DIN 67510-1 (DIN, 2002) and ISO 16069:2004 (ISO, 2004a), specifying a normalized way for excitation and measurement of decay times and intensities. In summary, materials should be excited during 5 min with a surface illumination of 1000 lux, using an unfiltered Xe-arc as the light source. Decay should be measured using a photometer, calibrated in photopic units cd/m^2 . Please note that this illumination source is far from representative for indoor lighting, since it is both very bright and contains a very large fraction of UV, obviously absent in any indoor lighting. Later in this chapter, we will also discuss the validity of measuring the light emission in photopic cd/m^2 .

In order to be able to assess the performance of persistent phosphors under more realistic lighting conditions, ISO standard 17398 (ISO, 2004b) has been published, which requires the manufacturer to provide additional information on the luminance for specified excitation scenarios. This includes (a) excitation with standard illuminant D65 for 20 min at 200 lux, (b) excitation with a fluorescent lamp (4300 K) for 15 min at 50 lux, and (c) excitation with a fluorescent lamp (3000 K) for 15 min at 25 lux. In order not to make things more complicated than necessary, we will not discuss these additional requirements further.

Based on their luminance decay profile, persistent phosphors are subdivided in classes, as shown in Table 1. For both manufacturers and customers, this classification is an easy and fast way to select materials based on a single specification.

TABLE 1 Minimum Specifications for Different Classes of Persistent Phosphors, Following CIE Standard 67510-4

Class	2 min	10 min	30 min	60 min
A	108	23	7	3
B	210	50	15	7
C	690	140	45	20
D	1100	260	85	35
E	2000	500	160	60
F	4000	1000	320	120

Values are in photopic units, mcd/m^2 . Classes E and F are newly developed standards, in view of the constant improvement of luminescent materials.

TABLE 2 Minimum Photopic Luminance of Persistent Luminescent Materials in Safety Way Guidance Systems, as Specified in ISO Standard 16069

Time After Excitation (min)	Luminance (mcd/m^2)
10	20
60	2.8
340	0.3

Next to the different classifications and standards, minimum requirements have been specified for phosphors in safety way guidance systems, as per ISO 16069 and DIN67510-1, as shown in [Table 2](#).

The value of 0.3 mcd/m^2 in the table is approximately 100 times the limit of eye sensitivity and the time to reach this value is defined as the decay time of the material. Remark that a value of 0.32 mcd/m^2 is also often used and already appears in [Matsuzawa et al. \(1996\)](#).

5.2 Performance of Persistent Luminescent Emission

In order to be able to discuss realistic spectra and decay curves instead of synthetic ones, a set of four persistent phosphor powders was selected from Glo-Tech Inc. ([WebGloTech, 2014](#)), covering the entire visible spectrum. Details of the different benchmark materials and their properties are given in [Table 3](#).

TABLE 3 Properties of Commercial Persistent Phosphor Materials, Selected as Benchmarks

GloTech Code	Color	Peak λ (nm)	<i>S/P</i>	PLE	Host
GTP3000A	Violet	438	14.1	46	CaAl ₂ O ₄
GTBL3500A	Blue	470	7.8	153	Sr ₂ MgSi ₂ O ₇
GTG3000A	Green	520	2.4	423	SrAl ₂ O ₄
GTE3000A	Red	626	0.37	201	Y ₂ O ₂ S

PLE, photopic luminous efficacy; *S/P*, ratio of scotopic to photopic efficacy (see Section 6.1).

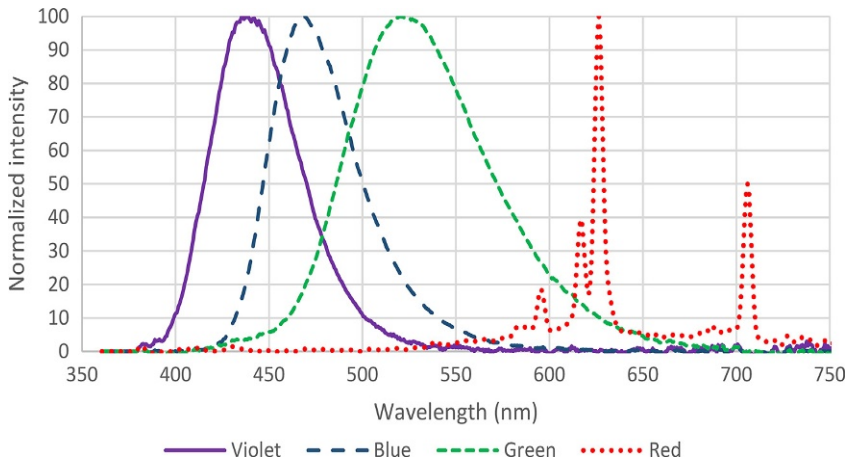


FIGURE 9 Normalized spectra of the benchmark persistent phosphors in Table 3. Adapted from Poelman and Smet (2010).

Samples were made by mixing about 25% of phosphor in a polyurethane paint and spreading this homogeneously over a flat surface. While this does not yield the maximum possible luminance for these phosphors, it yielded stable benchmark samples which are used as test objects for the rest of this section. Normalized persistent emission spectra of the different samples are shown in Fig. 9.

Following the procedure described above (using a 5-min illumination with 1000 lux of an unfiltered Xe-arc), decay profiles were collected. These were measured using a calibrated photometer (International Light Technologies ILT1700, using an SPM068 photomultiplier detector) as shown in Fig. 10.

By extrapolating the data from these measurements, one can estimate the decay time of the different samples, until the luminance has decreased to 0.3 mcd/m². These calculated times are shown in Table 4 as photopic decay times.

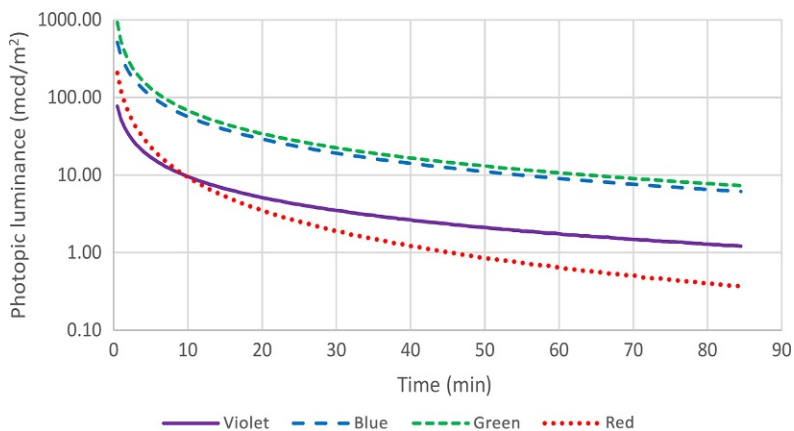


FIGURE 10 Luminance decay curves of the benchmark phosphors in photopic mcd/m^2 . Adapted from *Poelman and Smet (2010)*.

TABLE 4 Decay Time of the Different Benchmark Phosphors Till a Luminance of 0.3 mcd/m^2 is Reached, Both for Photopic Luminance and for Mesopic Luminance According to CIE191:2010

Ref. Sample	Photopic Decay Time (min)	Mesopic Decay Time (min)
Violet	313	4070
Blue	981	4420
Green	1230	1860
Red	97	54

TC-1-58 (2010).

6 OBSERVATION BY THE HUMAN EYE

6.1 Introduction

For many years, standards for measuring the brightness and color of artificial light sources, such as lamps and displays, have been well established. The units involved are photometric: they take into account the average human eye sensitivity and color perception. Usually, the same photometric quantities are used for specifying low level light sources, such as persistent luminescent materials, although it is realized these are not valid at low light

levels (Stockman and Sharpe, 2006). A complete description of the photochemical and neurological processes governing vision is far beyond the scope of this chapter. Therefore, only the basics of color and brightness perception will be covered here.

The range of wavelengths of electromagnetic radiation which gives rise to a visible impression is very limited; for human eyes, this is typically the range from 380 to 780 nm. During daylight conditions, known as the photopic regime, human vision uses three types of so-called cones, which are mainly localized in the central area of retina (the fovea). Thanks to these three types of photoreceptors, we can distinguish different wavelengths as different colors. The International Commission on Illumination (CIE) has been published the overall sensitivity of the average human eye as a function of wavelength as $V(\lambda)$, a function which is peaking at 555 nm (CIE, 2005). The SI unit of light intensity, the candela, is only defined at this specific wavelength:

The candela is the luminous intensity, in a given direction, of a source that emits monochromatic radiation of frequency 540×10^{12} hertz and that has a radiant intensity in that direction of 1/683 watt per steradian.

This definition effectively means that at a frequency of 540×10^{12} Hz (corresponding to a wavelength of 555.07 nm), 1 W of optical power corresponds to a luminous flux of 683 lumens. This number of 683 lm/W is sometimes referred to as the luminous efficacy of the radiation (LER) or the photopic luminous efficacy (PLE). For any spectral distribution, the PLE equals the average eye sensitivity (in lm/W) for the given spectrum, and is calculated as:

$$\text{PLE}(\text{lm/W}) = 683 \frac{\int_{380 \text{ nm}}^{830 \text{ nm}} I(\lambda) \cdot V(\lambda) d\lambda}{\int_{380 \text{ nm}}^{830 \text{ nm}} I(\lambda) d\lambda}$$

For monochromatic light sources, the PLE reduces to 683 times the value of $V(\lambda)$ at the given wavelength (shown in Fig. 11).

Under night time conditions (the so-called scotopic regime), the cones in the retina are inactive. Human vision is then governed by rods, which are more evenly spread over the retina, except in the fovea. They are more light sensitive than the cones, but do not allow color vision. Rods show a sensitivity as a function of wavelength which is different from that of cones. The corresponding relative sensitivity function, as determined by the CIE, is $V'(\lambda)$, peaking at 507 nm.

In order to facilitate further calculations, the tables for $V(\lambda)$ and $V'(\lambda)$ (CIE, 2005) were fitted to multiple Gaussian functions as follows (Poelman and Smet, 2010):

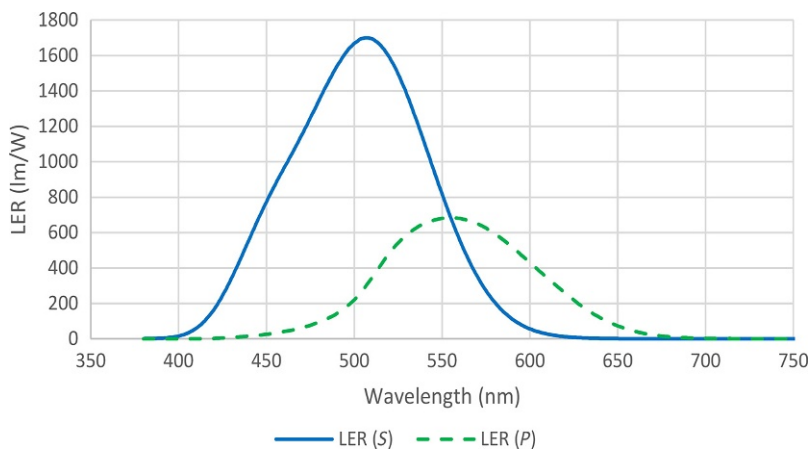


FIGURE 11 Luminous efficacy of the radiation (LER) at different wavelengths, for scotopic (S) and photopic (P) vision. These traces are proportional to CIE standard curves V' and V , multiplied by 1699 and 683, respectively. Note that the intersection of the two traces at a value of 683 lm/W at 555 nm. Adapted from *Poelman and Smet (2010)*.

$$\begin{aligned}
 V(\lambda) &= 0.239 \exp \left[-\frac{(\lambda - 531)^2}{851} \right] + 0.911 \exp \left[-\frac{(\lambda - 566)^2}{3320} \right] \\
 &\quad + 0.0310 \exp \left[-\frac{(\lambda - 464)^2}{658} \right] V'(\lambda) \\
 &= 0.999 \left[-\frac{(\lambda - 507)^2}{2520} \right] + 0.182 \exp \left[-\frac{(\lambda - 449)^2}{647} \right]
 \end{aligned}$$

where wavelengths are given in nanometers.

As rods are more light sensitive than cones, one would expect a totally different value for the luminous efficacy during nighttime, based on the sensitivity ratio of rods and cones. However, this is not possible due to the definition of the candela at the single wavelength of 555 nm. Therefore, the luminous efficacy for scotopic vision (now denoted as SLE or scotopic luminous efficacy) should take the same value of 683 lm/W at 555 nm as for photopic vision. The resulting SLE as a function of wavelength is shown in Fig. 11.

Due to the shape of the $V'(\lambda)$ function and the fixed value at 555 nm, the maximum of the curve is automatically defined; at 507 nm, the curve peaks at 1699 lm/W. This leads to the following calculation of the SLE for an arbitrary spectrum:

$$\text{SLE}(\text{lm/W}) = 1699 \frac{\int_{380 \text{ nm}}^{830 \text{ nm}} I(\lambda) \cdot V'(\lambda) d\lambda}{\int_{380 \text{ nm}}^{830 \text{ nm}} I(\lambda) d\lambda}$$

As will be described in [Section 6.3](#), the relative sensitivity of rods and cones is highly dependent on the overall luminance and on the physical and photochemical dark adaptation of the eyes. At intermediate light levels, in the twilight regime, both rods and cones are active, which is the regime of mesopic vision.

6.2 CIE Model for Mesopic Luminance Measurements

The combined effect of the difference in wavelength range and sensitivity between photopic and scotopic vision and the gradual shift between the two during twilight has been subject of research for a long time. Notably, the nineteenth century Czech anatomist Jan Evangelista Purkyně gave his name to the Purkinje effect, which describes the phenomenon qualitatively: when flowers look bright red compared to their relatively dull green leaves in bright sunlight, this contrast changes at dusk, when the green leaves look much brighter than the red flowers.

Since it is important to take these effects into account for photometric measurements during twilight or during the night, especially for road markings and road lighting, several models have been developed to describe vision in the mesopic regime. An important contribution to this subject was delivered by the European project MOVE (Mesopic Optimisation of Visual Efficiency), which proposed a set of equations for describing luminance in the mesopic region, using a weighted average eye sensitivity in between the sensitivity curves for photopic and scotopic vision ([Eloholma and Halonen, 2006](#)). Stated otherwise, they used a sensitivity function which, referring to [Fig. 11](#), gradually shifted from one graph to the other. Rea published an overview of the existing models for mesopic vision, including the one from MOVE, and proposed a slightly different model ([Poelman et al., 2009](#); [Rea et al., 2004](#)). Finally, in 2010 and after decades of meetings and preliminary documents, the CIE published a “Recommended system for visual performance based mesopic photometry” in technical report CIE191:2010 ([TC-1-58, 2010](#)). The system yields results which are very close to, for example, the MOVE project or the model by Rea. However, it has the advantage that now an internationally recognized organization has provided the scientific community with a standard that can be used as reference. We will not go into all details of this report, but only briefly describe the main results.

Just like the older models, the new CIE model relies on a “mesopic” sensitivity function which is a linear combination of the photopic and scotopic functions:

$$M(m) \cdot V_{\text{mes}}(\lambda) = m \cdot V(\lambda) + (1 - m) \cdot V'(\lambda)$$

and the resulting mesopic luminance is

$$L_{\text{mes}} = \frac{683}{V_{\text{mes}}(\lambda_0)} \int V_{\text{mes}}(\lambda) L_e(\lambda) d\lambda$$

where $M(m)$ is a normalizing function such that V_{mes} has a maximum value of 1 and $L_e(\lambda)$ is the spectral radiance in $\text{W}/\text{m}^2/\text{sr}/\text{nm}$. $V_{\text{mes}}(\lambda_0)$ is the value of V_{mes} at 555 nm. When $L_{\text{mes}} \geq 5.0 \text{ cd}/\text{m}^2$ then $m = 1$ and if $L_{\text{mes}} \leq 0.005 \text{ cd}/\text{m}^2$ then $m = 0$. In these cases, the mesopic luminance reduces to the photopic and scotopic luminance, respectively.

Both the coefficient m and the mesopic luminance are calculated using an iterative procedure as follows:

$$\begin{aligned} m_0 &= 0.5 \\ L_{\text{mes},0} &= \frac{1699 \cdot m_{n-1} \cdot P + 683 \cdot (1 - m_{n-1}) \cdot S}{1699 \cdot m_{n-1} + 683 \cdot (1 - m_{n-1})} \\ m_n &= 0.767 + 0.333 \log_{10}(L_{\text{mes},n}) \quad \text{for } 0 \leq m_n \leq 1 \end{aligned}$$

where P and S are the photopic and scotopic luminance, respectively. $683/1699$ is the value of the scotopic spectral sensitivity function $V'(\lambda)$ at 555 nm. It is easily seen that this last equation can be written in terms of P , the photopic luminance, and S/P , the ratio of scotopic to photopic luminance. It is the latter ratio S/P , which is typically used to quantify the appropriateness of a certain light source for low light level illumination applications, since high S/P values lead to higher mesopic luminance under near-scotopic conditions.

This effect is seen in Table 5, where the photopic and mesopic luminance of the different benchmark phosphors are shown at different times after excitation. The violet and blue emitters, having a high S/P ratio (see also Table 3), show a mesopic luminance that is considerably higher than their photopic counterpart, while the red-emitting phosphor, with $S/P = 0.37$, performs considerably worse in the mesopic region. The unified luminance as a function of time according to the model of Rea and the mesopic luminance according to the CIE recommended system are shown for the benchmark phosphors in

TABLE 5 Measured Photopic Luminance/Calculated Mesopic Luminance of the Benchmark Phosphors at Different Times (in mcd/m^2)

Phosphor	2 min	10 min	30 min	60 min	340 min
Violet	33.6/166	9.54/64.2	3.51/29.9	1.75/17.6	0.275/4.15
Blue	216/470	56.6/164	19.2/70.3	9.03/38.8	1.48/11.5
Green	298/376	68.2/99.7	22.5/37.4	10.7/19.6	1.16/2.71
Red	64.1/46.6	9.41/3.78	1.90/0.765	0.649/0.261	0.042/0.0169

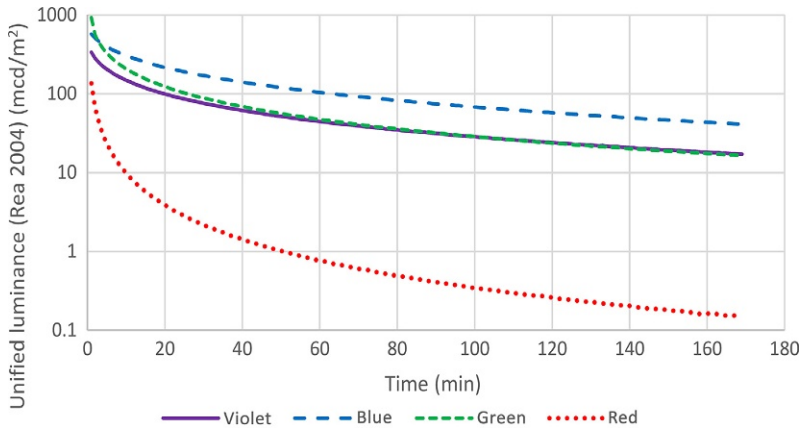


FIGURE 12 Unified luminance of the benchmark phosphors (Table 3) as a function of time.

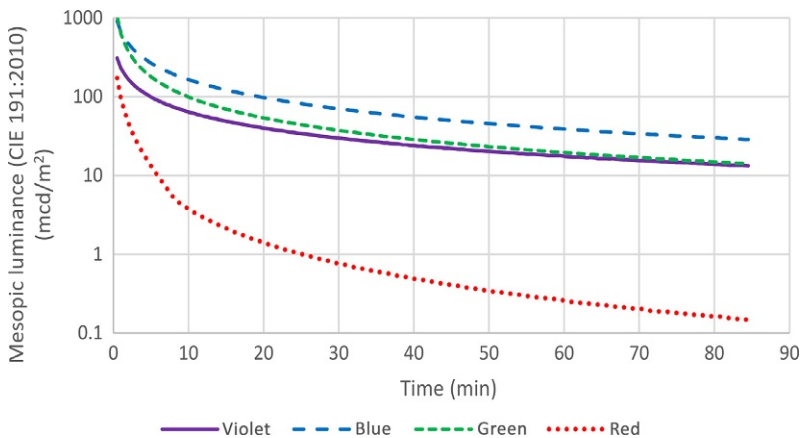


FIGURE 13 Mesopic luminance, following CIE191:2010, of the benchmark phosphors (Table 3) as a function of time.

Figs. 12 and 13, respectively. Even though the unified luminance model makes some approximations compared to the CIE model, it is seen that even for quite extreme S/P ratios, such as the benchmark phosphors, the differences remain quite small.

6.3 Accounting for Dark Adaptation: Visibility Index

The new recommended system for mesopic photometry is a good and relatively easy way—apart from the iterative procedure—to evaluate and to compare the light sources having strongly different spectral distributions,

corresponding to different S/P ratios. However, it fails to describe the performance of, for example, persistent luminescent materials in actual situations for two main reasons. First of all, the rods in the human eye are much more sensitive compared to the cones than the ratio 1699/683 would seem to imply: in practice, the ratio is 2–3 orders of magnitude. Second, upon lowering the light intensity, the eyes undergo both physical changes (an increase in pupil diameter) and photochemical changes, which leads to an ever increasing eye sensitivity until full dark adaptation is achieved after approximately 30 min.

During the first few minutes, the eye sensitivity rapidly increases, due to photochemical changes in the cones and dilatation of the pupils. This is shown in Fig. 14. After 5–10 min, the cones reach their ultimate sensitivity (Hecht and Shlaer, 1948). The second part of the graph is due to the dark adaptation of the rods, which takes about 30–45 min. The discontinuity in the graph is described as the cone–rod breakdown. The photopic and scotopic thresholds, which we call photopic threshold (PT) and scotopic threshold (ST), respectively, were approximated as continuous curves in order to facilitate calculations:

$$PT_{460}(t) = 0.00270 + 0.0533 \exp\left(\frac{-t}{0.0314}\right) + 0.0292 \exp\left(\frac{-t}{0.740}\right)$$

$$ST_{460}(t) = 2.98 \times 10^{-6} + 0.601 \exp\left(\frac{-t}{1.21}\right) + 1.97 \times 10^{-5} \exp\left(\frac{-t}{13.6}\right)$$

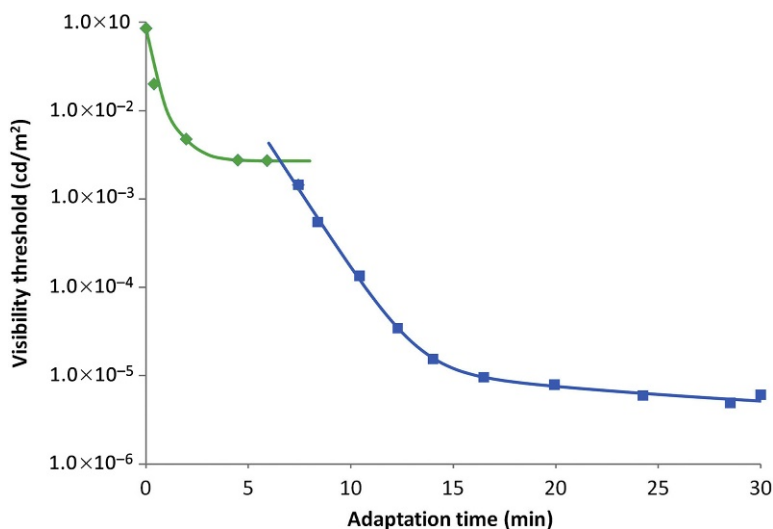


FIGURE 14 Dark adaptation of the human eye using violet light (wavelengths below 460 nm), after light adaptation to about 5000 cd/m^2 . Adapted from Davson (1962).

In these equations, the adaptation time is given in minutes and the threshold is in cd/m^2 . Subscripts 460 are used, as the adaptation curve was recorded for blue light below 460 nm.

The curves are based on the measurements on humans with normal eye sight, but variations of about an order of magnitude exist among individuals, so the graph and the corresponding equations should only be used as approximations. The human eye also suffers from a strong loss in sensitivity with age: a factor of 200 between the age of 20–80 (Valberg, 2007).

Figure 14 has been measured with violet light below 460 nm; as an approximation, we have assumed that it was measured at a constant wavelength of 460 nm. At other wavelengths, the curve for the PT remains the same, since the wavelength-dependent cone sensitivity is incorporated in the definition of the (photopic) candela, but the rod threshold will change. The shape of the curves for the photopic and scotopic threshold now becomes (Poelman and Smet, 2011):

$$\begin{aligned} \text{PT}(\lambda, t) &= \text{PT}_{460}(t) \\ \text{ST}(\lambda, t) &= \text{ST}_{460}(t) \cdot \frac{1699 \cdot V'(460)}{683 \cdot V(460)} \cdot \frac{P}{S} \end{aligned}$$

The fact that eye sensitivity not only changes with luminance, but also with time, makes it necessary to include this dark adaptation in the description of perceived brightness of low level light sources. Since this dark adaptation is—among others—a function of the previous light adaptation and the background illumination of our test samples, we cannot hope to describe the time-dependent brightness of persistent phosphors in a single set of equations. In the rest of this paragraph, we will only describe a very simple, but still realistic situation: a person is fully light adapted, subject to $5000 \text{ cd}/\text{m}^2$ white light, for which Fig. 14 is valid, when there is a power shutdown and the test person is left in the dark, except for our benchmark afterglow phosphor emergency exit signs.

In order to evaluate the brightness of the phosphors at any given time, their luminance should be compared to the visibility thresholds calculated in the equations for $\text{ST}(\lambda, t)$ and $\text{PT}(\lambda, t)$. The choice between these two thresholds, photopic or scotopic, should obviously depend on the contribution of rods and cones to vision at that given time. The latter is dependent on the luminance of the light source, and we will use a linear combination of both contribution. The visibility of the source can then be described by a “visibility index” (VI) as:

$$\text{VI} = X \frac{P}{\text{PT}(\lambda, t)} + (1 - X) \frac{P}{\text{ST}(\lambda, t)}$$

This equation can be simplified in case only one of the two types of vision is active. For night-blind people, the rods are inactive, and the visibility of a

source only depends on the sensitivity threshold of the rods. On the other hand, for rod monochromats, which have no active cones, only the value of the rod threshold plays a role. When both rods and cones are active, it is safe to assume that the relative weight of their contribution to vision is determined by their relative threshold: the most sensitive detector will contribute the most to vision. Therefore, the mixing parameter X in the above equation for VI should be dependent on the ratio of ST and PT at that specific time and for that specific wavelength distribution.

Several different formulas for X were evaluated, but the overall result on the VI was found to be relatively insensitive to the exact equation. Finally, the following very simple form was chosen:

$$X = \frac{ST}{ST + PT} = 1 - \frac{PT}{ST + PT}$$

When, for example, the ST is much higher than the PT, for example during the first few minutes of dark adaptation, vision is governed by photopic vision, and the mixing parameter will be close to 1. In the equation for the VI, it is seen that in this case, vision is indeed dominated by the contribution from the cones. From the symmetry of the equations for X and VI, it is seen that a similar reasoning applies when the rods are most sensitive.

The resulting VI as a function of time is shown for the four benchmark persistent phosphors in Fig. 15.

It is clear from Figs. 10, 12, 14, and 15 that the predicted apparent brightness is entirely different from both the photopic luminance and the mesopic luminance as per different models for mesopic photometry. The most

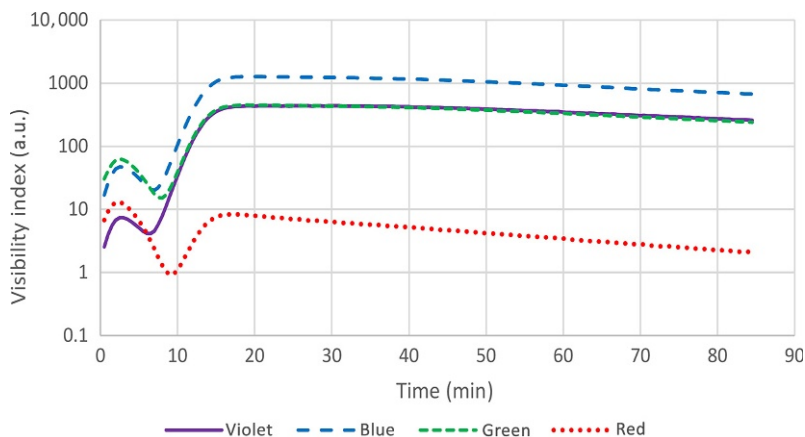


FIGURE 15 Apparent brightness, called “visibility index” VI, of the benchmark persistent phosphors, after charging for 5 min with 1000 lux of an unfiltered Xe-arc. The observer is fully light adapted at time zero. Adapted from *Poelman and Smet (2011)*.

pronounced effect is the wavelength shift of the eye sensitivity toward the blue; indeed, violet and red-emitting phosphors have a similar (photopic) luminance at all times (Fig. 10), while, except for the very first minutes of the decay curve, the red phosphor has a VI which is about two orders of magnitude lower than the other phosphors (Fig. 15).

The luminance of typical persistent phosphors follows a very fast nonexponential decay (Yen et al., 2006) (Fig. 10). Despite this rapid decay, after the first few minutes of dark adaptation, the visibility remains constant for a long time. The phenomena during the first minutes are due to the combined effect of an increasing eye sensitivity for both rods and cones, and the fast luminescence decay of the phosphor materials. After the rod–cone breakdown at around 8 min, the eye sensitivity keeps increasing at a slower rate (Fig. 13), which then almost perfectly compensates for the decreasing light output of the phosphor materials. It is well known by researchers in persistent luminescence, and probably also by people staring at the glowing stars on their bedroom ceiling, that the brightness of many glow in the dark phosphors remains constant for a very long time: this effect is seen in Fig. 15, but cannot be described using the usual photometric quantities or the models for mesopic vision.

6.4 Conclusions

For several years, both individual researchers and standards organizations like the CIE have undertaken research to develop better photometric practices in low light level conditions. This has led to several models which extend photometry into the mesopic region (TC-1-58, 2010). However, such models do not take into account the slow dark adaptation of the human eye and therefore provide no accurate description of observed brightness in the case of slowly decaying light intensities.

Due to the intricacies of human vision and its complex dependence on background illumination, light/dark adaptation, wavelength, age, angular dependence, etc. It is not possible to describe perceived brightness in a single set of equations or a single unit. Therefore, we limited ourselves to the simple case of a fully light adapted observer who is suddenly left in complete darkness, except for some low intensity persistent luminescent materials as emergency exit signs.

The proposed preliminary model takes into account the contribution of both rods and cones, their respective spectral sensitivities and dark adaptation behavior, and is summarized in a VI. While the model has to be refined in several ways, and made applicable to more realistic situations, it gives a much more reasonable description of the actually observed brightness than the currently used photometric quantities.

From the results obtained, it is seen that the VI of typical persistent phosphors is low during the first minutes, and then increases to a constant level. Therefore, it might be advantageous to include an additional high brightness phosphor with a short decay time (of the order of 10 min) in emergency lighting applications, in order to correct for this initial lack of brightness.

In support of the new model for mesopic photometry, as recommended by the CIE, we can see that the ratios of visibility indices for the different benchmark phosphors are almost identical to the ratios of the mesopic luminances. Therefore, while the CIE model cannot describe the subjectively observed brightness of persistent phosphors as a function of time, it is still very useful to evaluate materials with different emission spectra (and thus different S/P ratios) against each other.

7 PERSISTENT PHOSPHORS: MATERIALS

7.1 Introduction: Host and Dopants

The discovery of $\text{SrAl}_2\text{O}_4:\text{Eu,Dy}$ by Matsuzawa et al. (1996) and Murayam et al. (1994) marked the beginning of a renewed search for different and better persistent luminescent materials. Initially, this research was focused on other Eu^{2+} -doped alkaline earth aluminates, and it took a few years before other types of host materials and activators came into view. The number of materials where persistent luminescence has been observed has grown continuously over time. By now, over 250 combinations of host materials and activating ions have been described. This section aims to provide a comprehensive overview of these compounds and their luminescent properties. Further details can be found in the appropriate references mentioned in the table.

After 1995, the persistent luminescence research remained focused on Eu^{2+} -doped alkaline earth aluminates. It took a few years before other types of host materials and activators came into view. By now, only 10% of all known persistent phosphors use aluminates as a host, and about 25% are based on Eu^{2+} as the luminescent ion (Figs. 16 and 17).

The popularity of Eu^{2+} as activator is not only based on the historical reasons. It shows excellent afterglow properties in a large number of host lattices, with an afterglow duration which is often longer than 5 h. Additionally, its broadband emission depends strongly on the host lattice and can be modified by changing the composition of the host lattice or the local coordination of the ion. Finally, the persistent luminescence can be induced via excitation into the lowest $4f^65d$ state, which is favorable in conditions where the energy of the excitation light is limited, e.g., in indoor applications of safety signage.

The research on persistent luminescent materials with other dopant ions is largely driven by the lack of efficient red persistent phosphors. While blue or green afterglow is rather common in oxide hosts, it is much more difficult to

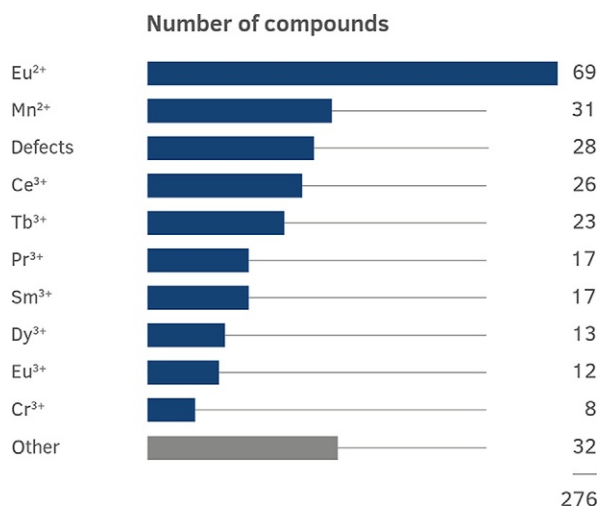


FIGURE 16 Number of known persistent luminescent compounds grouped by luminescent center.

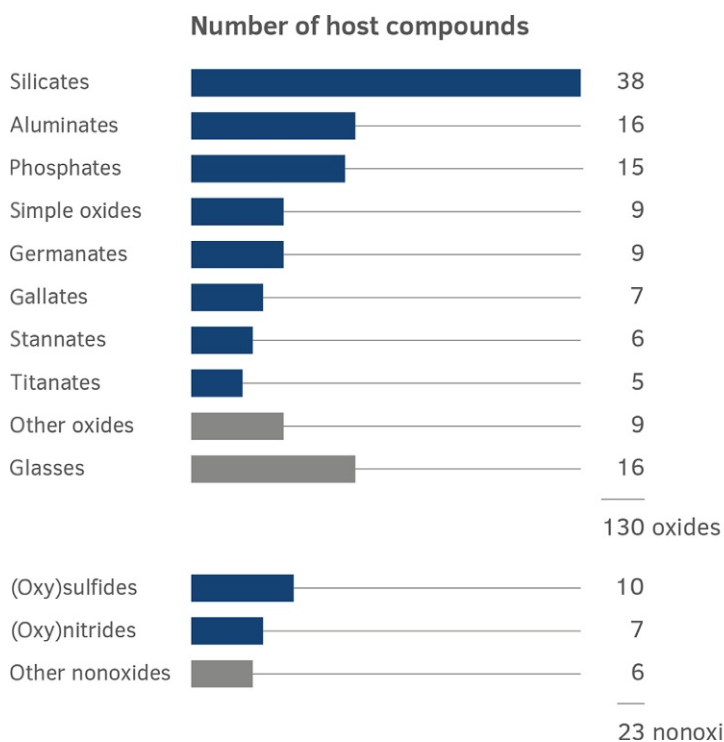


FIGURE 17 Number of known host compounds where persistent luminescence has been reported.

find a suitable host material with sufficient red shift in order to obtain red (persistent) luminescence. Although there are a number of red-emitting Eu^{2+} -doped persistent phosphors, such as CaS:Eu,Ln (Jia, 2006a; Jia et al., 2000a,c) and $\text{Ca}_2\text{Si}_5\text{N}_8\text{:Eu,Ln}$ (Miyamoto et al., 2009; Van den Eeckhout et al., 2009), the choice is limited and the host lattices are chemically unstable or difficult to prepare. This is especially unfortunate, since red afterglow phosphors are strongly desired for applications in safety signage, paints, and as tracer particles for *in vivo* medical imaging (Section 10).

A popular choice for long-wavelength luminescence is Mn^{2+} , known for its typical yellow–red emission in octahedral sites (Yen et al., 2007). In several compounds, an energy transfer from Eu^{2+} to Mn^{2+} has been observed, leading to a red afterglow color originating from Mn^{2+} , but with a long afterglow duration defined by Eu^{2+} . The NIR emission of Cr^{3+} is an interesting candidate for medical imaging (Section 10).

Not only red-emitting activators are being explored. Other common choices are the different trivalent rare earth ions, such as Ce^{3+} and Tb^{3+} . The spectral properties of Ce^{3+} are to large extent similar to those of Eu^{2+} , with 4f–5d transitions driving the excitation and the emission. Yet, significantly less Ce^{3+} -based persistent phosphors have been reported. This is presumably related to the observation that excitation into the lowest 5d excited state of Ce^{3+} is often not sufficient to lead to trap filling at RT, which necessitates excitation in the UV (Ueda et al., 2013). This behavior was related to the energy barrier between the lowest 5d excited state and the bottom of the conduction band, which is typically larger for Ce^{3+} compared to Eu^{2+} when incorporated in the same host. However, band gap engineering was possible by compositionally modifying the $\text{Y}_3\text{Al}_5\text{O}_{12}\text{:Ce}$ garnet, positioning the 5d levels in such a way that trapping can occur after excitation into the lowest 5d excited state (Ueda et al., 2014a,b). In that respect, the persistent luminescence of Yb^{2+} has hardly been explored, despite its similarity to Eu^{2+} (Kanno et al., 2013; Yu et al., 2015).

The other trivalent lanthanides showing $4f^n\text{--}4f^n$ emission have the main drawback that ultraviolet light (often with $\lambda < 300$ nm) is required to fill traps, despite their excellent emissive properties, which have proven beneficial in for instance fluorescence lighting ($\text{Tb}^{3+}, \text{Eu}^{3+}$). An interesting case is Dy^{3+} , which shows a whitish emission color due to three different emissions around 480, 575, and 665 nm. Such a white emission is very difficult to obtain with Eu^{2+} doping alone. Finally, several compounds are known to exhibit an afterglow without the (deliberate) addition of dopants, purely based on the intrinsic luminescence of the host material.

An enormous variety of host materials are used as (general) luminescent compounds, but when it comes to persistent luminescence, the number of known hosts is relatively low. The majority of research is concentrated around the silicates, with $\text{Sr}_2\text{MgSi}_2\text{O}_7$ as most famous representative, and the

aluminates, represented by SrAl_2O_4 . These two main classes of materials add up to over one-third of all host compounds where persistent luminescence has been observed. All together, the oxides represent about 85% of all host lattices (Fig. 17). The sulfides, having the longest recorded history of all persistent luminescent compounds (Section 2.2), form the largest group of nonoxide hosts.

7.2 Literature Overview: Notes

Below, we provide an extensive overview of all compounds where persistent luminescence has been reported. It contains an update on the overview given in Van den Eeckhout et al. (2010) for Eu^{2+} -based persistent phosphors and in Van den Eeckhout et al. (2013b) for persistent phosphors with other dopant ions.

For every combination of host compound and activator relevant references are indicated in the last column. In the case of energy transfer between two different dopants or luminescent centers both the sensitizer and the activator are indicated. We use the symbol “ \gg ” for efficient energy transfer and “ $>$ ” for partial energy transfer, as derived from the emission spectra. For clarity, the materials are divided into five groups: silicates, aluminates, other oxides, nonoxides, and glasses. If a property was not mentioned explicitly in the text of the reference(s), but inferred from it or from a figure, it is put between parentheses.

The afterglow durations were taken directly from the mentioned references. However, not all of these were measured in a single, clearly defined way. The most common criterion is the visibility by the naked, dark-adapted eye. Only a few authors use the threshold value of 0.3 mcd/m^2 (see Section 5.1). Also the exact excitation conditions (wavelength, intensity, and duration) are not always clear, although 254 nm is a common excitation wavelength. For details on the excitation conditions, we refer to the mentioned references. A more thorough discussion on these issues can be found in Section 8.2.1.

The emission colors are abbreviated as near-UV (NUV), indigo (I), blue (B), green (G), yellow (Y), orange (O), red (R), white (W), pink (P), near-IR (NIR), and infrared (IR).

7.3 Silicates

The silicates are used as the host crystal for a large part of the reported persistent luminescent compounds, both with Eu^{2+} and other luminescent ions. Especially, the alkaline earth aluminum and magnesium silicates have been studied extensively. Some of the longest afterglow times (>5 – 10 h) have been observed in $\text{Sr}_2\text{MgSi}_2\text{O}_7:\text{Eu}^{2+},\text{Dy}^{3+}$ (Lin et al., 2001b) and in rare earth-doped

CdSiO₃, although the role of host and self-trapped exciton (STE) luminescence remain the subject of discussion in this latter compound (Kuang and Liu, 2006c; Liu et al., 2005c). A full list of persistent luminescent silicates can be found in Table 6.

7.4 Aluminates

Ever since the discovery of SrAl₂O₄:Eu,Dy, the aluminates have been at the center of the attention in persistent luminescent research, especially the Eu²⁺-based materials. The aluminate compounds that are known to exhibit persistent luminescent properties are listed in Table 7.

The alkaline earth aluminates MA₂O₄ ($M = \text{Ca, Sr, Ba}$) and Sr₄Al₁₄O₂₅ are by far the most studied family of persistent luminescent materials. It is interesting to note that, as mentioned before, even the noncodoped SrAl₂O₄:Eu shows a considerable afterglow, indicating that the presence of codopants is not imperative to obtain persistent luminescence.

7.5 Other Oxides

The oxides make up the majority of persistent luminescent compounds. Besides the silicates and the aluminates, many more types have been explored, also those in which Eu²⁺ cannot be stabilized. This includes, for example, the stannates, titanates, and germanates. An exceptional case is the NIR afterglow of Cr³⁺ in LiGa₅O₈ and Zn₃Ga₂Ge₂O₁₀ (Section 10.3), which lasts several weeks and could be used for night-vision surveillance or *in vivo* bioimaging (Liu et al., 2013; Pan et al., 2012). Allix et al. found that the latter compound is a variant of the solid solution, Zn_{1+x}Ga_{2-2x}Ge_xO₄:Cr³⁺, for $x = 0.5$. They report even better afterglow properties for the composition with $x = 0.1$ (Allix et al., 2013).

It should be noted again that there is no agreed definition of the afterglow duration for wavelengths which cannot be detected by the human eye. This makes it difficult to compare the various reported afterglow durations. A full list of persistent luminescent oxides, other than silicates and aluminates, can be found in Table 8.

7.6 Nonoxide Hosts

The sulfides are the most important nonoxide compounds in persistent luminescence. In fact, the famous Bologna Stone (Section 2.1) consisted mainly of copper-doped BaS (Lastusaari et al., 2012). Nowadays, the use of ZnS:Cu,Co has much decreased in favor of SrAl₂O₄:Eu,Dy. Y₂O₂S:Eu³⁺, Ti⁴⁺,Mg²⁺ is one of the few commercialized red-emitting phosphors. Nevertheless, the afterglow intensity is much weaker than the Eu²⁺-doped

TABLE 6 Persistent Luminescent Silicates

Host Material	Activators	Emission Maximum (nm)	Afterglow Emission	Afterglow Duration	References
Ca ₂ Al ₂ SiO ₇	Ce ³⁺	400–417 (B)	Identical	>1 h	Kodama et al. (1999, 2000) , Yamaga et al. (2002) , and Wu et al. (2011a)
	Ce ³⁺ ≫ Mn ²⁺	550 (Y)	Identical	>10 h	Wang et al. (2003a)
Ca _{0.5} Sr _{1.5} Al ₂ SiO ₇	Ce ³⁺ > Tb ³⁺	386, 483 + 542 + 591 (W)	B–W	>1 min	Ito et al. (2006)
Sr ₂ Al ₂ SiO ₇	Ce ³⁺	400 (NUV)	Identical	(>2 min)	Gutiérrez-Martín et al. (2010)
	Ce ³⁺ > Dy ³⁺	408, 491 + 573 (W)	(Identical)	±1 h	Gong et al. (2010)
	Ce ³⁺ > Tb ³⁺	410, 482 + 543 + 588 (W)	(Identical)	(>1 min)	Pan et al. (2008)
	Eu ²⁺	485 (B/G)	Identical	>2 h	Ding et al. (2009)
Sr ₃ Al ₁₀ SiO ₂₀	Eu ²⁺	465 (B)	Identical	>6 h	Kuang et al. (2005a, 2006b)
CaAl ₂ Si ₂ O ₈	Eu ²⁺	435 (B)	435/510 (B)	>3 h	Wang et al. (2004c) and Clabau et al. (2008)
	Eu ²⁺ > Mn ²⁺	418, 580 (B)	Identical	>1 h	Zhang et al. (2012b)
	Mn ²⁺	?	?	±20 min	Chen et al. (2011)
Sr ₆ Al ₁₈ Si ₂ O ₃₇	Eu ²⁺	469 (B)	Identical	±4 h	Zhao et al. (2014)

Continued

TABLE 6 Persistent Luminescent Silicates—Cont'd

Host Material	Activators	Emission Maximum (nm)	Afterglow Emission	Afterglow Duration	References
CaMgSi ₂ O ₆	Dy ³⁺	480+575+667 (W)	Identical	±2 h	Chen et al. (2009)
	Eu ²⁺	445 (B)	Identical	>4 h	Jiang et al. (2003a, 2004)
	Eu ²⁺ > Mn ²⁺	450, 580+680 (?)	Identical	(±30 min)	Lecointre et al. (2010b)
	Mn ²⁺	580+680 (R)	680 nm (R)	>1 h	Bessiere et al. (2012), Lecointre et al. (2010b), and Maldiney et al. (2011a, 2012a)
SrMgSi ₂ O ₆	Dy ³⁺	455, 576 (B)	Identical	>5 min	He et al. (2007)
	Mn ²⁺	455, 612 (P)	(Identical)	(±15 min)	He et al. (2007)
Ba ₂ Mg ₂ Si ₂ O ₇	Ce ³⁺ > Mn ²⁺	408, 680 (R)	(Identical)	>2 h	Gong et al. (2012)
	Eu ²⁺ > Mn ²⁺	400, 630–680 (R)	(Identical)	>2 min	Abe et al. (2006), Aitasalo et al. (2008), and Ye et al. (2007a)
	Mn ²⁺	630–680 (R)	(Identical)	>30 min	Gong et al. (2012) and Ye et al. (2007b)
Ba ₂ MgSi ₂ O ₇	Eu ²⁺	505 (G)	Identical	>5 h	Aitasalo et al. (2005, 2007b)
Ca ₂ MgSi ₂ O ₇	Dy ³⁺	480+575+667 (W)	Identical	>3 h	Chen et al. (2009) and Lin et al. (2009)
	Eu ²⁺	515–535 (G)	Identical	>5 h	Aitasalo et al. (2007a), Blasse et al. (1968), and Jiang et al. (2003a)

Sr ₂ MgSi ₂ O ₇	Dy ³⁺	441, 480+575 +668 (W)	Only Dy ³⁺	±40 min	Liu et al. (2007)
	Eu ²⁺	470 (B)	Identical	>10 h	Lin et al. (2003b, 2001b) and Liu et al. (2005b)
Ba ₃ MgSi ₂ O ₈	Eu ²⁺	440 (B)	Identical	>1 h	Lin et al. (2003d)
Ca ₃ MgSi ₂ O ₈	Dy ³⁺	480+575+667 (W)	Identical	>5 min	Chen et al. (2009)
	Eu ²⁺	470 (B)	Identical	>5 h	Lin et al. (2001c, 2003d)
Sr ₃ MgSi ₂ O ₈	Eu ²⁺	460 (B)	Identical	>10 h	Lin et al. (2003d) and Sabbagh Alvani et al. (2005)
	Eu ²⁺ > Mn ²⁺	457, 670 (?)	Identical	>2 h	Gong et al. (2011)
SrMgAl ₂ SiO ₇	Ce ³⁺	402 (NUV)	(Identical)	>2 min	Gutiérrez-Martín et al. (2010)
Ca ₁₄ Mg ₂ (SiO ₄) ₈	Eu ²⁺	505 (G)	523 (G)	±30 min	Sun et al. (2014b)
CaSnSiO ₅	Intrinsic	420 (B)	(Identical)	(>1 min)	Xu et al. (2013c)
Ca ₃ SnSi ₂ O ₉	Dy ³⁺	485+573 (W)	Identical	>1 h	Xu et al. (2013b,c)
	Pr ³⁺	489 (B)	(Identical)	(>15 min)	Xu et al. (2013c)
	Sm ³⁺	600 (R)	(Identical)	(>10 min)	Xu et al. (2013c)
	Tb ³⁺	542 (G)	(Identical)	(>1 h)	Xu et al. (2013c)
	Defects	426 (B)	(Identical)	(±10 min)	Xu et al. (2011c)
	Dy ³⁺	426, 484+572 +670 (W)	(Identical)	(±10 min)	Xu et al. (2011c) and Wei et al. (2009)

Continued

TABLE 6 Persistent Luminescent Silicates—Cont'd

Host Material	Activators	Emission Maximum (nm)	Afterglow Emission	Afterglow Duration	References
	Pr ³⁺	426, 488 (B–G)	(Identical)	(±10 min)	Xu et al. (2011c)
	Sm ³⁺	426, 565+600+650 (R)	(Identical)	(±10 min)	Xu et al. (2011c)
	Tb ³⁺	426, 495+542+590 (G)	(Identical)	(±10 min)	Xu et al. (2011c)
Ca _{0.2} (ZnMg) _{0.9} Si ₂ O ₆	Eu ²⁺ ≫ Mn ²⁺	450, 580+680 (NIR)	Identical	±1 h	le Masne de Chermont et al. (2007) and Lecointre et al. (2009)
Ca ₂ ZnSi ₂ O ₇	Eu ²⁺	580 (Y)	(Identical)	>10 h	Jiang et al. (2013)
Sr ₂ ZnSi ₂ O ₇	Eu ²⁺	460 (B)	Identical	>5 min	Jiang et al. (2004) and Wang et al. (2005c)
	Eu ³⁺	617 (R)	Identical	>20 s	Lin et al. (2012)
CdSiO ₃	Intrinsic/STE	380+467+560 (?)	±420 (B)	±5 h	Kuang and Liu (2006c) and Liu et al. (2005c)
	Dy ³⁺	410, 486+580 (W)	(Identical)	>5 h	Lei et al. (2004d) and Liu et al. (2005d)
	Eu ³⁺ , Mn ²⁺	587, 610 (O)	(Identical)	>1 h	Qu et al. (2009)
	Mn ²⁺	575–587 (O)	Identical	±1–5 h	Kuang et al. (2006b) , Lei et al. (2004c) , and Qu et al. (2010, 2012b)

	Mn ²⁺ , Tb ³⁺	486+548, 587 (O)	(Identical)	>1 h	Qu et al. (2012a)
	Pb ²⁺	498 (G)	Identical	>2 h	Kuang and Liu (2006a)
	STE > Dy ³⁺	420, 480+575 (W)	Identical	±5 h	Liu et al. (2005c)
	STE > Eu ³⁺	420, 615 (R)	Identical	±5 h	Liu et al. (2005c)
	STE > Pr ³⁺	420, 600 (R)	Identical	±5 h	Liu et al. (2005c) and Kuang and Liu (2006b)
	STE > Sm ³⁺	420, 565+600 (P)	Identical	±5 h	Liu et al. (2005c) and Lei et al. (2004a)
	STE > Tb ³⁺	420, 485+540 (G)	Identical	±5 h	Liu et al. (2005c)
	Tb ³⁺	495+545+590 (G)	Identical	?	Rodrigues et al. (2012)
Lu ₂ SiO ₅	Ce ³⁺	400+430 (B)	(Identical)	>3 h	Dorenbos et al. (1994) and Yamaga et al. (2012)
Ba ₃ SiO ₅	Eu ²⁺	590 (O)	Identical	(>15 min)	Yamaga et al. (2005)
Sr ₃ SiO ₅	Eu ²⁺	570 (Y)	Identical	±6 h	Sun et al. (2008)
MgSiO ₃	Eu ²⁺ ≫ Mn ²⁺	(456), 660–665 (?)	665 (R)	±4 h	Lin et al. (2008a) and Wang et al. (2003a)
Mg ₂ SiO ₄	Mn ²⁺	650 (R)	(Identical)	±20 min	Lin et al. (2008b)
NaAlSiO ₄	Eu ²⁺	550 (Y)	Identical	>30 min	Pang et al. (2014b)
SrSiO ₃	Dy ³⁺	480+572+664 (W)	Identical	±1 h	Kuang et al. (2006a)

Continued

TABLE 6 Persistent Luminescent Silicates—Cont'd

Host Material	Activators	Emission Maximum (nm)	Afterglow Emission	Afterglow Duration	References
Ba ₂ SiO ₄	Eu ²⁺	510 (G)	Identical	(±5 min)	Yamaga et al. (2005)
Sr ₂ SiO ₄	Dy ³⁺	480+575+665 (W)	Identical	>1 h	Kuang and Liu (2005)
	Eu ²⁺	480 (G)	Identical	>5 min	Lakshminarasimhan and Varadaraju (2008)
	Tb ³⁺	486+546 (G)	Identical	±30 min	Wang et al. (2014b)
Ca ₃ Si ₂ O ₇	Eu ²⁺	620 (O)	Identical	>15 min	Jin et al. (2014c)
Zn ₂ SiO ₄	Mn ²⁺	? (G)	?	(>5 min)	Avouris and Morgan (1981) and Garlick and Gibson (1948)
BaZrSi ₃ O ₉	Intrinsic/Ti ⁴⁺	460–470 (B)	Identical	>20 s	Iwasaki et al. (2009) and Takahashi et al. (2008)
Ca ₂ ZrSi ₄ O ₁₂	Intrinsic	490 (G)	Identical	>1 h	Feng et al. (2013)
Gd _{0.33} (SiO ₄) ₆ O ₂	Sm ³⁺	570+606+648 (R)	(Identical)	>20 min	Li et al. (2013)
Ba ₄ (Si ₃ O ₈) ₂	Eu ²⁺	494 (B)	Identical	(±40 min)	Wang et al. (2014a)

See [Section 7.2](#) for symbols and notation.

TABLE 7 Persistent Luminescent Aluminates

Host Material	Activators	Emission Maximum (nm)	Afterglow Emission	Afterglow Duration	References
BaAl ₂ O ₄	Ce ³⁺	402+450 (B)	(Identical)	>10 h	Jia et al. (2002c)
	Eu ²⁺	500 (G)	Identical	>2 h	Lin et al. (2001d) and Sakai et al. (1999)
CaAl ₂ O ₄	Ce ³⁺	400 (I)	±413	>10 h	Jia et al. (2002b, 2003) and Jia and Yen (2003b)
	Ce ³⁺ ≫ Mn ²⁺	525 (G)	(Identical)	>10 h	Wang et al. (2003a)
	Ce ³⁺ ≫ Tb ³⁺	543 (G)	Identical	>10 h	Jia et al. (2002b, 2003)
	Dy ³⁺	477+491+577+668 (W)	Identical	>30 min	Liu et al. (2005a)
	Eu ²⁺	440 (B)	430	>5 h	Hölsä et al. (2001), Katsumata et al. (1998a), and Lin et al. (2003c)
	Eu ²⁺ > Mn ²⁺	440, 545 (G)	±440 (B)	(>3 h)	Xu et al. (2009)
	Tb ³⁺	493+543+590+621 (G)	Identical	±1 h	Jia et al. (2002b,d)
MgAl ₂ O ₄	Defects	520 (G)	Identical	±1 h	Jia and Yen (2003a)
	Cr ³⁺	260, 520, 710	520, 710	(>2 h)	Lorincz et al. (1982)
	Tb ³⁺	(G)	?	±1 h	Nakagawa et al. (2003)

Continued

TABLE 7 Persistent Luminescent Aluminates—Cont'd

Host Material	Activators	Emission Maximum (nm)	Afterglow Emission	Afterglow Duration	References
SrAl ₂ O ₄	Ce ³⁺	375–385+427 (B)	Only 385	>10 h	Jia (2006b), Jia et al. (2007), and Xu et al. (2011a)
	Ce ³⁺ > Mn ²⁺	375, 515 (G)	Identical	(±5 h)	Xu et al. (2011a)
	Eu ²⁺	520 (G)	Identical	>30 h	Katsumata et al. (1997) and Matsuzawa et al. (1996)
	Eu ²⁺ > Ce ³⁺	515+760 (G)	(Identical)	(>15 min)	Teng et al. (2014)
	Eu ²⁺ > Er ³⁺	525, 1530 (G/IR)	Mainly 525	±10 min	Yu et al. (2009)
	Eu ²⁺ > Nd ³⁺	515, 882 (G/NIR)	Mainly 515	>15 min	Teng et al. (2011)
CaAl ₄ O ₇	Ce ³⁺	325, 420 (B)	Only 420	>10 h	Jia (2006b)
SrAl ₄ O ₇	Eu ²⁺	480 (B)	Identical	>3 h	Katsumata et al. (1998b) and Preethi et al. (2004)
BaCa ₂ Al ₈ O ₁₅	Eu ²⁺	435–440 (B)	Identical	>15 min	Wei et al. (2013) and Yerpude et al. (2013)
Ca ₁₂ Al ₁₄ O ₃₃	Eu ²⁺	440 (I)	Identical	>10 min	Zhang et al. (2003)
BaAl ₁₂ O ₁₉	Eu ²⁺	440 (B)	(Identical)	(±10 min)	Matsui et al. (2013)
SrAl ₁₂ O ₁₉	Eu ²⁺	400 (B)	Identical	>3 min	Katsumata et al. (1998b)
Sr ₃ Al ₂ O ₆	Eu ²⁺	510/610 (disputed)	Identical	(Disputed)	Chang et al. (2010) and Zhang et al. (2007a)

Sr ₄ Al ₁₄ O ₂₅	Ce ³⁺	472+511 (B/G)	(Identical)	±10 min	Sharma et al. (2009)
	Eu ²⁺	490 (B)	Identical	>20 h	Lin et al. (2001a, 2002) and Nakazawa et al. (2006)
	Eu ²⁺ > Cr ³⁺	490, 693 (B/R)	Mainly 490	>2 h	Luitel et al. (2009) and Zhong et al. (2006a,b)
	Tb ³⁺	542 (G)	±380 (B)	?	Zhang et al. (2010b)
	Yb ²⁺	407+510	(Identical)	(>15 min)	Kanno et al. (2013)
BaMgAl ₁₀ O ₁₇	Eu ²⁺	450 (B)	Identical	>5 min	Jüstel et al. (2003)
SrMgAl ₁₀ O ₁₇	Eu ²⁺	460 (B)	515 (G)	>3 min	Wanjun et al. (2009)
Y ₃ Al ₅ O ₁₂	Ce ³⁺	525 (Y)	Identical	±2 min	Mu et al. (2011b) and Zhang et al. (2011c)
	Mn ²⁺	580 (Y/O)	585 (O)	±18 min	Mu et al. (2011a)
	Defects, Pr ³⁺	300–460, 490 +610 (?)	380, 490 +610	?	Zhang et al. (2011b)
CaYAl ₃ O ₇	Ce ³⁺	425 (B)	(Identical)	±min	Kodama et al. (1999)

See [Section 7.2](#) for symbols and notation.

TABLE 8 Other Oxide Persistent Luminescent Compounds

Host Material	Activators	Emission Maximum (nm)	Afterglow Emission	Afterglow Duration	References
CaO	Eu ³⁺	594+616 (R)	(O)	>2 h	Fu (2000, 2002)
	Pr ³⁺	489+620 (O/R)	Identical	±1 h	Jin et al. (2013e)
	Sm ³⁺	400, 576 +616 (?)	Only Sm ³⁺ (O)	±40 min	Jin et al. (2014b)
	Tb ³⁺	550 (G)	(Identical)	?	Kuang et al. (2005b)
Ga ₂ O ₃	Cr ³⁺	720 (NIR)	Identical	>4 h	Lu et al. (2011)
HfO ₂	Defects	480 (bluish W)	Identical	>1 min	Pejakovic (2010) and Wiatrowska et al. (2010)
Lu ₂ O ₃	Eu ³⁺	611 (R)	583+594 +611	>3 min	Zych and Trojan-Piegza (2007)
	Tb ³⁺	490+550 (G)	Identical	±5–7 h	Chen et al. (2012), Trojan-Piegza et al. (2008, 2009), and Zych et al. (2003)
SnO ₂	Sm ³⁺	567+607 +625 (R)	Identical	±40 min	Zhang et al. (2012d)
SrO	Eu ³⁺	594+616 (O)	Identical	>1 h	Fu (2002)
	Pb ²⁺	390 (violet)	Identical	>1 h	Fu (2002)
	Tb ³⁺	543 (G)	(Identical)	?	Kuang et al. (2005b)

Y ₂ O ₃	Eu ³⁺	612 (R)	(Identical)	±90 min	Lin et al. (2003a) and Xie et al. (2010)
(Zn,Mg)O	Unknown	520 (O)	(Identical)	±10 min	Zhang et al. (2004a, 2006b)
ZrO ₂	Sm ³⁺	570+614 (R)	(Identical)	±15 min	Zhao and Wang (2012)
	Ti (?)	(353+) 470–500 (B)	Only 470 +500	±1 h	Carvalho et al. (2012), Cong et al. (2007, 2008), Liu et al. (2010), and Wang et al. (2012b)
Ba ₂ SnO ₄	Sm ³⁺	580+611 +623 (R)	(Identical)	±20 min	Xu et al. (2011b) and Zhang et al. (2012c)
Ca ₂ SnO ₄	Eu ³⁺	585+618 +633 (R)	(Identical)	±50 min	Gao et al. (2011) and Lei et al. (2010e)
	STE	410+466 (B)	(Identical)	±3 h	Gao et al. (2011)
	STE≫Eu ³⁺	585+618 +633 (R)	(Identical)	±100 min	Gao et al. (2011)
	Pr ³⁺	450, 605 +625 (R)	605+625 (R)	±20 min	Jin et al. (2013b)
	Sm ³⁺	566+609 +653 (R)	Identical	>1–7 h	Ju et al. (2011a,b), Lei et al. (2011), and Xu et al. (2011b)
	Tb ³⁺	435, 483+545 (B/G)	483+545 (G)	±3 h	Jin et al. (2013a)
Mg ₂ SnO ₄	Defects	490–495 (G)	Identical	±5 h	Zhang et al. (2010a, 2011a, 2012e)
	Mn ²⁺	500 (G)	Identical	>5 h	Lei et al. (2006)
Sr ₂ SnO ₄	Sb ³⁺	550 (Y–W)	Identical	>2 min	Wang et al. (2012a)
	Sm ³⁺	582+624 +672 (R)	Identical	>1 h	Xu et al. (2010, 2011b), Lei et al. (2010a), and Yu et al. (2011)
	Tb ³⁺	542 (G)	(Identical)	±8 min	Qin et al. (2012)

Continued

TABLE 8 Other Oxide Persistent Luminescent Compounds—Cont'd

Host Material	Activators	Emission Maximum (nm)	Afterglow Emission	Afterglow Duration	References
CaSnO ₃	Nd ³⁺	903+950 +1079 (NIR)	Identical	(±1 h)	Kamimura et al. (2014)
	Pr ³⁺	488+541 +620+653 (W)	Identical	>3 h	Lei et al. (2007b)
	Sm ³⁺	566+601 +649+716 (R)	(Identical)	?	Lei et al. (2007a)
	Tb ³⁺	491+545 +588+622 (G)	Identical	±4 h	Lei et al. (2007b) , Liang et al. (2013) , and Liu and Liu (2005b)
Sr ₃ Sn ₂ O ₇	Sm ³⁺	580+621 +665+735 (R)	Identical	>1 h	Lei et al. (2010d)
Ca ₉ Bi(PO ₄) ₇	Eu ²⁺	475 (B–G)	Identical	±5 h	Jia et al. (2014)
Ca ₉ Gd(PO ₄) ₇	Mn ²⁺	602+628, 660 (R)	Only 660 (R)	(>20 min)	Bessière et al. (2012)
Ca ₉ Lu(PO ₄) ₇	Mn ²⁺	660 (R)	Identical	(>20 min)	Bessière et al. (2012)
Ca ₉ Tb(PO ₄) ₇	Tb ³⁺	490+545 (G)	(Identical)	(>20 min)	Bessière et al. (2012)
Ca ₃ (PO ₄) ₂	Mn ²⁺	645–660 (R)	Identical	±1 h	Bessiere et al. (2013) and Lecointre et al. (2011a)

SrMg ₂ (PO ₄) ₂	Eu ²⁺	400 (B)	Identical	>2 h	Liu et al. (2006b)
	Eu ³⁺ , Zr ⁴⁺	500, 588 (W)	(Identical)	±1.5 h	Wang et al. (2011b)
Ca ₃ Mg ₃ (PO ₄) ₄	Eu ²⁺	433 (B)	Identical	(>15 min)	Ju et al. (2014b)
SrZn ₂ (PO ₄) ₂	Eu ²⁺ > Mn ²⁺	421, 547 (W)	(Identical)	±1 min	Jeong et al. (2009)
	Mn ²⁺	547 (G)	(Identical)	±1 min	Jeong et al. (2009)
Zn ₃ (PO ₄) ₂	Hf ⁴⁺	470 (B)	Identical	>40 min	Peng et al. (2008)
	Mn ²⁺	616 (R)	Identical	>2 h	Song et al. (2007) and Wang et al. (2004a,b, 2005a)
	Mn ²⁺ , Zr ⁴⁺	475, 616 (B/R)	Mainly 616	±3 h	Wang et al. (2005b)
YPO ₄	Pr ³⁺	600+620 (O/R)	(Identical)	>30 min	Lecointre et al. (2011b)
LiBaPO ₄	Eu ²⁺	470 (B)	Identical	(>20 min)	Ju et al. (2014a) and Zhang et al. (2011d)
Ca ₂ P ₂ O ₇	Eu ²⁺	415 (B)	Identical	>6 h	Pang et al. (2009b)
Sr ₂ P ₂ O ₇	Eu ²⁺	420 (B)	Identical	>8 h	Pang et al. (2009a)
Zn ₂ P ₂ O ₇	Mn ²⁺	690 (R)	Identical	±10 h	Pang et al. (2014a)
	Tm ³⁺	368+454 (B)	Identical	(±10 h)	Pang et al. (2014a)
Ba ₃ P ₄ O ₁₃	Eu ²⁺	450 (B)	(Identical)	±85 min	Guo et al. (2015)
Ca _{0.8} Mg _{0.2} TiO ₃	Pr ³⁺	613 (R)	(Identical)	?	Zhang et al. (2004d)
CaTiO ₃	Pr ³⁺	612 (R)	Identical	>2 h	Boutinaud et al. (2009a) , Jia et al. (2006) , Pan et al. (2003) , and Zhang et al. (2007b,c)
(Ca,Zn)TiO ₃	Pr ³⁺	612 (R)	(Identical)	±20 min	Haranath et al. (2006) , WanJun and Donghua (2007) , and Yuan et al. (2009)

Continued

TABLE 8 Other Oxide Persistent Luminescent Compounds—Cont'd

Host Material	Activators	Emission Maximum (nm)	Afterglow Emission	Afterglow Duration	References
$\text{Ca}_2\text{Zn}_4\text{Ti}_{16}\text{O}_{38}$	Pr^{3+}	614 + 644 (R)	Mainly 614	?	Lian et al. (2010) and Qi et al. (2009)
$\text{La}_2\text{Ti}_2\text{O}_7$	Pr^{3+}	611 (R)	Identical	>1 h	Chu et al. (2010)
$\text{CaAl}_2\text{B}_2\text{O}$	Eu^{2+}	465 (B)	Identical	>1 h	Li and Su (2006b)
$\text{LiSr}_4(\text{BO}_3)_3$	Eu^{2+}	630 (O)	Identical	± 20 min	Li et al. (2014a)
$\text{Gd}_2\text{O}_2\text{CO}_3$	Yb^{3+}	970 (NIR)	Identical	± 6 days	Caratto et al. (2014)
$\text{Gd}_3\text{Ga}_5\text{O}_{12}$	Ce^{3+}	697 + 716 (R)	(Identical)	?	Blasse et al. (1993) and Kostyk et al. (2009)
$\text{Gd}_3\text{Al}_2\text{Ga}_3\text{O}_{12}$	$\text{Ce}^{3+}, \text{Cr}^{3+}$	540, 700 (Y)	Identical	(>2 h)	Ueda et al. (2014b)
MgGa_2O_4	Mn^{2+}	506 (G)	(Identical)	?	Matsui et al. (2000)
LiGa_5O_8	Cr^{3+}	716 (NIR)	Identical	>1000 h	Liu et al. (2013)
ZnGa_2O_4	Defects	410 + 540 (W)	Identical	± 40 min	Zhuang et al. (2012)
	Cr^{3+}	650–750 (R)	Identical	± 1 h	Allix et al. (2013) and Bessi�re et al. (2011)
	Mn^{2+}	504 (G)	(Identical)	>15 min	Uheda et al. (1997)
$(\text{Zn}, \text{Mg})\text{Ga}_2\text{O}_4$	Mn^{2+}	505 (G)	(Identical)	>15 min	Uheda et al. (1997)
$\text{SrGa}_{12}\text{O}_{19}$	Cr^{3+}	750 (NIR)	(Identical)	>2 h	Xu et al. (2014)
$\text{Cd}_2\text{Ge}_7\text{O}_{16}$	Mn^{2+}	585 (O)	Identical	>3 h	Che et al. (2008a)
	Pb^{2+}	352 + 497 (B)	Only 497	± 10 min	Yi et al. (2004)
MgGeO_3	Mn^{2+}	650–670 (R)	Identical	± 30 min	Cong et al. (2009) and Iwasaki et al. (2003)

Zn ₂ GeO ₄	Bi ³⁺	455 (B)	Identical	±3 min	Zhang et al. (2014a)
	Eu ²⁺	474 (B)	Identical	±1 h	Wan et al. (2014)
	Mn ²⁺	530 (G)	Identical	>2 h	Sun (2012) and Wan et al. (2014)
Li ₂ ZnGeO ₄	Intrinsic	(B)	(Identical)	±5 h	Jin et al. (2014d)
	Mn ²⁺	(G)	(Identical)	±8 h	Jin et al. (2014d)
CaZnGe ₂ O ₆	Dy ³⁺	(W)	(Identical)	>3 h	Che et al. (2008c)
	Mn ²⁺	648 (R)	Identical	>3 h	Che et al. (2008b)
	Tb ³⁺	488 + 552 + 583 + 622 (G)	Identical	±4 h	Liu et al. (2009a) and Woo et al. (2011)
Cd ₃ Al ₂ Ge ₃ O ₁₂	Defects > Dy ³⁺	437, 485 + 580 (?)	(Identical)	±1 h	Liu and Liu (2005a)
Na ₂ CaSn ₂ Ge ₃ O ₁₂	Sm ³⁺	566 + 605 + 664 (O)	(Identical)	±5 h	Xu et al. (2013a)
La ₃ Ga ₅ GeO ₁₄	Cr ³⁺	785, 960–1030 (NIR)	Only 960–1030	>1–8 h	Jia et al. (2010) and Yan et al. (2010)
Zn ₃ Ga ₂ Ge ₂ O ₁₀	Cr ³⁺	696 + 713 (NIR)	Identical	>360 h	Allix et al. (2013), Abdukayum et al. (2013), and Pan et al. (2012)
CaMoO ₄	Eu ³⁺	616 (R)	Identical	>5 min	Kang et al. (2011)
NaNbO ₃	Pr ³⁺	620 (R)	Identical	?	Boutinaud et al. (2009b)
YTaO ₄	Tb ³⁺	492 + 543 + 590 + 624 (G)	(Identical)	±2 h	Takayama et al. (2005)

Continued

TABLE 8 Other Oxide Persistent Luminescent Compounds—Cont'd

Host Material	Activators	Emission Maximum (nm)	Afterglow Emission	Afterglow Duration	References
CaWO ₄	Defects > Pr ³⁺	415, 490 + 650 (B/W)	Identical	>10 min	Wu et al. (2012a)
	Bi ³⁺	425 (B)	436 (B)	±45 min	Jin et al. (2013d)
	Eu ³⁺	592 + 616 (R)	Identical	±40 min	Kang et al. (2012a) , Liu et al. (2004) , and Wu et al. (2012b)
	Sm ³⁺ ≫ Eu ³⁺	592 + 616 (R)	(Identical)	>35 min	Kang et al. (2012b)
	Tb ³⁺	490 + 546 (G)	Identical	(>10 min)	Wu et al. (2011b)
BaZrO ₃	Defects (F _A)	408 (B)	Identical	±30 min	Moon et al. (2009)
	Eu ³⁺	574 + 596 + 614 (R)	(Identical)	(±10 min)	Sun et al. (2012)
	Ti ≫ Eu ³⁺	574 + 596 + 614 (R)	(Identical)	(±10 min)	Sun et al. (2012)
SrZrO ₃	Intrinsic	395 (violet-B)	400 (violet-B)	(±100 s)	Wang et al. (2013b)
	STE, Pr ³⁺	380, 489 + 499 (B)	Identical	(±10 min)	Jin et al. (2013c)

See [Section 7.2](#) for symbols and notation.

TABLE 9 Nonoxide Persistent Luminescent Compounds

Host Material	Activators	Emission Maximum (nm)	Afterglow Emission	Afterglow Duration	References
BaS	Cu ⁺	610 (O)	(Identical)	>30 min	Lastusaari et al. (2012)
CaS	Bi ³⁺	448 (B)	(Identical)	(±20 min)	Jia et al. (2000c), Garlick and Mason (1949), Lawangar et al. (1972), and Pawar and Narlikar (1976)
	Ce ³⁺	508+568 (G)	(Identical)	±5 min	Jia et al. (2002a)
	Eu ²⁺	650 (R)	Identical	>1 h	Jia (2006a) and Jia et al. (2000a,c)
	Sm ³⁺	569 (G)	?	(±3 h)	Paulose et al. (2007)
(Ca,Sr)S	Bi ³⁺	453 (B)	(Identical)	(>15 min)	Jia et al. (2000b)
SrS	Defects	517 (G)	(Identical)	(±20 min)	Pitale et al. (2008)
	Eu ²⁺	611 (O–R)	Identical	>16 h	Kojima et al. (2014)
	Yb ²⁺	605 (R)	(Identical)	>5 min	Yang et al. (2014)
ZnS	Cu ⁺	540 (G)	(Identical)	(>3 h)	Clabau et al. (2006), Garlick and Gibson (1948), Ma and Chen (2011), and Yen et al. (2007)
Gd ₂ O ₂ S	Ti/defects	590 (O)	Identical	±2 h	Lei et al. (2010b) and Zhang et al. (2006c)
	Ti > Er ³⁺	555+675 (G)	555+675, 590	>1 h	Lei et al. (2010b) and Zhang et al. (2006a)
	Ti ≫ Eu ³⁺	504+536+620 (R)	Identical	(>5 min)	Hang et al. (2008), Lei et al. (2010b), and Mao et al. (2008)
	Ti > Sm ³⁺	607 (R)	590, 607	?	Lei et al. (2010b)
	Ti > Tm ³⁺	513+800 (?)	590, 800	?	Lei et al. (2010b)

Continued

TABLE 9 Nonoxide Persistent Luminescent Compounds—Cont'd

Host Material	Activators	Emission Maximum (nm)	Afterglow Emission	Afterglow Duration	References
La ₂ O ₂ S	Sm ³⁺	605+625+ 656 (R)	(Identical)	(>1 min)	Liu et al. (2012)
Y ₂ O ₂ S	Ti/defects	540–594 (O)	Identical	>5 h	Kang et al. (2003), Liu and Che (2006), Wang et al. (2009), and Zhang et al. (2004c, 2005)
	Dy ³⁺	486+577 (W)	Identical	>30 min	Huang et al. (2013)
	Eu ³⁺	590+614+ 627 (R)	Identical	±3 h	Wang et al. (2003b), Wang and Wang (2006), Yuan et al. (2007), and Zhang et al. (2004b)
	Sm ³⁺	570+606+ 659 (R)	(Identical)	>1 h	Lei et al. (2003a, 2004b) and Yao et al. (2006)
	Tb ³⁺	417+546 (G)	(Identical)	>20 min	Liu et al. (2006a)
	Ti > Eu ³⁺	616+625 (R)	565, 616 +625	±10 min, 5 h	Holsa et al. (2009) and Hong et al. (2007)
	Tm ³⁺	495+545+ 588 (O)	Identical	±1 h	Lei et al. (2003b)
CaGa ₂ S ₄	Eu ²⁺	555 (Y)	Identical	>30 min	Guo et al. (2004, 2007) and Najafov et al. (2002)
Ca ₂ SiS ₄	Eu ²⁺	660 (R)	Identical	>30 min	Capek et al. (2009)
AlN	Mn ²⁺	600 (R)	Identical	>1 h	Zhang et al. (2013a)
BN	C, O	520 (G)	Identical	>2 h	Liu et al. (2009b) and Wang et al. (2011a)
Sr ₃ Al ₂ O ₅ Cl ₂	Ce ³⁺	435 (B)	Identical	±2 h	Chen et al. (2014a)

	Eu ²⁺	620 (O)	Identical	±6 h	Chen et al. (2014a) and Li et al. (2010)
	Tb ³⁺	490+544+ 588 (G)	Identical	>1 h	Chen et al. (2014b)
Ca ₂ BO ₃ Cl	Eu ²⁺	580 (Y)	(Identical)	>3 h	Zeng et al. (2013, 2014)
Sr ₅ (BO ₃) ₃ Cl	Eu ²⁺	610 (O)	Identical	±15 min	Jin et al. (2014a)
Ba ₅ (PO ₄) ₃ Cl	Ce ³⁺ ≫ Eu ²⁺	350, 435 (B)	Only 435	(>5 min)	Ju et al. (2012)
Sr ₅ (PO ₄) ₃ F _{0.25} Cl _{0.75}	Eu ²⁺	445 (B)	(Identical)	±30 min	Deng et al. (2013)
KY ₃ F ₁₀	Sm ³⁺	558+597+ 651 (R)	(Identical)	(>2 min)	Zhang et al. (2012a)
BaSi ₇ N ₁₀	Eu ²⁺	475 (B-G)	Identical	(>10 min)	Qin et al. (2014)
Ca ₂ Si ₅ N ₈	Eu ²⁺	610 (O)	620	>1 h	Miyamoto et al. (2009) and Van den Eeckhout et al. (2009)
SrSi ₂ O ₂ N ₂	Eu ²⁺	550 (Y)	(Identical)	>2.5 h	Qin et al. (2013)
BaAlSi ₅ N ₇ O ₂	Eu ²⁺	515 (G)	(Identical)	>40 min	Zhang et al. (2013b)
ZnSiN ₂	Mn ²⁺	620 (R)	(Identical)	±min	Uheda et al. (2001)

See [Section 7.2](#) for symbols and notation.

TABLE 10 Persistent Luminescent Glasses

Host Material	Activators	Emission Maximum (nm)	Afterglow Emission	Afterglow Duration	References
Ca ₄ Al ₆ Si ₃ O ₁₉	Ce ³⁺	? (B)	(Identical)	>1 h	Qiu et al. (1998)
	Pr ³⁺	? (R)	(Identical)	>1 h	Qiu et al. (1998)
	Tb ³⁺	350–600 (G)	Identical	>1 h	Qiu et al. (1998)
Ca ₅₉ Al ₅₄ Si ₇ Mg ₇ O ₁₆₁	Mn ²⁺	540 (Y)	(Identical)	>1 h	Kinoshita and Hosono (2000)
	Pr ³⁺	493+610 (R)	(Identical)	>1 h	Kinoshita and Hosono (2000)
	Tb ³⁺	543 (G)	(Identical)	>2 h	Hosono et al. (1998) , Kinoshita and Hosono (2000) , and Kinoshita and Yamazaki (1999)
GeO ₂	Defects	465 (B)	Identical	(±20 min)	Qiu et al. (2002b) and Wada et al. (2005)
SiO ₂	Defects	290+390 (B)	Identical	±1 h	Qiu et al. (2001)
Na ₂ AlB ₁₅ O ₂₅	Mn ²⁺	590 (O)	Identical	±5 min	Qiu et al. (1999)
Na ₄ CaGa ₈ Si ₃ O ₂₁	Tb ³⁺	542 (G)	Identical	±1 h	Yamazaki and Kojima (2004)
Na ₄ CaSi ₇ O ₁₇	Cu ⁺ /Cu ²⁺	510 (B/G)	Identical	>30 min	Qiu et al. (2002a)
SrB ₂ O ₄	Eu ²⁺	430 (B)	Identical	?	Zhang et al. (2006d)
Sr ₇ B ₂₆ O ₄₆	Eu ²⁺ ,Ce ³⁺	350, 430 (B)	Mainly 430	(>2 min)	Zhang et al. (2006d)
ZnB ₂ O ₄	Mn ²⁺	600 (R)	(Identical)	±12 h	Lian and Su (2014)

ZnGe_3O_7	Mn^{2+}	534 (G)	Identical	>1 h	Sanada et al. (2010)
Zn_2GeO_4	Mn^{2+}	540 (G)	Identical	(>10 s)	Takahashi et al. (2011)
$\text{Zn}_3\text{B}_2\text{SiO}_8$	Pr^{3+}	495 + 603 (O)	Identical	(>30 min)	Jiang et al. (2003b)
	Tb^{3+}	542 (G)	Identical	± 1 h	Wang et al. (2006) and Yamazaki et al. (1998)
$\text{Zn}_{11}\text{B}_8\text{Si}_5\text{O}_{33}$	Mn^{2+}	525–606 (G/Y)	Identical	± 12 h	Li et al. (2002)
$\text{Zn}_{11}\text{B}_{10}\text{Si}_4\text{O}_{34}$	Mn^{2+}	590 (R)	Identical	(± 20 min)	Li et al. (2003)
	$\text{Mn}^{2+}, \text{Sm}^{3+}$	600 (R)	Identical	± 10 h	Li and Su (2004, 2006a)
	$\text{Mn}^{2+}, \text{Yb}^{3+}$	605, 980 (R/IR)	Identical	(± 10 min)	Li et al. (2007)
$\text{Zn}_{60}\text{B}_{40}\text{Si}_{17}\text{Ge}_3\text{Al}_{14}\text{O}_{160}$	Defects	410 (B)	Identical	± 2 h	Lin et al. (2010)

See [Section 7.2](#) for symbols and notation.

aluminates or silicates (Poelman et al., 2009). An interesting case of persistent luminescence is observed in carbon- and oxygen-doped BN, where the emission wavelength can be shifted from blue to orange purely by changing the preparation conditions (Liu et al., 2009b; Wang et al., 2011a). The nonoxide persistent luminescent compounds are summarized in Table 9.

7.7 Glasses

A final group of persistent luminescent compounds are the glasses. Although it is sometimes difficult to accurately infer the exact composition of these glasses from literature reports, some clear trends can be observed. Especially, the calcium aluminum silicate- and zinc boron silicate-based glasses have a long afterglow of more than 1 h. A full list of persistent luminescent glasses can be found in Table 10.

8 TL AND AFTERGLOW CURVES

8.1 Thermoluminescence

8.1.1 Motivation

As discussed in Section 4.3.4, TL offers an alternative to lengthy afterglow measurements and allows one to extract several parameters relevant for the trapping process. As such it is an almost indispensable research tool for persistent phosphors. Unfortunately, creating the right conditions for TL measurements and reliable interpretation of the obtained TL glow curves is not straightforward. In this section, guidelines are given to confidently extract trap depths from TL spectroscopy in the case of persistent phosphors.

For the basic processes behind TL, the reader is referred to the textbooks by Chen and McKeever (1997) and Furetta (2003). A tutorial paper by Bos (2006) provides a good insight on the influence of heating rates, the escape frequency, retrapping, and the role of thermal quenching.

A standard TL investigation can reveal at a *qualitative* level how useful a certain trap distribution is for a specific application. Shallow traps, which are emptied well below RT, will not play a significant role in the afterglow at RT. Traps which are too deep will not be emptied within a reasonable time frame. Consequently, they are not relevant to the afterglow process, as the traps can be expected to remain permanently filled.

Performing TL measurements under identical conditions on persistent phosphors with well-chosen compositional variation can answer specific questions. For instance, is the main trap depth a function of the type of (rare earth) codopant (Fig. 18)? Can intrinsic traps (e.g., related to defects in the host compound) be separated from trap states introduced by the codoping? Although the results from a brief TL study are very helpful, it often remains at a qualitative level, labeling traps by their TL peak temperature.

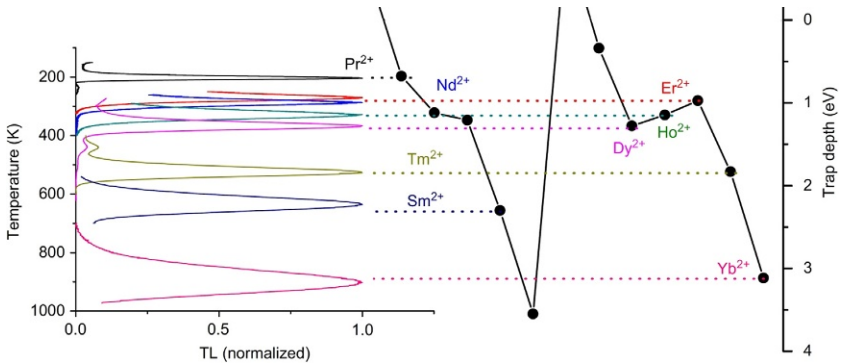


FIGURE 18 (Left) TL glow curves recorded at a heating rate of 0.1 K/s on $\text{YPO}_4:\text{Ce}^{3+},\text{Ln}^{3+}$ samples. (Right) The Ln^{2+} ground state below the conduction band bottom in YPO_4 . Dashed lines illustrate the relationship between predicted trapping depth and peak temperature of the TL glow. Note that most traps are not in the suitable temperature range to yield persistent luminescence at RT. (Right) Adapted from *Dorenbos et al. (2013)*.

8.1.2 Experimental Considerations and Guidelines

TL investigations should preferably be conducted at different levels to enable the determination of trap depths and/or distributions. Unfortunately, it is rather common practice to present only a single TL glow curve for a specific phosphor composition. From this single measurement, often two or more trap depths are derived in a *quantitative* way. Additionally, the degree of re-trapping, frequency factors, and trap concentrations are simultaneously derived. Eventually, (too) many independent fitting parameters are determined from a single glow curve and it remains questionable how close this information is to the real, underlying trap distribution.

What considerations should thus be made when conducting an in-depth TL study?

- A prospective TL analysis should be performed at the qualitative level first. It should be evaluated what temperature range is needed to empty the relevant traps. This also includes a study of the reproducibility of TL glow curves, to assess possible thermal damage to the studied phosphors, which is especially important for novel, less studied compositions.
- In a second step, the dose dependency should be evaluated. *Dose* should be considered in its broadest sense, and not only limited to the case of ionizing radiation, but also as this term is indeed more commonly used in radiation dosimetry. However, also when exciting with visible or UV light, the combination of excitation intensity and duration can be considered as a dose. The dose dependency should be evaluated for several reasons: (i) if the dose is too low (i.e., much lower than what is used during determination of afterglow duration and intensity), then minority traps might be studied compared to those strongly contributing to the afterglow.

(ii) evaluating the dose dependency is required to anticipate the glow curve fitting, where a shift to lower temperature for higher dose rate might be an indication for second-order kinetics. and (iii) if ionizing radiation is used, a high dose might cause irreversible damage to the persistent phosphor.

In persistent phosphors, not only the dose used for trap filling is important but also the combination of excitation intensity and time. For dosimetry or storage phosphors, the traps are normally sufficiently deep to avoid emptying during the irradiation. Consequently, the received dose is proportional to the duration multiplied by the intensity and the same dose can be achieved in several combinations. For persistent phosphors, this is not the case, as upon excitation at RT a significant fraction of trapped charges leads to recombination during the excitation, which is not taken into account anymore during the afterglow or the TL measurement. Hence, exciting longer but at lower excitation intensity is likely to result in a lower number of trapped charges at the end of the excitation. This aspect is important when correcting for instance TL excitation spectra for the spectral light output of the light source. These issues can to some extent be overcome by exciting the persistent phosphors below RT, when premature emptying of traps is limited.

- The heating rate during the TL measurement is an important parameter. Often, a higher heating rate (well above 1 K/s) is chosen to improve the signal-to-noise ratio (SNR), as in this way the emitted TL light is collected in a relatively short time frame. However, using faster heating (5 K/s or higher) induces the risk of temperature differences between the heating element and the persistent phosphor, especially if loose powder or a thick pellet is used. Upon poor thermal contact, temperature gradients cannot be excluded over the measured phosphor surface, which would artificially broaden TL glow peaks. Therefore, measuring at moderate heating rate on a well-characterized heating stage and by using thin pressed pellets of persistent phosphor in good thermal contact with the heat exchanger are of importance. These guidelines are even more strict, if one wants to apply peak shape or the Hoogenstraaten method to derive trap depths (Chen and McKeever, 1997; Hoogenstraaten, 1958).
- While practical applications of afterglow generally occur at constant ambient temperature, for a TL measurement elevated temperatures are used, which can go up to the same range where thermal quenching (as found in the steady-state photoluminescence) sets in (Bos, 2006). This is especially the case if elevated heating rates are used, shifting TL peaks to higher temperatures. In principle, the TL glow curve profile should be corrected for the thermal quenching behavior to determine the number of released charges, rather than the number of charges which eventually led to the emission of a photon. Nevertheless, in-depth studies on whether thermal quenching effects can be straightforwardly corrected are lacking.

- Collecting the TL emission spectrum during the TL measurement is advisable, to determine contributions from different emission centers, to exclude the presence of impurity phase, and to overcome erroneously collected black body radiation. The latter effect is more important for deep traps, which are less important for persistent luminescence, in contrast to the case of storage phosphors.
- When correlating TL glow curve measurements with afterglow analysis, similar excitation wavelength and conditions as used for the afterglow experiments should be chosen. Also, the time between the end of the excitation and the start of the TL measurement should be minimized, not to overlook the shallower traps, responsible for the initial part of the afterglow.
- Thermal barriers for trapping can be identified by performing a TL analysis after excitation at various temperatures. This can especially be relevant for Eu^{2+} - and Ce^{3+} -based persistent phosphors, where excitation into the lower 5d excited states at low temperature is not necessarily leading to charge trapping. Ideally, the TL measurements are performed after excitation with different wavelengths, corresponding to the different absorption bands of the persistent phosphor (Fig. 19).

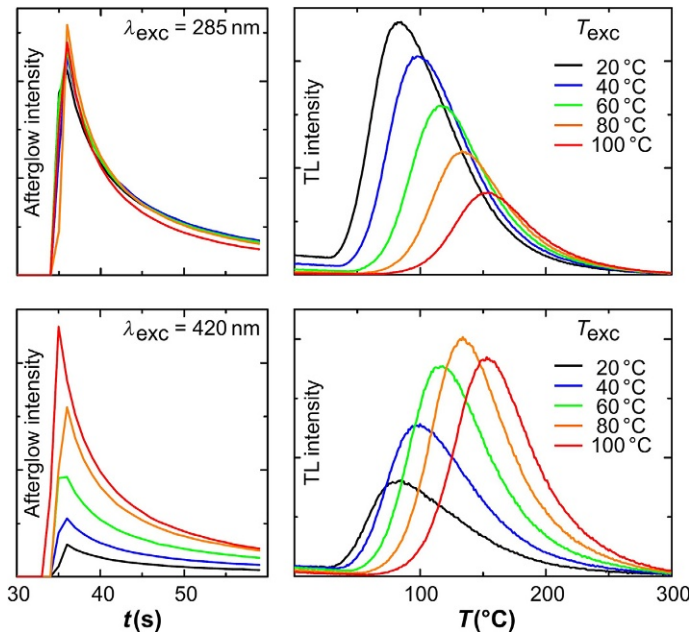


FIGURE 19 Influence of excitation wavelength (λ_{exc}) and temperature during the excitation (T_{exc}) on the afterglow intensity and subsequent TL glow curve of $\text{Ba}_2\text{Si}_5\text{N}_8:\text{Eu}$. A clear thermal barrier is found for excitation via the lowest excited 5d band for Eu^{2+} (at 420 nm), as an increase in temperature leads to a larger fraction of trapped charges, resulting in a stronger afterglow and higher TL intensity. Note also that the gradual shift in TL peak position (top, right) points at the presence of a trap depth distribution. *Reproduced from Smet et al. (2012c).*

8.1.3 Extraction of Trap Depths from TL

The approach used to extract trap depths from TL glow curves depends strongly on the precise shape of the glow curve, and from the peripheral knowledge gathered from the research approach presented above. If the peaks are well resolved, which is actually rarely the case for persistent phosphors, the shape of the TL peak can be used to assess the trap depth and the fraction of retrapping. In case two or more TL peaks are present, one can resort to a peak fitting software package. However, this should be used with care, and only when individual TL peaks are well recognizable. Otherwise, insufficient data are available to reliably pin all the experimental parameters. Fitting results should be interpreted cautiously and nonrealistic frequency factors or strong retrapping are indicative of an unrealistic fitting. In these cases, it is advisable to record TL glow curves for different doses and heating rates and to fit these with the same set of parameters. For instance, if a considerable fraction of the thermally released charges are retrapped, this will lead to peak shifts in the TL glow curve for different doses. Hence, one can easily extend the dataset to allow more parameters to be fitted reliably.

In the case of a broad TL glow peak, TL analysis software might come up with unrealistically low frequency factor when trying to fit a single, discrete trap. Instead, it is rather a sign of the presence of a *trap depth distribution*. Several methods, such as the initial rise method (Furetta, 2003; Van den Eeckhout et al., 2013a) or the $T_{\max}-T_{\text{stop}}$ method (Brylew et al., 2014) are available to extract parameters from this distribution. Before going into detail, note that having a *Gaussian-shaped trap distribution* is markedly different from fitting a number of *Gaussian-shaped TL peaks* to an experimentally obtained TL glow curve. In the former case, one has a large set of trap depths, with their relative abundance obeying a Gaussian-shape function, each contributing to the measured TL glow curve (typically following first-order kinetics). In the latter case, one is fitting a TL curve without physical background. A Gaussian-shaped TL glow curve is close to the case where retrapping is equally probable as recombination upon release of the trapped charge, which is called second-order kinetics (Bos, 2006). Making this assumption is most often not substantiated, e.g., by evaluation of the dose dependency. Consequently, feeding Gaussian-shaped TL fittings into TL peak fitting software to extract the corresponding trap depth does not make sense, although it is often encountered in literature.

In the case separate or clearly identifiable TL glow peaks are found, several methods are available to extract trap depths. Chen's peak shape method (Chen, 1969) makes use of general-order kinetics. Retrapping has an influence of the shape of the TL glow curve, i.e., a broadening toward the high temperature side, leading toward almost Gaussian-shape peaks for second-order kinetics, fitting the peak shape can be used to assess the retrapping.

Obviously, the method is not reliable in the case of many overlapping glow peaks.

If the afterglow is obeying first-order kinetics, then Hoogenstraaten's method can be used to determine the trap depth, by evaluating the shift in the glow peak maximum as a function of the heating rate. Consequently, it is very important to have a good control over the temperature (of the sample), for different heating rates.

If one encounters broad TL glow curves, then the above-mentioned techniques are not suitable. Still, several approaches are available to determine the underlying trap distribution, although they require a more elaborate TL analysis typically involving tens of TL measurements. The $T_{\max} - T_{\text{stop}}$ method sequentially probes the trap distribution, by thermal cleaning of shallower traps and evaluation of the shift of (local) TL glow maxima. An interesting example, showing the power of the method, is shown in Fig. 20 for the shallow traps in $\text{Lu}_3\text{Al}_5\text{O}_{12}:\text{Pr}^{3+}$ (Brylew et al., 2014). Simulation of TL glow curve based on the obtained trap depth distribution showed good agreement with the experimentally obtained glow curve (Brylew et al., 2014).

A similar method employs excitation prior to the TL measurement at different temperatures, after which the initial part of the rising slope of the TL glow curve is taken into account using the initial rise method. From these sequential measurements, a trap depth distribution can be reconstructed. In the case of $\text{CaAl}_2\text{O}_4:\text{Eu},\text{Nd}$, it was found that this distribution could be

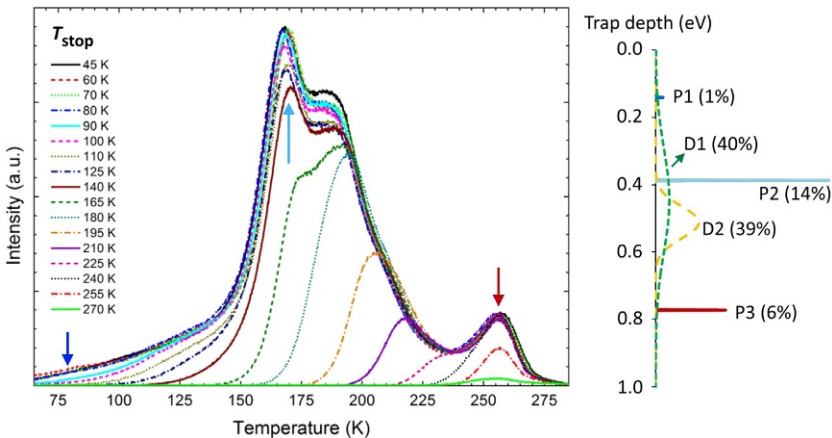


FIGURE 20 TL glow curves for $\text{Lu}_3\text{Al}_5\text{O}_{12}:\text{Pr}^{3+}$ as function of T_{stop} (left). Corresponding trap depth distribution, showing three discrete traps (P1, P2, and P3) and two Gaussian-shaped contributions (D1 and D2). The relative contribution to the total trapping is given between parentheses. The position of the glow peaks related to the discrete trap depths are indicated by arrows in the left figure. Adapted from Brylew et al. (2014).

approximated by a Gaussian-shaped distribution, centered around a trap depth of 0.91 eV (Van den Eeckhout et al., 2013a).

In conclusion, TL spectroscopy is a powerful tool to reveal the trap depth distribution in persistent phosphors. Although it is tempting to feed a single TL curve into TL analysis software, this does not necessarily yield reliable data as such, on the contrary. One should cautiously interpret the derived numbers and in general a complete TL study is required, involving multiple measurements to extend the dataset on which fittings are applied.

8.2 Afterglow Curves

8.2.1 Absolute Measurements and Procedure

Measuring the (isothermal) afterglow curve for a persistent phosphor is crucial to assess its usefulness for a particular application. Such a curve has two key parameters: the shape of the glow curve and the absolute intensity. The former yields an intensity curve in relative units and is typically measured with any luminescence spectrometer. A specific emission wavelength (or emission band) characteristic for the investigated material is typically followed, which can be useful if multiple emission centers are available. The latter requires a specific, calibrated luminance detector, yielding values adjusted to the human observer (in cd/m^2) or in radiometric units (in $\text{W}/\text{sr}/\text{m}^2$). The luminance unit and the perception by the human eye were discussed in detail in Section 6. If such equipment is not available, then the output of the luminescence spectrometer can be converted to cd/m^2 , provided a calibrated light source is available. Furthermore, the shape of the afterglow emission spectrum should be taken into account, via the luminous efficacy.

Although showing the afterglow decay curve—on a logarithmic scale to improve readability—is most informative, it is useful to put a single number on the afterglow duration. It is commonly taken as the time after excitation for the afterglow intensity to drop to $0.3 \text{ mcd}/\text{m}^2$, which is nowadays an accepted standard. This threshold luminance is however not equal to the lower light perception limit of the human eye, as this is about a 100 times lower (Section 5.1). It is, however, rather common to find publications with the ambiguous statement “*the afterglow duration (to $0.3 \text{ mcd}/\text{m}^2$) was determined by the unaided dark-adapted human eye,*” which is an inconsistent definition. This complicates the interpretation of the usefulness of such a reported persistent phosphor, as it contains two orders of magnitude of uncertainty.

An interesting approach revealing the trapping capacity of a persistent phosphor in the case no absolute measurements can be made, is by measuring the phosphor’s light output during and after the excitation in the same experiment. This is shown in Fig. 21 for the benchmark $\text{SrAl}_2\text{O}_4:\text{Eu},\text{Dy}$ phosphor. When the emission intensity saturates, i.e., the number of filled traps reaches a stationary number, almost 80% of the steady-state emission is actually composed of “afterglow” emission, i.e., luminescence originating from

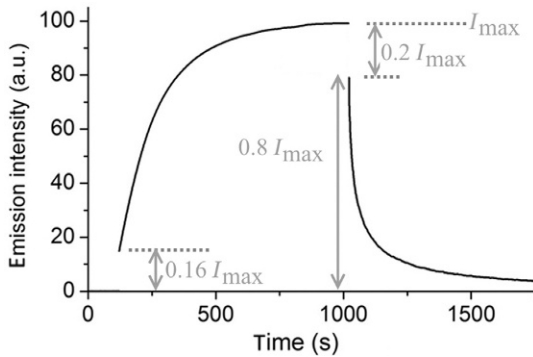


FIGURE 21 Evolution of the light output of $\text{SrAl}_2\text{O}_4:\text{Eu,Dy}$ upon excitation at 450 nm, with constant intensity. At $t=1000$ s, the excitation source is switched off. Adapted from *Botterman et al. (2014)*.

recombination after release of trap charges, as judged from the initial afterglow intensity. Displaying the steady-state output and the initial part of the afterglow curve is a straightforward experimental method to assess the trapping capacity of a persistent phosphor. If a persistent phosphor with relatively short decay time immediately drops to a low afterglow intensity compared to the steady-state intensity, then this is indicative of a very limited number of thermally accessible traps.

Another difficulty in the determination of the afterglow duration is caused by the choice of excitation conditions prior to the afterglow measurement. One could argue that taking “1000 lux of an unfiltered Xe-arc, during 5 min” corresponds best to the industrial standard (Section 5.1), and should therefore be promoted. However, this emission spectrum contains a lot of ultraviolet light, even with $\lambda < 300$ nm, which is not available in daylight, let alone in artificial (indoor) lighting. Consequently, a persistent phosphor which can only be excited by ultraviolet light will be characterized by a long afterglow duration, yet its application potential is rather limited for indoor safety signage. For these applications, excitation by means of (blue or white) LED light source is far more appropriate.

The most important message is to describe in sufficient detail the excitation conditions, with a light source appropriate for the foreseen application. Furthermore, information on what wavelength ranges are able to induce the persistent luminescence is useful additional information.

8.2.2 Fitting and Interpretation

For a single, discrete trap depth, the afterglow intensity is expected to decay in an exponential way, at least in the case of first-order kinetics. However, this is most often not the case and a more complex shape of the afterglow curve is found. This is obviously related to the commonly broad TL glow curves, often

with substructure, indicating different trap depths or even a distribution of trap depths. If all these trap depths contribute by an exponentially decaying curve with different slope, then the combined afterglow profile is often too complex to be fitted with multiple components in a reliable way.

Consequently, fitting the afterglow curve to identify each contribution will probably not be successful, especially if only a small fraction of the afterglow (e.g., the first few minutes) is taken into account. If retrapping would play a role (i.e., in case of general-order kinetics), then fitting with exponential functions does not make sense. At a qualitative level, it can however be useful, for instance, if one wants to assess the role of codoping on the depth of the main contributing traps, which should be reflected in the afterglow curve as well.

If one measures the afterglow intensity on a long timescale (e.g., for several hours), then plotting $\log(I)$ as function of $\log(t)$ increases readability. Especially, if one wants to investigate the tell-tale sign of tunneling processes (Pan et al., 2012), in case the afterglow intensity is proportional to t^{-1} . Note, however, that certain trap distributions can give rise to an apparent t^{-1} decay behavior.

The afterglow curve can also be helpful in validating a TL glow curve analysis. Especially, if more advanced TL analysis methods are used, e.g., the $T_{\max}-T_{\text{stop}}$ or the initial rise method (as discussed in Section 8.1.3), a fairly detailed trap distribution should result from the analysis. Then one can calculate the *expected* afterglow intensity curve and compare it to the obtained *experimental* curve to assess the reliability of the derived trap distribution. This is shown in Fig. 22 for the derived Gaussian trap distribution in $\text{CaAl}_2\text{O}_4:\text{Eu},\text{Nd}$ (Van den Eeckhout et al., 2013a), where an excellent correlation between the calculated and experimental afterglow curve is found. By repeating this experiment at different temperatures, the same trap distribution could “predict” the different isothermal afterglow curves.

Note that if fading would be present in a persistent phosphor—being the nonradiative recombination of the trapped charge and the (ionized) luminescent ion—this should also be taken into account, due to the largely different timescales for the collection of the afterglow and the TL curves.

In conclusion, afterglow curves are highly relevant from an application point of view, especially if they are given in absolute units and the excitation conditions are clear. Furthermore, they nicely complement the information extracted from TL glow curve analysis.

9 APPLICATIONS

9.1 Safety Signage

Safety signage is the main application area of persistent phosphors, with signs to indicate emergency exits or guiding lines in the aisle of airplanes as typical examples. Upon an incident where the regular lighting fails (power failure or

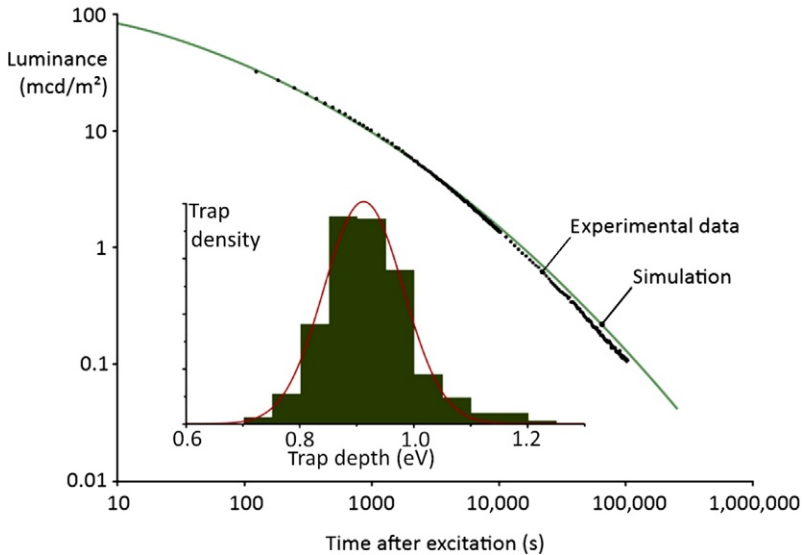


FIGURE 22 Measured afterglow intensity (dots) for $\text{CaAl}_2\text{O}_4:\text{Eu,Nd}$ (Van den Eeckhout et al., 2013a). Based on the trap distribution (bars, inset) and the fitted Gaussian trap depth distribution (trace, inset), the corresponding afterglow intensity was calculated assuming first-order kinetics (trace). An excellent agreement is found over many orders of magnitude. Adapted from Van den Eeckhout et al. (2013a).

smoke), the persistent phosphor is supposed to yield an appreciable light emission to allow safe evacuation. An important aspect is of course the perceived brightness by the human eye, which depends on many factors, including the emission spectrum of the phosphor (Section 6.2), the preceding light conditions and the dark adaptation (Section 6.3), and the initial emission intensity and afterglow profile of the phosphor (Section 8.2.1), which are strongly determined by the preceding lighting conditions. It is clear that the usefulness of a persistent phosphor—even when having an appropriate trap depth—is in the first place determined by its energy storage capacity. In the next section, the *potential* energy storage capacity of persistent phosphors is estimated.

9.2 Potential Energy Storage Capacity

The brightness and afterglow behavior of persistent phosphors depend on many parameters, of which several are related to the intrinsic properties of the persistent phosphor. These include the trap density, the trap depth distribution, and the (quantum) efficiency of the recombination process. In principle, these parameters can be steered—whether or not in a controlled way—by changing synthesis conditions or the composition of the persistent phosphor.

In addition, the perceived brightness of the phosphor depends on how it is applied. Let us consider the most common application, namely a flat layer of phosphor embedded in a transparent binder material, as in the case of safety signage. Initially, the brightness of the phosphor layer can be increased by increasing the thickness of the layer or by increasing the volume fraction. Clearly, if the phosphor density (in g/cm^3) increases, the total storage capacity increases as well. There are however limits to this approach, as for thick layers, the light extraction efficiency for deeply embedded particles drops due to the scattering losses. Furthermore, the fraction of useful light reaching the deeper parts of the phosphor layer in order to fill traps, is then limited. By appropriately designing the morphology of phosphor particles (e.g., size distribution and surface roughness) and carefully choosing the optical properties of the binder (e.g., refractive index and volume fraction), the effective phosphor density can be optimized to yield the highest afterglow intensity.

It is clear that the final afterglow intensity which can be achieved with persistent phosphors ultimately depends on the energy storage capacity on the phosphor itself. For the remainder of the discussion, we will use an effective phosphor thickness, as if the phosphor embedded in a binder material would be condensed into a dense phosphor layer where the scattering losses are eliminated. For estimating the maximum storage capacity, a number of known parameters are used as input, such as the physical density, molar mass, and emission spectrum of the persistent phosphors. In this example, we consider the green-emitting persistent phosphor $\text{SrAl}_2\text{O}_4:\text{Eu},\text{Dy}$. We consider an optimum dopant concentration of 1% for the Eu ions, i.e., 1% of the strontium ions are substituted by europium ions. For other dopant concentrations, the calculated values can simply be scaled proportionally.

The main assumption to be made is on the fraction of lattice sites which are contributing to the trapping process. We keep this as a free parameter and Table 11 shows the results for a trapping efficiency of 10%, 50%, and 100% relative to the dopant concentration. Based on a XAS study on $\text{SrAl}_2\text{O}_4:\text{Eu},\text{Dy}$, a lower limit for the trapping efficiency of 5% was put forward, relative to the number of Eu dopant ions (Korthout et al., 2011). Given that $\text{SrAl}_2\text{O}_4:\text{Eu},\text{Dy}$ still shows strong photoluminescence at low temperature—when all accessible traps can be assumed to be filled after sufficiently long excitation—the trapping efficiency is certainly not 100%. As the trap filling in $\text{SrAl}_2\text{O}_4:\text{Eu},\text{Dy}$ occurs via excitation of Eu^{2+} and its subsequent ionization, it seems not likely that more charges can be trapped in the phosphor than the number of europium ions. So, a trapping efficiency of 100% should indeed be considered as an absolute upper limit. More research, by means of a detailed bookkeeping of excitation, absorption, and afterglow intensities, is required to pinpoint this number. In this respect, it would be extremely helpful to settle the nature of the trapping centers.

As an example, the total energy storage capacity for $\text{SrAl}_2\text{O}_4:\text{Eu}[1\%],\text{Dy}$ with full trapping capacity is about 2.2 J/cm^3 or 0.6 J/g . The calculated

TABLE 11 Calculated Maximum Afterglow Luminance (in Photopic cd/m²) for SrAl₂O₄:Eu,Dy as a Function of the Thickness of the Phosphor Layer and the Trapping Efficiency

Thickness	Trapping Efficiency								
	10%			50%			100%		
50 μm	18 ^a			92			184		
	30 ^b	4.4 ^c	2.1 ^d	151	22	10	302	44	21
200 μm	74			368			736		
	121	18	8.4	604	88	42	1207	176	84
1 mm	295			1473			2945		
	483	70	34	2415	352	168	4830	704	336

^aAverage luminance during the first 12 h of the decay.
^bLuminance value at 1 h into the decay.
^cLuminance value at 6 h into the decay.
^dLuminance value at 12 h into the decay.

afterglow intensities (in mcd/m²) for a certain effective phosphor thickness were then derived by assuming that light emitted toward the backside of the phosphor layer (e.g., toward the substrate) is reflected back toward the forward direction, without losses. An afterglow decay profile (measured at RT) was used as input to calculate the afterglow intensity at different times after stopping the excitation. It was derived that after 12 h, approximately 80% of all traps were emptied for this particular persistent phosphor, which was confirmed by TL measurements to assess the number of remaining trapped charges.

From Table 11, and assuming a trapping efficiency of 10%, a 50-μm phosphor thickness would correspond to class C, whereas 200 μm is needed for the highest class F (Section 5.1). It is clear that currently available persistent phosphors do not reach a performance characterized by a trapping efficiency of 50% or higher. Hence, the numbers in the table should be regarded as an optimum case.

Persistent phosphors-like SrAl₂O₄:Eu,Dy are optimized to yield a fairly high initial brightness, in view of emergency situations where a power cut induces a rapid transition from bright conditions (leading to fully charged persistent phosphors) to dark conditions. Consequently, after 1 h of afterglow, about 56% of all trapped charges have already been released. This means that the requirement to still have a substantial emission much further along the decay curve, for instance at the end of a 12 h night, is not met in this particular persistent phosphor. For instance, an afterglow intensity of 500 mcd/m²

after 12 h is not maintained, even in 1 mm thick phosphors and with 100% trapping efficiency.

Note that embedding such a large effective phosphor thickness in a binder will inevitably lead to strong light scattering losses. Going to ceramic-like phosphor plates with low pore density can overcome these extraction issues. Recently, high afterglow intensities were found in $\text{SrAl}_2\text{O}_4:\text{Eu},\text{Dy}$ and $\text{CaAl}_2\text{O}_4:\text{Eu},\text{Nd}$, synthesized by means of the frozen sorbet technique (Nakanishi et al., 2015) and electron beam annealing (Smet et al., 2012a), respectively. The much higher production cost, compared to the established synthesis methods for bulk powder phosphors, are of course not compatible with large area applications.

Does this imply that the energy storage capacity of persistent phosphors is intrinsically relatively low? The key parameter is obviously the trapping capacity and the—assumed—connection to the number of europium ions, as these ions are the presumed source of the trapped charge carriers. With a molar dopant concentration of 1%, only 0.14% of all atoms in the SrAl_2O_4 lattice are replaced by europium. The optimum dopant concentration for divalent europium is typically well below a few percent of substitution, above which concentration quenching sets in and nonradiative decay becomes prominent. This presumably also has a negative effect on the trapping capacity, as fading will start to play a strong role, as well. Taking $\text{YPO}_4:\text{Ce},\text{Sm}$ as an example, it was found that fading was much more prominent for higher dopant concentrations (Dorenbos et al., 2013). Alternatively, other types of dopant–defect combinations might be more effective in creating a higher trapping capacity. The recent reports on Cr^{3+} -based gallate phosphors, and their high storage capacity, are hopeful and perhaps indicative of a new road to follow, instead of the established Eu^{2+} -based phosphors (Section 10.3).

9.3 Mechanoluminescence

ML, also called piezoluminescence or elasticoluminescence, is the process where upon application of pressure, a previously excited material emits light (Fig. 23). The process is repeatable after recharging the material by illumination and goes on as long as trapped charges are available in the material. ML is related to persistent luminescence as it is also based on the release of previously trapped charges. In the case of ML, pressure induces a piezoelectric field which can reduce the trap depth or it can cause band bending (Botterman et al., 2012; Chandra, 2011; Chandra et al., 2011). Trapped charges are then released to give luminescence upon recombination, due to a reduction in trap depth or to tunneling processes, respectively. ML can thus be used as smart sensors to monitor stress distributions and deformations (Kamimura et al., 2012; Chandra et al., 2010; Xu et al., 1999, 2000).

ML phosphors are closely related to persistent phosphors. If the relevant traps for the ML process would be very shallow, they will quickly be emptied

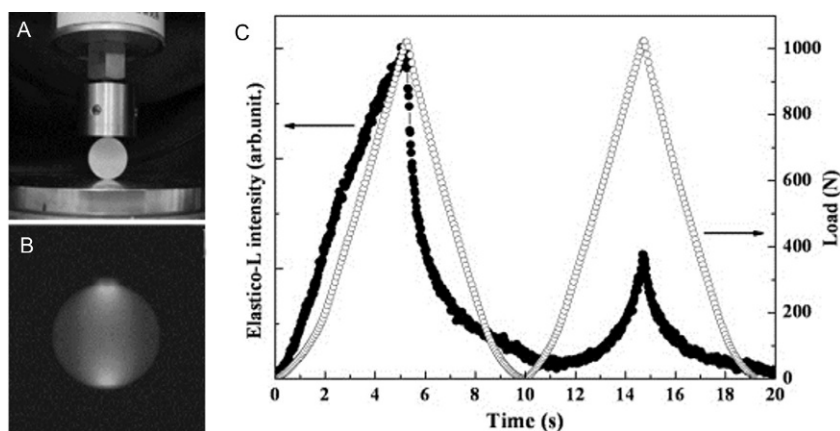


FIGURE 23 (A) Sample pellet (composite of $\text{SrMg}_2(\text{PO}_4)_2:\text{Eu}$ in an optical epoxy resin) in a testing machine. (B) Image of the ML obtained from the pellet subjected to compressive load. (C) ML response to loading applied in a triangular wave mode. *Adapted from Kamimura et al. (2012).*

by the available thermal energy, yielding afterglow, before a ML experiment can be conducted. If the traps are too deep, the required pressure is too high to sufficiently reduce the trap depths. Consequently, ML is addressing the somewhat deeper traps than those responsible for the initial parts of the thermally induced afterglow. Not all persistent phosphors do show ML behavior. First of all, only the piezoelectric host compounds are appropriate. Second, the intensity of the ML is not straightforwardly related to the afterglow intensity, as the crystallographic properties, such as stiffness and local coordination, are playing an important role in the pressure sensitivity (Akiyama et al., 2002). For the bluish-green ML in $\text{BaSi}_2\text{O}_2\text{N}_2:\text{Eu}$, the occurrence of ML was used to deduce crystallographic information (Botterman et al., 2012). Other materials classes showing ML include the strontium aluminates, $\text{CaZnOS}:\text{Mn}$ (Zhang et al., 2013c), and $\text{ZnS}:\text{Mn}$ (Chandra et al., 2010).

10 PERSISTENT LUMINESCENCE FOR *IN VIVO* IMAGING

In vivo biomedical imaging is a promising and emerging application for persistent luminescent materials that have received considerable interest in recent years (Bessière et al., 2011; Frangioni, 2003; le Masne de Chermont et al., 2007; Maldiney et al., 2012b; Zhuang et al., 2014b). Luminescent nanoparticles could become a viable alternative to traditional radioactive tracer molecules for tracking, for instance in studying vascularization and targeting of tumors in the body of a patient. Within this category of luminescent particles, red- or NIR-emitting persistent luminescent particles hold several advantages over the use of other types of fluorescent materials, such as quantum dots or

organic fluorophores. For example, autofluorescence of living tissue is avoided because persistent luminescent particles can be excited before they are injected in the body. This increases the SNR (where the background autofluorescence can be considered as “noise”) for imaging methods making use of these persistent luminescent materials. Although other luminescent labels, including quantum dots, will show much higher emission intensity upon excitation, the excitation light inevitably induces a large autofluorescence background, lowering the SNR, unless time-resolved detection is used.

10.1 Requirements for *In Vivo* Imaging

The proof-of-principle of using persistent luminescent materials for medical imaging was demonstrated by [le Masne de Chermont et al. \(2007\)](#). In this imaging method, small luminescent particles are optically charged *ex situ* and subsequently injected ([Singh, 2014](#)). If the afterglow intensity and duration are sufficiently large and if the tissues are sufficiently transparent for the emitted light, movement, or accumulation of the particles can be detected using a sensitive camera outside the body ([Fig. 24](#)).

For the development of persistent luminescent materials for usage in medical imaging, several issues should be considered, which are covered in the following paragraphs: emission wavelength, afterglow duration, biodistribution, chemical stability and cytotoxicity, and possibility of *in situ* reexcitation. A recent review on this topic can be found in [Singh \(2014\)](#).

10.1.1 Emission Spectrum

The ideal emission range of particles for bioimaging lies in the NIR region, between 650 and 950 nm. This is the so-called first optical window of living tissues, where absorption and scattering of photons are minimal ([Chance, 1998](#); [Frangioni, 2003](#); [Hemmer et al., 2013](#); [Lim et al., 2003](#)). [Figure 25](#) shows how the combination of the absorption curves of several prominent components of blood leads to this transparency window. There exists also a second window, between 1000 and 1350 nm, which from a physical point of view is even better suited for optical imaging, due to the smaller autofluorescence from tissue in this wavelength range ([Smith et al., 2009](#)). However, the

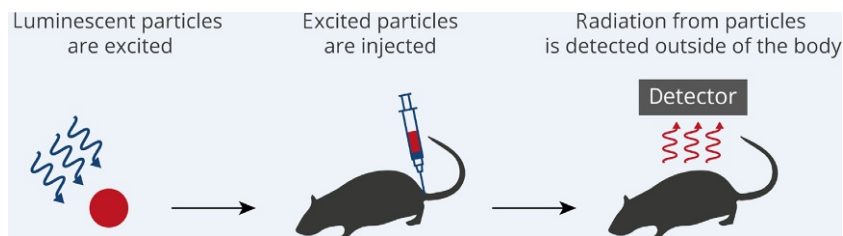


FIGURE 24 Principle of *in vivo* imaging via NIR-emitting persistent phosphors.

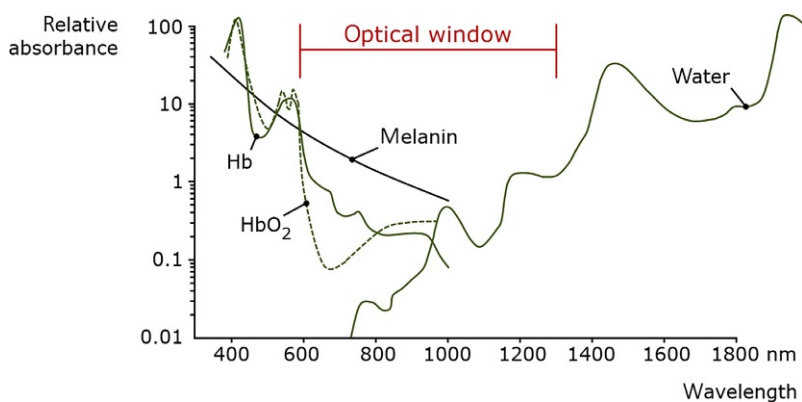


FIGURE 25 Near-infrared optical window of biological tissue. Hb: hemoglobin; HbO₂: oxygenated hemoglobin. Adapted with permission from [Huang et al. \(2009\)](#), ©2009, SPIE.

possibility of using typical Si- or GaAs-based CCD cameras for photon detection in the first window, combined with the relative lack of materials emitting in the second window, make this 1000–1350 nm range less suited for practical applications. An excellent overview of red- and NIR-emitting persistent phosphors (doped with transition metal ions) can be found in [Zhuang et al. \(2014b\)](#).

10.1.2 Afterglow Intensity

The afterglow of the persistent luminescent materials should be long enough, so that the emitted light can be followed through the body for diagnosis or treatment. For commercially available persistent phosphors emitting in the visible part of the spectrum, the decay time is often defined as the time it takes for the luminance of the phosphor to drop below a value of 0.3 mcd/m² ([Section 5.1](#)) ([Clabau et al., 2007](#)). However, this quantity cannot be used as a benchmark for NIR-emitting phosphors, because it takes the wavelength sensitivity of the human eye into consideration, which, by definition, is zero in the IR. Therefore, a shift toward a description in terms of radiance (in W/sr/m²) is desirable. With this in mind, the decay time of NIR-emitting persistent phosphors could be defined as the time it takes for the radiance of the phosphor to drop below 10⁻³ mW/sr/m², a value that roughly corresponds to the luminance of 0.3 mcd/m² for the green emission of the SrAl₂O₄:Eu²⁺, Dy³⁺ phosphor ([Zhuang et al., 2014b](#)).

For practical *in vivo* applications, other evaluation methods should also be considered. Depending on the process to be studied, a different time frame can be required in which the observed radiant intensity should exceed the sensitivity of detection via Si-based CCD cameras by a sufficiently large factor after background subtraction ([le Masne de Chermont et al., 2007](#)). This will require the proper design or optimization of the trap depth distribution, where it

should be kept in mind that the operating temperature will be higher than the usual “room temperature” at which persistent phosphors are normally evaluated.

10.1.3 Biodistribution

The biodistribution of injected particles depends on the size of the injected particles and the functionalization with surface groups (Alexis et al., 2008; Maldiney et al., 2011b). Biodistribution should be fast and targeted in order to reduce background noise by fluorescence from particles remaining in the blood flow. Furthermore, the particles should be retained by the target in order to enable prolonged imaging of the regions of interest. Particles with hydrodynamic diameters of more than 150 nm tend to accumulate very fast in organs, such as the liver or spleen, that identify and filter foreign and toxic substances in the body. On the other hand, particles with diameters smaller than 10 nm are rapidly cleared via excretion from kidneys (le Masne de Chermont et al., 2007; Maldiney et al., 2011b). Functionalization of particles with surface groups drastically affects distribution and circulation time. Functional groups which lead to negative surface charges, such as hydroxyl or carboxyl groups, tend to show a rapid uptake in liver and spleen, thus reducing circulation time. Alternatively, functionalization with amino groups leads to accumulation in the lungs. So far, the most suited surface modification method seems to be the functionalization of nanoprobe with polyethylene glycol (PEG). PEG-ylation leads to charge-neutral particles, due to shielding of the nanoprobe surface by the long alkyl chains, which delays the uptake by liver and spleen (Alexis et al., 2008; Kamps et al., 1997, 1999).

10.1.4 Chemical Stability and Cytotoxicity

The used host materials for persistent phosphors should obviously be chemically stable in an aqueous environment, both for concerns of toxicity and for retention of optical properties. Therefore, phosphors with otherwise excellent NIR emission properties, such as CaS:Eu^{2+} , $\text{Y}_2\text{O}_2\text{S:Eu}^{3+}$, Ti^{4+} , Mg^{2+} , or other sulfides cannot be used for *in vivo* imaging without precautions. Materials that contain heavy metal elements should also be avoided. However, if nanoparticles are synthesized via wet-chemical methods, as opposed to size-reduction techniques, several methods for applying passivating coatings have been described (Bardhan et al., 2011; Bellah et al., 2012).

Next to the stability of the particles during the imaging experiments, it is important that they are excreted afterward within a reasonable amount of time. If they do not get completely removed from the body, their long-term stability becomes an issue and prolonged experiments are necessary to evaluate their toxicity and stability.

Nanoprobe toxicity is also heavily influenced by the size of the particles and their surface functionalization. Very small nanoparticles with diameters

comparable to natural proteins can cross-cell barriers. Increased interaction with cellular components is also possible because of nanoparticles' larger surface-to-volume ratio (Soenen et al., 2011; Zhang et al., 2014b).

10.1.5 In Situ Reexcitation

Up to date, the longest detection duration possible after *ex situ* excitation and injection is of the order of several hours (Maldiney et al., 2011a, 2012b). When the nanoprobes have reached and accumulated sufficiently in the regions of interest, which could take, e.g., between 2 and 24 h for tumor studies, the afterglow intensity can already have dropped by a factor 100. Therefore, *in situ* reexcitation by long-wavelength visible or NIR light can be a valuable asset for the consideration of NIR-emitting persistent phosphors for medical imaging applications. Obviously, this requires that (part of) the excitation spectrum of the particles lies in or near the edge of the tissue optical transparency window, which is not an easy task to accomplish.

Note, however, that the presence of such excitation bands forms by no means a certitude for efficient repeated charging of the nanoprobes at these wavelengths, as excitation of the dopant ion is not necessarily leading to trapping. Although phosphor dependent, excitation into the lower excitation bands has often a lower trapping efficiency, which necessitates high optical power of the excitation source. Furthermore, the charging efficiency can depend on the temperature during excitation (Li et al., 2015; Maldiney et al., 2014; Smet et al., 2012c).

Alternatively, the persistent luminescence can temporarily be increased through photostimulation of deep trap levels in storage phosphors by IR light (Liu et al., 2013; Sharma et al., 2014b; Zhuang et al., 2013b), to allow imaging with higher SNR at regular intervals. Note, however, that the integrated light output is limited by the energy stored prior to injection. Only upconversion luminescence, where two IR photons are absorbed and give rise to one photon with a shorter wavelength, can yield additional light emission (Liu et al., 2014; Wang et al., 2010; Zhou et al., 2012). The discussion of the latter effect falls outside the present scope.

10.2 Lanthanide-Based Phosphors

Commercially available blue- and green-emitting persistent phosphors are almost exclusively based on divalent europium as their luminescent center, which outperforms other dopant ions. Therefore, first-generation probes for *in vivo* imaging were based on Eu^{2+} -based phosphors (Van den Eeckhout et al., 2010).

The Eu^{2+} emission wavelength depends on the employed host material, with aluminates and silicates yielding mostly blue or green emission. The required red shift of the Eu^{2+} emission for *in vivo* applications, can only be

TABLE 12 Deep Red-Emitting Persistent Phosphors Based on Ln Doping

Host	Dopants	Emission Max. (nm)	References
CaMgSi ₂ O ₆	Eu ²⁺ , Pr ³⁺ , Mn ²⁺	685	Maldiney et al. (2011a)
Ca _{0.2} Zn _{0.9} Mg _{0.9} Si ₂ O ₆	Eu ²⁺ , Dy ³⁺ , Mn ²⁺	690	le Masne de Chermont et al. (2007)
CaS	Eu ²⁺ , Tm ³⁺ (Ce ³⁺)	650	Jia (2006a) and Jia et al. (2000a,c)
Y ₂ O ₂ S	Eu ³⁺ , Ti ⁴⁺ , Mg ²⁺	626	Poelman et al. (2009), Holsa et al. (2009), and Hong et al. (2007)
Ca ₂ Si ₄	Eu ²⁺ , Nd ³⁺	660	Smet et al. (2009)
Ca ₂ Si ₅ N ₈	Eu ²⁺ , Tm ³⁺	610	Maldiney et al. (2012b) and Van den Eeckhout et al. (2011)

achieved in a limited number of compounds (Table 12) (Smet et al., 2011). Therefore, transition metals, such as manganese that have longer emission wavelengths, have been used as codopants alongside the Eu²⁺ ions. Eu²⁺ then acts as sensitizer ion for these transition metals via (so-called persistent) energy transfer. Host modification of MgSiO₃ with Ca and Zn resulted in the desired red shifting in the case of Ca_{0.2}Zn_{0.9}Mg_{0.9}Si₂O₆:Eu²⁺, Dy³⁺, Mn²⁺ (le Masne de Chermont et al., 2007). With a maximum afterglow emission intensity around 690 nm, this phosphor was shown to be applicable as proof-of-concept for injection in white Swiss mice, obtaining a SNR > 5. PEG-ylation resulted in delayed uptake by liver and spleen, and the injected particles could be monitored for about 30 min (le Masne de Chermont et al., 2007). Introduction of Pr³⁺ in CaMgSi₂O₆:Eu²⁺, Pr³⁺, Mn²⁺, instead of Dy³⁺ codoping, optimized the trap depth (Maldiney et al., 2011a).

Another promising first-generation Eu²⁺-based probe was the phosphor Ca₂Si₅N₈:Eu²⁺, Tm³⁺, part of the nitride-silicate family (Maldiney et al., 2012b; Van den Eeckhout et al., 2011). One of the key features of this phosphor is its excellent stability in an aqueous medium, losing only 2% of afterglow emission intensity after 2-year storage in water. Its orange emission at 610 nm lies at the short wavelength edge of the first optical window of tissue, which is not ideal, but the width of the emission band and the high emission intensity somewhat compensates this drawback. PEG-ylated particles in mice could be monitored for 15 min after excitation and injection, before uptake in

reticuloendothelial system (RES) organs took place. $\text{Ca}_2\text{Si}_5\text{N}_8:\text{Eu}^{2+},\text{Tm}^{3+}$ can also be recharged via excitation into the lowest 5d level of Eu^{2+} , with reasonable efficiency (Smet et al., 2012c).

10.3 Cr^{3+} -Based Phosphors

Recent developments in NIR-emitting persistent phosphors have mostly been focusing on introducing Cr^{3+} dopants in spinel hosts (Table 13), with a structural formula of AB_2O_4 (Zhuang et al., 2014b). Spinel compounds have a cubic crystal structure, with two different cation lattice sites A and B. A is

TABLE 13 Known Compounds of Red to NIR Persistent Phosphors Activated by Cr^{3+}

Host	Incorporated Site	Emission Region (nm)	References
ZnGa_2O_4	Ga^{3+} (VI)	650–730	Zhuang et al. (2013a,b, 2014a), Maldiney et al. (2014), and Bessière et al. (2011, 2014)
MgGa_2O_4	Ga^{3+} (VI)	650–770	Basavaraju et al. (2015) and Zhang et al. (2013d)
$\text{Zn}_{1+x}\text{Ga}_2-2x\text{Ge}_x\text{O}_4$	Ga^{3+} (VI)	680–800	Pan et al. (2012), Allix et al. (2013), Abdukayum et al. (2013), and Li et al. (2014b)
$\text{Zn}_{1.5}\text{GaSn}_{0.5}\text{O}_4$	Ga^{3+} (VI)	680–800	Allix et al. (2013) and Li et al. (2014c)
$\text{La}_3\text{Ga}_5\text{GeO}_{14}$	Ga^{3+} (VI)	660–1100	Jia et al. (2010) and Yan et al. (2010)
LiGa_5O_8	Ga^{3+} (VI)	680–760	Fu et al. (2014) and Liu et al. (2013)
Ga_2O_3	Ga^{3+} (VI)	650–850	Lu et al. (2011) and Wang et al. (2013a)
$\text{SrGa}_{12}\text{O}_{19}$	Ga^{3+} (VI)	660–900	Xu et al. (2014)
$\text{Y}_3\text{Al}_2\text{Ga}_3\text{O}_{10}$	Ga^{3+} (VI)	660–750	Xu et al. (2015) and Ueda et al. (2014b)
$\text{Gd}_3\text{Ga}_5\text{O}_{10}$	Ga^{3+} (VI)	660–800	Blasse et al. (1993) and Kostyk et al. (2009)

Reproduced from Zhuang et al. (2014b).

typically a Zn^{2+} or Mg^{2+} ion in tetrahedral coordination with oxygen ions. B is an octahedral site, usually occupied by Al^{3+} or Ga^{3+} . The currently most efficient red-emitting persistent spinel phosphor is $\text{ZnGa}_2\text{O}_4:\text{Cr}^{3+}$, with an emission band peaking at a wavelength of 695 nm (Bessière et al., 2011, 2014; Gourier et al., 2014). The Cr^{3+} ions mostly substitute Ga^{3+} in the octahedral site, because Cr^{3+} and Ga^{3+} have the same ionic radius in spinel (0.62 Å). However, inversion between Ga^{3+} and Zn^{2+} in octahedral and tetrahedral lattice sites is possible, a common effect in spinel compounds. This creates antisite defects and it has been shown that persistent luminescence of Cr^{3+} in ZnGa_2O_4 most probably stems from chromium ions influenced by a perturbed crystal field due to such antisite defects, located within the first cationic neighbors of Cr^{3+} (Gourier et al., 2014); 0.5% Cr^{3+} concentration appears to be the optimal dopant amount, as higher Cr^{3+} concentrations lead to quenching effects (Sharma et al., 2014a).

The strength of the crystal field changes with the metal ions used. This explains the differences between Cr^{3+} -doped ZnGa_2O_4 , ZnAl_2O_4 , MgGa_2O_4 , and MgAl_2O_4 with regard to excitation and emission wavelengths, as well as persistent luminescent behavior (Basavaraju et al., 2015; Sharma et al., 2014b). For example, MgGa_2O_4 shows a lower persistent luminescence intensity when compared to ZnGa_2O_4 , but the upper excitation band is red shifted from 580 to around 600 nm, closer to the optical tissue window, meaning that for *in vivo* imaging applications, this material may be more efficiently re-excited. Alternatively, because of the deeper trap levels in ZnAl_2O_4 , this host could be used as storage phosphor in the future.

$\text{ZnGa}_2\text{O}_4:\text{Cr}^{3+}$ nanoprobes, injected in lab mice, could be monitored for 2 h without need for reexcitation (Maldiney et al., 2014). The persistent luminescence diminished after 15 h, after which the particles could be reexcited *in vivo* with a 5000 lm orange/red LED source.

Several modifications to the zinc gallate spinels have improved the persistent luminescent properties of the phosphor. Partial substitution of Ga^{3+} with Ge^{4+} or Sn^{4+} has led to a largely increased afterglow time (detectable for >300 h with night vision equipment) (Allix et al., 2013; Pan et al., 2012). This increase is due to the distortion of octahedral sites occupied by Cr^{3+} by the substitution of Ga by Sn or Ge in neighboring sites, which creates additional efficient deep trap levels, aside from the inherent antisite defects of nonsubstituted ZnGa_2O_4 . PEG-ylated $\text{Zn}_3\text{Ga}_2\text{Ge}_2\text{O}_{10}:\text{Cr}^{3+},\text{Pr}^{3+}$ nanoprobes injected in lab mice showed excellent imaging properties, obtaining a SNR of 5 for 7.5 h after injection (Abdukayum et al., 2013).

Codoping of $\text{ZnGa}_2\text{O}_4:\text{Cr}^{3+}$ with Bi_2O_3 resulted in a 10 times increased afterglow intensity (Zhuang et al., 2013a). The incorporation of Bi^{3+} helps in mitigating a self-reduction effect of Zn-deficient ZnGa_2O_4 . Ga^{3+} ions occupying tetragonal sites in the lattice will release electrons as a means of charge compensation. These electrons will then reduce Cr^{3+} ions, which leads to a

decrease in persistent luminescence. By codoping the phosphor with Bi^{3+} , the reduction of Cr^{3+} is eschewed because Bi^{3+} will be more easily reduced to lower valence states.

An alternative to the chromium-doped zinc gallate spinel hosts has recently been found in $\text{LiGa}_5\text{O}_8:\text{Cr}^{3+}$ (Fu et al., 2014; Liu et al., 2013). This phosphor has an afterglow emission wavelength of 716 nm and has been shown to have detectable afterglow for over 1000 h. Polyethylenimine-functionalized $\text{LiGa}_5\text{O}_8:\text{Cr}^{3+}$ nanoparticles injected into lab mice could be monitored for 4 h after excitation without the need for reexcitation. By using a white LED for reexcitation of the nanoparticles, the injected phosphors could be monitored for 10 days after injection.

A new development for chromium-doped spinel hosts is codoping $\text{ZnGa}_2\text{O}_4:\text{Cr}^{3+}$ with Gd^{3+} ions, which allows for multimodal imaging (Maldiney et al., 2015). Here, optical imaging of Cr^{3+} originating persistent luminescence can be combined with MRI imaging of the magnetic Gd^{3+} ions in the host. The combination of the two techniques greatly enhances the potential of *in vivo* monitoring applications.

10.4 Other Phosphors

Before the rise in interest in Cr^{3+} -based materials, Mn^{2+} doping seemed like the obvious alternative to Eu^{2+} , because of the typical yellow-to-red emission (Table 14) when incorporated into octahedral sites (Van den Eeckhout et al., 2013b; Zhuang et al., 2014b). Diopside structured ABO_3 hosts, where $A = \text{Cd}^{2+}, \text{Mg}^{2+}, \text{Ca}^{2+}$, or a combination of these ions and $B = \text{Si}^{4+}$, are mostly used (Abreu et al., 2013; Lecointre et al., 2010b, 2013; Wang et al., 2003a). Oxygen vacancies are suspected to act as trap levels after ionization of Mn^{2+} upon excitation, after which detrapping and recombination to Mn^{2+} can occur (Katayama et al., 2014). This results in an intense persistent luminescence around 700 nm. Codoping with various Ln^{3+} ions, such as Dy^{3+} or Pr^{3+} induces additional electron or hole traps, which can improve the persistent luminescence of Mn^{2+} . The afterglow in these materials typically lasts for about 1 h, which needs to be improved for these Mn-doped materials to be viable for practical applications.

Phosphate hosts, such as $\text{Zn}_3(\text{PO}_4)_2$, $\text{Ca}_3(\text{PO}_4)_2$, or $\text{Ca}_9\text{Ln}(\text{PO}_4)_7$, were also investigated for their persistent luminescent behavior when doped with Mn^{2+} (Lecointre et al., 2010a, 2011a; Wang et al., 2005a). The advantage of these phosphate hosts is their high biocompatibility. At low Mn^{2+} concentration, the Mn ions are incorporated in octahedral Ca^{2+} sites and show both red fluorescence and LLP around 655 nm. After synthesis, thermal annealing under reducing atmosphere improves the LLP intensity of these phosphors. Unfortunately, because of the shallow character of the electron traps, the afterglow duration of these phosphates is much lower than other red persistent phosphors.

TABLE 14 Known Compounds of Red to NIR Persistent Phosphors Activated by Mn^{2+}

Host	Incorporated Site	Emission Region (nm)	References
$MgSiO_3$	Mg^{2+} (VI)	600–750	Lin et al. (2008a)
$CdSiO_3$	Cd^{2+} (VI)	550–720	Abreu et al. (2013)
(Mg/Ca) SiO_3	Mg^{2+}/Ca^{2+} (VI)	550–800	Lecointre et al. (2010b, 2013)
(Mg/Sr) SiO_3	Mg^{2+}/Sr^{2+} (VI)	500–800	He et al. (2007)
$MgGeO_3$	Mg^{2+} (VI)	600–720	Cong et al. (2009) and Katayama et al. (2014)
$Zn_3(PO_4)_2$	Zn^{2+} (VI)	570–700	Song et al. (2007) and Wang et al. (2004b, 2005a)
$Ca_3(PO_4)_2$	Ca^{2+} (VI)	600–750	Bessiere et al. (2013) and Lecointre et al. (2011a)
$Ca_9Ln(PO_4)_7$	Ca^{2+} (VI)	600–750	Bessière et al. (2012)

Reproduced from [Zhuang et al. \(2014b\)](#).

11 OUTLOOK

During the last decade, there has been a large growth in the number of commercialized glow-in-the-dark ornamental objects, gadgets, and toys, most of them are based on the green-emitting strontium aluminate persistent phosphor. Obviously, this is a market segment which will keep growing, even if no new or more performing persistent phosphors become available.

If we consider applications with higher technological or societal relevance, then safety signage is certainly the prime application of persistent phosphors. Also in this case, the awareness of the potential of the technology is constantly increasing. For example, Nissan has recently presented a prototype of a glow-in-the-dark car.

11.1 Safety Signage

Currently, these materials are applied in many public spaces and other situations where emergency exit routes have to be visible upon electrical power failure. Their application range, however, depends on local regulations, e.g., in the case of requirements on minimum light levels within certain spaces (i.e., in lux) rather than specifications for the visibility of the safety signage (in cd/m^2). Clearly, the phosphor area or the light output should be increased

by many orders of magnitude to act as a replacement for battery powered light sources, even when using “ideal” and yet to be developed persistent phosphors (Table 11).

Present safety signage is based on green-emitting strontium aluminate phosphors. One could argue that developing a broader color gamut is desirable, as one is now limited to a single color. Specifically, red phosphors would make sense as this color is used in many reflective pictograms (e.g., stop- and fire-related signs). There are, however, a number of technical and physiological issues with full color emergency signage. First, it is far from trivial to develop a blue-emitting phosphor which can be pumped with violet or blue light. Indeed, for indoor applications, the available spectrum is limited on the short wavelength side—especially in the case of white LEDs based on blue pumping LEDs—so it is questionable whether a blue persistent phosphor can be sufficiently charged. On the long wavelength side, there is still a lack of suitable persistent phosphors. Although a number of yellow persistent phosphors have been described, chemically stable red phosphors are scarce. For safety applications, every photon counts, at least those detected by the human eye. Consequently, red emission beyond 650 nm is not very energy efficient, as the eye sensitivity becomes low. This rules out the recent class of performing Cr^{3+} persistent phosphors with remarkably high storage capacity. Persistent red Eu^{2+} emission can be found in certain nitride materials, although the storage capacity of for instance $\text{Ca}_2\text{Si}_5\text{N}_8:\text{Eu},\text{Tm}$ is still limited. Eu^{3+} -based persistent phosphors offer in principle an excellent compromise between color purity and eye sensitivity, but they are notoriously difficult to charge by means of visible light.

Hypothesizing the development of novel, high-performance persistent phosphors in the coming years, application into full color safety signage is not straightforward. If the different colors are characterized by different afterglow decay curves, this will lead to changes in the overall appearance. Furthermore, in the later stages after the power failure, when the luminance of the signage has strongly decreased, the eye becomes less color sensitive, which would make blue, green, and yellow emission indistinguishable, and red even invisible, thereby making certain signage unreadable.

To achieve white persistent luminescence, different roads can be followed. Simply mixing of persistent phosphors with different colors is not desirable due to color shifts which are likely to occur during the afterglow, for the reason mentioned earlier.

A reasonable approach is by using a so-called “persistent energy transfer,” from the ion—typically europium—responsible for the afterglow emission to a second dopant—often Mn^{2+} —which is not taking part in the afterglow process directly. Consequently, the emission spectrum is stable throughout the afterglow duration. Alternatively, white luminescence based on a single ion, such as in the case of Bi^{3+} in ZnGa_2O_4 , is a viable approach (Zhuang et al., 2012).

Persistent phosphors based on Dy^{3+} would make sense in this respect, as the emission is characterized by two emission peaks around 480 and 575 nm. The combination of both blue and yellow emission yields a whitish emission. Although this type of narrow-banded emission spectrum has an extremely poor color rendering, making it useless for general illumination, it is appropriate for direct viewing, with the eye sensitivity being high for both components. The major drawback is the poor absorption strength of Dy^{3+} in the NUV to visible part of the spectrum, which would require some energy transfer from the actual recombination center.

11.2 Persistent Phosphors in Outdoor Applications

The use of persistent phosphors in road markings has been suggested for quite some time (Fig. 26). It would improve road safety at relatively low cost, by avoiding installation, maintenance, and electricity costs inherent to electrical street lighting. Charging of the persistent phosphors would occur during the daytime. The distribution of traps depths within such a phosphor should be designed in a way that the afterglow can remain above an acceptable level during the entire night. This is in contrast to the common safety signage phosphors which have to maintain certain light levels during “only” the first 30 min to 1 h. Note that a winter’s night at higher latitudes can easily last 16 h.

In 2014, a field test was performed in Oss in The Netherlands, initiated by Roosegaarde (WebBBC, 2014; WebSmartHighway, 2015). It turned out that the light output dropped too fast to maintain an acceptable level throughout the night. Upon evaluation of $\text{SrAl}_2\text{O}_4:\text{Eu},\text{Dy}$ for this particular application, it was found that the trap depth distribution in this material is favorable to counteract the different temperature regimes during winter and summer (Botterman and Smet, 2015). However, a temperature drop during the night



FIGURE 26 Day and night appearance of a LEGO® scene containing persistent luminescent road marks and signage.

is detrimental for the light output, due to the reduction in the thermal energy available for the release of the (remaining) trapped charges (Botterman and Smet, 2015).

For clear visibility, the light output of the road marks should be in the 0.5–1 cd/m² luminance range, throughout the entire night. Based on the simulation in Table 11, it is clear that this will require a large effective phosphor thickness.

11.3 Solar and Energy Storage Applications

It was suggested that persistent phosphors could be used to drive solar cells during the night, or to prolong the use of photocatalytic materials (Ma et al., 2013; Mei et al., 2015; Sun et al., 2014a). It should, however, be kept in mind that the total storage capacity of persistent phosphors is fairly limited, on the order of 0.6 J/g (for the best case scenario in SrAl₂O₄:Eu,Dy, see Section 9.2). This is approximately 0.5% of the storage capacity of rechargeable NiMH batteries. When a 100- μ m thick phosphor layer would be deposited onto a solar cell, then the storage capacity is about 0.022 J/cm². When released overnight, this gives an average irradiance of the order of 0.5 μ W/cm² or 5 mW/m² (supposing all the emitted light is collected), which is negligible. Note that this hypothetical phosphor layer would be fully charged on a sunny day (1000 W/m², with 14% of the spectrum being useful to fill traps) in less than 2 s. Viewed from the perspective of the solar cell, the storage capacity within the persistent phosphor is equivalent to at most 2 s of solar irradiance, which will easily be outbalanced by losses induced by the addition of the phosphor layer.

11.4 *In Vivo* Imaging

It is clear from the discussion in Section 10 that bioimaging by means of NIR persistent phosphors is a novel application area for persistent phosphors. Novel materials were developed, especially the Cr³⁺-based materials, which would otherwise have been of little use in the traditional application area of safety signage. The coming years are crucial to lift this approach from material development and a proof-of-principle status toward a routinely applied and established *in vivo* imaging technique, translating the technique to medical researchers.

11.5 Final Remarks

Twenty years after the development of SrAl₂O₄:Eu,Dy, the field of persistent luminescence appears lively and is still growing. Hundreds of compounds showing afterglow emission have been identified and reported. There is however a caveat. Few materials are finding their way to applications and strontium aluminates are still the main commercially used materials.

An improved understanding of the mechanisms behind persistent luminescence would be welcomed, as this would steer the development of novel materials. The observation that—although by trial-and-error—hundreds of novel materials emerged which are not even on par with $\text{SrAl}_2\text{O}_4:\text{Eu},\text{Dy}$, suggests that the wonder material with much larger storage capacity is very difficult to find, or even nonexistent. Apart from the use in *in vivo* imaging, the number of viable applications is strongly lagging behind. The related phenomena, such as ML (or piezoluminescence) and optically stimutable phosphors can possibly be a way to justify prolonged research efforts. The phenomenon of *glow-in-the-dark* remains nevertheless very fascinating, just as it triggered the curiosity of scientists since the early seventeenth century.

ABBREVIATIONS

CCD	charge-coupled device
CIE	Commission Internationale de l'Éclairage
EDX	energy-dispersive X-ray spectroscopy
ESR	electron spin resonance
MOVE	mesopic optimisation of visual efficiency
NIR	near-infrared
OSL	optically stimulated luminescence
PEG	polyethylene glycol
PT	photopic threshold
RT	room temperature
SEM	scanning electron microscopy
SNR	signal-to-noise ratio
ST	scotopic threshold
STE	self-trapped exciton
TL	thermoluminescence
TOF-SIMS	time of flight secondary ion mass spectroscopy
VI	visibility index
XANES	X-ray absorption near-edge structure
XAS	X-ray absorption spectroscopy
XRD	X-ray diffraction

REFERENCES

- Abbruscato, V., 1971. Optical and electrical properties of $\text{SrAl}_2\text{O}_4:\text{Eu}^{2+}$. *J. Electrochem. Soc.* 118 (6), 930–933.
- Abdukayum, A., Chen, J.-T., Zhao, Q., Yan, X.-P., 2013. Functional near infrared-emitting $\text{Cr}^{3+}/\text{Pr}^{3+}$ co-doped zinc gallogermanate persistent luminescent nanoparticles with super-long afterglow for *in vivo* targeted bioimaging. *J. Am. Chem. Soc.* 135 (38), 14125–14133.
- Abe, S., Uematsu, K., Toda, K., Sato, M., 2006. Luminescent properties of red long persistence phosphors, $\text{BaMg}_2\text{Si}_2\text{O}_7:\text{Eu}^{2+},\text{Mn}^{2+}$. *J. Alloys Compd.* 408, 911–914.

- Abreu, C.M., Silva, R.S., Valerio, M.E.G., Macedo, Z.S., 2013. Color-control of the persistent luminescence of cadmium silicate doped with transition metals. *J. Solid State Chem.* 200, 54–59.
- Ahmad, I., Marinova, V., Vrielinck, H., Callens, F., Goovaerts, E., 2011. A photosensitive Cr^{3+} center in photorefractive $\text{Bi}_{12}\text{SiO}_{20}$ crystals co-doped with chromium and phosphorus. *J. Appl. Phys.* 109 (8), 083506.
- Aitasalo, T., Hölsä, J., Laamanen, T., Lastusaari, M., Lehto, L., Niittykoski, J., Pellé, F., 2005. Luminescence properties of Eu^{2+} doped dibarium magnesium disilicate, $\text{Ba}_2\text{MgSi}_2\text{O}_7:\text{Eu}^{2+}$. *Ceramics-Silikáty* 49 (1), 58–62.
- Aitasalo, T., Hölsä, J., Kirm, M., Laamanen, T., Lastusaari, M., Niittykoski, J., Raud, J., Valtonen, R., 2007a. Persistent luminescence and synchrotron radiation study of the $\text{Ca}_2\text{MgSi}_2\text{O}_7:\text{Eu}^{2+},\text{R}^{3+}$ materials. *Radiat. Meas.* 42 (4–5), 644–647.
- Aitasalo, T., Hreniak, D., Hölsä, J., Laamanen, T., Lastusaari, M., Niittykoski, J., Pellé, F., Stręk, W., 2007b. Persistent luminescence of $\text{Ba}_2\text{MgSi}_2\text{O}_7:\text{Eu}^{2+}$. *J. Lumin.* 122–123, 110–112.
- Aitasalo, T., Hietikko, A., Hreniak, D., Hölsä, J., Lastusaari, M., Niittykoski, J., Stręk, W., 2008. Luminescence properties of $\text{BaMg}_2\text{Si}_2\text{O}_7:\text{Eu}^{2+},\text{Mn}^{2+}$. *J. Alloys Compd.* 451 (1–2), 229–231.
- Akiyama, M., Xu, C.N., Liu, Y., Nonaka, K., Watanabe, T., 2002. Influence of Eu,Dy co-doped strontium aluminate composition on mechanoluminescence intensity. *J. Lumin.* 97 (1), 13–18.
- Alexis, F., Pridgen, E., Molnar, L.K., Farokhzad, O.C., 2008. Factors affecting the clearance and biodistribution of polymeric nanoparticles. *Mol. Pharm.* 5 (4), 505–515.
- Allix, M., Chenu, S., Véron, E., Poumeyrol, T., Kouadri-Boudjelthia, E.A., Alahraché, S., Porcher, F., Massiot, D., Fayon, F., 2013. Considerable improvement of long-persistent luminescence in germanium and tin substituted ZnGa_2O_4 . *Chem. Mater.* 25 (9), 1600–1606.
- Avcı, N., Korhouth, K., Newton, M.A., Smet, P.F., Poelman, D., 2012. Valence states of europium in $\text{CaAl}_2\text{O}_4:\text{Eu}$ phosphors. *Opt. Mater. Express* 2 (3), 321–330.
- Avouris, P., Morgan, T.N., 1981. A tunneling model for the decay of luminescence in inorganic phosphors: the case of $\text{Zn}_2\text{SiO}_4:\text{Mn}$. *J. Chem. Phys.* 74 (8), 4347–4355.
- Bardhan, R., Lal, S., Joshi, A., Halas, N.J., 2011. Theranostic nanoshells: from probe design to imaging and treatment of cancer. *Acc. Chem. Res.* 44, 936–946.
- Basavaraju, N., Priolkar, K.R., Gourier, D., Sharma, S.K., Bessiere, A., Viana, B., 2015. The importance of inversion disorder in the visible light induced persistent luminescence in Cr^{3+} doped AB_2O_4 ($A=\text{Zn}$ or Mg and $B=\text{Ga}$ or Al). *Phys. Chem. Chem. Phys.* 17 (3), 1790–1799.
- Bellah, M.M., Christensen, S., Iqbal, S.M., 2012. Nanostructures for medical diagnostics. *J. Nanomater.* 2012, 486301.
- Bessière, A., Jacquart, S., Priolkar, K., Lecointre, A., Viana, B., Gourier, D., 2011. $\text{ZnGa}_2\text{O}_4:\text{Cr}^{3+}$: a new red long-lasting phosphor with high brightness. *Opt. Express* 19 (11), 10131–10137.
- Bessière, A., Benhamou, R.A., Wallez, G., Lecointre, A., Viana, B., 2012. Site occupancy and mechanisms of thermally stimulated luminescence in $\text{Ca}_9\text{Ln}(\text{PO}_4)_7$ ($\text{Ln}=\text{lanthanide}$). *Acta Mater.* 60 (19), 6641–6649.
- Bessiere, A., Lecointre, A., Priolkar, K.R., Gourier, D., 2012. Role of crystal defects in red long-lasting phosphorescence of $\text{CaMgSi}_2\text{O}_6:\text{Mn}$ diopsides. *J. Mater. Chem.* 22 (36), 19039–19046.
- Bessiere, A., Lecointre, A., Benhamou, R.A., Suard, E., Wallez, G., Viana, B., 2013. How to induce red persistent luminescence in biocompatible $\text{Ca}_3(\text{PO}_4)_2$. *J. Mater. Chem. C* 1 (6), 1252–1259.
- Bessière, A., Sharma, S.K., Basavaraju, N., Priolkar, K.R., Binet, L., Viana, B., Bos, A.J.J., Maldiney, T., Richard, C., Scherman, D., Gourier, D., 2014. Storage of visible light for long-lasting phosphorescence in chromium-doped zinc gallate. *Chem. Mater.* 26, 1365–1373.

- Blasse, G., Wanmaker, W.L., ter Vrugt, J.W., Bril, A., 1968. Fluorescence of Eu^{2+} -activated silicates. *Philips Res. Rep.* 23, 189–200.
- Blasse, G., Grabmaier, B.C., Ostertag, M., 1993. The afterglow mechanism of chromium-doped gadolinium gallium garnet. *J. Alloys Compd.* 200, 17–18.
- Bos, A.J.J., 2006. Theory of thermoluminescence. *Radiat. Meas.* 41, S45–S56.
- Bos, A.J.J., van Duijvenvoorde, R.M., van der Kolk, E., Drozdowski, W., Dorenbos, P., 2011. Thermoluminescence excitation spectroscopy: a versatile technique to study persistent luminescence phosphors. *J. Lumin.* 131 (7), 1465–1471.
- Botterman, J., Smet, P.F., 2015. Persistent phosphor $\text{SrAl}_2\text{O}_4:\text{Eu},\text{Dy}$ in outdoor conditions: saved by the trap distribution. *Opt. Express* 23 (15), A868–A881.
- Botterman, J., Van den Eeckhout, K., De Baere, I., Poelman, D., Smet, P.F., 2012. Mechanoluminescence in $\text{BaSi}_2\text{O}_2\text{N}_2:\text{Eu}$. *Acta Mater.* 60 (15), 5494–5500.
- Botterman, J., Joos, J.J., Smet, P.F., 2014. Trapping and detrapping in $\text{SrAl}_2\text{O}_4:\text{Eu},\text{Dy}$ persistent phosphors: influence of excitation wavelength and temperature. *Phys. Rev. B* 90 (8), 085147.
- Boutinaud, P., Sarakha, L., Cavalli, E., Bettinelli, M., Dorenbos, P., Mahiou, R., 2009a. About red afterglow in Pr^{3+} doped titanate perovskites. *J. Phys. D Appl. Phys.* 42 (4), 045106.
- Boutinaud, P., Sarakha, L., Mahiou, R., 2009b. $\text{NaNbO}_3:\text{Pr}^{3+}$: a new red phosphor showing persistent luminescence. *J. Phys. Condes. Mater.* 21 (2), 025901.
- Boutinaud, P., Boyer, D., Perthue, A., Mahiou, R., Cavalli, E., Brik, M.G., 2015. Spectroscopic investigations on SrAl_2O_4 polymorphs. *J. Lumin.* 159, 158–165.
- Brito, H.F., Holsa, J., Laamanen, T., Lastusaari, M., Malkamaki, M., Rodrigues, L.C.V., 2012. Persistent luminescence mechanisms: human imagination at work. *Opt. Mater. Express* 2 (4), 371–381.
- Brylew, K., Drozdowski, W., Wojtowicz, A.J., Kamada, K., Yoshikawa, A., 2014. Studies of low temperature thermoluminescence of GAGG:Ce and LuAG:Pr scintillator crystals using the T-max–T-stop method. *J. Lumin.* 154, 452–457.
- Capek, R.K., Lambert, K., Dorfs, D., Smet, P.F., Poelman, D., Eychmuller, A., Hens, Z., 2009. Synthesis of extremely small CdSe and bright blue luminescent CdSe/ZnS nanoparticles by a prefocused hot-injection approach. *Chem. Mater.* 21 (8), 1743–1749.
- Caratto, V., Locardi, F., Costa, G.A., Masini, R., Fasoli, M., Panzeri, L., Martini, M., Bottinelli, E., Gianotti, E., Miletto, I., 2014. NIR persistent luminescence of lanthanide ion-doped rare-earth oxycarbonates: the effect of dopants. *ACS Appl. Mater. Interfaces* 6 (20), 17346–17351.
- Carvalho, J.M., Rodrigues, L.C.V., Holsa, J., Lastusaari, M., Nunes, L.A.O., Felinto, M.C.F.C., Malta, O.L., Brito, H.F., 2012. Influence of titanium and lutetium on the persistent luminescence of ZrO_2 . *Opt. Mater. Express* 2 (3), 331–340.
- Chance, B., 1998. Near-infrared images using continuous, phase-modulated, and pulsed light with quantitation of blood and blood oxygenation. *Ann. N. Y. Acad. Sci.* 838, 29–45.
- Chandra, B.P., 2011. Development of mechanoluminescence technique for impact studies. *J. Lumin.* 131 (6), 1203–1210.
- Chandra, B.P., Xu, C.N., Yamada, H., Zheng, X.G., 2010. Luminescence induced by elastic deformation of $\text{ZnS}:\text{Mn}$ nanoparticles. *J. Lumin.* 130 (3), 442–450.
- Chandra, B.P., Sonwane, V.D., Haldar, B.K., Pandey, S., 2011. Mechanoluminescence glow curves of rare-earth doped strontium aluminate phosphors. *Opt. Mater.* 33 (3), 444–451.
- Chang, C., Li, W., Huang, X., Wang, Z., Chen, X., Qian, X., Guo, R., Ding, Y., Mao, D., 2010. Photoluminescence and afterglow behavior of $\text{Eu}^{2+},\text{Dy}^{3+}$ and $\text{Eu}^{3+},\text{Dy}^{3+}$ in $\text{Sr}_3\text{Al}_2\text{O}_6$ matrix. *J. Lumin.* 130 (3), 347–350.

- Che, G., Li, X., Liu, C., Wang, H., Liu, Y., Xu, Z., 2008a. Long-lasting phosphorescence properties of Mn^{2+} -doped $\text{Cd}_2\text{Ge}_7\text{O}_{16}$ orange light-emitting phosphor. *Phys. Status Solidi (a)* 205 (1), 194–198.
- Che, G., Liu, C., Li, X., Xu, Z., Liu, Y., Wang, H., 2008b. Luminescence properties of a new Mn^{2+} -activated red long-afterglow phosphor. *J. Phys. Chem. Solids* 69 (8), 2091–2095.
- Che, G.B., Liu, C.B., Wang, Q.W., Xu, Z.L., 2008c. White-light-emission afterglow phosphor $\text{CaZnGe}_2\text{O}_6:\text{Dy}^{3+}$. *Chem. Lett.* 37 (2), 136–137.
- Chen, R., 1969. Glow curves with general order kinetics. *J. Electrochem. Soc.* 116 (9), 1254.
- Chen, R., McKeever, S.W.S., 1997. *Theory of Thermoluminescence and Related Phenomena*. World Scientific, Singapore.
- Chen, Y., Cheng, X., Liu, M., Qi, Z., Shi, C., 2009. Comparison study of the luminescent properties of the white-light long afterglow phosphors: $\text{Ca}_x\text{MgSi}_2\text{O}_{5+x}:\text{Dy}^{3+}$ ($x = 1, 2, 3$). *J. Lumin.* 129 (5), 531–535.
- Chen, B.S., Zheng, Z.S., Lin, Y.M., Chen, G.L., Zhou, L., Guo, H.X., Huang, L.F., 2011. Preparation of a novel red long lasting phosphorescent material $\text{CaAl}_2\text{Si}_2\text{O}_8:\text{Mn}^{2+}$ and investigation of its luminescent properties. In: Sun, D., Sung, W.P., Chen, R. (Eds.), *Frontiers of Green Building, Materials and Civil Engineering*. Trans Tech Publications Ltd., Stafa-Zurich, pp. 1–8.
- Chen, S., Yang, Y., Zhou, G., Wu, Y., Liu, P., Zhang, F., Wang, S., Trojan-Piegeza, J., Zych, E., 2012. Characterization of afterglow-related spectroscopic effects in vacuum sintered $\text{Tb}^{3+}, \text{Sr}^{2+}$ co-doped Lu_2O_3 ceramics. *Opt. Mater.* 35 (2), 240–243.
- Chen, R., Hu, Y.H., Chen, L., Wang, X.J., Jin, Y.H., Wu, H.Y., 2014a. Luminescent properties of a novel afterglow phosphor $\text{Sr}_3\text{Al}_2\text{O}_5\text{Cl}_2:\text{Eu}^{2+}, \text{Ce}^{3+}$. *Ceram. Int.* 40 (6), 8229–8236.
- Chen, W.B., Wang, Y.H., Zeng, W., Han, S.C., Li, G., 2014b. Filling of trap and green long persistent luminescence in $\text{Sr}_3\text{Al}_2\text{O}_5\text{Cl}_2:\text{Tb}^{3+}$. *Opt. Mater.* 36 (11), 1850–1854.
- Chu, M.-H., Jiang, D.-P., Zhao, C.-J., Li, B., 2010. Long-lasting phosphorescence properties of pyrochlore $\text{La}_2\text{Ti}_2\text{O}_7:\text{Pr}^{3+}$ phosphor. *Chin. Phys. Lett.* 27 (4), 047203.
- CIE, 2005. *CIE S 010/E:2004: Photometry—The CIE System of Physical Photometry*. CIE Central Bureau, Vienna, Austria.
- Clabau, F., Rocquefelte, X., Le Mercier, T., Deniard, P., Jobic, S., Whangbo, M.H., 2006. Formulation of phosphorescence mechanisms in inorganic solids based on a new model of defect conglomeration. *Chem. Mater.* 18 (14), 3212–3220.
- Clabau, F., Rocquefelte, X., Jobic, S., Deniard, P., Whangbo, M.H., Garcia, A., Le Mercier, T., 2007. On the phosphorescence mechanism in $\text{SrAl}_2\text{O}_4:\text{Eu}^{2+}$ and its codoped derivatives. *Solid State Sci.* 9, 608–612.
- Clabau, F., Garcia, A., Bonville, P., Gonbeau, D., Le Mercier, T., Deniard, P., Jobic, S., 2008. Fluorescence and phosphorescence properties of the low temperature forms of the $\text{MAl}_2\text{Si}_2\text{O}_8:\text{Eu}^{2+}$ ($\text{M} = \text{Ca}, \text{Sr}, \text{Ba}$) compounds. *J. Solid State Chem.* 181 (6), 1456–1461.
- Cong, Y., Li, B., Lei, B., Li, W., 2007. Long lasting phosphorescent properties of Ti doped ZrO_2 . *J. Lumin.* 126 (2), 822–826.
- Cong, Y., Li, B., Wang, X.-J., Lei, B., Li, W., 2008. Synthesis and optical property studies of nanocrystalline $\text{ZrO}_2:\text{Ti}$ long-lasting phosphors. *J. Electrochem. Soc.* 155 (11), K195–K198.
- Cong, Y., Li, B., Yue, S., Zhang, L., Li, W., Wang, X.-j., 2009. Enhanced red phosphorescence in $\text{MgGeO}_3:\text{Mn}^{2+}$ by addition of Yb^{3+} ions. *J. Electrochem. Soc.* 156 (4), H272–H275.
- Davson, H., 1962. *The Eye: The Visual Process*. Academic Press, New York.
- Deng, Y.M., Yi, S.P., Huang, J., Zhao, W.R., Fang, X.B., 2013. A novel long lasting phosphor $\text{Sr}_3(\text{PO}_4)3\text{F}_x\text{Cl}_{1-x}:\text{Eu}^{2+}, \text{Gd}^{3+}$ prepared in air condition. *J. Rare Earths* 31 (10), 962–968.

- DIN, 2002. Deutsche Norm DIN 67510-1: Langnachleuchtende Pigmente und Produkte, Teil 1: Messung und Kennzeichnung beim Hersteller. Institut für Normung, Deutsches.
- Ding, Y., Zhang, Y., Wang, Z., Li, W., Mao, D., Han, H., Chang, C., 2009. Photoluminescence of Eu single doped and Eu/Dy codoped $\text{Sr}_2\text{Al}_2\text{SiO}_7$ phosphors with long persistence. *J. Lumin.* 129 (3), 294–299.
- Dorenbos, P., 2005. Mechanism of persistent luminescence in Eu^{2+} and Dy^{3+} codoped aluminate and silicate compounds. *J. Electrochem. Soc.* 152 (7), H107–H110.
- Dorenbos, P., Van Eijk, C.W.E., Bos, A.J.J., Melcher, C.L., 1994. Afterglow and thermoluminescence properties of $\text{Lu}_2\text{SiO}_5:\text{Ce}$ scintillation crystals. *J. Phys. Condes. Mater.* 6 (22), 4167–4180.
- Dorenbos, P., Bos, A.J.J., Poolton, N.R.J., You, F., 2013. Photon controlled electron juggling between lanthanides in compounds. *J. Lumin.* 133, 45–50.
- Eloholma, M., Halonen, L., 2006. New model for mesopic photometry and its application to road lighting. *Leukos* 2 (4), 263–293.
- Feng, P.F., Zhang, J.C., Wu, C.Q., Liu, X., Wang, Y.H., 2013. Self-activated afterglow luminescence of un-doped $\text{Ca}_2\text{ZrSi}_4\text{O}_{12}$ material and explorations of new afterglow phosphors in a rare earth element-doped $\text{Ca}_2\text{ZrSi}_4\text{O}_{12}$ system. *Mater. Chem. Phys.* 141 (1), 495–501.
- Frangioni, J., 2003. In vivo near-infrared fluorescence imaging. *Curr. Opin. Chem. Biol.* 7, 626–634.
- Fu, J., 2000. Orange and red emitting long-lasting phosphors $\text{MO}:\text{Eu}^{3+}$ ($\text{M}=\text{Ca}, \text{Sr}, \text{Ba}$). *Electrochem. Solid-State Lett.* 3 (7), 350–351.
- Fu, J., 2002. Orange- and violet-emitting long-lasting phosphors. *J. Am. Ceram. Soc.* 85 (1), 255–257.
- Fu, X., Liu, C., Shi, J., Man, H., Xu, J., Zhang, H., 2014. Long persistent near infrared luminescence nanoprobes $\text{LiGa}_5\text{O}_8:\text{Cr}^{3+}\text{-PEG-OCH}_3$ for in vivo imaging. *Opt. Mater.* 36, 1792–1797.
- Furetta, C., 2003. Handbook of Thermoluminescence. World Scientific, Singapore.
- Gao, X., Zhang, Z., Wang, C., Xu, J., Ju, Z., An, Y., Liu, W., 2011. The persistent energy transfer and effect of oxygen vacancies on red long-persistent phosphorescence phosphors $\text{Ca}_2\text{SnO}_4:\text{Gd}^{3+}, \text{Eu}^{3+}$. *J. Electrochem. Soc.* 158 (12), J405–J408.
- Garlick, G.F.J., Gibson, A.F., 1948. The electron trap mechanism of luminescence in sulphide and silicate phosphors. *Proc. Phys. Soc.* 60 (6), 574–590.
- Garlick, G.F.J., Mason, D.E., 1949. Electron traps and infrared stimulation of phosphors. *J. Electrochem. Soc.* 96 (2), 90–113.
- Gong, Y., Wang, Y., Li, Y., Xu, X., 2010. $\text{Ce}^{3+}, \text{Dy}^{3+}$ Co-doped white-light long-lasting phosphor: $\text{Sr}_2\text{Al}_2\text{SiO}_7$ through energy transfer. *J. Electrochem. Soc.* 157 (6), J208–J211.
- Gong, Y., Wang, Y., Xu, X., Li, Y., Xin, S., Shi, L., 2011. The persistent energy transfer of Eu^{2+} and Mn^{2+} and the thermoluminescence properties of long-lasting phosphor $\text{Sr}_3\text{MgSi}_2\text{O}_8:\text{Eu}^{2+}, \text{Mn}^{2+}, \text{Dy}^{3+}$. *Opt. Mater.* 33 (11), 1781–1785.
- Gong, Y., Xu, X.H., Zeng, W., Wu, C.J., Wang, Y.H., 2012. $\text{Ce}^{3+}, \text{Mn}^{2+}$ co-doped red—light long—lasting phosphor: $\text{BaMg}_2\text{Si}_2\text{O}_7$ through energy transfer. In: Rand, S.C., Carmon, T., Jarrahi, M. (Eds.), Proceedings of the 16th International Conference on Luminescence and Optical Spectroscopy of Condensed Matter: Posters. Elsevier Science BV, Amsterdam.
- Gourier, D., Bessière, A., Sharma, S.K., Binet, L., Viana, B., Basavaraju, N., Priolkar, K.R., 2014. Origin of the visible light induced persistent luminescence of Cr^{3+} -doped zinc gallate. *J. Phys. Chem. Solids* 75, 826–837.
- Guo, C., Zhang, C., Lü, Y., Tang, Q., Su, Q., 2004. Luminescent properties of Eu^{2+} and Ho^{3+} co-doped CaGa_2S_4 phosphor. *Phys. Status Solidi (a)* 201 (7), 1588–1593.

- Guo, C., Tang, Q., Huang, D., Zhang, C., Su, Q., 2007. Influence of co-doping different rare earth ions on $\text{CaGa}_2\text{S}_4: \text{Eu}^{2+}, \text{RE}^{3+}$ ($\text{RE}=\text{Ln}$) phosphors. *J. Phys. Chem. Solids* 68 (2), 217–223.
- Guo, H.J., Chen, W.B., Zeng, W., Wang, Y.H., Li, Y.Y., 2015. A long-lasting phosphor $\text{Ba}_3\text{P}_4\text{O}_{13}:\text{Eu}^{2+}$. *ECS Solid State Lett.* 4 (1), R1–R3.
- Gutiérrez-Martín, F., Fernández-Martínez, F., Díaz, P., Colón, C., Alonso-Medina, A., 2010. Persistent UV phosphors for application in photo catalysis. *J. Alloys Compd.* 501 (2), 193–197.
- Hang, T., Liu, Q., Mao, D., Chang, C., 2008. Long lasting behavior of $\text{Gd}_2\text{O}_2\text{S}:\text{Eu}^{3+}$ phosphor synthesized by hydrothermal routine. *Mater. Chem. Phys.* 107 (1), 142–147.
- Haranath, D., Khan, A.F., Chander, H., 2006. Bright red luminescence and energy transfer of Pr^{3+} -doped $(\text{Ca}, \text{Zn})\text{TiO}_3$ phosphor for long decay applications. *J. Phys. D Appl. Phys.* 39 (23), 4956–4960.
- Harvey, E.N. (Ed.), 1957. *A History of Luminescence from the Earliest Times Until 1900*. American Philosophical Society, Philadelphia, PA, USA.
- He, Z., Wang, X.-j., Yen, W.M., 2007. Behavior of Mn^{2+} ions in the trapping process of $\text{SrMg}(\text{SiO}_3)_2:\text{Mn}, \text{Dy}$. *J. Lumin.* 122–123, 381–384.
- Hecht, S., Schlaer, S., 1948. The visual functions of the complete colorblind. *J. Gen. Physiol.* 31 (6), 459–472.
- Hemmer, E., Venkatachalam, N., Hyodo, H., Hattori, A., Ebina, Y., Kishimoto, H., Soga, K., 2013. Upconverting and NIR emitting rare earth based nanostructures for NIR-bioimaging. *Nanoscale* 5 (23), 11339–11361.
- Hölsä, J., Jungner, H., Lastusaari, M., Niittykoski, J., 2001. Persistent luminescence of Eu^{2+} doped alkaline earth aluminates, $\text{MAl}_2\text{O}_4:\text{Eu}^{2+}$. *J. Alloys Compd.* 323–324, 326–330.
- Holsa, J., Laamanen, T., Lastusaari, M., Malkamaki, M., Niittykoski, J., Zych, E., 2009. Effect of Mg^{2+} and Ti-IV doping on the luminescence of $\text{Y}_2\text{O}_2\text{S}:\text{Eu}^{3+}$. *Opt. Mater.* 31 (12), 1791–1793.
- Holsa, J., Laamanen, T., Lastusaari, M., Malkamaki, M., Welter, E., Zajac, D.A., 2010. Valence and environment of rare earth ions in $\text{CaAl}_2\text{O}_4:\text{Eu}^{2+}, \text{R}^{3+}$ persistent luminescence materials. *Spectrochim. Acta B Atom. Spectros.* 65 (4), 301–305.
- Hong, Z., Zhang, P., Fan, X., Wang, M., 2007. Eu^{3+} red long afterglow in $\text{Y}_2\text{O}_2\text{S}:\text{Ti}, \text{Eu}$ phosphor through afterglow energy transfer. *J. Lumin.* 124 (1), 127–132.
- Hoogenstraaten, W., 1958. Electron traps in zinc sulphide phosphors. *Philips Res. Rep.* 13, 515.
- Hoogenstraaten, W., Klasens, H.A., 1953. Some properties of zinc sulfide activated with copper and cobalt. *J. Electrochem. Soc.* 100 (8), 366–375.
- Hosono, H., Kinoshita, T., Kawazoe, H., Yamazaki, M., Yamamoto, Y., Sawanobori, N., 1998. Long lasting phosphorescence properties of Tb^{3+} -activated reduced calcium aluminate glasses. *J. Phys. Condens. Matter* 10 (42), 9541–9547.
- Huang, Y.-Y., Hamblin, M., Chen, A.C.-H., 2009. Low-level laser therapy: an emerging clinical paradigm. *SPIE Newsroom*. <http://dx.doi.org/10.1117/2.1200906.1669>.
- Huang, P., Yang, F., Cui, C.E., Wang, L., Lei, X., 2013. Luminescence properties of white-light long-lasting phosphor $\text{Y}_2\text{O}_2\text{S}:\text{Dy}^{3+}, \text{Mg}^{2+}, \text{Si}^{4+}$. *Ceram. Int.* 39 (6), 7193–7197.
- ISO, 2004a. International Standard ISO 16069:2004(E): Graphical Symbols—Safety Signs—Safety Way Guidance Systems (SWGS).
- ISO, 2004b. International Standard ISO 17398:2004(E): Safety Colours and Safety Signs—Classification, Performance and Durability of Safety Signs.
- Ito, Y., Komeno, A., Uematsu, K., Toda, K., Sato, M., 2006. Luminescence properties of long-persistence silicate phosphors. *J. Alloys Compd.* 408–412, 907–910.
- Iwasaki, M., Kim, D.N., Tanaka, K., Murata, T., Morinaga, K., 2003. Red phosphorescence properties of Mn ions in $\text{MgO}-\text{GeO}_2$ compounds. *Sci. Technol. Adv. Mater.* 2, 137–142.

- Iwasaki, K., Takahashi, Y., Masai, H., Fujiwara, T., 2009. Blue photoluminescence, greenish-blue afterglow and their Ti-concentration dependence in rare earth-free bazirite-type $\text{BaZr}_{1-x}\text{Ti}_x\text{Si}_3\text{O}_9$. *Opt. Express* 17 (20), 18054–18062.
- Jeong, J., Jayasimhadri, M., Lee, H.S., Jang, K., Yi, S.S., Jeong, J.H., Kim, C., 2009. Photoluminescence and phosphorescence properties of $\text{Sr}_{1-x}\text{Zn}_{2-y}(\text{PO}_4)_2:\text{Eu}^{2+}, \text{Mn}^{2+}$ phosphor for UV-based white-LEDs. *Phys. B Condens. Matter* 404 (14–15), 2016–2019.
- Jia, D.D., 2003. Charging curves and excitation spectrum of long persistent phosphor $\text{SrAl}_2\text{O}_4:\text{Eu}^{2+}, \text{Dy}^{3+}$. *Opt. Mater.* 22 (1), 65–69.
- Jia, D., 2006a. Enhancement of long-persistence by Ce co-doping in $\text{CaS}:\text{Eu}^{2+}, \text{Tm}^{3+}$ red phosphor. *J. Electrochem. Soc.* 153 (11), H198–H201.
- Jia, D., 2006b. Relocalization of Ce^{3+} 5d electrons from host conduction band. *J. Lumin.* 117 (2), 170–178.
- Jia, D., Yen, W.M., 2003a. Enhanced V_K^{3+} center afterglow in MgAl_2O_4 by doping with Ce^{3+} . *J. Lumin.* 101 (1–2), 115–121.
- Jia, D., Yen, W.M., 2003b. Trapping mechanism associated with electron delocalization and tunneling of $\text{CaAl}_2\text{O}_4:\text{Ce}^{3+}$, a persistent phosphor. *J. Electrochem. Soc.* 150 (3), H61–H65.
- Jia, D., Jia, W., Evans, D.R., Dennis, W.M., Liu, H., Zhu, J., Yen, W.M., 2000a. Trapping processes in $\text{CaS}:\text{Eu}^{2+}, \text{Tm}^{3+}$. *J. Appl. Phys.* 88 (6), 3402–3407.
- Jia, D., Zhu, J., Wu, B., 2000b. Improvement of persistent phosphorescence of $\text{Ca}_{0.9}\text{Sr}_{0.1}\text{S}:\text{Bi}^{3+}$ by codoping Tm^{3+} . *J. Lumin.* 91 (1–2), 59–65.
- Jia, D., Zhu, J., Wu, B., 2000c. Trapping centers in $\text{CaS}:\text{Bi}^{3+}$ and $\text{CaS}:\text{Eu}^{2+}, \text{Tm}^{3+}$. *J. Electrochem. Soc.* 147 (1), 386–389.
- Jia, D., Meltzer, R.S., Yen, W.M., 2002a. Ce^{3+} energy levels relative to the band structure in CaS : evidence from photoionization and electron trapping. *J. Lumin.* 99 (1), 1–6.
- Jia, D., Meltzer, R.S., Yen, W.M., Jia, W., Wang, X., 2002b. Green phosphorescence of $\text{CaAl}_2\text{O}_4:\text{Tb}^{3+}, \text{Ce}^{3+}$ through persistence energy transfer. *Appl. Phys. Lett.* 80, 1535–1537.
- Jia, D., Wang, X.-j., van der Kolk, E., Yen, W.M., 2002c. Site dependent thermoluminescence of long persistent phosphorescence of $\text{BaAl}_2\text{O}_4:\text{Ce}^{3+}$. *Opt. Commun.* 204 (1–6), 247–251.
- Jia, D., Wang, X.-j., Yen, W.M., 2002d. Electron traps in Tb^{3+} -doped CaAl_2O_4 . *Chem. Phys. Lett.* 363 (3–4), 241–244.
- Jia, D., Wang, X.J., Jia, W., Yen, W.M., 2003. Persistent energy transfer in $\text{CaAl}_2\text{O}_4:\text{Tb}^{3+}, \text{Ce}^{3+}$. *J. Appl. Phys.* 93 (1), 148–152.
- Jia, W., Jia, D., Rodríguez, T., Evans, D.R., Meltzer, R.S., Yen, W.M., 2006. UV excitation and trapping centers in $\text{CaTiO}_3:\text{Pr}^{3+}$. *J. Lumin.* 119–120, 13–18.
- Jia, D., Wang, X.-j., Jia, W., Yen, W.M., 2007. Trapping processes of 5d electrons in Ce^{3+} doped SrAl_2O_4 . *J. Lumin.* 122–123, 311–314.
- Jia, D., Lewis, L.A., Wang, X.-j., 2010. Cr^{3+} -doped lanthanum gallogermanate phosphors with long persistent IR emission. *Electrochem. Solid-State Lett.* 13 (4), J32–J34.
- Jia, Y.L., Li, H.F., Zhao, R., Sun, W.Z., Su, Q., Pang, R., Li, C.Y., 2014. Luminescence properties of a new bluish green long-lasting phosphorescence phosphor $\text{Ca}_9\text{Bi}(\text{PO}_4)_7:\text{Eu}^{2+}, \text{Dy}^{3+}$. *Opt. Mater.* 36 (11), 1781–1786.
- Jiang, L., Chang, C., Mao, D., 2003a. Luminescent properties of $\text{CaMgSi}_2\text{O}_6$ and $\text{Ca}_2\text{MgSi}_2\text{O}_7$ phosphors activated by $\text{Eu}^{2+}, \text{Dy}^{3+}$ and Nd^{3+} . *J. Alloys Compd.* 360 (1–2), 193–197.
- Jiang, X.-W., Qiu, J.-R., Zeng, H.-D., Zhu, C.-S., 2003b. Femtosecond laser-induced long-lasting phosphorescence in Pr^{3+} -doped $\text{ZnO}-\text{B}_2\text{O}_3-\text{SiO}_2$ glass. *Chin. Phys.* 12 (12), 1386.
- Jiang, L., Chang, C., Mao, D., Feng, C., 2004. Luminescent properties of $\text{CaMgSi}_2\text{O}_6$ -based phosphors co-doped with different rare earth ions. *J. Alloys Compd.* 377 (1–2), 211–215.

- Jiang, L.L., Xiao, S.G., Yang, X.L., Zhang, X.A., Liu, X.H., Zhou, B.Y., Jin, X.L., 2013. Preparation and luminescence properties of yellow long-lasting phosphor $\text{Ca}_2\text{ZnSi}_2\text{O}_7:\text{Eu}^{2+}, \text{Dy}^{3+}$. *Mater. Sci. Eng. B Adv. Funct. Solid State Mater.* 178 (2), 123–126.
- Jin, Y., Hu, Y., Chen, L., Wang, X., Ju, G., Mu, Z., 2013a. Luminescent properties of Tb^{3+} -doped Ca_2SnO_4 phosphor. *J. Lumin.* 138 (6), 83–88.
- Jin, Y.H., Hu, Y.H., Chen, L., Wang, X.J., Ju, G.F., 2013b. Luminescent properties of a red afterglow phosphor $\text{Ca}_2\text{SnO}_4:\text{Pr}^{3+}$. *Opt. Mater.* 35 (7), 1378–1384.
- Jin, Y.H., Hu, Y.H., Chen, L., Wang, X.J., Ju, G.F., Mou, Z.F., 2013c. Luminescence properties of dual-emission (UV/Visible) long afterglow phosphor $\text{SrZrO}_3:\text{Pr}^{3+}$. *J. Am. Ceram. Soc.* 96 (12), 3821–3827.
- Jin, Y.H., Hu, Y.H., Chen, L., Wang, X.J., Ju, G.F., Mu, Z.F., 2013d. Persistent luminescence in Bi^{3+} doped CaWO_4 matrix. *Radiat. Meas.* 51–52, 18–24.
- Jin, Y.H., Hu, Y.H., Chen, L., Wang, X.J., Mou, Z.F., Ju, G.F., Liang, F., 2013e. Luminescent properties of a reddish orange emitting long-lasting phosphor $\text{CaO}:\text{Pr}^{3+}$. *Mater. Sci. Eng. B Adv. Funct. Solid State Mater.* 178 (18), 1205–1211.
- Jin, Y.H., Hu, Y.H., Chen, L., Wang, X.J., 2014a. Synthesis and persistent luminescence mechanism of a novel orange emitting persistent phosphor $\text{Sr}_5(\text{BO}_3)_3\text{Cl}:\text{Eu}^{2+}$. *J. Am. Ceram. Soc.* 97 (8), 2573–2579.
- Jin, Y.H., Hu, Y.H., Chen, L., Wang, X.J., Ju, G.F., Mou, Z.F., Liang, F., 2014b. Luminescence properties of a novel orange emission long persistent phosphor $\text{CaO}:\text{Sm}^{3+}$. *Opt. Commun.* 311, 266–269.
- Jin, Y.H., Hu, Y.H., Chen, L., Wang, X.J., Mu, Z.F., Ju, G.F., Wang, T., 2014c. A novel orange emitting long afterglow phosphor $\text{Ca}_3\text{Si}_2\text{O}_7:\text{Eu}^{2+}$ and the enhancement by R^{3+} ions ($\text{R} = \text{Tm}, \text{Dy}$ and Er). *Mater. Lett.* 126, 75–77.
- Jin, Y.H., Hu, Y.H., Duan, H., Chen, L., Wang, X.J., 2014d. The long persistent luminescence properties of phosphors: $\text{Li}_2\text{ZnGeO}_4$ and $\text{Li}_2\text{ZnGeO}_4:\text{Mn}^{2+}$. *RSC Adv.* 4 (22), 11360–11366.
- Ju, Z.-H., Zhang, S.-H., Gao, X.-P., Tang, X.-L., Liu, W.-S., 2011a. Reddish orange long afterglow phosphor $\text{Ca}_2\text{SnO}_4:\text{Sm}^{3+}$ prepared by sol–gel method. *J. Alloys Compd.* 509 (31), 8082–8087.
- Ju, Z.H., Wei, R.P., Zheng, J.R., Gao, X.P., Zhang, S.H., Liu, W.S., 2011b. Synthesis and phosphorescence mechanism of a reddish orange emissive long afterglow phosphor Sm^{3+} -doped Ca_2SnO_4 . *Appl. Phys. Lett.* 98 (12), 121906.
- Ju, G., Hu, Y., Chen, L., Wang, X., 2012. Persistent luminescence and its mechanism of $\text{Ba}_5(\text{PO}_4)_3\text{Cl}:\text{Ce}^{3+}, \text{Eu}^{2+}$. *J. Appl. Phys.* 111 (11), 113508.
- Ju, G.F., Hu, Y.H., Chen, L., Wang, X.J., 2014a. Investigation of the persistent luminescence of $\text{LiBaPO}_4:\text{Eu}^{2+}$. *J. Mater. Res.* 29 (4), 519–526.
- Ju, G.F., Hu, Y.H., Chen, L., Wang, X.J., Mu, Z.F., 2014b. Blue persistent luminescence in Eu^{2+} doped $\text{Ca}_3\text{Mg}_3(\text{PO}_4)_4$. *Opt. Mater.* 36 (7), 1183–1188.
- Jüstel, T., Bechtel, H., Mayr, W., Wiechert, D.U., 2003. Blue emitting $\text{BaMgAl}_{10}\text{O}_{17}:\text{Eu}$ with a blue body color. *J. Lumin.* 104 (1–2), 137–143.
- Kamimura, S., Yamada, H., Xu, C.-N., 2012. Development of new elasticoluminescent material $\text{SrMg}_2(\text{PO}_4)_2:\text{Eu}$. *J. Lumin.* 132 (2), 526–530.
- Kamimura, S., Xu, C.N., Yamada, H., Terasaki, N., Fujihala, M., 2014. Long-persistent luminescence in the near-infrared from Nd^{3+} -doped Sr_2SnO_4 for in vivo optical imaging. *Jpn. J. Appl. Phys.* 53 (9), 092403.
- Kamps, J.A., Morselt, H.W., Swart, P.J., Meijer, D.K., Scherphof, G.L., 1997. Massive targeting of liposomes, surface-modified with anionized albumins, to hepatic endothelial cells. *Proc. Natl. Acad. Sci. U. S. A.* 94 (21), 11681–11685.

- Kamps, J.A., Morselt, H.W., Scherphof, G.L., 1999. Uptake of liposomes containing phosphatidylserine by liver cells in vivo and by sinusoidal liver cells in primary culture: in vivo—in vitro differences. *Biochem. Biophys. Res. Commun.* 256 (1), 57–62.
- Kang, C.-C., Liu, R.-S., Chang, J.-C., Lee, B.-J., 2003. Synthesis and luminescent properties of a new yellowish-orange afterglow phosphor $\text{Y}_2\text{O}_2\text{S}:\text{Ti},\text{Mg}$. *Chem. Mater.* 15 (21), 3966–3968.
- Kang, F.-W., Hu, Y.-H., Wu, H.-Y., Ju, G.-F., 2011. Red afterglow properties of Eu^{3+} in CaMoO_4 phosphor. *Chin. Phys. Lett.* 28 (10), 107201.
- Kang, F., Hu, Y., Chen, L., Wang, X., Mu, Z., Wu, H., Ju, G., 2012a. Eu^{3+} doped CaWO_4 —a potential red long afterglow phosphor. *Appl. Phys. B* 107 (3), 833–837.
- Kang, F., Hu, Y., Wu, H., Mu, Z., Ju, G., Fu, C., Li, N., 2012b. Luminescence and red long afterglow investigation of $\text{Eu}^{3+}\text{—Sm}^{3+}$ Co-doped CaWO_4 phosphor. *J. Lumin.* 132 (4), 887–894.
- Kanno, H., Noda, K., Matsui, K., 2013. New long-afterglow phosphors: Yb^{2+} -doped strontium aluminates. *Chem. Phys. Lett.* 580, 103–107.
- Katayama, Y., Ueda, J., Tanabe, S., 2014. Effect of Bi_2O_3 doping on persistent luminescence of $\text{MgGeO}_3:\text{Mn}^{2+}$ phosphor. *Opt. Mater. Express* 4, 613–623.
- Katsumata, T., Nabae, T., Sasajima, K., Komuro, S., Morikawa, T., 1997. Effects of composition on the long phosphorescent $\text{SrAl}_2\text{O}_4:\text{Eu}^{2+},\text{Dy}^{3+}$ phosphor crystals. *J. Electrochem. Soc.* 144 (9), L243–L245.
- Katsumata, T., Nabae, T., Sasajima, K., Matsuzawa, T., 1998a. Growth and characteristics of long persistent SrAl_2O_4 - and CaAl_2O_4 -based phosphor crystals by a floating zone technique. *J. Cryst. Growth* 183 (3), 361–365.
- Katsumata, T., Sasajima, K., Nabae, T., Komuro, S., Morikawa, T., 1998b. Characteristics of strontium aluminate crystals used for long-duration phosphors. *J. Am. Ceram. Soc.* 81 (2), 413–416.
- Kinoshita, T., Hosono, H., 2000. Materials design and example of long lasting phosphorescent glasses utilizing electron trapped centers. *J. Non-Cryst. Solids* 274 (1-3), 257–263.
- Kinoshita, T., Yamazaki, M., 1999. Long lasting phosphorescence and photostimulated luminescence in Tb-ion-activated reduced calcium. *J. Appl. Phys.* 86 (7), 3729.
- Kodama, N., Takahashi, T., Yamaga, M., Tani, Y., Qiu, J., Hirao, K., 1999. Long-lasting phosphorescence in Ce^{3+} -doped $\text{Ca}_2\text{Al}_2\text{SiO}_7$ and CaYAl_3O_7 crystals. *Appl. Phys. Lett.* 75 (12), 1715–1717.
- Kodama, N., Tani, Y., Yamaga, M., 2000. Optical properties of long-lasting phosphorescent crystals Ce^{3+} -doped $\text{Ca}_2\text{Al}_2\text{SiO}_7$ and CaYAl_3O_7 . *J. Lumin.* 87–89, 1076–1078.
- Kojima, Y., Takahashi, A., Umegaki, T., 2014. Synthesis of orange-red-emitting $\text{Eu}^{2+},\text{Pr}^{3+}$ codoped SrS long afterglow phosphor. *J. Lumin.* 146, 42–45.
- Korthout, K., Van den Eeckhout, K., Botterman, J., Nikitenko, S., Poelman, D., Smet, P.F., 2011. Luminescence and X-ray absorption measurements of persistent $\text{SrAl}_2\text{O}_4:\text{Eu},\text{Dy}$ powders: evidence for valence state changes. *Phys. Rev. B* 84 (8), 085140.
- Kostyk, L., Luchechko, A., Zakharko, Y., Tsvetkova, O., Kukliński, B., 2009. Cr-related centers in $\text{Gd}_3\text{Ga}_5\text{O}_{12}$ polycrystals. *J. Lumin.* 129 (3), 312–316.
- Kuang, J., Liu, Y., 2005. White-emitting long-lasting phosphor $\text{Sr}_2\text{SiO}_4:\text{Dy}^{3+}$. *Chem. Lett.* 34 (4), 598–599.
- Kuang, J., Liu, Y., 2006a. Luminescence properties of a Pb^{2+} activated long-afterglow phosphor. *J. Electrochem. Soc.* 153 (3), G245–G247.
- Kuang, J., Liu, Y., 2006b. Observation of energy transfer from host to rare earth ions in Pr^{3+} -doped CdSiO_3 long-lasting phosphor. *Chem. Phys. Lett.* 424 (1–3), 58–62.
- Kuang, J.Y., Liu, Y.L., 2006c. Trapping effects in $\text{CdSiO}_3:\text{In}^{3+}$ long afterglow phosphor. *Chin. Phys. Lett.* 23 (1), 204–206.

- Kuang, J., Liu, Y., Zhang, J., Huang, L., Rong, J., Yuan, D., 2005a. Blue-emitting long-lasting phosphor, $\text{Sr}_3\text{Al}_{10}\text{SiO}_{20}:\text{Eu}^{2+},\text{Ho}^{3+}$. *Solid State Commun.* 136 (1), 6–10.
- Kuang, J.Y., Liu, Y.L., Zhang, J.X., Yuan, D.S., Huang, L.H., Rong, J.H., 2005b. Long-lasting phosphorescence of Tb^{3+} doped MO (M=Ca, Sr). *Chin. J. Inorg. Chem.* 21 (9), 1383–1385.
- Kuang, J., Liu, Y., Zhang, J., 2006a. White-light-emitting long-lasting phosphorescence in Dy^{3+} -doped SrSiO_3 . *J. Solid State Chem.* 179 (1), 266–269.
- Kuang, J.Y., Liu, Y.L., Zhang, J.X., 2006b. Effects of RE^{3+} as a co-dopant in blue-emitting long-lasting phosphors, $\text{Sr}_3\text{Al}_{10}\text{SiO}_{20}:\text{Eu}^{2+}$. *J. Mater. Sci.* 41 (17), 5500–5503.
- Lakshminarasimhan, N., Varadaraju, U.V., 2008. Luminescence and afterglow in $\text{Sr}_2\text{SiO}_4:\text{Eu}^{2+}, \text{RE}^{3+}$ [RE=Ce, Nd, Sm and Dy] phosphors—role of co-dopants in search for afterglow. *Mater. Res. Bull.* 43 (11), 2946–2953.
- Lastusaari, M., Laamanen, T., Malkamäki, M., Eskola, K.O., Kotlov, A., Carlson, S., Welter, E., Brito, H.F., Bettinelli, M., Jungner, H., Hölsä, J., 2012. The Bologna Stone: history's first persistent luminescent material. *Eur. J. Mineral.* 24 (5), 885–890.
- Lastusaari, M., Brito, H.F., Carlson, S., Holsa, J., Laamanen, T., Rodrigues, L.C.V., Welter, E., 2014. Valences of dopants in Eu^{2+} persistent luminescence materials. *Phys. Scr.* 89 (4), 044004.
- Lawangar, R.D., Shalgaonkar, C.S., Pawar, S.H., Narlikar, A.V., 1972. Thermally stimulated luminescence of $\text{CaS}:\text{Bi}:\text{Pd}$ phosphors. *Solid State Commun.* 10 (12), 1241–1246.
- le Masne de Chermont, Q., Chanéac, C., Seguin, J., Pellé, F., Maîtrejean, S., Jolivet, J.-P., Gourier, D., Bessodes, M., Scherman, D., 2007. Nanoprobes with near-infrared persistent luminescence for in vivo imaging. *Proc. Natl. Acad. Sci.* 104 (22), 9266–9271.
- Leblans, P., Vandenbroucke, D., Willems, P., 2011. Storage phosphors for medical imaging. *Materials* 4 (6), 1034–1086.
- Lecointre, A., Viana, B., LeMasne, Q., Bessière, A., Chanéac, C., Gourier, D., 2009. Red long-lasting luminescence in clinooenstatite. *J. Lumin.* 129 (12), 1527–1530.
- Lecointre, A., Bessière, A., Viana, B., Ait Benhamou, R., Gourier, D., 2010a. Thermally stimulated luminescence of $\text{Ca}_3(\text{PO}_4)_2$ and $\text{Ca}_9\text{Ln}(\text{PO}_4)_7$ (Ln=Pr, Eu, Tb, Dy, Ho, Er, Lu). *Radiat. Meas.* 45, 273–276.
- Lecointre, A., Bessière, A., Viana, B., Gourier, D., 2010b. Red persistent luminescent silicate nanoparticles. *Radiat. Meas.* 45 (3–6), 497–499.
- Lecointre, A., Ait Benhamou, R., Bessière, A., Wallez, G., Elaammani, M., Viana, B., 2011a. Red long-lasting phosphorescence (LLP) in β -TCP type $\text{Ca}_9\text{Mn}(\text{PO}_4)_7$ compounds. *Opt. Mater.* 34 (2), 376–380.
- Lecointre, A., Bessière, A., Bos, A.J.J., Dorenbos, P., Viana, B., Jacquart, S., 2011b. Designing a red persistent luminescence phosphor: the example of $\text{YPO}_4:\text{Pr}^{3+},\text{Ln}^{3+}$ (Ln=Nd, Er, Ho, Dy). *J. Phys. Chem. C* 115 (10), 4217–4227.
- Lecointre, A., Bessière, A., Priolkar, K.R., Gourier, D., Wallez, G., Viana, B., 2013. Role of manganese in red long-lasting phosphorescence of manganese-doped diopside for in vivo imaging. *Mater. Res. Bull.* 48, 1898–1905.
- Lei, B.F., Liu, Y.L., Tang, G.B., Ye, Z.R., Shi, C.S., 2003a. A new orange-red long-lasting phosphor material $\text{Y}_2\text{O}_2\text{S}:\text{Sm}^{3+}$. *Chem. J. Chin. Univ. Chin.* 24 (2), 208–210.
- Lei, B.F., Liu, Y.L., Tang, G.B., Ye, Z.R., Shi, C.S., 2003b. Unusual afterglow properties of Tm^{3+} doped yttrium oxysulfide. *Chem. J. Chin. Univ.* 24 (5), 782–784.
- Lei, B., Liu, Y., Liu, J., Ye, Z., Shi, C., 2004a. Pink light emitting long-lasting phosphorescence in Sm^{3+} -doped CdSiO_3 . *J. Solid State Chem.* 177 (4–5), 1333–1337.
- Lei, B., Liu, Y., Tang, G., Ye, Z., Shi, C., 2004b. Spectra and long-lasting properties of Sm^{3+} -doped yttrium oxysulfide phosphor. *Mater. Chem. Phys.* 87 (1), 227–232.

- Lei, B., Liu, Y., Ye, Z., Shi, C., 2004c. Luminescence properties of $\text{CdSiO}_3\text{:Mn}^{2+}$ phosphor. *J. Lumin.* 109 (3–4), 215–219.
- Lei, B.F., Liu, Y.L., Ye, Z.R., Shi, C.S., 2004d. A novel white light emitting long-lasting phosphor. *Chin. Chem. Lett.* 15 (3), 335–338.
- Lei, B., Li, B., Wang, X., Li, W., 2006. Green emitting long lasting phosphorescence (LLP) properties of $\text{Mg}_2\text{SnO}_4\text{:Mn}^{2+}$ phosphor. *J. Lumin.* 118 (2), 173–178.
- Lei, B., Li, B., Zhang, H., Li, W., 2007a. Preparation and luminescence properties of $\text{CaSnO}_3\text{:Sm}^{3+}$ phosphor emitting in the reddish orange region. *Opt. Mater.* 29 (11), 1491–1494.
- Lei, B., Li, B., Zhang, H., Zhang, L., Cong, Y., Li, W., 2007b. Synthesis and luminescence properties of cube-structured $\text{CaSnO}_3\text{/RE}^{3+}$ (RE=Pr, Tb) long-lasting phosphors. *J. Electrochem. Soc.* 154 (7), H623–H630.
- Lei, B.-F., Yue, S., Zhang, Y.-Z., Liu, Y.-L., 2010a. Luminescence properties of $\text{Sr}_2\text{SnO}_4\text{:Sm}^{3+}$ afterglow phosphor. *Chin. Phys. Lett.* 27 (3), 037201.
- Lei, B., Liu, Y., Zhang, J., Meng, J., Man, S., Tan, S., 2010b. Persistent luminescence in rare earth ion-doped gadolinium oxysulfide phosphors. *J. Alloys Compd.* 495 (1), 247–253.
- Lei, B., Machida, K., Horikawa, T., Hanzawa, H., Kijima, N., Shimomura, Y., Yamamoto, H., 2010c. Reddish-orange long-lasting phosphorescence of $\text{Ca}_2\text{Si}_5\text{N}_8\text{:Eu}^{2+}, \text{Tm}^{3+}$ phosphor. *J. Electrochem. Soc.* 157 (6), J196–J201.
- Lei, B., Man, S.-Q., Liu, Y., Yue, S., 2010d. Luminescence properties of Sm^{3+} -doped $\text{Sr}_3\text{Sn}_2\text{O}_7$ phosphor. *Mater. Chem. Phys.* 124 (2–3), 912–915.
- Lei, B.F., Man, S.Q., Liu, Y.L., Yue, S., 2010e. Luminescence properties of $\text{Ca}_2\text{SnO}_4\text{:Eu}^{3+}$ red-light emitting afterglow phosphor. *Chin. J. Inorg. Chem.* 26 (7), 1259–1263.
- Lei, B., Zhang, H., Mai, W., Yue, S., Liu, Y., Man, S.-q., 2011. Luminescent properties of orange-emitting long-lasting phosphorescence phosphor $\text{Ca}_2\text{SnO}_4\text{:Sm}^{3+}$. *Solid State Sci.* 13 (3), 525–528.
- Li, C., Su, Q., 2004. Action of co-dopant in electron-trapping materials: the case of Sm^{3+} in Mn^{2+} -activated zinc borosilicate glasses. *Appl. Phys. Lett.* 85 (12), 2190–2192.
- Li, C., Su, Q., 2006a. Effect of samarium on Mn activated zinc borosilicate storage glasses. *J. Rare Earths* 24 (4), 506–508.
- Li, C., Su, Q., 2006b. A new blue phosphorescent glass-ceramic: rare-earth-doped calcium aluminoborate. *J. Alloys Compd.* 408–412, 875–878.
- Li, C., Su, Q., Wang, S., 2002. Multi-color long-lasting phosphorescence in Mn^{2+} -doped $\text{ZnO-B}_2\text{O}_3\text{-SiO}_2$ glass-ceramics. *Mater. Res. Bull.* 37 (8), 1443–1449.
- Li, C., Yu, Y., Wang, S., Su, Q., 2003. Photo-stimulated long-lasting phosphorescence in Mn^{2+} -doped zinc borosilicate glasses. *J. Non-Cryst. Solids* 321 (3), 191–196.
- Li, C., Wang, J., Liang, H., Su, Q., 2007. Near infrared long lasting emission of Yb^{3+} and its influence on the optical storage ability of Mn^{2+} -activated zinc borosilicate glasses. *J. Appl. Phys.* 101 (11), 113304.
- Li, Y., Wang, Y., Gong, Y., Xu, X., Zhou, M., 2010. Design, synthesis and characterization of an orange–yellow long persistent phosphor: $\text{Sr}_3\text{Al}_2\text{O}_5\text{Cl}_2\text{:Eu}^{2+}, \text{Tm}^{3+}$. *Opt. Express* 18 (24), 24853–24858.
- Li, G., Wang, Y.H., Han, S.C., Zeng, W., Chen, W.B., Gong, Y., 2013. A red long-lasting phosphorescence material $\text{Gd}_{0.33}(\text{SiO}_4)_6\text{O}_2\text{:Sm}^{3+}$ and effect of oxygen vacancies on its performance. *ECS J. Solid State Sci. Technol.* 2 (9), R161–R164.
- Li, G., Wang, Y.H., Zeng, W., Han, S.C., Chen, W.B., Li, Y.Y., Li, H., 2014a. Enhanced long persistence of $\text{LiSr}_4(\text{BO}_3)_3\text{:Eu}^{2+}$ orange phosphors by co-doping with Dy^{3+} . *Opt. Mater.* 36 (11), 1808–1813.

- Li, Y., Zhou, S., Dong, G., Peng, M., Wondraczek, L., Qiu, J., 2014b. Anti-stokes fluorescent probe with incoherent excitation. *Sci. Rep.* 4, 4059.
- Li, Y., Zhou, S., Li, Y., Sharafudeen, K., Ma, Z., Dong, G., Peng, M., Qiu, J., 2014c. Long persistent and photo-stimulated luminescence in Cr^{3+} -doped Zn–Ga–Sn–O phosphors for deep and reproducible tissue imaging. *J. Mater. Chem. C* 2, 2657.
- Li, Z., Zhang, Y., Wu, X., Wu, X., Maudgal, R., Zhang, H., Han, G., 2015. In vivo repeatedly charging near-infrared-emitting mesoporous $\text{SiO}_2/\text{ZnGa}_2\text{O}_4:\text{Cr}^{3+}$ persistent luminescence nanocomposites. *Adv. Sci.* 2(3), 1500001.
- Lian, Z.H., Su, Q., 2014. Long lasting phosphorescence in Mn^{2+} -activated $\text{ZnO}-\text{B}_2\text{O}_3$ glass. In: Li, D., Zheng, D., Shi, J. (Eds.), *Materials Research and Applications*. Trans Tech Publications Ltd., Stafa-Zurich, pp. 1–3.
- Lian, S.X., Qi, Y., Rong, C.Y., Yu, L.P., Zhu, A.L., Yin, D.L., Liu, S.B., 2010. Effectively leveraging solar energy through persistent dual red phosphorescence: preparation, characterization, and density functional theory study of $\text{Ca}_2\text{Zn}_4\text{Ti}_{16}\text{O}_{38}:\text{Pr}^{3+}$. *J. Phys. Chem. C* 114 (15), 7196–7204.
- Liang, Z., Zhang, J., Sun, J., Li, X., Cheng, L., Zhong, H., Fu, S., Tian, Y., Chen, B., 2013. Enhancement of green long lasting phosphorescence in $\text{CaSnO}_3:\text{Tb}^{3+}$ by addition of alkali ions. *Phys. B Condens. Matter* 412, 36–40.
- Lim, Y.T., Kim, S., Nakayama, A., Stott, N.E., Bawendi, M.G., Frangioni, J.V., 2003. Selection of quantum dot wavelengths for biomedical assays and imaging. *Mol. Imaging* 2, 50–64.
- Lin, Y., Tang, Z., Zhang, Z., 2001a. Preparation of long-afterglow $\text{Sr}_4\text{Al}_{14}\text{O}_{25}$ -based luminescent material and its optical properties. *Mater. Lett.* 51 (1), 14–18.
- Lin, Y., Tang, Z., Zhang, Z., Wang, X., Zhang, J., 2001b. Preparation of a new long afterglow blue-emitting $\text{Sr}_2\text{MgSi}_2\text{O}_7$ -based photoluminescent phosphor. *J. Mater. Sci. Lett.* 20 (16), 1505–1506.
- Lin, Y., Zhang, Z., Tang, Z., Wang, X., Zhang, J., Zheng, Z., 2001c. Luminescent properties of a new long afterglow Eu^{2+} and Dy^{3+} activated $\text{Ca}_3\text{MgSi}_2\text{O}_8$ phosphor. *J. Eur. Ceram. Soc.* 21 (5), 683–685.
- Lin, Y., Zhang, Z., Tang, Z., Zhang, J., Zheng, Z., Lu, X., 2001d. The characterization and mechanism of long afterglow in alkaline earth aluminates phosphors co-doped by Eu_2O_3 and Dy_2O_3 . *Mater. Chem. Phys.* 70 (2), 156–159.
- Lin, Y., Tang, Z., Zhang, Z., Nan, C.W., 2002. Anomalous luminescence in $\text{Sr}_4\text{Al}_{14}\text{O}_{25}:\text{Eu},\text{Dy}$ phosphors. *Appl. Phys. Lett.* 81 (6), 996–998.
- Lin, Y., Nan, C.-W., Cai, N., Zhou, X., Wang, H., Chen, D., 2003a. Anomalous afterglow from Y_2O_3 -based phosphor. *J. Alloys Compd.* 361 (1–2), 92–95.
- Lin, Y., Nan, C.W., Zhou, X., Wu, J., Wang, H., Chen, D., Xu, S., 2003b. Preparation and characterization of long afterglow $\text{M}_2\text{MgSi}_2\text{O}_7$ -based (M: Ca, Sr, Ba) photoluminescent phosphors. *Mater. Chem. Phys.* 82 (3), 860–863.
- Lin, Y., Tang, Z., Zhang, Z., Nan, C., 2003c. Influence of co-doping different rare earth ions on the luminescence of CaAl_2O_4 -based phosphors. *J. Eur. Ceram. Soc.* 23 (1), 175–178.
- Lin, Y., Tang, Z., Zhang, Z., Nan, C.W., 2003d. Luminescence of Eu^{2+} and Dy^{3+} activated $\text{R}_3\text{MgSi}_2\text{O}_8$ -based (R = Ca, Sr, Ba) phosphors. *J. Alloys Compd.* 348 (1–2), 76–79.
- Lin, L., Shi, C., Wang, Z., Zhang, W., Yin, M., 2008a. A kinetics model of red long-lasting phosphorescence in $\text{MgSiO}_3:\text{Eu}^{2+},\text{Dy}^{3+},\text{Mn}^{2+}$. *J. Alloys Compd.* 466 (1–2), 546–550.
- Lin, L., Yin, M., Shi, C., Zhang, W., 2008b. Luminescence properties of a new red long-lasting phosphor: $\text{Mg}_2\text{SiO}_4:\text{Dy}^{3+},\text{Mn}^{2+}$. *J. Alloys Compd.* 455 (1–2), 327–330.

- Lin, L., Zhao, Z., Zhang, W., Zheng, Z., Yin, M., 2009. Photo-luminescence properties and thermo-luminescence curve analysis of a new white long-lasting phosphor: $\text{Ca}_2\text{MgSi}_2\text{O}_7:\text{Dy}^{3+}$. *J. Rare Earths* 27 (5), 749–752.
- Lin, G., Dong, G., Tan, D., Liu, X., Zhang, Q., Chen, D., Qiu, J., Zhao, Q., Xu, Z., 2010. Long lasting phosphorescence in oxygen-deficient zinc–boron–germanosilicate glass–ceramics. *J. Alloys Compd.* 504 (1), 177–180.
- Lin, H., Xu, A.X., Chen, G.L., Zheng, Z.S., Lin, H., Chen, B.S., Huang, L.F., Guo, H.X., Xu, Y., 2012. Synthesis of a new red long persistent phosphor $\text{Sr}_2\text{ZnSi}_2\text{O}_7:\text{Eu}^{3+}, \text{Lu}^{3+}$ via sol–gel method and investigation of its luminescence. In: Chen, R., Sung, W.P. (Eds.), *Biotechnology, Chemical and Materials Engineering*. Trans Tech Publications Ltd., Stafa-Zurich, pp. 1–3.
- Liu, C.B., Che, G.B., 2006. Observation of enhanced long-lasting phosphorescence in $\text{Y}_2\text{O}_3:\text{RE}^{3+}$ (RE=Lu, Gd) phosphors. *Phys. Status Solidi (a) Appl. Mater. Sci.* 203 (3), 558–564.
- Liu, Z., Liu, L.Y., 2005a. Afterglow energy transfer in $\text{Cd}_3\text{Al}_2\text{Ge}_3\text{O}_{12}:\text{Dy}$. *Phys. Status Solidi (a)* 202 (9), 1814–1817.
- Liu, Z., Liu, Y., 2005b. Synthesis and luminescent properties of a new green afterglow phosphor $\text{CaSnO}_3:\text{Tb}$. *Mater. Chem. Phys.* 93 (1), 129–132.
- Liu, Z.W., Liu, Y.L., Yuan, D.S., Zhang, J.X., Rong, J.H., Huang, L.H., 2004. Long-lasting phosphorescence in Eu^{3+} -doped CaWO_4 . *Chin. J. Inorg. Chem.* 20 (12), 1433–1436.
- Liu, B., Shi, C., Qi, Z., 2005a. Potential white-light long-lasting phosphor: Dy^{3+} -doped aluminate. *Appl. Phys. Lett.* 86 (19), 191111.
- Liu, B., Shi, C., Yin, M., Dong, L., Xiao, Z., 2005b. The trap states in the $\text{Sr}_2\text{MgSi}_2\text{O}_7$ and $(\text{Sr}, \text{Ca})\text{MgSi}_2\text{O}_7$ long afterglow phosphor activated by Eu^{2+} and Dy^{3+} . *J. Alloys Compd.* 387 (1–2), 65–69.
- Liu, Y., Kuang, J., Lei, B., Shi, C., 2005c. Color-control of long-lasting phosphorescence (LLP) through rare earth ion-doped cadmium metasilicate phosphors. *J. Mater. Chem.* 15 (37), 4025–4031.
- Liu, Y.L., Lei, B., Shi, C.H., 2005d. Luminescent properties of a white afterglow phosphor $\text{CdSiO}_3:\text{Dy}^{3+}$. *Chem. Mater.* 17 (8), 2108–2113.
- Liu, B., Shi, C., Qi, Z., 2006a. White-light long-lasting phosphorescence from Tb^{3+} -activated $\text{Y}_2\text{O}_3\text{S}$ phosphor. *J. Phys. Chem. Solids* 67 (8), 1674–1677.
- Liu, L., Li, C., Wang, S., Su, Q., 2006b. Redshift phenomenon of the excitation light of long life emission phosphor. *Appl. Phys. Lett.* 88 (24), 241107.
- Liu, B., Kong, L., Shi, C., 2007. White-light long-lasting phosphor $\text{Sr}_2\text{MgSi}_2\text{O}_7:\text{Dy}^{3+}$. *J. Lumin.* 122–123, 121–124.
- Liu, C., Che, G., Xu, Z., Wang, Q., 2009a. Luminescence properties of a Tb^{3+} activated long-afterglow phosphor. *J. Alloys Compd.* 474 (1–2), 250–253.
- Liu, X., Qiao, Y., Dong, G., Ye, S., Zhu, B., Zhuang, Y., Qiu, J., 2009b. BCNO-based long-persistent phosphor. *J. Electrochem. Soc.* 156 (5), P81–P84.
- Liu, Y.-h, Li, B., Cong, Y., 2010. Synthesis and optical property studies of long-lasting phosphor $\text{ZrO}_2:\text{Ti}$ electrospinning fibers. *Spectrosc. Spectr. Anal.* 30 (4), 887–891.
- Liu, G., Zhang, Q., Wang, H., Li, Y., 2012. A reddish $\text{La}_2\text{O}_3\text{S}$ -based long-afterglow phosphor with effective absorption in the visible light region. *Mater. Sci. Eng. B* 177 (3), 316–320.
- Liu, F., Yan, W., Chuang, Y.-J., Zhen, Z., Xie, J., Pan, Z., 2013. Photostimulated near-infrared persistent luminescence as a new optical read-out from Cr^{3+} -doped LiGa_5O_8 . *Sci. Rep.* 3, 1554.
- Liu, F., Liang, Y., Pan, Z., 2014. Detection of up-converted persistent luminescence in the near infrared emitted by the $\text{Zn}_3\text{Ga}_2\text{GeO}_8:\text{Cr}^{3+}, \text{Yb}^{3+}, \text{Er}^{3+}$ phosphor. *Phys. Rev. Lett.* 113, 177401.

- Lorincz, A., Puma, M., James, F.J., Crawford, J.H.J., 1982. Thermally stimulated processes involving defects in gamma- and x-irradiated spinel (MgAl_2O_4). *J. Appl. Phys.* 53 (2), 927–932.
- Lu, Y.-Y., Liu, F., Gu, Z., Pan, Z., 2011. Long-lasting near-infrared persistent luminescence from $\beta\text{-Ga}_2\text{O}_3\text{:Cr}^{3+}$ nanowire assemblies. *J. Lumin.* 131 (12), 2784–2787.
- Luitel, H.N., Watari, T., Torikai, T., Yada, M., 2009. Luminescent properties of Cr^{3+} doped $\text{Sr}_4\text{Al}_{14}\text{O}_{25}$: Eu/Dy blue–green and red phosphor. *Opt. Mater.* 31 (8), 1200–1204.
- Ma, L., Chen, W., 2010. ZnS:Cu, Co water-soluble afterglow nanoparticles: synthesis, luminescence and potential applications. *Nanotechnology* 21 (38), 385604.
- Ma, L., Chen, W., 2011. Enhancement of afterglow in ZnS:Cu, Co water-soluble nanoparticles by aging. *J. Phys. Chem. C* 115 (18), 8940–8944.
- Ma, X., Zhang, J., Li, H., Duan, B., Guo, L., Que, M., Wang, Y., 2013. Violet blue long-lasting phosphorescence properties of Mg-doped BaZrO_3 and its ability to assist photocatalysis. *J. Alloys Compd.* 580, 564–569.
- Ma, L., Zou, X., Bui, B., Chen, W., Song, K.H., Solberg, T., 2014. X-ray excited ZnS:Cu, Co afterglow nanoparticles for photodynamic activation. *Appl. Phys. Lett.* 105 (1), 013702.
- Maldiney, T., Lecointre, A., Viana, B., Bessiere, A., Bessodes, M., Gourier, D., Richard, C., Scherman, D., 2011a. Controlling electron trap depth to enhance optical properties of persistent luminescence nanoparticles for in vivo imaging. *J. Am. Chem. Soc.* 133 (30), 11810–11815.
- Maldiney, T., Richard, C., Seguin, J., Wattier, N., Bessodes, M., Scherman, D., 2011b. Effect of core diameter, surface coating, and PEG chain length on the biodistribution of persistent luminescence nanoparticles in mice. *ACS Nano* 5 (2), 854–862.
- Maldiney, T., Lecointre, A., Viana, B., Bessiere, A., Gourier, D., Bessodes, M., Richard, C., Scherman, D., 2012a. Trap depth optimization to improve optical properties of diopside-based nanophosphors for medical imaging. In: Teherani, F.H., Look, D.C., Rogers, D.J. (Eds.), *Oxide-Based Materials and Devices III*. Spie-Int Soc Optical Engineering, Bellingham.
- Maldiney, T., Sraiki, G., Viana, B., Gourier, D., Richard, C., Scherman, D., Bessodes, M., Van den Eeckhout, K., Poelman, D., Smet, P.F., 2012b. In vivo optical imaging with rare earth doped $\text{Ca}_2\text{Si}_2\text{N}_8$ persistent luminescence nanoparticles. *Opt. Mater. Express* 2, 261–268.
- Maldiney, T., Bessière, A., Seguin, J., Teston, E., Sharma, S.K., Viana, B., Bos, A.J.J., Dorenbos, P., Bessodes, M., Gourier, D., Scherman, D., Richard, C., 2014. The in vivo activation of persistent nanophosphors for optical imaging of vascularization, tumours and grafted cells. *Nat. Mater.* 13, 418–426.
- Maldiney, T., Doan, B.-T., Alloyeau, D., Bessodes, M., Scherman, D., Richard, C., 2015. Gadolinium-doped persistent nanophosphors as versatile tool for multimodal in vivo imaging. *Adv. Funct. Mater.* 25 (2), 331–338.
- Mao, S., Liu, Q., Gu, M., Mao, D., Chang, C., 2008. Long lasting phosphorescence of $\text{Gd}_2\text{O}_2\text{S}$: Eu,Ti,Mg nanorods via a hydrothermal routine. *J. Alloys Compd.* 465 (1–2), 367–374.
- Matsui, H., Xu, C.-N., Akiyama, M., Watanabe, T., 2000. Strong mechanoluminescence from UV-irradiated spinels of $\text{ZnGa}_2\text{O}_4\text{:Mn}$ and $\text{MgGa}_2\text{O}_4\text{:Mn}$. *Jpn. J. Appl. Phys.* 39 (Pt. 1, No. 12A), 6582.
- Matsui, K., Arima, M., Kanno, H., 2013. Luminescence of barium aluminate phosphors activated by Eu^{2+} and Dy^{3+} . *Opt. Mater.* 35 (11), 1947–1951.
- Matsuzawa, T., Aoki, Y., Takeuchi, N., Murayama, Y., 1996. A new long phosphorescent phosphor with high brightness, $\text{SrAl}_2\text{O}_4\text{:Eu}^{2+},\text{Dy}^{3+}$. *J. Electrochem. Soc.* 143 (8), 2670–2673.
- Mei, Y., Xu, H., Zhang, J., Ci, Z., Duan, M., Peng, S., Zhang, Z., Tian, W., Lu, Y., Wang, Y., 2015. Design and spectral control of a novel ultraviolet emitting long lasting phosphor for assisting TiO_2 photocatalysis: $\text{Zn}_2\text{SiO}_4\text{:Ga}^{3+},\text{Bi}^{3+}$. *J. Alloys Compd.* 622, 908–912.

- Miyamoto, Y., Kato, H., Honna, Y., Yamamoto, H., Ohmi, K., 2009. An orange-emitting, long-persistent phosphor, $\text{Ca}_2\text{Si}_5\text{N}_8:\text{Eu}^{2+}, \text{Tm}^{3+}$. *J. Electrochem. Soc.* 156 (9), J235–J241.
- Moon, C., Nishi, M., Miura, K., Hirao, K., 2009. Blue long-lasting phosphorescence of Ti-doped BaZrO_3 perovskites. *J. Lumin.* 129 (8), 817–819.
- Mu, Z., Hu, Y., Wang, Y., Wu, H., Fu, C., Kang, F., 2011a. The structure and luminescence properties of long afterglow phosphor $\text{Y}_{3-x}\text{Mn}_x\text{Al}_{5-x}\text{Si}_x\text{O}_{12}$. *J. Lumin.* 131 (4), 676–681.
- Mu, Z.F., Wang, Y.H., Hu, Y.H., Wu, H.Y., Deng, L.Y., Xie, W., Fu, C.J., Liao, C.X., 2011b. The afterglow and thermoluminescence properties of $\text{Y}_3\text{Al}_5\text{O}_{12}:\text{Ce}^{3+}$. *Acta Phys. Sin.* 60 (1), 013201.
- Murayam, Y., Takeuchi, N., Aoki, Y., Matsuzawa, T., 1994. Phosphorescent phosphor. EP0622440.
- Najafov, H., Kato, A., Toyota, H., Iwai, K., Bayramov, A., Iida, S., 2002. Effect of Ce co-doping on $\text{CaGa}_2\text{S}_4:\text{Eu}$ phosphor: II. Thermoluminescence. *Jpn. J. Appl. Phys.* 41 (Pt. 1, No. 4A), 2058–2065.
- Nakagawa, H., Ebisu, K., Zhang, M., Kitaura, M., 2003. Luminescence properties and afterglow in spinel crystals doped with trivalent Tb ions. *J. Lumin.* 102–103, 590–596.
- Nakanishi, T., Watanabe, K., Ueda, J., Fushimi, K., Tanabe, S., Hasegawa, Y., 2015. Enhanced light storage of SrAl_2O_4 glass-ceramics controlled by selective Europium reduction. *J. Am. Ceram. Soc.* 98 (2), 423–429.
- Nakazawa, E., Murazaki, Y., Saito, S., 2006. Mechanism of the persistent phosphorescence in $\text{Sr}_4\text{Al}_{14}\text{O}_{25}:\text{Eu}$ and $\text{SrAl}_2\text{O}_4:\text{Eu}$ codoped with rare earth ions. *J. Appl. Phys.* 100, 113113.
- Palilla, F.C., Levine, A.K., Tomkus, M.R., 1968. Fluorescent properties of alkaline earth aluminates of the type MAl_2O_4 activated by divalent europium. *J. Electrochem. Soc.* 115 (6), 642–644.
- Pan, Y.X., Su, Q., Xu, H.F., Chen, T.H., Ge, W.K., Yang, C.L., Wu, M.M., 2003. Synthesis and red luminescence of Pr^{3+} -doped CaTiO_3 nanophosphor from polymer precursor. *J. Solid State Chem.* 174 (1), 69–73.
- Pan, W., Ning, G., Lin, Y., Yang, X., 2008. Sol–gel processed $\text{Ce}^{3+}, \text{Tb}^{3+}$ codoped white emitting phosphors in $\text{Sr}_2\text{Al}_2\text{SiO}_7$. *J. Rare Earths* 26 (2), 207–210.
- Pan, Z., Lu, Y.-Y., Liu, F., 2012. Sunlight-activated long-persistent luminescence in the near-infrared from Cr^{3+} -doped zinc gallogermanates. *Nat. Mater.* 11, 58–63.
- Pang, R., Li, C., Shi, L., Su, Q., 2009a. A novel blue-emitting long-lasting pyrophosphate phosphor $\text{Sr}_2\text{P}_2\text{O}_7:\text{Eu}^{2+}, \text{Y}^{3+}$. *J. Phys. Chem. Solids* 70 (2), 303–306.
- Pang, R., Li, C., Zhang, S., Su, Q., 2009b. Luminescent properties of a new blue long-lasting phosphor $\text{Ca}_2\text{P}_2\text{O}_7:\text{Eu}^{2+}, \text{Y}^{3+}$. *Mater. Chem. Phys.* 113 (1), 215–218.
- Pang, R., Jia, Y.L., Zhao, R., Li, H.F., Fu, J.P., Sun, W.Z., Jiang, L.H., Zhang, S., Li, C.Y., Su, Q., 2014a. Tunable long lasting phosphorescence due to the selective energy transfer from defects to luminescent centres via tunnelling in Mn^{2+} and Tm^{3+} co-doped zinc pyrophosphate. *Dalton Trans.* 43 (25), 9661–9668.
- Pang, R., Zhao, R., Jia, Y.L., Li, C.Y., Su, Q., 2014b. Luminescence properties of a new yellow long-lasting phosphorescence phosphor $\text{NaAlSiO}_4:\text{Eu}^{2+}, \text{Ho}^{3+}$. *J. Rare Earths* 32 (9), 792–796.
- Paulose, P.I., Joseph, J., Rudra Warrior, M.K., Jose, G., Unnikrishnan, N.V., 2007. Relaxation kinetics of Sm: Ce-doped CaS phosphors. *J. Lumin.* 127 (2), 583–588.
- Pawar, S.H., Narlikar, A.V., 1976. Mechanism of luminescence in $\text{CaS}:\text{Bi}$ phosphor. *Mater. Res. Bull.* 11 (7), 821–826.
- Pejakovic, D.A., 2010. Studies of the phosphorescence of polycrystalline hafnia. *J. Lumin.* 130 (6), 1048–1054.
- Peng, Z., Xu, Z., Luo, C., Yu, J., Zhang, G., 2008. Synthesis and luminescent properties of a novel bluish-white afterglow phosphor, $\text{b-Zn}_3(\text{PO}_4)_2:\text{Hf}^{4+}$. *Luminescence* 23 (1), 14–16.

- Pitale, S.S., Sharma, S.K., Dubey, R.N., Qureshi, M.S., Malik, M.M., 2008. TL and PL studies on defect-assisted green luminescence from doped strontium sulfide phosphor. *J. Lumin.* 128 (10), 1587–1594.
- Poelman, D., Smet, P.F., 2010. Photometry in the dark: time dependent visibility of low intensity light sources. *Opt. Express* 18 (25), 26293–26299.
- Poelman, D., Smet, P.F., 2011. Photometry in the dark: time dependent visibility of low intensity light sources (vol 18, pg 26293, 2010). *Opt. Express* 19 (20), 18808–18809.
- Poelman, D., Avci, N., Smet, P.F., 2009. Measured luminance and visual appearance of multi-color persistent phosphors. *Opt. Express* 17 (1), 358–364.
- Preethi, K.R.S., Lu, C.H., Thirumalai, J., Jagannathan, R., Natarajan, T.S., Nayak, N.U., Radhakrishna, I., Jayachandran, M., Trivedi, D.C., 2004. $\text{SrAl}_4\text{O}_7:\text{Eu}^{2+}$ nanocrystals: synthesis and fluorescence properties. *J. Phys. D Appl. Phys.* 37 (19), 2664–2669.
- Qi, Y., Lian, S.X., Yu, L.P., Zhou, W., Yin, D.L., 2009. Synthesis and red persistent properties of phosphor $\text{Ca}_2\text{Zn}_4\text{Ti}_{16}\text{O}_{38}:\text{Pr}^{3+},\text{Na}^+$. *Chin. J. Inorg. Chem.* 25 (2), 218–222.
- Qin, Q.S., Ma, X.L., Shao, Y., Yang, X.Y., Sheng, H.F., Yang, J.Z., Yin, Y., Zhang, J.C., 2012. Synthesis and infrared up-conversion photostimulated luminescence properties of a novel optical storage material $\text{Sr}_2\text{SnO}_4:\text{Tb}^{3+},\text{Li}^+$. *Acta Phys. Sin.* 61 (9), 097804.
- Qin, J.L., Lei, B.F., Li, J.F., Liu, Y.L., Zhang, H.R., Zheng, M.T., Xiao, Y., Chao, K.F., 2013. Temperature-dependent long-lasting phosphorescence in $\text{SrSi}_2\text{O}_2\text{N}_2:\text{Eu}^{2+}$. *ECS J. Solid State Sci. Technol.* 2 (3), R60–R64.
- Qin, J.L., Zhang, H.R., Lei, B.F., Dong, H.W., Liu, Y.L., Meng, J.X., Zheng, M.T., Xiao, Y., 2014. Preparation and afterglow properties of highly condensed nitridosilicate $\text{BaSi}_7\text{N}_{10}:\text{Eu}^{2+}$ phosphor. *J. Lumin.* 152, 230–233.
- Qiu, J., Miura, K., Inouye, H., Kondo, Y., Mitsuyu, T., Hirao, K., 1998. Femtosecond laser-induced three-dimensional bright and long-lasting phosphorescence inside calcium aluminosilicate glasses doped with rare earth ions. *Appl. Phys. Lett.* 73, 1763–1765.
- Qiu, J., Kondo, Y., Miura, K., Mitsuyu, T., Hirao, K., 1999. Infrared femtosecond laser induced visible long-lasting phosphorescence in Mn^{2+} -doped sodium borate glasses. *Jpn. J. Appl. Phys.* 38 (Pt. 2, No. 6A/B), L649.
- Qiu, J., Gaeta, A.L., Hirao, K., 2001. Long-lasting phosphorescence in oxygen-deficient Ge-doped silica glasses at room temperature. *Chem. Phys. Lett.* 333 (3–4), 236–241.
- Qiu, J., Miyauchi, K., Kawamoto, Y., Kitamura, N., Qiu, J., Hirao, K., 2002a. Long-lasting phosphorescence in $\text{Sn}^{2+}\text{--Cu}^{2+}$ codoped silicate glass and its high-pressure treatment effect. *Appl. Phys. Lett.* 81 (3), 394–396.
- Qiu, J., Wada, N., Ogura, F., Kojima, K., Hirao, K., 2002b. Structural relaxation and long-lasting phosphorescence in sol–gel-derived GeO_2 glass after ultraviolet light irradiation. *J. Phys. Condens. Matter* 14 (10), 2561–2567.
- Qu, X., Cao, L., Liu, W., Su, G., Wang, P., 2009. Luminescence properties of $\text{CdSiO}_3:\text{Mn}^{2+},\text{RE}^{3+}$ (RE = Sm, Dy, Eu) phosphors. *J. Alloys Compd.* 487 (1–2), 387–390.
- Qu, X., Cao, L., Liu, W., Su, G., Xu, C., Wang, P., 2010. Preparation and properties of $\text{CdSiO}_3:\text{Mn}^{2+},\text{Dy}^{3+}$ phosphor. *J. Alloys Compd.* 494 (1–2), 196–198.
- Qu, X., Cao, L., Liu, W., Su, G., 2012a. Preparation and properties of $\text{CdSiO}_3:\text{Mn}^{2+},\text{Tb}^{3+}$ phosphor. *Ceram. Int.* 38 (3), 1765–1769.
- Qu, X.F., Cao, L.X., Liu, W., Su, G., 2012b. Sol–gel synthesis and luminescence properties of $\text{CdSiO}_3:\text{Mn}^{2+},\text{Eu}^{3+}$ phosphor. *J. Alloys Compd.* 533, 83–87.
- Rea, M., Bullough, J., Freyssinier-Nova, J., Bierman, A., 2004. A proposed unified system of photometry. *Light. Res. Technol.* 36 (2), 85–109.

- Rodrigues, L.C.V., Brito, H.F., Hölsä, J., Stefani, R., Felinto, M.C.F.C., Lastusaari, M., Laamanen, T., Nunes, L.A.O., 2012. Discovery of the persistent luminescence mechanism of $\text{CdSiO}_3:\text{Tb}^{3+}$. *J. Phys. Chem. C* 116 (20), 11232–11240.
- Rodrigues, L.C.V., Holsa, J., Carvalho, J.M., Pedroso, C.C.S., Lastusaari, M., Felinto, M.C.F.C., Watanabe, S., Brito, H.F., 2014. Co-dopant influence on the persistent luminescence of $\text{BaAl}_2\text{O}_4:\text{Eu}^{2+},\text{R}^{3+}$. *Phys. B Condens. Matter* 439, 67–71.
- Sabbagh Alvani, A.A., Moztafzadeh, F., Sarabi, A.A., 2005. Effects of dopant concentrations on phosphorescence properties of Eu/Dy-doped $\text{Sr}_3\text{MgSi}_2\text{O}_8$. *J. Lumin.* 114 (2), 131–136.
- Sakai, R., Katsumata, T., Komuro, S., Morikawa, T., 1999. Effect of composition on the phosphorescence from $\text{BaAl}_2\text{O}_4:\text{Eu}^{2+},\text{Dy}^{3+}$ crystals. *J. Lumin.* 85 (1–3), 149–154.
- Sanada, T., Seto, H., Morimoto, Y., Yamamoto, K., Wada, N., Kojima, K., 2010. Luminescence and long-lasting afterglow in Mn^{2+} and Eu^{3+} co-doped $\text{ZnO}-\text{GeO}_2$ glasses and glass ceramics prepared by sol–gel method. *J. Sol–Gel Sci. Technol.* 56 (1), 82–86.
- Sharma, S.K., Pitale, S.S., Manzar Malik, M., Dubey, R.N., Qureshi, M.S., 2009. Luminescence studies on the blue-green emitting $\text{Sr}_4\text{Al}_{14}\text{O}_{25}:\text{Ce}^{3+}$ phosphor synthesized through solution combustion route. *J. Lumin.* 129 (2), 140–147.
- Sharma, S.K., Bessière, A., Basavaraju, N., Priolkar, K.R., Binet, L., Viana, B., Gourier, D., 2014a. Interplay between chromium content and lattice disorder on persistent luminescence of $\text{ZnGa}_2\text{O}_4:\text{Cr}^{3+}$ for in vivo imaging. *J. Lumin.* 155, 251–256.
- Sharma, S.K., Gourier, D., Viana, B., Maldiney, T., Teston, E., Scherman, D., Richard, C., 2014b. Persistent luminescence of $\text{AB}_2\text{O}_4:\text{Cr}^{3+}$ (A = Zn, Mg, B = Ga, Al) spinels: new biomarkers for in vivo imaging. *Opt. Mater.* 36, 1901–1906.
- Singh, S.K., 2014. Red and near infrared persistent luminescence nano-probes for bioimaging and targeting applications. *RSC Adv.* 4 (102), 58674–58698.
- Smet, P.F., Van Haecke, J.E., Loncke, F., Vrielinck, H., Callens, F., Poelman, D., 2006. Anomalous photoluminescence in $\text{BaS}:\text{Eu}$. *Phys. Rev. B* 74 (3), 035207.
- Smet, P.F., Avci, N., Poelman, D., 2009. Red persistent luminescence in $\text{Ca}_2\text{SiS}_4:\text{Eu},\text{Nd}$. *J. Electrochem. Soc.* 156, H243.
- Smet, P.F., Parmentier, A.B., Poelman, D., 2011. Selecting conversion phosphors for white light-emitting diodes. *J. Electrochem. Soc.* 158, R37–R54.
- Smet, P.F., Avci, N., Van den Eeckhout, K., Poelman, D., 2012a. Extending the afterglow in $\text{CaAl}_2\text{O}_4:\text{Eu}, \text{Nd}$ persistent phosphors by electron beam annealing. *Opt. Mater. Express* 2 (10), 1306–1313.
- Smet, P.F., Poelman, D., Hehlen, M.P., 2012b. Focus issue introduction: persistent phosphors. *Opt. Mater. Express* 2 (4), 452–454.
- Smet, P.F., Van den Eeckhout, K., Bos, A.J.J., van der Kolk, E., Dorenbos, P., 2012c. Temperature and wavelength dependent trap filling in $\text{M}_2\text{Si}_5\text{N}_8:\text{Eu}$ (M = Ca, Sr, Ba) persistent phosphors. *J. Lumin.* 132 (3), 682–689.
- Smith, A.M., Mancini, M.C., Nie, S., 2009. Bioimaging: second window for in vivo imaging. *Nat. Nanotechnol.* 4, 710–711.
- Soenen, S.J., Rivera-Gil, P., Montenegro, J.-M., Parak, W.J., De Smedt, S.C., Braeckmans, K., 2011. Cellular toxicity of inorganic nanoparticles: common aspects and guidelines for improved nanotoxicity evaluation. *Nano Today* 6, 446–465.
- Song, Y.H., Zou, H.F., Gan, S.C., Deng, Y.F., Hong, G.Y., Meng, J., 2007. Phase conversion and spectral properties of long lasting phosphor $\text{Zn}_3(\text{PO}_4)_2:\text{Mn}^{2+}, \text{Ga}^{3+}$. *J. Mater. Sci.* 42 (13), 4899–4904.
- Stockman, A., Sharpe, L.T., 2006. Into the twilight zone: the complexities of mesopic vision and luminous efficiency. *Ophthalmic Physiol. Opt.* 26 (3), 225–239.

- Sun, Z.X., 2012. Enhanced green-light-emitting afterglow in $\text{Zn}_2\text{GeO}_4:\text{Mn}^{2+}$ phosphor by Yb^{3+} codoping. *Chin. J. Inorg. Chem.* 28 (6), 1229–1233.
- Sun, X., Zhang, J., Zhang, X., Luo, Y., Wang, X.-J., 2008. Long lasting yellow phosphorescence and photostimulated luminescence in $\text{Sr}_3\text{SiO}_5:\text{Eu}^{2+}$ and $\text{Sr}_3\text{SiO}_5:\text{Eu}^{2+},\text{Dy}^{3+}$ phosphors. *J. Phys. D Appl. Phys.* 41 (19), 195414.
- Sun, D., Li, D., Zhu, Z., Xiao, J., Tao, Z., Liu, W., 2012. Photoluminescence properties of europium and titanium co-doped BaZrO_3 phosphors powders synthesized by the solid-state reaction method. *Opt. Mater.* 34 (11), 1890–1896.
- Sun, H., Pan, L., Zhu, G., Piao, X., Zhang, L., Sun, Z., 2014a. Long afterglow $\text{Sr}_4\text{Al}_{14}\text{O}_{25}:\text{Eu},\text{Dy}$ phosphors as both scattering and down converting layer for CdS quantum dot-sensitized solar cells. *Dalton Trans.* 43 (40), 14936–14941.
- Sun, W.Z., Jia, Y.L., Zhao, R., Li, H.F., Fu, J.P., Jiang, L.H., Zhang, S., Pang, R., Li, C.Y., 2014b. A novel green long-lasting phosphorescence phosphor $\text{Ca}_{14}\text{Mg}_2(\text{SiO}_4)_8:\text{Eu}^{2+},\text{Dy}^{3+}$. *Opt. Mater.* 36 (11), 1841–1845.
- Swart, H.C., Terblans, J.J., Ntwaeaborwa, O.M., Kroon, R.E., Coetsee, E., Nagpure, I.M., Kumar, V., Kumar, V., Kumar, V., 2014. Applications of AES, XPS and TOF SIMS to phosphor materials. *Surf. Interface Anal.* 46 (10–11), 1105–1109.
- Takahashi, Y., Masai, H., Fujiwara, T., Kitamura, K., Inoue, S., 2008. Afterglow in synthetic bazirite, $\text{BaZrSi}_3\text{O}_9$. *J. Ceram. Soc. Jpn.* 116 (1350), 357–360.
- Takahashi, Y., Ando, M., Ihara, R., Fujiwara, T., 2011. Green-emissive Mn-activated nanocrystallized glass with willemite-type Zn_2GeO_4 . *Opt. Mater. Express* 1 (3), 372–378.
- Takayama, T., Katsumata, T., Komuro, S., Morikawa, T., 2005. Growth and characteristics of a new long afterglow phosphorescent yttrium tantalate crystal. *J. Cryst. Growth* 275 (1–2), e2013–e2017.
- TC-1-58, C.T.C., 2010. CIE technical report 191:2010: Recommended system for mesopic photometry based on visual performance. CIE Central Bureau.
- Teng, Y., Zhou, J., Ma, Z., Smedskjaer, M.M., Qiu, J., 2011. Persistent near infrared phosphorescence from rare earth ions co-doped strontium aluminate phosphors. *J. Electrochem. Soc.* 158 (2), K17–K19.
- Teng, Y., Zhou, J.J., Khisro, S.N., Zhou, S.F., Qiu, J.R., 2014. Persistent luminescence of $\text{SrAl}_2\text{O}_4:\text{Eu}^{2+},\text{Dy}^{3+},\text{Cr}^{3+}$ phosphors in the tissue transparency window. *Mater. Chem. Phys.* 147 (3), 772–776.
- Trojan-Piegza, J., Niittykoski, J., Hölsä, J., Zych, E., 2008. Thermoluminescence and kinetics of persistent luminescence of vacuum-sintered Tb^{3+} -doped and $\text{Tb}^{3+}, \text{Ca}^{2+}$ -codoped Lu_2O_3 materials. *Chem. Mater.* 20 (6), 2252–2261.
- Trojan-Piegza, J., Zych, E., Holsa, J., Niittykoski, J., 2009. Spectroscopic properties of persistent luminescence phosphors: $\text{Lu}_2\text{O}_3:\text{Tb}^{3+}, \text{M}^{2+}$ ($\text{M}=\text{Ca}, \text{Sr}, \text{Ba}$). *J. Phys. Chem. C* 113 (47), 20493–20498.
- Ueda, J., Aishima, K., Tanabe, S., 2013. Temperature and compositional dependence of optical and optoelectronic properties in Ce^{3+} -doped $\text{Y}_3\text{Sc}_2\text{Al}_{3-x}\text{Ga}_x\text{O}_{12}$ ($x=0, 1, 2, 3$). *Opt. Mater.* 35 (11), 1952–1957.
- Ueda, J., Kuroishi, K., Tanabe, S., 2014a. Bright persistent ceramic phosphors of $\text{Ce}^{3+}-\text{Cr}^{3+}$ -codoped garnet able to store by blue light. *Appl. Phys. Lett.* 104 (10), 101904.
- Ueda, J., Kuroishi, K., Tanabe, S., 2014b. Yellow persistent luminescence in $\text{Ce}^{3+}-\text{Cr}^{3+}$ -codoped gadolinium aluminum gallium garnet transparent ceramics after blue-light excitation. *Appl. Phys. Express* 7 (6), 062201.
- Ueda, J., Shinoda, T., Tanabe, S., 2015. Evidence of three different Eu^{2+} sites and their luminescence quenching processes in $\text{CaAl}_2\text{O}_4:\text{Eu}^{2+}$. *Opt. Mater.* 41, 84–89.

- Uheda, K., Maruyama, T., Takizawa, H., Endo, T., 1997. Synthesis and long-period phosphorescence of $\text{ZnGa}_2\text{O}_4:\text{Mn}^{2+}$ spinel. *J. Alloys Compd.* 262–263, 60–64.
- Uheda, K., Takizawa, H., Endo, T., Miura, C., Shimomura, Y., Kijima, N., Shimada, M., 2001. Photo- and thermo-luminescence of zinc silicon nitride doped with divalent manganese. *J. Mater. Sci. Lett.* 20 (19), 1753–1755.
- Valberg, A., 2007. *Light Vision Color*. Wiley, Chichester, England.
- Van den Eeckhout, K., Smet, P.F., Poelman, D., 2009. Persistent luminescence in rare-earth codoped $\text{Ca}_2\text{Si}_5\text{N}_8:\text{Eu}^{2+}$. *J. Lumin.* 129 (10), 1140–1143.
- Van den Eeckhout, K., Smet, P.F., Poelman, D., 2010. Persistent luminescence in Eu^{2+} -doped compounds: a review. *Materials* 3, 2536–2566.
- Van den Eeckhout, K., Smet, P.F., Poelman, D., 2011. Luminescent afterglow behavior in the $\text{M}_2\text{Si}_5\text{N}_8:\text{Eu}$ family (M = Ca, Sr, Ba). *Materials* 4, 980–990.
- Van den Eeckhout, K., Bos, A.J.J., Poelman, D., Smet, P.F., 2013a. Revealing trap depth distributions in persistent phosphors. *Phys. Rev. B* 87 (4), 045126.
- Van den Eeckhout, K., Poelman, D., Smet, P., 2013b. Persistent luminescence in non- Eu^{2+} -doped compounds: a review. *Materials* 6, 2789–2818.
- Vercaemst, R., Poelman, D., Fiermans, L., Vanmeirhaeghe, R.L., Laflere, W.H., Cardon, F., 1995a. A detailed XPS study of the rare-earth compounds EuS and EuF_3 . *J. Electron Spectrosc. Relat. Phenom.* 74 (1), 45–56.
- Vercaemst, R., Poelman, D., Vanmeirhaeghe, R.L., Fiermans, L., Laflere, W.H., Cardon, F., 1995b. An XPS study of the dopants' valence states and the composition of $\text{CaS}_{1-x}\text{Se}_x:\text{Eu}$ and $\text{SrS}_{1-x}\text{Se}_x:\text{Ce}$ thin-film electroluminescent devices. *J. Lumin.* 63 (1–2), 19–30.
- Wada, N., Ogura, F., Yamamoto, K., Kojima, K., 2005. White luminescence and afterglow in germanium oxide glasses prepared by the sol-gel method. *Glass Technol.* 46 (2), 163–170.
- Wan, M.H., Wang, Y.H., Wang, X.S., Zhao, H., Li, H.L., Wang, C., 2014. Long afterglow properties of $\text{Eu}^{2+}/\text{Mn}^{2+}$ doped Zn_2GeO_4 . *J. Lumin.* 145, 914–918.
- Wang, Y.H., Wang, Z.L., 2006. Characterization of $\text{Y}_2\text{O}_2\text{S}:\text{Eu}^{3+}, \text{Mg}^{2+}, \text{Ti}^{4+}$ long-lasting phosphor synthesized by flux method. *J. Rare Earths* 24 (1), 25–28.
- Wang, X.-J., Jia, D., Yen, W.M., 2003a. Mn^{2+} activated green, yellow, and red long persistent phosphors. *J. Lumin.* 102–103, 34–37.
- Wang, X., Zhang, Z., Tang, Z., Lin, Y., 2003b. Characterization and properties of a red and orange $\text{Y}_2\text{O}_2\text{S}$ -based long afterglow phosphor. *Mater. Chem. Phys.* 80 (1), 1–5.
- Wang, J., Wang, S., Su, Q., 2004a. The role of excess Zn^{2+} ions in improvement of red long lasting phosphorescence (LLP) performance of $\beta\text{-Zn}_3(\text{PO}_4)_2:\text{Mn}$ phosphor. *J. Solid State Chem.* 177 (3), 895–900.
- Wang, J., Wang, S.B., Su, Q., 2004b. Synthesis, photoluminescence and thermostimulated-luminescence properties of novel red long-lasting phosphorescent materials $\beta\text{-Zn}_3(\text{PO}_4)_2:\text{Mn}^{2+}, \text{M}^{3+}$ (M = Al and Ga). *J. Mater. Chem.* 14 (16), 2569–2574.
- Wang, Y., Wang, Z., Zhang, P., Hong, Z., Fan, X., Qian, G., 2004c. Preparation of Eu^{2+} and Dy^{3+} co-activated $\text{CaAl}_2\text{Si}_2\text{O}_8$ -based phosphor and its optical properties. *Mater. Lett.* 58 (26), 3308–3311.
- Wang, J., Su, Q., Wang, S., 2005a. A novel red long lasting phosphorescent (LLP) material $\beta\text{-Zn}_3(\text{PO}_4)_2:\text{Mn}^{2+}, \text{Sm}^{3+}$. *Mater. Res. Bull.* 40, 590–598.
- Wang, J., Su, Q., Wang, S.B., 2005b. Blue and red long lasting phosphorescence (LLP) in $\beta\text{-Zn}_3(\text{PO}_4)_2:\text{Mn}^{2+}, \text{Zr}^{4+}$. *J. Phys. Chem. Solids* 66 (7), 1171–1176.
- Wang, X.J., He, Z.Y., Jia, D., Streck, W., Pazik, R., Hreniak, D., Yen, W.M., 2005c. Crystal size dependence of the persistent phosphorescence in $\text{Sr}_2\text{ZnSi}_2\text{O}_7:\text{Eu}^{2+}, \text{Dy}^{3+}$. *Microelectron. J.* 36 (3–6), 546–548.

- Wang, Z.-Y., Zhang, F.-a, Guo, X.-r., Wang, Y.-h., Fan, X.-p, Qian, G.-d, 2006. Study on long-lasting phosphorescent mechanism of Tb^{3+} doped $ZnO-B_2O_3-SiO_2$ glass. *J. Zhejiang Univ.* 40 (8), 1454–1457.
- Wang, L., Zhang, L., Huang, Y., Jia, D., Lu, J., 2009. Effects of Gd^{3+} and Lu^{3+} co-doping on the long afterglow properties of yellowish-orange phosphor $Y_2O_3:Ti^{4+},Mg^{2+}$. *J. Lumin.* 129 (9), 1032–1035.
- Wang, F., Banerjee, D., Liu, Y., Chen, X., Liu, X., 2010. Upconversion nanoparticles in biological labeling, imaging, and therapy. *Analyst* 135, 1839–1854.
- Wang, W.-N., Ogi, T., Kaihatsu, Y., Iskandar, F., Okuyama, K., 2011a. Novel rare-earth-free tunable-color-emitting BCNO phosphors. *J. Mater. Chem.* 21 (14), 5183–5189.
- Wang, X., Du, F., Wei, D., Huang, Y., Seo, H.J., 2011b. A new long-lasting phosphor Zr^{4+} and Eu^{3+} co-doped $SrMg_2(PO_4)_2$. *Sens. Actuator B Chem.* 158 (1), 171–175.
- Wang, Z.-L., Zheng, G.-S., Wang, S.-Q., Qin, Q.-S., Zhou, H.-L., Zhang, J.-C., 2012a. The luminescence properties of a novel electron trapped material $Sr_2SnO_4:Sb^{3+}$ for optical storage. *Acta Phys. Sin.* 61 (12), 127805.
- Wang, Z., Zhang, J., Zheng, G., Liu, Y., Zhao, Y., 2012b. The unusual variations of photoluminescence and afterglow properties in monoclinic ZrO_2 by annealing. *J. Lumin.* 132 (11), 2817–2821.
- Wang, X.S., Wan, M.H., Wang, Y.H., Zhao, H., Hu, Z.F., Li, H.L., 2013a. Structure and luminescence properties of $Ga_2O_3:Cr^{3+}$ by Al doping. *Spectrosc. Spectr. Anal.* 33 (11), 2921–2925.
- Wang, Z.L., Zhang, J.C., Zheng, G.S., Peng, X.J., Dai, H.X., 2013b. Violet-blue afterglow luminescence properties of non-doped $SrZrO_3$ material. *J. Lumin.* 144, 30–33.
- Wang, P.J., Xu, X.H., Qiu, J.B., Yu, X., Wang, Q., 2014a. Effects of Er^{3+} doping on the long-persistent luminescence properties of $Ba_4(Si_3O_8)_2:Eu^{2+}$ phosphor. *Opt. Mater.* 36 (11), 1826–1829.
- Wang, Q., Qiu, J.B., Song, Z.G., Zhou, D.C., Xu, X.H., 2014b. Green long-after-glow luminescence of Tb^{3+} in Sr_2SiO_4 . *Chin. Phys. B* 23 (6), 064211.
- Wanjuan, T., Donghua, C., 2007. Photoluminescent properties of (Ca, Zn)TiO₃:Pr, B particles synthesized by the peroxide-based route method. *J. Am. Ceram. Soc.* 90 (10), 3156–3159.
- Wanjuan, T., Donghua, C., Ming, W., 2009. Luminescence studies on $SrMgAl_{10}O_{17}:Eu,Dy$ phosphor crystals. *Opt. Laser Technol.* 41 (1), 81–84.
- WebBBC, 2014. Glow in the dark road unveiled in the Netherlands [Online]. Available: <http://www.bbc.com/news/technology-27021291> (accessed 22.04.15).
- WebGloTech, 2014. GloTech International [Online]. Available: <http://www.glo-techint.com/> (accessed 11.12.14).
- WebSmartHighway, 2015. Smart Highway [Online]. Available: <http://www.smarthighway.net/> (accessed 01.08.15).
- Wei, R.-P., Ju, Z.-H., Ma, J.-X., Zhang, D., Zang, Z.-P., Liu, W.-S., 2009. A novel white afterglow phosphorescent phosphor $Ca_3SnSi_2O_9: Dy^{3+}$. *J. Alloys Compd.* 486 (1–2), L17–L20.
- Wei, D.L., Qin, L., Huang, Y.L., Seo, H.J., 2013. Photoluminescence properties of Eu^{2+} -activated $BaCa_2Al_8O_{15}$ nanophosphors. *Ceram. Int.* 39 (3), 2383–2387.
- Wiatrowska, A., Zych, E., Kepinski, L., 2010. Monoclinic $HfO_2:Eu$ X-ray phosphor. *Radiat. Meas.* 45 (3–6), 493–496.
- Woo, B.K., Luo, Z., Li, Y., Singh, S.P., Joly, A.G., Hossu, M., Liu, Z., Chen, W., 2011. Luminescence enhancement of $CaZnGe_2O_6:Tb^{3+}$ afterglow phosphors synthesized using ZnO nanopowders. *Opt. Mater.* 33 (8), 1283–1290.
- Wu, H., Hu, Y., Ju, G., Chen, L., Wang, X., Yang, Z., 2011a. Photoluminescence and thermoluminescence of Ce^{3+} and Eu^{2+} in $Ca_2Al_2SiO_7$ matrix. *J. Lumin.* 131 (12), 2441–2445.

- Wu, H., Hu, Y., Kang, F., Chen, L., Wang, X., Ju, G., Mu, Z., 2011b. Observation on long afterglow of Tb^{3+} in $CaWO_4$. *Mater. Res. Bull.* 46 (12), 2489–2493.
- Wu, H., Hu, Y., Kang, F., Li, N., Ju, G., Mu, Z., Yang, Z., 2012a. Luminescent properties of praseodymium in $CaWO_4$ matrix. *J. Am. Ceram. Soc.* 95 (10), 3214–3219.
- Wu, H.Y., Hu, Y.H., Kang, F.W., Li, N.N., 2012b. Enhancement on afterglow properties of Eu^{3+} by Ti^{4+}, Mg^{2+} incorporation in $CaWO_4$ matrix. *J. Mater. Res.* 27 (6), 959–964.
- Xie, W., Wang, Y.H., Hu, Y.H., Luo, L., Wu, H.Y., Deng, L.Y., 2010. Preparation and red long-afterglow luminescence of $Y_2O_3:Eu,Dy$. *Acta Phys. Sin.* 59 (5), 3344–3349.
- Xu, C.N., Watanabe, T., Akiyama, M., Zheng, X.G., 1999. Direct view of stress distribution in solid by mechanoluminescence. *Appl. Phys. Lett.* 74 (17), 2414–2416.
- Xu, C.N., Zheng, X.G., Akiyama, M., Nonaka, K., Watanabe, T., 2000. Dynamic visualization of stress distribution by mechanoluminescence image. *Appl. Phys. Lett.* 76 (2), 179–181.
- Xu, X., Wang, Y., Li, Y., Gong, Y., 2009. Energy transfer between Eu^{2+} and Mn^{2+} in long-afterglow phosphor $CaAl_2O_4:Eu^{2+}, Nd^{3+}$, and Mn^{2+} . *J. Appl. Phys.* 105 (8), 083502.
- Xu, X., Wang, Y., Gong, Y., Zeng, W., Li, Y., 2010. Effect of oxygen vacancies on the red phosphorescence of $Sr_2SnO_4:Sm^{3+}$ phosphor. *Opt. Express* 18 (16), 16989–16994.
- Xu, X., Wang, Y., Yu, X., Li, Y., Gong, Y., 2011a. Investigation of Ce–Mn energy transfer in $SrAl_2O_4:Ce^{3+}, Mn^{2+}$. *J. Am. Ceram. Soc.* 94 (1), 160–163.
- Xu, X., Wang, Y., Zeng, W., Gong, Y., 2011b. Luminescence and storage properties of Sm-doped alkaline-earth titanates. *J. Electrochem. Soc.* 158 (10), J305–J309.
- Xu, X., Wang, Y., Zeng, W., Gong, Y., Liu, B., 2011c. Luminescent properties of the multicolor afterglow phosphors $Ca_3SnSi_2O_9:Re^{3+}$ ($Re=Pr, Tb, Sm$). *J. Am. Ceram. Soc.* 94 (11), 3632–3635.
- Xu, J., Ju, Z.H., Gao, X.P., An, Y.Q., Tang, X.L., Liu, W.S., 2013a. $Na_2CaSn_2Ge_3O_{12}$: a novel host lattice for Sm^{3+} -doped long-persistent phosphorescence materials emitting reddish orange light. *Inorg. Chem.* 52 (24), 13875–13881.
- Xu, X.H., He, Q.L., Yan, L.T., 2013b. White-light long persistent and photo-stimulated luminescence in $CaSnSiO_5:Dy^{3+}$. *J. Alloys Compd.* 574, 22–26.
- Xu, X.H., Qiu, J.B., Xue, Y., 2013c. Multicolor long persistent luminescence phosphors $CaSnSiO_5:R^{3+}$ ($R=Pr, Tb, Sm, Dy$). *ECS Solid State Lett.* 2 (3), R9–R11.
- Xu, J., Chen, D.Q., Yu, Y.L., Zhu, W.J., Zhou, J.C., Wang, Y.S., 2014. Cr^{3+} : $SrGa_{12}O_{19}$: a broadband near-infrared long-persistent phosphor. *Chem. Asian J.* 9 (4), 1020–1025.
- Xu, J., Ueda, J., Zhuang, Y., Viana, B., Tanabe, S., 2015. $Y_3Al_{5-x}Ga_xO_{12}:Cr^{3+}$: a novel red persistent phosphor with high brightness. *Appl. Phys. Express* 8, 042602.
- Yamaga, M., Tani, Y., Kodama, N., Takahashi, T., Honda, M., 2002. Mechanism of long-lasting phosphorescence process of Ce^{3+} -doped $Ca_2Al_2SiO_7$ melilite crystals. *Phys. Rev. B* 65 (23), 235108.
- Yamaga, M., Masui, Y., Sakuta, S., Kodama, N., Kaminaga, K., 2005. Radiative and nonradiative decay processes responsible for long-lasting phosphorescence of Eu^{2+} -doped barium silicates. *Phys. Rev. B* 71 (20), 205102.
- Yamaga, M., Ohsumi, Y., Nakayama, T., Han, T.P.J., 2012. Persistent phosphorescence in Ce-doped Lu_2SiO_5 . *Opt. Mater. Express* 2 (4), 413–419.
- Yamazaki, M., Kojima, K., 2004. Long-lasting afterglow in Tb^{3+} -doped $SiO_2-Ga_2O_3-CaO-Na_2O$ glasses and its sensitization by Yb^{3+} . *Solid State Commun.* 130 (9), 637–639.
- Yamazaki, M., Yamamoto, Y., Nagahama, S., Sawanobori, N., Mizuguchi, M., Hosono, H., 1998. Long luminescent glass: Tb^{3+} -activated $ZnO-B_2O_3-SiO_2$ glass. *J. Non-Cryst. Solids* 241 (1), 71–73.

- Yan, W., Liu, F., Lu, Y.-Y., Wang, X.-J., Yin, M., Pan, Z., 2010. Near infrared long-persistent phosphorescence in $\text{La}_3\text{Ga}_5\text{GeO}_{14}:\text{Cr}^{3+}$ phosphor. *Opt. Express* 18 (19), 20215–20221.
- Yang, Y.M., Li, X.D., Su, X.Y., Li, Z.Q., Liu, L.L., Liu, Y.Z., Zhang, J., Mi, C., Yu, F., 2014. A novel Yb^{2+} doped SrS long persistent luminescence phosphors. *Opt. Mater.* 36 (11), 1822–1825.
- Yao, K., Wang, M., Liu, S., Zhang, L., Li, W., 2006. Effects of host doping on spectral and long-lasting properties of Sm^{3+} -doped $\text{Y}_2\text{O}_3\text{S}$. *J. Rare Earths* 24 (5), 524–528.
- Ye, S., Zhang, J., Zhang, X., Lu, S., Ren, X., Wang, X.-j., 2007a. Mn^{2+} activated red phosphorescence in $\text{BaMg}_2\text{Si}_2\text{O}_7$: $\text{Mn}^{2+}, \text{Eu}^{2+}, \text{Dy}^{3+}$ through persistent energy transfer. *J. Appl. Phys.* 101 (6), 063545.
- Ye, S., Zhang, J., Zhang, X., Wang, X., 2007b. Mn^{2+} activated red long persistent phosphors in $\text{BaMg}_2\text{Si}_2\text{O}_7$. *J. Lumin.* 122–123, 914–916.
- Yen, W.M., Shionoya, S., Yamamoto, H., 2006. *Fundamentals of Phosphors*. CRC Press, Boca Raton.
- Yen, W.M., Shionoya, S., Yamamoto, H., 2007. *Phosphor Handbook*. CRC Press/Taylor and Francis, Boca Raton, FL, USA.
- Yerpude, A.N., Dhoble, S.J., Haranath, D., 2013. Synthesis and characterization of blue long-lasting $\text{BaCa}_2\text{Al}_8\text{O}_{15}:\text{Eu}^{2+}, \text{Dy}^{3+}$ phosphor. *Luminescence* 28 (4), 437–441.
- Yi, S.-J., Liu, Y.-L., Zhang, J.-X., Yuan, D.-S., 2004. Long phosphorescence persistence property of $\text{Cd}_2\text{Ge}_7\text{O}_{16}:\text{Pb}^{2+}$. *Chem. J. Chin. Univ.* 25 (8), 1400–1402.
- Yu, N., Liu, F., Li, X., Pan, Z., 2009. Near infrared long-persistent phosphorescence in SrAl_2O_4 : $\text{Eu}^{2+}, \text{Dy}^{3+}, \text{Er}^{3+}$ phosphors based on persistent energy transfer. *Appl. Phys. Lett.* 95 (23), 231110.
- Yu, X., Xu, X., Qiu, J., 2011. Enhanced long persistence of $\text{Sr}_2\text{SnO}_4:\text{Sm}^{3+}$ red phosphor by co-doping with Dy^{3+} . *Mater. Res. Bull.* 46 (4), 627–629.
- Yu, F., Yang, Y., Su, X., Mi, C., Seo, H.J., 2015. Novel long persistent luminescence phosphors: Yb^{2+} codoped MAI_2O_4 ($M = \text{Ba}, \text{Sr}$). *Opt. Mater. Express* 5 (3), 585–595.
- Yuan, S., Yang, Y., Fang, B., Chen, G., 2007. Effects of doping ions on afterglow properties of $\text{Y}_2\text{O}_3:\text{Eu}$ phosphors. *Opt. Mater.* 30 (4), 535–538.
- Yuan, X., Shi, X., Shen, M., Wang, W., Fang, L., Zheng, F., Wu, X., 2009. Luminescent properties of Pr^{3+} doped $(\text{Ca}, \text{Zn})\text{TiO}_3$: powders and films. *J. Alloys Compd.* 485 (1–2), 831–836.
- Yukihara, E.G., McKeever, S.W.S., Akselrod, M.S., 2014. State of art: optically stimulated luminescence dosimetry—frontiers of future research. *Radiat. Meas.* 71, 15–24.
- Zeng, W., Wang, Y.H., Han, S.C., Chen, W.B., Li, G., Wang, Y.Z., Wen, Y., 2013. Design, synthesis and characterization of a novel yellow long-persistent phosphor: $\text{Ca}_2\text{BO}_3\text{Cl}:\text{Eu}^{2+}, \text{Dy}^{3+}$. *J. Mater. Chem. C* 1 (17), 3004–3011.
- Zeng, W., Wang, Y.H., Han, S.C., Chen, W.B., Li, G., 2014. Investigation on long-persistent luminescence of $\text{Ca}_2\text{BO}_3\text{Cl}:\text{Eu}^{2+}, \text{Ln}^{3+}$ ($\text{Ln} = \text{Nd}, \text{Dy}, \text{Er}$). *Opt. Mater.* 36 (11), 1819–1821.
- Zhang, J., Zhang, Z., Wang, T., Hao, W., 2003. Preparation and characterization of a new long afterglow indigo phosphor $\text{Ca}_{12}\text{Al}_{14}\text{O}_{33}:\text{Nd}, \text{Eu}$. *Mater. Lett.* 57 (26–27), 4315–4318.
- Zhang, J., Zhang, Z., Wang, T., 2004a. A new luminescent phenomenon of ZnO due to the precipitate trapping effect of MgO . *Chem. Mater.* 16 (5), 768–770.
- Zhang, J.Y., Zhang, Z.T., Tang, Z.L., Wang, T.M., 2004b. A new method to synthesize long afterglow red phosphor. *Ceram. Int.* 30 (2), 225–228.
- Zhang, P.Y., Wang, M.Q., Hong, Z.L., Fang, X.P., Qian, G.D., Wang, Z.Y., 2004c. A new yellow long lasting phosphor $\text{Y}_2\text{O}_3:\text{Ti}$. *J. Rare Earths* 22 (1), 75–78.

- Zhang, X.Y., Cheng, G., Mi, X.Y., Xiao, Z.Y., Jiang, Z.Z., Hujingjie, H.U., 2004d. Preparation and long persistence red luminescence of $M_{0.2}Ca_{0.8}TiO_3:Pr^{3+}$ ($M=Mg^{2+}, Sr^{2+}, Ba^{2+}, Zn^{2+}$). *J. Rare Earths* 22 (1), 137–139.
- Zhang, P., Hong, Z., Wang, M., Fang, X., Qian, G., Wang, Z., 2005. Luminescence characterization of a new long afterglow phosphor of single Ti-doped Y_2O_3 . *J. Lumin.* 113 (1–2), 89–93.
- Zhang, J., Liu, Y.-L., Man, S.-q., 2006a. Afterglow phenomenon in erbium and titanium codoped Gd_2O_3 phosphors. *J. Lumin.* 117 (2), 141–146.
- Zhang, J., Pan, F., Hao, W., Wang, T., 2006b. Effect of MgO doping on the luminescent properties of ZnO. *Mater. Sci. Eng. B* 129 (1–3), 93–95.
- Zhang, J.W., Liu, Y.L., Zhang, J.X., Yuan, D.S., Rong, J.H., Huang, L.H., 2006c. Long afterglow property and mechanism on $Gd_2O_3:Ti$. *Rare Metal Mater. Eng.* 35 (5), 766–769.
- Zhang, L., Li, C., Su, Q., 2006d. Long lasting phosphorescence in Eu^{2+} and Ce^{3+} co-doped strontium borate glasses. *J. Rare Earths* 24, 196–198.
- Zhang, P., Xu, M., Zheng, Z., Sun, B., Zhang, Y., 2007a. Rapid formation of red long afterglow phosphor $Sr_3Al_2O_6:Eu^{2+}, Dy^{3+}$ by microwave irradiation. *Mater. Sci. Eng. B* 136 (2–3), 159–164.
- Zhang, X., Zhang, J., Nie, Z., Wang, M., Ren, X., Wang, X.-j., 2007b. Enhanced red phosphorescence in nanosized $CaTiO_3:Pr^{3+}$ phosphors. *Appl. Phys. Lett.* 90 (15), 151911.
- Zhang, X., Zhang, J., Zhang, X., Chen, L., Lu, S., Wang, X.-J., 2007c. Enhancement of red fluorescence and afterglow in $CaTiO_3:Pr^{3+}$ by addition of Lu_2O_3 . *J. Lumin.* 122–123, 958–960.
- Zhang, J., Yu, M., Qin, Q., Zhou, H., Zhou, M., Xu, X., Wang, Y., 2010a. The persistent luminescence and up conversion photostimulated luminescence properties of nondoped Mg_2SnO_4 material. *J. Appl. Phys.* 108 (12), 123518.
- Zhang, S., Pang, R., Li, C., Su, Q., 2010b. Green photoluminescence, but blue afterglow of Tb^{3+} activated $Sr_4Al_4O_{25}$. *J. Lumin.* 130 (11), 2223–2225.
- Zhang, J.-C., Qin, Q.-S., Yu, M.-H., Zhou, H.-L., Zhou, M.-J., 2011a. Photoluminescence and persistent luminescence properties of non-doped and Ti^{4+} -doped Mg_2SnO_4 phosphors. *Chin. Phys. B* 20 (9), 094211.
- Zhang, S., Li, C., Pang, R., Jiang, L., Shi, L., Su, Q., 2011b. Energy transfer and excitation wavelength dependent long-lasting phosphorescence in Pr^{3+} activated $Y_3Al_5O_{12}$. *J. Lumin.* 131 (12), 2730–2734.
- Zhang, S., Li, C., Pang, R., Jiang, L., Shi, L., Su, Q., 2011c. Long-lasting phosphorescence study on $Y_3Al_5O_{12}$ doped with different concentrations of Ce^{3+} . *J. Rare Earths* 29 (5), 426–430.
- Zhang, S., Nakai, Y., Tsuboi, T., Huang, Y., Seo, H.J., 2011d. Luminescence and microstructural features of Eu-activated $LiBaPO_4$ phosphor. *Chem. Mater.* 23 (5), 1216–1224.
- Zhang, J.-S., Zhong, H.-Y., Sun, J.-S., Cheng, L.-H., Li, X.-P., Chen, B.-J., 2012a. Reddish orange long-lasting phosphorescence in $KY_3F_{10}:Sm^{3+}$ for X-ray or cathode ray tubes. *Chin. Phys. Lett.* 29 (1), 017101.
- Zhang, J., Chen, B., Sun, J., Li, X., Cheng, L., Zhong, H., 2012b. White long-lasting phosphorescence generation in a $CaAl_2Si_2O_8:Eu^{2+}, Mn^{2+}, Dy^{3+}$ system through persistent energy transfer. *J. Phys. D Appl. Phys.* 45 (32), 325105.
- Zhang, J., Hu, R., Qin, Q., Wang, D., Liu, B., Wen, Y., Zhou, M., Wang, Y., 2012c. The origin of two quenching concentrations and unusual afterglow behaviors of $Ba_2SnO_4:Sm^{3+}$ phosphor. *J. Lumin.* 132 (10), 2590–2594.

- Zhang, J., Ma, X., Qin, Q., Shi, L., Sun, J., Zhou, M., Liu, B., Wang, Y., 2012d. The synthesis and afterglow luminescence properties of a novel red afterglow phosphor: $\text{SnO}_2:\text{Sm}^{3+},\text{Zr}^{4+}$. *Mater. Chem. Phys.* 136 (2–3), 320–324.
- Zhang, J., Qin, Q., Yu, M., Zhou, M., Wang, Y., 2012e. The photoluminescence, afterglow and up conversion photostimulated luminescence of Eu^{3+} doped Mg_2SnO_4 phosphors. *J. Lumin.* 132 (1), 23–26.
- Zhang, H.R., Zheng, M.T., Lei, B.F., Liu, Y.L., Xiao, Y., Dong, H.W., Zhang, Y.C., Ye, S.P., 2013a. Luminescence properties of red long-lasting phosphorescence phosphor $\text{AlN}:\text{Mn}^{2+}$. *ECS J. Solid State Sci. Technol.* 2 (7), R117–R120.
- Zhang, H.R., Zheng, M.T., Lei, B.F., Xiao, Y., Dong, H.W., Liu, Y.L., Liu, X.T., Deng, J.J., Deng, J.W., Huang, Z.L., 2013b. Preparation and long-lasting phosphorescence properties of $\text{BaAlSi}_5\text{N}_7\text{O}_2:\text{Eu}^{2+}$. *ECS Solid State Lett.* 2 (6), R16–R18.
- Zhang, J.-C., Xu, C.-N., Kamimura, S., Terasawa, Y., Yamada, H., Wang, X., 2013c. An intense elasto-mechanoluminescence material $\text{CaZnOS}:\text{Mn}^{2+}$ for sensing and imaging multiple mechanical stresses. *Opt. Express* 21 (11), 12976–12986.
- Zhang, W.-X., Wang, Y.-H., Li, H.-L., Wang, X.-S., Zhao, H., 2013d. Structure and luminescence properties of $\text{MgGa}_2\text{O}_4:\text{Cr}^{3+}$ with Zn substituted for Mg. *Spectrosc. Spectr. Anal.* 33, 31–35.
- Zhang, S.A., Hu, Y.H., Chen, R., Wang, X.J., Wang, Z.H., 2014a. Photoluminescence and persistent luminescence in Bi^{3+} -doped Zn_2GeO_4 phosphors. *Opt. Mater.* 36 (11), 1830–1835.
- Zhang, Y., Wei, W., Das, G.K., Yang Tan, T.T., 2014b. Engineering lanthanide-based materials for nanomedicine. *J. Photochem. Photobiol. C Photochem. Rev.* 20, 71–96.
- Zhao, Z., Wang, Y., 2012. The synthesis and afterglow luminescence properties of a novel red afterglow phosphor: $\text{ZrO}_2:\text{Sm}^{3+}, \text{Sn}^{4+}$. *J. Lumin.* 132 (11), 2842–2846.
- Zhao, R., Pang, R., Li, H.F., Jia, Y.L., Jiang, L.H., Sun, W.Z., Li, C.Y., 2014. Luminescent properties of blue long-lasting phosphorescence phosphors $\text{Sr}_6\text{Al}_{18}\text{Si}_2\text{O}_{37}:\text{Eu}^{2+},\text{RE}^{3+}$. *J. Rare Earths* 32 (9), 797–801.
- Zhong, R., Zhang, J., Zhang, X., Lu, S., Wang, X.-j., 2006a. Energy transfer and red phosphorescence in strontium aluminates co-doped with $\text{Cr}^{3+},\text{Eu}^{2+}$ and Dy^{3+} . *J. Lumin.* 119–120, 327–331.
- Zhong, R., Zhang, J., Zhang, X., Lu, S., Wang, X.-j., 2006b. Red phosphorescence in $\text{Sr}_4\text{Al}_{14}\text{O}_{25}:\text{Cr}^{3+},\text{Eu}^{2+},\text{Dy}^{3+}$ through persistent energy transfer. *Appl. Phys. Lett.* 88, 201916.
- Zhou, J., Liu, Z., Li, F., 2012. Upconversion nanophosphors for small-animal imaging. *Chem. Soc. Rev.* 41, 1323–1349.
- Zhuang, Y., Ueda, J., Tanabe, S., 2012. Photochromism and white long-lasting persistent luminescence in Bi^{3+} -doped ZnGa_2O_4 ceramics. *Opt. Mater. Express* 2 (10), 1378–1383.
- Zhuang, Y., Ueda, J., Tanabe, S., 2013a. Enhancement of red persistent luminescence in Cr^{3+} -doped ZnGa_2O_4 phosphors by Bi_2O_3 codoping. *Appl. Phys. Express* 6, 4–7.
- Zhuang, Y., Ueda, J., Tanabe, S., 2013b. Tunable trap depth in $\text{Zn}(\text{Ga}_{1-x}\text{Al}_x)_2\text{O}_4:\text{Cr}$, Bi red persistent phosphors: considerations of high-temperature persistent luminescence and photostimulated persistent luminescence. *J. Mater. Chem. C* 1, 7849.
- Zhuang, Y., Ueda, J., Tanabe, S., Dorenbos, P., 2014a. Band-gap variation and a self-redox effect induced by compositional deviation in $\text{Zn}_x\text{Ga}_{2-3x}\text{O}_{3+x}:\text{Cr}^{3+}$ persistent phosphors. *J. Mater. Chem. C* 2, 5502.
- Zhuang, Y.X., Katayama, Y., Ueda, J., Tanabe, S., 2014b. A brief review on red to near-infrared persistent luminescence in transition-metal-activated phosphors. *Opt. Mater.* 36 (11), 1907–1912.

- Zomer, G., Hastings, J.W., Berthold, F., Lundin, A., Garcia Campana, A.M., Niessner, R., Christopolous, T.K., Lowik, C., Branchini, B., Daunert, S., Blum, L., Kricka, L.J., 2011. Chemiluminescence and Bioluminescence. Past, Present and Future (A. Roda, Ed.). The Royal Society of Chemistry, pp. P001–590. ISBN: 978-1-84755-812-1. <http://dx.doi.org/10.1039/9781849732024>.
- Zych, E., Trojan-Piegza, J., 2007. Anomalous activity of Eu^{3+} in S_6 site of Lu_2O_3 in persistent luminescence. *J. Lumin.* 122–123, 335–338.
- Zych, E., Trojan-Piegza, J., Hreniak, D., Strek, W., 2003. Properties of Tb-doped vacuum-sintered Lu_2O_3 storage phosphor. *J. Appl. Phys.* 94 (3), 1318.

Chapter 275

Quaternary $R_2X_3-PbX-ZX_2$ ($X = S, Se; Z = Si, Ge, Sn$) Chalcogenides

Lubomir D. Gulay*, Marek Daszkiewicz^{†,1} and Oleg V. Marchuk[‡]

*Department of Ecology and Protection of Environment, Eastern European National University, Lutsk, Ukraine

[†]Institute of Low Temperature and Structure Research, Polish Academy of Sciences, Wrocław, Poland

[‡]Department of Inorganic and Physical Chemistry, Eastern European National University, Lutsk, Ukraine

¹Corresponding author: e-mail: m.daszkiewicz@int.pan.wroc.pl

Chapter Outline

1 Introduction	110	4.3 Phase Diagrams of the $R_2S_3-PbS-GeSe_2$ Systems	126
2 Synthesis Conditions	110	4.4 Phase Diagrams of the $R_2Se_3-PbSe-GeSe_2$ Systems	127
3 Ternary Compounds in the $Pb-Z-X$ ($X = S, Se; Z = Si, Ge, Sn$) Systems	110	4.5 Phase Diagrams of the $R_2S_3-PbS-SnS_2$ Systems	130
3.1 Structure Type Pb_2SiS_4	112	4.6 Structure Types of Quaternary Compounds	133
3.2 Structure Type Pb_2SiSe_4	113	4.7 Crystallographic Description of Quaternary Compounds in the $R_2X_3-PbX-ZX_2$ ($X = S, Se; Z = Si, Ge, Sn$) Systems	144
3.3 Structure Type Pb_2GeS_4	114	4.8 Formation of Superstructures	154
3.4 Structure Type Pb_2GeS_4 : High-Temperature Phase	115	5 Magnetic Properties of Quaternary Compounds in the $R_2X_3-PbX-ZX_2$ ($X = S, Se; Z = Si, Ge, Sn$) Systems	158
3.5 Structure Type $PbGeS_3$	115	6 Conclusions and Outlook	159
3.6 Structure Type GeS	115	References	160
3.7 Structure Type $NaCl$	117		
3.8 Structure Type $[NH_4]CdCl_3$	118		
4 Quaternary $R_2X_3-PbX-ZX_2$ ($X = S, Se; Z = Si, Ge, Sn$) Systems	119		
4.1 Phase Diagrams of the $R_2S_3-PbS-SiS_2$ Systems	119		
4.2 Phase Diagrams of the $R_2Se_3-PbSe-SiSe_2$ Systems	124		

1 INTRODUCTION

Rare-earth chalcogenides are of broad interest for both basic and applied science, and they have been intensely studied in the recent past due to their interesting optical, thermal, magnetic, and electrical properties. Complex rare-earth-based chalcogenide materials have found applications as components of infrared and nonlinear optical devices. Synthesis and discovery of new compounds with increasingly complex compositions is vital for modern materials science, and systematic investigations of complex chalcogenide systems is an essential part of the ever-important effort that may lead to novel materials with both interesting and practically significant properties.

The present chapter consists of three main parts. The first part (Section 3) deals with crystal structures of ternary compounds. Since crystallography of ternary compounds in R_2X_3 —PbX and R_2X_3 — ZX_2 ($X = S, Se; Z = Si, Ge, Sn$) ($X = S, Se; Z = Si, Ge, Sn$) systems has been previously reviewed in detail (Gulay and Daszkiewicz, 2011), only the crystal structures of ternary compounds found in Pb—Z—X ($X = S, Se; Z = Si, Ge, Sn$) systems are described here. Most of these compounds exist along the pseudo-binary cross section PbX— ZX_2 . The second part (Section 4) deals with phase diagrams and crystal structures of the known compounds in quaternary systems R_2X_3 —PbX— ZX_2 ($X = S, Se; Z = Si, Ge, Sn$). Crystallographic peculiarities of quaternary rare-earth chalcogenides are discussed. The last part (Section 5) describes magnetic properties of some quaternary compounds described in Section 4.

2 SYNTHESIS CONDITIONS

All samples of quaternary R_2X_3 —PbX— ZX_2 ($X = S, Se; Z = Si, Ge, Sn$) systems reviewed in this chapter were prepared using direct synthesis starting from high purity elemental constituents. The purity of the ingredients was generally better than 99.9 wt%. The typical synthesis protocol is as follows: appropriate amounts of the components corresponding to desired stoichiometry are weighed and sealed in evacuated silica ampoules under argon atmosphere. The synthesis is then carried out in a tube furnace by a gradual heating of the ampoules with a heating rate of 30 K h^{-1} to the maximum temperature (typically 1370 K). The ampoules are kept at this temperature for several hours (typically 4 h). Later, they are cooled slowly with a cooling rate of 10 K h^{-1} down to 770 K and annealed at these conditions for 500 h. After annealing, the ampoules with the samples are quenched in cold water. The exact experimental conditions are described in details in the original papers referenced throughout this chapter.

3 TERNARY COMPOUNDS IN THE Pb—Z—X ($X = S, Se; Z = Si, Ge, Sn$) SYSTEMS

Stoichiometries and crystallographic data of ternary compounds that are known to form in the Pb—Z—X ($X = S, Se; Z = Si, Ge, Sn$) systems are summarized in Table 1. Most of the compounds can have been reported to exist

TABLE 1 Crystallographic Data for Ternary Chalcogenides of the Pb—Z—X (X = S, Se; Z = Si, Ge, Sn) Systems

Compound	Structure Type	Space Group	Lattice Parameters (nm)			Reference(s)
			a	b	c	
Pb ₂ SiS ₄	Pb ₂ SiS ₄	<i>P2₁/c</i>	0.64721	0.66344 $\beta = 108.805^\circ$	1.6832	Iglesias and Steinfink (1973)
Pb ₂ SiSe ₄	Pb ₂ SiSe ₄	<i>P2₁/c</i>	0.85670	0.70745 $\beta = 108.355^\circ$	1.36160	Iglesias and Steinfink (1973)
Pb ₂ GeS ₄	Pb ₂ GeS ₄	<i>P2₁/c</i>	0.79742	0.89255 $\beta = 114.171^\circ$	1.08761	Susa and Steinfink (1971)
Pb ₂ GeS ₄ (ht)	Pb ₂ GeS ₄	<i>I$\bar{4}$3d</i>	1.4096	—	—	Poduska et al. (2002)
PbGeS ₃	PbGeS ₃	<i>P2₁/c</i>	0.7224	1.0442 $\beta = 105.7^\circ$	0.6825	Ribes et al. (1974)
Pb ₂ GeSe ₄	Pb ₂ GeSe ₄	<i>I$\bar{4}$3d</i>	1.4573	—	—	Poduska et al. (2002)
Pb _{0.2} Ge _{0.8} Se	GeS	<i>Pnma</i>	1.114	0.3928	0.4407	Krebs and Langner, 1964
Pb _{0.9} Ge _{0.1} Se	NaCl	<i>Fm$\bar{3}$m</i>	0.6089	—	—	Krebs and Langner (1964)
PbSnS ₃	[NH ₄]CdCl ₃	<i>Pnma</i>	0.8738	0.3792	1.4052	Jumas et al. (1972)
Pb _{0.5} Sn _{0.5} S	GeS	<i>Pnma</i>	1.043	0.4065	0.4284	Krebs and Langner (1964)
Pb _{0.9} Sn _{0.1} S	NaCl	<i>Fm$\bar{3}$m</i>	0.5922	—	—	Krebs and Langner (1964)
Pb _{0.25} Sn _{0.75} Se	GeS	<i>Pnma</i>	1.160	0.4210	0.4483	Krebs et al. (1961)
Pb _{0.6} Sn _{0.4} Se	NaCl	<i>Fm$\bar{3}$m</i>	0.6077	—	—	Woolley and Berolo (1968)

along the pseudo-binary cross sections PbX—ZX_2 . In the case of the PbSe—SnSe_2 system, no ternary compounds are known.

3.1 Structure Type Pb_2SiS_4

Structure type Pb_2SiS_4 (Iglesias and Steinfink, 1973) (Fig. 1, Table 2). Space group (SG) $P2_1/c$, $Z=4$, $a=0.64721$, $b=0.66344$, $c=1.6832$ nm, and $\beta=108.805^\circ$. The sulfur atoms form distorted monocapped trigonal prismatic arrangements around each of the Pb1 and Pb2 atoms. The shortest Pb—S distances are 0.2826 and 0.2798 nm, for Pb1 and Pb2, respectively. The sulfur atoms create a distorted tetrahedral coordination sphere around the Si atom. The shortest Si—S distance is 0.2099 nm. The S1 atom is located just outside

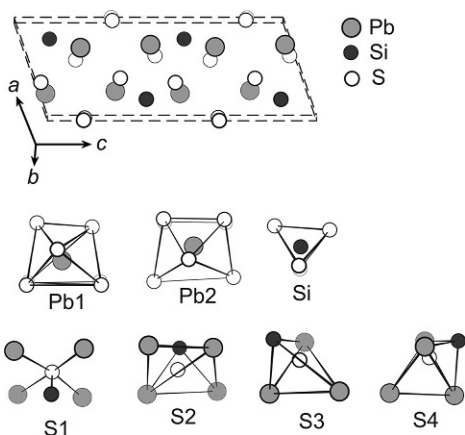


FIGURE 1 Crystal structure of Pb_2SiS_4 and CPs of atoms.

TABLE 2 Atomic Parameters for Pb_2SiS_4

Atom	Position	Fractional Coordinates			Coordination	
		x	y	z		
Pb1	4e	0.2363	0.2494	0.0223	7S	
Pb2	4e	0.2631	0.3117	0.2854	7S	
Si	4e	0.7939	0.2483	0.1064	4S	
S1	4e	0.0052	-0.0007	0.1355	4Pb	1Si
S2	4e	-0.0008	0.0014	0.3612	4Pb	1Si
S3	4e	0.5791	0.2279	0.1768	3Pb	1Si
S4	4e	0.6221	0.2398	0.4773	4Pb	1Si

a tetragonal pyramid formed by 4Pb and 1Si atoms. The S2 atom is located inside a tetragonal pyramid formed by 4Pb and 1Si atoms. The S3 atom has a tetrahedral arrangement and is coordinated by 3Pb and 1Si atoms. 4Pb and 1Si atoms create trigonal bipyramidal coordination sphere around the S4 atom.

3.2 Structure Type Pb_2SiSe_4

Structure type Pb_2SiSe_4 (Iglesias and Steinfink, 1973) (Fig. 2, Table 3). SG $P2_1/c$, $Z=4$, $a=0.85670$, $b=0.70745$, $c=1.36160$ nm, and $\beta=108.355^\circ$.

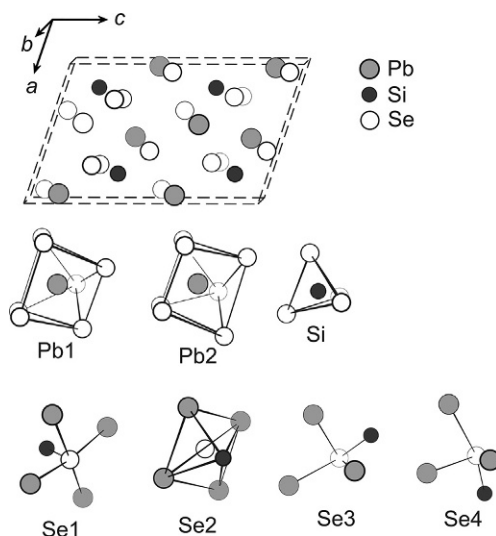


FIGURE 2 Crystal structure of Pb_2SiSe_4 and CPs of atoms.

TABLE 3 Atomic Parameters for Pb_2SiSe_4

Atom	Position	Fractional Coordinates			Coordination	
		x	y	z		
Pb1	4e	0.0543	0.1581	0.3715	7Se	
Pb2	4e	0.5602	0.1479	0.3672	7Se	
Si	4e	0.2037	0.2400	0.1449	4Se	
Se1	4e	0.2737	0.4779	0.2640	4Pb	1Si
Se2	4e	0.7437	0.4726	0.2603	4Pb	1Si
Se3	4e	0.3668	0.2626	0.0420	3Pb	1Si
Se4	4e	0.9313	0.2602	0.0557	3Pb	1Si

The selenium atoms create monocapped trigonal prismatic arrangement around each of the Pb1 and Pb2 atoms. The shortest Pb—Se distances are 0.2974 and 0.2875 nm for Pb1 and Pb2, respectively. The selenium atoms create tetrahedral coordination sphere around the Si atom. The shortest Si—Se distance is 0.2254 nm. The Se1 atom is located outside a tetragonal pyramid formed by 4Pb and 1Si atoms. The Se2 atom is located in a tetragonal pyramid formed by 4Pb and 1Si atoms. Each of the Se3 and Se4 atoms is located outside a tetrahedron formed by 3Pb and 1Si atoms.

3.3 Structure Type Pb_2GeS_4

Structure type Pb_2GeS_4 (Susa and Steinfink, 1971) (Fig. 3, Table 4). SG $P2_1/c$, $Z=4$, $a=0.79742$, $b=0.89255$, $c=1.08761$ nm, and $\beta=114.171^\circ$. The sulfur atoms create distorted pentagonal bi-pyramidal arrangement around the Pb1 atom. The shortest Pb—S distance is 0.2833 nm. The Pb2 atom is located in a tetragonal bipyramid formed by the sulfur atoms. The shortest Pb—S distance is 0.2810 nm. The sulfur atoms create a tetrahedral coordination sphere around the Ge atom. The shortest Ge—S distance is 0.2185 nm. Each of the S1, S2, and S4 atoms has a tetrahedral arrangement, coordinated by 3Pb and 1Ge atoms. The coordination polyhedron for S4 is centered outside. The S3 atom is located in a trigonal bipyramid formed by 4Pb and 1Ge atoms.

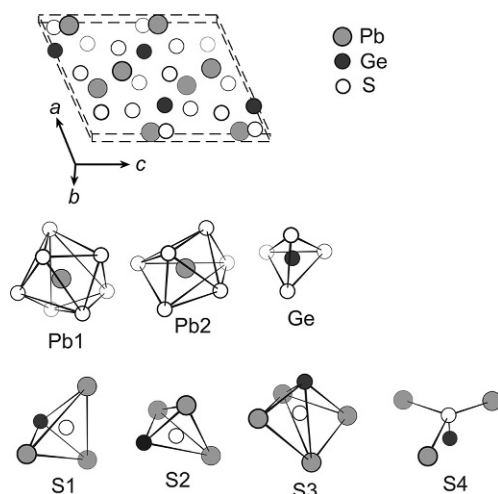


FIGURE 3 Crystal structure of Pb_2GeS_4 and CPs of atoms.

TABLE 4 Atomic Parameters for Pb_2GeS_4

Atom	Position	Fractional Coordinates			Coordination	
		x	y	z		
Pb1	4e	0.0356	0.3161	0.3407	7S	
Pb2	4e	0.4124	0.4326	0.1551	6S	
Ge	4e	0.7137	0.1908	0.0063	4S	
S1	4e	0.2465	−0.0171	0.1256	3Pb	1Ge
S2	4e	0.7644	0.0900	0.2027	3Pb	1Ge
S3	4e	0.4437	0.2002	0.3980	4Pb	1Ge
S4	4e	0.9193	0.3691	0.0610	3Pb	1Ge

3.4 Structure Type Pb_2GeS_4 : High-Temperature Phase

Structure type Pb_2GeS_4 high-temperature phase (ht) was reported by Poduska et al. (2002) (Fig. 4, Table 5). SG $I\bar{4}3d$, $Z=16$ and $a=1.4096$ nm. The sulfur atoms create octahedral arrangement around the Pb1 and Pb2 atoms. The shortest Pb—S distances are 0.2856 and 0.2879 nm for Pb1 and Pb2, respectively. The sulfur atoms create tetrahedral coordination sphere around the Ge atom. The shortest Ge—S distance is 0.2211 nm. The S1 atom has a tetrahedral arrangement coordinated by 3Pb and 1Ge atoms. The S2 atom is located in trigonal bipyramid formed by 4Pb and 1Ge atoms.

3.5 Structure Type PbGeS_3

Structure type PbGeS_3 was published by Ribes et al., 1974 (Fig. 5, Table 6). SG $P2_1/c$, $Z=4$, $a=0.7224$, $b=1.0442$, $c=0.6825$ nm, and $\beta=105.7^\circ$. The sulfur atoms create a distorted octahedral arrangement around the Pb atom. The shortest Pb—S distance is 0.2736 nm. The sulfur atoms create tetrahedral coordination sphere around the Ge atom. The shortest Ge—S distance is 0.2174 nm. The S1 atom has a tetrahedral arrangement coordinated by 2Pb and 2Ge atoms. The S2 atom has a triangular surrounding formed by 2Pb and 1Ge atoms. The S3 atom has a tetrahedral arrangement coordinated by 3Pb and 1Ge atoms.

3.6 Structure Type GeS

Structure type GeS (Zachariasen, 1932) (Fig. 6, Table 7). SG $Pnma$, $Z=4$, $a=1.114$, $b=0.3928$, and $c=0.4407$ nm for $\text{Pb}_{0.2}\text{Ge}_{0.8}\text{Se}$ (Krebs and Langner, 1964). The randomly distributed Pb and Ge atoms (M) are located

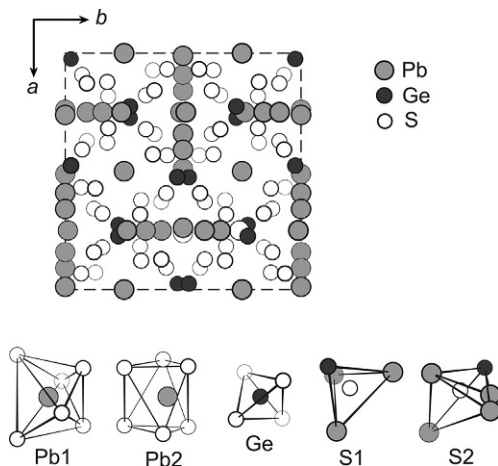


FIGURE 4 Crystal structure of Pb_2GeS_4 (ht) and CPs of atoms.

TABLE 5 Atomic Parameters for Pb_2GeS_4 (ht)

Atom	Position	Fractional Coordinates			Coordination	
		<i>x</i>	<i>y</i>	<i>z</i>		
Pb1	24 <i>d</i>	3/4	0.2611(1)	0	6S	
Pb2 ^a	24 <i>d</i>	3/4	0.5912(2)	0	6S	
Ge	16 <i>c</i>	0.9756(1)	0.4756(1)	0.0244(1)	4S	
S1	16 <i>c</i>	0.0676(2)	0.5676(2)	0.9324(2)	3Pb	1Ge
S2	48 <i>e</i>	0.0719(3)	0.3719(3)	0.0921(3)	4Pb	1Ge

^aOccupancy 32.4% Pb.

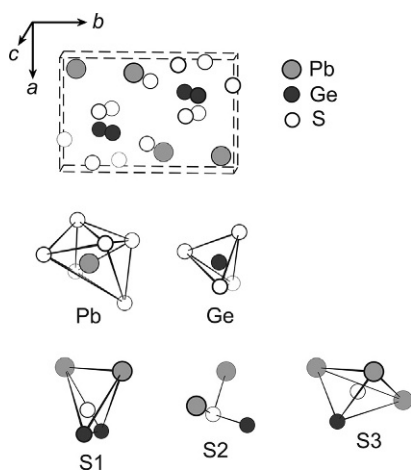


FIGURE 5 Crystal structure of PbGeS_3 and CPs of atoms.

TABLE 6 Atomic Parameters for PbGeS_3

Atom	Position	Fractional Coordinates			Coordination	
		x	y	z		
Pb	4e	0.1371	0.0796	0.2808	6S	
Ge	4e	0.3183	0.7063	0.4908	4S	
S1	4e	0.4870	0.2191	0.6904	2Pb	2Ge
S2	4e	0.2305	0.5079	0.4159	2Pb	1Ge
S3	4e	0.0573	0.8209	0.4103	3Pb	1Ge

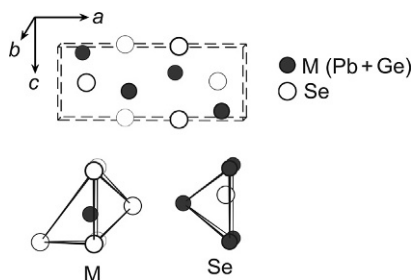

FIGURE 6 Crystal structure of GeS and CPs of atoms.

TABLE 7 Atomic Parameters for $\text{Pb}_{0.2}\text{Ge}_{0.8}\text{Se}$

Atom	Position	Fractional Coordinates			Coordination
		x	y	z	
M^a	4c	0.120	1/4	0.115	6Se
Se	4c	0.350	1/4	0.000	5M

^aOccupancy 20% Pb+80% Ge.

in heavily distorted octahedra formed by the selenium atoms. The shortest M—Se distance is 0.2572 nm. The Se atom has a tetragonal pyramidal arrangement coordinated by 5M atoms.

3.7 Structure Type NaCl

Structure type NaCl (Straumanis and Ieviņš, 1936) (Fig. 7, Table 8). SG $Fm\bar{3}m$, $Z=4$ and $a=0.6089$ nm for $\text{Pb}_{0.9}\text{Ge}_{0.1}\text{Se}$ (Krebs and Langner,

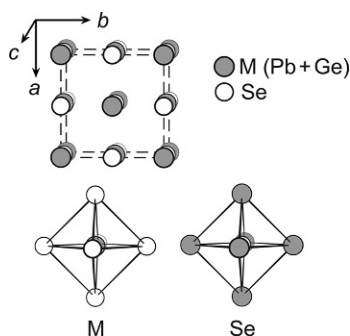


FIGURE 7 Crystal structure of NaCl and CPs of atoms.

TABLE 8 Atomic Parameters for $\text{Pb}_{0.9}\text{Ge}_{0.1}\text{Se}$

Atom	Position	Fractional Coordinates			Coordination
		x	y	z	
M^a	4a	0	0	0	6Se
Se	4b	1/2	1/2	1/2	6M

^aOccupancy 90% Pb+10% Ge.

1964). The randomly distributed Pb and Ge atoms (M) are located in octahedra formed by the selenium atoms. The shortest M—Se distance is 0.3044 nm. The Se atom has an octahedral arrangement coordinated by 6M atoms.

3.8 Structure Type $[\text{NH}_4]\text{CdCl}_3$

Structure type $[\text{NH}_4]\text{CdCl}_3$ (Rolies and De Ranter, 1978) (Fig. 8, Table 9). SG $Pnma$, $Z=4$, $a=0.8738$, $b=0.3792$, and $c=1.4052$ nm for PbSnS_3 (Jumas et al., 1972). The sulfur atoms create bicapped trigonal prismatic arrangement around the Pb atoms. The shortest Pb—S distance is 0.2781 nm. The sulfur atoms create octahedral coordination sphere around the Sn atoms. The shortest Sn—S distance is 0.2470 nm. The S1 atom has a tetrahedral arrangement coordinated by 1Pb and 3Sn atoms. The S2 atom is located in a tetragonal pyramid formed by 3Pb and 2Sn atoms. The S3 atom is situated in a tetragonal pyramid formed by 4Pb and 1Sn atoms.

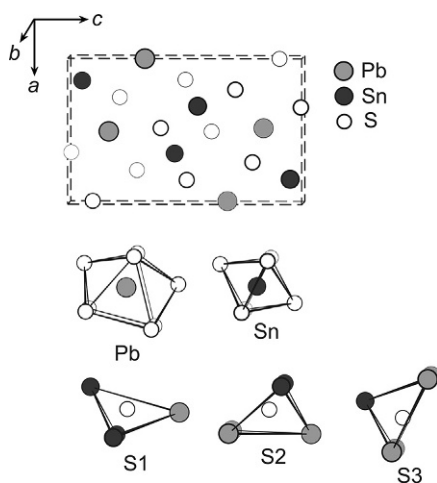

FIGURE 8 Crystal structure of $[\text{NH}_4]\text{CdCl}_3$ and CPs of atoms.

TABLE 9 Atomic Parameters for PbSnS_3

Atom	Position	Fractional Coordinates			Coordination	
		x	y	z		
Pb	4c	0.5063	3/4	0.1729	8S	
Sn	4c	0.1685	1/4	0.0524	6S	
S1	4c	-0.0167	3/4	0.1048	1Pb	3Sn
S2	4c	0.3387	3/4	-0.0063	3Pb	2Sn
S3	4c	0.2827	1/4	0.2132	4Pb	1Sn

4 QUATERNARY $R_2X_3\text{—PbX—ZX}_2$ ($X = S, Se; Z = Si, Ge, Sn$) SYSTEMS

The information about investigations of the $R_2X_3\text{—PbX—ZX}_2$ ($X = S, Se; Z = Si, Ge, Sn$) systems is summarized in [Table 10](#). Isothermal sections of 17 quaternary systems have been constructed.

4.1 Phase Diagrams of the $R_2S_3\text{—PbS—SiS}_2$ Systems

Phase diagrams of the $R_2S_3\text{—PbS—SiS}_2$ ($R = Y, La, \text{ and } Er$) systems have been constructed. Quaternary compounds that form in these systems are listed in [Table 11](#). Only one quaternary compound of the $\text{La}_2\text{PbSi}_2\text{S}_8$ structure type

TABLE 10 Investigations of the $R_2X_3-PbX-ZX_2$ ($X = S, Se; Z = Si, Ge, Sn$) Systems

Z	X	R														
		Y	La	Ce	Pr	Nd	Sm	Eu	Gd	Tb	Dy	Ho	Er	Tm	Yb	Lu
Si	S	⊕, 1	⊕, 1	-, 1	-, 1	-, 1	-, 1	-, ...	-, 1	-, 1	-, 1	-, 1	⊕, 1	-, ...	-, ...	-, ...
	Se	⊕, 0	⊕, 1	-, 1	-, 1	-, 1	-, 1	-, ...	-, 1	-, ...	-, ...	-, ...	-, ...	-, ...	-, ...	-, ...
Ge	S	⊕, 0	⊕, 1	-, 1	⊕, 1	-, ...	-, ...	-, ...	-, ...	-, ...	-, ...	-, ...	-, ...	-, ...	-, ...	-, ...
	Se	⊕, 1	⊕, 2	-, 1	-, 1	-, 1	⊕, 1	-, ...	-, 1	-, 1	-, 1	-, 1	⊕, 0	-, ...	-, ...	-, ...
Sn	S	⊕, 1	⊕, 1	-, 1	⊕, 1	-, 1	⊕, 1	-, ...	-, 1	-, 1	-, 1	⊕, 1	-, 1	-, 1	-, ...	-, ...

"⊕, n "—isothermal section of the respective system has been constructed, n quaternary compounds have been found in the respective system.

"-, n "—isothermal section of the respective system has been not constructed, n quaternary compounds have been found in the respective system.

"-, ..."—isothermal section of the respective system has been not constructed, no quaternary compounds have been found in the respective system.

TABLE 11 Crystallographic Data for Quaternary Chalcogenides of the R_2X_3 —PbX— ZX_2 (X = S, Se; Z = Si, Ge, Sn) Systems

Compound	Structure Type	Space Group	Lattice Parameters (nm)			Reference(s)
			a	b	c	
Y ₂ PbSi ₂ S ₈	La ₂ PbSi ₂ S ₈	$R\bar{3}C$	0.88433	—	2.59745	Daszkiewicz et al. (2012)
La ₂ PbSi ₂ S ₈	La ₂ PbSi ₂ S ₈	$R\bar{3}C$	0.90522	—	2.6964	Gulay et al. (2010)
Ce ₂ PbSi ₂ S ₈	La ₂ PbSi ₂ S ₈	$R\bar{3}C$	0.90030	—	2.6765	Daszkiewicz et al. (2012)
Pr ₂ PbSi ₂ S ₈	La ₂ PbSi ₂ S ₈	$R\bar{3}C$	0.89744	—	2.6640	Daszkiewicz et al. (2012)
Nd ₂ PbSi ₂ S ₈	La ₂ PbSi ₂ S ₈	$R\bar{3}C$	0.8942	—	2.6492	Daszkiewicz et al. (2012)
Sm ₂ PbSi ₂ S ₈	La ₂ PbSi ₂ S ₈	$R\bar{3}C$	0.88854	—	2.6283	Daszkiewicz et al. (2012)
Gd ₂ PbSi ₂ S ₈	La ₂ PbSi ₂ S ₈	$R\bar{3}C$	0.88633	—	2.6185	Daszkiewicz et al. (2012)
Tb ₂ PbSi ₂ S ₈	La ₂ PbSi ₂ S ₈	$R\bar{3}C$	0.88604	—	2.61184	Daszkiewicz et al. (2012)
Dy ₂ PbSi ₂ S ₈	La ₂ PbSi ₂ S ₈	$R\bar{3}C$	0.88422	—	2.60033	Daszkiewicz et al. (2012)
Ho ₂ PbSi ₂ S ₈	La ₂ PbSi ₂ S ₈	$R\bar{3}C$	0.88428	—	2.5963	Daszkiewicz et al. (2012)
Er ₂ PbSi ₂ S ₈	La ₂ PbSi ₂ S ₈	$R\bar{3}C$	0.8830	—	2.584	Kozlynets et al. (2014)
La ₂ PbSi ₂ Se ₈	La ₂ PbSi ₂ S ₈	$R\bar{3}C$	0.93984	—	2.8089	Daszkiewicz et al. (2012)
Ce ₂ PbSi ₂ Se ₈	La ₂ PbSi ₂ S ₈	$R\bar{3}C$	0.9351	—	2.7908	Daszkiewicz et al. (2012)
Pr ₂ PbSi ₂ Se ₈	La ₂ PbSi ₂ S ₈	$R\bar{3}C$	0.93264	—	2.7779	Daszkiewicz et al. (2012)

Continued

TABLE 11 Crystallographic Data for Quaternary Chalcogenides of the R_2X_3 —PbX— ZX_2 (X = S, Se; Z = Si, Ge, Sn) Systems—
Cont'd

Compound	Structure Type	Space Group	Lattice Parameters (nm)			Reference(s)
			a	b	c	
Nd ₂ PbSi ₂ Se ₈	La ₂ PbSi ₂ S ₈	$R\bar{3}c$	0.92998	—	2.7670	Daszkiewicz et al. (2012)
Sm ₂ PbSi ₂ Se ₈	La ₂ PbSi ₂ S ₈	$R\bar{3}c$	0.92620	—	2.7487	Daszkiewicz et al. (2012)
Gd ₂ PbSi ₂ Se ₈	La ₂ PbSi ₂ S ₈	$R\bar{3}c$	0.92320	—	2.7329	Daszkiewicz et al. (2012)
La ₂ PbGe ₂ S ₈	La ₂ PbSi ₂ S ₈	$R\bar{3}c$	0.90613	—	2.7187	Marchuk et al. (2010)
Ce ₂ PbGe ₂ S ₈	La ₂ PbSi ₂ S ₈	$R\bar{3}c$	0.90176	—	2.6980	Daszkiewicz et al. (2012)
Pr ₂ PbGe ₂ S ₈	La ₂ PbSi ₂ S ₈	$R\bar{3}c$	0.89840	—	2.68670	Daszkiewicz et al. (2012)
Y _{1.32} Pb _{1.68} Ge _{1.67} Se ₇	Y _{1.32} Pb _{1.68} Ge _{1.67} Se ₇	$P6_3$	1.0394	—	0.66361	Ruda et al. (2007)
La ₂ PbGe ₂ Se ₈	La ₂ PbSi ₂ S ₈	$R\bar{3}c$	0.93994	—	2.8098	Marchuk et al. (2010)
La _{1.32} Pb _{1.68} Ge _{1.67} Se ₇	Y _{1.32} Pb _{1.68} Ge _{1.67} Se ₇	$P6_3$	1.0590	—	0.6612	Ruda et al. (2007)
Ce _{1.32} Pb _{1.68} Ge _{1.67} Se ₇	Y _{1.32} Pb _{1.68} Ge _{1.67} Se ₇	$P6_3$	1.0542	—	0.6604	Ruda et al. (2007)
Pr _{1.32} Pb _{1.68} Ge _{1.67} Se ₇	Y _{1.32} Pb _{1.68} Ge _{1.67} Se ₇	$P6_3$	1.0520	—	0.6623	Ruda et al. (2007)
Nd _{1.32} Pb _{1.68} Ge _{1.67} Se ₇	Y _{1.32} Pb _{1.68} Ge _{1.67} Se ₇	$P6_3$	1.0499	—	0.6640	Ruda et al. (2007)
Sm _{1.32} Pb _{1.68} Ge _{1.67} Se ₇	Y _{1.32} Pb _{1.68} Ge _{1.67} Se ₇	$P6_3$	1.0442	—	0.6627	Ruda et al. (2007)
Gd _{1.32} Pb _{1.68} Ge _{1.67} Se ₇	Y _{1.32} Pb _{1.68} Ge _{1.67} Se ₇	$P6_3$	1.0428	—	0.6638	Ruda et al. (2007)

$Tb_{1.32}Pb_{1.68}Ge_{1.67}Se_7$	$Y_{1.32}Pb_{1.68}Ge_{1.67}Se_7$	$P6_3$	1.0406	–	0.66384	Ruda et al. (2007)
$Dy_{1.32}Pb_{1.68}Ge_{1.67}Se_7$	$Y_{1.32}Pb_{1.68}Ge_{1.67}Se_7$	$P6_3$	1.0389	–	0.6647	Ruda et al. (2007)
$Ho_{1.32}Pb_{1.68}Ge_{1.67}Se_7$	$Y_{1.32}Pb_{1.68}Ge_{1.67}Se_7$	$P6_3$	1.0381	–	0.6646	Ruda et al. (2007)
$Y_2Pb_3Sn_3S_{12}$	$Y_2Pb_3Sn_3S_{12}$	$Pmc2_1$	0.39021	2.01003	1.15169	Marchuk et al. (2007)
$La_2Pb_3Sn_3S_{12}$	$Y_2Pb_3Sn_3S_{12}$	$Pmc2_1$	0.39697	2.0329	1.1606	Gulay et al. (2008)
$Ce_2Pb_3Sn_3S_{12}$	$Y_2Pb_3Sn_3S_{12}$	$Pmc2_1$	0.39575	2.0275	1.1590	Gulay et al. (2008)
$Pr_2Pb_3Sn_3S_{12}$	$Y_2Pb_3Sn_3S_{12}$	$Pmc2_1$	0.39448	2.0071	1.1702	Gulay et al. (2008)
$Nd_2Pb_3Sn_3S_{12}$	$Y_2Pb_3Sn_3S_{12}$	$Pmc2_1$	0.39361	2.0049	1.1680	Gulay et al. (2008)
$Sm_2Pb_3Sn_3S_{12}$	$Y_2Pb_3Sn_3S_{12}$	$Pmc2_1$	0.39230	2.0119	1.1611	Gulay et al. (2008)
$Gd_2Pb_3Sn_3S_{12}$	$Y_2Pb_3Sn_3S_{12}$	$Pmc2_1$	0.39153	2.0206	1.1556	Gulay et al. (2008)
$Tb_2Pb_3Sn_3S_{12}$	$Y_2Pb_3Sn_3S_{12}$	$Pmc2_1$	0.39076	2.0174	1.1532	Gulay et al. (2008)
$Dy_2Pb_3Sn_3S_{12}$	$Y_2Pb_3Sn_3S_{12}$	$Pmc2_1$	0.39000	2.0153	1.1524	Gulay et al. (2008)
$Ho_2Pb_3Sn_3S_{12}$	$Y_2Pb_3Sn_3S_{12}$	$Pmc2_1$	0.38992	2.01175	1.15140	Gulay et al. (2008)
$Er_2Pb_3Sn_3S_{12}$	$Y_2Pb_3Sn_3S_{12}$	$Pmc2_1$	0.39006	2.0029	1.1513	Gulay et al. (2008)
$Tm_2Pb_3Sn_3S_{12}$	$Y_2Pb_3Sn_3S_{12}$	$Pmc2_1$	0.38936	2.0056	1.1501	Gulay et al. (2008)

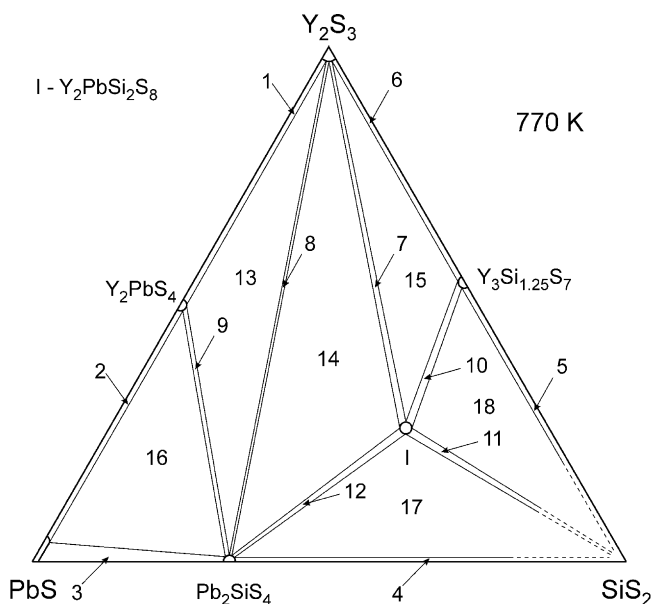


FIGURE 9 Isothermal section of the Y_2S_3 —PbS— SiS_2 system at 770 K. On the basis of Marchuk et al. (2008) with permission.

(space group $R\bar{3}c$) exists in each of the R_2S_3 —PbS— SiS_2 ($R = Y, La,$ and Er) systems.

The isothermal sections of the Y_2S_3 —PbS— SiS_2 (Marchuk et al., 2008), La_2S_3 —PbS— SiS_2 (Marchuk and Gulay, 2012), and Er_2S_3 —PbS— SiS_2 (Kozlynets et al., 2014) systems at 770 K are shown in Figs. 9–11, respectively. The phase fields in the Y_2S_3 —PbS— SiS_2 , La_2S_3 —PbS— SiS_2 , and Er_2S_3 —PbS— SiS_2 systems at 770 K are listed in Tables 12–14, respectively.

4.2 Phase Diagrams of the R_2Se_3 —PbSe— $SiSe_2$ Systems

Phase diagrams of the R_2Se_3 —PbSe— $SiSe_2$ ($R = Y$ and La) systems have been constructed. Quaternary compounds that form in these systems are listed in Table 11. No quaternary compounds exist in the Y_2Se_3 —PbSe— $SiSe_2$ system. Only one quaternary compound of the $La_2PbSi_2S_8$ structure type (space group $R\bar{3}c$) exists in the La_2Se_3 —PbSe— $SiSe_2$ system.

The isothermal sections of the Y_2Se_3 —PbSe— $SiSe_2$ (Marchuk et al., 2008) and La_2Se_3 —PbSe— $SiSe_2$ (Marchuk and Gulay, 2012) systems at 770 K are shown in Figs. 12 and 13, respectively. The phase fields in the Y_2Se_3 —PbSe— $SiSe_2$ and La_2Se_3 —PbSe— $SiSe_2$ systems at 770 K are listed in Tables 15 and 16, respectively.

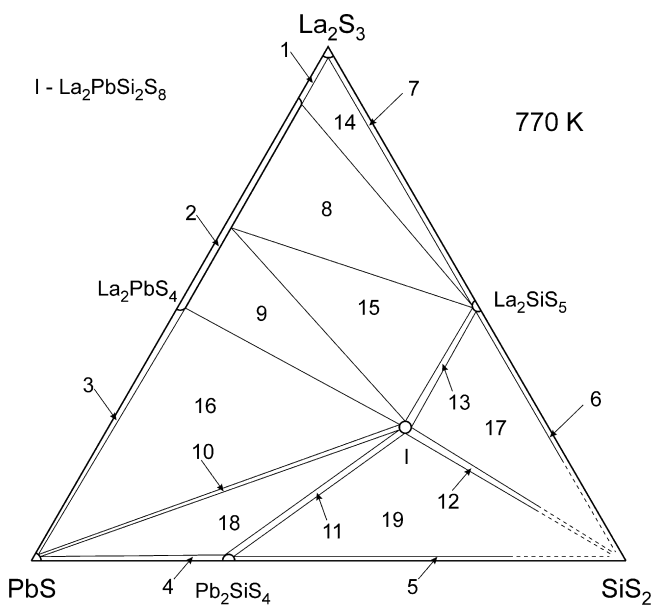


FIGURE 10 Isothermal section of the La_2S_3 — PbS — SiS_2 system at 770 K. On the basis of *Marchuk and Gulay (2012)* with permission.

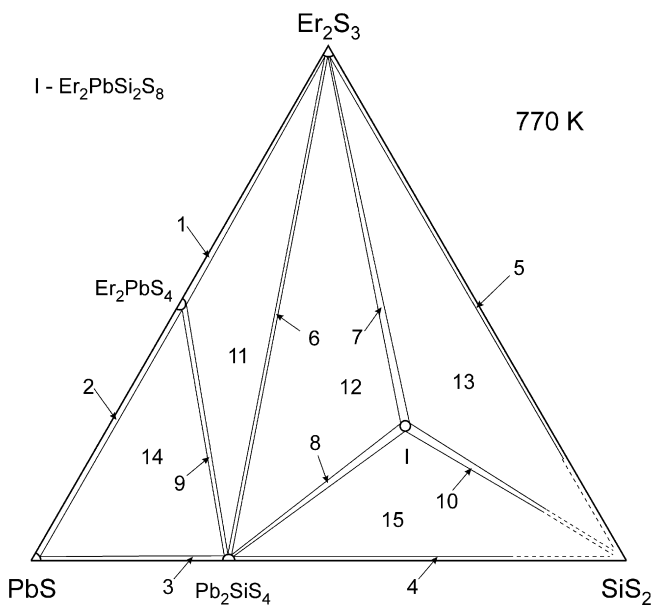


FIGURE 11 Isothermal section of the Er_2S_3 — PbS — SiS_2 system at 770 K.

TABLE 12 Phase Fields in the Y_2S_3 —PbS— SiS_2 System at 770 K

Phase Field	Phases
1	$Y_2S_3 + Y_2PbS_4$
2	$PbS + Y_2PbS_4$
3	$PbS + Pb_2SiS_4$
4	$SiS_2 + Pb_2SiS_4$
5	$SiS_2 + Y_3Si_{1.25}S_7$
6	$Y_2S_3 + Y_3Si_{1.25}S_7$
7	$Y_2S_3 + Y_2PbSi_2S_8$
8	$Y_2S_3 + Pb_2SiS_4$
9	$Y_2PbS_4 + Pb_2SiS_4$
10	$Y_3Si_{1.25}S_7 + Y_2PbSi_2S_8$
11	$SiS_2 + Y_2PbSi_2S_8$
12	$Pb_2SiS_4 + Y_2PbSi_2S_8$
13	$Y_2S_3 + Y_2PbS_4 + Pb_2SiS_4$
14	$Y_2S_3 + Pb_2SiS_4 + Y_2PbSi_2S_8$
15	$Y_2S_3 + Y_3Si_{1.25}S_7 + Y_2PbSi_2S_8$
16	$PbS + Y_2PbS_4 + Pb_2SiS_4$
17	$SiS_2 + Pb_2SiS_4 + Y_2PbSi_2S_8$
18	$SiS_2 + Y_3Si_{1.25}S_7 + Y_2PbSi_2S_8$

4.3 Phase Diagrams of the R_2S_3 —PbS— GeS_2 Systems

Phase diagrams of the R_2S_3 —PbS— GeS_2 ($R = Y, La, \text{ and } Pr$) systems have been constructed. Quaternary compounds that form in these systems are listed in Table 11. No quaternary compounds exist in the Y_2S_3 —PbS— GeS_2 system. Only one quaternary compound of the $La_2PbSi_2S_8$ structure type (space group $R\bar{3}c$) exists in each of the R_2S_3 —PbS— GeS_2 ($R = La \text{ and } Pr$) systems.

The isothermal sections of the Y_2S_3 —PbS— GeS_2 (Ruda et al., 2008), La_2S_3 —PbS— GeS_2 (Marchuk et al., 2010), and Pr_2S_3 —PbS— GeS_2 (Marchuk et al., 2012) systems at 770 K are shown in Figs. 14–16, respectively. The phase fields in the Y_2S_3 —PbS— GeS_2 , La_2S_3 —PbS— GeS_2 , and Pr_2S_3 —PbS— GeS_2 systems at 770 K are listed in Tables 17–19, respectively.

TABLE 13 Phase Fields in the La_2S_3 —PbS— SiS_2 System at 770 K

Phase Field	Phases
1	$La_2S_3 + La_{2+2/3x}Pb_{1-x}S_4$ ($x=0.86$)
2	$La_{2+2/3x}Pb_{1-x}S_4$ ($x=0-0.86$)
3	$PbS + La_2PbS_4$
4	$PbS + Pb_2SiS_4$
5	$SiS_2 + Pb_2SiS_4$
6	$SiS_2 + La_2SiS_5$
7	$La_2S_3 + La_2SiS_5$
8	$La_2SiS_5 + La_{2+2/3x}Pb_{1-x}S_4$ ($x=0.39-0.86$)
9	$La_{2+2/3x}Pb_{1-x}S_4$ ($x=0-0.39$) + $La_2PbSi_2S_8$
10	$PbS + La_2PbSi_2S_8$
11	$Pb_2SiS_4 + La_2PbSi_2S_8$
12	$SiS_2 + La_2PbSi_2S_8$
13	$La_2SiS_5 + La_2PbSi_2S_8$
14	$La_2S_3 + La_2SiS_5 + La_{2+2/3x}Pb_{1-x}S_4$ ($x=0.86$)
15	$La_2SiS_5 + La_2PbSi_2S_8 + La_{2+2/3x}Pb_{1-x}S_4$ ($x=0.39$)
16	$PbS + La_2PbS_4 + La_2PbSi_2S_8$
17	$SiS_2 + La_2SiS_5 + La_2PbSi_2S_8$
18	$PbS + Pb_2SiS_4 + La_2PbSi_2S_8$
19	$SiS_2 + Pb_2SiS_4 + La_2PbSi_2S_8$

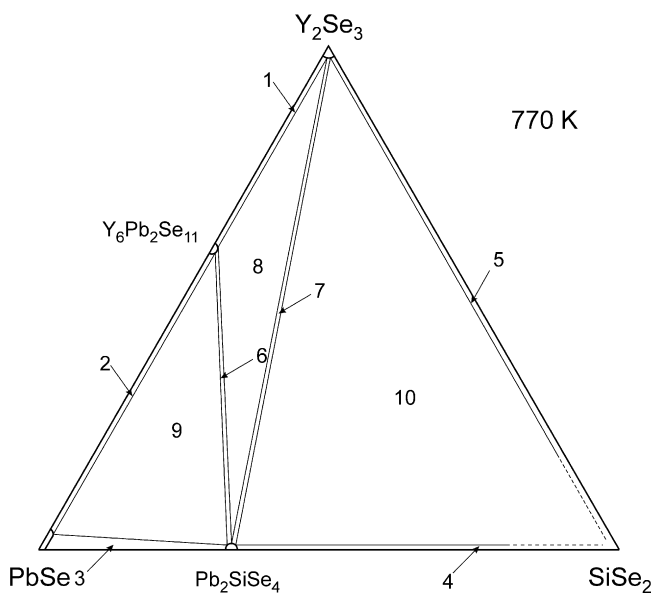
4.4 Phase Diagrams of the R_2Se_3 —PbSe— $GeSe_2$ Systems

Phase diagrams of the R_2Se_3 —PbSe— $GeSe_2$ (R = Y, La, Sm, and Er) systems have been constructed. Quaternary compounds that form in these systems are listed in Table 11. No quaternary compounds exist in the Er_2Se_3 —PbSe— $GeSe_2$ system. Only one quaternary compound of the $Y_{1.32}Pb_{1.68}Ge_{1.67}Se_7$ structure type (space group $P6_3$) exists in each of the R_2Se_3 —PbSe— $GeSe_2$ (R = Y and Sm) systems. Two quaternary compounds of the structure types $La_2PbSi_2S_8$ (space group $R\bar{3}c$) and $Y_{1.32}Pb_{1.68}Ge_{1.67}Se_7$ (space group $P6_3$) exist in the La_2Se_3 —PbSe— $GeSe_2$ system.

The isothermal sections of the Y_2Se_3 —PbSe— $GeSe_2$ (Ruda et al., 2008), La_2Se_3 —PbSe— $GeSe_2$ (Marchuk et al., 2010), Sm_2Se_3 —PbSe— $GeSe_2$

TABLE 14 Phase Fields in the Er_2S_3 — PbS — SiS_2 System at 770 K

Phase Field	Phases
1	$\text{Er}_2\text{S}_3 + \text{Er}_2\text{PbS}_4$
2	$\text{PbS} + \text{Er}_2\text{PbS}_4$
3	$\text{PbS} + \text{Pb}_2\text{SiS}_4$
4	$\text{SiS}_2 + \text{Pb}_2\text{SiS}_4$
5	$\text{SiS}_2 + \text{Er}_2\text{S}_3$
6	$\text{Er}_2\text{S}_3 + \text{Pb}_2\text{SiS}_4$
7	$\text{Er}_2\text{S}_3 + \text{Er}_2\text{PbSi}_2\text{S}_8$
8	$\text{Pb}_2\text{SiS}_4 + \text{Er}_2\text{PbSi}_2\text{S}_8$
9	$\text{Er}_2\text{PbS}_4 + \text{Pb}_2\text{SiS}_4$
10	$\text{SiS}_2 + \text{Er}_2\text{PbSi}_2\text{S}_8$
11	$\text{Er}_2\text{S}_3 + \text{Er}_2\text{PbS}_4 + \text{Pb}_2\text{SiS}_4$
12	$\text{Er}_2\text{S}_3 + \text{Pb}_2\text{SiS}_4 + \text{Er}_2\text{PbSi}_2\text{S}_8$
13	$\text{SiS}_2 + \text{Er}_2\text{S}_3 + \text{Er}_2\text{PbSi}_2\text{S}_8$
14	$\text{PbS} + \text{Pb}_2\text{SiS}_4 + \text{Er}_2\text{PbS}_4$
15	$\text{SiS}_2 + \text{Pb}_2\text{SiS}_4 + \text{Er}_2\text{PbSi}_2\text{S}_8$

**FIGURE 12** Isothermal section of the Y_2Se_3 — PbSe — SiSe_2 system at 770 K. On the basis of Marchuk *et al.* (2008) with permission.

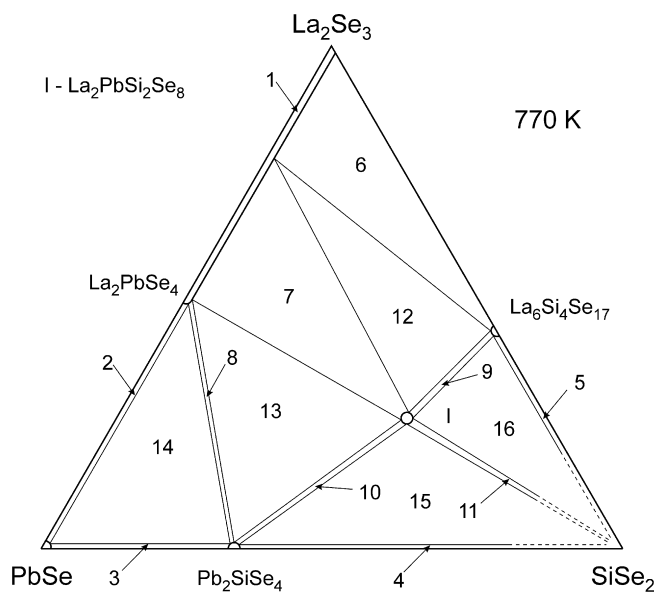


FIGURE 13 Isothermal section of the La_2Se_3 — $PbSe$ — $SiSe_2$ system at 770 K. On the basis of *Marchuk and Gulay (2012)* with permission.

TABLE 15 Phase Fields in the Y_2Se_3 — $PbSe$ — $SiSe_2$ System at 770 K

Phase Field	Phases
1	$Y_2Se_3 + Y_6Pb_2Se_{11}$
2	$PbSe + Y_6Pb_2Se_{11}$
3	$PbSe + Pb_2SiSe_4$
4	$SiSe_2 + Pb_2SiSe_4$
5	$Y_2Se_3 + SiSe_2$
6	$Y_6Pb_2Se_{11} + Pb_2SiSe_4$
7	$Y_2Se_3 + Pb_2SiSe_4$
8	$Y_2Se_3 + Y_6Pb_2Se_{11} + Pb_2SiSe_4$
9	$PbSe + Y_6Pb_2Se_{11} + Pb_2SiSe_4$
10	$Y_2Se_3 + SiSe_2 + Pb_2SiSe_4$

TABLE 16 Phase Fields in the $\text{La}_2\text{Se}_3\text{—PbSe—SiSe}_2$ System at 770 K

Phase Field	Phases
1	$\text{La}_{2+2/3x}\text{Pb}_{1-x}\text{Se}_4$ ($x=0\text{--}1$)
2	$\text{PbSe} + \text{La}_2\text{PbSe}_4$
3	$\text{PbSe} + \text{Pb}_2\text{SiSe}_4$
4	$\text{SiSe}_2 + \text{Pb}_2\text{SiSe}_4$
5	$\text{SiSe}_2 + \text{La}_6\text{Si}_4\text{Se}_{17}$
6	$\text{La}_6\text{Si}_4\text{Se}_7 + \text{La}_{2+2/3x}\text{Pb}_{1-x}\text{Se}_4$ ($x=0.66\text{--}1$)
7	$\text{La}_{2+2/3x}\text{Pb}_{1-x}\text{Se}_4$ ($x=0\text{--}0.66$) + $\text{La}_2\text{PbSi}_2\text{Se}_8$
8	$\text{La}_2\text{PbSe}_4 + \text{Pb}_2\text{SiSe}_4$
9	$\text{La}_6\text{Si}_4\text{Se}_{17} + \text{La}_2\text{PbSi}_2\text{Se}_8$
10	$\text{Pb}_2\text{SiSe}_4 + \text{La}_2\text{PbSi}_2\text{Se}_8$
11	$\text{SiSe}_2 + \text{La}_2\text{PbSi}_2\text{Se}_8$
12	$\text{La}_{2+2/3x}\text{Pb}_{1-x}\text{Se}_4$ ($x=0.66$) + $\text{La}_6\text{Si}_4\text{Se}_{17} + \text{La}_2\text{PbSi}_2\text{Se}_8$
13	$\text{La}_2\text{PbSe}_4 + \text{Pb}_2\text{SiSe}_4 + \text{La}_2\text{PbSi}_2\text{Se}_8$
14	$\text{PbSe} + \text{La}_2\text{PbSe}_4 + \text{Pb}_2\text{SiSe}_4$
15	$\text{SiSe}_2 + \text{Pb}_2\text{SiSe}_4 + \text{La}_2\text{PbSi}_2\text{Se}_8$
16	$\text{SiSe}_2 + \text{La}_6\text{Si}_4\text{Se}_{17} + \text{La}_2\text{PbSi}_2\text{Se}_8$

(Olekseyuk et al., 2009), and $\text{Er}_2\text{Se}_3\text{—PbSe—GeSe}_2$ (Olekseyuk et al., 2009) systems at 770 K are shown in Figs. 17–20, respectively. The phase fields in the $\text{Y}_2\text{Se}_3\text{—PbSe—GeSe}_2$, $\text{La}_2\text{Se}_3\text{—PbSe—GeSe}_2$, $\text{Sm}_2\text{Se}_3\text{—PbSe—GeSe}_2$, and $\text{Er}_2\text{Se}_3\text{—PbSe—GeSe}_2$ systems at 770 K are listed in Tables 20–23, respectively.

4.5 Phase Diagrams of the $\text{R}_2\text{S}_3\text{—PbS—SnS}_2$ Systems

Phase diagrams of the $\text{R}_2\text{S}_3\text{—PbS—SnS}_2$ ($\text{R} = \text{Y, La, Pr, Sm, and Ho}$) systems have been constructed. Quaternary compounds that form in these systems are listed in Table 11. Only one quaternary compound of the $\text{Y}_2\text{Pb}_3\text{Sn}_3\text{S}_{12}$ structure type (space group $Pmc2_1$) exists in each of the $\text{R}_2\text{S}_3\text{—PbS—SnS}_2$ ($\text{R} = \text{Y, La, Pr, Sm, and Ho}$) systems.

The isothermal sections of the $\text{Y}_2\text{S}_3\text{—PbS—SnS}_2$ (Marchuk et al., 2007), $\text{La}_2\text{S}_3\text{—PbS—SnS}_2$ (Marchuk et al., 2010), $\text{Pr}_2\text{S}_3\text{—PbS—SnS}_2$ (Marchuk

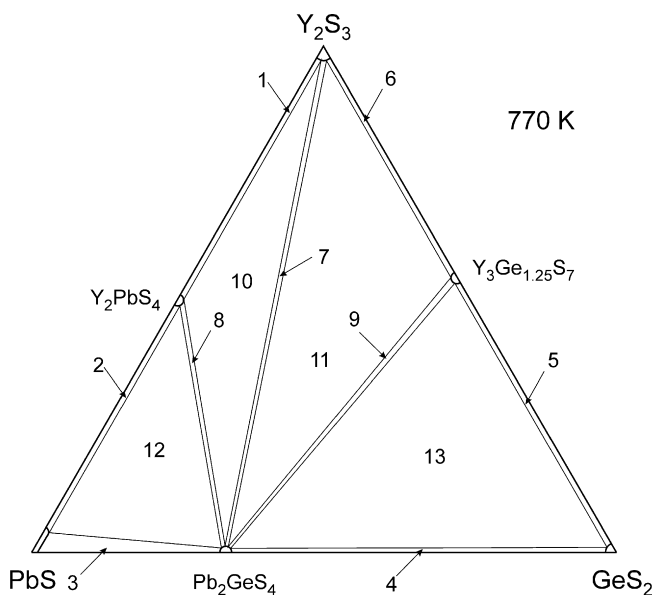


FIGURE 14 Isothermal section of the Y_2S_3 — PbS — GeS_2 system at 770 K.

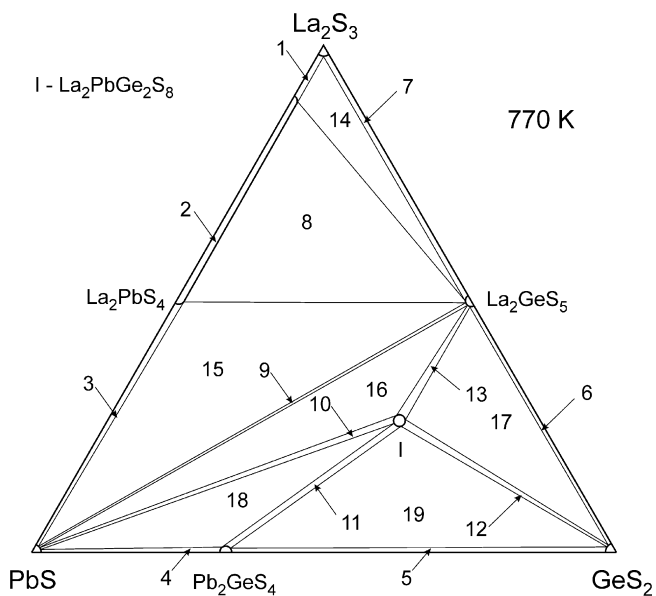


FIGURE 15 Isothermal section of the La_2S_3 — PbS — GeS_2 system at 770 K.

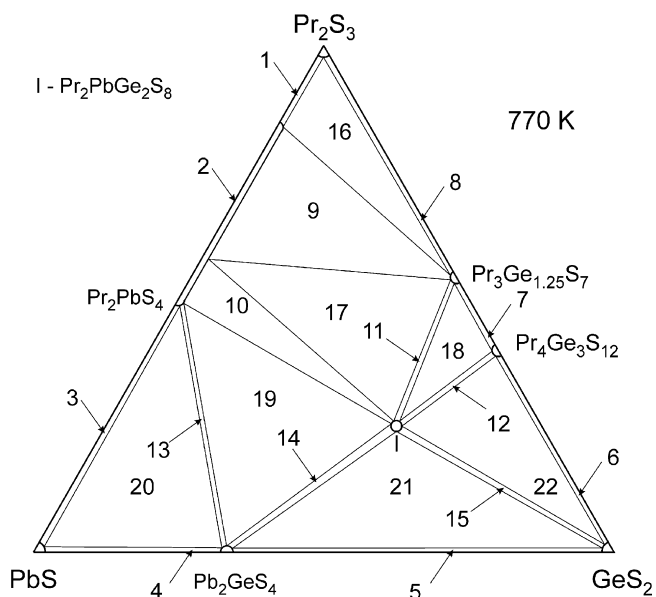


FIGURE 16 Isothermal section of the Pr_2S_3 — PbS — GeS_2 system at 770 K.

TABLE 17 Phase Fields in the Y_2S_3 — PbS — GeS_2 System at 770 K

Phase Field	Phases
1	$\text{Y}_2\text{S}_3 + \text{Y}_2\text{PbS}_4$
2	$\text{PbS} + \text{Y}_2\text{PbS}_4$
3	$\text{PbS} + \text{Pb}_2\text{GeS}_4$
4	$\text{GeS}_2 + \text{Pb}_2\text{GeS}_4$
5	$\text{GeS}_2 + \text{Y}_3\text{Ge}_{1.25}\text{S}_7$
6	$\text{Y}_2\text{S}_3 + \text{Y}_3\text{Ge}_{1.25}\text{S}_7$
7	$\text{Y}_2\text{S}_3 + \text{Pb}_2\text{GeS}_4$
8	$\text{Y}_2\text{PbS}_4 + \text{Pb}_2\text{GeS}_4$
9	$\text{Y}_3\text{Ge}_{1.25}\text{S}_7 + \text{Pb}_2\text{GeS}_4$
10	$\text{Y}_2\text{S}_3 + \text{Y}_2\text{PbS}_4 + \text{Pb}_2\text{GeS}_4$
11	$\text{Y}_2\text{S}_3 + \text{Y}_3\text{Ge}_{1.25}\text{S}_7 + \text{Pb}_2\text{GeS}_4$
12	$\text{PbS} + \text{Y}_2\text{PbS}_4 + \text{Pb}_2\text{GeS}_4$
13	$\text{GeS}_2 + \text{Y}_3\text{Ge}_{1.25}\text{S}_7 + \text{Pb}_2\text{GeS}_4$

TABLE 18 Phase Fields in the La_2S_3 —PbS— GeS_2 System at 770 K

Phase Field	Phases
1	$La_2S_3 + La_{2+2/3x}Pb_{1-x}S_4$ ($x=0.86$)
2	$La_{2+2/3x}Pb_{1-x}S_4$ ($x=0-0.86$)
3	PbS + La_2PbS_4
4	PbS + Pb_2GeS_4
5	$GeS_2 + Pb_2GeS_4$
6	$GeS_2 + La_2GeS_5$
7	$La_2S_3 + La_2GeS_5$
8	$La_{2+2/3x}Pb_{1-x}S_4$ ($x=0-0.86$) + La_2GeS_5
9	PbS + La_2GeS_5
10	PbS + $La_2PbGe_2S_8$
11	$Pb_2GeS_4 + La_2PbGe_2S_8$
12	$GeS_2 + La_2PbGe_2S_8$
13	$La_2GeS_5 + La_2PbGe_2S_8$
14	$La_2S_3 + La_{2+2/3x}Pb_{1-x}S_4$ ($x=0.86$) + La_2GeS_5
15	PbS + $La_2PbS_4 + La_2GeS_5$
16	PbS + $La_2GeS_5 + La_2PbGe_2S_8$
17	$GeS_2 + La_2GeS_5 + La_2PbGe_2S_8$
18	PbS + $Pb_2GeS_4 + La_2PbGe_2S_8$
19	$GeS_2 + Pb_2GeS_4 + La_2PbGe_2S_8$

et al., 2014), Sm_2S_3 —PbS— SnS_2 (Gulay and Marchuk, 2010), and Ho_2S_3 —PbS— SnS_2 (Gulay and Marchuk, 2010) systems at 770 K are shown in Figs. 21–25, respectively. The phase fields in the Y_2S_3 —PbS— SnS_2 , La_2S_3 —PbS— SnS_2 , Pr_2S_3 —PbS— SnS_2 , Sm_2S_3 —PbS— SnS_2 , and Ho_2S_3 —PbS— SnS_2 systems at 770 K are listed in Tables 24–28, respectively.

4.6 Structure Types of Quaternary Compounds

All quaternary compounds of the R_2X_3 —PbX— ZX_2 (X = S, Se; Z = Si, Ge, Sn) systems which crystallize in three structure types are summarized in Table 11.

TABLE 19 Phase Fields in the Pr_2S_3 — PbS — GeS_2 System at 770 K

Phase Field	Phases
1	$\text{Pr}_2\text{S}_3 + \text{Pr}_{2+2/3x}\text{Pb}_{1-x}\text{S}_4$ ($x=0.78$)
2	$\text{Pr}_{2+2/3x}\text{Pb}_{1-x}\text{S}_4$ ($x=0-0.78$)
3	$\text{PbS} + \text{Pr}_2\text{PbS}_4$
4	$\text{PbS} + \text{Pb}_2\text{GeS}_4$
5	$\text{GeS}_2 + \text{Pb}_2\text{GeS}_4$
6	$\text{GeS}_2 + \text{Pr}_4\text{Ge}_3\text{S}_{12}$
7	$\text{Pr}_3\text{Ge}_{1.25}\text{S}_7 + \text{Pr}_4\text{Ge}_3\text{S}_{12}$
8	$\text{Pr}_2\text{S}_3 + \text{Pr}_3\text{Ge}_{1.25}\text{S}_7$
9	$\text{Pr}_3\text{Ge}_{1.25}\text{S}_7 + \text{Pr}_{2+2/3x}\text{Pb}_{1-x}\text{S}_4$ ($x=0.22-0.78$)
10	$\text{Pr}_{2+2/3x}\text{Pb}_{1-x}\text{S}_4$ ($x=0-0.22$) + $\text{Pr}_2\text{PbGe}_2\text{S}_8$
11	$\text{Pr}_3\text{Ge}_{1.25}\text{S}_7 + \text{Pr}_2\text{PbGe}_2\text{S}_8$
12	$\text{Pr}_4\text{Ge}_3\text{S}_{12} + \text{Pr}_2\text{PbGe}_2\text{S}_8$
13	$\text{Pr}_2\text{PbS}_4 + \text{Pb}_2\text{GeS}_4$
14	$\text{Pb}_2\text{GeS}_4 + \text{Pr}_2\text{PbGe}_2\text{S}_8$
15	$\text{GeS}_2 + \text{Pr}_2\text{PbGe}_2\text{S}_8$
16	$\text{Pr}_2\text{S}_3 + \text{Pr}_{2+2/3x}\text{Pb}_{1-x}\text{S}_4$ ($x=0.78$) + $\text{Pr}_3\text{Ge}_{1.25}\text{S}_7$
17	$\text{Pr}_{2+2/3x}\text{Pb}_{1-x}\text{S}_4$ ($x=0.22$) + $\text{Pr}_3\text{Ge}_{1.25}\text{S}_7 + \text{Pr}_2\text{PbGe}_2\text{S}_8$
18	$\text{Pr}_3\text{Ge}_{1.25}\text{S}_7 + \text{Pr}_4\text{Ge}_3\text{S}_{12} + \text{Pr}_2\text{PbGe}_2\text{S}_8$
19	$\text{Pr}_2\text{PbS}_4 + \text{Pb}_2\text{GeS}_4 + \text{Pr}_2\text{PbGe}_2\text{S}_8$
20	$\text{PbS} + \text{Pb}_2\text{GeS}_4 + \text{Pr}_2\text{PbS}_4$
21	$\text{GeS}_2 + \text{Pb}_2\text{GeS}_4 + \text{Pr}_2\text{PbGe}_2\text{S}_8$
22	$\text{GeS}_2 + \text{Pr}_4\text{Ge}_3\text{S}_{12} + \text{Pr}_2\text{PbGe}_2\text{S}_8$

4.6.1 Structure Type $\text{La}_2\text{PbSi}_2\text{S}_8$

Structure type $\text{La}_2\text{PbSi}_2\text{S}_8$ (Gulay et al., 2010) (Fig. 26, Table 29). SG $R\bar{3}c$, $Z=9$, $a=0.90522$, and $c=2.6964$ nm. One site is disordered and occupied by the La and Pb atoms (M). The sulfur atoms create bicapped trigonal prismatic arrangement around the M atoms. The shortest M—S distance is 0.28800 nm. The sulfur atoms create a tetrahedral coordination sphere around the Si atoms. The shortest Si—S distance is 0.21203 nm. The S1 atom is

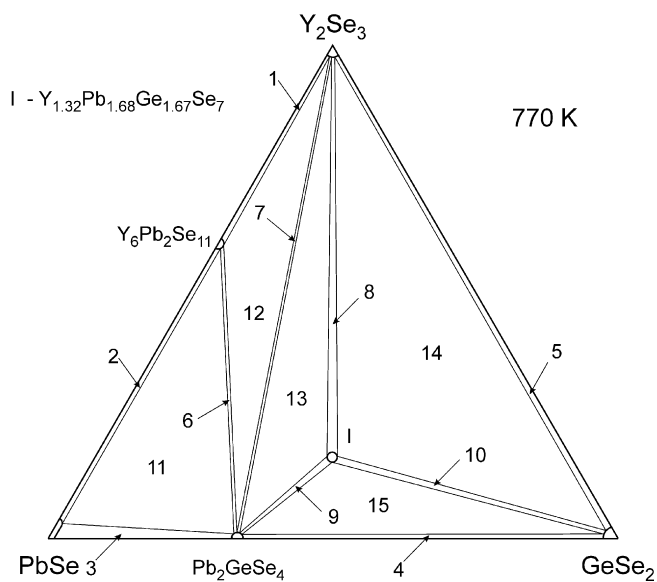


FIGURE 17 Isothermal section of the Y_2Se_3 — $PbSe$ — $GeSe_2$ system at 770 K.

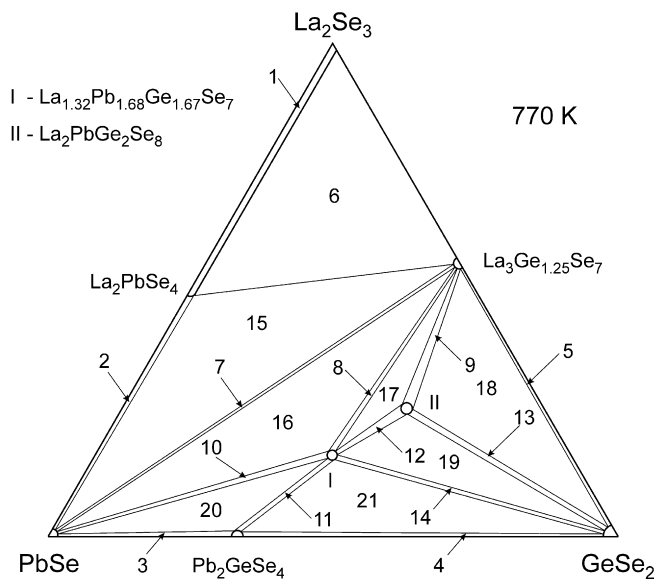


FIGURE 18 Isothermal section of the La_2Se_3 — $PbSe$ — $GeSe_2$ system at 770 K.

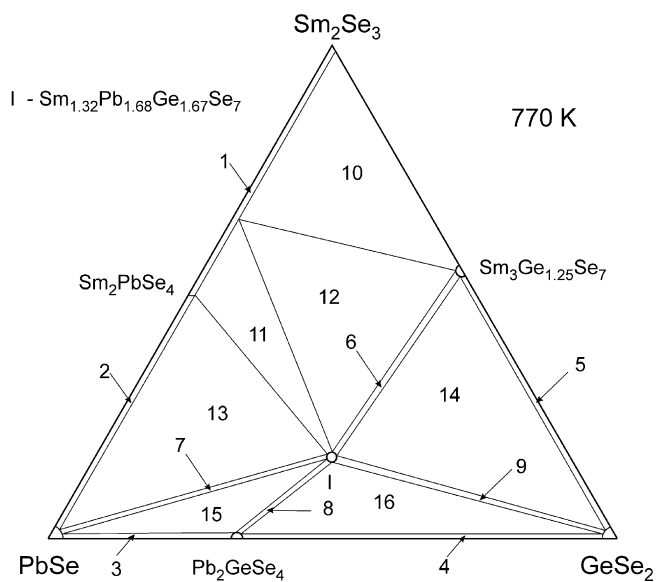


FIGURE 19 Isothermal section of the Sm_2Se_3 — PbSe — GeSe_2 system at 770 K. On the basis of Olekseyuk et al. (2009) with permission.

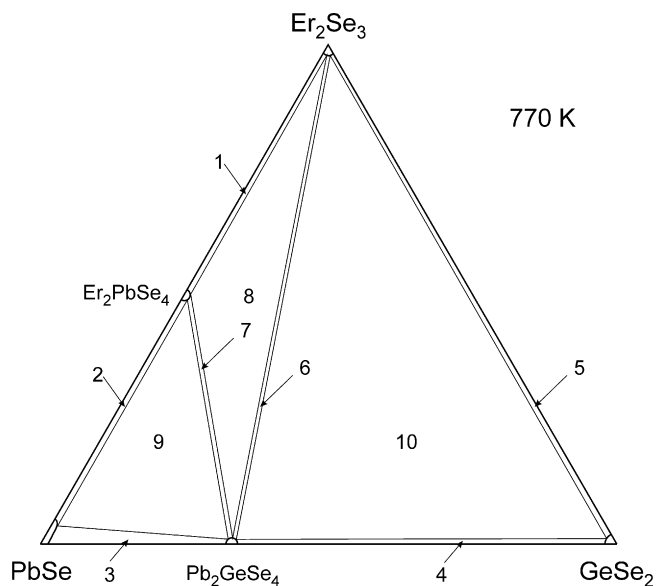


FIGURE 20 Isothermal section of the Er_2Se_3 — PbSe — GeSe_2 system at 770 K. On the basis of Olekseyuk et al. (2009) with permission.

TABLE 20 Phase Fields in the Y_2Se_3 — $PbSe$ — $GeSe_2$ System at 770 K

Phase Field	Phases
1	$Y_2Se_3 + Y_6Pb_2Se_{11}$
2	$PbSe + Y_6Pb_2Se_{11}$
3	$PbSe + Pb_2GeSe_4$
4	$GeSe_2 + Pb_2GeSe_4$
5	$Y_2Se_3 + GeSe_2$
6	$Y_6Pb_2Se_{11} + Pb_2GeSe_4$
7	$Y_2Se_3 + Pb_2GeSe_4$
8	$Y_2Se_3 + Y_{1.32}Pb_{1.68}Ge_{1.67}Se_7$
9	$Pb_2GeSe_4 + Y_{1.32}Pb_{1.68}Ge_{1.67}Se_7$
10	$GeSe_2 + Y_{1.32}Pb_{1.68}Ge_{1.67}Se_7$
11	$PbSe + Y_6Pb_2Se_{11} + Pb_2GeSe_4$
12	$Y_2Se_3 + Y_6Pb_2Se_{11} + Pb_2GeSe_4$
13	$Y_2Se_3 + Pb_2GeSe_4 + Y_{1.32}Pb_{1.68}Ge_{1.67}Se_7$
14	$Y_2Se_3 + GeSe_2 + Y_{1.32}Pb_{1.68}Ge_{1.67}Se_7$
15	$GeSe_2 + Pb_2GeSe_4 + Y_{1.32}Pb_{1.68}Ge_{1.67}Se_7$

located outside a tetrahedron formed by 3M and 1Si atoms. The S2 atom has a tetrahedral arrangement, coordinated by 3M and 1Si atoms. Twenty one quaternary compounds of the $La_2PbSi_2S_8$ type of structure exist in the R_2X_3 — PbX — ZX_2 ($X=S, Se; Z=Si, Ge$) systems (Table 11).

4.6.2 Structure Type $Y_{1.32}Pb_{1.68}Ge_{1.67}Se_7$

Structure type $Y_{1.32}Pb_{1.68}Ge_{1.67}Se_7$ (Ruda et al., 2007) (Fig. 27, Table 30). SG $P6_3$, $Z=2$, $a=1.0394$, and $c=0.66361$ nm. One site is disordered and occupied by the mixture of the randomly distributed Y and Pb atoms (M). The selenium atoms create monocapped trigonal prismatic arrangement around the M atoms. The shortest M—Se distance is 0.296 nm. The selenium atoms create a tetrahedral coordination sphere around the Ge1 atoms. The shortest Ge—Se distance is 0.236 nm. The Ge2 atom is located at the sixfold screw axis and has triangular surrounding formed by the selenium atoms. The shortest Ge—Se distance is 0.230 nm. The Se1 atom is located outside a tetrahedron formed by 3M and 1Ge atoms. The Se2 and Se3 atoms have CN=4 and a tetrahedral arrangement of 3M and 1Ge atoms. Ten quaternary

TABLE 21 Phase Fields in the $\text{La}_2\text{Se}_3\text{—PbSe—GeSe}_2$ System at 770 K

Phase Field	Phases
1	$\text{La}_{2+2/3x}\text{Pb}_{1-x}\text{Se}_4$ ($x=0\text{--}1$)
2	$\text{PbSe} + \text{La}_2\text{PbSe}_4$
3	$\text{PbSe} + \text{Pb}_2\text{GeSe}_4$
4	$\text{GeSe}_2 + \text{Pb}_2\text{GeSe}_4$
5	$\text{GeSe}_2 + \text{La}_3\text{Ge}_{1.25}\text{Se}_7$
6	$\text{La}_{2+2/3x}\text{Pb}_{1-x}\text{Se}_4$ ($x=0\text{--}1$) + $\text{La}_3\text{Ge}_{1.25}\text{Se}_7$
7	$\text{PbSe} + \text{La}_3\text{Ge}_{1.25}\text{Se}_7$
8	$\text{La}_3\text{Ge}_{1.25}\text{Se}_7 + \text{La}_{1.32}\text{Pb}_{1.68}\text{Ge}_{1.67}\text{Se}_7$
9	$\text{La}_3\text{Ge}_{1.25}\text{Se}_7 + \text{La}_2\text{PbGe}_2\text{Se}_8$
10	$\text{PbSe} + \text{La}_{1.32}\text{Pb}_{1.68}\text{Ge}_{1.67}\text{Se}_7$
11	$\text{Pb}_2\text{GeSe}_4 + \text{La}_{1.32}\text{Pb}_{1.68}\text{Ge}_{1.67}\text{Se}_7$
12	$\text{La}_2\text{PbGe}_2\text{Se}_8 + \text{La}_{1.32}\text{Pb}_{1.68}\text{Ge}_{1.67}\text{Se}_7$
13	$\text{GeSe}_2 + \text{La}_2\text{PbGe}_2\text{Se}_8$
14	$\text{GeSe}_2 + \text{La}_{1.32}\text{Pb}_{1.68}\text{Ge}_{1.67}\text{Se}_7$
15	$\text{PbSe} + \text{La}_3\text{Ge}_{1.25}\text{Se}_7 + \text{La}_2\text{PbSe}_4$
16	$\text{PbSe} + \text{La}_3\text{Ge}_{1.25}\text{Se}_7 + \text{La}_{1.32}\text{Pb}_{1.68}\text{Ge}_{1.67}\text{Se}_7$
17	$\text{La}_3\text{Ge}_{1.25}\text{Se}_7 + \text{La}_2\text{PbGe}_2\text{Se}_8 + \text{La}_{1.32}\text{Pb}_{1.68}\text{Ge}_{1.67}\text{Se}_7$
18	$\text{GeSe}_2 + \text{La}_3\text{Ge}_{1.25}\text{Se}_7 + \text{La}_2\text{PbGe}_2\text{Se}_8$
19	$\text{GeSe}_2 + \text{La}_2\text{PbGe}_2\text{Se}_8 + \text{La}_{1.32}\text{Pb}_{1.68}\text{Ge}_{1.67}\text{Se}_7$
20	$\text{PbSe} + \text{Pb}_2\text{GeSe}_4 + \text{La}_{1.32}\text{Pb}_{1.68}\text{Ge}_{1.67}\text{Se}_7$
21	$\text{GeSe}_2 + \text{Pb}_2\text{GeSe}_4 + \text{La}_{1.32}\text{Pb}_{1.68}\text{Ge}_{1.67}\text{Se}_7$

compounds of the $\text{Y}_{1.32}\text{Pb}_{1.68}\text{Ge}_{1.67}\text{Se}_7$ type of structure exist in the $\text{R}_2\text{Se}_3\text{—PbSe—GeSe}_2$ systems (Table 11).

4.6.3 Structure Type $\text{Y}_2\text{Pb}_3\text{Sn}_3\text{S}_{12}$

Structure type $\text{Y}_2\text{Pb}_3\text{Sn}_3\text{S}_{12}$ (Marchuk et al., 2007) (Fig. 28, Table 31). SG $\text{Pmc}2_1$, $Z=9$, $a=0.39021$, $b=2.01003$, and $c=1.15169$ nm. Two independent yttrium atoms (Y1 and Y2) are situated in bicapped and monocapped trigonal prisms formed exclusively by the sulfur atoms. The shortest Y—S

TABLE 22 Phase Fields in the $\text{Sm}_2\text{Se}_3\text{—PbSe—GeSe}_2$ System at 770 K

Phase Field	Phases
1	$\text{Sm}_{2+2/3x}\text{Pb}_{1-x}\text{Se}_4$ ($x=0\text{--}1$)
2	$\text{Sm}_2\text{PbSe}_4 + \text{PbSe}$
3	$\text{PbSe} + \text{Pb}_2\text{GeSe}_4$
4	$\text{GeSe}_2 + \text{Pb}_2\text{GeSe}_4$
5	$\text{GeSe}_2 + \text{Sm}_3\text{Ge}_{1.25}\text{Se}_7$
6	$\text{Sm}_3\text{Ge}_{1.25}\text{Se}_7 + \text{Sm}_{1.32}\text{Pb}_{1.68}\text{Ge}_{1.67}\text{Se}_7$
7	$\text{PbSe} + \text{Sm}_{1.32}\text{Pb}_{1.68}\text{Ge}_{1.67}\text{Se}_7$
8	$\text{Pb}_2\text{GeSe}_4 + \text{Sm}_{1.32}\text{Pb}_{1.68}\text{Ge}_{1.67}\text{Se}_7$
9	$\text{GeSe}_2 + \text{Sm}_{1.32}\text{Pb}_{1.68}\text{Ge}_{1.67}\text{Se}_7$
10	$\text{Sm}_{2+2/3x}\text{Pb}_{1-x}\text{Se}_4$ ($x=0.39\text{--}1$) + $\text{Sm}_3\text{Ge}_{1.25}\text{Se}_7$
11	$\text{Sm}_{2+2/3x}\text{Pb}_{1-x}\text{Se}_4$ ($x=0\text{--}0.39$) + $\text{Sm}_{1.32}\text{Pb}_{1.68}\text{Ge}_{1.67}\text{Se}_7$
12	$\text{Sm}_{2+2/3x}\text{Pb}_{1-x}\text{Se}_4$ ($x=0.39$) + $\text{Sm}_3\text{Ge}_{1.25}\text{Se}_7 + \text{Sm}_{1.32}\text{Pb}_{1.67}\text{Ge}_{1.67}\text{Se}_7$
13	$\text{Sm}_2\text{PbSe}_4 + \text{PbSe} + \text{Sm}_{1.32}\text{Pb}_{1.68}\text{Ge}_{1.67}\text{Se}_7$
14	$\text{GeSe}_2 + \text{Sm}_3\text{Ge}_{1.25}\text{Se}_7 + \text{Sm}_{1.32}\text{Pb}_{1.68}\text{Ge}_{1.67}\text{Se}_7$
15	$\text{PbSe} + \text{Pb}_2\text{GeSe}_4 + \text{Sm}_{1.32}\text{Pb}_{1.68}\text{Ge}_{1.67}\text{Se}_7$
16	$\text{GeSe}_2 + \text{Pb}_2\text{GeSe}_4 + \text{Sm}_{1.32}\text{Pb}_{1.68}\text{Ge}_{1.67}\text{Se}_7$

TABLE 23 Phase Fields in the $\text{Er}_2\text{Se}_3\text{—PbSe—GeSe}_2$ System at 770 K

Phase Field	Phases
1	$\text{Er}_2\text{Se}_3 + \text{Er}_2\text{PbSe}_4$
2	$\text{Er}_2\text{PbSe}_4 + \text{PbSe}$
3	$\text{PbSe} + \text{Pb}_2\text{GeSe}_4$
4	$\text{Pb}_2\text{GeSe}_4 + \text{GeSe}_2$
5	$\text{Er}_2\text{Se}_3 + \text{GeSe}_2$
6	$\text{Er}_2\text{Se}_3 + \text{Pb}_2\text{GeSe}_4$
7	$\text{Pb}_2\text{GeSe}_4 + \text{Er}_2\text{PbSe}_4$
8	$\text{Er}_2\text{Se}_3 + \text{Er}_2\text{PbSe}_4 + \text{Pb}_2\text{GeSe}_4$
9	$\text{PbSe} + \text{Er}_2\text{PbSe}_4 + \text{Pb}_2\text{GeSe}_4$
10	$\text{Er}_2\text{Se}_3 + \text{Pb}_2\text{GeSe}_4 + \text{GeSe}_2$

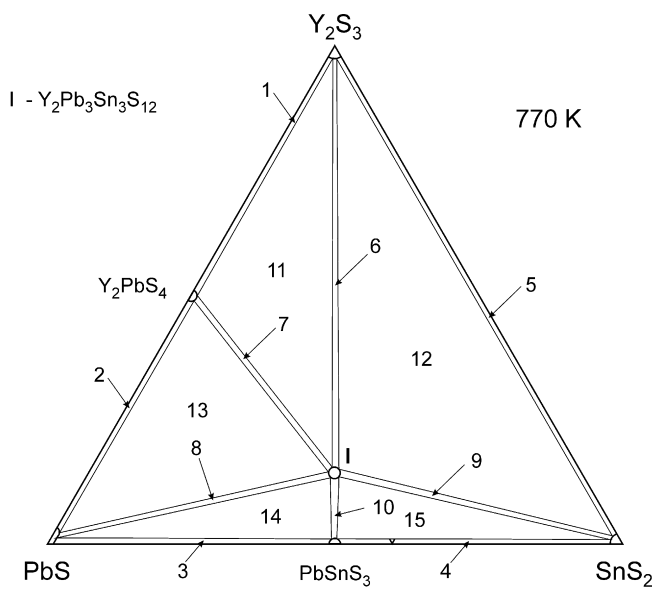


FIGURE 21 Isothermal section of the Y_2S_3 —PbS— SnS_2 system at 770 K.

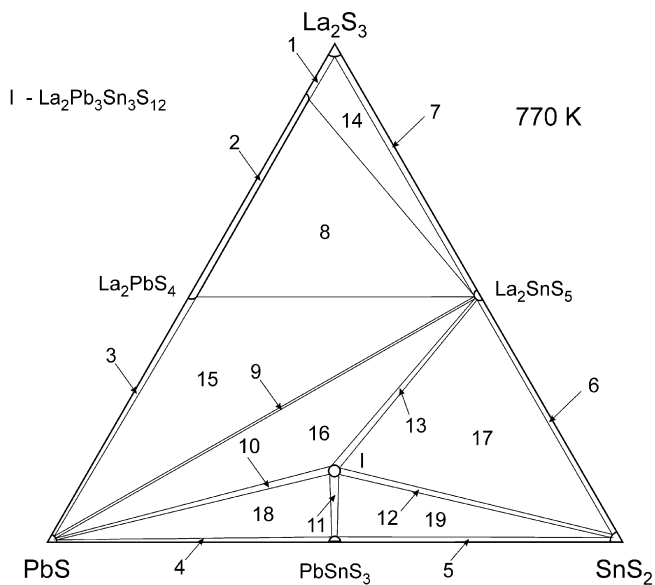


FIGURE 22 Isothermal section of the La_2S_3 —PbS— SnS_2 system at 770 K.

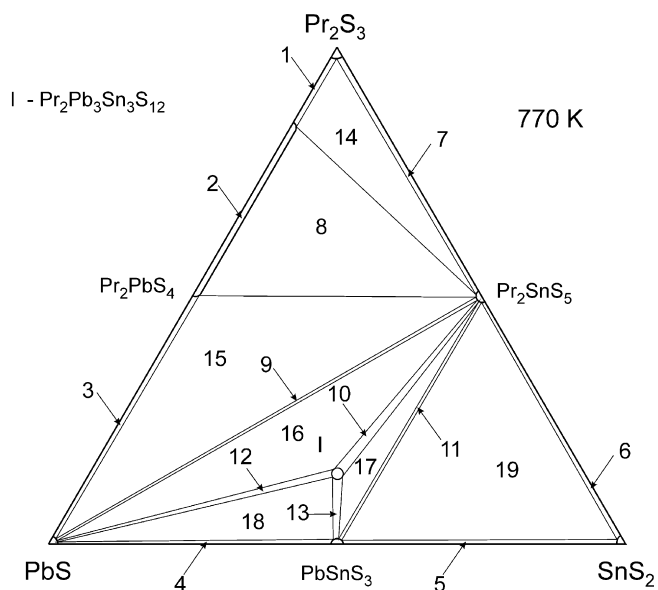


FIGURE 23 Isothermal section of the Pr_2S_3 — PbS — SnS_2 system at 770 K.

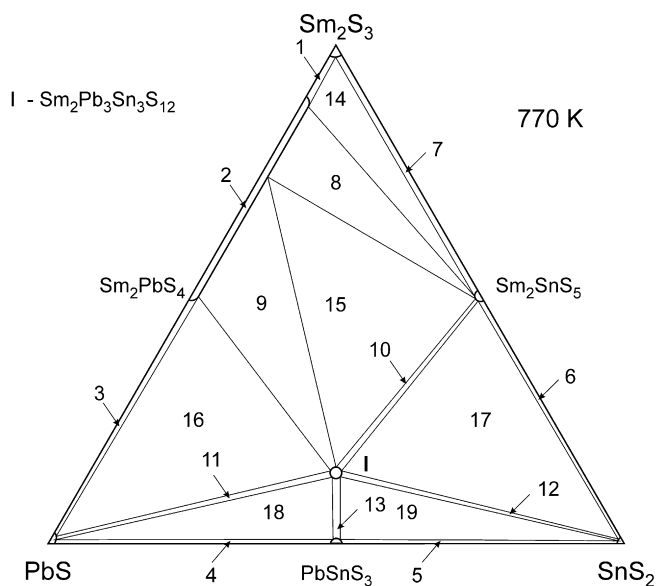


FIGURE 24 Isothermal section of the Sm_2S_3 — PbS — SnS_2 system at 770 K. *On the basis of Gulay and Marchuk (2010) with permission.*

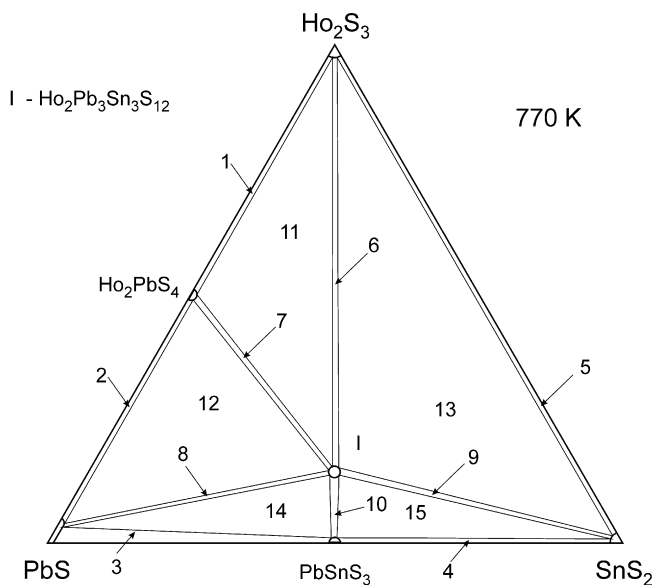


FIGURE 25 Isothermal section of the Ho_2S_3 — PbS — SnS_2 system at 770 K. On the basis of Gulay and Marchuk (2010) with permission.

TABLE 24 Phase Fields in the Y_2S_3 — PbS — SnS_2 System at 770 K

Phase Field	Phases
1	$\text{Y}_2\text{S}_3 + \text{Y}_2\text{PbS}_4$
2	$\text{PbS} + \text{Y}_2\text{PbS}_4$
3	$\text{PbS} + \text{PbSnS}_3$
4	$\text{PbSnS}_3 + \text{SnS}_2$
5	$\text{Y}_2\text{S}_3 + \text{SnS}_2$
6	$\text{Y}_2\text{S}_3 + \text{Y}_2\text{Pb}_3\text{Sn}_3\text{S}_{12}$
7	$\text{Y}_2\text{PbS}_4 + \text{Y}_2\text{Pb}_3\text{Sn}_3\text{S}_{12}$
8	$\text{PbS} + \text{Y}_2\text{Pb}_3\text{Sn}_3\text{S}_{12}$
9	$\text{Y}_2\text{Pb}_3\text{Sn}_3\text{S}_{12} + \text{SnS}_2$
10	$\text{Y}_2\text{Pb}_3\text{Sn}_3\text{S}_{12} + \text{PbSnS}_3$
11	$\text{Y}_2\text{S}_3 + \text{Y}_2\text{PbS}_4 + \text{Y}_2\text{Pb}_3\text{Sn}_3\text{S}_{12}$
12	$\text{Y}_2\text{S}_3 + \text{Y}_2\text{Pb}_3\text{Sn}_3\text{S}_{12} + \text{SnS}_2$
13	$\text{PbS} + \text{Y}_2\text{PbS}_4 + \text{Y}_2\text{Pb}_3\text{Sn}_3\text{S}_{12}$
14	$\text{PbS} + \text{PbSnS}_3 + \text{Y}_2\text{Pb}_3\text{Sn}_3\text{S}_{12}$
15	$\text{PbSnS}_3 + \text{Y}_2\text{Pb}_3\text{Sn}_3\text{S}_{12} + \text{SnS}_2$

TABLE 25 Phase Fields in the La_2S_3 —PbS— SnS_2 System at 770 K

Phase Field	Phases
1	$La_2S_3 + La_{2+2/3x}Pb_{1-x}S_4$ ($x=0.86$)
2	$La_{2+2/3x}Pb_{1-x}S_4$ ($x=0-0.86$)
3	PbS + La_2PbS_4
4	PbS + PbSnS ₃
5	$SnS_2 + PbSnS_3$
6	$SnS_2 + La_2SnS_5$
7	$La_2S_3 + La_2SnS_5$
8	$La_2SnS_5 + La_{2+2/3x}Pb_{1-x}S_4$ ($x=0-0.86$)
9	PbS + La_2SnS_5
10	PbS + $La_2Pb_3Sn_3S_{12}$
11	PbSnS ₃ + $La_2Pb_3Sn_3S_{12}$
12	$SnS_2 + La_2Pb_3Sn_3S_{12}$
13	$La_2SnS_5 + La_2Pb_3Sn_3S_{12}$
14	$La_2S_3 + La_2SnS_5 + La_{2+2/3x}Pb_{1-x}S_4$ ($x=0.86$)
15	PbS + $La_2SnS_5 + La_2PbS_4$
16	PbS + $La_2SnS_5 + La_2Pb_3Sn_3S_{12}$
17	$SnS_2 + La_2SnS_5 + La_2Pb_3Sn_3S_{12}$
18	PbS + PbSnS ₃ + $La_2Pb_3Sn_3S_{12}$
19	$SnS_2 + PbSnS_3 + La_2Pb_3Sn_3S_{12}$

distances are 0.275 and 0.267 nm for Y1 and Y2, respectively. The sulfur atoms create bicapped trigonal prismatic arrangement around the Pb1 and Pb2 atoms. The shortest Pb—S distances are 0.291 and 0.287 nm for Pb1 and Pb2, respectively. The Pb3 atom is situated in a monocapped trigonal prism formed by the sulfur atoms. The shortest Pb—S distance is 0.292 nm. The sulfur atoms create octahedral coordination spheres around the Sn1 and Sn2 atoms with the shortest Sn—S distances 0.256 and 0.255 nm for Sn1 and Sn2, respectively. The Sn3 atom is located in a trigonal bipyramid formed by the sulfur atoms. The shortest Sn—S distance is 0.230 nm. Each of the S1–S4 atom has tetrahedral surrounding of 1Y, 1Pb, and 2Sn atoms. The S5 atom is located in a trigonal bipyramid formed by 2Y, 1Pb, and 2Sn atoms. Each of the S6, S7, S10–S12 atom has tetragonal pyramidal surrounding of

TABLE 26 Phase Fields in the $\text{Pr}_2\text{S}_3\text{—PbS—SnS}_2$ System at 770 K

Phase Field	Phases
1	$\text{Pr}_2\text{S}_3 + \text{Pr}_{2+2/3x}\text{Pb}_{1-x}\text{S}_4$ ($x=0.78$)
2	$\text{Pr}_{2+2/3x}\text{Pb}_{1-x}\text{S}_4$ ($x=0-0.78$)
3	$\text{PbS} + \text{Pr}_2\text{PbS}_4$
4	$\text{PbS} + \text{PbSnS}_3$
5	$\text{SnS}_2 + \text{PbSnS}_3$
6	$\text{SnS}_2 + \text{Pr}_2\text{SnS}_5$
7	$\text{Pr}_2\text{S}_3 + \text{Pr}_2\text{SnS}_5$
8	$\text{Pr}_{2+2/3x}\text{Pb}_{1-x}\text{S}_4$ ($x=0-0.78$) + Pr_2SnS_5
9	$\text{PbS} + \text{Pr}_2\text{SnS}_5$
10	$\text{Pr}_2\text{SnS}_5 + \text{Pr}_2\text{Pb}_3\text{Sn}_3\text{S}_{12}$
11	$\text{PbSnS}_3 + \text{Pr}_2\text{SnS}_5$
12	$\text{PbS} + \text{Pr}_2\text{Pb}_3\text{Sn}_3\text{S}_{12}$
13	$\text{PbSnS}_3 + \text{Pr}_2\text{Pb}_3\text{Sn}_3\text{S}_{12}$
14	$\text{Pr}_2\text{S}_3 + \text{Pr}_{2+2/3x}\text{Pb}_{1-x}\text{S}_4$ ($x=0.78$) + Pr_2SnS_5
15	$\text{PbS} + \text{Pr}_2\text{PbS}_4 + \text{Pr}_2\text{SnS}_5$
16	$\text{PbS} + \text{Pr}_2\text{SnS}_5 + \text{Pr}_2\text{Pb}_3\text{Sn}_3\text{S}_{12}$
17	$\text{PbSnS}_3 + \text{Pr}_2\text{SnS}_5 + \text{Pr}_2\text{Pb}_3\text{Sn}_3\text{S}_{12}$
18	$\text{PbS} + \text{PbSnS}_3 + \text{Pr}_2\text{Pb}_3\text{Sn}_3\text{S}_{12}$
19	$\text{SnS}_2 + \text{PbSnS}_3 + \text{Pr}_2\text{SnS}_5$

2Y, 2Pb, and 1Sn atoms. The S8 atom also has a tetragonal pyramidal surrounding formed by 4Pb and 1Sn atoms. The S9 atom is located outside a tetragonal pyramid formed by 4Pb and 1Sn atoms. Twelve quaternary compounds of the $\text{Y}_2\text{Pb}_3\text{Sn}_3\text{S}_{12}$ type of structure exist in the $\text{R}_2\text{S}_3\text{—PbS—SnS}_2$ systems (Table 11).

4.7 Crystallographic Description of Quaternary Compounds in the $\text{R}_2\text{X}_3\text{—PbX—ZX}_2$ ($\text{X} = \text{S, Se; Z} = \text{Si, Ge, Sn}$) Systems

All quaternary compounds of the $\text{R}_2\text{X}_3\text{—PbX—ZX}_2$ ($\text{X} = \text{S, Se; Z} = \text{Si, Ge, Sn}$) systems summarized in Table 11 crystallize in three structure types.

TABLE 27 Phase Fields in the Sm_2S_3 — PbS — SnS_2 System at 770 K

Phase Field	Phases
1	$Sm_2S_3 + Sm_{2+2/3x}Pb_{1-x}S_4$ ($x=0.86$)
2	$Sm_{2+2/3x}Pb_{1-x}S_4$ ($x=0-0.86$)
3	$PbS + Sm_2PbS_4$
4	$PbS + PbSnS_3$
5	$SnS_2 + PbSnS_3$
6	$SnS_2 + Sm_2SnS_5$
7	$Sm_2S_3 + Sm_2SnS_5$
8	$Sm_{2+2/3x}Pb_{1-x}S_4$ ($x=0.60-0.86$) + Sm_2SnS_5
9	$Sm_{2+2/3x}Pb_{1-x}S_4$ ($x=0-0.60$) + $Sm_2Pb_3Sn_3S_{12}$
10	$Sm_2SnS_5 + Sm_2Pb_3Sn_3S_{12}$
11	$PbS + Sm_2Pb_3Sn_3S_{12}$
12	$SnS_2 + Sm_2Pb_3Sn_3S_{12}$
13	$PbSnS_3 + Sm_2Pb_3Sn_3S_{12}$
14	$Sm_2S_3 + Sm_{2+2/3x}Pb_{1-x}S_4$ ($x=0.86$) + Sm_2SnS_5
15	$Sm_{2+2/3x}Pb_{1-x}S_4$ ($x=0.60$) + $Sm_2SnS_5 + Sm_2Pb_3Sn_3S_{12}$
16	$PbS + Sm_2PbS_4 + Sm_2Pb_3Sn_3S_{12}$
17	$SnS_2 + Sm_2SnS_5 + Sm_2Pb_3Sn_3S_{12}$
18	$PbS + PbSnS_3 + Sm_2Pb_3Sn_3S_{12}$
19	$SnS_2 + PbSnS_3 + Sm_2Pb_3Sn_3S_{12}$

4.7.1 Quaternary Compounds with $La_2PbSi_2S_8$ Structure Type

The crystal structure of the $La_2PbSi_2S_8$ compound (Gulay et al., 2010) is related to the structure of the $Eu_3As_2S_8$ compound (Bera et al., 2007). The position of Eu and As in the structure of $Eu_3As_2S_8$ corresponds to the position of the randomly distributed La and Pb atoms (M) and Si in the structure of $La_2PbSi_2S_8$. The positions of sulfur atoms S1 and S2 in both structures are the same.

The packing of the coordination polyhedra of the Eu and As atoms in the structure of $Eu_3As_2S_8$ is shown in Fig. 29. The Eu and As atoms are located in bicapped trigonal prisms and tetrahedra, respectively, formed by sulfur atoms.

TABLE 28 Phase Fields in the $\text{Ho}_2\text{S}_3\text{—PbS—SnS}_2$ System at 770 K

Phase Field	Phases
1	$\text{Ho}_2\text{S}_3 + \text{Ho}_2\text{PbS}_4$
2	$\text{PbS} + \text{Ho}_2\text{PbS}_4$
3	$\text{PbS} + \text{PbSnS}_3$
4	$\text{SnS}_2 + \text{PbSnS}_3$
5	$\text{Ho}_2\text{S}_3 + \text{SnS}_2$
6	$\text{Ho}_2\text{S}_3 + \text{Ho}_2\text{Pb}_3\text{Sn}_3\text{S}_{12}$
7	$\text{Ho}_2\text{PbS}_4 + \text{Ho}_2\text{Pb}_3\text{Sn}_3\text{S}_{12}$
8	$\text{PbS} + \text{Ho}_2\text{Pb}_3\text{Sn}_3\text{S}_{12}$
9	$\text{SnS}_2 + \text{Ho}_2\text{Pb}_3\text{Sn}_3\text{S}_{12}$
10	$\text{PbSnS}_3 + \text{Ho}_2\text{Pb}_3\text{Sn}_3\text{S}_{12}$
11	$\text{Ho}_2\text{S}_3 + \text{Ho}_2\text{PbS}_4 + \text{Ho}_2\text{Pb}_3\text{Sn}_3\text{S}_{12}$
12	$\text{PbS} + \text{Ho}_2\text{PbS}_4 + \text{Ho}_2\text{Pb}_3\text{Sn}_3\text{S}_{12}$
13	$\text{SnS}_2 + \text{Ho}_2\text{S}_3 + \text{Ho}_2\text{Pb}_3\text{Sn}_3\text{S}_{12}$
14	$\text{PbS} + \text{PbSnS}_3 + \text{Ho}_2\text{Pb}_3\text{Sn}_3\text{S}_{12}$
15	$\text{PbSnS}_3 + \text{Ho}_2\text{Pb}_3\text{Sn}_3\text{S}_{12} + \text{SnS}_2$

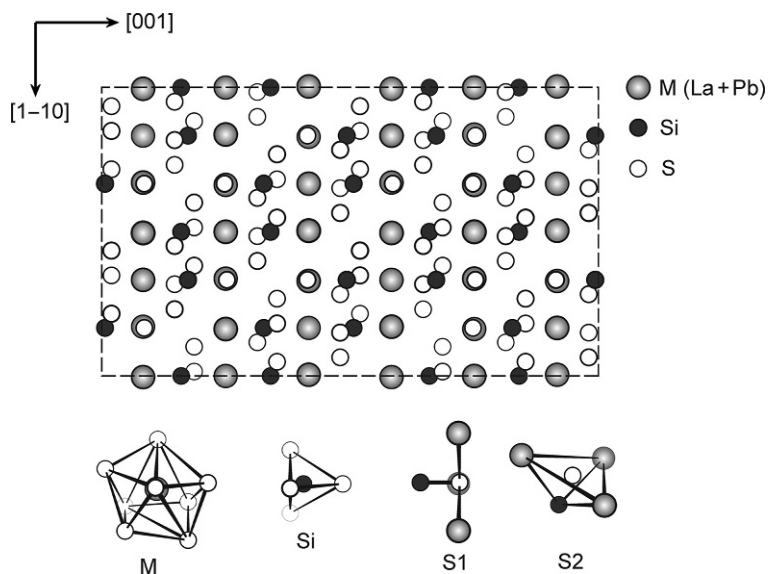
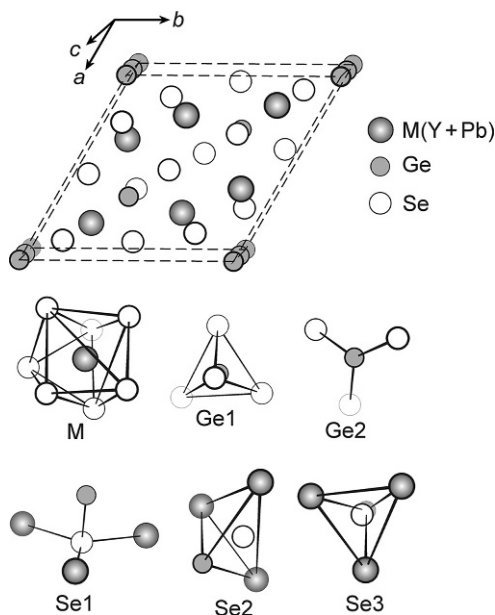
**FIGURE 26** Crystal structure of $\text{La}_2\text{PbSi}_2\text{S}_8$ and CPs of atoms.

TABLE 29 Atomic Parameters for $\text{La}_2\text{PbSi}_2\text{S}_8$

Atom	Position	Fractional Coordinates			Coordination	
		x	y	z		
M^a	18e	0.31864	0	1/4	8S	
Si	12c	0	0	0.15983	4S	
S1	12c	0	0	0.08092	3M	1Si
S2	36f	0.20301	0.23434	0.18649	3M	1Si

^aOccupancy 67% La + 33% Pb.

**FIGURE 27** Crystal structure of $\text{Y}_{1.32}\text{Pb}_{1.68}\text{Ge}_{1.67}\text{Se}_7$ and CPs of atoms. On the basis of *Ruda et al. (2007)* with permission.

The packing of the coordination polyhedra of the M (La+Pb) and Si atoms in the structure of $\text{La}_2\text{PbSi}_2\text{S}_8$ is shown in Fig. 29. Each M (La+Pb) atom is eight coordinated by the sulfur atoms which form bicapped trigonal prisms. Each Si atom is located in tetrahedra formed by sulfur atoms. Similar packing of cation-centered polyhedra illustrates the relations between the structure of

TABLE 30 Atomic Parameters for $Y_{1.32}Pb_{1.68}Ge_{1.67}Se_7$

Atom	Position	Fractional Coordinates			Coordination	
		x	y	z		
M ^a	6c	0.3843	0.1631	0.402	7Se	
Ge1	2b	1/3	2/3	0.324	4Se	
Ge2 ^b	2a	0	0	0.000	3Se	
Se1	6c	0.255	0.106	0.986	3M	1Ge
Se2	6c	0.529	0.441	0.692	3M	1Ge
Se3	2b	1/3	2/3	0.679	3M	1Ge

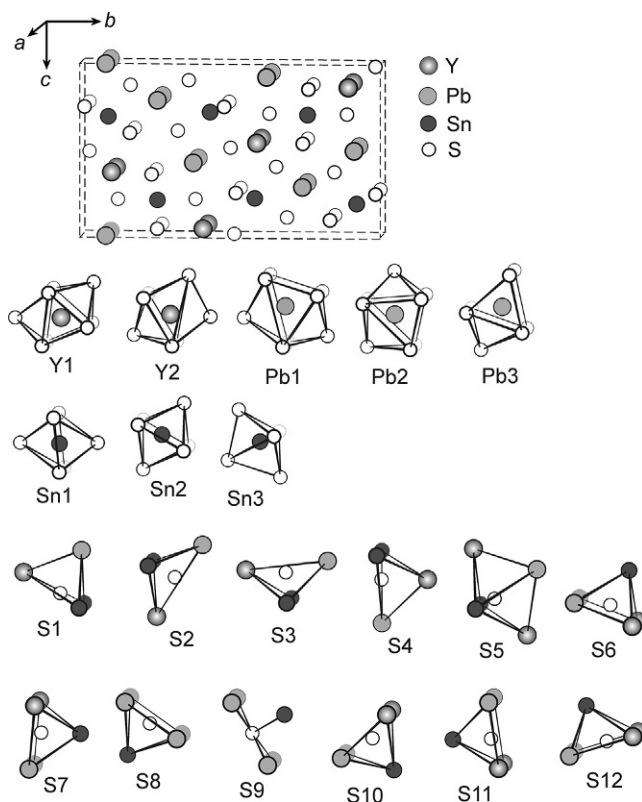
^aOccupancy 44% Y+56% Pb.^bOccupancy 67% Ge.**FIGURE 28** Crystal structure of $Y_2Pb_3Sn_3S_{12}$ and CPs of atoms. Reprinted with permission from Elsevier (Gulay et al., 2008).

TABLE 31 Atomic Parameters for $Y_2Pb_3Sn_3S_{12}$

Atom	Position	Fractional Coordinates			Coordination		
		x	y	z			
Y1	2a	0	0.4108	0.9567	8S		
Y2	2a	0	0.1061	0.6305	7S		
Pb1	2a	0	0.3782	0.5739	8S		
Pb2	2a	0	0.2589	0.2121	8S		
Pb3	2a	0	0.0869	0.0000	7S		
Sn1	2b	1/2	0.2501	0.8060	6S		
Sn2	2b	1/2	0.0868	0.3214	6S		
Sn3	2b	1/2	0.4258	0.2927	5S		
S1	2a	0	0.015	0.251	1Y	1Pb	2Sn
S2	2a	0	0.166	0.402	1Y	1Pb	2Sn
S3	2a	0	0.238	0.643	1Y	1Pb	2Sn
S4	2a	0	0.257	0.959	1Y	1Pb	2Sn
S5	2a	0	0.480	0.247	2Y	1Pb	2Sn
S6	2b	1/2	0.024	0.524	2Y	2Pb	1Sn
S7	2b	1/2	0.119	0.802	2Y	2Pb	1Sn
S8	2b	1/2	0.160	0.138	4Pb	1Sn	
S9	2b	1/2	0.318	0.402	4Pb	1Sn	
S10	2b	1/2	0.354	0.109	2Y	2Pb	1Sn
S11	2b	1/2	0.377	0.800	2Y	2Pb	1Sn
S12	2b	1/2	0.493	0.499	2Y	2Pb	1Sn

the $Eu_3As_2S_8$ and $La_2PbSi_2S_8$ compounds. Each $[SiS_4]$ tetrahedron in the structure of $La_2PbSi_2S_8$ is surrounded by six $[M(La+Pb)S_8]$ bicapped trigonal prism. These coordination polyhedra are connected to each other by common edges.

Two-dimensional nets 3^6 and 6^3 formed by the respective M (La+Pb) and Si atoms exist in the structure of the $La_2PbSi_2S_8$ compound (Fig. 30). These nets are parallel to the ab plane.

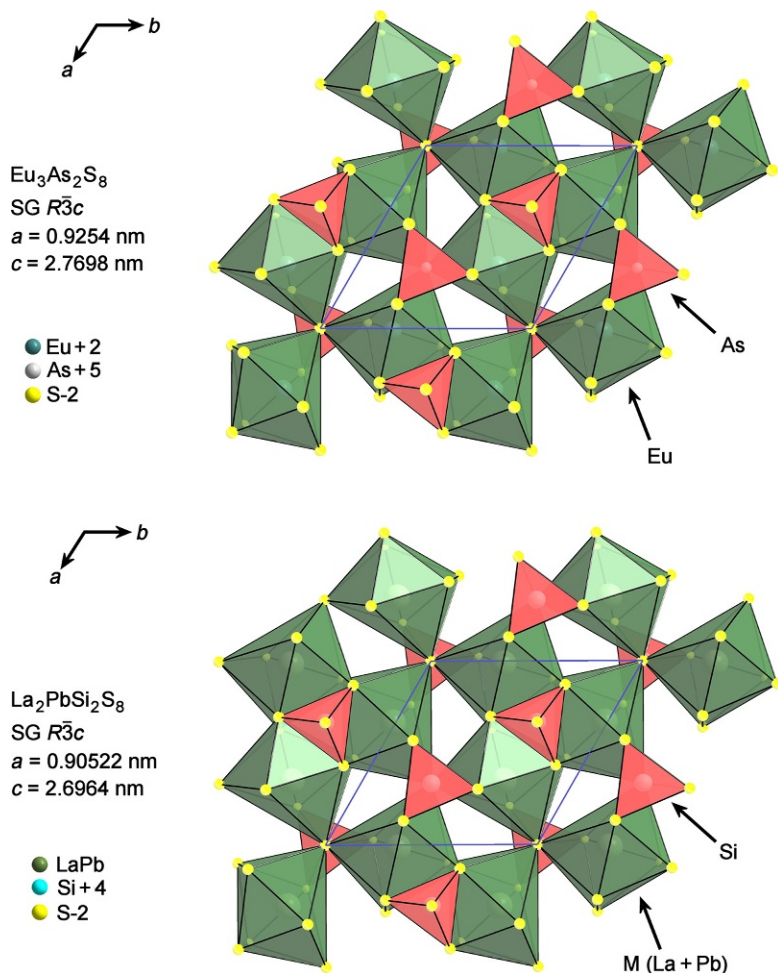


FIGURE 29 Cation-centered polyhedra in the structure of the $\text{Eu}_3\text{As}_2\text{S}_8$ and $\text{La}_2\text{PbSi}_2\text{S}_8$ compounds. Reprinted with permissions from IUCr (Gulay *et al.*, 2010) and Elsevier (Daszkiewicz *et al.*, 2012).

4.7.2 Quaternary Compounds with $\text{Y}_{1.32}\text{Pb}_{1.68}\text{Ge}_{1.67}\text{Se}_7$ Structure Type

Structure type $\text{Y}_{1.32}\text{Pb}_{1.68}\text{Ge}_{1.67}\text{Se}_7$ (Ruda *et al.*, 2007) is realized for $\text{Sm}_{1.32}\text{Pb}_{1.68}\text{Ge}_{1.67}\text{Se}_7$ (Ruda *et al.*, 2007). The crystal structure of the $\text{Sm}_{1.32}\text{Pb}_{1.68}\text{Ge}_{1.67}\text{Se}_7$ compound (SG $P6_3$, $a = 1.0442$, $c = 0.6627 \text{ nm}$) is built by $[\text{M}(\text{Sm}+\text{Pb})\text{Se}_7]$ monocapped trigonal prisms, $[\text{Ge}_1\text{Se}_4]$ tetrahedra, and $[\text{Ge}_2\text{Se}_3]$ triangles which are connected by corners and faces (Fig. 31).

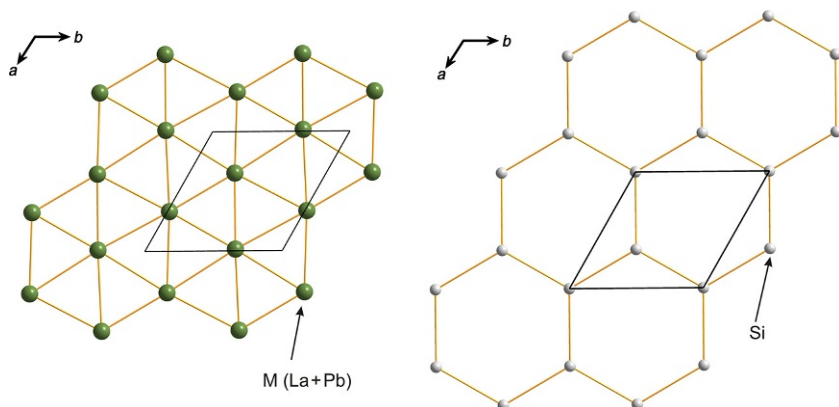


FIGURE 30 Two-dimensional nets 3^6 and 6^3 in the structure of the $\text{La}_2\text{PbSi}_2\text{S}_8$ compound. Reprinted with permission from IUCr (Gulay *et al.*, 2010).

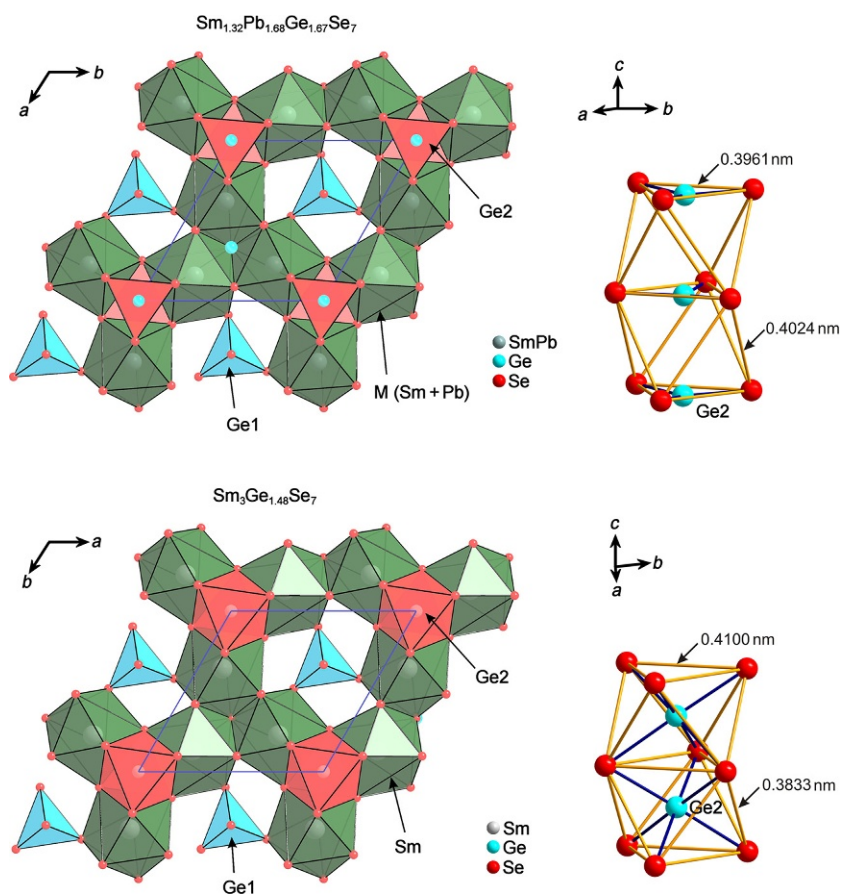


FIGURE 31 Cation-centered polyhedra in the structure of the $\text{Sm}_3\text{Ge}_{1.48}\text{Se}_7$ and $\text{Sm}_{1.32}\text{Pb}_{1.68}\text{Ge}_{1.67}\text{Se}_7$ compounds. Reprinted with permission from Elsevier (Daszkiewicz *et al.*, 2010) and on the basis of Ruda *et al.* (2007) with permission.

Actually, the Ge2 atom lies inside the octahedron formed by six Se atoms. However, it is located near one face of this octahedron; therefore, real coordination polyhedron for Ge2 is a triangle. The $\text{Sm}_3\text{Ge}_{1.48}\text{Se}_7$ compound (Daszkiewicz et al., 2010) of ternary Sm—Ge—Se system crystallizes in $\text{Dy}_3\text{Ge}_{1.25}\text{S}_7$ (Michelet et al., 1975) type of structure. The crystal structure of the $\text{Sm}_3\text{Ge}_{1.48}\text{Se}_7$ compound (SG $P6_3$, $a = 1.04419$ and $c = 0.60283$ nm) is built by $[\text{SmSe}_7]$ monocapped trigonal prisms, $[\text{Ge}_1\text{Se}_4]$ tetrahedra, and $[\text{Ge}_2\text{Se}_6]$ octahedra which are connected by corners and faces (Fig. 31). Generally, both $\text{Sm}_{1.32}\text{Pb}_{1.68}\text{Ge}_{1.67}\text{Se}_7$ and $\text{Sm}_3\text{Ge}_{1.48}\text{Se}_7$ compounds have similar structural motifs. The differences are only for the occupations of octahedra located along the c axes. The Ge2 atoms in the structure of $\text{Sm}_3\text{Ge}_{1.48}\text{Se}_7$ are located almost in the centers of the octahedra formed by the Se atoms, whereas the Ge2 atoms in the structure of $\text{Sm}_{1.32}\text{Pb}_{1.68}\text{Ge}_{1.67}\text{Se}_7$ are located near one of the triangular faces of such octahedra. The structure of the $\text{Sm}_{1.32}\text{Pb}_{1.68}\text{Ge}_{1.67}\text{Se}_7$ compound can be obtained from the $\text{Sm}_3\text{Ge}_{1.48}\text{Se}_7$ structure by random substitution of the Sm atoms, which occupies a single independent crystallographic position, by the Pb atoms. The substitution of Sm^{3+} in $\text{Sm}_3\text{Ge}_{1.48}\text{Se}_7$ by Pb^{2+} with formation of $\text{Sm}_{1.32}\text{Pb}_{1.68}\text{Ge}_{1.67}\text{Se}_7$ is supported by increasing of the Ge content in octahedra (position Ge2) to satisfy charge balance requirement.

The unit cell volume of the $\text{Sm}_{1.32}\text{Pb}_{1.68}\text{Ge}_{1.67}\text{Se}_7$ compound equals 0.6257 nm^3 and is larger than that for $\text{Sm}_3\text{Ge}_{1.48}\text{Se}_7$, 0.5692 nm^3 . The lattice parameter a for both compounds has approximately the same values, whereas the parameter c for $\text{Sm}_{1.32}\text{Pb}_{1.68}\text{Ge}_{1.67}\text{Se}_7$ is significantly larger than the same for $\text{Sm}_3\text{Ge}_{1.48}\text{Se}_7$ (Fig. 32). Similar situation exist for both series of ternary chalcogenides $\text{R}_3\text{Ge}_{1+x}\text{Se}_7$ ($\text{R} = \text{La, Ce, Pr, Sm, Gd, and Tb}$; $x = 0.43\text{--}0.49$) (Daszkiewicz et al., 2010) and quaternary compounds $\text{R}_{1.32}\text{Pb}_{1.68}\text{Ge}_{1.67}\text{Se}_7$ ($\text{R} = \text{Y, La, Ce, Pr, Nd, Sm, Gd, Tb, Dy, and Ho}$) (Ruda et al., 2007). The differences of the lattice parameter a between ternary $\text{R}_3\text{Ge}_{1+x}\text{Se}_7$ and quaternary $\text{R}_{1.32}\text{Pb}_{1.68}\text{Ge}_{1.67}\text{Se}_7$ compounds is not significant in comparison with differences of lattice parameter c (Fig. 32). The values of parameters c for quaternary $\text{R}_{1.32}\text{Pb}_{1.68}\text{Ge}_{1.67}\text{Se}_7$ compounds are significantly larger than those for the ternary $\text{R}_3\text{Ge}_{1+x}\text{Se}_7$ compounds. Such increasing of the c/a ratio for quaternary $\text{R}_{1.32}\text{Pb}_{1.68}\text{Ge}_{1.67}\text{Se}_7$ compounds when compared with ternary $\text{R}_3\text{Ge}_{1+x}\text{Se}_7$ compounds is related to the existence of large Pb^{2+} ions in the quaternary chalcogenides. As a result, elongation of the $[\text{Ge}_2\text{Se}_6]$ octahedron along the c axis in the structure of $\text{R}_{1.32}\text{Pb}_{1.68}\text{Ge}_{1.67}\text{Se}_7$ ($\text{R} = \text{Y, La, Ce, Pr, Nd, Sm, Gd, Tb, Dy, and Ho}$) compounds is observed. Besides, an increase of the Se—Se distances in the c direction and a decrease of the Se—Se distances in the ab plane are observed for $\text{Sm}_{1.32}\text{Pb}_{1.68}\text{Ge}_{1.67}\text{Se}_7$ when compared to $\text{Sm}_3\text{Ge}_{1.48}\text{Se}_7$.

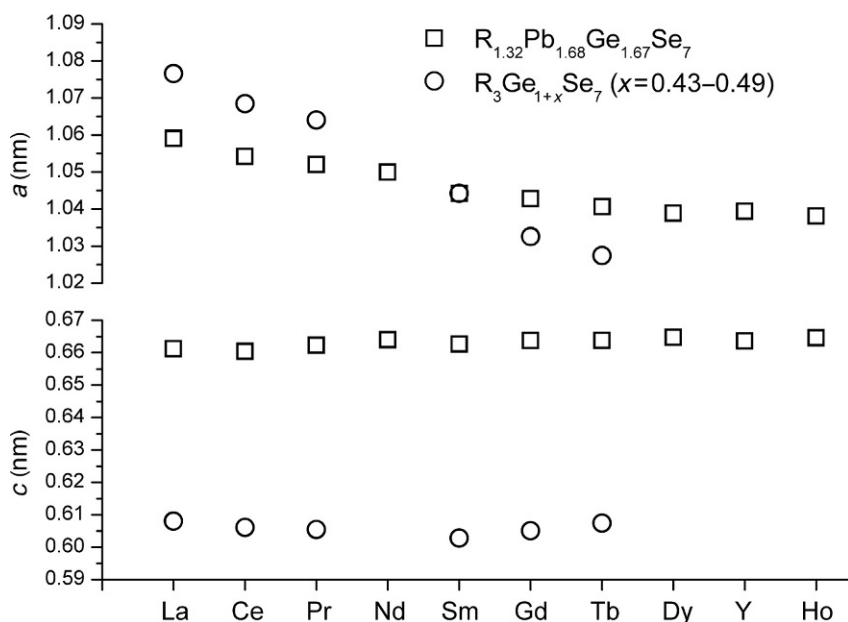


FIGURE 32 Lattice parameters of ternary $R_3Ge_{1+x}Se_7$ ($R=La, Ce, Pr, Sm, Gd,$ and Tb ; $x=0.43\text{--}0.49$) and quaternary $R_{1.32}Pb_{1.68}Ge_{1.67}Se_7$ ($R=Y, La, Ce, Pr, Nd, Sm, Gd, Tb, Dy,$ and Ho) compounds. Reprinted with permission from Elsevier (Daszkiewicz et al., 2010).

4.7.3 Quaternary Compounds with $Y_2Pb_3Sn_3S_{12}$ Structure Type

The crystal structure of the $Y_2Pb_3Sn_3S_{12}$ compound (Marchuk et al., 2007) is related to the structure of the $Eu_5Sn_3S_{12}$ compound (Jaulmes and Julien-Pouzol, 1977a). Two positions are occupied by Eu^{3+} and three positions are occupied by Eu^{2+} in the structure of $Eu_5Sn_3S_{12}$. The positions of Eu^{3+} and Eu^{2+} in the structure of $Eu_5Sn_3S_{12}$ correspond to the positions of Y^{3+} and Pb^{2+} , respectively, in the isostructural $Y_2Pb_3Sn_3S_{12}$. The positions of tin and sulfur in both structures are identical.

The packing of coordination polyhedra of $Eu, Y, Pb,$ and Sn atoms in the structures of the $Eu_5Sn_3S_{12}$ and $Y_2Pb_3Sn_3S_{12}$ compounds is shown in Fig. 33. The Eu atoms in the structure of $Eu_5Sn_3S_{12}$ or Y and Pb atoms in the structure of $Y_2Pb_3Sn_3S_{12}$ are located in trigonal prisms formed by sulfur atoms. The Sn atoms in both structures are located in octahedra (two positions) and trigonal bipyramids (one position) formed by the sulfur atoms. Each type of polyhedron forms chains along the a direction.

The unit cell of the $Eu_5Sn_3S_{12}$ compound is completely build from the fragments of the unit cells of La_2Sn_5 (Jaulmes, 1974) and $Eu_3Sn_2S_7$ (Jaulmes and Julien-Pouzol, 1977b). The crystal structure of the $Y_2Pb_3Sn_3S_{12}$

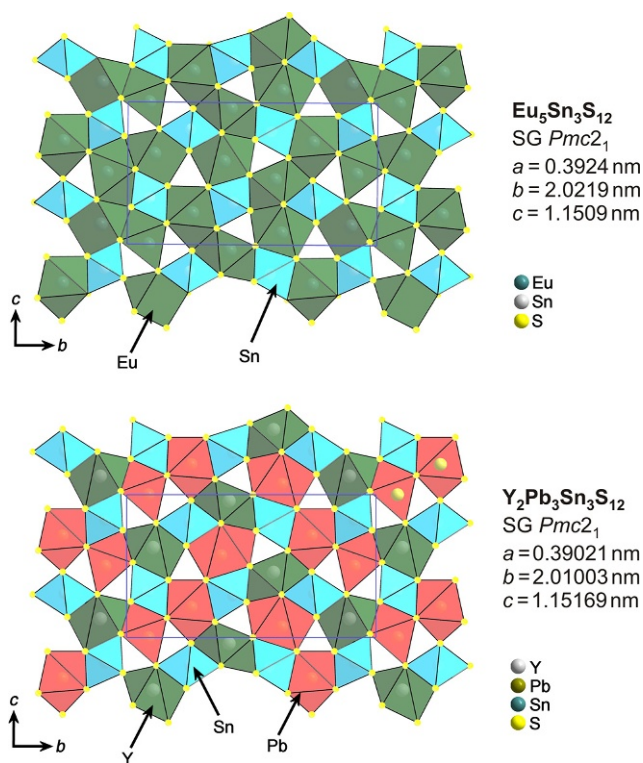


FIGURE 33 Cation-centered polyhedra in the structure of the $\text{Eu}_5\text{Sn}_3\text{S}_{12}$ and $\text{Y}_2\text{Pb}_3\text{Sn}_3\text{S}_{12}$ compounds.

compound is obtained from the structure of $\text{Eu}_5\text{Sn}_3\text{S}_{12}$ by ordered substitution of the Eu atoms by the Y and Pb atoms. Fragments of the unit cells of La_2SnS_5 and $\text{Eu}_3\text{Sn}_2\text{S}_7$ compounds are also observed in the structure of the $\text{Y}_2\text{Pb}_3\text{Sn}_3\text{S}_{12}$ compound (Fig. 34), highlighting their close structural relationships.

4.8 Formation of Superstructures

All of the interatomic distances in the crystal structure of quaternary compounds of the $\text{R}_2\text{X}_3\text{—PbX—ZX}_2$ ($\text{X} = \text{S, Se; Z} = \text{Si, Ge, Sn}$) systems are in good agreement with the sum of the respective ionic radii (Shannon, 1976). We assume the existence of cations and anions in the structures of quaternary compounds of the $\text{R}_2\text{X}_3\text{—PbX—ZX}_2$ ($\text{X} = \text{S, Se; Z} = \text{Si, Ge, Sn}$) systems. The sizes of anions are larger than sizes of cations. We assume the existence of sublattices of cations and anions. The sublattice of anions is completely

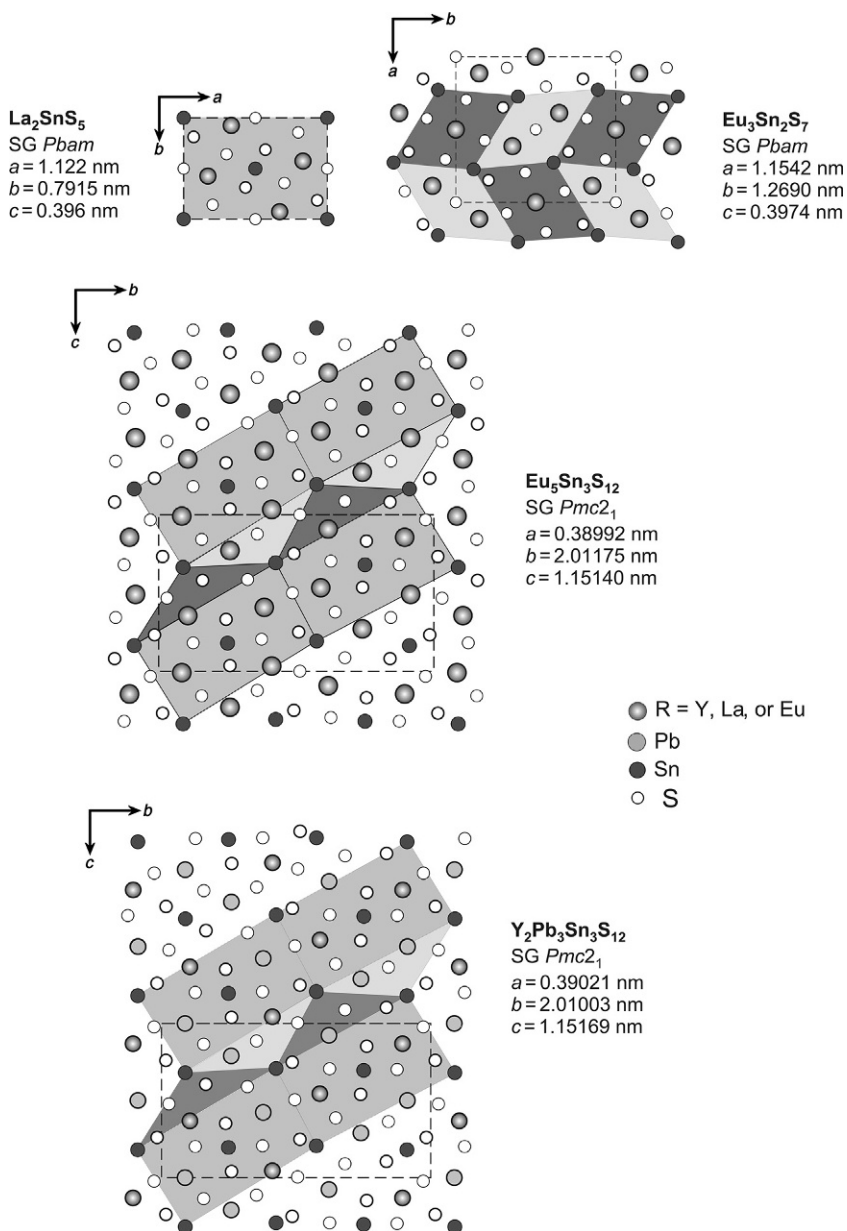


FIGURE 34 The fragments of the unit cells of the La_2SnS_5 and $\text{Eu}_3\text{Sn}_2\text{S}_7$ compounds in the structure of the $\text{Eu}_5\text{Sn}_3\text{S}_{12}$ and $\text{Y}_2\text{Pb}_3\text{Sn}_3\text{S}_{12}$ compounds. Reprinted with permission from Elsevier (*Gulay et al., 2008*).

ordered. Tetrahedral, octahedral, and trigonal prismatic voids exist in sublattice of anions. During description of the formation of superstructures, we assume that sublattice of anions is not changed. The changes exist only for the positions of cations. The crystal structure of quaternary compounds of the $R_2X_3\text{—PbX—ZX}_2$ ($X = S, Se$; $Z = Si, Ge, Sn$) systems can be formed according to the following principles:

- (I) *Partial substitution of the atoms of original structure by the atoms with another charge.* Both types of atoms form the mixture of the randomly distributed atoms. They occupy the same position(s) as in the parent structure. The change of a charge for one position of cations results in the change of charge for another one. This type of substitution is observed for the structures of $La_2PbSi_2S_8$ and $Y_{1.32}Pb_{1.68}Ge_{1.67}Se_7$ compounds. Two possibilities are observed:
- The comparison of the crystal structures of $La_2PbSi_2S_8$ and $Eu_3As_2S_8$ compounds is given in Table 32 using standardized crystallographic data for both compounds. Trigonal prismatic and tetrahedral sites of cations are observed in the crystal structure of both compounds. The substitution of Eu^{2+} by the mixture of the randomly distributed La^{3+} and Pb^{2+} causes the increasing of the positive charge in the trigonal prismatic positions. At the same time, a decrease of the positive charge is observed for the tetrahedral position during the substitution of As^{5+} by Si^{4+} and the positions of As and Si are fully occupied.
 - The comparison of the crystal structure of the $Y_{1.32}Pb_{1.68}Ge_{1.67}Se_7$ and $Dy_3Ge_{1.25}S_7$ compounds is described in Table 33. Trigonal prismatic, tetrahedral, and octahedral sites of cations are observed in the crystal structures of both compounds. The substitution of Dy^{3+} by

TABLE 32 The Comparison of the Crystal Structure of the $La_2PbSi_2S_8$ and $Eu_3As_2S_8$ Compounds

	$Eu_3As_2S_8$	$La_2PbSi_2S_8$
	SG $R\bar{3}c$	SG $R\bar{3}c$
	$a = 0.9254$ nm	$a = 0.90522$ nm
	$c = 2.7698$ nm	$c = 2.6964$ nm
Position		
Trigonal prismatic site 18e ($x, 0, 1/4$)	Eu ($x = 0.32110$)	M^a ($x = 0.31864$)
Tetrahedral site 12c ($0, 0, z$)	As ($z = 0.15951$)	Si ($z = 0.15983$)

^aOccupancy 67% La+33% Pb.

TABLE 33 The Comparison of the Crystal Structure of the $Y_{1.32}Pb_{1.68}Ge_{1.67}Se_7$ and $Dy_3Ge_{1.25}S_7$ Compounds

	$Dy_3Ge_{1.25}S_7$	$Y_{1.32}Pb_{1.68}Ge_{1.67}Se_7$
	SG $P6_3$	SG $P6_3$
	$a = 0.9254$ nm	$a = 0.90522$ nm
Position	$c = 2.7698$ nm	$c = 2.6964$ nm
Trigonal prismatic site 6e (x, y, z)	Dy ($x=0.359, y=0.140,$ $z=0.250$)	M ^a ($x=0.3843,$ $y=0.1631, z=0.402$)
Tetrahedral site 2b (1/3, 2/3, z)	Ge1 ($z=0.175$)	Ge1 ($z=0.324$)
Octahedral site 2a (0, 0, z)	Ge2 ^b ($x=0.047$)	Ge2 ^c ($x=0.000$)
^a Occupancy 44% Y+56% Pb. ^b Occupancy 25% Ge. ^c Occupancy 67% Ge.		

the mixture of randomly distributed Y^{3+} and Pb^{2+} causes a decrease of the positive charge in the trigonal prismatic position. The tetrahedral positions are fully occupied and have the same charge in both structures. The octahedral positions in both structures are partially occupied by Ge. The increase of the charge in the octahedral position is caused by the increase of site occupancy factor of Ge atom.

- (II) *Ordered substitutions of atoms carrying identical charges.* This kind of substitution is observed in the formation of the quaternary $Y_2Pb_3Sn_3S_{12}$ structure from the ternary $Eu_5Sn_3S_{12}$ parent. Three positions of Eu^{3+} and two positions of Eu^{2+} exist in the structure of $Eu_5Sn_3S_{12}$. The crystal structure of $Y_2Pb_3Sn_3S_{12}$ can be derived from $Eu_5Sn_3S_{12}$ by the substitution of Eu^{3+} by Y^{3+} and Eu^{2+} by Pb^{2+} (Fig. 33). This kind of substitution of ternary and quaternary rare-earth lead chalcogenides has been described by Gulay and Daszkiewicz (2011).
- (III) *The crystal structure of a complex compound contains fragments of simpler structures.* This kind of formation of superstructures is observed for the quaternary $Y_2Pb_3Sn_3S_{12}$ structure as well as for the ternary $Eu_5Sn_3S_{12}$ one. The unit cell of $Y_2Pb_3Sn_3S_{12}$ and $Eu_5Sn_3S_{12}$ can be completely constructed from the fragments of the unit cells of La_2SnS_5 and $Eu_3Sn_2S_7$ (Fig. 34). This kind of substitution of ternary and quaternary rare-earth lead chalcogenides has been also described earlier (Gulay and Daszkiewicz, 2011).

A general scheme illustrating the formation of the crystal structures of quaternary compounds in the R_2X_3 —PbX— ZX_2 ($X = S, Se$; $Z = Si, Ge, Sn$) systems is shown in Fig. 35.

5 MAGNETIC PROPERTIES OF QUATERNARY COMPOUNDS IN THE R_2X_3 —PbX— ZX_2 ($X = S, Se$; $Z = Si, Ge, Sn$) SYSTEMS

Magnetic properties have been investigated only for the series $R_2PbSi_2X_8$ ($R = La, Ce, Pr, Sm$; $X = S, Se$) (Daszkiewicz et al., 2012) (Table 34). Magnetic measurements have been performed using a Quantum Design MPMS-5 superconducting quantum interface device magnetometer in the temperature range 1.72–400 K and in applied magnetic fields up to 5 T. The $La_2PbSi_2S_8$ and $La_2PbSi_2Se_8$ are weak diamagnets (D, Table 34). The reciprocal magnetic susceptibility of $R_2PbSi_2S_8$ and $R_2PbSi_2Se_8$ ($R = Ce$ and Pr) in a wide range

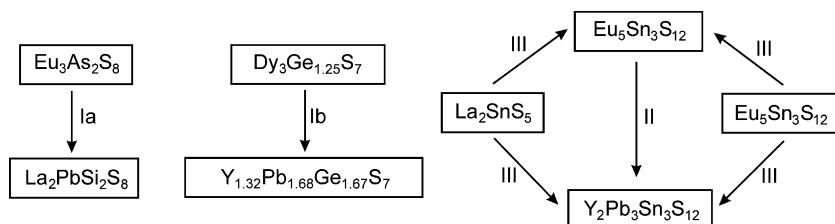


FIGURE 35 General scheme of formation of the crystal structure of quaternary compounds of the R_2X_3 —PbX— ZX_2 ($X = S, Se$; $Z = Si, Ge, Sn$) systems.

TABLE 34 Magnetic Properties of $R_2PbSi_2X_8$ ($R = La, Ce, Pr, Sm$; $X = S, Se$)

Compound	Magnetism	Θ_P (K)	μ_R (μ_B) [Theory]	Reference(s)
$La_2PbSi_2S_8$	D			Daszkiewicz et al. (2012)
$Ce_2PbSi_2S_8$	CW	38	2.51 [2.54]	Daszkiewicz et al. (2012)
$Pr_2PbSi_2S_8$	CW	54	3.65 [3.58]	Daszkiewicz et al. (2012)
$Sm_2PbSi_2S_8$	MCW	−3	0.57 [0.85]	Daszkiewicz et al. (2012)
$La_2PbSi_2Se_8$	D			Daszkiewicz et al. (2012)
$Ce_2PbSi_2Se_8$	CW	9	2.30 [2.54]	Daszkiewicz et al. (2012)
$Pr_2PbSi_2Se_8$	CW	39	3.53 [3.58]	Daszkiewicz et al. (2012)
$Sm_2PbSi_2Se_8$	MCW	−9	0.87 [0.85]	Daszkiewicz et al. (2012)

below room temperature can be approximated by the Curie-Weiss (CW) law. The inverse magnetic susceptibility of $Sm_2PbSi_2S_8$ and $Sm_2PbSi_2Se_8$ in the whole temperature range is strongly curvilinear and can be approximated by the modified Curie-Weiss (MCW) law. No long-range magnetic ordering has been found down to 1.72 K for $R_2PbSi_2S_8$ and $R_2PbSi_2Se_8$ (R=Ce, Pr, and Sm).

6 CONCLUSIONS AND OUTLOOK

Isothermal sections of phase diagrams of 17 systems R_2X_3 —PbX— ZX_2 (X=S, Se; Z=Si, Ge, Sn) that have been constructed at 770 K are briefly reviewed in this chapter. Even though experimental data are far from being complete, their analysis enables one to predict specific phase relations for the remaining systems, i.e., those for which only formation of quaternary compounds has been established. Thus, quaternary compounds have been reported to form only for the larger rare-earth elements in all of the investigated systems containing Si, Ge, and Sn. The interactions of the components in the systems with Si and Ge are generally similar. However, the Ge systems appear to be more complex compared to respective Si systems. On the other hand, the Sn systems differ significantly from the related systems containing Si.

The crystal structures of all quaternary compounds in the Si, Ge, and Sn systems are based and derived from known ternary structures by partial substitutions of rare-earth atoms by Pb atoms. In the quaternary compounds formed in the Si and Ge systems, a random distribution of rare earth and Pb atoms in the same sites is commonly observed. For quaternary compounds that exist in the Sn systems, the rare earth and Pb atoms exhibit tendency toward occupying independent positions.

All of the information presented in this chapter is derived from a thorough analysis of several R_2X_3 —PbX— ZX_2 (X=S, Se; Z=Si, Ge, Sn) systems based on the X-ray crystal structures of known ternary and quaternary chalcogenides. The systems with lead are of special importance because of possible substitutions of lead atoms by rare-earth atoms, which leads to new crystalline phases. On the other hand, even though the parent structure is generally preserved by such substitutions, magnetic and optical properties of these new, substituted chalcogenides are expected to be modified significantly. For instance, similar investigations have been carried out for oxides and fluorides as potential light emitting materials. It is worth noting here, that new phases can also be found in the nano scale, which are of potential importance in nanotechnology incorporated into other branches of science such as biotechnology, catalysis, or medicine. This question, although not discussed here, is still open and all of the results described in this chapter provide a good foundation for future studies.

SYMBOLS AND ABBREVIATIONS

<i>a, b, c</i>	unit cell dimensions (nm)
CN	coordination number
CP	coordination polyhedron
CW	Curie-Weiss behavior
D	diamagnetism
ht	high-temperature modification
MCW	modified Curie-Weiss behavior
R	rare-earth element
SG	space group
X	Group 16 element (S, Se)
<i>x, y, z</i>	fractional atomic coordinates (same as $x/a, y/b, z/c$)
Z	Group 14 element (Si, Ge, Sn)
Z	number of formula units per unit cell
α, β, γ	unit cell angles (degrees)

REFERENCES

- Bera, T.K., Iyer, R.G., Malliakas, C.D., Kanatzidis, M.G., 2007. $\text{Eu}_3(\text{AsS}_4)_2$ and $\text{A}_x\text{Eu}_{3-y}\text{As}_{5-z}\text{S}_{10}$ (A=Li, Na): compounds with simple and complex thioarsenate building blocks. *Inorg. Chem.* 46, 8466.
- Daszkiewicz, M., Strok, O.M., Gulay, L.D., Kaczorowski, D., 2010. Crystal structure of $\text{R}_3\text{Ge}_{1+x}\text{Se}_7$ (R=La, Ce, Pr, Sm, Gd and Tb, $x=0.43\text{--}0.49$) and magnetic properties of $\text{Ce}_3\text{Ge}_{1.47}\text{Se}_7$. *J. Alloys Compd.* 508, 258.
- Daszkiewicz, M., Marchuk, O.V., Gulay, L.D., Kaczorowski, D., 2012. Crystal structures and magnetic properties of $\text{R}_2\text{PbSi}_2\text{S}_8$ (R=Y, Ce, Pr, Nd, Sm, Gd, Tb, Dy, Ho), $\text{R}_2\text{PbSi}_2\text{Se}_8$ (R=La, Ce, Pr, Nd, Sm, Gd) and $\text{R}_2\text{PbGe}_2\text{S}_8$ (R=Ce, Pr) compounds. *J. Alloys Compd.* 519, 85.
- Gulay, L.D., Daszkiewicz, M., 2011. Ternary and quaternary chalcogenides of Si, Ge, Sn, Pb, and In. In: Gschneidner Jr., K.A., Bünzli, J.-C.G., Pecharsky, V.K. (Eds.), *Handbook on the Physics and Chemistry of Rare Earths*. vol. 41. North-Holland Elsevier, AE Amsterdam, The Netherlands, pp. 157–273 (ch. 250).
- Gulay, L.D., Marchuk, O.V., 2010. Phase equilibria in the $\text{Sm}(\text{Ho})_2\text{S}_3\text{--PbS--SnS}_2$ systems at 770 K. *Visnyk Volyn University, Khim. Nauky* 16, 50 (in Ukrainian).
- Gulay, L.D., Ruda, I.P., Marchuk, O.V., Olekseyuk, I.D., 2008. Crystal structures of the $\text{R}_2\text{Pb}_3\text{Sn}_3\text{S}_{12}$ (R=La, Ce, Pr, Nd, Sm, Gd, Tb, Dy, Ho, Er and Tm) compounds. *J. Alloys Compd.* 457, 204.
- Gulay, L.D., Daszkiewicz, M., Ruda, I.P., Marchuk, O.V., 2010. $\text{La}_2\text{Pb}(\text{SiS}_4)_2$. *Acta Crystallogr.* C66, i19.
- Iglesias, J.E., Steinfink, H., 1973. Ternary chalcogenide compounds AB_2X_4 : the crystal structure of SiPb_2S_4 and SiPb_2Se_4 . *J. Solid State Chem.* 6, 93.
- Jaulmes, S., 1974. Structure cristalline du sulfure d'Étain et de lanthane, La_2SnS_5 . *Acta Crystallogr.* B30, 2283.
- Jaulmes, S., Julien-Pouzol, M., 1977a. Structure cristalline du sulfure mixte d'euporium et d'étain $\text{Eu}_5\text{Sn}_3\text{S}_{12}$. *Acta Crystallogr.* B33, 1191.
- Jaulmes, S., Julien-Pouzol, M., 1977b. Sulfure d'euporium et d'étain $\text{Eu}_3\text{Sn}_2\text{S}_7$. *Acta Crystallogr.* B33, 3898.

- Jumas, J.C., Ribes, M., Philippot, E., Maurin, V., 1972. Chimie minérale. Sur le système SnS_2 — PbS . Structure cristalline de $PbSn_3S_3$. C.R. Seances Acad. Sci. (Ser. C) 275, 269–272.
- Kozlynets, V.S., Marchuk, O.V., Olekseyuk, I.D., Gulay, L.D., 2014. Phase equilibria in the Er_2S_3 — PbS — SiS_2 system at 770 K. In: Trokhimchuck, P. (Ed.), Proc. Seventh Int. Workshop “Relaxed, Nonlinear and Acoustic Optical Processes and Materials”, Lutsk, pp. 153–157 (in Ukrainian).
- Krebs, H., Langner, D., 1964. Über struktur und eigenschaften der halbmetalle. XVI. Mischkristallsysteme zwischen halbleitenden chalcogeniden der vierten hauptgruppe. II. Z. Anorg. Allg. Chem. 334, 37.
- Krebs, H., Grün, K., Kallen, D., 1961. Über struktur und eigenschaften der halbmetalle. XIV. Mischkristallsysteme zwischen halbleitenden chalcogeniden der vierten hauptgruppe. Z. Anorg. Allg. Chem. 312, 307.
- Marchuk, O.V., Gulay, L.D., 2012. Phase equilibria in the La_2X_3 — PbX — SiX_2 (X=S, Se) systems at 770 K. Visnyk Volyn University, Khim. Nauky 17, 93 (in Ukrainian).
- Marchuk, O.V., Ruda, I.P., Gulay, L.D., Olekseyuk, I.D., 2007. Investigation of the Y_2S_3 — PbS — SnS_2 system at 770 K. Pol. J. Chem. 81, 425.
- Marchuk, O.V., Ruda, I.P., Gulay, L.D., Olekseyuk, I.D., 2008. Phase equilibria in the $Y_2S(Se)_3$ — $PbS(Se)$ — $SiS(Se)_2$ systems at 770 K. Visnyk Volyn University, Khim. Nauky 13, 24 (in Ukrainian).
- Marchuk, O.V., Ruda, I.P., Gulay, L.D., 2010. Phase equilibria and crystal structure of the compounds in quaternary La_2X_3 — PbX — $D^{IV}X_2$ (D^{IV} —Si, Ge, Sn; X—S, Se) systems. In: Davydyuck, G. (Ed.). Proc. Fifth Int. Workshop “Relaxed, Nonlinear and Acoustic Optical Processes; Materials—Growth and Optical Properties”. Volyn’ University Press, Lutsk (in Ukrainian).
- Marchuk, O.V., Gulay, L.D., Blashko, N.M., 2012. Phase equilibria in the PbS — GeS_2 — Pr_2S_3 system at 770 K. In: Trokhimchuck, P. (Ed.). Proc. Sixth Int. Workshop “Relaxed, Nonlinear and Acoustic Optical Processes and Materials”, Lutsk, pp. 158–160 (in Ukrainian).
- Marchuk, O.V., Gulay, L.D., Shemet, V.Ya., 2014. Phase equilibria in the PbS — Pr_2S_3 — SnS_2 system at 770 K. Scientific notes. - Luck: LNTU 47, 99 (in Ukrainian).
- Michelet, A., Mazurier, A., Collin, G., Laruelle, P., Flahaut, J., 1975. Etude structurale des systèmes Ln_2S_3 — GeS_2 . J. Solid State Chem. 13, 65.
- Olekseyuk, I.D., Gulay, L.D., Marchuk, O.V., 2009. Isothermal sections of the $Sm(Er)_2Se_3$ — $PbSe$ — $GeSe_2$ systems at 770 K and crystal structure of the $Sm_{1.32}Pb_{1.68}Ge_{1.67}Se_7$ compound. Visnyk Volyn University, Khim. Nauky 24, 14 (in Ukrainian).
- Poduska, K.M., Cario, L., DiSalvo, F.J., Min, K., Halasyamani, P.S., 2002. Structural studies of a cubic, high-temperature (α) polymorph of Pb_2GeS_4 and the isostructural $Pb_{2-x}Sn_xGe_{4-y}Se_y$ solid solution. J. Alloys Compd. 335, 105.
- Ribes, M., Olivier-Fourcade, J., Philippot, E., Maurin, M., 1974. Structure cristalline d’un thiogermanate de plomb à chaînes infinies $(PbGeS_3)_n$. Acta Crystallogr. B30, 1391.
- Rolies, M.M., De Ranter, C.J., 1978. A new investigation of ammonium cadmium chloride. Acta Crystallogr. B34, 3057.
- Ruda, I.P., Marchuk, O.V., Gulay, L.D., Olekseyuk, I.D., 2007. Crystal structure of the $R_{1.32}Pb_{1.68}Ge_{1.67}Se_7$ (R=Y, La, Ce, Pr, Nd, Sm, Gd, Tb, Dy and Ho) compounds. Visnyk Volyn University, Khim. Nauky 13, 7 (in Ukrainian).
- Ruda, I.P., Marchuk, O.V., Gulay, L.D., Olekseyuk, I.D., 2008. Phase equilibria and crystal structure of the compounds in quaternary Y_2X_3 — PbX — $D^{IV}X_2$ (D^{IV} —Si, Ge, Sn; X—S, Se) systems. In: Davydyuck, G. (Ed.). Proc. Fourth Int. Workshop “Relaxed, Nonlinear and Acoustic Optical Processes; Materials—Growth and Optical Properties”. Volyn’ University Press “Vezha”, Lutsk, pp. 72–76 (in Ukrainian).

- Shannon, R.D., 1976. Revised effective ionic radii and systematic studies of interatomic distances in halides and chalcogenides. *Acta Crystallogr.* A32, 751.
- Straumanis, M., Ieviš, A., 1936. Die gitterkonstanten des NaCl und des steinsalzes. *Z. Phys.* 102, 353.
- Susa, K., Steinfink, H., 1971. Ternary sulfide compounds AB_2X_4 : the crystal structures of $GePb_2S_4$ and $SnBa_2S_4$. *J. Solid State Chem.* 3, 75.
- Woolley, J.C., Berolo, O., 1968. Phase studies of the $Pb_{1-x}Sn_xSe$ alloys. *Mater. Res. Bull.* 3, 445.
- Zachariasen, W.H., 1932. The crystal lattice of germano sulphide, GeS . *Phys. Rev.* 40, 917.

Chapter 276

Hybrid Materials of the f-Elements Part II: The Uranyl Cation

Robert G. Surbella III and Christopher L. Cahill¹

Department of Chemistry, The George Washington University, Washington, District of Columbia, USA

¹*Corresponding author: e-mail: cahill@gwu.edu*

Chapter Outline

1 Introduction	164	7.2 Coordinating Species: N-Donor “Capping” Ligands	208
2 Uranyl Crystal Chemistry	165	7.3 Noncoordinating Species: Structure Influencing Guests	216
3 Inorganic Uranyl Phases	167	8 Heterometallic Uranyl Hybrid Materials	222
4 Introduction to Hybrid Materials and Coordination Polymers	170	8.1 Homofunctional Ligands	223
5 Common Ligands Arranged by Functional Group	172	8.2 Heterofunctional Ligands	225
5.1 Carboxylates	172	8.3 Metalloligands	233
5.2 Phosphonates	185	8.4 Postsynthetic Modification	236
5.3 Carboxyphosphonates	192	9 A Hybrid Approach to Uranyl-Containing Coordination Polymer Syntheses	239
5.4 Sulfonates	195	9.1 Carboxyphosphonates Revisited	240
6 Chelating Ligands	199	9.2 Noncoordinating Nitrogen Donor Species	241
6.1 Heterofunctional Ligands: Nitrogen and Oxygen Donors	200	10 Combining Direct Coordination and Supramolecular Chemistry	243
6.2 Heterofunctional Ligands: Sulfonate and Carboxylate Donors	204	10.1 Assembly with 4-Halobenzoic Acid Ligands	245
7 Uranyl Hybrid Materials Containing Ancillary Organic Species	205		
7.1 Coordinating Species: Heterofunctional N-Donor and O-Donor Ligands	205		

10.2 Chelidamic Acid Derivatives for Hybrid Assembly	248	11.3 High Anion Media: A General Approach	259
10.3 Summary	251	12 Expanding the Supramolecular Strategy: Accessing the “yl” Oxygens	261
11 Introducing Control: Restricting Uranyl Speciation in Aqueous Media	251	13 Concluding Remarks	266
11.1 High Halide Media	252	Acknowledgments	266
11.2 Intermediate Concentrations of Halide Media	257	References	268

1 INTRODUCTION

Efforts to synthesize and develop structure–property relationships within crystalline, uranyl ($[\text{UO}_2]^{2+}$) containing hybrid materials have expanded dramatically over the past 10–15 years. The motivations for these studies are many and include exploratory syntheses with relevance to the nuclear fuel cycle, particularly with respect to spent fuel stewardship, separations and reprocessing, as well as transport in the environment. Crystalline coordination polymers (CPs) in general provide a forum for (indirect) study of these issues as there exist a number of parallels between synthesis conditions and either environmental or industrial settings. For example, the speciation profile of the uranyl cation under mild hydro- or solvothermal conditions is of interest to the materials chemist as knowledge thereof can direct synthesis efforts and promote desirable or targeted compositions. This same information is of course key for appreciating uranyl interaction with environmental species such as mineral surfaces, organic molecules, and inorganic anions.

The following section is an overview of recent developments in the synthesis and crystal chemistry of uranyl-containing crystalline hybrid materials. It is in many ways a continuation of our previous chapter in this series (Carter and Cahill, 2015b) wherein we presented a similar treatment of Ln(III)-containing hybrids. As with our Ln(III) presentation, this chapter will also be admittedly selfish in that we intend to highlight a number of examples from our group that illustrate either design principles or themes that we have developed over the years. We intend to promote a theme of structural diversity, stemming from a diverse aqueous speciation profile coupled with a nearly limitless selection of organic ligands. We will then (selectively!) present examples from other groups that are (mostly!) consistent with these themes. Given the frequency with which new uranyl materials are being published, we regret that this cannot be a comprehensive review, yet hope to be at least illustrative and sufficiently inclusive to serve as a firm foundation and/or introduction to the subject matter. Moreover, we will be limiting our discussion to crystalline hybrid materials—that is, those which have had their crystal structures determined by X-ray diffraction. We will define “hybrid” more rigorously within, yet at this juncture, one may consider such materials to be

composed of inorganic and organic components interacting on a molecular level. Finally, this presentation is rather “materials-centric” in that we are simply unable to attempt any treatment of some of the outstanding developments in the coordination chemistry of the uranyl cation, nor are we in a position to address some of the exciting chemistry of other oxidation states (Arnold, 2012; Ephritikhine, 2006, 2013; Hayton, 2013; Liddle, 2015; Qiu and Burns, 2012; Wang and Chen, 2011).

2 URANYL CRYSTAL CHEMISTRY

The most common and environmentally relevant oxidation state of uranium is U(VI), which occurs almost exclusively as the linear triatomic UO_2^{2+} ion (Brandel et al., 1996; Ephritikhine, 2006). The $\angle \text{O—U—O}$ bond angle tends to vary from 178° to 180° , and the average $\text{U—O}_{\text{axial}}$ bond lengths are approximately 1.8 Å in solid-state compounds. As such, the axial oxygen atoms (also known as the “yl” oxygen atoms) tend to be largely terminal and subsequent coordination typically occurs in the equatorial plane (Burns et al., 1997). This gives rise to three primary building units (PBUs): square, pentagonal, and hexagonal bipyramidal (Fig. 1). Whereas a full molecular orbital treatment of the uranyl bond and bond valence consideration (equatorial and axial ligand donation) is beyond the scope of this contribution, readers are encouraged to look to the following references (Burns et al., 1997; Denning, 2007; Natrajan, 2012).

The uranyl cation is subject to hydrolysis under aqueous conditions as shown in Eq. (1) (Andrews and Cahill, 2012a; Grenthe et al., 2004; Knope and Soderholm, 2013; Loiseau et al., 2014). The net result is the formation of oligomeric species (or secondary building units, SBUs) via the formation of oxo or hydroxo bridges as a function of temperature, concentration, and pH; Scheme 1 presents this as a function of pH only (Loiseau et al., 2014). Of note is the tendency toward polynuclear species with increasing pH, a

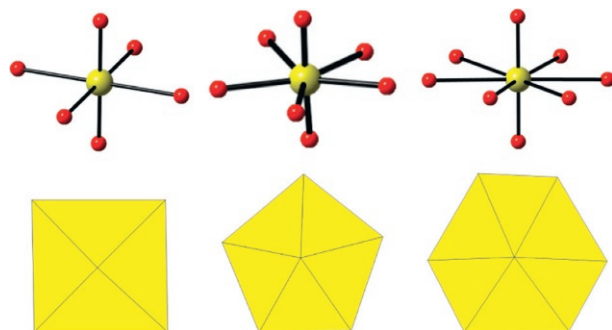
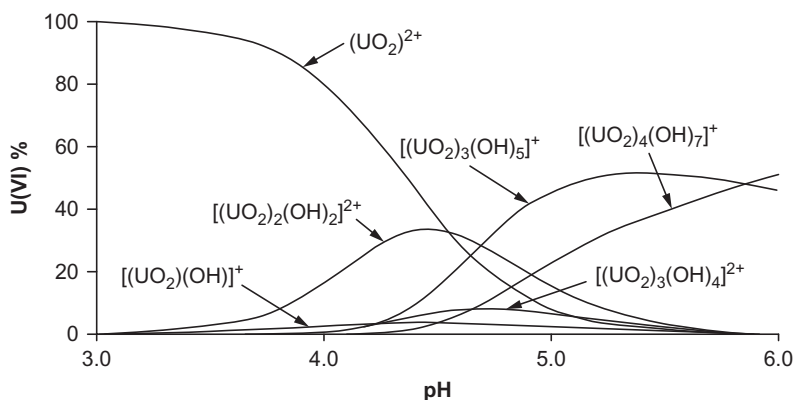
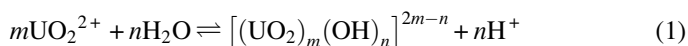


FIGURE 1 Left to right: A ball-and-stick and polyhedral representation of the three primary uranyl building units—square, pentagonal, and hexagonal bipyramids. The yellow (light gray in the print version) polyhedra represent the U(VI) metal center and are oriented such that they are viewed down the uranyl bond.



SCHEME 1 Uranyl speciation in aqueous media as a function of pH. Reprinted with permission from Loiseau *et al.* (2014). Copyright 2014 Elsevier.

theme that we will return to throughout this chapter when appropriate. Moreover, low concentrations (<1 mmol/L) tend to favor monomeric species and higher temperatures tend to promote oligomerization. Moreover still, a strict correlation of solution phase speciation and manifestation thereof in the solid state is indeed rather speculative. That said, one may use these observations as a loose guideline that are perhaps applied more successfully in retrospect. We will of course describe SBUs in more detail as they are presented, yet for now, we offer Fig. 2 as foreshadowing for the types of building units we will encounter in crystalline uranyl hybrids:



Speciation resulting from hydrolysis is of course of interest to a range of scientists, yet for the synthetic chemist, the intrigue stems from the fact that there is a range of possible BUs from which to construct an extended solid-state compound. This is a bit of a double-edged sword as a diverse range of building blocks can of course lead to a wide variety of crystal structures, yet as we will see, predicting which BU will manifest in the solid state is indeed a challenge and is often a complex function of reaction conditions, coordination preferences, and ligand sterics.

Going forward in this manuscript, we will describe the structural features of various uranyl-containing CPs and where appropriate (or possible), draw conclusions that correlate the observed BUs with synthetic reaction conditions. Given this agenda, we start with a brief treatment of UO_2^{2+} inorganic species (e.g., minerals) to highlight coordination chemistry preferences. One will note a natural progression from purely inorganic oxyanion containing compounds to analogous hybrids, as one replaces an inorganic building unit (e.g., CO_3^{2-} , SO_4^{2-} , or PO_4^{3-}) with an organic analog thereof (e.g., R-CO_2^- , R-SO_4^{2-} , R-PO_3^{2-}).

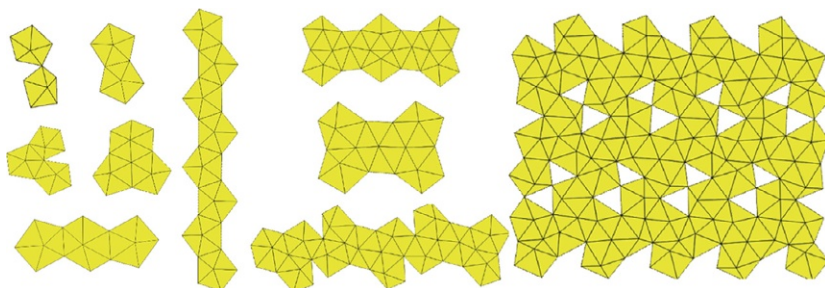


FIGURE 2 A representation of several polynuclear secondary building units resulting from uranyl hydrolysis and oxo/hydroxo bridge formation.

3 INORGANIC URANYL PHASES

Despite the nature of this chapter being restricted to hybrid materials, it is worth a brief departure to mineral phases to introduce a few concepts, namely some basic uranyl crystal chemistry, but also the affinity of various inorganic anions for $[\text{UO}_2]^{2+}$. The latter will serve as an inorganic foundation for the choices of functional groups going forward.

Naturally occurring uranyl mineral phases typically crystallize as hydroxide and oxide-bridged species that commonly give rise to sheet, chain, and to a lesser extent framework and cluster-type structural topologies (Burns, 2005; Burns et al., 1996, 1997). These inorganic oxide compounds dominate the uranyl mineral landscape as the rather hard $[\text{UO}_2]^{2+}$ has a strong tendency to coordinate anionic oxygen-rich donor species such as carbonate (CO_3^{2-}) (Hughes and Burns, 2003; Hughes Kubatko and Burns, 2004; Kubatko et al., 2005; Li and Burns, 2001), phosphate (PO_4^{3-}) (Burns et al., 2004; Locock and Burns, 2002; Locock et al., 2004), and sulfate (SO_4^{2-}) (Burns, 2001; Burns et al., 2003; Ling et al., 2010b) anions. A quick glance at the structural topology of three common uranyl mineral phases, namely bayleyite, autunite, and zippelite (each containing the carbonate, phosphate, or sulfate oxyanion, respectively), provides a glimpse into the diverse array of possible PBUs and SBUs present in the crystalline solid state (Figs. 3–5). The structure of bayleyite, $\text{Mg}_2[\text{UO}_2(\text{CO}_3)_3] \cdot (\text{H}_2\text{O})_{18}$, consists of hexagonal uranyl monomers that are coordinated by three bidentate carbonate anions and charge balanced by $\text{Mg}(\text{H}_2\text{O})_6^{2+}$ octahedra (Fig. 3) (Mayer and Mereiter, 1986). Water molecules occupy the spaces between the two isolated metal-centered PBUs and facilitate an elaborate hydrogen bonding network that constitutes the structural connectivity, as the carbonate ligands are terminating.

In contrast to the “molecular” structure of bayleyite, the structure of autunite, $\text{Ca}_2[(\text{UO}_2)_2(\text{PO}_4)] \cdot 11\text{H}_2\text{O}$, consists of 2D sheets that are composed of $[\text{UO}_2(\text{PO}_4)]^-$ building units (Fig. 4); each phosphate anion coordinates to a total of four uranyl cations in bridging bidentate fashions (Locock Andrew and Burns Peter, 2003). The resulting anionic sheets stack to form layers that

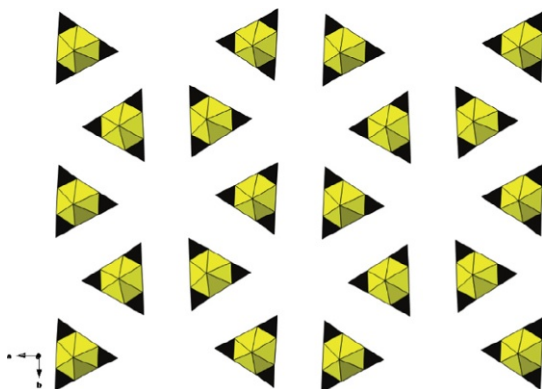


FIGURE 3 The structure of bayleyite features hexagonal bipyramidal uranyl monomers coordinated by three carbonate (polyhedrons) anions to form a molecular structure. The water molecules and magnesium cations are omitted for clarity.

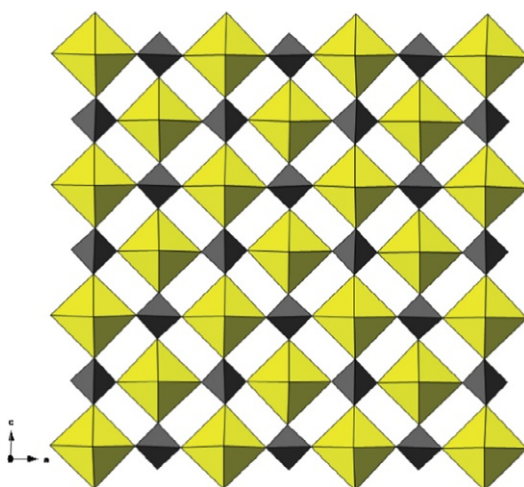


FIGURE 4 The structure of autunite features square bipyramidal uranyl monomers coordinated by four phosphate anions (polyhedrons) to form sheets. The water molecules and calcium cations are omitted for clarity.

are occupied by charge-balancing hydrated calcium cations and water molecules. The difference between the dimensionality of these two structures, “molecular” (bayleyite) and layered (autunite), is mentioned in order to identify that changes in the geometry of the uranyl building unit and/or oxyanion coordination preferences can influence resulting structural topologies.

When one then considers the structure of zippelite, $\text{K}[(\text{UO}_2)_4\text{O}_2(\text{SO}_4)_2(\text{OH})_2](\text{H}_2\text{O})_4$, one will notice pentagonal bipyramidal uranyl polyhedra

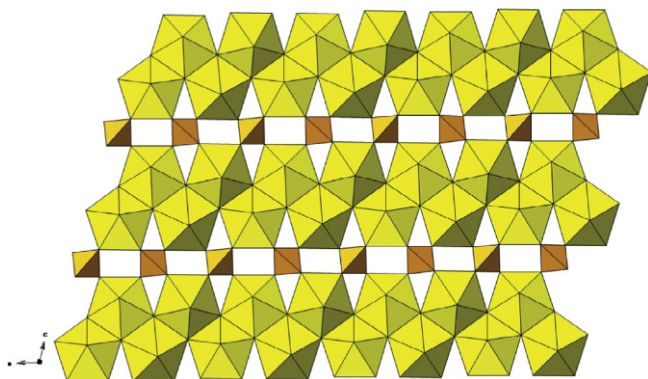


FIGURE 5 The structure of zippelite features chains of pentagonal bipyramidal uranyl building units that form sheets via sulfate linkages (orange (gray in the print version) polyhedra). The water molecules and potassium cations are omitted for clarity.

(PBUs) that are oxo and hydroxo bridged to form chains (SBUs), which are then linked together via monodentate bridging sulfate anions to form sheets (Fig. 5) (Plášil et al., 2011). This is our first example of many materials that contain oligomerized uranyl species. Moreover, the layered topology is particularly common among mineral structures, and readers are encouraged to examine the comprehensive structural review of inorganic uranyl phases (Burns, 2005).

Finally, one may consider the structure of agrinierite, $K_2(\text{Ca}_{0.65}\text{Sr}_{0.35})[(\text{UO}_2)_3\text{O}_3(\text{OH})_2]_2 \cdot 5\text{H}_2\text{O}$, which consists of anionic sheets that stack to form layers, between which reside water molecules and charge-balancing cations (Fig. 6) (Cahill and Burns, 2000). In this example, the sheets are formed exclusively of edge-sharing uranyl polyhedra and perhaps represent an “extreme” example of uranyl hydrolysis considering the extent of the oligomerization. The topology of the sheets, in terms of the uranyl building unit coordination and arrangement, is not uncommon in inorganic and mineral structures such as $\alpha\text{-U}_3\text{O}_8$, billietite, protasite, and becquerelite.

Here, we now have three examples of an anionic sheet topology (zippelite, autunite, and agrinierite) that each contain three different types of PBUs (square, pentagonal, and hexagonal bipyramids) as well as different ranges of oligomerization. The theme that we wish to begin to develop is that the resulting topologies of uranyl materials are influenced by both the local coordination geometry and degree to which the uranyl BUs are oligomerized. Moreover, we note that there is no additional coordination to the axial “yl” oxygen atoms in these structures, and as a consequence, the structures are at most two-dimensional. For a more thorough treatment of the topological diversity that stems from the unique geometry of the uranyl cation, combined with its susceptibility to undergo hydrolysis, in naturally occurring mineral

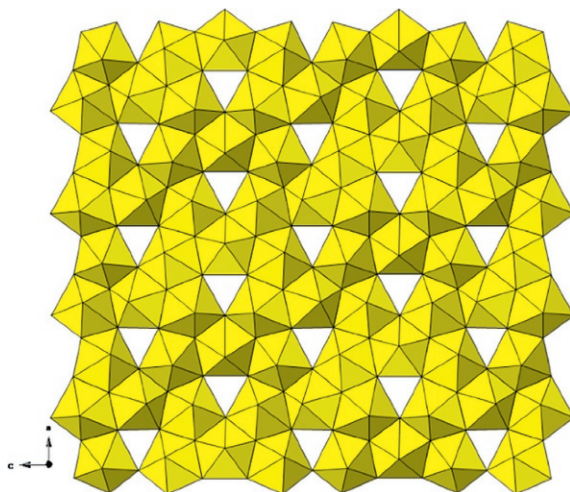


FIGURE 6 Edge-sharing uranyl polyhedra form anionic sheets in the structure of agrinierite. The interlayer water molecules and potassium, calcium, and strontium cations are omitted for clarity.

forms, the reader is directed to the following reviews: Burns (1999, 2007) and Knope and Soderholm (2013).

The structural diversity of uranyl compounds is just as rich in materials containing tetrahedral oxyanions (TO_4)—arsenates (AsO_4^{3-}) (Liu et al., 2014; Locock, 2007), chromates (CrO_4^{2-}) (Krivovichev and Burns, 2003b; Krivovichev Sergey and Burns Peter, 2003; Siidra et al., 2012), selenates (SeO_4^{2-}) (Krivovichev et al., 2009; Krivovichev Sergey et al., 2009; Ling et al., 2009; Wylie and Burns, 2012), molybdates (MoO_4^{2-}) (Krivovichev and Burns, 2003a), germanates (GeO_4^{4-}) (Lin and Lii, 2008; Ling et al., 2010a), silicates (SiO_4^{4-}) (Huang et al., 2003; Sureda et al., 2011), and vanadates (VO_4^{3-}) (Jouffret et al., 2010; Rivenet et al., 2007)—as the flexible An—O—T bonds give rise to various topologies and geometries (Krivovichev, 2010; Krivovichev et al., 2013; Nyman and Burns, 2012). As the crystal chemistry of the uranyl cation in both mineral and purely (inorganic) synthetic systems has been reviewed extensively, those topics will not be discussed in detail herein. There are of course opportunities, however, to draw structural parallels and highlight themes that transcend naturally occurring uranyl mineral phases within the context of the crystalline hybrid materials discussed here.

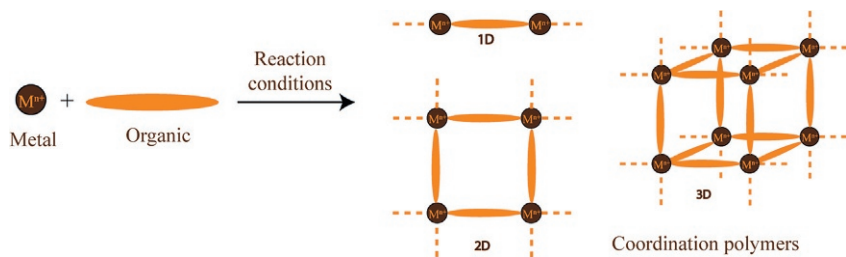
4 INTRODUCTION TO HYBRID MATERIALS AND COORDINATION POLYMERS

Some definitions are in order as we move toward our discussion of hybrid materials and CPs (and indeed metal–organic frameworks or

“MOFs”). Whereas these definitions were presented in our earlier Ln(III) contribution, we reiterate now in order to clearly identify the varieties of material types that will be covered in this contribution. Put simply, a hybrid material consists of at least two moieties (inorganic and organic) blended together on the molecular scale (Kickelbick, 2007). This definition covers both crystalline and amorphous phases, yet we will only concentrate on the former as crystallographic comparison will be the driver in this text. Kickelbick defines two classes of hybrid materials, the first of which to be discussed, class II, is identified by highly directional covalent or ionic-covalent chemical interactions that facilitate chemical bonds (Kickelbick, 2007). Of these materials, those which are crystalline constructed of “repeating coordination entities extending in 1, 2, or 3 dimensions” will be referred to as CPs (Batten et al., 2013). We will give a full treatment and definition to those uranyl-containing hybrid materials belonging to class I, those which are constructed via noncovalent interactions (NCIs) (e.g., hydrogen or halogen bonding (XB), etc.) at the conclusion of this chapter as they represent more recent development in the study of uranyl materials. That said, we will also highlight examples where both covalent *and* noncovalent interactions contribute to assembly.

The synthetic strategy for preparing uranyl-containing CPs relies upon strong covalent metal–ligand bonding, as metal ion “nodes” (mono or polynuclear) are connected via organic “linker” ligands to form extended structures (Scheme 2). Owing to the presence of the terminal oxygen atoms of the uranyl cation, dimensionality is often limited and 1D and 2D CPs are by far the most prevalent. The use of a flexible ligand, however, or sometimes uranyl speciation or secondary metal centers can lead to the formation of 3D architectures, some of which have accessible void spaces. Materials with 3D structures that contain accessible void spaces are effectively a subset of CPs and will be referred to as MOFs (Batten et al., 2013). The often mis- and overused term of MOFs will be employed judiciously.

The chemistry of CPs and MOFs of the 5f-elements is arguably less mature than those containing transition elements. Transition metal MOFs in particular have been developed to explore applications in a number of areas



SCHEME 2 A typical, nodal representation of coordination polymers. Metal ions (spheres) are linked together to form infinite 1D, 2D, or 3D networks via an organic linkers (orange (gray color in the print version) lines).

such as gas storage (Bae and Snurr, 2011; Li et al., 2009; Suh et al., 2011; Sumida et al., 2011), chemical sensing (Chen et al., 2010; Kreno et al., 2011), and catalysis (Dhakshinamoorthy et al., 2011, 2012; Lee et al., 2009; Wang et al., 2012; Yoon et al., 2011), among others (Allendorf et al., 2009, 2011; Furukawa et al., 2013; Meek et al., 2011; Shekha et al., 2011; Wang et al., 2013). Although the pursuit of transition metal MOFs and CPs may be driven by application, the motivation for the synthesis of 5f-element (in particular uranyl) containing CPs and MOFs is admittedly more exploratory and tangentially related to spent fuel stewardship and environmental issues. Over the past several years, synthetic efforts have expanded remarkably and have resulted in the emergence of new structure types and indeed function (Andrews and Cahill, 2012a; Baker, 2012; Burns, 2011; Burns et al., 2010; Fortier and Hayton, 2010; Hayton, 2010; Wang and Chen, 2011; Wang et al., 2011; Wu et al., 2012). We will attempt to focus our own discussion on the structural diversity of uranyl-containing hybrid materials that arises from the combined effects of uranyl speciation/oligomerization and ligand selection. These effects, while vital assets to exploratory studies, often prohibit the ability to implement a single synthetic philosophy that allows for the systematic assembly of uranyl-containing CPs with desired topologies. We will develop our presentation by using selected examples of uranyl CPs and MOFs (organized by functional group) to illustrate the structural diversity that can arise even under similar synthetic conditions. Moreover, we will highlight, albeit sparingly, structure–property relationships as appropriate.

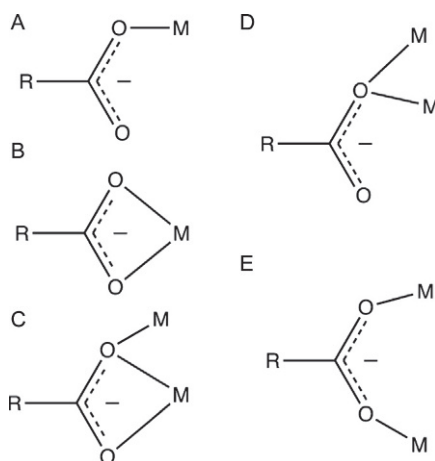
5 COMMON LIGANDS ARRANGED BY FUNCTIONAL GROUP

5.1 Carboxylates

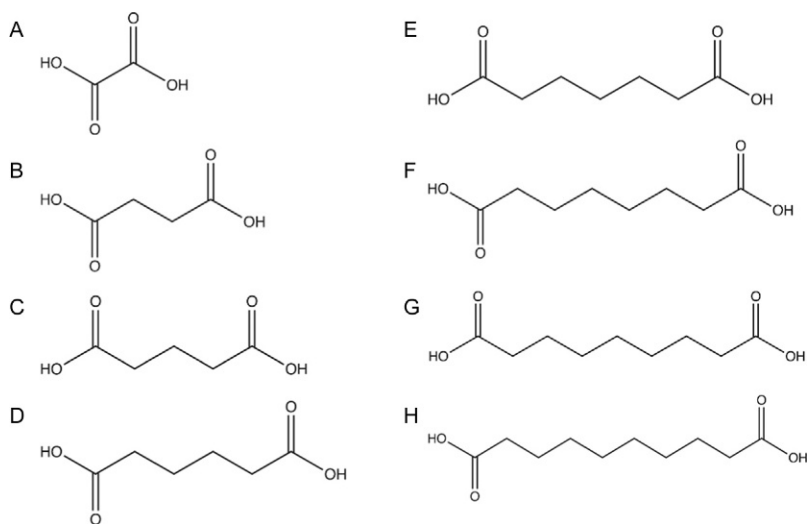
Carboxylate-functionalized organic ligands are perhaps the most widely used linkers in uranyl CP synthesis, owing to their tendency to coordinate strongly to the uranyl cation (Andrews and Cahill, 2012a), as well as their diversity of conformations and environmental relevance. The carboxylate functional group can adopt a number of coordination modes, such as mono- and bidentate, and can chelate a single metal ion or bridge multiple metal ions together (Scheme 3). The combined coordination strength and possible geometric conformations of the carboxylate group have led to a wealth of compounds that have been reviewed extensively (Leciejewicz et al., 1995; Loiseau et al., 2014). As such, our contribution will focus on examples that highlight topological themes within the context of uranyl BU diversity as a function of a fixed organic species (aliphatic, aromatic, and polycarboxylic acids) (Scheme 4).

5.1.1 Aliphatic Dicarboxylic Acids

Adipic acid ($C_6H_{10}O_4$) and uranyl nitrate salts were combined hydrothermally to produce both compounds **1**, $[UO_2(C_6H_8O_4)(H_2O)_2]$, and **2**,



SCHEME 3 Various coordination modes that the carboxylate functional group has been observed to coordinate the uranyl cation. (A) Monodentate (η^1) (B) Bidentate (η^2) (C) Bridging Tridentate ($\mu_2\text{-}\eta^2 \eta^1$) (D) Bridging Bidentate ($\mu_2\text{-}\eta^1 \eta^1$) (E) Bridging Bidentate ($\mu_2\text{-}\eta^1 \eta^1$).



SCHEME 4 The aliphatic dicarboxylic acid molecules referenced in this manuscript: (A) oxalic acid, (B) succinic acid, (C) glutaric acid, (D) adipic acid, (E) pimelic acid, (F) suberic acid, (G) azelaic acid, (H) sebacic acid.

$[(\text{UO}_2)_2(\text{C}_6\text{H}_8\text{O}_4)_2]$ (Borkowski and Cahill, 2003). The structure of compound **1** features PBUs (hexagonal bipyramids) that are formed by the coordination of two water molecules and two bidentate adipic acid linkers; the organic carboxylates give rise to chains (Fig. 7). In **2**, dimers constructed from edge-shared pentagonal bipyramidal uranyl PBUs coordinated by three adipate

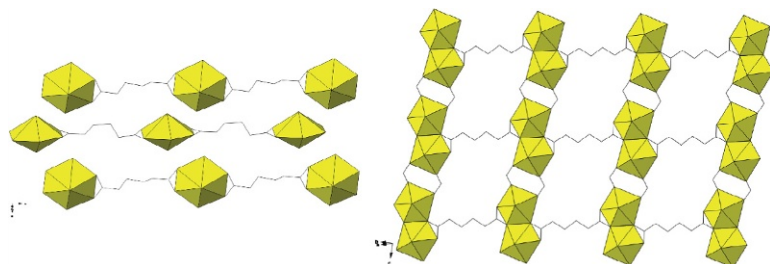


FIGURE 7 Left: Compound **1** consists of hexagonal bipyramidal uranyl building units that are linked together by adipic acid molecules to form chains. Right: Compound **2** consists of uranyl dimers that are linked together via adipic acid molecules to form sheets. The hydrogen atoms are omitted here for clarity and throughout the remainder of this text.

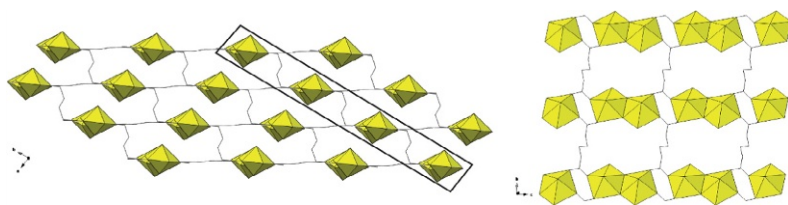


FIGURE 8 Left: The 3D structure of **2** contains voids that are created by the linking (outlined) of adjacent sheets via bridging bidentate adipate ligands. Right: A cross section of the 3D structure (outlined on the left) is shown to highlight the coordination between the adjacent sheets.

ligands, two of which via bridging bidentate and one that is bidentate. The bridging bidentate adipate ligands function to link the dimers into chains (that propagate parallel to one another), whereas those that coordinate in a bidentate fashion connect adjacent chains into sheets (Fig. 7). The bridging bidentate ligands link adjacent sheets together to form a 3D MOF with channels that propagate along the [001] directions (Fig. 8).

Looking beyond the interesting, yet straightforward coordination chemistry featured in **1** and **2** allows one to begin the discussion regarding the factors that influence uranyl BU formation and ultimately, inclusion into the solid state. The synthetic conditions used to prepare **1** and **2** were nearly identical, yet two different types of uranyl BUs crystallized. The key difference in reaction conditions, however, was a 14-fold increase in UO_2^{2+} concentration used in the synthesis of **2**. If we recall the equation used to describe uranyl hydrolysis (Eq. 1), a higher concentration of dissolved uranyl in solution should promote oligomerization. In this case, it appears that there is a clear correlation between aqueous uranyl speciation and the type of BU observed in the crystalline solid state.

Similar synthetic conditions as those that led to the formation of **2** were used in synthesis of compound **3**, $[\text{UO}_2(\text{C}_5\text{H}_6\text{O}_4)]$ (Borkowski and Cahill, 2005). Pentagonal bipyramidal uranyl BUs edge-share to form dimers ($[(\text{UO}_2)_2\text{O}_8]$) that are coordinated by a total of six glutaric acid linkers (two bidentate and

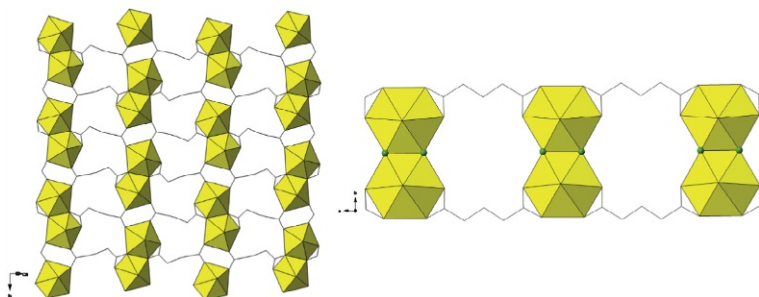


FIGURE 9 Left: Pentagonal bipyramidal dimers in **3** form 2D sheets via glutarate linkages. Right: The hexagonal bipyramidal dimers in **4** are joined together by glutarate ligands to form chains.

four bridging bidentate) to give rise to sheets (Fig. 9). The local coordination geometry of the uranyl SBUs in **3** is identical to that observed in **2**, yet the structure of **3** is only 2D. The apparent reason for this is that the glutaric acid linkers (compared to the longer adipic acid ligands featured in **2**) do not perform the same function of linking adjacent sheets into a 3D structure. In this case, the ligand is shown to influence the dimensionality of the resulting topology.

A second glutarate example, compound **4** $[\text{UO}_2\text{F}(\text{C}_5\text{H}_6\text{O}_4)] \cdot 2\text{H}_2\text{O}$, was crystallized out of a solution of uranyl nitrate and glutaric acid, postsolvothermal treatment (water, DMF, HF), that was allowed to evaporate slowly (Fig. 9) (Kim et al., 2003). The structure of **4** contains hexagonal bipyramidal $[(\text{UO}_2)_2\text{O}_6\text{F}_2]$ dimers that are coordinated by a total of four bidentate glutarate ligands to form chains. The presence of HF in the synthesis of **4** led to the inclusion of bridging fluoride ligands that connect the hexagonal bipyramidal BUs into dimers. The hexagonal geometry can only accommodate the coordination of two bidentate glutarate ligands, which results in the formation of a chain, and therefore does not support further bridging interactions akin to those in **3**. Thus, the overall dimensionality in **4** is limited to chains.

A brief review of the structures of compounds **2–4** reveals a decrease in overall dimensionality of the resulting topologies from $3\text{D} \rightarrow 1\text{D}$. The structures of **2** and **3** are constructed of similar uranyl SBUs (with the same local coordination) yet feature ligands of different lengths, as the shorter ligand (in **3**) appears to limit the dimensionality to 2D. Whereas aliphatic ligands of the same length are featured in **3** and **4**, the dimensionality is further decreased ($3 \rightarrow 4$) as the hexagonal uranyl building units in **4** support the formation of chains. This limited collection of structures is simply meant to demonstrate that subtle changes to reaction conditions or ligand properties can result in significant differences to the overall dimensionality of the CP.

Taking a step back from examining the use of intermediate in length aliphatic O-donor ligands to assemble uranyl CPs, one may expect a rather short

and nonflexible linker such as oxalic acid to yield a limited set of structure types. In reality, the opposite is true as a number of crystal structures containing a range of uranyl BUs and various topologies are known. For instance, compounds **5–7** are constructed of oxalate linkers and different uranyl BUs that give rise to structures of varying dimensionality.

Compound **5**, $[(\text{UO}_2)_2(\text{C}_2\text{O}_4)(\text{OH})_2(\text{H}_2\text{O})_2]$, was synthesized under hydrothermal conditions by combining U_3O_8 , oxalic acid, and water (Duvieubourg et al., 2005). The structure of **5** features hydroxide-bridged pentagonal bipyramidal uranyl dimers that are linked via oxalate ligands to form an overall 1D structure comprised of chains (Fig. 10). It is worth noting that by changing the reaction temperature and time (from 190 to 150 °C and 2 weeks to 1) yet keeping all other synthetic factors identical, respectively, compound **5** forms a polymorph (not depicted here) that consists of uranyl chains and is 2D overall (Duvieubourg et al., 2005). The hydrothermal treatment of uranyl and sodium nitrate salts in the presence of oxalic acid led to the formation of compound **6**, $[(\text{UO}_2)_2(\text{C}_2\text{O}_4)(\text{OH})(\text{H}_2\text{O})_2]\cdot\text{H}_2\text{O}$ (Duvieubourg et al., 2005). In **6**, point-sharing pentagonal bipyramidal uranyl dimers (via hydroxyl bridges) form tetramers that are linked into a puckered sheet-like network via bridging oxalate ligands (Fig. 10).

In a separate study, compound **7**, $\text{Rb}_2[(\text{UO}_2)_2(\text{C}_2\text{O}_4)_3]$, was formed from aqueous solution by heating a suspension of uranyl acetate and rubidium oxalate in the presence of acetic acid (Serezhkina et al., 2010). Here, the presence of acid likely induces the formation of pentagonal bipyramidal uranyl monomers, which are coordinated by a total of three oxalate ligands (Fig. 11). Two of the oxalate ligands coordinate in a bidentate fashion, whereas the third is monodentate. These coordination modes of the oxalate ligands give rise to a 3D CP that contains channels that run parallel to the [100] direction (Fig. 11). The framework is anionic and is charge balanced by rubidium cations that occupy the channels. These three selected examples (**5–7**) feature a range of uranyl building units and as a consequence of

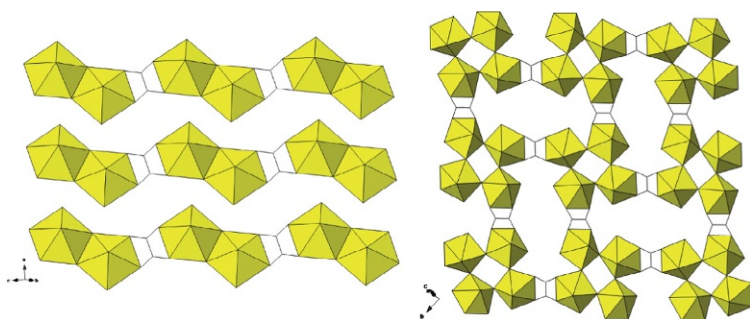


FIGURE 10 Left: Oxalate-bridged dimers form chains in the structure of **5**. Right: Oxalate-bridged link point-sharing SBUs in **6** form sheets.

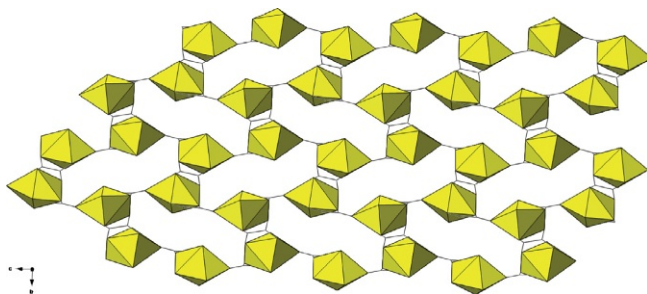


FIGURE 11 Pentagonal bipyramidal uranyl monomers in **7** are linked via oxalate ligands to form a 3D coordination polymer that contains channels. Rubidium cations occupy the channels, yet are omitted for clarity.

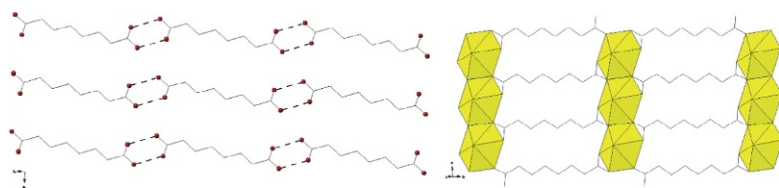


FIGURE 12 Left: Hydrogen bonding in the crystal structure of sebacic acid gives rise to sheets. Right: Uranyl SBUs are coordinated by sebacic acid linkers in **8** to form sheets.

speciation and the ligand coordination one-, two-, and three-dimensional coordination networks are accessible.

Aside from the influence of the ligand as a coordinating species that functions to link uranyl BUs into 1D, 2D, and 3D CPs, one must also consider the packing influence of the organic species. For instance, the crystal structure of suberic acid ($C_8H_{14}O_4$) consists of 2D sheets (Fig. 12) (Housty and Hospital, 1965), where each molecule aligns in an approximately linear fashion, via “head-to-head” $O-H\cdots O$ hydrogen bonds that stem between the carboxylate groups of neighboring molecules. Upon coordination with the uranyl cation, a similar sheet motif is observed (Fig. 12). Structure **8**, $UO_2(C_8H_{12}O_4)$, consists of edge-sharing hexagonal bipyramidal uranyl BUs, which form chains, that are in turn coordinated by bidentate sebacic linkers to form sheets (Borkowski and Cahill, 2006a). The sheet structures of both sebacic acid and **8** are very similar, and the role of the uranyl species is perhaps secondary as the organic ligand instead functions to influence structure. This effect is not entirely uncommon, especially among longer chain aliphatic species as the hydrophobic nature of these alkanes can have a strong influence over crystal packing (Thalladi et al., 2000).

The aliphatic dicarboxylic acid linker is arguably one of the simplest O-donor ligands that has been utilized in uranyl CP synthesis. Despite this, structural diversity is seemingly infinite when a collective look is taken over

the portfolio of uranyl/aliphatic CPs. Not only are a number of different structural topologies present (of different degrees of dimensionality), but they are constructed of a wide array of PBUs and SBUs. For more examples of structure types that we did not cover herein, we direct the reader to some of our past contributions utilizing longer chain aliphatics (C₇–C₁₀) (Borkowski and Cahill, 2006a) and those of varied length (C₃–C₁₀) which can be paired with either coordinating or structure influencing dipyriddy species (Borkowski and Cahill, 2006b; Kerr and Cahill, 2011). Provided in Table 1 is a summary of the crystal structures that resulted from the pairing of the aliphatic linkers with various dipyriddy species, some of which will be highlighted in subsequent sections of this contribution. The reader is also referred to several studies that further highlight the breadth of accessible structure types utilizing straight chain dicarboxylic acid linkers and the uranyl cation (Benetollo et al., 1979; Bombieri et al., 1980; Grigor'ev et al., 2005; Kim et al., 2003; Rojas et al., 1979; Thuéry, 2008b, 2011b).

5.1.2 Aromatic Carboxylic Acids

Aromatic mono- and poly-substituted carboxylic acids afford similar coordination modes (mono-bidentate and bridging) as the aliphatics, yet present new opportunities as the rigidity of the linker must be considered. Loiseau has explored and recently reviewed (Loiseau et al., 2014) the use of aromatic linkers in the synthesis of uranyl CPs and thus we proceed spartanly, as

TABLE 1 The Results of Two Studies Aimed at Assembly Of Uranyl CPs Using Aliphatic Carboxylates and Dipyriddy Species Are Summarized and Presented

Aliphatic Linker	4,4'-Dipyriddy	1,2-Bis(4-pyridyl) ethane	<i>trans</i> -1,2-Bis(4-pyridyl)ethylene
Sebacic (C ₁₀)	▲ ^a	▲ ^b	▲ ^b
Azelaic (C ₉)	▲ ^a	▲ ^a	*▲ ^b ● ^b
Suberic (C ₈)	▲ ^a	▲ ^a	*▲ ^b ● ^b
Pimelic (C ₇)	*▲ ^a ● ^a	● ^a	Not observed
Adipic (C ₆)	▲ ^a	● ^a	Not observed
Glutaric (C ₅)	● ^a	Not observed	● ^b

Role of N-donor species: ▲ direct coordination; ● noncoordinating.

*Two separate compounds.

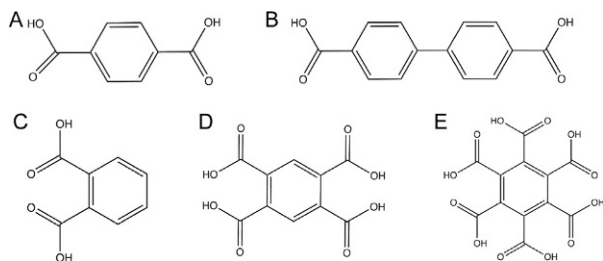
^aBorkowski and Cahill (2006b).

^bKerr and Cahill (2011).

Borkowski and Cahill (2006b) and Kerr and Cahill (2011).

necessary for theme development, and we focus on a few examples as shown in [Scheme 5](#).

The hydrothermal synthesis of uranyl nitrate and acetate salts in the presence of 1,4-benzenedicarboxylic acid (1,4-BDC) and 1,4-dicyanobenzene led to the formation of compounds **9**, $[\text{UO}_2(1,4\text{-BDC})]$ ([Mihalcea et al., 2012a](#)), and **10**, $(\text{NH}_4)[\text{UO}_2(1,4\text{-BDC})_{1.5}]$ ([Go et al., 2007](#)), respectively ([Fig. 13](#)). These compounds were synthesized as part of larger independent studies, and consequently, their reaction conditions differed greatly (e.g., time, temperature, and initial uranyl concentration), yet they both incorporate monomeric uranyl PBUs, albeit of different geometries. Square bipyramidal PBUs are featured in **9** where each monomer is coordinated in a bridging bidentate fashion by a total of four 1,4-BDC ligands to facilitate the formation of a sheet topology. In **10**, the primary uranyl building units are hexagonal bipyramids and are coordinated by a total of three bidentate 1,4-BDC ligands ([Fig. 13](#)). The hexagonal uranyl geometry and rigid aromatic linker lends itself to the formation of an open (6,3) honeycomb sheet with large cavities (22.4–23.1 Å). The



SCHEME 5 The aromatic carboxylate linkers featured throughout this manuscript: (A) 1,4-benzenedicarboxylic acid (1,4-BDC), (B) 4,4'-biphenylcarboxylic acid (4,4'-BPDC), (C) phthalic acid (1,2-BDC), (D) 1,2,4,5-benzenetetracarboxylic acid (BTEC), (E) mellitic acid.

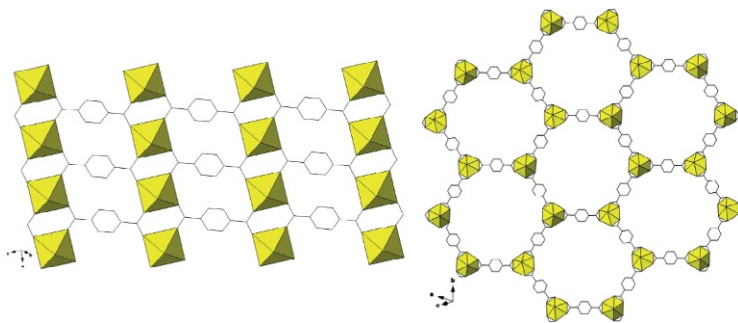


FIGURE 13 Left: Monomeric uranyl building units in **9** are bridged together by 1,4-BDC linkers to form sheets. Right: Hexagonal bipyramidal uranyl PBUs in **10** are coordinated by 1,4-BDC ligands, which give rise to a honeycomb topology. Ammonium cations and water molecules (not shown) occupy the interstitial sites.

overall structure is best described as a 2D network considering the successive (twofold) interpenetration of each layer, the latter of which is not unusual as CPs often have a tendency to form entangled or interpenetrated network topologies when large void spaces are present (Batten and Robson, 1998; Yaghi, 2007). Controlling the extent of interpenetration within hybrid materials in general is in fact an area of considerable interest, as it clearly relates to the properties (e.g., catalytic, absorption, etc.) of materials (He et al., 2013; Park et al., 2014; Rankine et al., 2012; Song et al., 2012; Zhang et al., 2009; Zhao et al., 2010).

The same study and similar synthetic conditions that resulted in the formation of **9** also gave rise to compound **11**, [UO₂(4,4'-BPDC)] (Mihalcea et al., 2012a). Compound **11** features a nearly identical sheet topology to that found in **9**, as square bipyramidal uranyl BUs in **11** are conjoined by 4,4'-biphenylcarboxylic acid (4,4'-BPDC) ligands (Fig. 14). The monomeric uranyl BUs in **11** are of no surprise as the synthetic conditions took place in the pH range of 2.6–3.1, where the dominate uranyl species in solution is expected to be the unhydrolyzed UO₂²⁺ ion (Scheme 1).

A study from our own group, aimed at monitoring the hydrothermal formation of several [UO₂]²⁺/4,4'-BPDC CPs by *in situ* Raman spectroscopy, led to the cocrystallization of two uranyl phases that each feature polynuclear SBUs (Cantos et al., 2013a). The first of the two compounds (**12**: (NH₄)[(UO₂)₂(4,4'-BPDC)₂(OH)]·(H₂O)) features pentagonal bipyramidal uranyl BUs that point-share to form dimers (Fig. 15). The uranyl SBUs are in turn linked to one another via a number of bidentate and bridging bidentate coordination modes stemming from the 4,4'-BPDC linker to ultimately give rise to an anionic 3D assembly. Charge-balancing ammonium cations and solvent water molecules occupy extra-framework sites throughout the 3D network.

Compound **13**, [(UO₂)₂(4,4'-BPDC)(OH)₂], contains highly oligomerized uranyl SBUs that give rise to slabs containing regular voids (Fig. 16). The slabs are composed of uranyl tetramers that are linked together via uranyl cation–cation interactions to give rise to the infinite SBUs. A uranyl cation–cation interaction occurs when the axial oxygen atom of one uranyl cation

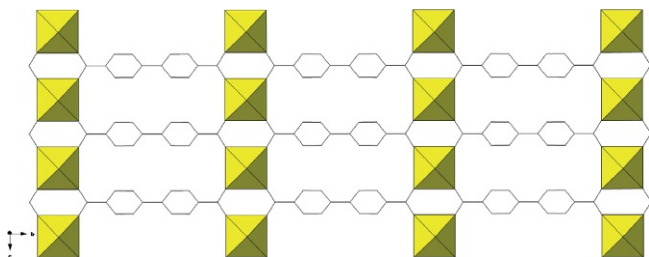


FIGURE 14 A sheet topology is formed in **11** as square bipyramid PBUs are linked via 4,4'-BPDC ligands.

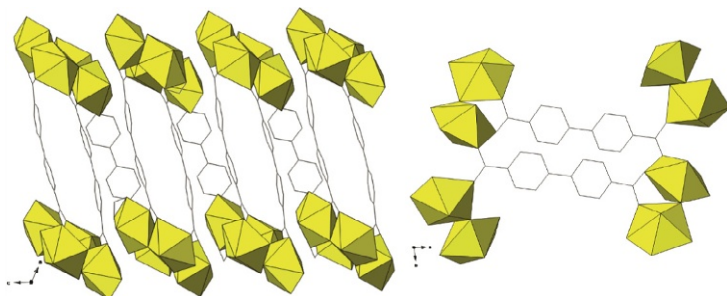


FIGURE 15 Left: Point-sharing uranyl dimers in **12** are linked via 4,4'-BPDC ligands to form a 3D coordination polymer. Right: The 4,4'-BPDC ligands bridge and link the dimeric SBUs together.

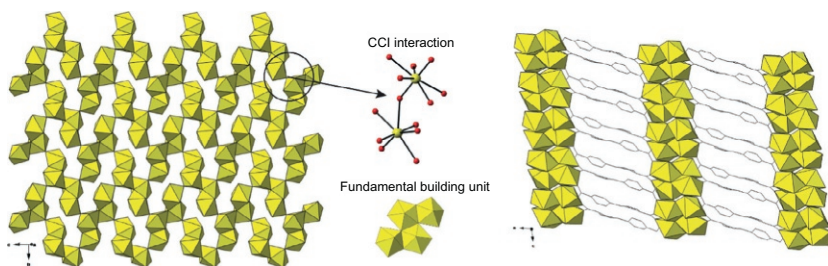


FIGURE 16 Left: Tetrameric uranyl SBUs in **13** are joined via CCIs to form highly oligomerized slabs, which contain regular voids. Right: The slabs are linked via 4,4'-BPDC ligands to form a 3D structure.

is further coordinated to the equatorial plane of a second uranyl cation. Cation–cation interactions are being reported more frequently, yet their occurrence remains largely serendipitous (Severance et al., 2011a). As such, a comprehensive treatment of uranyl cation–cation interactions is beyond the scope of this contribution and we will only describe these interactions as they arise. The slabs in **13** are in turn directly coordinated to one another via 4,4'-BPDC linkers to give rise to a 3D assembly.

This sampling of uranyl CPs containing the 4,4'-BPDC linker affords an opportunity to relate structural changes to reaction conditions across two different research groups. The initial pH values of the reaction solutions of which these materials were synthesized are: pH 2.6–3.1 (**11**) and pH 7.95 (**12–13**). There is a clear trend for the incorporation of oligomeric uranyl BUs as the pH is increased: **11** features square bipyramidal monomers, whereas **12** features dimers and **13** slabs. One may retroactively speculate on the nature of the uranyl building unit (monomer vs. dimer and slab) based upon pH, yet the ability to predict speciation *a priori* is beyond our current abilities.

5.1.3 Polyfunctional Carboxylic Acids

The ability to systematically vary the number and location of functional groups within carboxylate-containing ligands allows for extensive study of related uranyl-carboxylate compounds. As such, several derivatives of benzene dicarboxylic acids including benzenedicarboxylic acids (Kim et al., 2003; Mihalcea et al., 2011a,b, 2012a, 2014), benzenetricarboxylic acids (Borkowski and Cahill, 2004; Liao et al., 2010), mellitic acid (Mel) (Cantos and Cahill, 2014b; Go et al., 2007; Volkringer et al., 2011), and other related ligands (Liao et al., 2008; Thuéry, 2009e) are provided for presenting additional examples of uranyl-containing CPs that contain a wealth of PBUs and SBUs and exhibit an array of One-to-three dimensional topologies.

In particular, a closer look will be taken at a series of uranyl CPs that feature a common ligand, 1,2,4,5-benzenetetracarboxylic acid (BTEC), in order to further highlight building unit and topological diversity among carboxylate systems. Compounds **14**, $(\text{NH}_4)_2[(\text{UO}_2)_6\text{O}_2(\text{OH})_4(\text{BTEC})_{1.5}]\cdot 11\text{H}_2\text{O}$, and **15**, $(\text{NH}_4)[(\text{UO}_2)_2(\text{OH})(\text{H}_2\text{O})(\text{BTEC})]\cdot 1.75\text{H}_2\text{O}$, form MOFs that contain void spaces that are occupied by charge-balancing ammonium cations (Mihalcea et al., 2011c). Compound **14** contains polynuclear “double-wide” chains that are formed of pentagonal bipyramidal uranyl dimers that edge-share (Fig. 17). The SBUs in **14** are bridged together via tetradentate BTEC linkers to form a 3D structure that contains channels, which propagate along the [100] direction. Compound **15** contains a mixture of primary (hexagonal bipyramids) and secondary (pentagonal bipyramidal dimers) building units that introduce diversity to assembly. The smaller and more readily arranged building units (compared to **14**) are assembled via coordination to BTEC linkers, which exhibit rotation about the carboxylate bonds, to give rise to the overall 3D open framework.

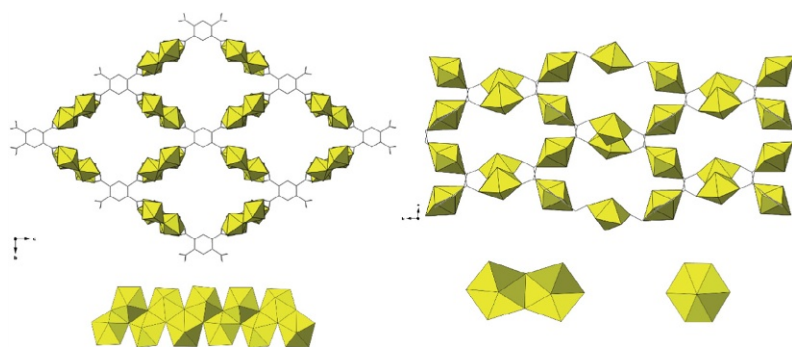


FIGURE 17 Left: The structure of **14** features double-wide uranyl chains (below) that are linked via BTEC ligands to form a three-dimensional coordination polymer. Right: The structure of **15** contains a mix of primary and secondary building units (below) that ultimately give rise to a 3D coordination polymer.

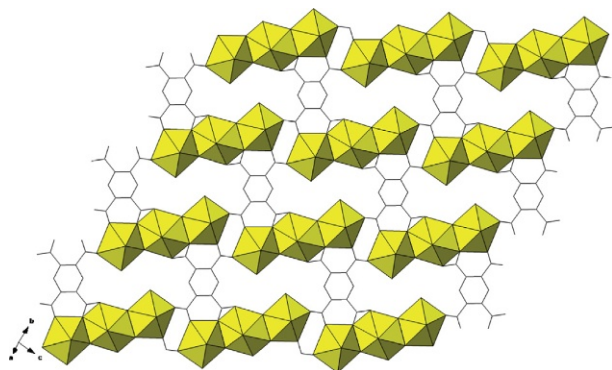
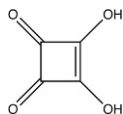


FIGURE 18 Pentagonal bipyramidal (2) and hexagonal (1) building units in **16** edge-share to form discrete trimers. The trimers are coordinated by BTEC ligands to form sheets.



SCHEME 6 The structure of squaric acid ($C_4H_2O_2$).

In contrast to **14** and **15**, compound **16**, $[(UO_2)_3(OH)_2(H_2O)_2(BTEC)]$, consists of a trimeric SBU that is part of a 2D assembly (Fig. 18) (Mihalcea et al., 2011c). The uranyl trimers in **16** consist of edge-sharing pentagonal (2) and hexagonal (1) pyramidal building units and are bridged together to form sheets via BTEC linkers. Unfortunately, with only the final pH values of the solutions being provided (pH 2.7 (**14**), 4.0 (**15**), 2.8 (**16**)) a definitive ranking of oligomerization versus initial solution pH cannot be made. We may comment, however, that SBU diversity even at low pH values is the norm, despite a tendency toward mononuclear species as suggest by hydrolysis (*vide infra*).

5.1.4 Uranyl Squarates

Squaric acid, while not a carboxylic acid *per se*, has been combined with the uranyl cation to result in a rich family of hybrid materials (Scheme 6). Our group in particular has used the squarate anion as a platform for systematic studies of the relationship between reaction conditions (time, temperature, pH, and concentration) and the resulting BUs observed in the solid state (Rowland and Cahill, 2010a,b). The resulting compounds demonstrate the tendency for syntheses at lower pH values and lower temperatures to yield monomeric PBUs, while alkaline conditions and higher reaction temperatures give way to building units of higher nuclearity. This is more of a guideline than a steadfast rule as few exceptions are noted. Compounds **17–19** demonstrate a

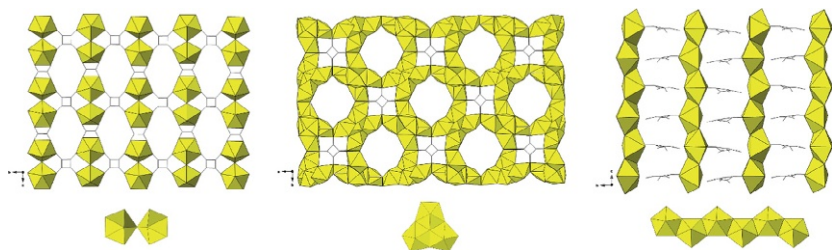


FIGURE 19 Left: Dimers formed via point sharing in **17** form sheets via squarate and oxalate coordination. Middle: Trimeric uranyl units in **18** are bound by squarate linkers to form a 3D structure that contains channels. The channels are occupied by water molecules and amine cations, which are not shown. Right: Oligomeric uranyl chains in **19** align parallel to one another and are each flanked by coordinating squarate ligands.

progression of uranyl hydrolysis as a function of pH: dimers (pH 3.0), trimers (pH 5.5), and chains (pH 6.8) are incorporated into the resulting crystal structures (Fig. 19). Compound **17**, $\text{NH}_4 [(\text{UO}_2)_2(\text{C}_4\text{O}_4)(\text{C}_2\text{O}_4)] \cdot \text{H}_2\text{O}$, was synthesized at pH 3.0 and contains point-sharing pentagonal bipyramidal uranyl dimers that are linked together via squarate and oxalate (generated *in situ*) ligands to form sheets. The sheets stack to form layers that contain charge-balancing ammonium cations and water molecules (Rowland and Cahill, 2010b). At pH 5.5, the formation of compound **18**, $(\text{NH}_4)_4 [(\text{UO}_2)_6(\text{C}_4\text{O}_4)_3(\text{OH})_6\text{O}_2] \cdot 9\text{H}_2\text{O}$, is observed and features uranyl trimers that consists of edge-sharing pentagonal (2) and hexagonal (1) bipyramids (Fig. 19) (Rowland and Cahill, 2010a). Owing to the degree of freedom in their coordination geometry, the uranyl trimers are assembled via squarate molecule to form an open 3D MOF. The channels propagate along the [010] direction and are occupied by ammonium cations and water molecules. The degree of oligomerization is greatest in **19**, $(\text{NH}_4)_2 [(\text{UO}_2)_6(\text{C}_4\text{O}_4)_3(\text{OH})_4]$, as chains that consist of edge-sharing uranyl pentagonal bipyramidal building units predominate (Fig. 19). These chains propagate along the [001] direction and are decorated by squarate molecules that protrude into the lattice and undergo no further covalent coordination. Although a clear trend emerges—an increase to oligomerization as pH increases—there does not seem to be an obvious connection between building unit and the resulting topologies.

Although the examples in this section are by no means exhaustive, they are meant to illustrate the effect of reaction conditions and ligand geometries uranyl speciation and subsequent topologies (Fig. 20). As we have stated, the effects are difficult to predict with certainty on the front end, yet are often retroactively explicable. That said, the trends that we observed over this limited suite of examples are in some cases contradicted by the formation of an unanticipated structure type with unanticipated SBUs. As such, synthesizing a uranyl-bearing CP with a desired topology without some exploratory efforts remains a considerable challenge. This will be a recurrent theme throughout

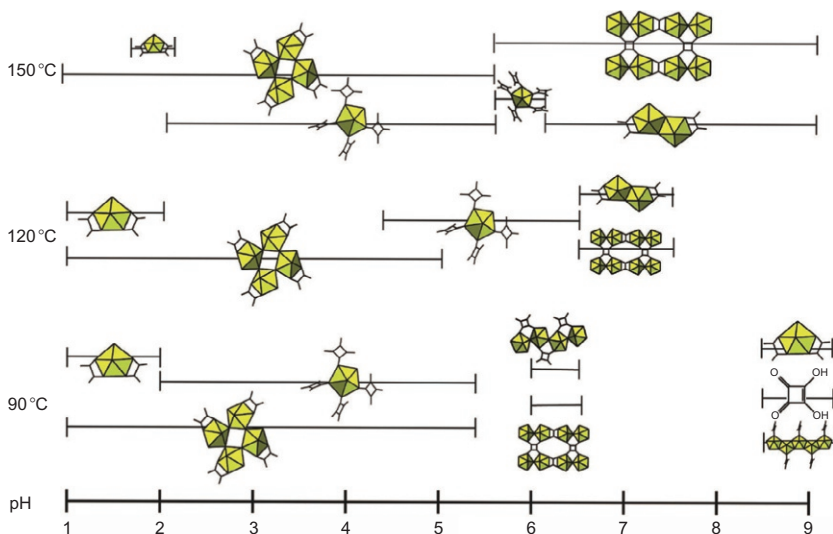
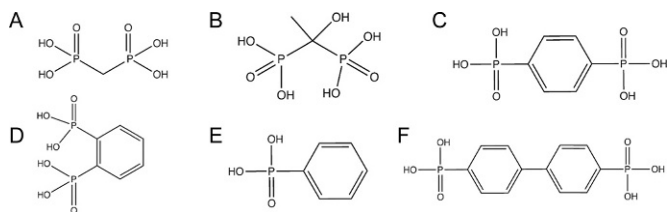


FIGURE 20 The local structures of uranyl CPs formed from 1:1 U:L ratio reactions as a function of temperature and initial pH. Reprinted with permission from Rowland and Cahill (2010b). Copyright 2010 American Chemical Society.

the remainder of the CP section of this chapter and we will endeavor not to overstate it.

5.2 Phosphonates

Metal phosphonate coordination chemistry and materials science has been a topic of study due to the large number of interesting structure types with properties appropriate for applications in catalysis, ion exchange, intercalation chemistry, photochemistry, and others (Bujoli et al., 2005; Clearfield, 2007; Gagnon et al., 2011; Clearfield and Demadis, 2011; Mao, 2007; Yin et al., 2001). In particular, f-element phosphonate chemistry is partially motivated by its relevance to separations and partitioning of actinides in application to advanced nuclear fuel cycles (Nash, 1994, 1997; Nash and Choppin, 1997). The strong affinity of the R-PO_3^{2-} functional group, due to its higher charge density, for the uranyl cation and the increase to geometrical versatility of the ligands (compared to a carboxylate) due to the degree of freedom added by the third oxygen atom have led to the formation of many coordination compounds, making it one of the most well-represented functional groups among uranyl crystal chemistry (Aranda et al., 1998; Britel et al., 1986; Doran et al., 2003; Grohol and Clearfield, 1997a,b; Grohol et al., 1996; Knope and Cahill, 2012b; Poojary et al., 1995a,b, 1996). Perhaps the greatest characteristic of phosphonate systems, however, is the variability of the organic (R) portion of the R-PO_3^{2-} functional group, as it is easily modified to fine tune the



SCHEME 7 A sampling of the aliphatic and aromatic diphosphonates ligands described throughout this manuscript: (A) methylenediphosphonic acid (MDP), (B) 1-hydroxyethylidenediphosphonic acid (LDP), (C) 1,4-benzenediphosphonic acid (1,4-BDP), (D) 1,2-phenyldiphosphonic acid (1,2-PDA), (E) phenylphosphoric acid (PhPA), (F) 4,4'-biphenylenbisphosphonic acid (4,4'-BPBP).

ligand and in turn material properties (Scheme 7). These factors have led to a modest suite of uranyl CPs that demonstrate similar synthetic and structural themes developed within the uranyl carboxylates.

5.2.1 Aliphatic Diphosphonates

Aliphatic diphosphonate linkers such as methylene diphosphonate (MDP) are flexible and ditopic, meaning that they can adopt various conformations as they exhibit a degree of flexibility (dependent upon length) and two coordination sites. The reaction of MDP with the UO_2^{2+} led to the formation of compounds **20**, $[\text{UO}_2(\text{CH}_2(\text{PO}_3\text{H})_2)(\text{H}_2\text{O})]\cdot 2\text{H}_2\text{O}$, and **21**, $(\text{C}_2\text{H}_{10}\text{N}_2)[\text{UO}_2(\text{CH}_2(\text{PO}_3)_2)]\cdot \text{H}_2\text{O}$, which each contain pentagonal bipyramidal uranyl monomers (Fig. 21) (Diwu and Albrecht-Schmitt, 2012a; Knope and Cahill, 2010a). The uranyl monomers in **20** are coordinated by a water molecule and three MDP ligands which bridged the PBUs together to form molecular chains that propagate along the [010] direction (Knope and Cahill, 2010a). The chains in turn pack and water molecules reside between chains. Whereas each uranyl monomer in **20** is linked to two neighboring monomers, in **21**, however, each monomer is bridged to three others (Fig. 21) (Diwu and Albrecht-Schmitt, 2012a). This additional linkage, combined with ligand flexibility, promotes the formation of a higher dimensional (compared to **21**) 3D CP with a channel structure. The channels are occupied by charge-balancing ethylenediamine cations and water molecules; the cations may be considered as templates, a topic to be discussed in a later section (Diwu and Albrecht-Schmitt, 2012a). Although **20** and **21** both incorporate the same pentagonal bipyramidal PBUs, the resulting structural topologies and dimensionality differ considerably.

In a separate study, the same MDP ligand was used in the hydrothermal synthesis, albeit under slightly different synthetic conditions, of two uranyl CPs, compounds **22**, $[(\text{UO}_2)_2(\text{CH}_2(\text{PO}_3)_2)(\text{H}_2\text{O})_3]\cdot \text{H}_2\text{O}$, and **23**, $[\text{UO}_2(\text{CH}_2(\text{PO}_3\text{H})_2)]\cdot \text{H}_2\text{O}$ (Fig. 22) (Nelson et al., 2008). Compound **22** contains both square and pentagonal bipyramidal PBUs that are bridged together by MPD ligands to form 2D corrugated sheets that stack to form an overall

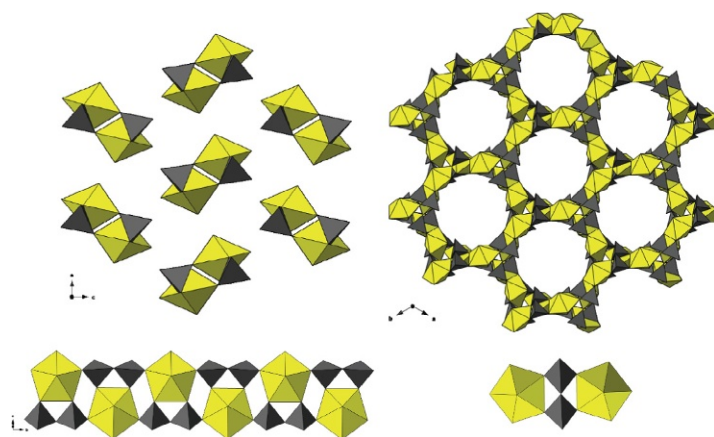


FIGURE 21 Left: Pentagonal bipyramidal uranyl monomers in **20** are linked into chains (bottom) via bridging MDP ligands to give rise to an overall 1D assembly (top). Right: The pentagonal bipyramidal uranyl building units in **21** are linked via MDP ligands to promote an open 3D coordination network.

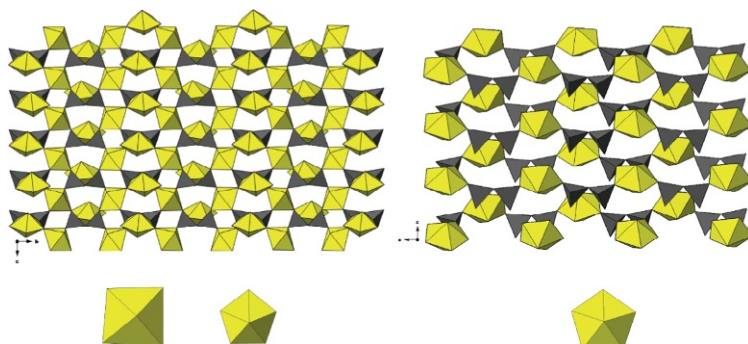


FIGURE 22 Left: Square and pentagonal bipyramidal uranyl BUs in **22** are coordinated by MDP ligands to form sheets. Right: Pentagonal bipyramidal uranyl BUs in **23** give rise to a 3D network via MDP linkages. Water molecules (not drawn) occupy the cavities in **23**.

layered structure. The square bipyramidal building units are coordinated in a monodentate fashion by four MPD ligands, whereas the uranyl pentagonal bipyramids are coordinated by one MPD ligand and three water molecules. The uranyl pentagonal bipyramidal building units point above and below the (011) plane and form hydrogen bonds with the interlayer water molecules. The structure of **23** contains pentagonal bipyramidal uranyl building units (similar to **20** and **21**) that are coordinated by three MPD ligands (two monodentate, one chelating) and one water molecule. The bridging interactions of the flexible MPD linkers give rise to an overall 3D CP (Fig. 22). Compounds

20–22 feature a common ligand and nearly constant PBU (with the exception of **22**), yet none share a common structure type as an MOF and two (2 and 3D) CPs result. For further examples of the well-explored chemistry of the uranyl aliphatic diphosphonates, the reader is guided to several publications that contain both hetero- and homometallic compounds featuring a wide range of PBUs and SBUs and resulting structure types (Diwu and Albrecht-Schmitt, 2012b; Nelson et al., 2012, 2013; Piskula et al., 2012; Tian et al., 2013a, 2014; Yang et al., 2012, 2014).

5.2.2 Aromatic Diphosphonates

The use of a rigid aromatic diphosphonate linkers, such as 1,4-benzenediphosphonic acid (1,4-BDP), is well represented among uranyl CP syntheses (Knope and Cahill, 2012). Compound **24**, $((\text{CH}_3\text{CH}_2)_4\text{N})[(\text{UO}_2)(\text{C}_6\text{H}_4(\text{PO}_3\text{H})\text{PO}_3\text{H}_{1.5}))_2 \cdot \text{H}_2\text{O}$, and **25**, $\text{Cs}[(\text{UO}_2)(\text{C}_6\text{H}_4(\text{PO}_3\text{H}_{0.5}))_2]$, are examples of aromatic diphosphonates containing materials that each incorporate uranyl monomers (Adelani and Albrecht-Schmitt, 2012; Adelani et al., 2011). Pentagonal bipyramidal PBUs are featured in the structure of **24** and are each coordinated (monodentate) by four 1,4-BDP linkers and one water molecule. The coordination of the 1,4-BDP linkers gives rise to chains that propagate in an undulatory fashion along the [010] direction (Fig. 23). These molecular chains are in turn linked in the [100] direction via strong hydrogen bonding interactions that stem from the coordinated water molecules and unbound phosphonate oxygen atoms. These pseudo-sheets pack and participate in

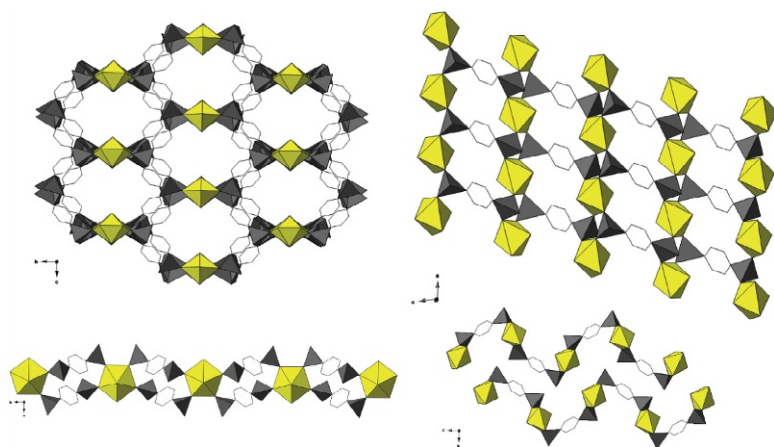


FIGURE 23 Left: In **24**, discrete anionic chains (bottom), formed by uranyl PBUs and 1,4-BDP linkers, propagate in a corrugated fashion and arrange such that channels are formed along the a -axis. Charge-balancing tetraethylammonium cations occupy the channels, yet are omitted for clarity. Right: Square bipyramidal uranyl building units in **25** are linked via 1,4-BDP ligands to form anionic corrugated sheets. Bottom right: The interlayer space is occupied by cesium cations (not drawn).

further hydrogen bonding interactions in the [001] direction to give rise to a 3D hydrogen-bonded open assembly that contains channels. The channels propagate along the [100] direction and are occupied by tetraethylammonium cations. In contrast to **24**, the structure of **25** contains square bipyramidal uranyl building blocks that are each coordinated by four (bridging bidentate) 1,4-BDP ligands to give rise to anionic sheets in the (011) plane (Fig. 23) (Adelani and Albrecht-Schmitt, 2012). The structure is overall layered as the anionic sheets (which contain open spaces) stack and are charge balanced by cesium cations that reside in the interlayer spaces.

Looking at two additional studies that feature the 1,4-BDP ligand, we will examine the structures of compounds **26**, $(C_4H_{12}N_2)[(UO_2)_2(C_6H_4(PO_3H)_2)_3] \cdot 2H_2O$, and **27**, $(H_3O)_2[(UO_2)_6(C_6H_4(PO_3)(PO_2OH))_2(C_6H_4(PO_2OH)_2)_2(C_6H_4(PO_3)_2)] \cdot 2H_2O$ (Adelani and Albrecht-Schmitt, 2009, 2011c). Compound **26** contains pentagonal bipyramidal building units that are coordinated to a total of five 1,4-BDP ligands in monodentate fashion that bridge adjacent metal sites together (Adelani and Albrecht-Schmitt, 2009). The bridging interactions link the uranyl metal centers together to give rise to a chain-like motif that propagates in the [010] direction (Fig. 24). Additional 1,4-BDP ligands oriented normal to [010] link the uranyl chains to form corrugated sheets that are in turn connected to yield an anionic 3D framework. The overall structure contains cavities that are occupied by charge-balancing piperazine cations and water molecules. Compounds **23–27**, containing the same ligand, feature

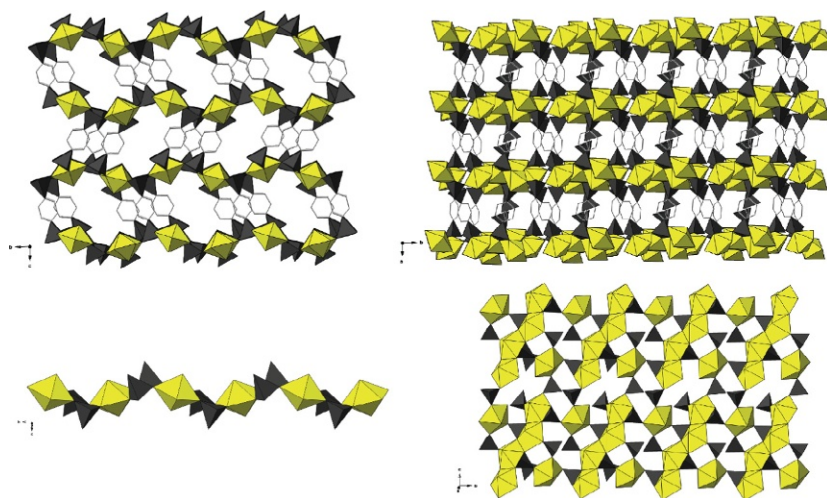


FIGURE 24 Left: Pentagonal bipyramidal uranyl building units in **26** form chains (below) that give rise to corrugated sheets (above) which are linked into a 3D network. Right: Uranyl monomeric and tetrameric BUs in **27** are linked via phosphonate bridges into anionic sheets (below) that are linked by 1,4-BDP ligands into 3D network. The 3D network is charge balanced by hydronium cations (not shown) that reside between the layers.

monomeric uranyl BUs and form a range of topologies (3D networks, sheets, and chains) that vary in dimensionality. The ambiguous relationship between building unit and resulting topology, established in [Sec. 5.1](#) (uranyl carboxylates), is echoed here.

An overall change to the uranyl building unit (compared to **23–25**) is observed in **27**, $(\text{H}_3\text{O})_2[(\text{UO}_2)_6(\text{C}_6\text{H}_4(\text{PO}_3)(\text{PO}_2\text{OH}))_2(\text{C}_6\text{H}_4(\text{PO}_2\text{OH}))_2(\text{C}_6\text{H}_4(\text{PO}_3)_2)] \cdot 2\text{H}_2\text{O}$, as pentagonal bipyramidal monomers and discrete uranyl tetramers predominate ([Adelani and Albrecht-Schmitt, 2011c](#)). The PBUs and SBUs in **27** are directly coordinated to one another via phosphonate linkages that give rise to sheets in the (011) plane ([Fig. 24](#)). The 1,4-BDP ligands are oriented normal to the (011) plane and go on to directly coordinate adjacent sheets together to form an open structured, 3D CP wherein the cavities are occupied by charge-balancing hydronium cations.

The use of a longer bisphosphonate linker, such as 4,4'-biphenylenbisphosphonic acid (4,4'-BPBP), promotes discrete 2D CPs that form uranyl nanotubes ([Fig. 25](#)). Compound **28**, $\text{M}_2[(\text{UO}_2)_2\text{F}(\text{PO}_3\text{HC}_6\text{H}_4\text{C}_6\text{H}_4\text{PO}_3\text{H})(\text{PO}_3\text{HC}_6\text{H}_4\text{C}_6\text{H}_4\text{PO}_3)] \cdot 2\text{H}_2\text{O}$, where $\text{M} = \text{Cs}^+$ or Rb^+ , contains point-sharing pentagonal bipyramidal uranyl dimers that link via a fluorine atom. The fluorine is a result of HF being used as part of the synthetic procedure to promote crystallization ([Adelani and Albrecht-Schmitt, 2011b](#)). The uranyl fluoro-dimers are bridged together by the phosphonate functional groups of the 4,4'-BPBP ligands to form anionic chains that propagate along [010]. The ditopic 4,4'-BPBP ligands facilitate the formation of a second chain that together form discrete molecular nanotubes that close pack. These tubes contain porous channels that are occupied by charge-balancing Cs^+ or Rb^+ cations that can undergo exchange with Ag^+ ions ([Adelani and Albrecht-Schmitt, 2011b](#)). Secondary metal ion incorporation in these materials has been further studied by the Burns research group ([Adelani et al., 2014](#)) who explored Cu^{2+} inclusion utilizing a dual ligand strategy.

To conclude the discussion of uranyl CPs containing aromatic phosphonate ligands, we highlight two structures that contain phenylphosphonic acid (PhPA). PhPA consists of a single aromatic benzene ring affixed with a single phosphonate group and has been demonstrated to be viable in the synthesis of uranyl CPs ([Wu et al., 2013](#)), including those that contain pores ([Poojary](#)

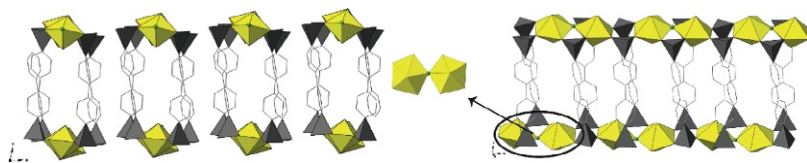
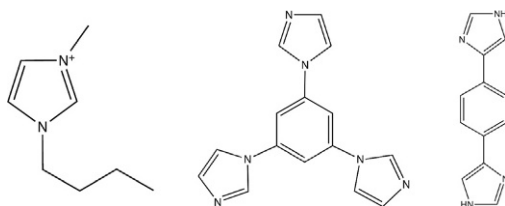


FIGURE 25 Left: Discrete and anionic nanotubes in **28** are formed along the [010] direction. The channels are occupied by water molecules and charge-balancing cesium cations (not shown). Right: A view along the [100] direction of two uranyl chains, linked via 4,4'-BPBP ligands, that give rise to the nanotubes.

et al., 1995b) and nanotubular assemblies (Aranda et al., 1998; Poojary et al., 1996). Compounds **29**, (Bmin)[$\text{UO}_2(\text{C}_6\text{H}_5\text{PO}_3\text{H})(\text{C}_6\text{H}_5\text{PO}_3)$] where Bmin = 1-butyl-3-methylimidazolium, and **30**, $(\text{H}_2\text{TIB})[(\text{UO}_2)_3(\text{PO}_3\text{C}_6\text{H}_5)_4] \cdot 2\text{H}_2\text{O}$ where TIB = 1,3,5-tri(1*H*-imidazol-1-yl)benzene (Scheme 8), are two examples that incorporate different uranyl building units and result in topologies of different dimensionality (Parker et al., 2013; Yang et al., 2013b). Compound **29** features square bipyramidal uranyl PBUs that are bridged by the phosphonate groups of the PhPA ligands to give rise to anionic chains (Fig. 26) (Yang et al., 2013b). Each PhPA ligand that facilitates the formation of the chain is oriented opposite to one another and is terminating considering their monotopic nature. The cationic Bmin molecules act as charge-balancing species. In **30**, a mixture of PBUs and SBUs are incorporated into the solid state as edge-sharing pentagonal bipyramidal uranyl dimers and square bipyramidal monomers predominate. The uranyl building units are bridged to one another by the phosphonate groups of the PhPA ligands and give rise to anionic sheets, where the interlayers are occupied by charge-balancing TIB cations. Although not stated as the authors' intent, the use of PhPA can potentially act to limit the dimensionality (i.e., the degree of connectivity) of the overall structure considering the single functional group.



SCHEME 8 Left to right: The structures of 1-butyl-3-methylimidazolium (Bmin), 1,3,5-tri(1*H*-imidazol-1-yl)benzene (Tib), and 1,4-di(1*H*-imidazol-4-yl)benzene (DIB).

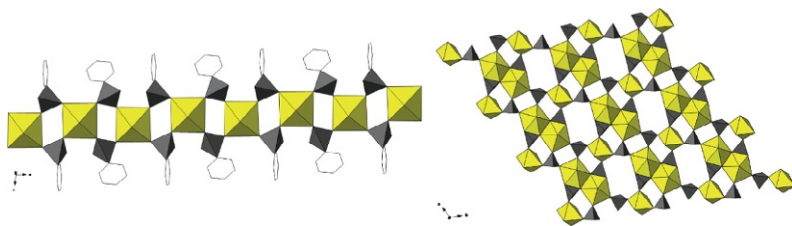
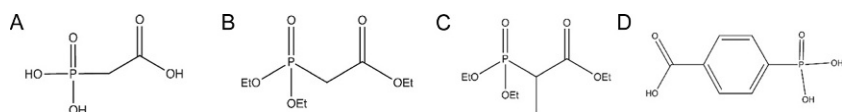


FIGURE 26 Left: Square bipyramidal uranyl PBUs in **29** are linked via PhPA ligands to form anionic chains that are charge balanced by Bmin cations (not shown). Right: Pentagonal bipyramidal uranyl dimers and square bipyramidal building units in **30** are bridged via PhPA ligands to form anionic sheets. The sheets are charge balanced by TIB molecules (not shown).

5.3 Carboxyphosphonates

Having seen just a small sampling of the crystal structures that contain both the uranyl cation and organic ligands containing carboxylic and/or phosphonate groups, one can begin to appreciate the diversity of coordination geometries and accessible topologies. Carboxyphosphonate ligands offer the possibility of expanding this diversity even further by introducing distinct coordination modes, as well as a platform for possible heterometallic constructs that make use of coordination preferences of the (R-CO_2^{2-}) and (R-PO_3^{2-}) groups (Scheme 9). With respect to the latter, it is generally observed that the phosphonate moieties tend to coordinate primarily to the uranyl centers, whereas the carboxylates either remain unbound or coordinate to remaining metal centers in both hetero- and homometallic systems—all three cases will be addressed in the coming sections of this text.

In the first example, we will examine a study performed in our group where phosphonoacetic acid (PPA-Scheme 9) was combined with the UO_2^{2+} to form a series of related 1D and 2D CPs in which O-donor moieties (phosphonate and carboxylate) contribute to assembly by different roles. Compound **31**, $[\text{UO}_2(\text{O}_3\text{PCH}_2\text{CO}_2\text{H})(\text{H}_2\text{O})]\cdot 2\text{H}_2\text{O}$, contains pentagonal bipyramidal uranyl monomers that are coordinated by three PPA ligands, two via phosphonate oxygen atoms (monodentate) and one by way of a carboxylate oxygen (Fig. 27) (Knope and Cahill, 2010b). The PPA ligand coordination



SCHEME 9 The carboxyphosphonate molecules commonly referred to throughout this text: (A) phosphonoacetic acid (PPA), (B) triethylphosphonoacetate (teppa), (C) triethyl-2-phosphonopropionate (te-2-pp), (D) carboxyphenylphosphonic acid (CPPA).

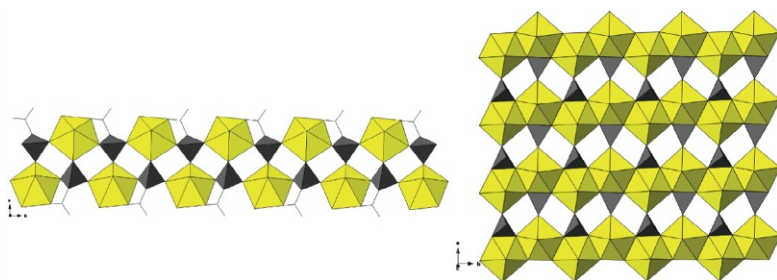


FIGURE 27 Left: Compound **31** features pentagonal bipyramidal monomers that form chains as a result of PPA linkages. Right: Oligomeric chains of uranyl pentagonal bipyramids in **32** are linked via PPA ligands to form sheets in the (110) plane. The carbon atoms have been omitted for clarity.

mode promotes the formation of chains ([010]) as O—P—O-bridging interactions link neighboring uranyl groups together. In contrast to **31**, compound **32**, $[\text{UO}_2(\text{O}_3\text{PCH}_2\text{CO}_2\text{H})]$, contains highly oligomerized pentagonal bipyramidal uranyl SBUs, chains that propagate along the [010] direction (Knope and Cahill, 2008). Each uranyl of the chain is coordinated by a total of two PPA ligands, in monodentate and bidentate fashions, which facilitate the formation of sheets (Fig. 27). The sheets featured in **32** are analogous to those found in the U(VI) mineral structure of uranophane (Burns, 2007; Locock, 2007). The carboxylate groups remain noncoordinating and protrude into the interlayer where they participate in hydrogen bonding interactions with adjoining layers. One may argue retroactively the effect of temperature and perhaps pressure upon uranyl speciation as the ligand, uranyl, and water ratio in the synthesis of compounds **31** and **32** was identical, yet **31** was produced via room temperature evaporation, whereas **32** by way of hydrothermal synthesis at 160 °C.

Triethylphosphonoacetate, teppa, was used in the synthesis of compounds **33** and **34**, yet *in situ* ligand hydrolysis led to the inclusion of PPA into the solid state. Compound **33**, $\text{NH}_4[(\text{UO}_2)(\text{O}_3\text{PCH}_2\text{CO}_2)] \cdot \text{H}_2\text{O}$, consists of pentagonal bipyramidal uranyl monomers that are bridged together by both the carboxylate and phosphonate moieties of the PPA linkers to form anionic sheets (110) (Knope and Cahill, 2008). The layered structure contains charge-balancing ammonium cations and solvent water molecules in the interlayer region. Although the synthetic parameters are nearly identical, the absence of an ammonium salt in the synthesis of **34**, $[(\text{UO}_2)_4(\text{HO}_3\text{PCH}_2\text{CO}_2)(\text{O}_3\text{PCH}_2\text{CO}_2)_2(\text{H}_2\text{O})_4] \cdot 3\text{H}_2\text{O}$, leads to the formation of uranyl carboxyphosphonate slabs that contain channels ([100]) (Fig. 28) (Knope and Cahill, 2008). The PPA ligands link the point-sharing uranyl dimers together, giving rise to chains (along [100]) that are further coordinated to isolated uranyl monomers (pentagonal bipyramids) via additional PPA coordination to ultimately form sheets. These sheets are in turn linked to one another via

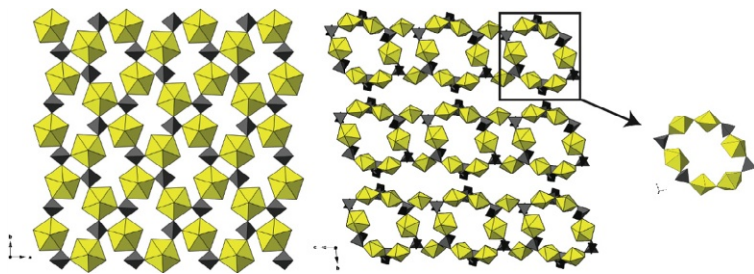


FIGURE 28 Left: Uranyl monomers in **33** are linked via bridging PPA ligands to form sheets. The ammonium cations and interlayer water molecular are omitted. Right: Hexagonal uranyl monomers in **34** form slabs that contain channels. The channels are occupied by water molecules that are not shown for clarity.

phosphonate linkages to give rise to thick slabs that contain channels (occupied by water molecules) that stack along the [010] direction.

A methyl-substituted PPA ligand (2-phosphonopropionate (2-PP)), under synthetic conditions identical to those used in the synthesis of **33**, was used in the synthesis of **35**, $(\text{NH}_4)_2 [(\text{UO}_2)_3(\text{O}_3\text{PCH}(\text{CH}_3)\text{CO}_2)_2(\text{O}_3\text{PCH}(\text{CH}_3)\text{CO}_2\text{H})] \cdot \text{H}_2\text{O}$ (Knope and Cahill, 2008). Presumably, these two syntheses took place under similar pH ranges, yet in **35** pentagonal bipyramidal uranyl BUs point-share to form trimers (Fig. 29). The coordination of the trimeric SBUs by the phosphonate and carboxylate moieties of the 2-PP ligands gives rise to anionic sheets that span the (110) plane in a corrugated fashion. The inter-layers are occupied by charge-balancing ammonium cations and water molecules. Despite sharing a common set of synthetic parameters, the BUs incorporated into the structures of **33** and **35** differ, as do the resulting sheet topologies. The role of both the ligand and uranyl speciation may contribute to these differences.

To close the section of carboxyphosphonate chemistry, we turn to a series of related structures synthesized via hydrothermal means using various alkali metal salts or hydroxides, PPA, and UO_3 (Alsobrook and Albrecht-Schmitt, 2009). In each case, alkali metal cations are incorporated into the structure and play a charge-balancing role. Synthesis performed using KCl and RbCl under acidic conditions pH 1.18 and 1.01, respectively, yielded compounds with the formula $\text{M}[(\text{UO}_2)_2(\text{PO}_3\text{CH}_2\text{CO}_2)(\text{PO}_3\text{CH}_2\text{CO}_2\text{H})(\text{H}_2\text{O})] \cdot 3\text{H}_2\text{O}$ ($\text{M} = \text{K}^+, \text{Rb}^+$), that featured sheet topologies that were comprised of pentagonal bipyramidal uranyl dimers. In the pH range of these syntheses, one may expect monomeric BUs to predominate; however, this is not the case as dimers are incorporated. Interestingly, synthesis performed with a cesium salt

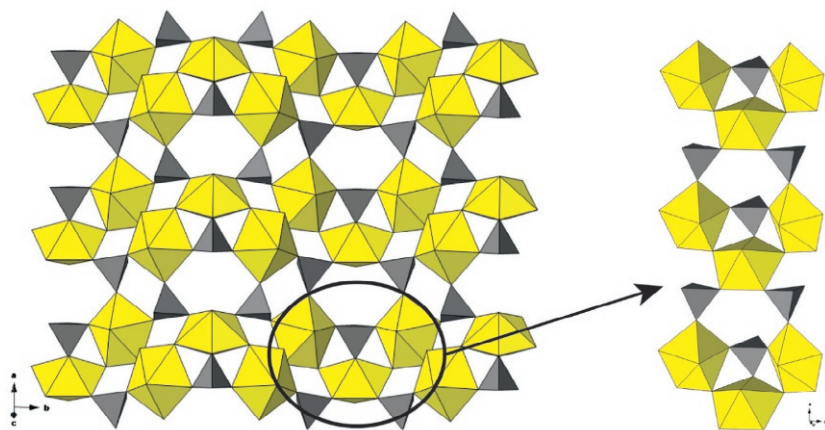


FIGURE 29 Trimeric uranyl SBUs formed via point sharing in **35** are linked into sheets via 2-PP ligands.

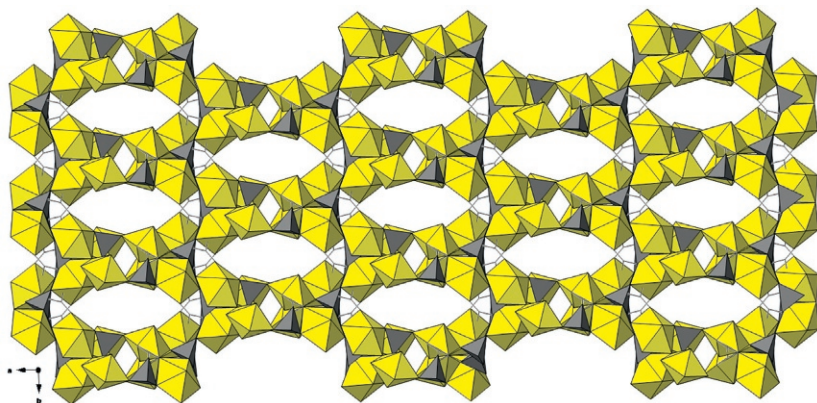


FIGURE 30 The structure of **36** consists of uranyl dimers that are linked by PPA ligands to form a 3D coordination polymer that contains regular channels. The channels are occupied by water molecules and charge-balancing cesium cations (not shown).

(CsCl) under analogous conditions leads to the formation of an MOF. Compound **36**, $\text{Cs}_3[(\text{UO}_2)_4(\text{PO}_3\text{CH}_2\text{O}_2)_2(\text{PO}_3\text{CH}_2\text{CO}_2\text{H}_{0.5})_2] \cdot n\text{H}_2\text{O}$, contains point-sharing pentagonal bipyramidal uranyl dimers that are coordinated by both the phosphonate and carboxylate moieties of the PPA ligands to result in a three-dimensional anionic framework that contains channels ($9.3 \text{ \AA} \times 14.0 \text{ \AA}$) which propagate along the [001] direction (Fig. 30). The channels are occupied by charge-balancing cesium cations and water molecules. This seemingly simple study highlights that the presence and perhaps size of a charge-balancing cation has the ability to affect structural formation which presents an additional variable.

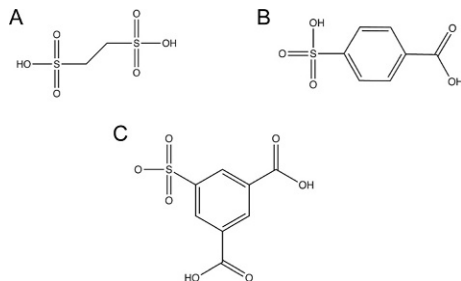
5.4 Sulfonates

CPs constructed from ligands bearing sulfonate functional groups (R-SO_3^-) have been explored to a much lesser degree than the geometrically similar phosphonates (Scheme 10). This is true from transition metal as well as actinide compositions, and arguments have been made that the relatively weak metal–sulfonate coordination is the cause (Cai, 2004; Côté and Shimizu, 2003; Videnova-Adrabinska, 2007). The most obvious difference between the phosphonate and sulfonate functional groups that attributes to the difference in bond strengths is the lower degree of negative charge associated with the latter (Thuéry, 2014). Furthermore, sulfonates tend to be weak bonding partners for hard metal ions in particular as these species tend to remain highly hydrated in solution (Shimizu et al., 2009). Thus, considering the principles of hard–soft acid–base pairing, the ligating ability of sulfonates (vs. phosphonates) for hard metal ions such as uranyl is inferior. As such, the body of uranyl–sulfonate containing CPs is much less developed compared to those

constructed from other functional groups (R-CO_2^- , R-PO_3^{2-} , etc.). This is in contrast to the rich body of uranyl sulfate materials (Doran et al., 2002, 2005; Norquist et al., 2003, 2005) and minerals (Burns, 2001; Burns et al., 2003) where perhaps the higher charge of the SO_4^{2-} anion provides a more favorable interaction and thus a larger body of structures. Recent efforts, however, have demonstrated that the sulfonate functional group can be utilized effectively in uranyl CP synthesis and therefore opportunities for novel structure types may exist and thus warrant further study (Thuéry, 2011a, 2012b,c).

5.4.1 Aliphatic Sulfonates

Owing to the relatively underexplored nature of uranyl–sulfonate CPs, examples are few and descriptions thereof are brief and meant to be introductory. The first example in this class of materials was reported by Thuéry and contains the aliphatic disulfonate linker 1,2-ethanedisulfonate (EDS) (Thuéry, 2014). Compound **37**, $[\text{UO}_2(\text{EDS})(\text{H}_2\text{O})_3]$, contains pentagonal bipyramidal uranyl monomers that are coordinated by two EDS ligands and three water molecules (Fig. 31). The EDS ligands coordinate in a bridging bidentate fashion to yield neutral chains. Comparing this structure type to those formed by similarly sized phosphonate (ethylenediphosphonic acid) (Tian et al., 2013a) and carboxylate (succinic acid) (Bombieri et al., 1979) linkers one can



SCHEME 10 The sulfonate containing ligands that are discussed in section(s): (A) 1,2-ethanedisulfonate (EDS), (B) 4-sulfobenzoate (4-SB), (C) 5-sulfoisophthalic acid (5-SB).

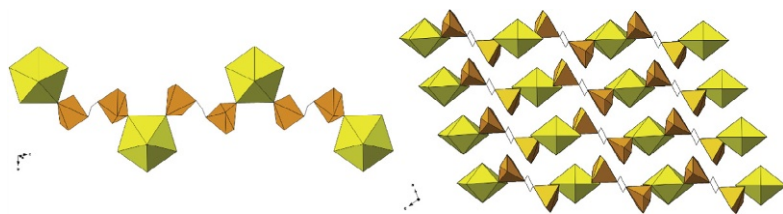


FIGURE 31 Left: Pentagonal bipyramidal uranyl monomers in **36** are linked into chains by EDS linkers. Right: The overall packing of **36** is shown down the $[100]$ direction. The sulfonate functional groups are drawn as orange (gray in the print version) polyhedrons.

observe an overall difference in both connectivity and resulting dimensionality. The phosphonate linkers coordinated in a multidentate fashion and gave rise to a 2D layered topology, whereas the carboxylate linkers coordinated via bridging bidentate to yield an overall 3D framework. This comparison is in no means exhaustive, yet presents a localized opportunity to highlight the diversity among uranyl CPs that can arise via functional group substitution.

5.4.2 Carboxysulfonates

As mentioned above, the relatively weak affinity of the sulfonate group for the uranyl cation makes synthesis and structural characterization of uranyl-sulfonates challenging. As such, the pairing of a sulfonate moiety with that of a strongly coordinating functional group, such as a carboxylate, can circumvent this challenge. Heterofunctional ligands that offer both R-SO₂OH and R-COOH functional groups can coordinate to the uranyl cation in one of two modes: via direct coordination, where each functional group coordinates a discrete metal ion, or via chelation. The latter can be an effective use of a ligand to increase the likelihood of a weakly coordinating functional group to form a bond. Essentially, a moiety with a tendency to be noncoordinating, such as R-SO₃⁻, is positioned in close proximity to a strongly coordinating group (R-CO₂⁻) such that the two functional groups form a chelation site where metal coordination is more likely to occur. The latter will be discussed in a following section, whereas direct coordination will be discussed now. The synthetic mindset behind pairing a weakly (sulfonate) and strongly (carboxylate) coordinating functional group together is that the stronger group is presumed to quickly form a complex in solution with a metal ion, which can induce the weaker moiety to either coordinate or in some cases remain unbound and free to participate in secondary interactions. We will examine a few crystal structures containing benzoic acids substituted with sulfonate and additional carboxylate groups in order to demonstrate their role in promoting structural diversity within uranyl-containing systems.

The 4-sulfobenzoate (4-SB) ligand contains two functional group sites (carboxylic and sulfonic acids) that are independently capable of coordinating a uranyl metal ion, yet instances where both have done so and been structurally characterized are rare with only a few crystal structures containing both the 4-SB ligand and the uranyl cation having been reported (Thuéry, 2011c, 2014). Compound **37**, K[(UO₂)₃(4-SB)O(OH)₃(H₂O)_{1.5}].0.5H₂O, features pentagonal bipyramidal uranyl building units that edge- and point-share to give rise to highly oligomerized polynuclear chains (Fig. 32). The infinite uranyl SBUs are coordinated, in an alternating fashion, in a bridging bidentate geometry by the sulfonate and carboxylate functional groups of the 4-SB ligands. These interactions link the chains to one another and promote an anionic sheet. The sheets in turn stack to form layers between which reside solvent water molecules and charge-balancing K⁺ ions.

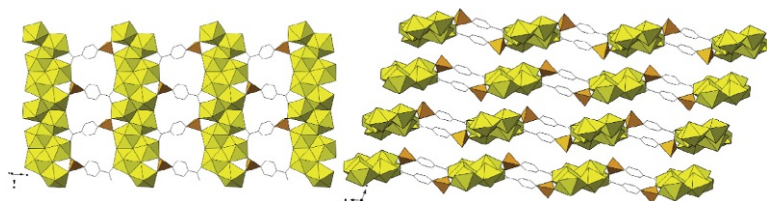


FIGURE 32 Left: Highly oligomerized uranyl SBUs are linked via 4-SB ligands to form sheets. Right: The sheets form a layered arrangement that is displayed looking down the [010] direction.

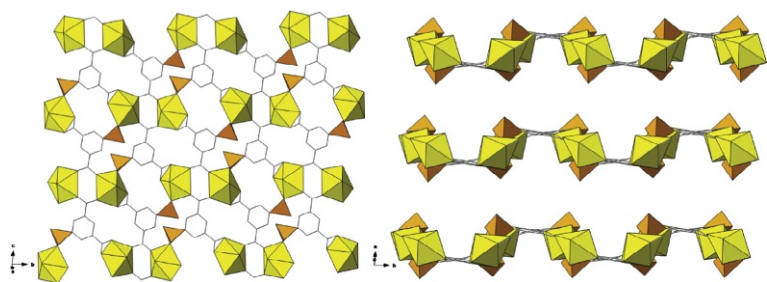


FIGURE 33 Left: Pentagonal bipyramidal uranyl monomers in **38** are coordinated via the carboxylate and sulfonate moieties of 5-SIP ligands to form anionic sheets. Right: The anionic sheets form a layered structure that is charge balanced by interlayer trimethylammonium cations (not shown).

Compounds **38**, $(C_8H_{23}N)[UO_2(5-SIP)]$, and **39**, $(Hdib)_2[(UO_2)_2(OH)(O)(5-SIP)]$ (dib = 1,4-di(1*H*-imidazol-1-yl)benzene—Scheme 8, 5-SIP = 5-sulfoisophthalic acid), were formed from the hydrothermal treatment of the uranyl cation with 5-SIP (Thuéry, 2013b; Yang et al., 2013b). Compound **38** consists of pentagonal bipyramidal uranyl monomers that are coordinated in bridging bidentate (by two ligands) and bidentate fashion via the carboxylate oxygen atoms of the 5-SIP ligands (Fig. 33) (Thuéry, 2013b). The local uranyl coordination sphere is completed by a monodentate sulfonate functional group. The bridging carboxylate interactions link the monomers into “pseudodimers” that are in turn conjoined to give rise to an overall 2D coordination network. The network consists of anionic layers that are charge balanced by trimethylamine cations residing in the interlayer regions.

Compound **39**, $(Hdib)_2[(UO_2)_2(OH)(O)(5-SIP)]$, features uranyl pentagonal bipyramids that edge-share to form discrete tetramers (Fig. 34) (Yang et al., 2013b). Each tetramer is coordinated by six 5-SIP ligands: four ligands coordinate via the carboxylic acid functional group (2—bridging bidentate and 2—bidentate), while two coordinate via the sulfonate functional group (monodentate). The six total coordination modes (three types) link the tetramers into a sheet. The previous two structures (**37** and **38**) share similarities to the metal-to-ligand coordination environments in spite of featuring uranyl

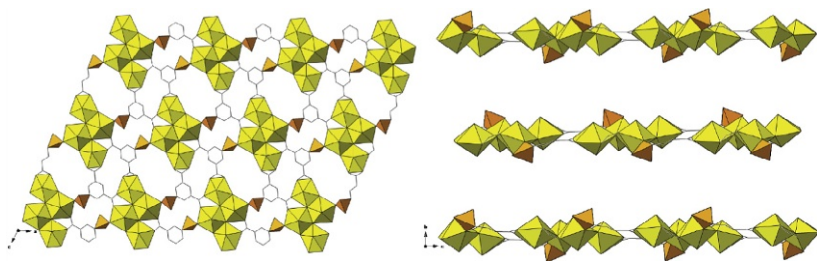
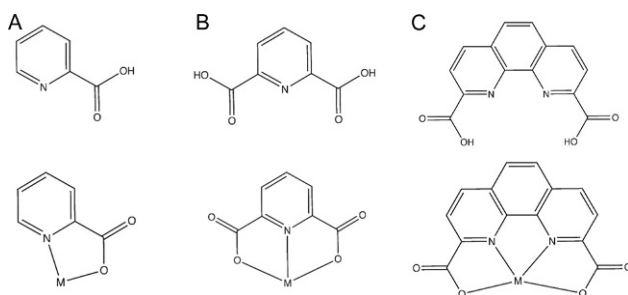


FIGURE 34 Left: Tetrameric SBUs in **39** are linked into sheets. Right: The sheets stack to form layers that are charge balanced by protonated dib cations (not shown).



SCHEME 11 Various nitrogen- and oxygen-donating chelating ligands referenced throughout this chapter. The ligands are also drawn chelating a generic metal (M): (A) pyridine-2-carboxylic acid (picolinic acid), (B) 2,6-pyridine dicarboxylic acid (2,6-PYDC), (C) 1,10-phenanthroline-2,9-dicarboxylic acid (PhenDCA).

BUs that vary in nuclearity. Further, there is a proclivity among structures **36–39** to form 1D and 2D assemblies regardless of the primary or SBUs incorporated into the solid state.

6 CHELATING LIGANDS

The compounds presented in the following section contain examples of chelating ligands, i.e., those which can form bonds or attractive interactions with metal ions via two or more separate binding sites (Muller, 1994). Chelating ligands are often chosen such that the binding sites (e.g., carboxylate moieties or coordinating pyridyl species) are positioned in close proximity to one another in order to form a chelation pocket. This pocket serves as a site where favorable metal ion coordination can occur as the formation of multiple concerted bonding interactions is possible. For instance, a ligand such as pyridine-2-carboxylic acid (picolinic acid) pairs the pyridyl nitrogen atom with a carboxylic acid moiety in the 2-position to form a bidentate site (Scheme 11). Nitrogen- and oxygen-donating ligands are considered to be heterofunctional as the coordination sites consist of different organic functional

groups. The pairing of rather soft nitrogen-donating sites with that of hard O-donor moieties (i.e., carboxylates) has been employed in the synthesis of uranyl CPs as these N- and O-donor chelation sites form favorable complexes to the UO_2^{2+} .

6.1 Heterofunctional Ligands: Nitrogen and Oxygen Donors

Compound **40**, $[\text{UO}_2(\text{C}_6\text{H}_4\text{NO}_2)_2]$, combines the picolinic ligand and the uranyl cation to result in an overall 1D structure (Severance et al., 2011b). Pentagonal bipyramidal uranyl monomers are found in **40** and are coordinated by three picolinic ligands (Fig. 35). The uranyl cation sits in the N,O-chelation pocket of two picolinic ligands to form a “uranyl-picolinic subunit.” One of the nonchelating oxygen atoms of the carboxylate group forms a bridging interaction to a neighboring subunit to give rise to neutral chains. This basic system demonstrates the favorable nature of the chelation pocket as uranyl coordination is not observed solely at the carboxylate oxygen atoms but primarily in the N/O site. As such, pyridine-2-carboxylic acid (and derivatives thereof) has been the focus of several studies that have yielded many diverse uranyl-containing CPs with the N/O site as a dominate structural theme (Andrews and Cahill, 2011; Cantos et al., 2010; Frisch and Cahill, 2006; Mishkevich et al., 2012; Severance et al., 2013; Silverwood et al., 1998; Thuéry, 2009c).

A study by our group involving picolinic acid yielded compound **41**, $[\text{UO}_2(\text{C}_6\text{H}_3\text{NO}_2)(\text{OH})]$ (Andrews and Cahill, 2011) which contains pentagonal bipyramidal uranyl building units that edge-share to form dimers (Fig. 36). Each dimer is chelated by two picolinic ligands that in turn link the dimers together via the nonchelating carboxylate oxygen atoms to form chains. Despite the incorporation of dimers in **41** the resulting chain topology is very similar to that of the one constructed from monomers in **40**. In this study by Andrews and Cahill, **40** was isolated as a coproduct in a reaction of uranyl nitrate and picolinic acid at pH 1.47, whereas pure **41** was isolated from the reaction mixture of uranyl acetate and picolinic acid at pH 3.94.

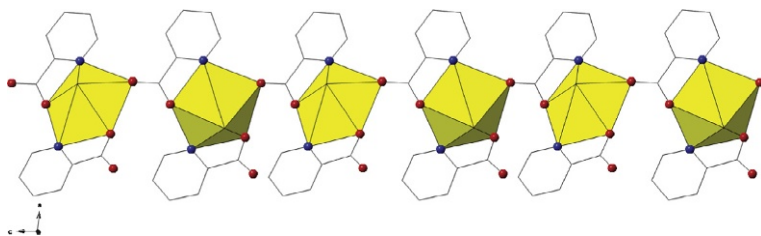


FIGURE 35 Pentagonal bipyramidal uranyl monomers in **40** are chelated by two picolinic acid ligands. The nonchelating oxygen atoms of the carboxylate group bridges the monomers into chains. The oxygen (red (gray in the print version)) and nitrogen (blue (dark gray in the print version)) atoms are drawn as spheres.

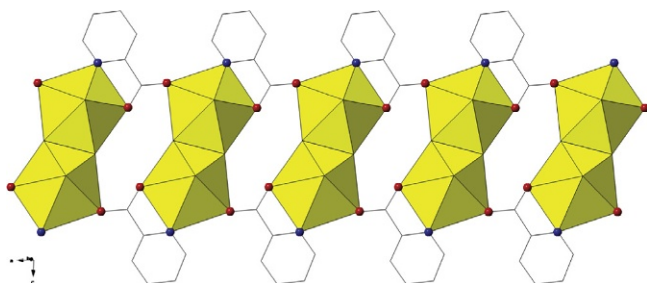


FIGURE 36 Edge-sharing pentagonal bipyramidal uranyl SBUs in **41** are chelated by picolinic acid molecules that bridge the dimers into chains.

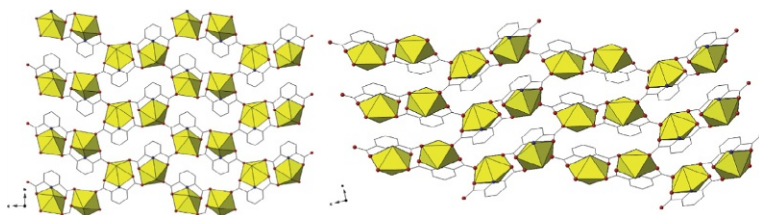


FIGURE 37 Left: Pentagonal bipyramidal uranyl monomers in **42** are chelated by 2,6-PYDC ligands that bridge the PBUs into sheets. Right: The nonchelating oxygen atoms of the 2,6-PYDC ligands afford an additional degree of connectivity to form a 3D network topology.

As with the bifunctional carboxylic acids discussed above, readily substituted “backbones” of a given ligand often provide for systematic study on steric or other influences within a class of materials. As such, pairing derivatives of pyridine-2-carboxylic acid with uranyl has led to numerous crystal structures (Cantos et al., 2010; Frisch and Cahill, 2006; Zheng et al., 2005). The 2,6-pyridine dicarboxylic acid (2,6-PYDC) ligand in particular features an O,N,O site that exhibits a rather high affinity for the uranyl cation (Scheme 11).

Compounds **42**, $[\text{UO}_2(\text{C}_7\text{H}_3\text{NO}_4)]$, and **43**, $[(\text{UO}_2)_2(\text{C}_7\text{H}_3\text{NO}_4)(\text{O})(\text{H}_2\text{O})]$, each contain pentagonal bipyramidal uranyl building units, yet differ as **42** contains monomers, whereas **43** contains polynuclear chains of SBUs (Fig. 37) (Frisch and Cahill, 2006). In compound **42**, the uranyl ion is chelated by the tridentate 2,6-PYDC at the pyridine nitrogen atom and the two flanking carboxylic acid groups. The carboxylate oxygen atoms that do not chelate are free to participate in further coordination and often serve as bridges between uranyl centers. In **42**, these oxygen atoms link neighboring uranyl-PYDC units together to give rise to chains that propagate with additional connectivity resulting in 2D sheets.

In **43**, $[(\text{UO}_2)_2(\text{C}_7\text{H}_3\text{NO}_4)(\text{O})(\text{H}_2\text{O})]$, pentagonal bipyramidal uranyl building units edge-share to form discrete linear tetramers that conjoin to form a

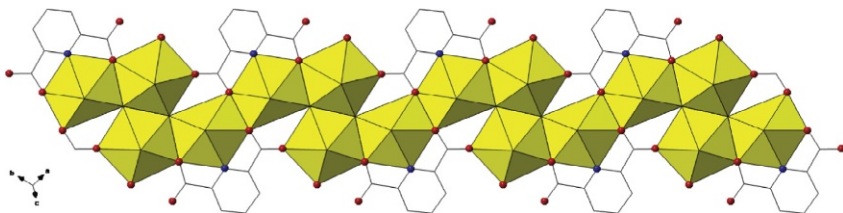


FIGURE 38 Pentagonal bipyramidal uranyl BUs in **43** compose tetramers that edge-share to form a notched chains. 2,6-PYDC ligands decorate the chains and chelate the uranyl BUs.

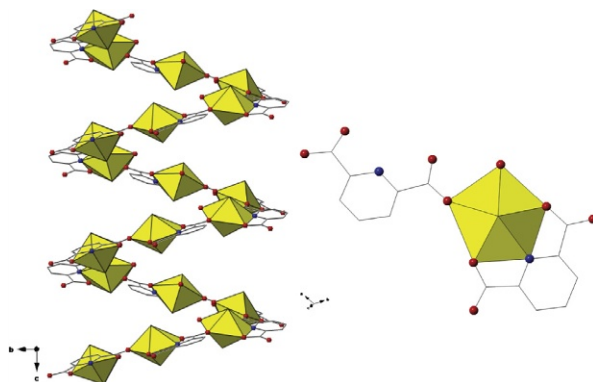


FIGURE 39 Left: Uranyl monomers in **44** are chelated via 2,6-PYDC linkers to form helical chains. Right: The local coordination geometry of the PBUs in **44** consist of two 2,6-PYDC ligands (one chelating and one bridging monodentate) and a water molecule.

polynuclear, notched chain (Fig. 38). The infinite chains are in turn decorated by 2,6-PYDC ligands as the middle two uranyl cations of each tetrameric unit are chelated. The nonchelating carboxylate oxygen atoms both stabilize the formation of the chain by bridging the tetrameric units together and protrude into the lattice. Although the synthetic conditions that produce these two compounds (**42** and **43**) differ (temperature, and the presence of zinc nitrate in **43**) demonstrate that even chelating ligands with a geometrically constrained coordination site are capable of forming structurally diverse compounds upon the incorporation of monomeric or polynuclear species.

The last example we would like to highlight clearly predates the current context of CPs, yet it is a particularly attractive compound, if only for aesthetics and more structural diversity. Compound **44**, $[\text{UO}_2(\text{C}_7\text{H}_3\text{O}_4)(\text{H}_2\text{O})]$, consists of pentagonal bipyramidal monomers that are coordinated by two 2,6-PYDC ligands and a water molecule (Fig. 39) (Immirzi et al., 1975). One 2,6-PYDC ligand chelates the uranyl cation via the three coordinate O, N, O chelation pocket, leaving two carboxylate oxygen atoms nonchelating. One of these nonchelating oxygen atoms coordinates in a bridging bidentate

fashion to a neighboring uranyl-2,6-PYDC unit to form a neutral helical chain along [001]. The helical arrangement is stabilized by hydrogen bonds that stem between the coordination water molecules and the second “free” carboxylate oxygen of the 2,6-PYDC ligand. It is not entirely clear what the driving force is behind the formation of this chiral structure as synthetic conditions were similar to many other studies, perhaps making it all the more intriguing. The influence of secondary NCIs such as the H-bonds herein will be explored in greater depth below.

Additional examples that highlight the range of uranyl CPs containing N- and O-donor heterofunctional pyridine-based ligands may be found in studies that incorporate both molecular (Harrowfield et al., 2006; Marangoni et al., 1974; Masci and Thuéry, 2005; Mirzaei et al., 2011; Xu et al., 2013) and polymeric (Harrowfield et al., 2006; Henry et al., 2011) PBUs and SBUs, some of which are heterometallic (Andreev et al., 2010; Frisch and Cahill, 2006; Harrowfield et al., 2006; Severance et al., 2013; Yu et al., 2003, 2004).

Traditional *N*-donating chelating ligands such as 1,10-phenanthroline (Phen), which contains an *N,N*-chelation site, are capable of forming complexes with the uranyl ion (Alcock et al., 1988; Jiang et al., 2006; Schettini et al., 2009; Sun et al., 2010). These ligands are also easily substituted with carboxylate functional groups in order to tailor a chelation site to a specific size, denticity, and type (N vs. O vs. N/O). In the following example, a Phen ligand is substituted with two carboxylic acid functional groups to yield 1,10-phenanthroline-2,9-dicarboxylic acid (PhenDCA), a chelating ligand that contains an O,N,N,O-chelating pocket (Scheme 11).

Compound **45**, [UO₂(PhenDCA)], incorporated pentagonal bipyramidal uranyl PBUs that are chelated by PhenDCA ligands (Fig. 40) (Dean et al., 2008). Each uranyl-PhenDCA subunit is in turn linked to another by the nonchelating carboxylate oxygen atoms of the PhenDCA ligands to give rise to chains. The chains in turn pack and are stabilized by π -interactions that stem from the aromaticity of the PhenDCA ligands. For additional examples of ligands featuring multidentate N- and O-chelation pockets, the reader is encouraged to see the following studies (Asadi and Shorkaei, 2013; Gatto et al., 2004; Hall et al., 1967; Paolucci et al., 1980; Takao and Ikeda, 2007; Xiao et al., 2014).

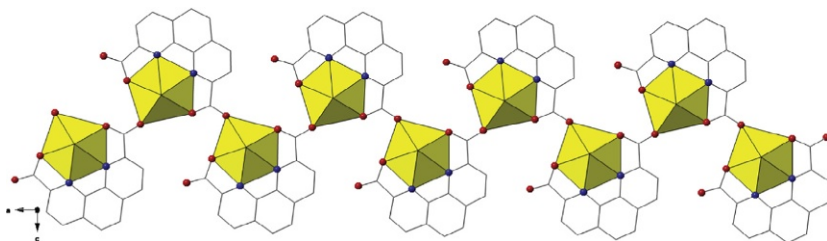


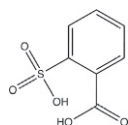
FIGURE 40 Pentagonal bipyramidal uranyl building units in **45** are chelated by PhenDCA ligands that bridge the PBUs into chains.

6.2 Heterofunctional Ligands: Sulfonate and Carboxylate Donors

As discussed previously, the sulfonate ($R-SO_2OH$) functional group exhibits weaker coordination to hard Lewis acids, such as the uranyl cation. One pathway for promoting uranyl–sulfonate coordination is to utilize a neighboring functional group with a greater affinity for $[UO_2]^{2+}$. For instance, a strongly coordinating carboxylic acid can be paired with a sulfonate to create an O,S chelation site, as in 2-sulfobenzoate (2-SB), and when in close proximity, can induce the coordination of a metal species that would otherwise be largely noncoordinating (Scheme 12).

Sulfobenzoate ligands are exemplary in this regard and the hydrothermal reaction of 2-SB with the uranyl cation led to the formation of several 1D and 2D CPs that will be discussed herein (Thuéry, 2012a). Compound **46**, $[UO_2(2-SB)(H_2O)]$, contains pentagonal bipyramidal uranyl monomers that are coordinated by a total of three 2-SB ligands and one water molecule (Fig. 41). Each uranyl monomer is connected via bridging bidentate carboxylate oxygen atoms to form pseudo-dimeric units. Each of these “dimer-like” subgroups is in turn linked to one another via bridging sulfonate groups to give rise to neutral 1D chains.

Similar reaction conditions, save for the addition of trimethylamine and copper nitrate, led to the formation of compound **47**, $(C_4H_{12}N)_2[(UO_2)_3(2-SB)_2O_2]$, which contains highly oligomerized SBUs (Fig. 42) (Thuéry, 2012a). The incorporation and edge-sharing of both pentagonal and hexagonal bipyramidal building units give rise to infinite polynuclear anionic chains. Each pentagonal bipyramidal PBU shares an edge to form a dimer; each dimer in turn shares two edges (on both sides) with a hexagonal



SCHEME 12 The structure of 2-sulfobenzoate (2-SB).

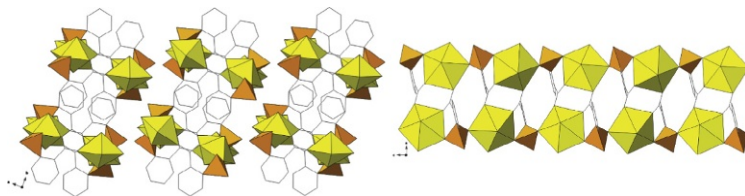


FIGURE 41 Left: A view down the [001] direction of the chains formed in **46**. Right: Pentagonal bipyramidal uranyl BUs are linked into chains via bridging carboxylate and sulfonate moieties of the 2-SB ligands.

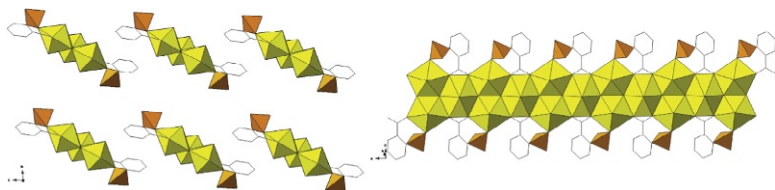


FIGURE 42 Left: A view of the 1D structure of **47** down the [100] direction. Right: 2-SB ligands decorate and coordinate to the oligomeric SBUs (chains) in **47**.

bipyramidal PBU to form the chain. The chains are then decorated by the 2-SB ligands which coordinate via the carboxylate and sulfonate oxygen atoms. The ligands are terminal and thus a 1D CP results as a function of the chains packing. Trimethylamine cations are interdispersed among the lattice to act as charge-balancing species.

7 URANYL HYBRID MATERIALS CONTAINING ANCILLARY ORGANIC SPECIES

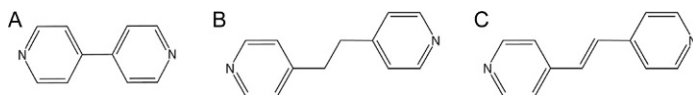
By now we hope to have highlighted a sufficient number of examples of uranyl CPs to demonstrate structural diversity—both on the topological and local coordination geometry levels. Hydrolysis and SBU “selection” for crystallization has been the norm as we have considered a range of ligands with varying functional groups. A natural progression of these efforts is to include ancillary species, such as a secondary organic molecule, that influence structure and in some cases, properties. Broadly speaking, ancillary species can take on a few definitions or meanings. The literature is fraught with examples of syntheses that only work when one uses a nitrate salt, for example, as a starting material, yet nitrate is nowhere to be found in the crystal structure. The same can be said for attempts at heterometallic materials (below) where the secondary metal never incorporates, yet the uranyl “end-member” cannot be prepared without it. Rather than dwell on these (sometime confounding) reactions, we will restrict our definition of “ancillary” to an organic molecule intentionally introduced to a reaction mixture with the goal of influencing structure. As we will see, results of these efforts come in essentially two families of materials: those in which the organic is coordinated directly to a metal center, and those in which the organic is not. For the latter, we will develop a theme of templating and host–guest relationships.

7.1 Coordinating Species: Heterofunctional N-Donor and O-Donor Ligands

Commonly observed secondary coordinating species or coligands often contain nitrogen-donating sites such as dipyridyls and their derivatives. Dipyridyl coligands can be paired with the more strongly coordinating O-donor

carboxylic acids and used to form a wide range of uranyl hybrid materials. A focused study from our group investigated the pairing of the uranyl cation with aliphatic carboxylic acid linkers (oxalic–sebacic) and dipyriddy (4,4'-bipyridine, 1,2-bis(4-pyridyl)ethane (BPE) and *trans*-1,2-bis(4-pyridyl)ethylene (BPE')—Scheme 13) species acting as coligands or structure influencing guest species (Borkowski and Cahill, 2006b; Kerr and Cahill, 2011).

Sebacic acid is an aliphatic ($C_{10}H_{18}O_4$) dicarboxylic linker that has been demonstrated to be viable in the synthesis of uranyl CPs (Borkowski and Cahill, 2006a). To begin our discussion of N-donor coligands we will compare the structures that resulted from the hydrothermal synthesis of uranyl nitrate salts with sebacic acid and then those formed by the combination of sebacic acid and BPE or BPE'. Compound **48**, $[UO_2(C_{10}H_{16}O_4)]$, was formed by the hydrothermal synthesis of uranyl nitrate and sebacic acid. Pentagonal bipyramidal uranyl dimers that edge-share are incorporated into **48** (Fig. 43). The uranyl dimers are coordinated by sebacic acid linkers that bridge them into chains that propagate along the [100] direction. These chains are further coordinated in the [001] direction to form 2D layers in the (101) plane. The layers are distinct as the sebacic acid linkers exhibit slightly different uranyl coordination geometries in each and ultimately form an A:B:B:A stacking sequence.



SCHEME 13 Various dipyriddy species that are mentioned throughout this text. (A) 4,4'-Dipyriddy (4,4'-BIPY), (B) 1,2-bis(4-pyridyl)ethane (BPE), (C) *trans*-1,2-bis(4-pyridyl)ethylene (BPE').

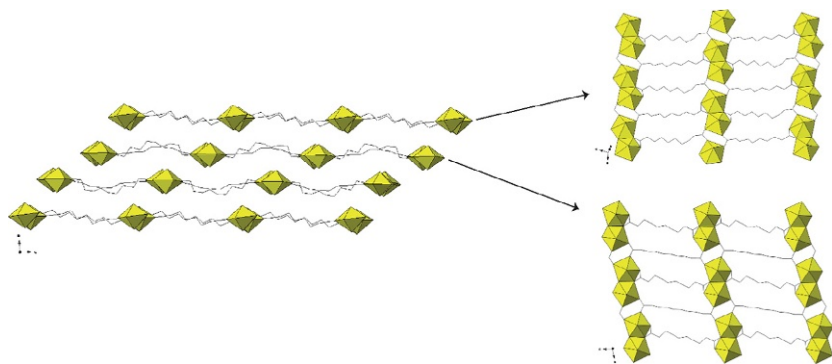


FIGURE 43 Right: Uranyl dimers (edge-sharing) in **48** are linked via sebacic acid ligands to form a layered structure. Left: Two unique types of uranyl sebacic layers are formed as a result of differing ligand coordination.

The addition of the N-donor BPE and BPE' coligands using a similar set of synthetic parameters resulted in the formation of compounds **49**, $[(\text{UO}_2)_2(\text{C}_{10}\text{H}_{16}\text{O}_4)_2(\text{C}_{12}\text{H}_{12}\text{N}_2)\text{H}_2\text{O}]$, and **50**, $[(\text{UO}_2)_2(\text{OH})_2(\text{C}_{10}\text{H}_{16}\text{O}_4)(\text{C}_{12}\text{H}_{10}\text{N}_2)]$ (Fig. 44) (Kerr and Cahill, 2011). Pentagonal bipyramidal uranyl monomers are featured in **49** and are linked together by bridging carboxylate groups to form chains along [101]. The chains are in turn cross-linked above and below the direction of their propagation via sebacic linkers to result in a 3D network that contains channels. Every fourth uranyl PBU in the chain is additionally coordinated by two BPE molecules that protrude into and occupy the channels; the presence of the BPE molecules may promote the formation of the channels.

In contrast to compound **49**, pentagonal bipyramidal uranyl building units point-share in **50** to form chains that propagate in the [010] direction (Fig. 45). The uranyl chains are coordinated by both sebacic and BPE' ligands that function to directly link adjacent chains into sheets that in turn stack along [001]. The overall neutral sheets form a 2D CP that differs from **48** in terms of layer continuity. When looking strictly at compounds **49** and **50**, the differences in synthetic conditions (pH 4.95 vs. 7.09, respectively) and potentially, yet likely less important, the subtle changes in the conjugation of the dipyriddy ligands lead to changes in building units and the resulting topologies. This admittedly limited comparison of three structures (**48–50**) that share similar synthetic conditions (save for pH), and a common carboxylic acid linker all show structural differences in terms of uranyl building unit incorporation and resulting topology. For further examples comparing uranyl CP synthesis using aliphatic linkers with and without dipyriddy ligands, as well as a more comprehensive treatment of incorporation criteria based on ligand/coligand size matching, the reader is referred to the following publications (Borkowski and Cahill, 2006a,b; Kerr and Cahill, 2011).

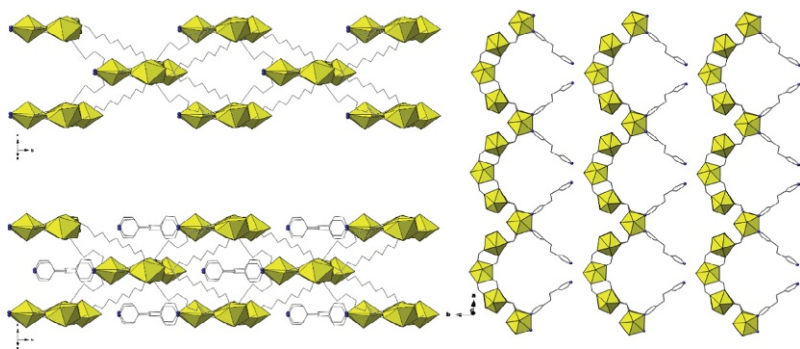


FIGURE 44 Left: A view down the 3D channel structure of **49** with (above) and without (below) the coordinating BPE ligands. Right: Pentagonal bipyramidal uranyl BUs are bridged via sebacic linkers into chains. Every fourth uranyl cation (of the chain) is coordinated by two BPE ligands.

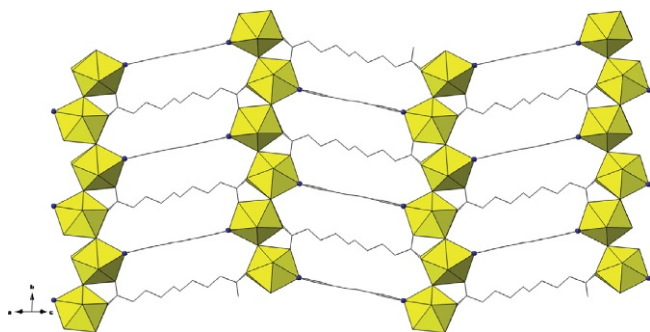
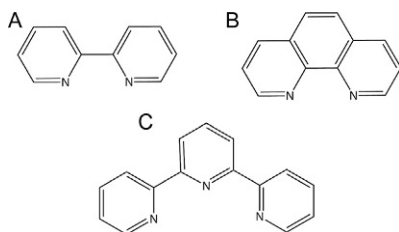


FIGURE 45 Pentagonal bipyramidal uranyl BUs in **50** point-share to form oligomeric SBUs (chains) that are linked via sebacic and BPE ligands to form sheets.

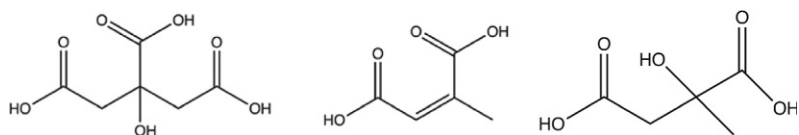


SCHEME 14 Various nitrogen-donating molecules that are mentioned throughout this chapter: (A) 2,2'-dipyridyl (2,2'-BIPY), (B) 1,10-phenanthroline (Phen), (C) 2,2':6',2''-terpyridine (TPY).

7.2 Coordinating Species: N-Donor “Capping” Ligands

N-donor-chelating ligands such as 2,2'-dipyridyl (2,2'-BIPY), Phen, and 2,2':6',2''-terpyridine (TPY) are unique as these organic molecules can be used in the synthesis of hybrid uranyl materials in a variety of roles that influence structure (Scheme 14). We have already seen cases where these ligands can be substituted with oxygen donors to create multidentate chelation sites; thus we now turn our attention to the nonsubstituted ligands. Particularly, we will focus on their roles as chelating coligands and their influence upon the resulting structural topologies. This class of ligand features a fixed coordination site and a ridged structure that can increase or decrease the structural dimensionality by restricting or promoting further ligand-to-metal coordination in one or more directions (Rodríguez-Dieguez et al., 2009; Thangavelu et al., 2013; Thuéry, 2013a).

In our first example, we will examine two of the many structures reported in 2013 by Thuéry that resulted from the hydrothermal synthesis of a uranyl salt, citraconic acid (citen) (Scheme 15) and either 2,2'-BIPY or Phen (Thuéry, 2013a). Compounds **51**, [UO₂(citen)(2,2'-BIPY)], and **52**, [UO₂(citen)(Phen)], are isomorphous as the similar coordination environments of the 2,2'-BIPY



SCHEME 15 Right to left: The structures of citraconic acid (citcn), citric acid (Cit), and D-(-)-citramalic acid (Citml).

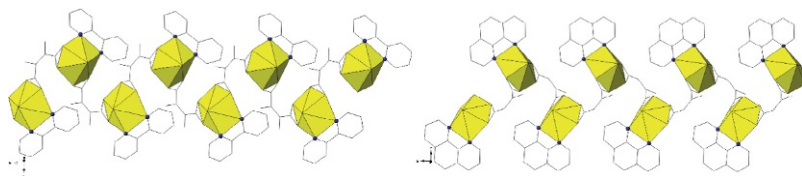


FIGURE 46 Left: Hexagonal bipyramidal uranyl building units in **51** are capped by 2,2'-bipy ligands and linked by citcn ligands to form chains. Right: Hexagonal uranyl PBUs in **52** are capped and linked via Phen and citcn ligands, respectively, to give rise to chains.

and Phen coligands promote nearly identical structures (Fig. 46). Each structure contains hexagonal uranyl bipyramidal monomers that are chelated by the respective N-donor ligand and by two bidentate citcn ligands. The citcn linkers connect adjoining uranyl monomers together to give rise to chains that propagate along the [010] direction. In these two examples, the overall dimensionality of the resulting structures is limited to 1D as the N-donors impede coordination in one direction. Moreover, a trend will emerge as this section progresses wherein such chelating coligands tend to restrict uranyl speciation to monomers, even over a range of reaction conditions.

The same study that produced compound **36** (Sec. 5.3) also explored the use of a capping ligand (Phen) in conjunction with the EDS linker (Thuéry, 2014). Compound **53**, $[(\text{UO}_2)_2(\text{EDS})(\text{OH})_2(\text{Phen})_2] \cdot 4\text{H}_2\text{O}$, contains edge-shared hydroxide-bridged pentagonal bipyramidal dimers (Fig. 47). The dimers are chelated by two bidentate Phen capping ligands and two EDS ligands via the oxygen atoms of the sulfonate functional groups (monodentate). The disulfonate-containing ligands function to bridge the dimers together to give rise to chains that propagate along the [010] direction. The neutral chains in turn pack and are stabilized by π -interactions that stem between the Phen molecules of neighboring chains, and these interactions propagate in the [100] direction.

It would appear that the use of a coligand that “caps” one side of the uranyl coordination sphere limits the potential dimensionality of the resulting structure. This is perhaps advantageous as there may be opportunity to promote or at the least increase the likelihood of forming a topology of a desired dimensionality—a topic to be revisited below. A means to promote assembly of a different dimensionality then presents itself by utilizing O-donor ligands

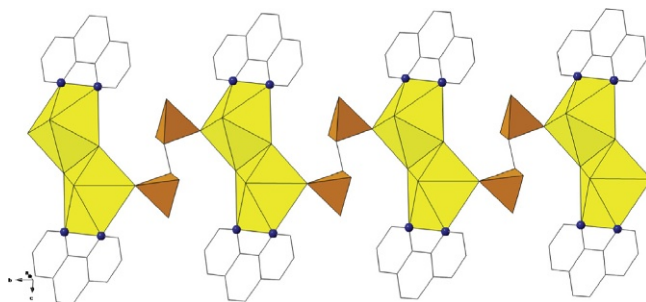


FIGURE 47 Uranyl SBUs (dimers) in **53** are capped by Phen ligands and subsequently form chains via EDS linkers.

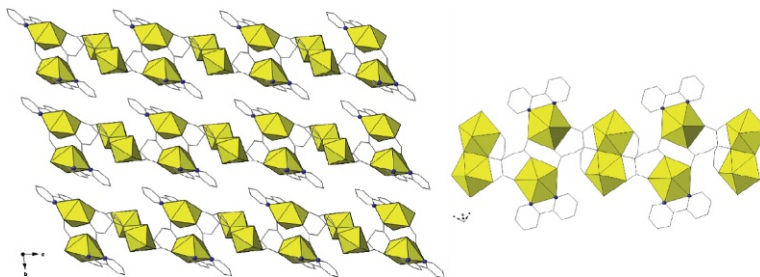


FIGURE 48 Left: A view down the [001] direction of the layered structure of **54**. Right: Uranyl PBUs are capped by 2,2'-Bipy ligands and linked to uranyl dimers via citric acid linkers to form a chain-like motif.

that exhibit polydentate coordination sites. An example of this is present in the same publication that featured compounds **51** and **52** as citric acid (Cit) and 2,2'-BIPY can be paired with the uranyl cation to form a 2D CP over the 1D dimensionality that resulted in the reaction with citcn (Thuéry, 2013a). When compared to citcn, citric acid is longer (C_5 vs. C_4), more flexible (saturated vs. conjugated) and contains an extra carboxylate group capable of coordination.

As a result, the combination of citric acid, 2,2'-BIPY and the uranyl cation yielded compound **54**, $[(UO_2)_2(Cit)(2,2'-BIPY)] \cdot 0.5H_2O$ (Thuéry, 2013a). Pentagonal bipyramidal monomers and edge-sharing dimers are incorporated into the structure of **54** (Fig. 48). The uranyl monomers are each chelated by one 2,2'-BIPY coligand and two Cit ligands: the first in a monodentate fashion, while the second in a bridging bidentate fashion that conjoins the monomers. The monomeric BU “groups” are in turn linked to the edge-sharing dimers via additional linkages from the Cit ligands to form chains, which in turn are linked to one another to result in the formation of a (101)-layered structure. This study was selected to serve as an example to highlight that in addition to the role of reaction conditions (a prevailing theme of this

contribution), one must also consider the role of each ligand in a dual ligand synthetic approach to the assembly of uranyl CPs.

Returning our attention to the familiar BTEC O-donor ligand (used in the synthesis of **14–16**) allows one to highlight further the use of a polycarboxylate ligand with a capping ligand (Phen) to influence the dimensionality of the resulting architecture. Compound **55**, $[\text{UO}_2(\text{Phen})(\text{BTEC})]$ features hexagonal bipyramidal uranyl PBUs that are capped by one chelating Phen ligand and further coordinated in a bidentate fashion via the carboxylate groups of two BTEC linkers (Jiang et al., 2006). The local coordination environment of the uranyl terminates in one direction (due to the Phen) but is linked in two directions by the polycarboxylate BTEC ligands to other monomers to form sheets (011) (Fig. 49). Interestingly, the Phen molecules are slightly twisted via rotation of the whole molecule relative to equatorial plane of the uranyl cation (dihedral angle of 23°) and protrude into the interlayer space (above and below the equatorial plane) and form edge-to-face π -interactions between adjacent Phen molecules of the same layer. Although the use of a polycarboxylate O-donor linker led to the formation of a 2D structure (as was the case in **54**) this method to assemble uranyl CPs is rather in its infancy. A concrete relationship between ligand use and resulting structural dimensionality is not well defined at present, yet certain trends of assembly (BU inclusion and dimensionality) should not be ignored.

The hydrothermal treatment of 2,2'-BIPY and 1,4-naphthalenedicarboxylate (NDC) ligand (Scheme 16) with a uranyl nitrate salt in the presence of silver nitrate (which was not incorporated) led to the formation of compound **56**, $[(\text{UO}_2)_2(\text{NDC})_2(2,2'\text{-BIPY})]$ (Fig. 50) (Liao et al., 2008). Hexagonal bipyramidal uranyl monomers in **56** are coordinated by a

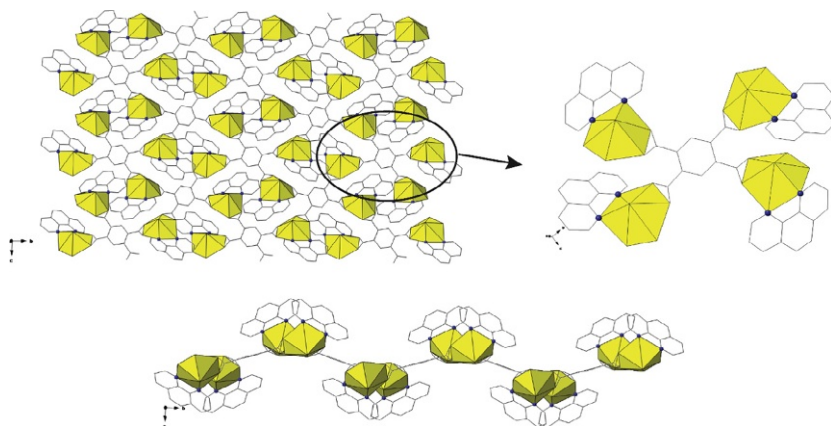
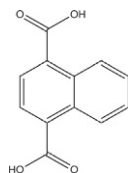


FIGURE 49 Above: Hexagonal bipyramidal uranyl building units in **55** are capped by Phen molecules and linked via BTEC ligands to form sheets. Below: The sheets are corrugated due to the alternating (above and below) coordination of the Phen ligands.



SCHEME 16 The structure of 1,4-naphthalenedicarboxylic acid (NDC).

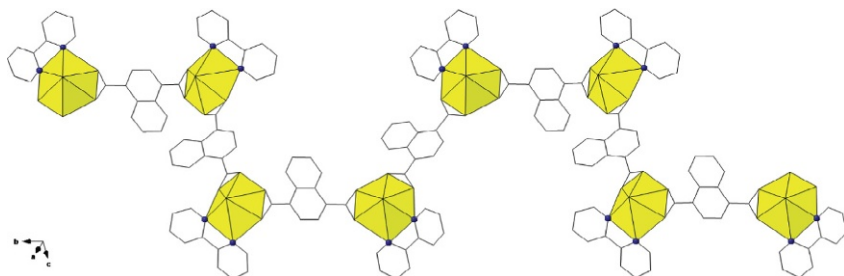


FIGURE 50 Hexagonal bipyramidal uranyl PBUs in **56** are capped and linked into chains by 2,2'-Bipy and NDC ligands, respectively.

chelating 2,2'-Bipy ligand and two NDC linkers via bidentate coordination. The bridging coordination of the NDC ligands links the monomers into chains that propagate in a zigzag fashion along the [010] direction.

These examples of lower dimensional structure formation provided by means of multiligand strategies (seemingly influenced by the functionality of the “linker” species) and the relative tendency of the chelating species to favor the coordination of monomeric species are of note. In fact, these motifs inspired studies in our group that aimed to probe control of nuclearity via chelating N-donor species. A study aimed at the pairing of various N-donor chelating ligands (e.g., TPY) with O-donor carboxylate-bridging ligands led to formation of six monomer-containing compounds via solvothermal synthesis (1:1.5 water:2-propanol) (Thangavelu et al., 2013). The highlighted example, **57**: $[\text{UO}_2(\text{C}_8\text{H}_4\text{O}_4)(\text{C}_{15}\text{H}_{11}\text{N}_3)]$, was prepared with the intent of promoting monomeric building units and lower dimensional solid-state structures. Compound **57** features N-donor TPY ligands bound to pentagonal bipyramidal uranyl monomers, which are further coordinated via two 1,4-BDC linkers (Fig. 51). The 1,4-BDC ligands bridge the uranyl monomers into chains that propagate along the [001] direction. Although we present only one structure from this contribution, all six compounds feature a common uranyl PBU that is coordinated by a terminal capping ligand and O-donor ligands. The effectiveness of this strategy to promote monomers and lower dimensional assemblies is clear, yet several (three of the six) of the compounds in this study consist of discrete molecular “pseudo-dimers” that result from nonbridging

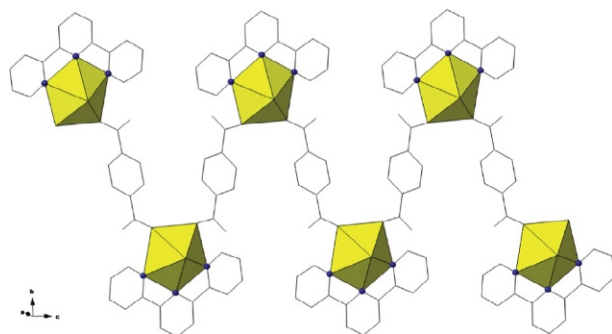
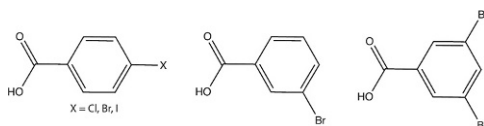


FIGURE 51 The pentagonal bipyramidal uranyl monomers in **55** are capped by chelating TPY ligands and subsequently linked into chains via bridging 1,4-BDC ligands.



SCHEME 17 Left to right: The structures of 4-halobenzoic acid ($X = \text{Cl, Br, I}$), 3-bromobenzoic acid, and 3,5-dibromobenzoic acid.

O-donor ligands. The cause and effect (dimer vs. extended structure) is not clear, which indicates that further investigation into this strategy is required.

The notion that this “cap and link”-based strategy favors monomeric building units is presented with a degree of caution as strictly aqueous systems have demonstrated that uranyl hydrolysis can ultimately prevail (Carter and Cahill, 2015a). For instance, our group has synthesized a series of uranyl compounds that contained TPY or Phen as a capping ligand, along with various halogen substituted benzoic acid O-donor ligands (Scheme 17). The hydrothermal treatment of uranyl nitrate, TPY and 4-bromobenzoic acid led to the formation of compounds **58**, $[\text{UO}_2(\text{C}_{15}\text{H}_{11}\text{N}_3)(\text{C}_7\text{H}_4\text{BrO}_2)_2]$, and **59**, $[(\text{UO}_2)_2(\text{C}_{15}\text{H}_{11}\text{N}_3)(\text{C}_7\text{H}_4\text{BrO}_2)_3]$. Compound **58** features pentagonal bipyramidal uranyl monomers that are chelated by TPY ligands and further coordinated by two monodentate 4-bromobenzoic acid ligands (Fig. 52). This structure is ultimately molecular as the benzoic acid ligands contain *terminal* halogen atoms as opposed to the ditopic carboxylate linkers in **57**. As the pH of the synthesis is adjusted from 2.8 (in **58**) to 6.8 with 5 M NaOH, the uranyl BUs change from monomers to point-sharing dimers. One uranyl of the dimer in **59** is chelated by a TPY ligand and is in turn bridged to the second uranyl via a bridging bidentate 4-bromobenzoic acid. The local coordination geometry of the second uranyl dimer is completed via coordination of two 4-bromobenzoic acid ligands. Although these structures are molecular and a bit out of place herein, they serve as illustrative examples that highlight the

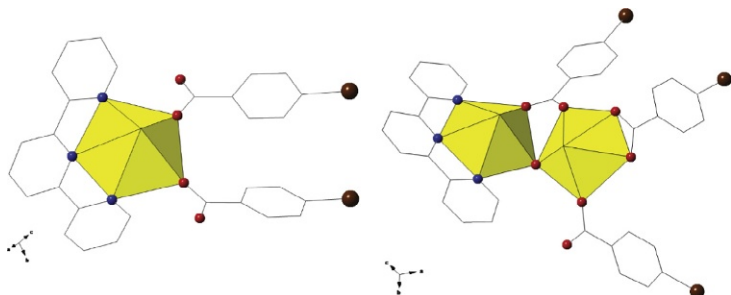


FIGURE 52 Left: Pentagonal bipyramidal uranyl monomers in **58** are capped by TPY ligands and coordinated via 4-bromobenzoic acid ligands. Right: Point-sharing uranyl dimers in **59** form molecular species as a result of coordination via TPY and 4-bromobenzoic acid ligands.

effect of hydrolysis on the nature of the uranyl BU. This reaffirms the message we have been developing regarding speciation and predictability as even when a strategy known to favor the formation of monomeric BUs is used, other factors may dominate and overrule a given approach.

Having had the opportunity to highlight the breadth of structure types that result from the combined use of chelating and bridging ligands in the syntheses of uranyl hybrid materials and CPs, we wish to close this section by featuring a few materials containing peroxide ligands, which have been introduced via *in situ* peroxy generation. The first example chosen contains a peroxo-bridged uranyl dimer that resulted from the room temperature evaporation of a solution containing uranyl nitrate and dimethylformamide. The result of the synthesis (a peroxo-bridged dimer) was unexpected and thus not formed by the authors own doing. Compound **60**, $[(\text{UO}_2)_2\text{O}_2(\text{C}_3\text{H}_7\text{NO})_4(\text{NO}_3)_2]$, features peroxo-bridged hexagonal bipyramidal uranyl dimers that are coordinated by two bidentate nitrate and four monodentate dimethylformamide ligands (Charpin et al., 1985). The coordination of six terminating ligands results in the formation of a molecular dimer (Fig. 53). We note that the authors did not introduce peroxide as part of their synthesis and instead, this ligand was formed *in situ*. This serendipitous occurrence is significant as the generation of peroxo species in uranyl-containing systems is relevant to spent nuclear fuel stewardship and catalysis (Forbes et al., 2011; Hanson Brady et al., 2005; McNamara et al., 2002; Nieweg et al., 2005; Wang et al., 1995). Moreover, and while not strictly the type of hybrid materials we have chosen to highlight, readers are encouraged to explore the exceedingly rich uranyl peroxo-cluster compounds prepared by the Burns group who have intentionally introduced peroxide species into their syntheses (Qiu and Burns, 2012).

Our group has explored promotion of *in situ* peroxy generation and its use as a synthetic strategy as opposed to a serendipitous occurrence. An early attempt at this approach came by way of a recent study where three structures containing uranyl dimers bridged via peroxo ligands were formed by

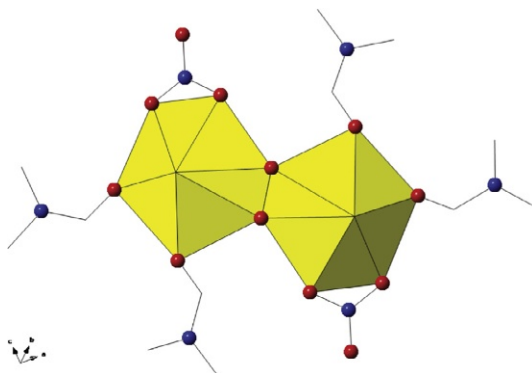


FIGURE 53 Peroxo-bridged uranyl dimers in **60** are coordinated by dimethylformamide and nitrate ligands.

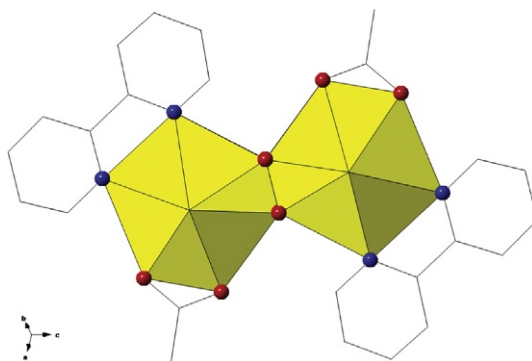


FIGURE 54 Hexagonal bipyramidal peroxo-bridged dimers in **61** are chelated and coordinated by 2,2'-BIPY and acetate ligands, respectively, to form molecular units.

photochemical means (Thangavelu and Cahill, 2015). The goal of the study was to understand the factors that influence the *in situ* generation of peroxo species and their contributions to the overall assembly. For instance, crystals of compound **61**, $[(\text{UO}_2)_2(\text{CH}_3\text{COO})_2(\text{O}_2)(\text{C}_{10}\text{H}_8\text{N}_2)]$, formed after 7 days as a result of combining 2,2'-BIPY and uranyl acetate in MeOH in the presence of sunlight (Fig. 54). The local coordination geometry of the uranyl peroxo-dimer featured in **61** consists of two chelating 2,2-BIPY capping ligands and two bidentate acetate species. This compound was only observed to form in the presence of light, indicating the presence of a photochemical process that led to the formation and ultimate inclusion of a peroxo species. For a detailed mechanistic explanation that covers the effect of sunlight and heating on the generation of the peroxo-bridged dimers the reader is referred to the original manuscript (Thangavelu and Cahill, 2015), as well as a number of the citations therein.

7.3 Noncoordinating Species: Structure Influencing Guests

An ancillary species can likewise adopt a noncoordinating role and incorporate into the solid state as a “guest” species—or simply a species that interacts with the primary compound “host” through noncovalent means. A guest species can serve a number of different roles: space filling, charge balancing, structure influencing with “templating” being a specific example of the latter. Up to this point, we have concentrated on direct ligand-to-metal coordination and uranyl speciation as the main drivers of assembly and largely ignored noncoordinated guests, as many have been solvent molecules or charge-balancing counter cations that occupy void spaces. We will now switch our attention to focus specifically on those instances where a noncoordinated guest species plays a significant role in the formation of the overall structure. We will begin by providing a general example of the effect a noncoordinated guest species can have and then focus specifically on cases where the guest species function as template molecules or those that participate in directional NCIs.

We begin this discussion by once again revisiting the pairing of aliphatic carboxylic acid linkers with N-donor dipyriddy molecules (introduced in an earlier section) by looking at the combination of suberic acid ($C_8H_{14}O_4$) and BPE' molecules. To highlight the influence that a noncoordinating species can have on a structure, we will revisit a previously discussed uranyl–suberic coordination compound and compare it with a BPE'-containing uranyl–suberic compound. Compound **9**, $[UO_2(C_8H_{12}O_4)]$, is formed during the hydrothermal reaction of suberic acid and uranyl nitrate and contains edge-sharing hexagonal bipyramids that form chains [010] (Fig. 12) (Borkowski and Cahill, 2006a). The polynuclear uranyl SBUs are coordinated and bridged together by suberic acid ligands to form sheets. Under similar synthetic conditions as those that produced **9**, save for the inclusion of BPE' to the reaction mixture, compound **62**, $(C_{12}N_2H_{12})[(UO_2)_2(C_8H_{12}O_4)]$, is formed—the pH of the synthesis is reported to be 4.86 (Kerr and Cahill, 2011). In contrast to **9**, hexagonal bipyramidal uranyl monomers that are linked together via suberic acid ligands to form anionic chains [101] constitute the structure of **62**. The anionic chains are in turn charge balanced by doubly protonated BPE' cations that reside in voids created by folds in the anionic chains (Fig. 55). The charge-balancing BPE' organic cations do not influence the structure via direct coordination, yet they clearly affect the resulting topology.

Recalling the structure of compound **42**, $[UO_2(2-SB)(H_2O)]$, it consisted of pentagonal bipyramidal uranyl monomers that were bridged by 2-SB ligands to yield chains (Fig. 41). Using analogous synthetic conditions—the syntheses only differed by the addition of pyrazine (Pyz—Scheme 18) and decreasing the synthesis time by 3 weeks—compound **63**, $[UO_2(2-SB)(H_2O)]_2 \cdot Pyz$, was formed (Thuéry, 2012a). This structure exhibits similar uranyl connectivity as pentagonal bipyramidal monomers are coordinated by

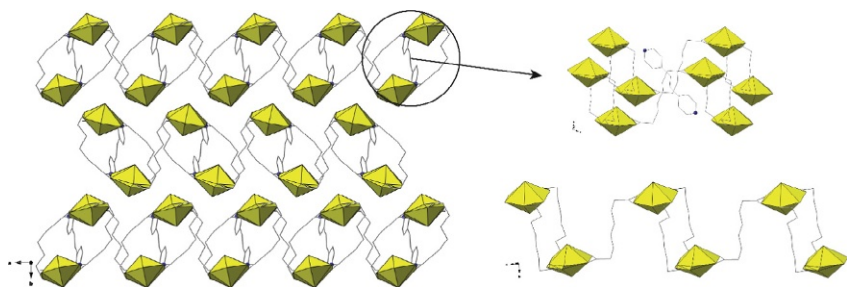
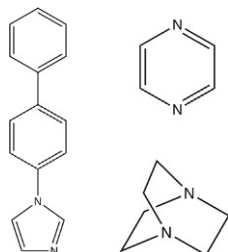


FIGURE 55 Left: A view down the [001] direction of the anionic chains in **62**. Right: Charge-balancing BPE⁺ cations occupy voids (above) that are formed from the folding of neighboring chains. The chains (below) are comprised of hexagonal bipyramidal uranyl BUs that are linked via suberic acid ligands.



SCHEME 18 Left: The structure of 1-biphenyl-4-yl-1-imidazole (BPI). Right: The structures of pyrazine (Pyz) (above) and 1,4-diazabicyclo[2.2.2]octane (DABCO) (below).

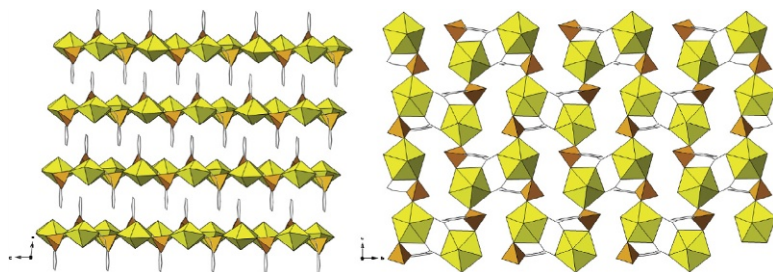


FIGURE 56 Left: A view down the [010] direction of the layered structure of **63**. Right: 2-SB ligands link pentagonal bipyramidal uranyl monomers into sheets.

three 2-SB ligands and one water molecule (Fig. 56). Despite a nearly identical local coordination geometry to that of **42** and similar connectivity, BU-to-BU, the formation of sheets in the (011) plane is observed. The overall 2D uranyl CP is layered, along [001], and contains Pyz guest molecules that reside in the interlayers. The Pyz guest form hydrogen bonds with the water molecules that are coordinated to the uranyl BUs forming each layer. The

presence of the Pyz molecules may favor the formation of sheets over that of chains.

The previous examples demonstrate the ability of a guest molecule to influence the overall structure and allow us to transition into a brief discussion on the templating effect. Templating (for structure direction) is a concept originated in the study of aluminosilicate zeolites, porous materials with considerable application to molecular separations, and size/shape-selective catalysis. As such, the desire to direct the formation of specific topologies and channel architectures led to using protonated organic molecules (such as amines) to serve as structure-directing agents and provide a platform about which an inorganic host could assemble. In the case of the thermal stable zeolites, this species could then be removed by calcination. Definitions and criteria emerged (Davis and Lobo, 1992) that obviously predate and are perhaps only tangentially relevant to CP systems. More recent definitions and categorization serve as a bit of an update to reflect more recent materials and suggest that templating can be divided into two categories: templating by the guest or templating for the guest (Tanaka and Kitagawa, 2007). The first case is referred to as primary templating and occurs when the guest or template incorporates (noncovalently) into a framework during synthesis and promotes the formation of/or influences the resulting structure type by creating voids, channels, or frameworks of various dimensionalities, etc. (Tanaka and Kitagawa, 2007). The second category or simply “secondary” templating involves cases where guests can induce reversible structural changes to a CP or MOF that formed of its own accord. We will focus and limit our discussion to the examination of primary templating in order to examine structure types that have resulted as a consequence of the structure-directing ability of select molecules. Moreover, some cases of templating are clearly serendipitous in nature or have been reported without explicitly stating that structure direction was the intent. We will not make these distinctions as doing so calls for too much speculation.

The hydrothermal reaction of uranyl nitrate and D-(–)-citramalic acid (Citml) led to the formation of compound **64**, $[\text{UO}_2(\text{Citml})]$ (Fig. 57) (Thuéry, 2008a). Pentagonal bipyramidal uranyl monomers are incorporated into the structure of **64** and each PBU is coordinated by three mono- and one bidentate Citml ligands via the carboxylate oxygen atoms. The Citml linkers each conjoin four uranyl PBUs to give rise to a sheet that spans the (110) plane. If the reaction conditions that yielded compound **64** are held (relatively) constant but phenanthroline is added, compound **65**, $(\text{H-Phen})_2[(\text{UO}_2)_5(\text{citml})_4(\text{H}_2\text{O})] \cdot 3\text{H}_2\text{O}$ results (Thuéry, 2013a). Compound **65** contains a mixture of PBUs and SBUs, as pentagonal bipyramidal uranyl monomers and edge-sharing dimers predominate. The uranyl monomers and dimers are bridged together via Citml linkers to yield an overall anionic 3D MOF that contains channels, which propagate along the [001] direction (Fig. 57). The channels are occupied by charge-balancing monoprotinated H-Phen

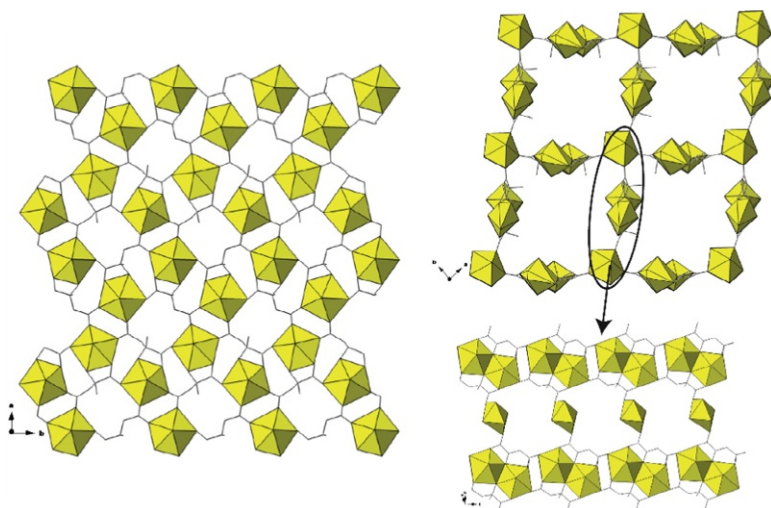


FIGURE 57 Left: Pentagonal bipyramidal uranyl monomers in **64** are conjoined via Citml linkers to form sheets. Right: The anionic 3D network of **64** (above) contains channels that are occupied by charge-balancing Phen guests (not drawn). The 3D framework contains pentagonal bipyramidal uranyl dimers and monomers (below) form bridged chains via Citml linkers.

molecules that participate in intermolecular π -interactions (Phen...Phen). Given the similarity between the two syntheses, it is clear that the presence of the Phen molecules induce the formation of a 3D framework and functions as a structure-directing agent.

To further illustrate this effect and its use among uranyl CPs and MOFs, we turn to the Albrecht-Schmitt research group as they synthesized a series of uranyl-diphosphonates under nearly identical conditions (Nelson et al., 2013). The hydrothermal synthesis of four uranyl-phosphonates was formed by holding the source of uranyl (UO_3) and type of coordinating phosphonate constant, while the incorporated organic guest species was varied. Two of the four structures were synthesized using 2,2'-BIPY and Phen, respectively, to yield compounds **66**, (2,2'-BIPY)[$\text{UO}_2(\text{H}_2\text{O})(\text{MDP})$], and **67**, (Phen)[$\text{UO}_2(\text{H}_2\text{O})(\text{MDP})$] (Fig. 58) (Nelson et al., 2013). In both compounds, uranyl pentagonal bipyramidal PBUs are coordinated by bridging diphosphonate ligands and a water molecule. In **66**, the PBUs are joined via the MPD linkers to give rise to anionic sheets in the (101) plane. The sheets in turn stack in the [010] direction to form an anionic layered structure that contains charge-balancing 2,2'-Bipy cations in the interlayer. In contrast, compound **67** consists of chains that propagate along the [010] direction. These chains are anionic and are flanked by charge-balancing Phen cations that facilitate the packing of the structure. In this case, the synthetic conditions remained constant, and thus a likely explanation for the variation in the structures can be attributed to the N-donor organic species acting as a structure-directing agent.

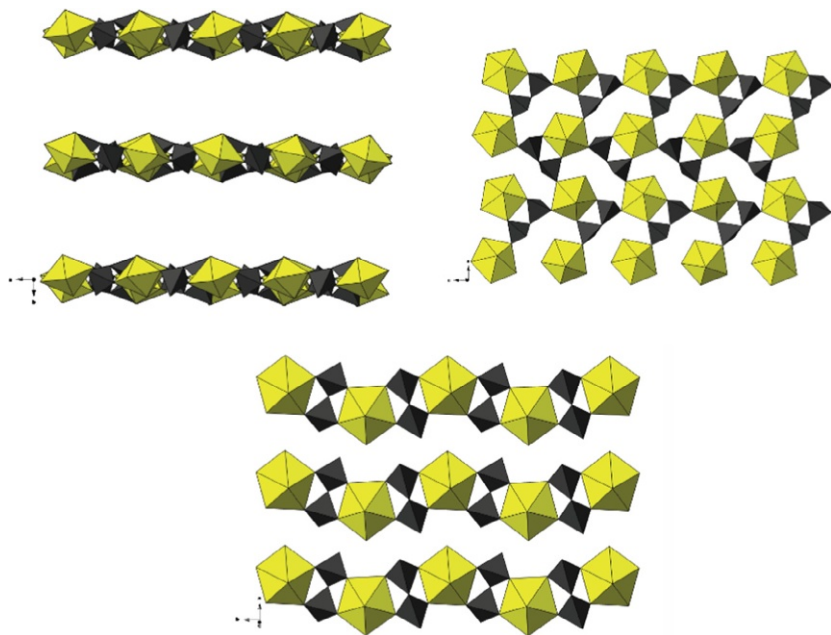


FIGURE 58 Above: The layered structure of **66** consists of sheets (right) formed by MDP linked pentagonal bipyramidal uranyl monomers. Below: Pentagonal bipyramidal uranyl PBUs in **67** are linked via MDP ligands into chains.

A final example to highlight the structure-directing influence that organic species can have upon the resulting topology comes by way of two uranyl-diphosphonates that contain 1-(biphenyl-4-yl)-1*H*-imidazole (BPI) and 2,2'-BIPY templates (Scheme 14). Compounds **68**, (H-BPI)[UO₂(H-LDP)H₂O], and **69**, (H₂-BIPY)[((UO₂(H₂O)₂)(UO₂(H₂O)₂))(LDP)₂·2H₂O], were formed via the hydrothermal synthesis of 1-hydroxyethylidenediphosphonic acid (LDP—Scheme 7), uranyl nitrate at pH 2.5 and 1.5, respectively (Fig. 59) (Yang et al., 2012). Compound **68** features pentagonal bipyramidal uranyl monomers that are coordinated three LDP ligands (one bidentate and two bridging bidentate) and one water molecule. The bridging interactions of the LDP ligands give rise to anionic sheets that span the (101) plane. The sheets stack to form layers that are occupied by monoprotonated 2,2'-BIPY cations that form hydrogen bonds to the layers (N—H...O 2.715 Å) to stabilize the arrangement (Yang et al., 2012).

The change in pH from the synthesis of **68** (pH 2.5) to **69** (pH 1.5) is likely responsible for the inclusion of doubly protonated 2,2'-BIPY molecules into the structure of **69**, which also features pentagonal bipyramidal monomers that are coordinated by LDP linkers and water molecules (Fig. 59). The uranyl PBUs exhibit similar coordination to those in **68**, as they are bound by three

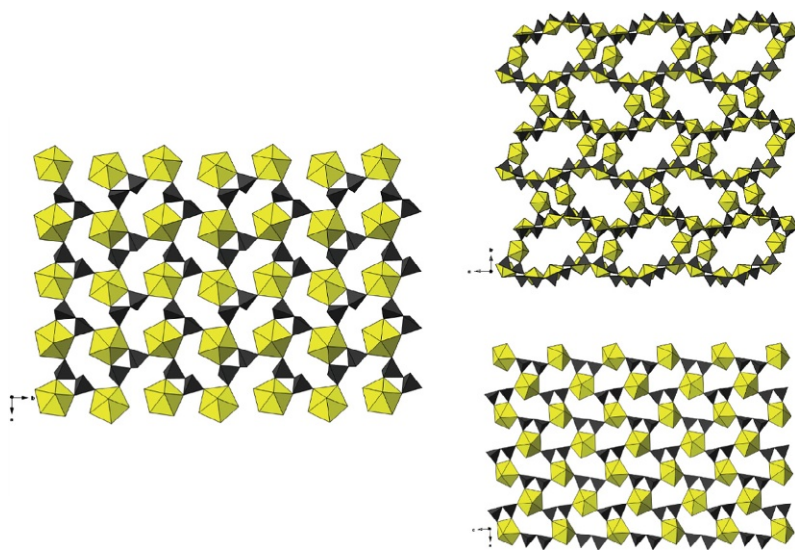


FIGURE 59 Left: Pentagonal bipyramidal uranyl monomers in **68** are linked via LDP ligands to form anionic sheets. Charge-balancing BPI cations (not shown) occupy the interlayer space. Right: The 3D structure (above) of **69** contains channels that are occupied by doubly protonated charge-balancing Phen molecules (not shown). The 3D structure consists of uranyl/LDP sheets (below) that are linked via additional PBU/LDP bridges. The carbon atoms have been omitted for clarity.

LDP ligands and one water molecule and give rise to sheets (101). The sheets are in turn connected in the [010] direction via bridging uranyl metal centers that are coordinated by two LDP ligands (one bidentate and one monodentate) and two water molecules. The connectivity in **69** results in the formation of a 3D anionic framework with channels that propagate along the [100] direction. The channels ($3.1 \times 6.9 \text{ \AA}$) are occupied by the doubly protonated bipyridinium cations. The ability of the organic cations in this system to direct the assembly of the resulting structures is clear as the presence of 2,2'-BIPY cations induces the formation of 2D and 3D CPs. In support of the bipyridinium cations functioning as templates are the differences in structural dimensionality that arises as a function of the protonation state of the cations, which ultimately is a function of reaction conditions. These two structures illustrate the diversity of both uranyl building unit coordination and the resulting structural topology as a function of the template effect. For further examples of the ability of the N-donor ligands to direct the formation of various architectures, the reader is referred to several studies (Adelani and Albrecht-Schmitt, 2011d; Adelani et al., 2011; Doran et al., 2003; Knope and Cahill, 2007; Nelson et al., 2013; Ok et al., 2006; Thuéry, 2009b, 2011b; Thuéry and Masci, 2009; Tian et al., 2013a, 2014; Wu et al., 2013; Yang et al., 2012).

The use of ancillary species in the synthesis of uranyl-bearing hybrid materials is rather common and encompasses a wide breadth of organic and inorganic species. We chose to cover and touch upon homofunctional oxygen and nitrogen donor species exclusively due to their abundance in the literature and the resulting rich catalog of structure types. Nitrogen-donating species in particular are extremely versatile due to their ability to function as space filling, charge-balancing, coordinating, or templating species. Thus, looking specifically at the pairing of N-donor species with O-donor ligands (the most widely represented coordinating species among uranyl CPs and MOFs) highlights the nearly limitless combinations of primary and secondary uranyl building units with the various coordinating and noncoordinating roles the organic species can adopt to capture the diversity that is fundamental to uranyl hybrid material synthesis. Recalling our previous chapter in this series exploring lanthanide hybrid materials (Carter and Cahill, 2015b), readers are also encouraged to look at examples of templating within Ln(III) compounds where there are some exceptional examples of directed assembly and indeed the influence of guest on luminescent properties.

8 HETEROMETALLIC URANYL HYBRID MATERIALS

The previous sections focused upon the role of the ligand or noncoordinating ancillary organic species in promoting structural diversity among uranyl-containing hybrid materials, whereas this section is dedicated to heterometallic systems. The influence of a secondary metal species on the structural topology and, in some cases, properties will be explored. From a structural standpoint, combining a metal ion that has a well-known coordination geometry (i.e., tetrahedral (3d and 4d) vs. spherical (Ln(III))) with that of the uranyl cation affords one new opportunity in promoting topological diversity. Moreover, as many transition and lanthanide metal complexes are of note for their physical and chemical properties, one of which being luminescence, their combination with the emissive uranyl species into a single coordination may promote a somewhat “blended” and perhaps, advantageous set of photophysical properties. The synthesis of these materials has primarily been pursued in three ways: via homofunctional or heterofunctional ligands, the use of metal-ligands, or by postsynthetic metalation (PSMe). Each of these three methods will be introduced and discussed individually. For additional references that highlight the breadth of structure types that have resulted from various heterometallic efforts, the reader is encouraged to see the following studies (Basile et al., 2015; Deb, 2010; Knope and Cahill, 2010c; Knope et al., 2011; Liu et al., 2013; Mougel et al., 2014; Olchowka et al., 2013a,b; Thuéry, 2007a, 2009a,c,d, 2010, 2011a, 2012a,b,c, 2013c; Thuéry and Harrowfield, 2014; Thuéry and Riviere, 2013; Tian et al., 2012, 2013b; Volkringer et al., 2011; Weng et al., 2014; Yang et al., 2014).

8.1 Homofunctional Ligands

One of the more common methods for the synthesis of heterometallic uranyl CPs and MOFs is direct assembly via hydro/solvothermal synthesis using homofunctional ligands, i.e., those with a single type of functional group. This approach combines uranyl and secondary metal salts or oxides with an organic linker in a one-step synthesis process. The use of a homofunctional ligand to synthesize a heterometallic hybrid material has inherent challenges as the metal ions need to have a similar affinity to a given functional group (i.e., pyridyl, carboxylate, phosphonate, etc.) such that incorporation of both metal centers is favored as opposed to phase separation.

We have already seen examples highlighting the proclivity of the uranyl cation to form various CPs with carboxylate containing groups. Thus, pairing the uranyl cation with a secondary metal such as a lanthanide (Ce, Nd, Pr, Eu, Tb, or Er) which shares a similar affinity to carboxylate functional groups can be a viable route to heterometallic hybrid materials. Looking specifically at a 2012 study by the Loiseau group, a series of heterometallic uranyl-Ln(III) (Ce or Nd) compounds were prepared hydrothermally from mixtures of uranyl and lanthanide nitrate salts with phthalic (1,2-BDC), pyromellitate (BTEC), or Mel (Mihalcea et al., 2012b). Of the six compounds that were synthesized, three were isostructural due to the substitution of Ce(III) for that of Nd(III).

The first structure type to be discussed is 1D and contains a mixed uranyl/lanthanide chain motif. Compound **70**, $(\text{NH}_4)[(\text{UO}_2)_4\text{O}_2(\text{Ln})(\text{H}_2\text{O})_7(1,2\text{-BDC})_4] \cdot x\text{H}_2\text{O}$ (Ln = Ce, Nd), features tetragonal uranyl SBUs (edge-sharing pentagonal and hexagonal bipyramids) and nine coordinate tricapped trigonal prismatic lanthanide monomers (Fig. 60). The uranyl tetramers are coordinated by a total of four phthalic linkers via bidentate and bridging bidentate fashion, the latter links the uranyl and lanthanide BUs together to form anionic chains along the [100] direction. The lanthanide coordination sphere consists of two oxygen atoms from the phthalic ligands and a total of seven water molecules. The anionic 1D coordination network is charge balanced via intercalated ammonium cations.

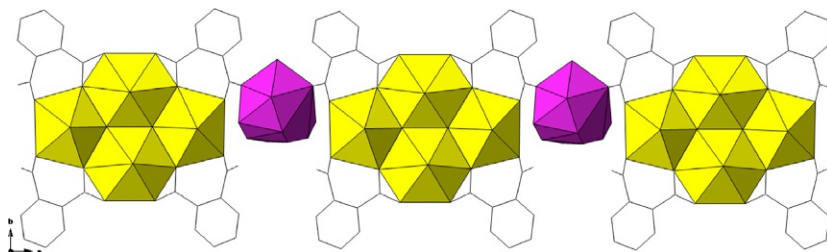


FIGURE 60 Uranyl SBUs (tetramers) in **70** are bridged to neodymium monomers via 1,2-BDC linkers to form chains along the [100] direction.

The use of a different linker, pyromellitate (BTEC), led to the formation of compound **71**, $[(\text{UO}_2)_3\text{Ln}(\text{H}_2\text{O})_{12}(\text{BTEC})_3] \cdot 5\text{H}_2\text{O}$, which contains monomeric uranyl and lanthanide BUs (Fig. 61). The coordination sphere of the pentagonal and hexagonal bipyramidal uranyl monomers are completed via coordination of the BTEC ligands, which result in the formation of corrugated sheets in the (110) plane. The lanthanide metal ions are also coordinated via the BTEC ligands (and six water molecules) and directly link the uranyl sheets along the [110] direction to form a 3D CP (Fig. 61).

The final compound in this series, **72**: $[(\text{UO}_2)_2(\text{OH})\text{Ln}(\text{H}_2\text{O})_7(\text{Mel})] \cdot 5\text{H}_2\text{O}$ ($\text{Ln} = \text{Ce}, \text{Nd}$), contains point-sharing pentagonal bipyramidal uranyl dimers and hydrated lanthanide monomers (Fig. 61). Each uranyl dimer is coordinated by four Mel linkers (two in bidentate and four in bridging bidentate fashion) that link each dimeric unit to a total of eight others; this connectivity gives rise to sheets in the (110) plane. Two of the bridging monodentate carboxylate groups of the Mel linkers are rotated normal to the (110) plane and link the uranyl BUs to the lanthanide metal ions to give rise to a neutral 3D framework. The interlayer space is occupied by solvent water molecules.

A total of six compounds (three isostructural) were published in this study and each contained a range of uranyl building units (tetramers, monomers, and dimers) and a common monomeric lanthanide BU. In each of the three examples, the lanthanide metal species contributed to the overall structural dimensionality by providing an additional degree of connectivity. Looking at the overall structures and noting the coordination geometry of the uranyl and the (mostly) spherical coordination of the Ln(III) sites suggests the

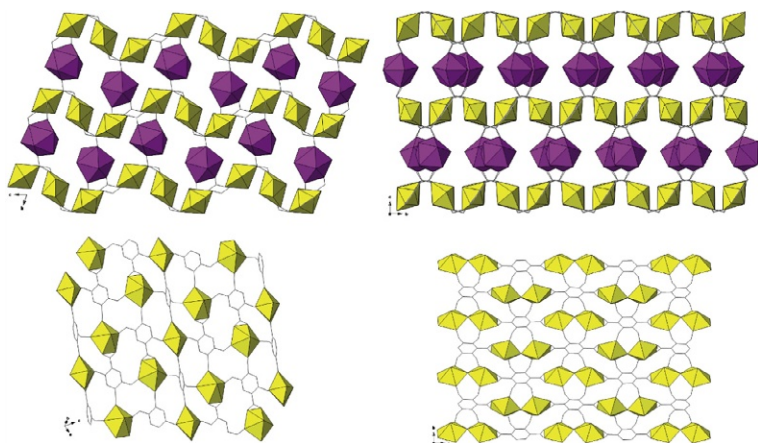


FIGURE 61 Left: Uranyl PBUs in **71** are linked in the (101) plane via BTEC ligands to form sheets (below) that ultimately give rise to a 3D network (above) through additional connectivity by way of interlayer neodymium monomers. Right: Point-sharing pentagonal bipyramidal uranyl dimers in **72** give rise to sheets (below) via melletic acid coordination. The layers are connected in the [001] direction (below) via interlayer neodymium metal centers, giving rise to a 3D network.

lanthanide “fills in where it can” after the uranyl–carboxylate “host” has formed. The use of polycarboxylate ligands in general are viable routes to the formation of uranyl heterometallic hybrid materials containing either transition metals (Olchowka et al., 2013a; Yang et al., 2013a) or lanthanide metals (Thuéry, 2010).

A ligand similar to the 1,2-BDC linker utilized in the synthesis of **74** is the phosphonate containing 1,2-phenyldiphosphonic (1,2-PDP) acid (Scheme 7). The Albrecht-Schmitt group used 1,2-PDP to probe the coordination chemistry of several bimetallic actinide and actinide/lanthanide compounds, namely Pu(IV)/Ce(IV) and U(VI)/Pu(VI) (Diwu et al., 2011). For brevity, we will only present the result of the hydrothermal reaction of ammonium cerium nitrate and uranyl nitrate in the presence of 2-PDP. Compound **74**, $[\text{UO}_2(\text{Ce}(\text{H}_2\text{O})(\text{C}_6\text{H}_3(\text{PO}_3)(\text{PO}_3\text{H}))_2]_2 \cdot \text{H}_2\text{O}$, features edge-sharing pentagonal bipyramidal uranyl and cerium (trigonal dodecahedrons) dimers (Fig. 62). The pentagonal bipyramidal coordination environment of the uranyl SBUs arises from the oxygen atoms of the phosphonate moieties of the 1,2-PDP linkers; these interactions link the uranyl and cerium dimers together to form an interwoven sheet. The cerium ions are each 10 coordinate as they are bound via the oxygen atoms of the phosphonate moieties and water molecules. The 2D CP contains solvent water molecules that occupy the interlayer sites.

8.2 Heterofunctional Ligands

A synthetic strategy centered upon heterofunctional ligands typically involves the pairing of two functional groups that differ in either coordination mode geometry or affinity for a given metal ion. The interplay of coordination geometry and affinity is used to preferentially bind dissimilar metal ions at each functional group selectively. For instance, the uranyl cation is a hard Lewis acid that prefers to coordinate highly charged anions and functional

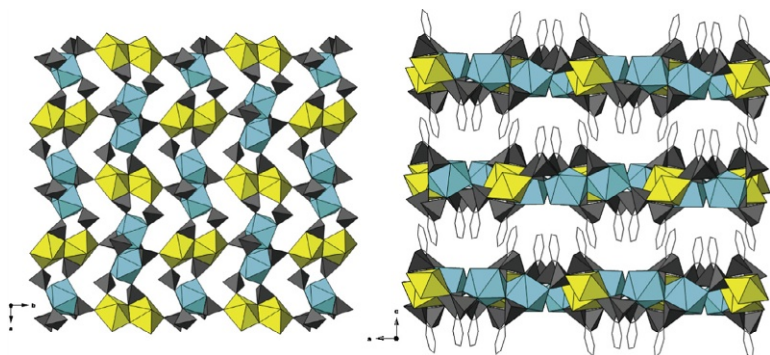


FIGURE 62 Left: Uranyl and cerium dimers in **73** are woven together via 2-PDP linkers to form sheets in the (101) plane. Right: The $\text{UO}_2^{2+}/\text{Ce(III)}$ sheets in **73** form a layered structure that contains solvent water molecules in the interlayer regions.

groups that contain hard donor atoms, i.e., phosphonate. The pairing of a phosphonate functional group with that of a carboxylate or pyridyl function group on the same ligand can then result in preferential uranyl coordination at the R-PO₃²⁻ site, leaving the second functionality free for further metal ion coordination. Although the basis of hard/soft pairing may be able to be exploited in pairing metal ions of different Lewis' acidity with functional groups of varying hardness, the reader is cautioned as this is merely a rough guide and as we will see, sterics cannot be ignored.

This synthetic strategy has been utilized by our own group to synthesize a series of heterometallic UO₂²⁺/Zn(II) hybrid materials via the use of the now familiar carboxyphosphonate ligands. Specifically, teppa was used to form several compounds that featured hydrated zinc monomers and pentagonal bipyramidal uranyl PBUs that gave rise to 1, 2, and 3D CPs (Knope and Cahill, 2010c). Compound **74**, (Zn(H₂O)₆)[(UO₂)₂(PPA)₂(H₂O)₂]₂·4H₂O, features uranyl monomers that are each coordinated by one water molecule and three PPA ligands, two of which are monodentate and coordinate via the phosphonate oxygen atoms, while the third is coordinated in a bidentate fashion via both the phosphonate and carboxylate functional groups (Fig. 63). The coordination of the PPA ligands bridges the uranyl PBUs together to form anionic chains, which propagate along [100] and feature noncoordinating carboxylate oxygen atoms (due to the monodentate PPA ligands) along the periphery. The chains are charge balanced by hydrated Zn(II) cations that occupy the interchain region along with several solvent water molecules.

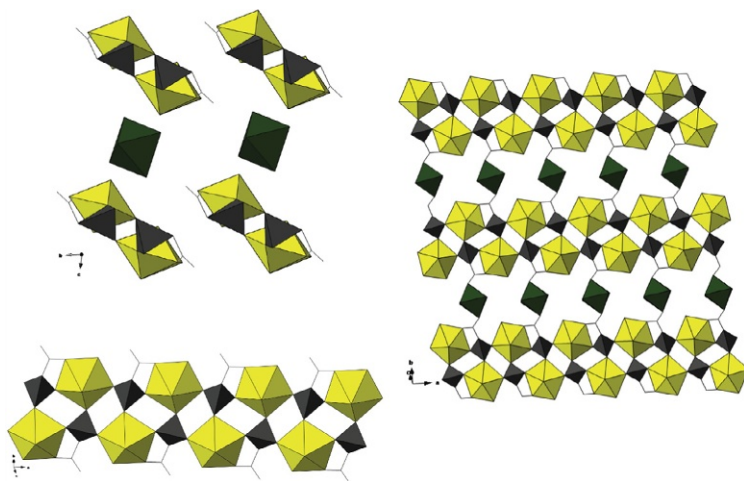


FIGURE 63 Left: Pentagonal bipyramidal uranyl monomers in **74** are joined via PPA linkers to form anionic chains (below) that are charge balanced by Zn(H₂O)₆²⁺ cations (above). The zinc atoms are drawn as green (gray in the print version) polyhedrons. Right: Monomeric uranyl PBUs in **75** form chains that are joined via Zn metal sites through carboxylate linkages to give rise to sheets.

The role of the zinc changes in **75** as it no longer simply charge balancing (as in **74**) but is now directly coordinated and has a more definitive structural contribution. Compound **75**, $[(\text{UO}_2)_2(\text{H}_2\text{O})_2(\text{PPA})_2\text{Zn}(\text{H}_2\text{O})_4]$, features a similar chain motif ($[100]$) to that of **75**, yet the Zn(II) sites are now coordinated axially by the previously noncoordinating carboxylate oxygen atoms at the periphery of the chains (Fig. 63). The coordination of the Zn(II) to these peripheral sites directly link the chains together, which results in the formation of sheets in the (011) plane. The octahedral coordination sphere of the zinc metal ions is completed by four equatorial water molecules.

The last structure chosen from this study, **76**: $[(\text{UO}_2)_2(\text{PPA})_2(\text{HPPA})\text{Zn}_2(\text{H}_2\text{O})_2]\cdot 3\text{H}_2\text{O}$, contains point-sharing uranyl dimers and oligomeric Zn(II) building units (Fig. 64). The uranyl SBUs are linked together via PPA ligands (via the phosphonate and carboxylate oxygen atoms) to form chains that propagate along the $[100]$ direction. The Zn(II) metal ions also form chains as each octahedron edge-shares to give rise to oligomeric SBUs that propagate along $[010]$. Additional PPA ligands form bridging interactions that link the uranyl and Zn(II) chains together to form a 3D CP that contains solvent (water molecules) accessible void spaces. A collective look over the uranyl/zinc system demonstrates, once again, the structural versatility that can be afforded by the addition of a secondary metal species, especially one capable of adopting a number of structure influencing roles.

The same PPA ligand used in the $\text{UO}_2^{2+}/\text{Zn}(\text{II})$ study was used to prepare a series of $\text{UO}_2^{2+}/\text{Ln}(\text{III})$ -containing compounds from the hydrothermal reactions of uranyl and lanthanide nitrate salts (Knöpe et al., 2011). As a result, four isostructural compounds with 2D sheet topologies and the formula $[(\text{UO}_2)_2(\text{PPA})(\text{HPPA})_2\text{Ln}(\text{H}_2\text{O})]\cdot 2\text{H}_2\text{O}$ ($\text{Ln}=\text{Sm}, \text{Tb}, \text{Er}, \text{Yb}$) were synthesized (Fig. 65). The structure of **77** (containing Sm(III)) features edge-sharing uranyl dimers, comprised of pentagonal and hexagonal BUs, that are

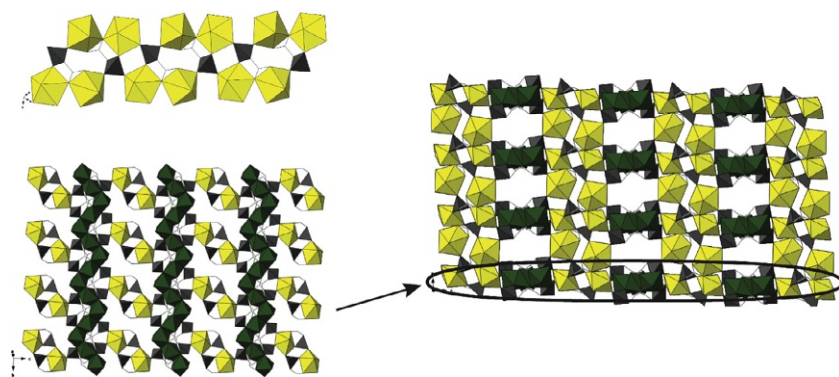


FIGURE 64 Left: Uranyl dimers in **76** give rise to chains (above) via PPA linkages. The chains are joined to oligomeric Zn(II) SBUs (chains) to give rise to sheets (below). Right: Additional linkages afforded by the uranyl chains results in the formation of a 3D coordination polymer.

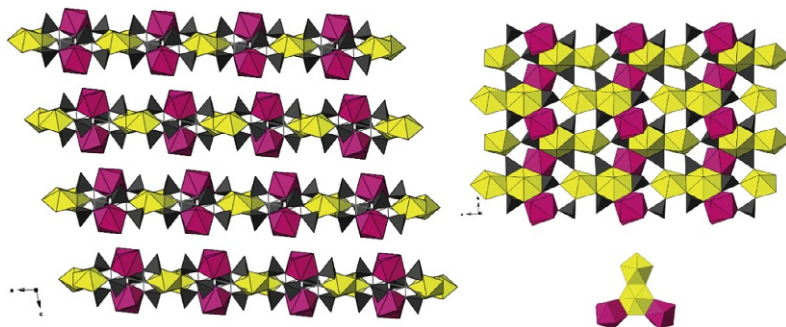


FIGURE 65 Left: Compound **77** forms a layered structure. Right: Two samarium PBUs (pink (gray in the print version) polyhedrons) edge-share with a uranyl dimer to form bimetallic units (below) that in turn give rise to sheets (above) via PPA linkers.

coordinated exclusively by the phosphonate groups of the PPA ligands. The Sm(III) ions edge-share with the hexagonal uranyl BUs (that make up the dimers) and are further coordinated by the carboxylate and phosphonate moieties of the PPA ligands. These uranyl/Sm groups are in turn linked to one another via phosphonate bridges that ultimately give rise to corrugated sheets in the (110) plane.

The difference in coordination preference of the carboxylate and phosphonate moieties in the previous examples (**74–76**) for the zinc and uranyl metal sites, respectively, can likely be attributed to differences in hard–soft pairing as is commonly observed in uranyl/transition metal heterometallic systems (Adelani and Albrecht-Schmitt, 2011a; Alsobrook et al., 2008, 2010, 2011b,c). In the case of **77**, however, the difference in terms of hardness between the UO_2^{2+} and Ln(III) metal ions is minimal and cannot alone explain coordination preferences (Nash and Choppin, 1997). As such, steric differences between the linear uranyl and spherical Ln(III) ions are likely contributors to the distinction as well.

Although it is not a primary focus to discuss the properties of the materials in this chapter, we would like to direct attention to the luminescent behavior of compound **77**. The material exhibits intense visible and near-IR emission, characteristic of Sm(III)-containing compounds, when excited directly at an absorption maximum of the UO_2^{2+} cation (Knope et al., 2011). This is significant as the absence of any uranyl emission is an indication that all of the absorbed energy is transferred to the Sm(III) metal centers and/or lost to a nonradiative decay process; the uranyl cation acts as an antenna to sensitize Sm(III) emission. The same phenomenon is not observed in the Tb(III), Er(III), and Yb(III) analogs, as these ions do not have excited states that match, in terms of energy, to the excited state of the UO_2^{2+} and thus do not undergo efficient energy transfer. Compound **77** is an example of a

compound where the bimetallic functionality has a distinct and measurable impact upon the structures properties.

To conclude the discussion of the versatility of carboxyphosphonate ligands in the synthesis of uranyl-bimetallic compounds, we turn to a series of compounds prepared via the hydrothermal reaction of UO_3 , cadmium acetate, and teppa (Alsobrook et al., 2011a). Compound **78**, $\text{Cd}_2[(\text{UO}_2)_6(\text{PO}_3\text{CH}_2\text{CO}_2)_3\text{O}_2(\text{OH})(\text{H}_2\text{O})_2]\cdot 16\text{H}_2\text{O}$, will be the only material from the study discussed as it is a rather unique material with respect to the uranyl SBUs and resulting topology (Fig. 66). The structure of compound **78** is a 3D open framework that features both pentagonal and hexagonal bipyramidal uranyl building units that edge-share to form octamers. The octomeric subunits, four in total, are coordinated via PPA linkers to discrete uranyl monomers (pentagonal bipyramids) that function to link the four octomers together; these linkages are also responsible for the three dimensionality. Once the octomers are linked together, they form the outer periphery of a large cavity that is capped (top and bottom) by additional octomeric units that are tethered together via PPA and uranyl monomeric linkages, giving rise to a cage. The spaces created in the joining of the octomers are filled by hydrated cadmium metal centers that form linkages with the carboxylate oxygen atoms of the PPA ligands (Fig. 66). The cavity of the cage is large (16 Å in diameter) and is occupied by solvent water molecules. The direct coordination of the cages creates permanent channels that propagate along the [010] direction and are occupied by cadmium cations and water molecules.

Bifunctional ligands with perhaps a more explicit difference between functional groups may be found in those featuring both nitrogen and oxygen donor sites, such as isonicotinic acid ($\text{C}_6\text{H}_5\text{NO}_2$) and *trans*-3-(3-pyridyl)acrylic acid

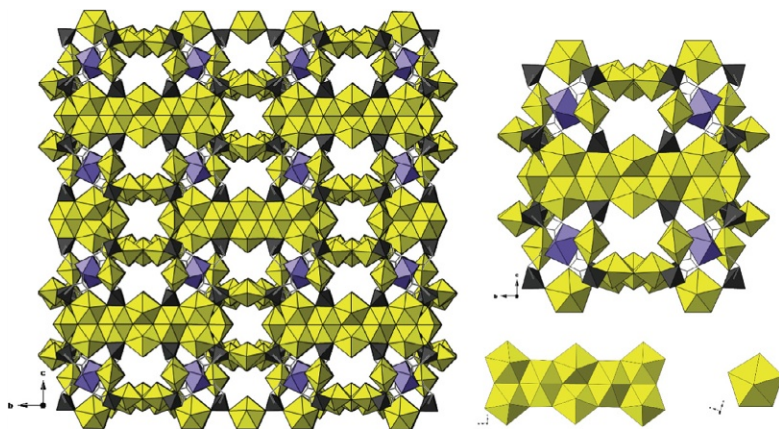
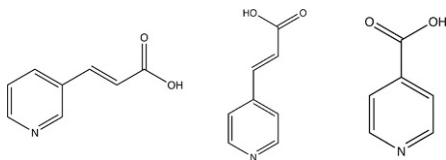


FIGURE 66 Left: A view down the [100] direction of the open 3D structure of **78**, water molecules (not shown) occupy the cavities. Right: PPA linked uranyl/cadmium cages (above) are constructed of both uranyl octomers and monomers (below). The cadmium atoms are depicted as lavender (gray in the print version) polyhedrons.

($C_8H_7NO_2$) (Scheme 19). In this case, the negatively charged carboxylate group (hard) would be expected to preferentially coordinate the hard UO_2^{2+} cation, leaving the soft pyridyl nitrogen site free to coordinate a softer metal such as copper. As an example, two compounds were prepared by the hydrothermal reaction of uranyl acetate and copper salts in the presence of isonicotinic acid (Weng et al., 2014). Compounds **79**, $[(UO_2)_3Cu(II)O_2(C_6H_4NO_2)_5]$, and **80**, $[(UO_2)Cu(I)(C_6H_4NO_2)_3]$, are both 3D bimetallic CPs that incorporate different uranyl building units (trimers vs. monomers) and stabilize two different oxidation states of Cu(II vs. I). Compound **79** features edge- and point-sharing pentagonal bipyramidal uranyl trimers that are coordinated by the carboxylate groups of five isonicotinate ligands that adopt two primary roles: bridging (4) and terminating (1) (Fig. 67). Those that bridge link the uranyl trimers to the copper (II) metal ions via the nitrogen atom of the pyridyl ring group to give rise to a sheet that contains voids. The copper (II) sites are octahedral, as the equatorial plane is occupied by four nitrogen coordinated isonicotinate ligands, whereas the axial sites are filled with oxygen atoms. The axial oxygen coordination motif (Cu—O=U) results from covalent bond formation between a shared “yl” oxygen of the uranyl with that of the copper metal ion. Two of these Cu—O=U bonds, above and below the plane of the sheet, form and give rise to an overall 3D CP. This shared oxygen bond is another example of the intriguing chemistry of the uranyl cation that can promote higher dimensions of connectivity and complexity. We will revisit this topic below, yet point the reader to a number of other examples (Liu et al., 2013; Mougél et al., 2014; Thuéry, 2009c; Tian et al., 2012, 2013b; Volkringer et al., 2011).



SCHEME 19 Left to right: The structures of *trans*-3-(3-pyridyl) acrylic acid (t33pa) and *trans*-3-(4-pyridyl) acrylic acid (t34pa).

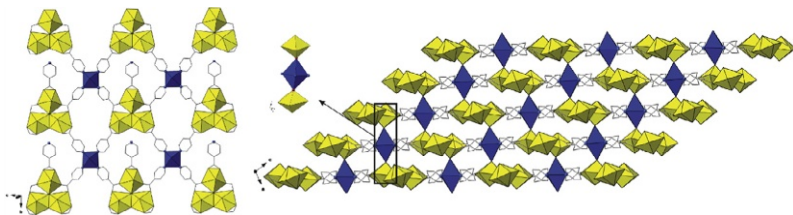


FIGURE 67 Left: Uranyl trimers in **79** are coordinated to octahedral Cu(II) metal centers via isonicotinate linkers to form sheets. Right: The sheets are stacked and directly linked via Cu—O=U bonds to form a 3D assembly.

Compound **80**, $[(\text{UO}_2)\text{Cu}(\text{I})(\text{C}_6\text{H}_4\text{NO}_2)_3]$, is unique in that it features copper in the +1 oxidation state, which is a rare occurrence in hydrothermally prepared uranyl-bearing hybrid materials (Weng et al., 2014). Pentagonal bipyramidal uranyl monomers are incorporated into **80** and are bridged together by the carboxylate oxygen atoms of two bridging bidentate isonicotinate ligands to form “pseudo-dimers” (Fig. 68). The pseudo-dimeric units are coordinated by an additional four isonicotinate ligands (two bidentate and two monodentate) that in turn further coordinate a Cu(I) metal ion at the pyridyl nitrogen. In addition, the two monodentate (carboxylate) isonicotinate ligands coordinate copper species above and below the dimeric groups to result in the formation of a 3D heterometallic CP. Structures **79** and **80** both result in an overall increase to the structural dimensionality as the coordination geometry of the secondary metal becomes important to assembly.

The second and final N,O-donor ligand to be discussed in the context of heterometallic materials synthesis is the pyridyl-based *trans*-3-(3-pyridyl) acrylic acid (t33pa). The solvothermal (water/acetonitrile) reaction of uranyl and copper nitrate in the presence of t33pa led to the formation of compound **81**, $[(\text{UO}_2)_2\text{Cu}(\text{t33pa})_3\text{O}(\text{H}_2\text{O})]\cdot\text{NO}_3$ (Fig. 69) (Thuéry and Harrowfield, 2014). The structure of **81** incorporates tetramers that consist of three pentagonal bipyramidal and one hexagonal bipyramidal uranyl building units that edge-share. Each tetramer is coordinated via the carboxylate group of six t33pa ligands (four bidentate and two monodentate), which go on to coordinate copper (II) metal species at each pyridyl nitrogen atom. The dual coordinating nature of the t-33pa ligands give rise to sheets that form a 3D network as secondary Cu—O=U bonds increase the connectivity of the CP (Fig. 69). The copper atoms in this structure adopt a distorted square bipyramidal coordination environment, which promotes dimensionality. The ability to incorporate metal atoms that can form several different coordination environments is viable to the synthesis of heterometallic systems.

As we have stated above, it is not a primary goal of this chapter to develop structure/property relationships comprehensively across all families of uranyl

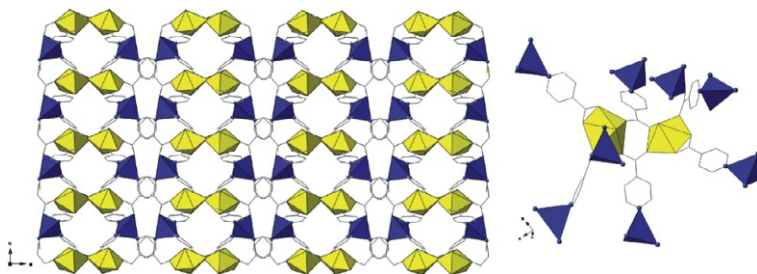


FIGURE 68 Left: Pentagonal bipyramidal uranyl monomers and tetrahedral Cu(I) PBUs in **80** are directly linked by isonicotinic ligands to form a 3D assembly. Right: Each uranyl monomer is coordinated to five Cu(I) tetrahedron via isonicotinic linkers.

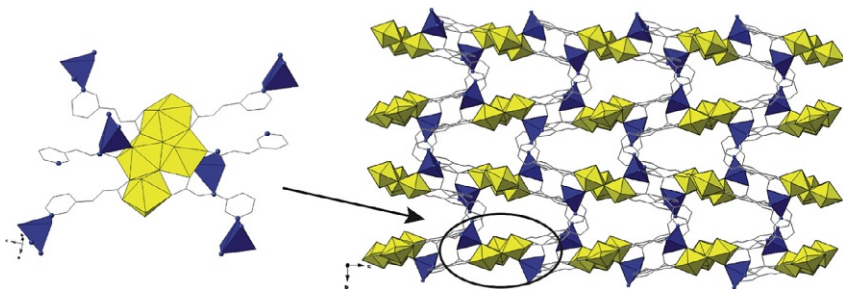
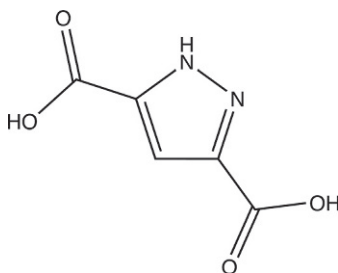


FIGURE 69 Uranyl secondary (tetramers) and Cu(II) primary (tetrahedral monomers) building units give rise to an open 3D network via t33pa and Cu—O=U linkages.



SCHEME 20 The structure of 3,5-pyrazoledicarboxylic acid.

hybrids. That said, the heterometallic materials warrant special mention considering the influence of the second metal center on uranyl emission. Whereas we have already seen the opposite uranyl impacting Sm(III) emission, more common is the influence of the secondary metal center on the luminescent properties of the uranyl. As such, we will close this section on heterofunctional ligands by looking at two examples where the N- and O-donor 3,5-pyrazoledicarboxylic acid (3,5-PDC, [Scheme 20](#)) linker was utilized in the synthesis of a homo- and heterometallic uranyl-containing CP ([Frisch and Cahill, 2005](#)).

The hydrothermal treatment of uranyl nitrate with 3,5-PDC led to the formation of compound **82**, $[\text{UO}_2(\text{C}_5\text{H}_2\text{N}_2\text{O}_4)(\text{H}_2\text{O})]$, which features pentagonal bipyramidal uranyl monomers ([Fig. 70](#)). Each uranyl monomer is coordinated by three 3,5-PDC ligands: (1) bidentate (carboxylate), (2) bridging bidentate (carboxylate), and (3) chelating (carboxylate and pyridyl nitrogen). The bridging interactions link the uranyl monomers into sheets in the (110) plane. The addition of copper nitrate to the reaction mixture yields compound **83**, $[(\text{UO}_2)\text{Cu}(\text{C}_5\text{H}_2\text{N}_2\text{O}_4)_2(\text{H}_2\text{O})_2]$, which is also comprised of sheets ([Fig. 70](#)). In this case, square bipyramidal uranyl monomers are each coordinated in a monodentate fashion by four 3,5-PDC ligands. Two of the 3,5-PDC ligands bridge the uranyl monomers to distorted octahedral copper BUs that are chelated by the carboxylate oxygen and pyridyl nitrogen to form an overall 2D

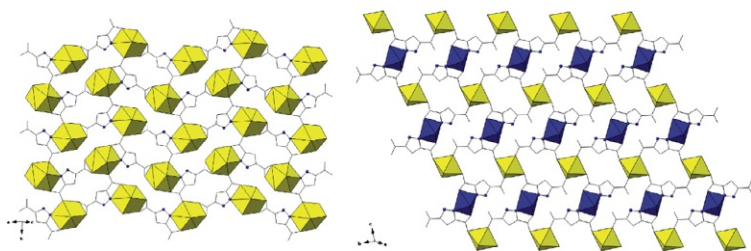


FIGURE 70 Left: Hexagonal bipyramidal uranyl PBUs in **82** are conjoined by 3,5-PDC linkers to form sheets. Right: Square bipyramidal uranyl and distorted octahedral Cu(II) building units in **83** are linked via 3,5-PDC ligands to form sheets.

topology. Conjugation within the pyrazole ring makes this ligand a candidate for facilitating energy transfer between metal centers. As such, the luminescent properties of compound **82** were investigated at several excitation wavelengths that correspond to both the ligand (248 nm) and uranyl (365 and 424 nm) absorption maxima. Upon excitation at all three wavelengths, compound **82** exhibited characteristic green uranyl emission of similar intensity. The same excitation wavelengths were used to study the emissive properties of **83**, where uranyl emission was absent. This indicates the presence of a possible energy transfer pathway from the uranyl cation to the copper metal centers with an accompanying nonradiative decay pathway. In this case (unlike **77**), energy transfer did not induce luminescence in the secondary metal species (as copper is not typically regarded as luminescent) but instead quenching of uranyl fluorescence was observed.

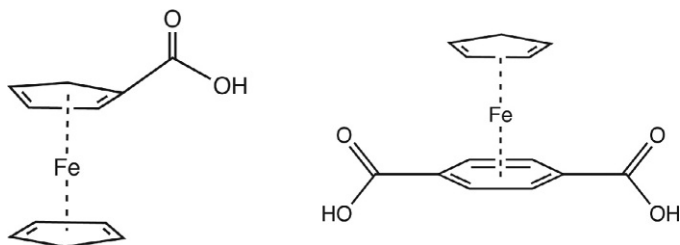
There are many more examples of heterofunctional ligands and that have proven effective for the synthesis of uranyl heterometallic materials, including those with the previously mentioned pyridine dicarboxylates and chelating capping ligands (2,2'-dipyridyl, 2,2'-bipyrimidine, and Phen) (Cahill et al., 2007; Cantos et al., 2010; Frisch and Cahill, 2006; Thuéry and Riviere, 2013). The recurring theme of speciation and building unit diversity leading to a vast structural portfolio is only further exemplified by the addition of a secondary metal center. Moreover, the ability of a secondary metal to donate its properties to the resulting CP renders heterometallic uranyl CPs an area of interest.

8.3 Metalloligands

The susceptibility of the uranyl cation to hydrolysis and the seemingly random inclusion of oligomeric species into the solid state are by no means less apparent in heterometallic systems. In many respects, efforts to promote inclusion of a secondary metal center complicate matters in the sense that additional metal species can undergo their own hydrolysis and, in some cases, are competing for the same binding sites as the uranyl. Thus, the use of metalloligands may offset some of these issues by introducing a secondary metal species in

a “prepackaged” form. Briefly, a metalloligand may be defined as a discrete molecular metal–organic complex that contains unreacted functional groups that can be utilized for further reaction or coordination (Scheme 21). Incumbent for the use of the metalloligand strategy in the synthesis of uranyl hybrid materials is ensuring that the “uncoordinated” functional groups of the metalloligand have a high affinity for coordination the UO_2^{2+} (Kerr et al., 2014). We will focus on examples where the secondary metal is precoordinated and contains carboxylate functional groups that can undergo further coordination to the uranyl cation. The use of carboxylate groups is significant as these species can be synthesized as soluble salts that can charge balance the UO_2^{2+} and in turn offset phase separation during crystallization.

The first example of this strategy comes from our own group as a η^5 -cyclopentadienyl-iron(II)-functionalized terephthalate ligand, $[\text{H}_2\text{CpFeTP}]^+$, can be paired with the uranyl cation under hydrothermal conditions to prepare compounds **84** and **85** (Fig. 71) (Kerr et al., 2014). The syntheses of **84**, $[(\text{UO}_2)_2(\text{CpFeTP})_4] \cdot 5\text{H}_2\text{O}$, and **85**, $[(\text{UO}_2)\text{F}(\text{HCpFeTP})(\text{PO}_4\text{H}_2)] \cdot 2\text{H}_2\text{O}$, were performed under similar conditions yet the pH of the two reactions differed significantly (5.20 and 0.90, respectively). Pentagonal bipyramidal uranyl



SCHEME 21 Left: The structure of η^5 -cyclopentadienyl-iron(II)-functionalized terephthalate ($[\text{H}_2\text{CpFeTP}]^+$). Right: The structure of ferrocenecarboxylic acid (FCA).

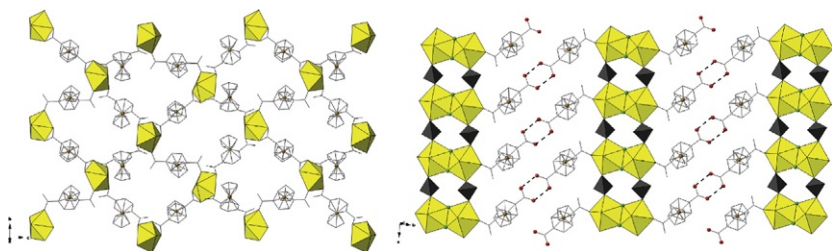


FIGURE 71 Left: Pentagonal bipyramidal uranyl monomers in **84** form sheets through $[\text{CpFeTP}]^+$ linkers. Right: Fluoride-bridged uranyl dimers in **85** are linked via phosphonate ligands to form chains that are coordinated by one of the carboxylate groups of the $[\text{CpFeTP}]^+$ ligands. The noncoordinating carboxylate group participates in head-to-head hydrogen bonding (dashed lines) that links the chains into a sheet-like network topology.

monomers are featured in **84** and are coordinated by the carboxylate groups of four [CpFeTP][−] ligands (one bidentate and three monodentate) to form neutral undulating sheets in the (011) plane. The layered structure contains solvent water molecules that reside in the interlayer regions. Compound **85** contains coordinating phosphate and fluoride anions, which were formed as a result of hydrothermal induced hexafluorophosphate (PF₆[−]) hydrolysis; the [H₂CpFeTP]⁺ metalloligands were prepared and introduced as PF₆[−] salts. In the structure of **85** pentagonal bipyramidal uranyl building units are bridged together via fluorine anions to form dimers. The dimers are then coordinated to one another via bridging phosphate ligands to form chains that propagate along the [100] direction. Each chain is further connected to one another via secondary head-to-head H-bonding interactions (O—H⋯O 2.604 Å) through the terminal carboxylic groups of the [HCpFeTP][−] ligands to give rise to a 2D sheet.

Somewhat surprising is the incorporation of monomeric building units into **84** where oligomerization of the uranyl BUs may have been expected due to the pH of 5.20 (Scheme 1 and Eq. 1). The converse is true for **85** (pH 0.90) as the incorporation of uranyl dimers is rather unexpected, yet can likely be rationalized by the high affinity of the fluoride ion for uranyl coordination and its proclivity to form bridged structures. These two compounds (like **83**) illustrate examples of a secondary metal influencing the properties of the material as the typical luminescence expected with most uranyl-containing CPs (~520 nm) is absent, likely as a result of an energy transfer to the Fe(II) metal centers followed by nonradiative decay (Kerr et al., 2014).

Compound **86**, [UO₂(FCA)₂(H₂O)]·tetrahydrofuran (THF), was isolated as a result of the reaction of uranyl acetate and ferrocenecarboxylic acid (FCA) in a CH₂Cl₂/THF mixture (Villiers et al., 2008). Although the synthesis conditions used for this compound are somewhat inconsistent with our predominantly hydrothermal presentation, we wish to include this structure to further illustrate the metalloligand strategy. Pentagonal bipyramidal uranyl monomers are featured in **86** and are coordinated by the carboxylate oxygen atoms of three FCA ligands (two monodentate and one bidentate) and one water molecule (Fig. 72). The monodentate FCA ligands bridge the uranyl monomers to one another to give rise to chains that propagate along the [100] direction. The chains arrange in a parallel fashion and feature intrachain hydrogen bonding interactions that stem between the oxygen atom of the coordinated water molecule and the noncoordinated carboxylate oxygen (O—H) of the monodentate FCA ligand (O—H⋯O 2.734 Å). The synthesis of heterometallic uranyl CPs using the metalloligand strategy is rather underexplored in comparison to other routes (i.e., homo- and heterofunctional ligands), yet affords a viable route to mixed metal systems with some degree of control over the prepacked metal center. For further examples where metalloligands have been explored in the synthesis of uranyl materials (not necessarily CPs and MOFs), the reader is directed to the following studies (Fong et al., 2002; Ghosh et al., 2013; Henderson et al., 2000; Schettini et al., 2012).

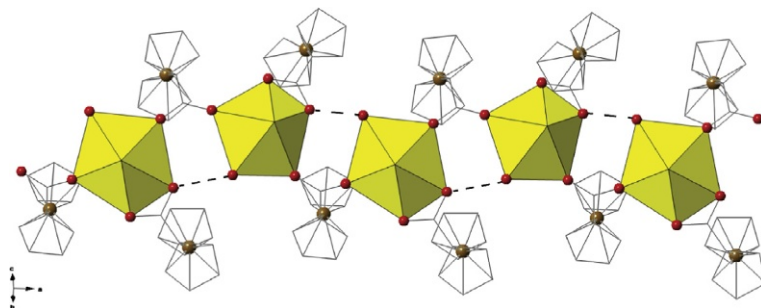


FIGURE 72 Pentagonal bipyramidal uranyl monomers in **86** are bridged by FCA ligands to form chains along the [100] direction. Interchain O—H...O hydrogen bonds form between the coordinated water molecules and the carboxylate oxygen atoms of neighboring PBUs.

8.4 Postsynthetic Modification

Postsynthetic modification (PSM) is the final method to be discussed with respect to preparing heterometallic uranyl-containing hybrid materials. The term PSM is defined as the chemical modification of a framework after it has been synthesized (Hoskins and Robson, 1990; Wang and Cohen, 2009). The basic concept that underlies this strategy is that the modification does not change the overall topology of a material, and instead is used to impart a desired functionality to an existing framework (Tanabe and Cohen, 2011). This approach allows one to exhibit a greater degree of control over the type and number of functional groups or metal centers that are postsynthetically incorporated into the framework (Tanabe and Cohen, 2011). Furthermore, this strategy does not often result in altering the stability of the framework and allows one to diversify (selectively) the secondary properties of a material with a fixed or desired topology (Tanabe and Cohen, 2011). In the case of uranyl-containing CPs, this synthetic mindset can be tangentially applied to the introduction of secondary metal centers. The cases that we will examine (albeit briefly) will all be similar in that the intent of the authors was to apply PSM to the synthesis of bimetallic uranyl hybrid materials. The results of these efforts led to the synthesis of several heterometallic compounds by way of “PSMe” (metalation) and rearrangement, the latter of which (unlike true PSM) involves a physical change to the original structure.

Compounds **87**, $[\text{UO}_2(\text{OH})(\text{C}_6\text{H}_4\text{NO}_2)_2\text{Ag}]$, and **88**, $[(\text{UO}_2)_2(\text{O})(\text{OH})(\text{C}_6\text{H}_4\text{NO}_2)_2\text{Cu}(\text{OH})_2\text{Cl}]$, were synthesized by the hydrothermal treatment of a preformed uranyl–isonicotinate coordination polymer (UICP) with secondary metal salts (Kerr and Cahill, 2014b). The structure of UICP, $[\text{UO}_2(\text{OH})(\text{C}_6\text{H}_5\text{NO}_2)(\text{C}_6\text{H}_4\text{NO}_2)]$, features pentagonal bipyramidal uranyl dimers (edge-sharing) that form chains along the [100] direction via isonicotinic acid linkages (Fig. 73) (Grechishnikov et al., 2005). The structure ultimately forms pseudo-sheets ((110)) via N—H...N hydrogen bonding interactions that stitch

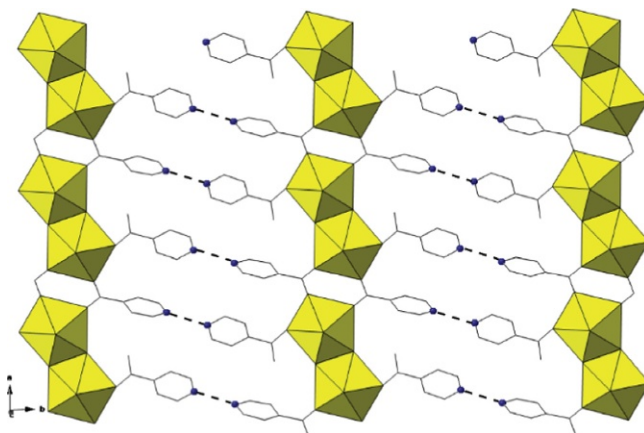


FIGURE 73 Dimers of pentagonal bipyramids in UICP form chains via isonicotinic acid linkages. Hydrogen bonding interactions give rise to a sheet-like network topology.

parallel chains together as every other isonicotinate ligand is protonated, which serves to charge balance the overall structure.

The hydrothermal treatment of the starting material (UICP) with Ag(I) led to the formation of compound **87**, where the original UICP structure remains largely unchanged (Fig. 74) (Kerr and Cahill, 2014b). The addition of the silver cations replaces the need for the pyridyl nitrogen atoms to remain protonated, as charge balancing is now performed by the silver ions. The nitrogen sites, which are now deprotonated, allow for the silver metal atoms to insert between the parallel chains and coordinate directly to the isonicotinate ligands. The linear N—Ag—N coordination of the secondary metal increases the overall dimensionality from 1D to 2D as sheets (110) predominate. It is worth noting that this structure can also be obtained via direct synthesis (hydrothermally) by combining uranyl and silver nitrate salts with isonicotinic acid.

Starting once again with UICP, under similar hydrothermal treatment of copper (II) chloride led to the formation of compound **88** (Fig. 75). The copper (II) metal ions coordinate to the nitrogen atoms of the isonicotinate ligands (similar to **87**) and have either an octahedral or a square planar geometry. One copper site is octahedral as the equatorial plane is filled by the two isonicotinate ligands and two coordinating water molecules, whereas the axial sites are occupied by bridging chloride ligands. The chloride ligands link the octahedral copper sites to those that exhibit a square planar geometry (consisting of two isonicotinate and two chloride ligands) to result in the formation of oligomeric chains of copper SBUs along the [100] direction. As a result of the copper coordination environment, the overall topology of the heterometallic CP consists of sheets. In contrast to **87**, however, the initial structure of UICP is not retained in the final product. An *in situ* rearrangement of the parent CP

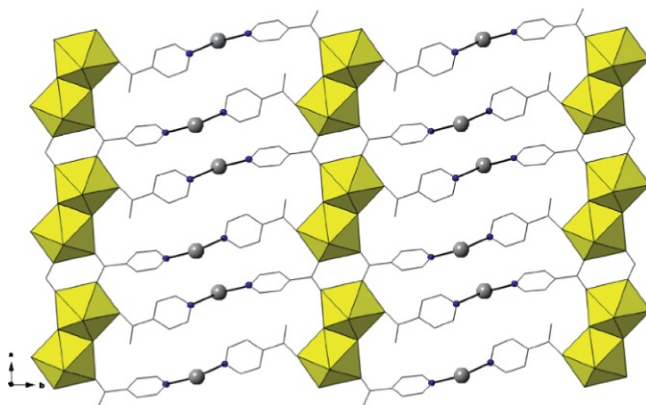


FIGURE 74 Silver metal ions (silver spheres) form bonds with the nitrogen atoms of the isonicotinic acid ligands in **88** to result in a 2D bimetallic structure with a sheet topology.

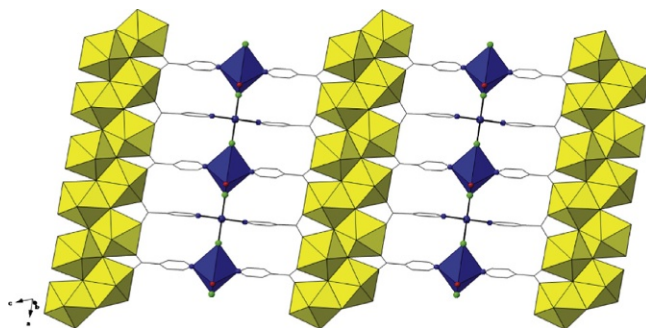


FIGURE 75 Isonicotinate ligands bridge uranyl SBUs (double-wide chains) in **88** to chains of alternating Cu(II) tetrahedral and octahedral BUs to form 2D sheets.

occurs as chains of polynuclear uranyl SBUs replace the previous dimeric BUs in the final structure. Moreover, the final product features a different isonicotinate to UO_2^{2+} ratio than that of UICP (UICP—2:1 and **88**—1:1) which may be suggestive of the mechanism governing the rearrangement.

Once again it is worth taking the opportunity to mention the photophysical properties of these materials as the inclusion of a secondary metal species quenches the luminescence emission that is so typical of uranyl-containing CPs and hybrid materials. The starting coordination polymer (UICP) is a luminescent compound that yields green light (~ 520 nm) upon excitation at 420 nm, which is an absorbance maxima associated with the uranyl cation. Compounds **87** and **88**, however, are both nonemissive as the inclusion of the Ag(I) and Cu(II) ions likely facilitate a nonradiative decay pathway. Kerr and Cahill further explored the effect of copper metal ions on the presence of uranyl luminescence in a subsequent study (Kerr and Cahill, 2014a).

The synthesis of heterometallic uranyl compounds is desirable as the inclusion of a secondary metal can increase the number of new structure types and topologies while potentially influencing the resulting properties of the material. Although one may speculate that the introduction of a metal with a more predictable coordination environment should (in theory) increase the ability to anticipate global topology, the structural diversity of the uranyl hybrids continues to complicate this notion. The structures that we have selected once again display a wide range of PBUs and SBUs and a wealth of topologies that echo the sentiments of [Sections 3–7](#).

9 A HYBRID APPROACH TO URANYL-CONTAINING COORDINATION POLYMER SYNTHESSES

A commonly occurring theme not only in this text, but throughout the field of hybrid materials chemistry is the reliance upon metal–ligand coordination and the exploitation of functional group affinity and ligand modification to assemble materials. Strong and highly directional covalent linkages have dominated CP and MOF chemistry, yet these primary synthetic tools can be combined with other less-directional interactions (hydrogen and XB, etc.) to prepare extended structures. We will now transition our attention to a “hybrid approach to hybrid material synthesis” and focus upon the intersection of covalent and noncovalent interactions in synthetic strategies.

Very simply, the “hybrid approach” presented in this section refers to the combination of both covalent and noncovalent interactions to assemble materials. Directional metal–ligand linkages will serve as the backbone in this approach, as these covalent bonds will generally be observed to give rise to 1D or 2D CPs. Structural motifs will in turn be further linked by secondary NCIs that function to increase the overall dimensionality of the structure, such as layers of a 2D sheet being joined by hydrogen bonds to form a 3D assembly. Whereas less-directional interactions such as hydrogen bonds and π -type interactions are individually weaker when compared to typical covalent bonds, their contribution to assembly of CPs is derived from their cooperative and synergistic influence. The following examples in this section will therefore consist of CPs that exhibit a dimensionality higher than that which is afforded by coordinative–covalent interactions alone as a result of substantive NCIs. We should also note that a number of ancillary NCIs have been mentioned already, yet we now make such examples explicit as we form a foundation for their intentional inclusion in design strategies. As such, it is important to note that not all of the compounds featured in this section were synthesized with the *intent* to combine both covalent and noncovalent interactions as a means to assembly. In fact, some of these materials merge the two interactions by pure happenstance. That said, the ability to observe and capitalize on these occurrences allows one to better understand the principles that govern these processes and to develop design principles. This section will

therefore include a number of examples that provide a broad foundation of covalent/noncovalent pairings, followed by a transition to intentional efforts (Section 10) that harness these principles.

9.1 Carboxyphosphonates Revisited

The carboxyphosphonate linkers have been featured rather extensively in this text owing to their propensity to form a diverse range of uranyl hybrid materials. We have demonstrated the utility of these ligands to form a number of homo- and heterometallic uranyl-containing architectures via direct coordination of the R-CO_2^- and R-PO_3^{2-} functional groups. The binding affinities and coordination geometries of these two functional groups can be further exploited during syntheses in acidic conditions. Under moderate to relatively harsh acidic conditions, the carboxylate moiety can be assumed to remain protonated (R-COOH) and unlikely to participate in coordination. Moreover, the high affinity of the phosphonate functional group to bind the uranyl cation is favored over protonation despite the presence of acid. These conditions can induce the formation of P-O-U linkages and leave the carboxylate group uncoordinated and free to participate in NCIs. To illustrate, we will look at two structures that are constructed of aliphatic and aromatic carboxyphosphonate linkers that feature significant H-bonding interactions.

We will begin by recalling and taking a closer look at the structure of compound **32**, $[\text{UO}_2(\text{O}_3\text{PCH}_2\text{CO}_2\text{H})]$ (Knöpe and Cahill, 2008). Recalling the layered structure, which consisted of uranyl/phosphonate sheets in (110) plane that featured noncoordinated carboxylate groups, which protruded into the interlayer regions (Fig. 76). The carboxylate functional groups are protonated and are able to form strong $[\text{O}-\text{H}\cdots\text{O} 2.658(5)\text{Å}]$ head-to-head hydrogen bonds with those of neighboring sheets to stitch the rigid 2D inorganic layers into an overall 3D assembly. These interactions are indeed nontrivial as a subsequent high-pressure crystallographic study revealed that the hydrogen bonding interactions between adjacent layers remain intact at pressures up to ~ 3.0 GPa (Spencer et al., 2014). Although these interactions were formed serendipitously, their presence is significant as the vitality of the NCI to contribute to assembly in a significantly meaningful way is demonstrated.

The structure of **89**, $[\text{UO}_2(\text{PO}_3\text{HC}_6\text{H}_4\text{CO}_2\text{H})_2]\cdot 2\text{H}_2\text{O}$, consists of square bipyramidal uranyl monomers that are bridged together by the phosphonate groups of the carboxyphenylphosphonic acid (CPPA) ligands (Fig. 77) (Adelani and Albrecht-Schmitt, 2010). These bridging interactions result in the formation of chains that propagate along the [100] direction. The CPPA ligands are oriented normal to the a -axis such that their carboxylate functional groups face adjacent chains to form similar head-to-head carboxyl pairs to those observed in **89**. The hydrogen bonding interactions that exist between the carboxyl pairs ($\text{O}-\text{H}\cdots\text{O} 2.601(4)\text{Å}$) effectively link the chains together to form sheets. Solvent water molecules occupy the interlayers and participate

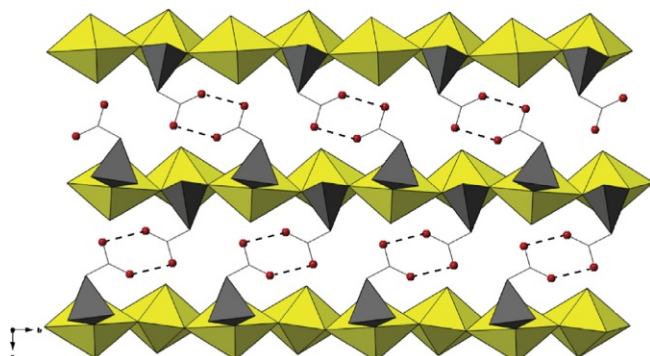


FIGURE 76 The layered structure of **32** is stabilized by head-to-head hydrogen bonding interactions that form between the noncoordinating carboxylate groups of the PPA ligands.

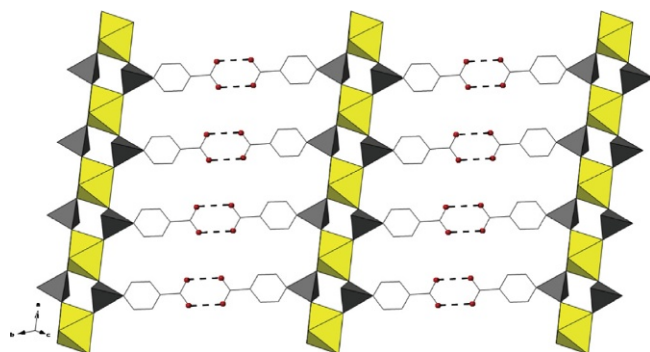


FIGURE 77 Square bipyramidal uranyl monomers in **89** are bridged into chains by the phosphate moiety of the CPPA ligands, whereas the carboxylate groups form head-to-head hydrogen bonds to form a 2D sheet-like network topology.

in further hydrogen bonding interactions. The conversation regarding complementary covalent and noncovalent interactions being used to assemble materials is started by compounds **32** and **89**. Both structures contain a well-studied and prevalent hydrogen bonding motif that has been demonstrated in other systems to be a robust entity capable of influencing structural arrangements (Etter, 1990; Sarkhel and Desiraju, 2004). The role of hydrogen bonds in these two structures may be seen as inspiration for their inclusion in future synthetic efforts.

9.2 Noncoordinating Nitrogen Donor Species

Nitrogen-donating ancillary species have thus far demonstrated ability to affect the resulting structure of uranyl-containing materials via coordinating and noncoordinating roles. The noncoordinating roles that have been

discussed thus far have ranged from space filling to templating, yet the ability of N-donor organic molecules to function as hydrogen bond donors or acceptors has been reserved until this section. The hydrogen bonding capacity of noncoordinating pyridyl species is well established in organic and main-block chemistry, yet remains underexplored, but applicable to actinide chemistry (Bhogala and Nangia, 2003; Etter, 1990, 1991; Long et al., 2013). Among uranyl-containing hybrid materials, pyridyl species are commonly protonated and serve as charge-balancing cations, yet these N—H⁺ residues can undergo further interactions as hydrogen bond donors. These interactions that arise from the ancillary species can be utilized to tie the primary components of the CP (1D- or 2D) together into an extended hydrogen-bonded structure.

Two examples that embody this concept arise from the hydrothermal treatment of uranyl nitrate, citric (Cit) or Citml acids and a pyridyl source (Thuéry, 2007b). Compounds **90**, (H₂-DABCO)[(UO₂(Citml))₂], and **91**, (4,4'-BIPY)[(UO₂(Hcit))₂], each contain 1D chain-like CPs that are further assembled into sheets via N—H...O hydrogen bonds that stem from 1,4-diazabicyclo[2.2.2]octane (DABCO) and 4,4'-dipyridyl (4,4'-BIPY) cations, respectively (Fig. 78). Pentagonal bipyramidal uranyl edge-sharing dimers are incorporated in **91** and are each coordinated by four Citml ligands that bridge the SBUs together to give rise to anionic chains that propagate along the [100] direction. The chains are flanked by doubly protonated DABCO cations that charge balance and form dual N—H...O hydrogen bonds between the pyridinium ion and the noncoordinated carboxylate groups of the Citml ligands (N—H...O 2.643 and 2.635 Å). The hydrogen bonding interactions link the chains into 2D sheets in the (101) plane. Although a different ligand (Cit vs. Citml) was used in the synthesis of **91**, the anionic chain motif is present along the [010] direction and is constructed in an analogous fashion to that of **90**. The 4,4'-bipyridinium cations in turn form dual hydrogen bonding interactions that stitch the chains into a sheet-like structure, yet in this case the hydrogen bonds are bifurcated. The pyridinium nitrogen forms a hydrogen bond with both the

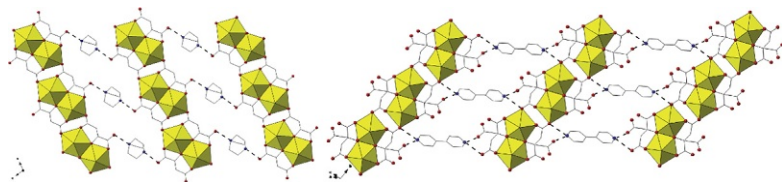


FIGURE 78 Left: Pentagonal bipyramidal uranyl dimers in **90** are linked into anionic chains that propagate along [100] direction by Citml ligands. Charge-balancing DABCO cations form bridging N—H...O hydrogen bonds that link the chains into a sheet-like network topology. Right: Uranyl SBUs (dimers) in **91** form anionic chains via bridging Cit ligands. Charge-balancing 4,4'-BIPY cations form bridging bifurcated N—H...O hydrogen bonds that link the chains into a sheet-like network topology.

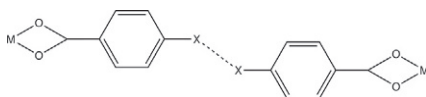
noncoordinated carboxylate oxygen of the Cit ligand and the oxygen atom of the carboxylate that bridges the uranyl dimers together (N—H...O 2.875 and N—H...O 3.053 Å).

Looking collectively, the role of an N-donating ancillary species is variable as it can function to influence and increase the structural dimensionality or merely exist as a space-filling cation. Perhaps the most useful concepts that can be extracted from compounds **90** and **91** are simply that NCIs contribute significantly to assembly of CPs. Looking ahead, we may take the perspective that these interactions are meaningful to the assembly and not merely result of packing. To perhaps convince the reader of this, we will now examine cases where NCIs have been included *intentionally* in the synthetic strategy. This is a crucial step in the use of NCIs in the synthesis of uranyl CPs as the strategy has changed from retrospective structural analysis to targeted efforts that include specific and desired interactions.

10 COMBINING DIRECT COORDINATION AND SUPRAMOLECULAR CHEMISTRY

We have thus far used the term “NCI” a bit loosely and in the context of describing, for example, H-bonds or π -interactions. It is perhaps more appropriate at this stage to use the term “supramolecular” (Minkin, 1999) as we begin to explore the intentional introduction of such interactions and their contributions to the assembly of uranyl hybrids. Moreover, as the materials we present begin to feature more and more NCIs, often synergistically with typical coordination chemistry, we will borrow some terms from the supramolecular community and refer to the assembly of “tectons” via “synthons,” the former being the molecular building blocks to be assembled by the favorable interactions of the latter. The term tecton was proposed to describe molecules “whose interactions are dominated by particular associative forces that induce the self-assembly or an organized network with specific architectural or functional features” and has been regularly used among the supramolecular community to describe molecular building units (Simard et al., 1991). The terminology regarding the supramolecular synthon has evolved and matured since its inception in 1995 (Desiraju, 1995), but will be used herein to describe those repeating interaction patterns and motifs that assemble molecular tectons into extended structures.

We have already seen cases where direct coordination and supramolecular interactions (i.e., hydrogen bonds) have been used to form extended structures, albeit in some cases serendipitously. In order to combine both of these synthetic strategies, in our own group, we decided to explore ligands that were capable of supporting both covalent and supramolecular interactions (Scheme 22). Such ligands should have a functional group at one end of the molecule capable of coordinating to the uranyl (such as those described



SCHEME 22 A representation of the synthetic strategy that utilizes both direct coordination and supramolecular assembly.

above), as well as a noncoordinating group that is capable of supporting supramolecular interactions. Our first attempt targeting this strategy utilized 4-halobenzoic acid ligands that contained “terminal” halogen atoms (Cl, Br, and I) (Scheme 17).

In reality, these “terminating” halogens are able to participate in XB and provide additional connectivity by noncovalent means. A halogen bond is defined as occurring when there is a “net attractive interaction between an electrophilic region associated with a halogen atom in a molecular entity and a nucleophilic region in another, or the same, molecular entity” (Desiraju Gautam et al., 2013). Although the definition of XB was not agreed upon until 2013, covalently bound halogen atoms have long been observed to interact attractively and in a highly directionally manner with both nucleophiles and electrophiles, the latter being a halogen bond (Murray-Rust and Motherwell, 1979; Murray-Rust et al., 1983; Ramasubbu et al., 1986). The presence of these interactions may be explained (yet perhaps oversimplified) considering an electrostatic model wherein polarization is induced in covalently bound halogen atoms. Essentially, when a halogen atom forms a covalent bond, some of its electronic charge is polarized toward the bond, which decreases its electronic density in its outer region, directly in line with the bond axis creating a positive region known as the sigma hole (Politzer et al., 2007, 2010, 2013). The polarization of the halogen atom does not affect the spherical regions normal to the covalent bond as these equatorial portions of the atom retain “more” negative charge (relative to the σ -hole); thus “like–like” attractions are favorable (Politzer et al., 2010). The favorable alignment of these polar regions can therefore produce attractive interactions whose strength can be influenced and tuned via the presence of any constituent that can affect the polarization of the halogen (e.g., electron-withdrawing or -donating entities) (Metrangolo et al., 2008a,b; Politzer et al., 2013). The polarizability of the halogen itself will influence the extent of the polarization and in turn the strength of the interactions as XB donor strength increases in the sequence $F < Cl < Br < I$ (with acceptor strength being the inverse) (Awwadi et al., 2007a; Politzer et al., 2007). XB in many systems has been reviewed of late and readers are encouraged to explore (Bertani et al., 2010; Clark, 2013; Gilday et al., 2015; Metrangolo et al., 2005, 2006, 2008a,b; Troff et al., 2013), especially with respect to classification schemes based on observed geometries. Our treatment within will be a bit more general and will of course be restricted to uranyl systems.

10.1 Assembly with 4-Halobenzoic Acid Ligands

With the concept of combining both covalent and noncovalent interactions in mind, we set out to use carboxylate linkages and halogen bonds to assembly uranyl-containing hybrid materials. As a result of these efforts, three compounds **92–94**, $[(\text{UO}_2)_2(\text{XC}_6\text{H}_4\text{COO})_4(\text{H}_2\text{O})_2]$ (where $\text{X} = \text{Cl}, \text{Br}, \text{I}$), were synthesized and contain discrete BUs that are stitched together via intermolecular halogen–halogen interactions (Deifel and Cahill, 2011). Each of these three compounds contain the same covalently bonded structural unit, and thus only one will be discussed in detail. The basic building unit, or tecton, consists of two pentagonal bipyramidal uranyl monomers that are linked together via two bridging monodentate 4-halobenzoic acid linkers to form discrete pseudo-dimeric molecular tectons (Fig. 79). The coordination sphere of each uranyl monomer is completed by a bidentate coordinating 4-halobenzoic acid and a water molecule. In **92**, $[(\text{UO}_2)_2(\text{ClC}_6\text{H}_4\text{COO})_4(\text{H}_2\text{O})_2]$, the pseudo-dimeric tectons have four total sites for additional interaction by way of the chlorine atoms, each of which supports the formation of a halogen–halogen ($\text{Cl}\cdots\text{Cl}$) interaction to a separate tecton. Relevant interaction distances and angles associated with this interaction are $\text{Cl}_1\cdots\text{Cl}_2$ 3.289 Å and $\theta_1 \sim \theta_2$, $\theta_1 = \angle \text{C} - \text{Cl}\cdots\text{Cl} = 146.51^\circ$ and $\theta_2 = \angle \text{C} - \text{Cl}\cdots\text{Cl} = 143.47^\circ$. The supramolecular halogen–halogen interactions link each molecular uranyl tecton to four others, giving rise to an extended 2D sheet in the (011) plane (Fig. 80). The supramolecular sheets contain large pores that are subsequently filled by the interpenetration of adjacent layers. The increase in connectivity in this structure is what demonstrates the potential of this synthetic strategy and the influence and directional nature of the halogen–halogen interactions.

Similar interactions are present in **93**, $[(\text{UO}_2)_2(\text{BrC}_6\text{H}_4\text{COO})_4(\text{H}_2\text{O})_2]$, where 4-bromobenzoic acid ligands coordinated to the uranyl centers each form one halogen–halogen interaction (similar to those in **92**), yet two of these interactions are required to join adjacent uranyl units together

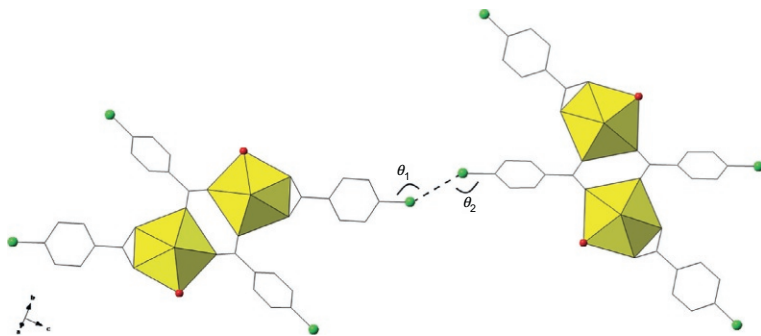


FIGURE 79 The nominally terminal chlorine atoms of the molecular dimers in **92** facilitate halogen–halogen interactions.

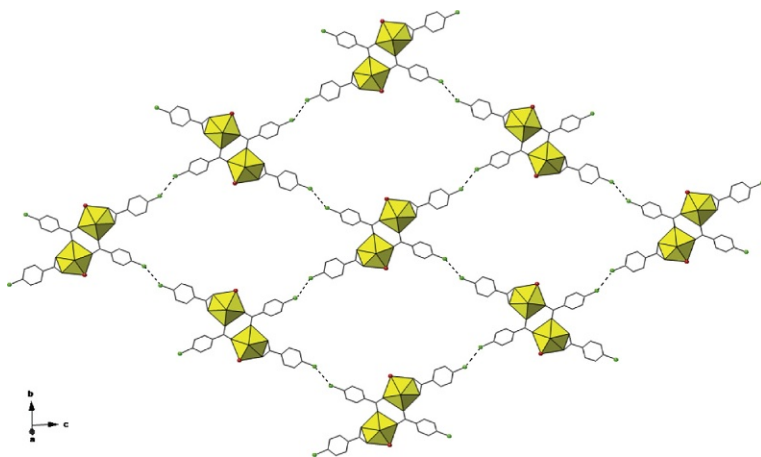


FIGURE 80 Halogen–halogen interactions in **92** direct the formation of supramolecular sheets that contain void spaces.

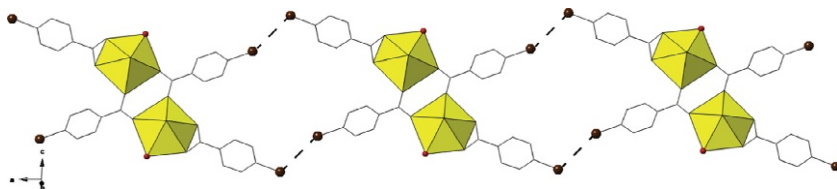


FIGURE 81 The bromine atoms of the molecular dimers in **93** form halogen–halogen interaction that link neighboring tectons into chains.

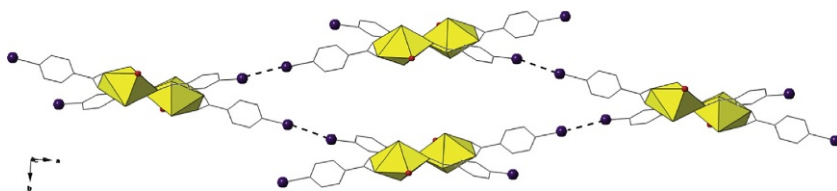


FIGURE 82 Halogen–halogen interaction stemming from the iodine atoms in **94** assemble molecular dimers into a 2D network.

(Fig. 81). The dual stitching interactions and reduction to the total number of conjoined uranyl tectons induce a change to the overall assembly from open sheets (**92**) to a neutral chain motif that propagates along the [100] (Fig. 82). The interaction distances and angles associated with the bromine–bromine halogen bonds in **85** are $\text{Br}_1 \cdots \text{Br}_2$ 3.75 Å and $\theta_1 \neq \theta_2$, $\theta_1 = \angle \text{C}-\text{Br}_1 \cdots \text{Br}_2 = 114.73^\circ$ and $\theta_2 = \angle \text{C}-\text{Br}_2 \cdots \text{Br}_1 = 156.10^\circ$.

The formation of a similar chain motif in **94** is facilitated by halogen–halogen (I \cdots I) interactions that form between the 4-iodobenzonic acid ligands

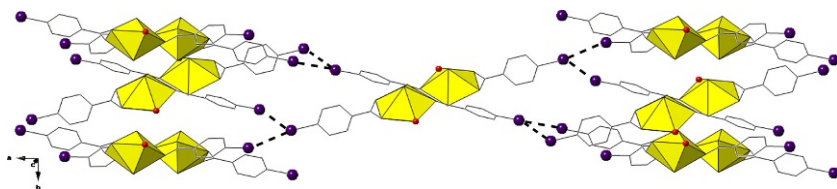


FIGURE 83 Bifurcated C—I...I halogen bonds in **94** link each uranyl tecton to six others to form a 3D network.

of adjoining uranyl tectons (Fig. 82). The halogen–halogen interactions in **94** differ than those found in **93**, as they become bifurcated and increase the complexity of the halogen-bonded network. The bifurcation of the iodine interactions stitches each uranyl tecton to a total of six others to yield an overall interpenetrating 3D woven structure (Fig. 83). The interactions distances and angles of the two interactions are $I_1 \cdots I_2$ 4.016 Å and $\theta_1 \neq \theta_2$, $\theta_1 = \angle C-I_1 \cdots I_2 = 156.40^\circ$ and $\theta_2 = \angle C-I_2 \cdots I_1 = 116.26^\circ$; $I_1 \cdots I_3$ 4.013 Å and $\theta_1 \neq \theta_2$, $\theta_1 = \angle C-I_1 \cdots I_3 = 119.94^\circ$ and $\theta_2 = \angle C-I_3 \cdots I_1 = 157.06^\circ$.

Compounds **92–94** provided our group with proof of concept and some validation of the strategy for combining direct coordination and supramolecular chemistry to form extended crystalline structures. When comparing the structures on the basis of halogen–halogen interaction strengths, one finds that the order decreases as $Cl \cdots Cl > Br \cdots Br > I \cdots I$. This becomes obvious when one considers two separate structural features of **92–94**: the number of uranyl tectons that are linked per interaction and the overall order to the assemblies. The $Cl \cdots Cl$ interactions in **92** link each uranyl tecton to four others while producing a relatively ordered structure based upon an open sheet motif. In contrast, two $Br \cdots Br$ interactions are required in **93** to join adjacent uranyl tectons and the resulting structure consists of chains. The bifurcation of the $I \cdots I$ interactions in **94** indicates that these are less directional and perhaps weaker than those found in both **92** and **93**. Furthermore, the iodo analog seems to form the least “ordered” structure as the interwoven assembly resembles what one may expect from a close packed molecular structure.

Aside from the qualitative structural assessment of these interactions, one can semiquantitatively rank their relative strengths by comparing these interactions on a relative scale by calculating the percentage of overlap between the halogen bond donor and acceptor atoms respective van der Waals radii (see Eq. 2) (Lommerse et al., 1996). Performing this simple calculation reveals the interaction strengths in **92–94** do in fact follow $Cl \cdots Cl$ (94% vdW) $>$ $Br \cdots Br$ (101% vdW) \geq $I \cdots I$ (101% vdW) where a smaller number corresponds to greater overlap. These results are significant because a metric can be established that not only ranks the effectiveness of these interactions but also provides an assessment of their contributions in assembly:

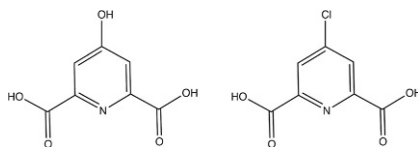
$$\% \text{ overlap} \left[\frac{(\text{interaction distance } (D \cdots A))}{((\text{vdW radii}_{(D)}) + (\text{vdW radii}_{(A)}))} \right] \times 100\% \quad (2)$$

10.2 Chelidamic Acid Derivatives for Hybrid Assembly

Recalling the nitrogen- and oxygen-donating heterofunctional 2,6-pyridinedicarboxylic acid ligand introduced earlier in this text, one can take note of its rather restricted geometry in terms of metal ion coordination. The geometric constraints of the unidirectional chelation site can be countered by the functionalization of the benzene ring with a hydroxyl or chloro group, as in chelidamic and chlorochelidamic acids (CICAs) (Scheme 23). As the hydroxyl (or chloro) functional group has been observed to adopt the role of either a coordinating or a noncoordinating entity, it is less predictable as an instrument of assembly. Therefore, subsequent substitution of the hydroxyl group in favor of a halogen or other functional group (e.g., nitro (Cantos and Cahill, 2014a)) capable of supporting a more reliable set of supramolecular interactions can increase the propensity for assembly in the solid state (Derikvand et al., 2013; Yang et al., 2013a).

As an example, we look to the results of the hydrothermal synthesis of compounds **95**, $[(\text{UO}_2)_2(\text{C}_7\text{H}_2\text{NO}_4\text{Cl})_2(\text{H}_2\text{O})_3] \cdot \text{H}_2\text{O}$, and **96**, $[(\text{UO}_2)(\text{C}_7\text{H}_2\text{NO}_4\text{Cl})_2(\text{H}_2\text{O})] \cdot \text{H}_2\text{O}$ (Fig. 84) (Cantos et al., 2013b). One-dimensional chains are predominant in **95** and are formed of CICA-bridged pentagonal bipyramidal uranyl monomers. The chains consist of discrete strands (four PBUs wide) of CICA-bridged uranyl monomers that span the [001] direction which are in turn linked to one another in the [010] direction by a single-bridging CICA ligand. The periphery of the chains contain CICA ligands that are oriented such that their chlorine atoms face the noncoordinated carboxylate oxygen atoms of adjacent CICA ligands of neighboring chains. This alignment allows for the formation of moderately strong $\text{Cl} \cdots \text{O}$ halogen bonds (2.938 \AA 89.9% vdW) that function to stitch the chains into sheets in the (011) plane.

Pentagonal bipyramidal uranyl monomers are incorporated into the structure of **96** and are each coordinated by two CICA ligands to form tetranuclear groupings (Fig. 85). Each tetranuclear group is directly coordinated via



SCHEME 23 Left: The structure of chelidamic acid. Right: The structure of chlorochelidamic acid (CICA).

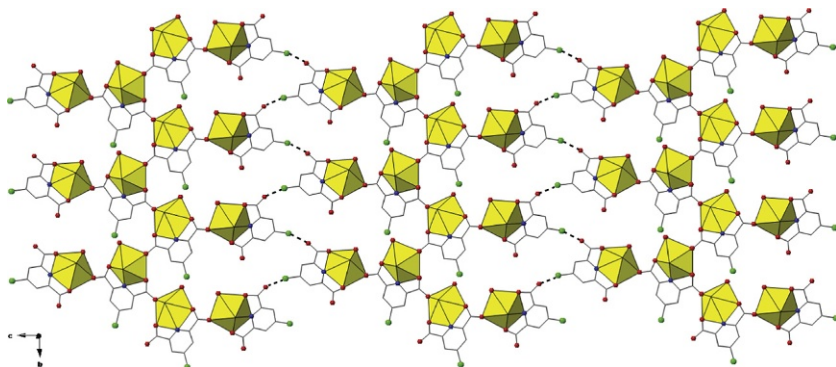


FIGURE 84 Pentagonal bipyramidal uranyl monomers in **95** are chelated and linked by CICA ligands to form chains that propagate along the [010] direction. Halogen bonding interactions (C—Cl \cdots O) link the chains into an extended sheet-like topology.

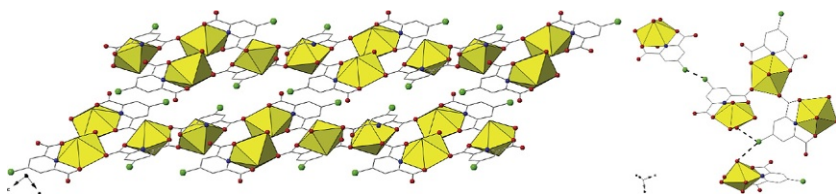


FIGURE 85 Left: Pentagonal bipyramidal uranyl monomers in **96** are chelated and linked into chains via CLCLA ligands. Right: The chains are linked into a 2D supramolecular network through C—Cl \cdots O and C—Cl \cdots Cl halogen bonding interactions.

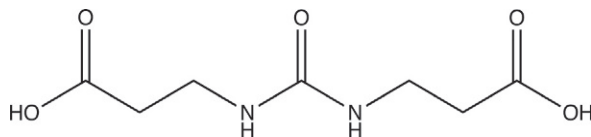
bridging CICA ligands that give rise to a 2D covalently bonded CP with a sheet topology. The periphery of the sheets is decorated with CICA ligands, which orient themselves in a position to form both halogen–oxygen and halogen–halogen interactions that link the sheets into a 3D assembly. The distances associated with the halogen interaction are as follows: Cl \cdots O 3.169 Å (93.2% vdW), Cl \cdots O 3.170 Å (93.2% vdW), and Cl \cdots Cl 3.438 Å (98.2% vdW).

Structures **95** and **96** each consist of either covalently constructed molecular units or CPs that utilize supramolecular interactions to form a higher degree of connectivity. The fact that these noncoordinating supramolecular interactions are (in some cases) strong enough to facilitate the assembly of both molecular and CP subunits is significant. Although the molecular and polymeric “subunits” of some of the previous five structures are the same or similar, none of materials exhibit the same global structure.

The final example of this section fully embraces judicious ligand choice in order to promote the supramolecular assembly of a uranyl CP. In this study, the authors cited others’ successful efforts using aliphatic dicarboxylates under harsh acidic conditions to synthesize uranyl CPs as their inspiration to

attempt similar studies in less-acidic and mild solvothermal environments, while utilizing a urea-functionalized aliphatic linker (Shu et al., 2013). Their selection of a urea functional group was not random, as it was targeted due to its ability to form intermolecular hydrogen bonding interactions and potentially facilitate supramolecular assembly. As a result of their efforts, compound **97**, $[\text{UO}_2(\text{udpa})]$, was synthesized from the combination of uranyl nitrate and 3,3'-ureylenedipropionic acid (udpa—Scheme 24) in the presence of DMF (Fig. 86) (Shu et al., 2013). The structure of **97** contains pentagonal bipyramidal uranyl monomers that are flanked (front and back) and coordinated by a total of three udpa ligands. The arrangement of the udpa ligands and their flexibility facilitate the formation of chains that propagate in a step-wise fashion. The coordination to the uranyl cation by the carbonyl oxygen atom of the urea functional groups orients the amine groups such that they face away from the chains. This orientation of the protonated amine groups facilitates the formation of dual interchain $\text{N}-\text{H}\cdots\text{O}$ hydrogen bonds with the coordinated carboxylate oxygen atoms of adjacent chains ($\text{N}-\text{H}\cdots\text{O}$ 2.986 and 3.035 Å, respectively).

It is probably appropriate at this point to (again) acknowledge the differences between dimensionality of a strict CP versus a material containing some component of supramolecular assembly. In CPs, the definition of



SCHEME 24 The structure of 3,3'-ureylenedipropionic acid (udpa).

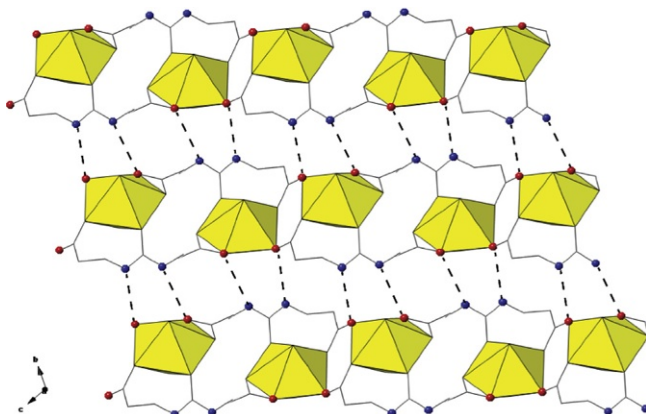


FIGURE 86 Urea-functionalized dipropionic acid linkers conjoin the uranyl PBUs in **97** to form chains. Interchain hydrogen bonding interactions support the formation of an extended 2D sheet-like topology.

dimensionality more often than not (or at least should!) refers to the degree of connectivity afforded by covalent linkages. When considering synergistic supramolecular interactions, we are careful to highlight additional degrees of connectivity presented by their contribution.

10.3 Summary

Our intent thus far has been to delineate a theme of structural diversity stemming from inclusion of a broad range of uranyl hydrolysis products and connectivity via coordinating functional groups. From a synthesis strategy perspective, the hydrothermal treatment of uranyl salts with organic ligands is without question a robust route to new structures, yet also remains challenging with respect to producing designed or desired topologies. A few trends and guidelines have of course emerged such as the ability to promote oligomerization via temperature and pH (as with the squarates), yet such “rules” are quickly offset by, for example, the observation of tetrameric building units prepared at low pH. Similar comments can be made for heterometallic systems wherein binding affinities may be invoked as a design principle only to have solid-state steric or topological influences dismiss what might have been a sound argument in aqueous media. As our presentation has progressed, we highlighted an increase in the contribution of supramolecular interactions to the assembly of hybrid materials. Many of these were noted in retrospect, yet such examples served as inspiration for the intentional introduction of noncovalent synthons as a means to influence structure. Moving forward, we will highlight these supramolecular interactions prominently.

11 INTRODUCING CONTROL: RESTRICTING URANYL SPECIATION IN AQUEOUS MEDIA

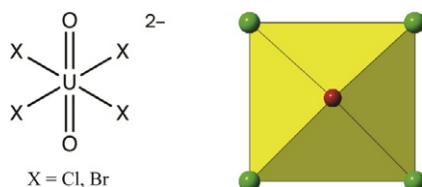
Whereas the diversity of speciation of uranyl building units in aqueous media and subsequent condensation thereof into the solid state is indeed attractive for exploratory synthesis of hybrid materials, such phenomena may also be confounding if one strives for predictable assembly or systematic study of a discrete family of materials. With respect to the latter, we have begun to think in almost purely supramolecular terms in that many of our current efforts focus on the assembly of tectons via appropriate synthons. Such an approach requires a reliable and reproducible portfolio of tectons, which may seem unattainable given the presentation thus far, yet turning to lower temperatures and high anion media promotes a restricted speciation profile (in the solid state) that nearly eliminates tecton diversity. Moreover, this approach prompts a revisit of the hybrid material definition introduced for CPs, i.e., Kickelbick’s class II (above). Materials hereafter perhaps best belong to class I: those inorganic–organic components that are coupled together via weak NCIs such as hydrogen and XB, van der Waals, or electrostatic interactions (Kickelbick,

2007). Moreover still, such a forum brings us full circle to the applied and environmental as the behavior of $[\text{UO}_2]^{2+}$ (and actinides in general) in high chloride or high thiocyanate conditions are relevant to the long-term geologic storage of nuclear waste and historical aqueous reprocessing, respectively (Chiarizia et al., 1973; Crouthamel and Johnson, 1952; Hennig et al., 2005; Surls and Choppin, 1957).

11.1 High Halide Media

Recall Scheme 1 where one can see that under acidic conditions ($\text{pH} < 3.0$) a monomeric speciation profile is favored as dissolved uranyl species will generally exist as but hydrated dications. Achieving low pH by way of concentrated HCl has a twofold influence. First, oligomerization is thwarted as hydrolysis is prevented and second, chloride anions undergo exchange reactions with water molecules in the first uranyl coordination sphere (Bean et al., 2002). As such, low pH, high halide media typically promote $[\text{UO}_2\text{X}_y]^{2-y}$ ($\text{X} = \text{Cl}, \text{Br}$ and $y = 1, 2, 3$) ions in solution, which ultimately condense into the solid state as the $[\text{UO}_2\text{X}_4]^{2-}$ dianion when paired with appropriate cations (Scheme 25). The uranyl tetrahalide tecton consists of the linear uranyl cation bonded, equatorially, by four halogen atoms to result in an overall square bipyramidal coordination environment. Appropriate synthetic conditions can lead to the formation of this uranyl building unit, reproducibly and thus serve as a platform for supramolecular assembly.

The second requirement for assembly of uranyl tetrachloride dianions is of course charge balance, and one may do this with a variety of cations capable of sustaining a range of NCIs. As a starting point, one may look to similar and well-studied transition metal-bound chloride complexes, as inspiration for the selecting and targeting of interaction pairings. Terminal metal-bound chlorine atoms in these materials demonstrate a proclivity to accept both hydrogen and halogen bonds and in fact do so rather strongly (Bertani et al., 2010; Brammer, 2004; Brammer et al., 2001, 2008; Metrangolo and Resnati, 2013; Zordan et al., 2005a). The ability of these chloride species to support the formation of strong supramolecular interactions renders them excellent candidates for use in the assembly of higher dimensional compounds based

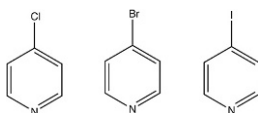


SCHEME 25 A schematic of the uranyl tetrahalide dianion $[\text{UO}_2\text{X}_4]^{2-}$ ($\text{X} = \text{Cl}, \text{Br}$) is provided on the left, whereas a view down the uranyl axis is shown as a polyhedral representation on the right.

on molecular building units (Awwadi et al., 2006, 2007b; Smart et al., 2013; Willett et al., 2003; Zordan and Brammer, 2006; Zordan et al., 2005a). Thus, using the transition metals as inspiration we decided to test the applicability of known structure types and interaction pairings present in MCl_4^{2-} ($M=Cu(II)$, $Pt(II)$, $Pd(II)$) systems with those of the uranyl tetrachloride dianion to evaluate its ability to serve as a building block in self-assembly processes.

An early study from our group demonstrated the pairing of the $[UO_2X_4]^{2-}$ tecton with a series of bipyridinium cations (Scheme 26) by means of slow isothermal aqueous evaporation, to result in the formation of seven supramolecular assembled compounds (Deifel and Cahill, 2009). The idea was to test the applicability of the previously reported perhalometallate and bipyridinium pairings ($M-X_2\cdots H-N$) ($M=Pt$, Pd , Cu and $X=Cl$, Br) to the uranyl system considering the similarities between square planar transition metal complexes and the square bipyramidal uranyl tetrahalides (Zordan and Brammer, 2006; Zordan et al., 2005a,b). The hallmark of a robust synthon or molecular motif is its applicability to a number of systems without being interrupted or disrupted; thus, presence of this motif in compounds **98**, (4,4'-BIPY)[UO_2Cl_4], **99**, (BPE)[UO_2Cl_4], **100**, (BPE')[UO_2Cl_4], and **101**, $(C_7H_7NCOOH)_2[UO_2Cl_4]$, demonstrates that the $M-X_2\cdots H-N$ synthon is in fact robust and applicable to uranyl systems (Deifel and Cahill, 2009).

Each compound features the square bipyramidal uranyl tetrachloride tecton as the PBU, all of which function as hydrogen bond acceptors. The pyridinium cations in **98**, **99**, and **100** form bifurcated hydrogen bonds to the chlorine atoms at the periphery of the $[UO_2Cl_4]^{2-}$ tectons to give rise to a 1D ribbon motif that is analogous to the $M-X_2\cdots H-N$ synthon of the perhalometallate systems (Fig. 87). The presence of this synthon in the $[UO_2Cl_4]^{2-}$ materials highlighted the important fact that this tecton was reproducible and a viable supramolecular building block. The next step was to interrupt or inhibit the 1D ribbon motif in order to test assembly through alternate means. This was accomplished in **101** by substituting the bipyridinium cation for a *trans*-3-(4-pyridyl)acrylic acid (t34pa); the cation is a pyridinium base with an acrylic group attached to the 4-position of the ring. In **101**, the pyridinium nitrogen forms the familiar $U-Cl_2\cdots H-N$ bifurcated hydrogen bond, while the carboxyl group is free to form an $O-H\cdots O=C$ hydrogen bond (Fig. 88). This head-to-head hydrogen bonding motif results in the formation of a 1D ribbon-like structural motif, akin to those observed in **98–100**. This



SCHEME 26 Left to right: The structures of 4-chloropyridine, 4-bromopyridine, and 4-iodopyridine.

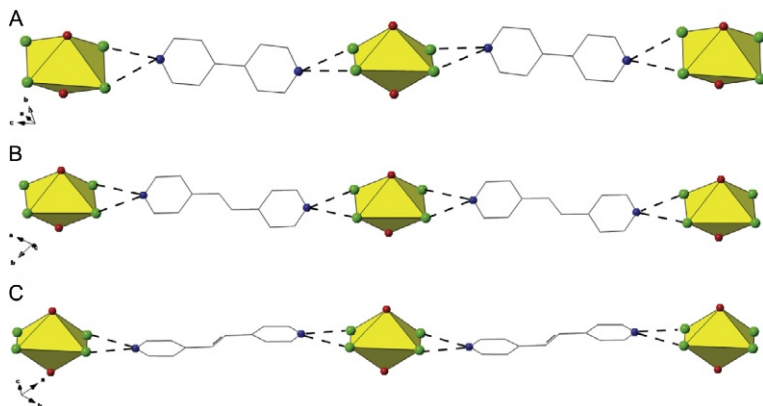


FIGURE 87 In **98** (A), **99** (B), and **100** (C), the N—H...Cl₂—U synthon gives rise to supramolecular chains (1D ribbons) comprised of [UO₂Cl₄]²⁻ and dipyrindinium tectons.

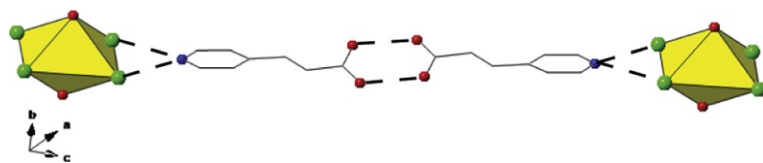


FIGURE 88 Bifurcated N—H...Cl and head-to-head O—H...O hydrogen bonding interactions in **101** stitch the [UO₂Cl₄]²⁻ and t34pa tectons together to form supramolecular chains.

result was significant as the ability to vary the functional groups attached to the organic molecule is then responsible for tuning NCIs.

An attractive feature of the supramolecular assembly process introduced above is the ability to systematically vary not only the cations (and hence NCIs) but also the composition of the uranyl tectons. As such, analogous reactions in concentrated HBr lead to the formation of the [UO₂Br₄]²⁻ tecton. Moreover, use of the same pyridinium cations featured in the previous study allows for a comparison of interaction pairings, acceptor–donor relationships, relative interaction strengths, and the presence or absence of synthons (Deifel and Cahill, 2010). Consequently, an analogous series of uranyl tetrabromide compounds were synthesized and found to contain a number of similarities, yet also some differences as compared to the tetrachlorides. For instance, the same acceptor–donor pairing that was observed in compounds **99** and **100** was also observed in the isomorphous uranyl tetrabromide analogs, **102**, (C₁₂H₁₄N₂)[UO₂Br₄], and **103**, (C₁₂H₁₂N₂)[UO₂Br₄] (Fig. 89). The key difference between the compounds containing the [UO₂Cl₄]²⁻ and [UO₂Br₄]²⁻ tectons is the relative strengths of the hydrogen bonding interactions that give rise to the 1D ribbon motif. In compounds **102** and **103**, the N—H...Br distances are longer than those of the analogous N—H...Cl interactions in **99** and **100** (Table 2).

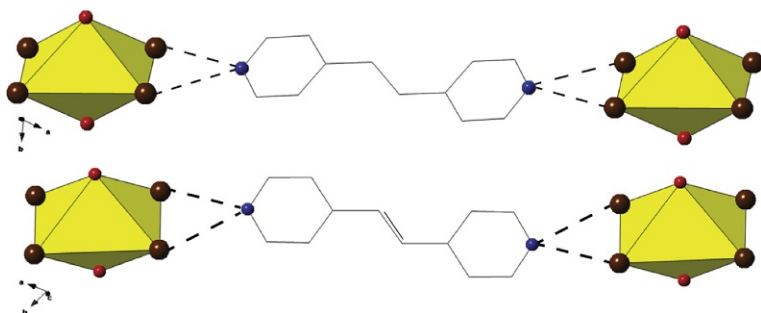


FIGURE 89 In **102** (above) and **103** (below) the N—H...Br₂—U synthon gives rise to supramolecular chains (1D ribbons) comprised of [UO₂Br₄]²⁻ and dipyrindinium tectons.

TABLE 2 Selected Interactions (Distances and Angles) Pertinent to the Assembly of 99–100 and 102–103

Compound	Interaction	Distance (D...A) (Å)	Angle (D—H...A) (°)	vdW Overlap (D—A) (Eq. 2) (%)
99	N—H...Cl	3.259(3)	148.1	98.8
	N—H...Cl	3.367(3)	122.6	102.0
100	N—H...Cl	3.218(2)	132.3	97.5
	N—H...Cl	3.318(2)	136.3	100.5
102	N—H...Br	3.456(3)	137.4	100.2
	N—H...Br	3.468(3)	131.1	100.5
103	N—H...Br	3.459(3)	146.4	100.2
	N—H...Br	3.487(3)	122.9	100.5

The increase in interaction distance is no surprise, as one may point to the larger halogen atoms in the bromo analogs. Comparison of interaction distances across compositions, however, requires a relative scale for the purpose of ranking strengths or significance thereof. As such, one may compare the percentage of overlap between donor and acceptor atoms by using the sum of their van der Waals radii (Eq. 2). In this approach, one may observe a very slight increase in the N—H...X distances in the [UO₂Br₄]²⁻ systems versus those of the [UO₂Cl₄]²⁻ which indicates the chloro atoms are slightly better acceptors of hydrogen bonds (capable of forming stronger interactions) than

the bromo ligands, which can be rationalized based upon size and polarizability (Table 2). The differences in these distances are very small and thus not likely to alter the assembly process (hence isostructural interaction pairings). These two studies provided an entry for our group to investigate the $[\text{UO}_2\text{X}_4]^{2-}$ ($\text{X}=\text{Cl}, \text{Br}$) tectons as halogen bond acceptors and an opportunity to establish a hierarchy of acceptor–donor pairings and strengths.

An effort to explore this potential further resulted in a total of six compounds synthesized by pairing 4-halopyridinium cations (Cl, Br, and I—Scheme 26) with the uranyl tetra-chloride and -bromide tectons (Andrews and Cahill, 2012b). The use of a multifunctional cation (both a halogen and hydrogen bond donor) allowed for a preliminary assessment of acceptor–donor pairings as the pyridinium nitrogen ($\text{N}-\text{H}\cdots\text{A}$) and the halogen ($\text{C}-\text{X}\cdots\text{A}$) atom both function as donor sites and their pairing can be observed crystallographically. Although the extended structures are not shown, the results in terms of observed synthons are summarized (below) and demonstrate a halogen–halogen interaction donor–acceptor pairing that is consistent with well-established trends in halogen bond pairing preferences (Table 3). The atoms involved in the halogen–halogen interactions follow the accepted trends of acceptor ($\text{I} < \text{Br} < \text{Cl}$) and donor ($\text{I} > \text{Br} > \text{Cl}$) strengths as pairing of the smaller acceptor (Cl vs. Br) with a larger donor (I vs. Br vs. Cl) results in stronger interactions. The assessment of strength is assigned as a function of increased overlap of the van der Waals radii of the halogen bond acceptor and donor atoms as pairing of a stronger donor (larger C—X atom) with that of a stronger acceptor (smaller X—U atom) results in the greatest overlap (Table 3). The hydrogen bonding acceptor atom ($\text{N}-\text{H}\cdots\text{A}$) is not fixed and varies as a function of the XB interaction; this result highlights the directional nature of the halogen bond compared to the rather ubiquitous nature of the hydrogen bond. Although these observations based upon crystallographic data

TABLE 3 Relevant Halogen Bonding Interactions and Distances

Compound	Interaction Type	Interaction Distance (Å)	vdW Overlap (D–A) (Eq. 2) (%)
$(\text{C}_5\text{H}_5\text{NCl})_2[\text{UO}_2\text{Cl}_4]$	$\text{C}-\text{Cl}\cdots\text{Cl}-\text{U}$	3.314	94
$(\text{C}_5\text{H}_5\text{NBr})_2[\text{UO}_2\text{Cl}_4]$	$\text{C}-\text{Br}\cdots\text{Cl}-\text{U}$	3.342	93
$(\text{C}_5\text{H}_5\text{NI})_2[\text{UO}_2\text{Cl}_4]$	$\text{C}-\text{I}\cdots\text{Cl}-\text{U}$	3.299	88
$(\text{C}_5\text{H}_5\text{NCl})_2[\text{UO}_2\text{Br}_4]$	$\text{C}-\text{Cl}\cdots\text{Br}-\text{U}$	3.405	95
$(\text{C}_5\text{H}_5\text{NBr})_2[\text{UO}_2\text{Br}_4]$	$\text{C}-\text{Br}\cdots\text{Br}-\text{U}$	3.374	91
$(\text{C}_5\text{H}_5\text{NI})_2[\text{UO}_2\text{Br}_4]$	$\text{C}-\text{I}\cdots\text{Br}-\text{U}$	3.497	91

Extracted from Andrews and Cahill (2012b).

are qualitative, the trends in acceptor–donor pairings and relative strengths (based on vdW overlap) allows one to begin to form a hierarchy of NCIs which may be applied judiciously to future design efforts.

11.2 Intermediate Concentrations of Halide Media

The utility of the uranyl tetrahalide species as a means to guided assembly studies led us to explore the potential of synthesizing other reliable inorganic tectons that can be used in similar studies. This curiosity led to the formation of three compounds containing the $[\text{UO}_2\text{Cl}_3(\text{NO}_3)]^{2-}$ dianion, an alternate tecton capable of supporting supramolecular assembly. The uranyl trichloronitrate tecton is an attractive species as it is reproducible and capable of forming a range of intermolecular interactions that have yet to be thoroughly studied in supramolecular syntheses (Andrews and Cahill, 2013). Although the chlorides behave similar to those of the uranyl tetrachloride tecton (as both hydrogen and halogen bond acceptors), the bound nitrate ligand contains electronegative oxygen atoms, which allows for support of both hydrogen and halogen bonds as well. The substitution of a chloride ligand for that of a nitrate group also provides a different conformation where sterics may affect both acceptor–donor pairings and strengths as well as provide geometry favorable to distinct synthons. As such, our group paired the $[\text{UO}_2\text{Cl}_3(\text{NO}_3)]^{2-}$ tecton with 4-halopyridinium cations ($X = \text{Cl}, \text{Br}, \text{I}$) to explore assembly and assess pertinent interactions contained therein (Andrews and Cahill, 2013). As a result, compounds **104**, $(\text{C}_5\text{H}_5\text{NCl})_2[\text{UO}_2\text{Cl}_3(\text{NO}_3)]$, **105**, $(\text{C}_5\text{H}_5\text{NBr})_2[\text{UO}_2\text{Cl}_3(\text{NO}_3)]$, and **106**, $(\text{C}_5\text{H}_5\text{NI})_3[\text{UO}_2\text{Cl}_3(\text{NO}_3)] \cdot \text{NO}_3$, were formed and all display a variety of intermolecular interactions (Figs. 90 and 91). Selected

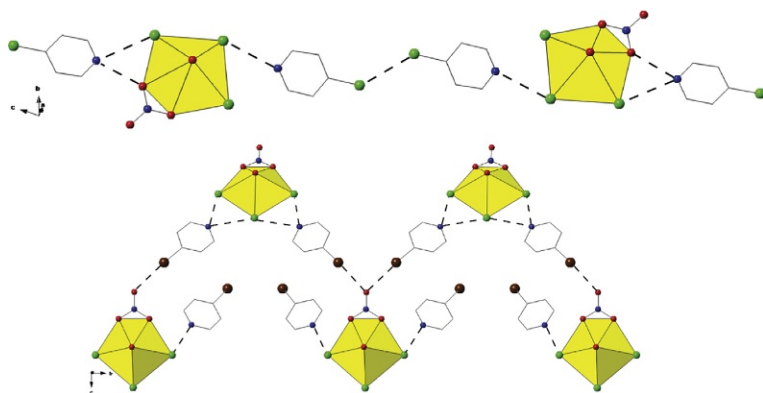


FIGURE 90 Above: Hydrogen ($\text{N}-\text{H}\cdots\text{Cl}$ and $\text{N}-\text{H}\cdots\text{Cl}/\text{O}$) and halogen ($\text{Cl}-\text{Cl}\cdots\text{Cl}$) bonding interactions in **104** stitch the $[\text{UO}_2\text{Cl}_3(\text{NO}_3)]^{2-}$ and 4-chloropyridinium tectons into chains. Below: Branched “zigzag” chains predominate in **105** as both hydrogen ($\text{N}-\text{H}\cdots\text{Cl}_2$ and $\text{N}-\text{H}\cdots\text{Cl}$) and halogen ($\text{C}-\text{Br}\cdots\text{O}$) bonding interactions facilitate the assembly of the $[\text{UO}_2\text{Cl}_3(\text{NO}_3)]^{2-}$ and 4-bromopyridinium tectons.

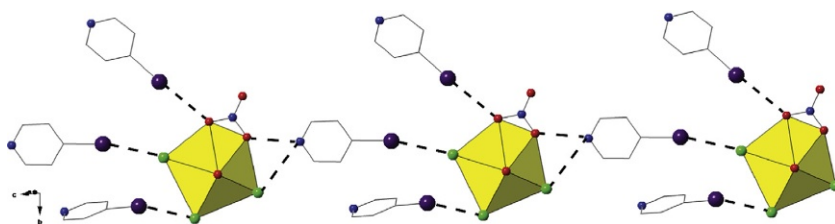


FIGURE 91 A series of halogen and hydrogen bonding interactions in **106** form a “decorated chain” motif.

TABLE 4 Selected Interaction Pairings and Distances of 104–106 Are Provided

Compound	Interaction Type	Interaction Distance (Å)	vdW Overlap (D–A) (Eq. 2) (%)
$(C_5H_5NCl)_2[UO_2Cl(NO_3)]$	C—Cl...Cl—C	3.266	93.3
	N—H...Cl—U/O—N (bifurcated)	3.300	100
		2.897	94.4
	N—H...Cl—U	3.190	96.7
$(C_5H_5NBr)_2[UO_2Cl(NO_3)]$	C—Br...O—N	3.094	91.8
	N—H...Cl—U/Cl—U (bifurcated)	3.177	96.3
		3.329	100.8
	N—H...Cl—U	3.135	95
$(C_5H_5NI)_2[UO_2Cl(NO_3)]$	C—I...O—N	3.382	96.6
	C—I...Cl—U	3.284	88.0
	C—I...Cl—U	3.522	94.4
	N—H...O—N/Cl—U	2.835	92.3
		3.435	104.1

interactions pertinent to the overall assembly of **104–106** are provided (Table 4) and were compared against each other in order to begin the process of establishing a hierarchy to interaction preferences and strengths. The ability to “rank” interactions in terms of strengths and pairing combined with the identification of robust synthons that transcend systems is the ultimate goal

of these efforts. At present however, we are offering qualitative rankings based strictly on which synthons are *observed* when a range of options in a given system are possible.

This study provided not only a platform for studying the interactions that influence assembly but also information regarding the reproducibility of the $[\text{UO}_2\text{Cl}_3(\text{NO}_3)]^{2-}$ tecton and its range of stability. Our initial studies utilizing the uranyl tetrahalide tectons as building blocks for assembly used highly acidic conditions in which the molar concentration of Cl^- to UO_2^{2+} was at least 10:1. If uranyl acetate is used as the UO_2^{2+} source, then much lower Cl:U concentrations can be used to yield the $\text{UO}_2\text{Cl}_4^{2-}$ tecton (Andrews and Cahill, 2013). If uranyl nitrate is substituted as the UO_2^{2+} source and low concentrations (mildly acidic) of Cl^- are utilized, the $[\text{UO}_2\text{Cl}_3(\text{NO}_3)]^{2-}$ tecton can be formed. This is likely a result of the protonation of the acetate ion in acidic solutions (inhibiting coordination), while the nitrate remains unprotonated and free to coordinate to the UO_2^{2+} . The ability to “tune” the aqueous synthetic conditions to produce the $[\text{UO}_2\text{Cl}_3(\text{NO}_3)]^{2-}$ species is significant as this tecton has only been formed hydrothermally (Nazarchuk et al., 2011) and in ionic liquids (Cocalia et al., 2010). Moreover, the ability to manipulate the uranyl speciation profile provides the opportunity to pursue other PBUs in inorganic–organic compound synthesis while, most importantly, avoiding uranyl hydrolysis.

11.3 High Anion Media: A General Approach

The generality of the restricted speciation (or anti-hydrolysis!) approach that has thus far been successful in promoting formation of the $[\text{UO}_2\text{X}_4]^{2-}$ ($\text{X} = \text{Cl}, \text{Br}$) and $[\text{UO}_2\text{Cl}_3(\text{NO}_3)]^{2-}$ tectons may be appreciated when one considers synthesis in high anion media across a range of compositions. In theory, any anion (N_3^- , CN^- , OCN^- , SCN^- , etc.) that demonstrates affinity to the uranyl cation could be used in sufficient concentration as a coordinating ligand to form a uranyl tecton. For instance, if a synthesis were to be performed under aqueous and acidic conditions (HCl), the anion of choice (e.g., OCN^-) would be required to have a higher binding affinity for the UO_2^{2+} cation than Cl^- , or be used at sufficient concentration as to out compete the Cl^- anions for coordination. An example of this concept in use is the synthesis of several uranyl isothiocyanate complexes that contain the $[\text{UO}_2(\text{NCS})_4(\text{H}_2\text{O})]^{2-}$ tecton. Although this tecton has been observed in systems containing rare earth (Ilyukhin et al., 2011; Novitchi et al., 2004), alkaline earth (Weber, 1982; Wei et al., 1987, 1988), and transition metals (Mesa et al., 1998; Vrabel et al., 1999), there are few systematic studies exploring interaction pairings, strengths, and their role in assembly. As such, we prepared the $[\text{UO}_2(\text{NCS})_4(\text{H}_2\text{O})]^{2-}$ tecton by aqueous means and explored pairing with carefully chosen pyridinium cations. The cations contained a fixed hydrogen bond donor ($\text{N}-\text{H}\cdots\text{A}$) and were substituted with halogen,

pseudo-halogen, and hydrogen bond-donating functional groups and led to the formation of eight compounds (Surbella and Cahill, 2014). Compounds **107**, $(C_5H_5NCl)_2[UO_2(NCS)_4(H_2O)]$, **108**, $(C_5H_5NBr)_2[UO_2(NCS)_4(H_2O)] \cdot H_2O$, **109**, $(C_5H_5NI)_2[UO_2(NCS)_4(H_2O)] \cdot (H_2O)$, each contain $[UO_2(NCS)_4(H_2O)]^{2-}$ tectons charge balanced by 4-halopyridinium cations ($X=Cl, Br, I$) (Fig. 92); these three compounds were chosen for consistency and comparison with previous examples using 4-halopyridines.

Each compound (**107–109**) is constructed of supramolecular chains of $[UO_2(NCS)_4(H_2O)]^{2-}$ tectons that are linked together via hydrogen bonding interactions stemming from the coordinated water molecule and the terminal S atoms of the adjoining tectons (Fig. 93). The 4-halopyridinium cations in turn charge balance and stitch together the supramolecular chains to form a structure that contains a 3D hydrogen and halogen-bonded system. The

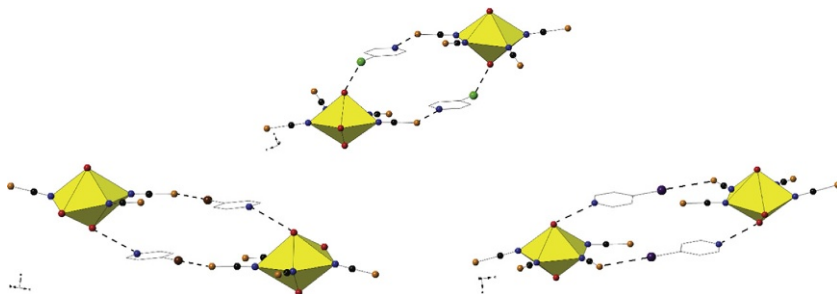


FIGURE 92 Above: The 4-chloropyridinium cations in **107** form $N-H \cdots S$ hydrogen bonds to the sulfur atoms of the $[UO_2(NCS)_4(H_2O)]^{2-}$ tectons and $C-Cl \cdots O$ halogen bonds to the uranyl oxygen atoms. Below: The 4-bromopyridinium (left) and 4-iodopyridinium (right) cations in **108** and **109**, respectively, form $N-H \cdots O$ hydrogen bonds to the uranyl oxygen atoms and $C-Br \cdots S$ halogen bonds to the terminal sulfur atoms.

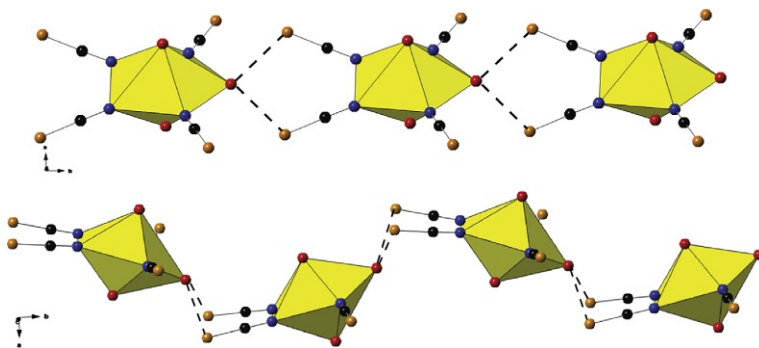


FIGURE 93 Above: Hydrogen bonding interactions ($O-H \cdots S$) in **107** link the $[UO_2(NCS)_4(H_2O)]^{2-}$ tectons into chains. Below: Undulating chains of $[UO_2(NCS)_4(H_2O)]^{2-}$ tectons are formed in **108** and **109** via $O-H \cdots S$ hydrogen bonding interactions.

TABLE 5 Selected Supramolecular Interactions and Distances from 107–109

Compound	Interaction Type	Interaction Distance (Å)	vdW Overlap (D–A) (Eq. 2)
(C ₅ H ₅ NCl) ₂ [UO ₂ (NCS) ₄ (H ₂ O)]	C—Cl...O	3.079(3)	94.1
	N—H...S	3.213(4)	95.9
(C ₅ H ₅ NBr) ₂ [UO ₂ (NCS) ₄ (H ₂ O)]·H ₂ O	C—Br...S	3.608(1)	98.7
	N—H...O	3.044(4)	99.1
(C ₅ H ₅ NI) ₂ [UO ₂ (NCS) ₄ (H ₂ O)]·H ₂ O	C—I...S	3.553 ^a	93.4
	N—H...O	3.029 ^a	98.7

^aAverage interaction distance due to two crystallographically unique 4-iodopyridinium cations in the crystal structure of **109**.

halogen atom of the pyridinium cations (in **107–109**) all forms halogen bonds that increase in strength as a function of interaction pairings that follow HSAB preferences (Table 5). The interaction pairings and relative strengths are as follows: C—Br...S (98.7% vdW), C—Cl...O (94.1% vdW), C—I...S (93.5% avg. vdW). The pyridinium nitrogen atom in turn forms a hydrogen bond with the best available acceptor as the directional halogen bonds tend to “lead” in terms of positioning and orienting the pyridinium cations. The trend of HSAB pairing is consistent among the various uranyl tectons presented within this section and has been invoked in other systems to explain acceptor–donor pairings (Gilday et al., 2015). Recently, several other examples of uranyl isothiocyanate, [UO₂(NCS)₅]³⁻, containing compounds have been synthesized and studied via Raman spectroscopy (Rowland et al., 2012) and visible (fluorescence and absorbance) spectroscopy to understand their photophysical and thermochromic properties (Aoyagi et al., 2011).

12 EXPANDING THE SUPRAMOLECULAR STRATEGY: ACCESSING THE “YL” OXYGENS

The terminal nature of the uranyl oxygen atoms arises from the relatively short U—O bond lengths and, consequently, a relatively satisfied bond valence requirement. As a result, many uranyl-bearing materials tend to form layered structures as a third dimension of connectivity is effectively “off-limits.” This is perhaps less apparent in hybrid materials and CPs where ligand flexibility, NCIs, or additional metal centers may contribute to a 3D topology. Purely inorganic and mineral structures, however, demonstrate this propensity rather extensively (Burns, 2005). We have already discussed

cation–cation interactions, where the axial oxygen of one uranyl cation is coordinated equatorially to another, and while increasing in frequency, their occurrences remain somewhat serendipitous (Cantos et al., 2013a; Severance et al., 2011a). Molecular and coordination chemists have had modest degrees of success with “activating” the uranyl oxygen atoms for interactions by influencing their Lewis basicity with strongly donating equatorial species, or by pairing with strong Lewis acids (Fortier and Hayton, 2010; Hayton and Wu, 2009; Sarsfield and Helliwell, 2004; Wilkerson et al., 2000). In this context, opportunities exist within hybrid materials synthesis to access the uranyl oxygen atoms through judicious selection of ligands and reaction conditions. We will conclude our chapter with two such examples as the “yl” oxygen atoms are in many ways the “frontier” of uranyl crystal chemistry. The first uses a combination of electron-donating equatorial ligands and a polarizable halogen to promote XB (Carter and Cahill, 2015a), whereas the second uses charge-assisted H-bonding within amino acids to coordinate to hydrolyzed SBUs (de Groot et al., 2014).

Compound **110**, $[\text{UO}_2(\text{C}_{12}\text{H}_8\text{N}_2)(\text{C}_7\text{H}_4\text{BrO}_2)_2]$, forms as a result of the hydrothermal treatment of uranyl nitrate salts (at pH 2.5) with 3-bromobenzoic acid and Phen (Carter and Cahill, 2015a). In **110**, molecular BUs are formed as pentagonal bipyramidal uranyl monomers are coordinated by a chelating Phen “cap” and two 3-bromobenzoic ligands in a monodentate and bidentate fashion (Fig. 94). These molecular units are in turn stitched together into molecular dimers, as the bromine atoms of the benzoic acid ligands are positioned such that attractive $\text{Br}\cdots\text{O}$ halogen bonds form with the “yl” oxygen of neighboring tectons. The $\text{Br}\cdots\text{O}$ interaction distance is relatively short at $3.271(3)\text{Å}$ (97% vdW) which indicates a relatively strong and favorable interaction. These pseudo-dimeric units arrange in a parallel fashion along the [010] direction. Secondary π -interactions form between neighboring parallel arranged dimers as the aromatic rings of the Phen “caps” overlap in a favorable manner to form a subtle chain motif (Fig. 94). The presence of a second bromine atom (3,5-dibromobenzoic acid) in **111** leads to the formation

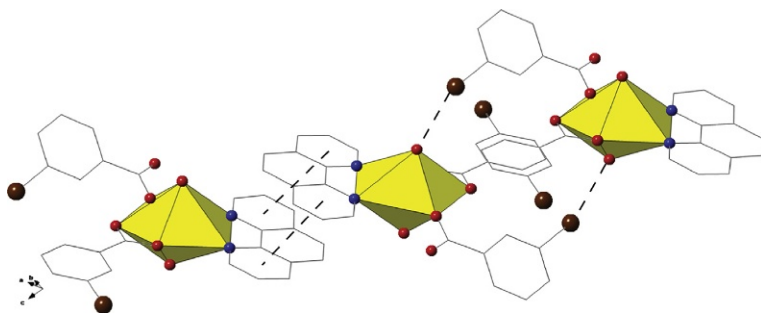


FIGURE 94 Molecular uranyl units in **110** form dimeric units via $\text{C}-\text{Br}\cdots\text{O}$ interactions. The aromatic rings of the Phen “caps” overlap to form π -interactions that link the dimeric groups.

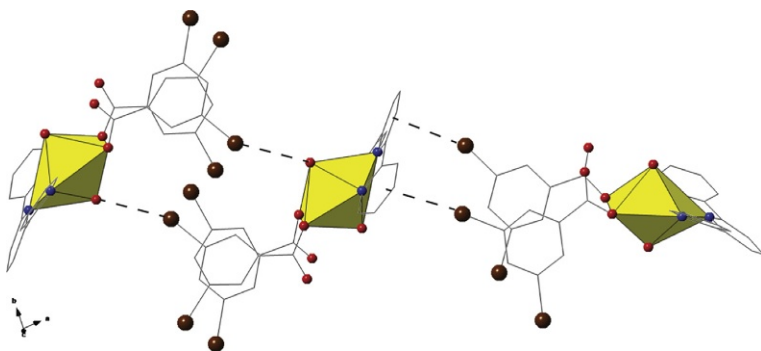
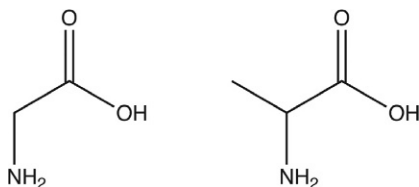


FIGURE 95 Halogen bonding interactions stemming from the terminal bromine atoms of the 3,5-dibromobenzoic acid ligands in **111** lead to the formation of chains.



SCHEME 27 Left: The structure of glycine (Gly). Right: The structure of L-alanine (Ala).

of chains (Fig. 95). In **111**, pentagonal bipyramidal uranyl BUs are chelated by TPY ligands and bound (monodentate) by two 3,5-dibromobenzoic acid ligands. This coordination results in the formation of molecular monomers. One bromine atom of a 3,5-dibromobenzoic acid ligand on each molecular monomer forms an attractive $\text{Br}\cdots\text{O}_{\text{yl}}$ interaction with a neighboring unit ($\text{Br}\cdots\text{O}$ 3.246(3) Å 96% vdW) that effectively forms pseudo-dimers. These “dimers” are in turn stitched together to form zigzag chains, along the [010] direction via additional halogen– π interactions that stem between the bromine atoms and the neighboring TPY ligands.

Additional examples of materials featuring interactions with the “yl” oxygen atoms have been prepared by the Forbes group. The preparation and subsequent isothermal evaporation of aqueous solutions containing uranyl nitrate salts and the amino acids glycine (Gly) or L-alanine (Ala) shown in Scheme 27 led to the formation of three compounds that all contained uranyl SBUs (chains) that were assembled into extended structures via intermolecular charge-assisted hydrogen bonds (de Groot et al., 2014).

Compounds **112**, $[(\text{UO}_2)_3(\text{Gly})_2(\text{O})_2(\text{OH})_2]\cdot 6 \text{H}_2\text{O}$, and **113**, $[(\text{UO}_2)_5(\text{Gly})_4(\text{O})_3(\text{OH})_3]\cdot \text{NO}_3\cdot 12 \text{H}_2\text{O}$, cocrystallize, with **114** being the minor phase (<1%), and both feature oligomerized uranyl SBUs that are decorated by bridging bidentate (via the carboxylate groups) zwitterionic glycine ligands. In **112**, the uranyl SBUs consist of regularly repeating uranyl trimers, whereas

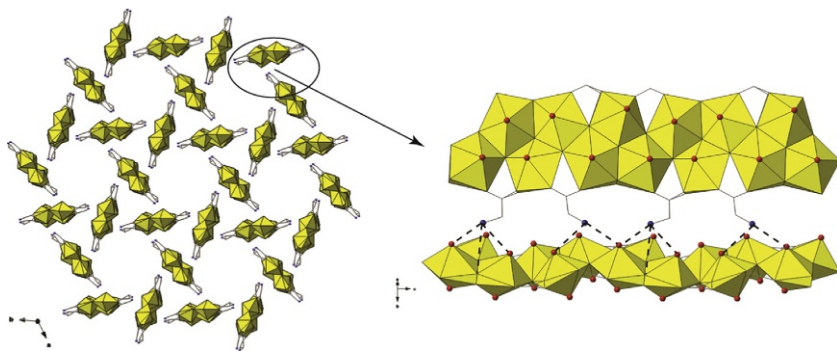


FIGURE 96 Left: Packed chains of oligomerized uranyl pentagonal bipyramids in **112**. The channels are occupied by water molecules (not shown). Right: Individual chains are hydrogen bonded to one another through $\text{N-H}\cdots\text{O}_{\text{yl}}$ and $\text{N-H}\cdots\text{O}_{\text{oxo}}$ interactions.

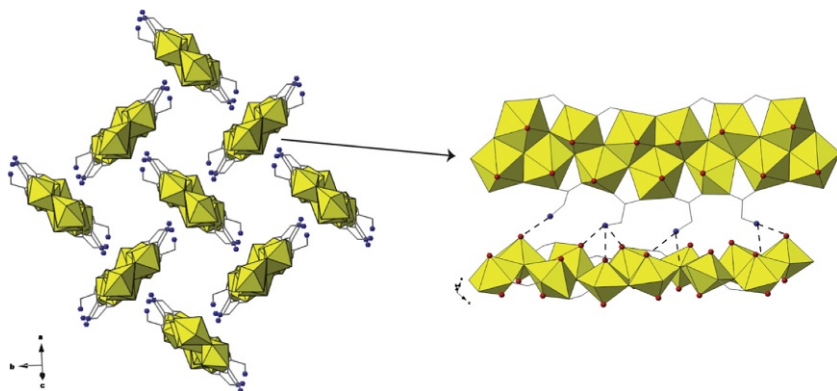


FIGURE 97 Left: Packed cationic chains of oligomerized uranyl pentagonal bipyramids in **113** are charge balanced by nitrate anions that occupy the lattice with solvent water molecules. The nitrate anions and water molecular are omitted for clarity. Right: Individual chains are hydrogen bonded to one another through $\text{N-H}\cdots\text{O}_{\text{yl}}$ and $\text{N-H}\cdots\text{O}_{\text{oxo}}$ interactions.

an alternating motif of trimers and dimers makes up the chains in **113** (Figs. 96 and 97). The uranyl chains in **112** are neutral and assemble in a circular fashion to yield an “open nanoporous architecture” that is occupied by water molecules (Fig. 96). This result is significant as the orientation of the uranyl chains is stabilized in this conformation by strong hydrogen bonds that stem from the positively charged amine residues (of the Gly), which extends into the lattice, to form charge-assisted multifurcated hydrogen bonds with the neighboring chains. The amine group(s)—two crystallographically unique Gly ligands are contained in **112**—form hydrogen bonds to the uranyl oxygen atoms as well as those that bridge the oligomeric SBUs together (O and OH). The $\text{N-H}\cdots\text{O}_{\text{axial}}$ hydrogen bonds range 2.97–3.05 Å, whereas the

$\text{N}-\text{H}\cdots\text{O}_{(\text{oxo})}$ are ~ 2.8 Å. In contrast, the coproduct, **113**, contains cationic uranyl chains that are charge balanced by nitrate molecules, which occupy the lattice along with solvent water molecules. The uranyl chains exhibit similar NCIs (to that of **112**) as $\text{N}-\text{H}\cdots\text{O}$ (axial and oxo) hydrogen bonds form and stabilize the arrangement of the chains. The overall structure is denser and contains less solvent accessible void space when compared to **113**, which may be a function of the charged chains (Fig. 97).

The final compound of this series, **114** $[(\text{UO}_2)_3(\text{Ala})_2\text{O}(\text{OH})_3]\bullet\text{NO}_3\cdot 3\text{H}_2\text{O}$, contains a similarly constructed chain motif to that contained in **112**, yet is similar to that of **113** as the chain is cationic (Fig. 98). Charge-balancing nitrate anions and solvent water molecules are interdispersed throughout the lattice. Once again, similar hydrogen bonding interactions $\text{N}-\text{H}\cdots\text{O}$ (axial and oxo) are formed and stabilize the arrangement of the chains. The absence of large solvent accessible voids are again noted.

This study is significant as it demonstrates the ability to purposefully utilize the supramolecular strategy in the assembly of uranyl-containing materials in media other than high anion and low pH. In fact, the previous compounds **112** and **113** were synthesized at a pH value of 3.8, while **114** was synthesized at pH 4.0 (de Groot et al., 2014). The authors did not restrict the uranyl speciation profile, but instead embraced uranyl hydrolysis and used it to their advantage in order to synthesize a supramolecular CP based off of uranyl chains. The inclusion of nearly identical and reproducible SBUs in three compounds that were further assembled through noncovalent charge-assisted hydrogen bonding interactions demonstrates the versatility and potential this synthetic strategy holds. Perhaps a less obvious, yet equally important, observation from this study is the occurrence of the porous structure (**112**) versus the dense packing in **113** and **114**. This result may be suggestive in terms of the influence charge has upon assembly in the supramolecular approach in uranyl-containing materials as the cationic uranyl chains tend to form more dense structures, whereas the neutral chains formed porous assemblies.

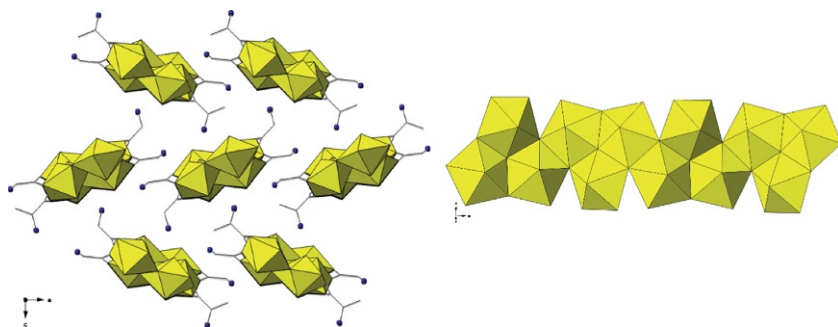


FIGURE 98 Left: Packed chains of oligomerized uranyl pentagonal bipyramids in **112**. Right: The oligomerized chains consist of edge-sharing uranyl trimers.

13 CONCLUDING REMARKS

As mentioned several times throughout this contribution, and perhaps to make sure we do not offend any of our colleagues in this arena, we have endeavored to be illustrative rather than comprehensive. The field of uranyl-bearing CPs is expanding rapidly, keeping pace with all of the current contributions and newcomers, has become all the more demanding—pleasantly so, of course! As such, this contribution has also been largely reflective of the mindset of our group as the evolution of its content mirrors that of our own efforts. In sum, a rich structural chemistry has been established through broad exploratory efforts. Attempts to extract structural themes and incorporate them intentionally into targeted structure types follow with modest success. At present, the “frontier” of uranyl hybrid materials synthesis relies upon a supra-molecular assembly platform, for which the “rules” are still being delineated. We are fortunate, however, to have well-developed criteria in d-metal or purely organic systems to serve as inspiration for use in the f-block.

Looking more broadly, it is clear that the rich structural diversity of the uranyl cation and opportunities to promote desired topologies and connectivities thereof are indeed attractive to a number of researchers. One should also bear in mind their relevance as well considering challenges facing all aspects of the nuclear fuel cycle, as well as legacy waste issues from both energy and weapons production. Beyond these areas, it is also our sense that the photo-physical properties of the uranyl cation are very much underutilized. While certainly not a focus of this chapter, one may speculate (as many have) on significant potential for *niche* applications in catalysis and solar energy conversion. We look forward to more development of this potential.

ACKNOWLEDGMENTS

This work was supported by the U.S. Department of Energy—Chemical Sciences, Geosciences and Biosciences Division, Office of Basic Sciences, Office of Science, Heavy Elements Program, under Grant Number DE-FG02-05ER15736.

ABBREVIATIONS

[H₂CpFeTP]⁺	η^5 -cyclopentadienyl-iron(II)-functionalized terephthalate
1,4-BDC	1,4-benzenedicarboxylic acid
1,4-BDP	1,4-benzenediphosphonic acid
1D	one-dimensional
2,2'-BIPY	2,2'-dipyridyl
2,6-PYDC	2,6-pyridine dicarboxylic acid
2D	two-dimensional
2-PDA	2-phenyldiphosphonic acid
2-PP	2-phosphonopropionate

2-SB	2-sulfobenzoate
3D	three-dimensional
3,5-PDC	3,5-pyrazoledicarboxylic acid
4,4'-BIPY	4,4'-dipyridyl
4,4'-BPBP	4,4'-biphenylenbisphosphonic acid
4,4'-BPDC	4,4'-biphenylcarboxylic acid
4-SB	4-sulfobenzoate
5-SIP	5-sulfoisophthalic acid
Ala	L-alanine
Bmin	1-butyl-3-methylimidazolium
BPE	1,2-bis(4-pyridyl)ethane
BPE'	<i>trans</i> -1,2-bis(4-pyridyl)ethylene
BTEC	1,2,4,5-benzenetetracarboxylic acid
Cit	citric acid
citn	citraconic acid
Citml	D-(−)-citramalic acid
CICA	chlorochelidamic acid
CP	coordination polymer
CPPA	carboxyphenylphosphonic acid
DABCO	1,4-diazabicyclo[2.2.2]octane
dib	1,4-di(1 <i>H</i> -imidazol-1-yl)benzene
DMF	<i>N,N'</i> -dimethylformamide
EDS	1,2-ethanedisulfonate
FCA	ferrocenecarboxylic acid
Gly	glycine
LDP	1-hydroxyethylidenediphosphonic acid
MDP	methylene diphosphonate
Mel	mellitic acid
MOF	metal–organic framework
NCI	noncovalent interaction
NDC	1,4-naphthalenedicarboxylate
PBU	primary building unit
Phen	1,10-phenanthroline
PhenDCA	1,10-phenanthroline-2,9-dicarboxylic acid
PhPA	phenylphosphonic acid
PPA	phosphonoacetic acid
PSM	postsynthetic modification
PSMe	postsynthetic metalation
Pyz	pyrazine
SBU	secondary building unit
t-33pa	<i>trans</i> -3-(3-pyridyl)acrylic acid
te-2-pp	triethyl-2-phosphonopropionate
teppa	triethylphosphonoacetate
THF	tetrahydrofuran

TIB	1,3,5-tri(1 <i>H</i> -imidazol-1-yl)benzene
TPY	2,2':6',2''-terpyridine
udpa	3,3'-ureylenedipropionic acid
UICP	[UO ₂ (OH)(C ₆ H ₅ NO ₂)(C ₆ H ₄ NO ₂)]
XB	halogen bonding

REFERENCES

- Adelani, P.O., Albrecht-Schmitt, T.E., 2009. Uranyl diphosphonates with pillared structures. *Inorg. Chem.* 48, 2732–2734.
- Adelani, P.O., Albrecht-Schmitt, T.E., 2010. Comparison of thorium(IV) and uranium(VI) carboxyphosphonates. *Inorg. Chem.* 49, 5701–5705.
- Adelani, P.O., Albrecht-Schmitt, T.E., 2011a. Heterobimetallic copper(II) uranyl carboxyphenylphosphonates. *Cryst. Growth Des.* 11, 4676–4683.
- Adelani, P.O., Albrecht-Schmitt, T.E., 2011b. Metal-controlled assembly of uranyl diphosphonates toward the design of functional uranyl nanotubules. *Inorg. Chem.* 50, 12184–12191.
- Adelani, P.O., Albrecht-Schmitt, T.E., 2011c. Pillared and open-framework uranyl diphosphonates. *J. Solid State Chem.* 184, 2368–2373.
- Adelani, P.O., Albrecht-Schmitt, T.E., 2011d. Syntheses of uranyl diphosphonate compounds using encapsulated cations as structure directing agents. *Cryst. Growth Des.* 11, 4227–4237.
- Adelani, P.O., Albrecht-Schmitt, T.E., 2012. Layered uranyl coordination polymers rigidly pillared by diphosphonates. *Cryst. Growth Des.* 12, 5800–5805.
- Adelani, P.O., Oliver, A.G., Albrecht-Schmitt, T.E., 2011. Hydrothermal synthesis and structural characterization of organically templated uranyl diphosphonate compounds. *Cryst. Growth Des.* 11, 1966–1973.
- Adelani, P.O., Cook, N.D., Babo, J.-M., Burns, P.C., 2014. Incorporation of Cu²⁺ ions into nanotubular uranyl diphosphonates. *Inorg. Chem.* 53, 4169–4176.
- Alcock, N.W., Flanders, D.J., Pennington, M., Brown, D., 1988. Actinide structural studies. 15. Two 1,10-phenanthroline complexes of uranium(VI). *Acta Crystallogr. C* 44, 247–250.
- Allendorf, M.D., Bauer, C.A., Bhakta, R.K., Houk, R.J.T., 2009. Luminescent metal-organic frameworks. *Chem. Soc. Rev.* 38, 1330–1352.
- Allendorf, M.D., Schwartzberg, A., Stavila, V., Talin, A.A., 2011. A roadmap to implementing metal-organic frameworks in electronic devices: challenges and critical directions. *Chem. Eur. J.* 17, 11372–11388.
- Alsobrook, A.N., Albrecht-Schmitt, T.E., 2009. Phosphonoacetate as a ligand for constructing layered and framework alkali metal uranyl compounds. *Inorg. Chem.* 48, 11079–11084.
- Alsobrook, A.N., Zhan, W., Albrecht-Schmitt, T.E., 2008. Use of bifunctional phosphonates for the preparation of heterobimetallic 5f–3d systems. *Inorg. Chem.* 47, 5177–5183.
- Alsobrook, A.N., Hauser, B.G., Hupp, J.T., Alekseev, E.V., Depmeier, W., Albrecht-Schmitt, T.E., 2010. Cubic and rhombohedral heterobimetallic networks constructed from uranium, transition metals, and phosphonoacetate: new methods for constructing porous materials. *Chem. Commun.* 46, 9167–9169.
- Alsobrook, A.N., Alekseev, E.V., Depmeier, W., Albrecht-Schmitt, T.E., 2011a. Uranyl carboxyphosphonates that incorporate Cd(II). *J. Solid State Chem.* 184, 1195–1200.
- Alsobrook, A.N., Alekseev, E.V., Depmeier, W., Albrecht-Schmitt, T.E., 2011b. Incorporation of Mn(II) and Fe(II) into uranyl carboxyphosphonates. *Cryst. Growth Des.* 11, 2358–2367.

- Alsobrook, A.N., Hauser, B.G., Hupp, J.T., Alekseev, E.V., Depmeier, W., Albrecht-Schmitt, T.E., 2011c. From layered structures to cubic frameworks: expanding the structural diversity of uranyl carboxyphosphonates via the incorporation of cobalt. *Cryst. Growth Des.* 11, 1385–1393.
- Andreev, G., Budantseva, N., Tananaev, I., Myasoedov, B., 2010. Novel mixed valence U(VI)/U(IV) dipicolinate. *Inorg. Chem. Commun.* 13, 577–579.
- Andrews, M.B., Cahill, C.L., 2011. In situ oxalate formation during hydrothermal synthesis of uranyl hybrid materials. *CrystEngComm* 13, 7068–7078.
- Andrews, M.B., Cahill, C.L., 2012a. Uranyl bearing hybrid materials: synthesis, speciation, and solid-state structures. *Chem. Rev.* 113, 1121–1136.
- Andrews, M.B., Cahill, C.L., 2012b. Utilizing hydrogen bonds and halogen-halogen interactions in the design of uranyl hybrid materials. *Dalton Trans.* 41, 3911–3914.
- Andrews, M.B., Cahill, C.L., 2013. Metal-organic hybrids involving the $[\text{UO}_2\text{Cl}_3(\text{NO}_3)]^{2-}$ tecton and the role of halogen polarizability. *CrystEngComm* 15, 3082–3086.
- Aoyagi, N., Shimojo, K., Brooks, N.R., Nagaishi, R., Naganawa, H., Hecke, K.V., Meervelt, L.V., Binnemans, K., Kimura, T., 2011. Thermochromic properties of low-melting ionic uranyl isothiocyanate complexes. *Chem. Commun.* 47, 4490–4492.
- Aranda, M.A.G., Cabeza, A., Bruque, S., Poojary, D.M., Clearfield, A., 1998. Polymorphism and phase transition in nanotubular uranyl phenylphosphonate: $(\text{UO}_2)_3(\text{HO}_3\text{PC}_6\text{H}_5)_2 \cdot (\text{O}_3\text{PC}_6\text{H}_5)_2 \cdot \text{H}_2\text{O}$. *Inorg. Chem.* 37, 1827–1832.
- Arnold, P.L., 2012. Single-molecule magnets: uranyl steps in the ring. *Nat. Chem.* 4, 967–969.
- Asadi, Z., Shorkaei, M.R., 2013. Synthesis, X-ray crystallography, thermal studies, spectroscopic and electrochemistry investigations of uranyl Schiff base complexes. *Spectrochim. Acta A* 105, 344–351.
- Awwadi, F.F., Willett, R.D., Haddad, S.F., Twamley, B., 2006. The electrostatic nature of aryl–bromine–halide synthons: the role of aryl–bromine–halide synthons in the crystal structures of the trans-bis(2-bromopyridine)dihalocopper(II) and trans-bis(3-bromopyridine)-dihalocopper(II) complexes. *Cryst. Growth Des.* 6, 1833–1838.
- Awwadi, F.F., Willett, R.D., Peterson, K.A., Twamley, B., 2007a. The nature of halogen...halide synthons: theoretical and crystallographic studies. *J. Phys. Chem. A* 111, 2319–2328.
- Awwadi, F.F., Willett, R.D., Twamley, B., 2007b. The aryl chlorine–halide ion synthon and its role in the control of the crystal structures of tetrahalocuprate(II) ions. *Cryst. Growth Des.* 7, 624–632.
- Bae, Y.-S., Snurr, R.Q., 2011. Development and evaluation of porous materials for carbon dioxide separation and capture. *Angew. Chem. Int. Ed. Engl.* 50, 11586–11596.
- Baker, R.J., 2012. New reactivity of the uranyl(VI) ion. *Chem. Eur. J.* 18, 16258–16271.
- Basile, M., Unruh, D.K., Flores, E., Johns, A., Forbes, T.Z., 2015. Structural characterization of environmentally relevant ternary uranyl citrate complexes present in aqueous solutions and solid state materials. *Dalton Trans.* 44, 2597–2605.
- Batten, S.R., Robson, R., 1998. Interpenetrating nets: ordered, periodic entanglement. *Angew. Chem. Int. Ed. Engl.* 37, 1460–1494.
- Batten, S.R., Champness, N.R., Chen, X.-M., Garcia-Martinez, J., Kitagawa, S., Öhrström, L., O’Keeffe, M., Paik Suh, M., Reedijk, J., 2013. Terminology of metal-organic frameworks and coordination polymers (IUPAC Recommendations 2013). *Pure Appl. Chem.* 85, 1715–1724.
- Bean, A.C., Xu, Y., Danis, J.A., Albrecht-Schmitt, T.E., Scott, B.L., Runde, W., 2002. Aqueous reactions of U(VI) at high chloride concentrations: syntheses and structures of new uranyl chloride polymers. *Inorg. Chem.* 41, 6775–6779.
- Benetollo, F., Bombieri, G., Herrero, J.A., Rojas, R.M., 1979. Structural studies on actinides carboxylates—III. Preparation, properties and crystal structure of lithium glutarate

- hydrogenlutarate dioxouranate(VI)tetrahydrate $\text{UO}_2(\text{C}_5\text{H}_6\text{O}_4)\text{Li}(\text{C}_5\text{H}_7\text{O}_4)\cdot 4\text{H}_2\text{O}$. *J. Inorg. Nucl. Chem.* 41, 195–199.
- Bertani, R., Sgarbossa, P., Venzo, A., Lelj, F., Amati, M., Resnati, G., Pilati, T., Metrangolo, P., Terraneo, G., 2010. Halogen bonding in metal–organic–supramolecular networks. *Coord. Chem. Rev.* 254, 677–695.
- Bhogala, B.R., Nangia, A., 2003. Cocrystals of 1,3,5-cyclohexanetricarboxylic acid with 4,4'-bipyridine homologues: acid···pyridine hydrogen bonding in neutral and ionic complexes. *Cryst. Growth Des.* 3, 547–554.
- Bombieri, G., Benetollo, F., Del Pra, A., Rojas, R., 1979. Structural studies on the actinide carboxylates—IV. The crystal and molecular structure of succinate dioxouranium(VI) monohydrate. *J. Inorg. Nucl. Chem.* 41, 201–203.
- Bombieri, G., Benetollo, F., Forsellini, E., Del Pra, A., 1980. Structural studies on actinides carboxylates—VI [1]: crystal structures of strontium uranyldimalonate trihydrate and barium uranyldimalonate trihydrate. *J. Inorg. Nucl. Chem.* 42, 1423–1430.
- Borkowski, L.A., Cahill, C.L., 2003. Topological evolution in uranyl dicarboxylates: synthesis and structures of one-dimensional $\text{UO}_2(\text{C}_6\text{H}_8\text{O}_4)(\text{H}_2\text{O})_2$ and three-dimensional $\text{UO}_2(\text{C}_6\text{H}_8\text{O}_4)$. *Inorg. Chem.* 42, 7041–7045.
- Borkowski, L.A., Cahill, C.L., 2004. A novel uranium-containing coordination polymer: poly [[aqua(benzene-1,3,5-tricarboxylato)dioxouranium(VI)] monohydrate]. *Acta Crystallogr. C* 60, m198–m200.
- Borkowski, L.A., Cahill, C.L., 2005. A novel uranium-containing coordination polymer: poly [dioxouranium(VI)- μ_4 -n-pentane-1,5-dicarboxylato]. *Acta Crystallogr. C* 61, m816–m817.
- Borkowski, L.A., Cahill, C.L., 2006a. Crystal engineering with the uranyl cation I. Aliphatic carboxylate coordination polymers: synthesis, crystal structures, and fluorescent properties. *Cryst. Growth Des.* 6, 2241–2247.
- Borkowski, L.A., Cahill, C.L., 2006b. Crystal engineering with the uranyl cation II. Mixed aliphatic carboxylate/aromatic pyridyl coordination polymers: synthesis, crystal structures, and sensitized luminescence. *Cryst. Growth Des.* 6, 2248–2259.
- Brammer, L., 2004. Developments in inorganic crystal engineering. *Chem. Soc. Rev.* 33, 476–489.
- Brammer, L., Bruton, E.A., Sherwood, P., 2001. Understanding the behavior of halogens as hydrogen bond acceptors. *Cryst. Growth Des.* 1, 277–290.
- Brammer, L., Minguez Espallargas, G., Libri, S., 2008. Combining metals with halogen bonds. *CrystEngComm* 10, 1712–1727.
- Brandel, V., Dacheux, N., Genet, M., 1996. Reexamination of uranium (IV) phosphate chemistry. *J. Solid State Chem.* 121, 467–472.
- Britel, A., Wozniak, M., Boivin, J.C., Nowogrocki, G., Thomas, D., 1986. Structure du complexe uranyle pentahydrate de l'acide hydroxyméthylphosphonique. *Acta Crystallogr. C* 42, 1502–1505.
- Bujoli, B., Lane, S.M., Nonglaton, G., Pipelier, M., Léger, J., Talham, D.R., Tellier, C., 2005. Metal phosphonates applied to biotechnologies: a novel approach to oligonucleotide microarrays. *Chem. Eur. J.* 11, 1980–1988.
- Burns, P.C., 1999. The crystal chemistry of uranium. *Rev. Mineral Geochem.* 38, 23–90.
- Burns, P.C., 2001. A new uranyl sulfate chain in the structure of uranophile. *Can. Mineral.* 39, 1139–1146.
- Burns, P.C., 2005. U^{6+} minerals and inorganic compounds: insights into an expanded structural hierarchy of crystal structures. *Can. Mineral.* 43, 1839–1894.
- Burns, P.C., 2007. Chapter 1—crystal chemistry of uranium oxocompounds: an overview. In: Tananaev, I.G.K., Burns, S.V., Peter, C. (Eds.), *Structural Chemistry of Inorganic Actinide Compounds*. Amsterdam, Elsevier, pp. 1–30.

- Burns, P.C., 2011. Nanoscale uranium-based cage clusters inspired by uranium mineralogy. *Mineral Mag.* 75, 1–25.
- Burns, P.C., Miller, M.L., Ewing, R.C., 1996. U (6+) minerals and inorganic phases; a comparison and hierarchy of crystal structures. *Can. Mineral.* 34, 845–880.
- Burns, P.C., Ewing, R.C., Hawthorne, F.C., 1997. The crystal chemistry of hexavalent uranium; polyhedron geometries, bond-valence parameters, and polymerization of polyhedra. *Can. Mineral.* 35, 1551–1570.
- Burns, P.C., Deely, K.M., Hayden, L.A., 2003. The crystal chemistry of the zippeite group. *Can. Mineral.* 41, 687–706.
- Burns, P.C., Alexopoulos, C.M., Hotchkiss, P.J., Locock, A.J., 2004. An unprecedented uranyl phosphate framework in the structure of $[(\text{UO}_2)_3(\text{PO}_4)\text{O}(\text{OH})(\text{H}_2\text{O})_2](\text{H}_2\text{O})$. *Inorg. Chem.* 43, 1816–1818.
- Burns, P.C., Ikeda, Y., Czerwinski, K., 2010. Advances in actinide solid-state and coordination chemistry. *MRS Bull.* 35, 868–876.
- Cahill, C.L., Burns, P.C., 2000. The structure of agrinierite: a Sr-containing uranyl oxide hydrate mineral. *Am. Mineral.* 85, 1294–1297.
- Cahill, C.L., de Lill, D.T., Frisch, M., 2007. Homo- and heterometallic coordination polymers from the f elements. *CrystEngComm* 9, 15–26.
- Cai, J., 2004. Structural chemistry and properties of metal arenesulfonates. *Coord. Chem. Rev.* 248, 1061–1083.
- Cantos, P.M., Cahill, C.L., 2014a. A family of UO_2^{2+} -5-nitro-1,3-dicarboxylate hybrid materials: structural variation as a function of pH and structure directing species. *Cryst. Growth Des.* 14, 3044–3053.
- Cantos, P.M., Cahill, C.L., 2014b. Poly[diammonium [diaqua(μ_7 -benzene-1,2,3,4,5,6-hexacarboxylato)tetraoxidodiuuranium(VI)]]. *Acta Crystallogr. C* 70, m142–m143.
- Cantos, P.M., Frisch, M., Cahill, C.L., 2010. Synthesis, structure and fluorescence properties of a uranyl-2,5-pyridinedicarboxylic acid coordination polymer: the missing member of the UO_2^{2+} -2,n-pyridinedicarboxylic series. *Inorg. Chem. Commun.* 13, 1036–1039.
- Cantos, P.M., Jouffret, L.J., Wilson, R.E., Burns, P.C., Cahill, C.L., 2013a. Series of uranyl-4,4'-biphenyldicarboxylates and an occurrence of a cation–cation interaction: hydrothermal synthesis and in situ raman studies. *Inorg. Chem.* 52, 9487–9495.
- Cantos, P.M., Pope, S.J.A., Cahill, C.L., 2013b. An exploration of homo- and heterometallic UO_2^{2+} hybrid materials containing chelidamic acid: synthesis, structure, and luminescence studies. *CrystEngComm* 15, 9039–9051.
- Carter, K.P., Cahill, C.L., 2015a. Combining coordination and supramolecular chemistry to explore uranyl assembly in the solid state. *Inorg. Chem. Front.* 2, 141–156.
- Carter, K.P., Cahill, C.L., 2015b. Hybrid materials of the f-Elements. Part 1: the lanthanides. In: Bunzli, J.-C.G., Pecharaky, V.K. (Eds.), *Handbook on the Physics and Chemistry of Rare Earths*. Elsevier, Amsterdam, pp. 147–208.
- Charpin, P., Folcher, G., Lance, M., Nierlich, M., Vigner, D., 1985. Structure d'un complexe binucléaire du nitrate d'uranyle et du N,N-diméthyl-formamide: μ -peroxo-bis[bis(N,N-diméthyl-formamide)nitratodioxouranium(VI)], $[(\text{UO}_2)_2(\text{NO}_3)_2\text{O}_2(\text{C}_3\text{H}_7\text{NO})_4]$. *Acta Crystallogr. C* 41, 1302–1305.
- Chen, B., Xiang, S., Qian, G., 2010. Metal–organic frameworks with functional pores for recognition of small molecules. *Acc. Chem. Res.* 43, 1115–1124.
- Chiarizia, R., Danesi, P.R., Scibona, G., Magon, L., 1973. Liquid anion exchange of thiocyanate–nitrate actinide and lanthanide complexes. *J. Inorg. Nucl. Chem.* 35, 3595–3604.
- Clark, T., 2013. σ -Holes. *WIREs Comput. Mol. Sci.* 3, 13–20.

- Clearfield, A., 2007. Metal Phosphonate Chemistry. Prog. Inorg. Chem., John Wiley & Sons, Inc.
- Clearfield, A., Demadis, K., 2011. Metal Phosphonate Chemistry: From Synthesis to Applications. Royal Society of Chemistry, Cambridge, U.K. <http://dx.doi.org/10.1039/9781849733571-00001>. ISBN:9781849733564.
- Cocalia, V., Smíglak, M., Kelley, S.P., Shamshina, J.L., Gurau, G., Rogers, R.D., 2010. Crystallization of uranyl salts from dialkylimidazolium ionic liquids or their precursors. Eur. J. Inorg. Chem. 2010, 2760–2767.
- Côté, A.P., Shimizu, G.K.H., 2003. The supramolecular chemistry of the sulfonate group in extended solids. Coord. Chem. Rev. 245, 49–64.
- Crouthamel, C.E., Johnson, C.E., 1952. Spectrophotometric determination of uranium by thiocyanate method in acetone medium. Anal. Chem. 24, 1780–1783.
- Davis, M.E., Lobo, R.F., 1992. Zeolite and molecular sieve synthesis. Chem. Mater. 4, 756–768.
- de Groot, J., Gojdas, K., Unruh, D.K., Forbes, T.Z., 2014. Use of charge-assisted hydrogen bonding in the supramolecular assembly of hybrid uranyl materials. Cryst. Growth Des. 14, 1357–1365.
- Dean, N.E., Hancock, R.D., Cahill, C.L., Frisch, M., 2008. Affinity of the highly preorganized ligand PDA (1,10-phenanthroline-2,9-dicarboxylic acid) for large metal ions of higher charge. A crystallographic and thermodynamic study of PDA complexes of thorium(IV) and the uranyl(VI) ion. Inorg. Chem. 47, 2000–2010.
- Deb, N., 2010. An investigation on the solid-state thermal decomposition behaviour of uranyl(II)-diaquatris(oxalato)lanthanate(III)octahydrate and cobalt(II)uranyl(II)pentaquatris(oxalato)lanthanate(III)octahydrate. J. Anal. Appl. Pyrolysis 87, 269–275.
- Deifel, N.P., Cahill, C.L., 2009. The uranyl tetrachloride anion as a tecton in the assembly of U(VI) hybrid materials. CrystEngComm 11, 2739–2744.
- Deifel, N.P., Cahill, C.L., 2010. Supramolecular chemistry with uranyl tetrahalide ($[\text{UO}_2\text{X}_4]^{2-}$) anions. CR Chim. 13, 747–754.
- Deifel, N.P., Cahill, C.L., 2011. Combining coordination and supramolecular chemistry for the formation of uranyl-organic hybrid materials. Chem. Commun. 47, 6114–6116.
- Denning, R.G., 2007. Electronic structure and bonding in actinyl ions and their analogs. J. Phys. Chem. A 111, 4125–4143.
- Derikvand, Z., Olmstead, M.M., Mercado, B.Q., Shokrollahi, A., Shahryari, M., 2013. Solution and solid state studies of three new supramolecular compounds of zinc(II), nickel(II) and uranium(VI) with chelidamic acid and 9-aminoacridine. Inorg. Chim. Acta 406, 256–265.
- Desiraju, G.R., 1995. Supramolecular synthons in crystal engineering—a new organic synthesis. Angew. Chem. Int. Ed. Engl. 34, 2311–2327.
- Desiraju Gautam, R., Ho, P.S., Kloos, L., Legon Anthony, C., Marquardt, R., Metrangolo, P., Politzer, P., Resnati, G., Rissanen, K., 2013. Definition of the halogen bond (IUPAC Recommendations 2013). Pure Appl. Chem. 85, 1711–1713.
- Dhakshinamoorthy, A., Alvaro, M., Garcia, H., 2011. Metal-organic frameworks as heterogeneous catalysts for oxidation reactions. Catal. Sci. Technol. 1, 856–867.
- Dhakshinamoorthy, A., Alvaro, M., Garcia, H., 2012. Commercial metal-organic frameworks as heterogeneous catalysts. Chem. Commun. 48, 11275–11288.
- Diwu, J., Albrecht-Schmitt, T.E., 2012a. Chiral uranium phosphonates constructed from achiral units with three-dimensional frameworks. Chem. Commun. 48, 3827–3829.
- Diwu, J., Albrecht-Schmitt, T.E., 2012b. Mixed-valent uranium(IV, VI) diphosphonate: synthesis, structure, and spectroscopy. Inorg. Chem. 51, 4432–4434.
- Diwu, J., Wang, S., Good, J.J., DiStefano, V.H., Albrecht-Schmitt, T.E., 2011. Deviation between the chemistry of Ce(IV) and Pu(IV) and routes to ordered and disordered heterobimetallic 4f/5f and 5f/5f phosphonates. Inorg. Chem. 50, 4842–4850.

- Doran, M., Norquist, A.J., O'Hare, D., 2002. $[\text{NC}_4\text{H}_{12}]_2[(\text{UO}_2)_6(\text{H}_2\text{O})_2(\text{SO}_4)_7]$: the first organically templated actinide sulfate with a three-dimensional framework structure. *Chem. Commun.* 24, 2946–2947.
- Doran, M.B., Norquist, A.J., O'Hare, D., 2003. Reactant-mediated diversity in uranyl phosphonates. *Chem. Mater.* 15, 1449–1455.
- Doran, M.B., Norquist, A.J., O'Hare, D., 2005. $(\text{C}_3\text{H}_{12}\text{N}_2)_2[\text{UO}_2(\text{H}_2\text{O})_2(\text{SO}_4)_2]_2 \cdot 2\text{H}_2\text{O}$: an organically templated uranium sulfate with a novel dimer type. *Acta Crystallogr. C* 61, m881–m884.
- Duvieubourg, L., Nowogrocki, G., Abraham, F., Grandjean, S., 2005. Hydrothermal synthesis and crystal structures of new uranyl oxalate hydroxides: α - and β - $[(\text{UO}_2)_2(\text{C}_2\text{O}_4)(\text{OH})_2(\text{H}_2\text{O})_2]$ and $[(\text{UO}_2)_2(\text{C}_2\text{O}_4)(\text{OH})_2(\text{H}_2\text{O})_2] \cdot \text{H}_2\text{O}$. *J. Solid State Chem.* 178, 3437–3444.
- Ephritikhine, M., 2006. The vitality of uranium molecular chemistry at the dawn of the XXIst century. *Dalton Trans.* (21), 2501–2516.
- Ephritikhine, M., 2013. Recent advances in organoactinide chemistry as exemplified by cyclopentadienyl compounds. *Organometallics* 32, 2464–2488.
- Etter, M.C., 1990. Encoding and decoding hydrogen-bond patterns of organic compounds. *Acc. Chem. Res.* 23, 120–126.
- Etter, M.C., 1991. Hydrogen bonds as design elements in organic chemistry. *J. Phys. Chem. US* 95, 4601–4610.
- Fong, S.W.A., Yap, W.T., Vittal, J.J., Henderson, W., Hor, T.S.A., 2002. Mass spectrometry-directed synthesis of 'early-late' sulfide-bridged heterobimetallic complexes from the metal-ligand $[\text{Pt}_2(\text{PPh}_3)_4(\mu\text{-S})_2]$ and oxo compounds of vanadium(V), molybdenum(VI) and uranium(VI). *J. Chem. Soc. Dalton* (8), 1826–1831. <http://dx.doi.org/10.1039/b107939p>. ISSN:1472-7773.
- Forbes, T.Z., Horan, P., Devine, T., McInnis, D., Burns, P.C., 2011. Alteration of dehydrated schoepite and soddyite to studtite, $[(\text{UO}_2)(\text{O}_2)(\text{H}_2\text{O})_2](\text{H}_2\text{O})_2$. *Am. Mineral.* 96, 202–206.
- Fortier, S., Hayton, T.W., 2010. Oxo ligand functionalization in the uranyl ion (UO_2^{2+}). *Coord. Chem. Rev.* 254, 197–214.
- Frisch, M., Cahill, C.L., 2005. Syntheses, structures and fluorescent properties of two novel coordination polymers in the U-Cu- H_3pdc system. *Dalton Trans.* (8), 1518–1523.
- Frisch, M., Cahill, C.L., 2006. Synthesis, structure and fluorescent studies of novel uranium coordination polymers in the pyridinedicarboxylic acid system. *Dalton Trans.* (39), 4679–4690.
- Furukawa, H., Cordova, K.E., O'Keeffe, M., Yaghi, O.M., 2013. The chemistry and applications of metal-organic frameworks. *Science* 341, 1230444.
- Gagnon, K.J., Perry, H.P., Clearfield, A., 2011. Conventional and unconventional metal-organic frameworks based on phosphonate ligands: MOFs and UMOFs. *Chem. Rev.* 112, 1034–1054.
- Gatto, C.C., Schulz Lang, E., Kupfer, A., Hagenbach, A., Wille, D., Abram, U., 2004. Dioxouranium complexes with acetylpyridine benzoylhydrazones and related ligands. *Z. Anorg. Allg. Chem.* 630, 735–741.
- Ghosh, S., Biswas, S., Bauzá, A., Barceló-Oliver, M., Frontera, A., Ghosh, A., 2013. Use of metalloligands $[\text{CuL}]$ ($\text{H}_2\text{L} = \text{salen}$ type di-Schiff bases) in the formation of heterobimetallic copper(II)-uranyl complexes: photophysical investigations, structural variations, and theoretical calculations. *Inorg. Chem.* 52, 7508–7523.
- Gilday, L.C., Robinson, S.W., Barendt, T.A., Langton, M.J., Mullaney, B.R., Beer, P.D., 2015. Halogen bonding in supramolecular chemistry. *Chem. Rev.* 115 (15), 7118–7195.
- Go, Y.B., Wang, X., Jacobson, A.J., 2007. (6,3)-honeycomb structures of uranium(VI) benzenedicarboxylate derivatives: the use of noncovalent interactions to prevent interpenetration. *Inorg. Chem.* 46, 6594–6600.

- Grechishnikov, E.V., Mikhailov, Y.N., Kanishcheva, A.S., Serezhkina, L.B., Serezhkin, V.N., 2005. Synthesis and structure of $[\text{UO}_2(\text{OH})(\text{C}_6\text{NO}_2\text{H}_4)(\text{C}_6\text{NO}_2\text{H}_3)]$. *Zh. Neorg. Khim.* 50, 1436–1441.
- Grenthe, I., Fuger, J., Konings, R.J.M., Lemire, R.J., Muller, A.B., Nguyen-Trun, C., Wanner, H., 2004. Chemical thermodynamics of uranium. In: Wanner, H., Forest, I. (Eds.), second ed. Nuclear Energy Agency, Organization for Economic Cooperation and Development, Issy-les-Moulineau (France).
- Grigor'ev, M.S., Antipin, M.Y., Krot, N.N., 2005. Crystal structure of uranyl malonate trihydrate $[\text{UO}_2(\text{OOC})_2\text{CH}_2(\text{H}_2\text{O})]\cdot 2\text{H}_2\text{O}$. *Radiochemistry* 47, 103–106.
- Grohol, D., Clearfield, A., 1997a. Alkali-ion-catalyzed transformation of two linear uranyl phosphonates into a tubular one. *J. Am. Chem. Soc.* 119, 9301–9302.
- Grohol, D., Clearfield, A., 1997b. Solid-state water-catalyzed transformation at room temperature of a nonluminescent linear-chain uranyl phenylphosphonate into a luminescent one. *J. Am. Chem. Soc.* 119, 4662–4668.
- Grohol, D., Subramanian, M.A., Poojary, D.M., Clearfield, A., 1996. Synthesis, crystal structures, and proton conductivity of two linear-chain uranyl phenylphosphonates. *Inorg. Chem.* 35, 5264–5271.
- Hall, D., Rae, A.D., Waters, T.N., 1967. The crystal structures of the chloroform solvate of dioxodi-8-quinolinolato-8-quinolinoluranium(VI). *Acta Crystallogr.* 22, 258–268.
- Hanson Brady, D., McNamara, B., Buck Edgar, C., Friese Judah, I., Jenson, E., Krupka, K., Arey Bruce, W., 2005. Corrosion of commercial spent nuclear fuel. 1. Formation of studtite and metastudtite. *Radiochim Acta* 93, 159–168.
- Harrowfield, J.M., Lugan, N., Shahverdizadeh, G.H., Soudi, A.A., Thuéry, P., 2006. Solid-state luminescence and π -stacking in crystalline uranyl dipicolinates. *Eur. J. Inorg. Chem.* 2006, 389–396.
- Hayton, T.W., 2010. Metal-ligand multiple bonding in uranium: structure and reactivity. *Dalton Trans.* 39, 1145–1158.
- Hayton, T.W., 2013. Recent developments in actinide-ligand multiple bonding. *Chem. Commun.* 49, 2956–2973.
- Hayton, T.W., Wu, G., 2009. Exploring the effects of reduction or lewis acid coordination on the UO bond of the uranyl moiety. *Inorg. Chem.* 48, 3065–3072.
- He, H., Ma, H., Sun, D., Zhang, L., Wang, R., Sun, D., 2013. Porous lanthanide–organic frameworks: control over interpenetration, gas adsorption, and catalyst properties. *Cryst. Growth Des.* 13, 3154–3161.
- Henderson, W., Oliver, A.G., Rickard, C.E.F., 2000. Synthesis and structure of the amidate-bridged platinum–uranium bimetallic complex $[\text{Pt}\{\text{NC}(\text{O})\text{CH}_2\text{CH}_2\}_2(\text{PPh}_3)_2]\cdot \text{UO}_2(\text{NO}_3)_2$. *Inorg. Chim. Acta* 307, 144–148.
- Hennig, C., Tutschku, J., Rossberg, A., Bernhard, G., Scheinost, A.C., 2005. Comparative EXAFS investigation of uranium(VI) and -(IV) aquo chloro complexes in solution using a newly developed spectroelectrochemical cell. *Inorg. Chem.* 44, 6655–6661.
- Henry, N., Lagrenée, M., Loiseau, T., Clavier, N., Dacheux, N., Abraham, F., 2011. Tetrameric entity resulting from two distinct dinuclear uranyl-centered motifs bridged through μ_2 -OH and pyridazine-3,6-dicarboxylate. *Inorg. Chem. Commun.* 14, 429–432.
- Hoskins, B.F., Robson, R., 1990. Design and construction of a new class of scaffolding-like materials comprising infinite polymeric frameworks of 3D-linked molecular rods. A reappraisal of the zinc cyanide and cadmium cyanide structures and the synthesis and structure of the diamond-related frameworks $[\text{N}(\text{CH}_3)_4][\text{Cu}(\text{I})\text{Zn}(\text{II})(\text{CN})_4]$ and $\text{Cu}[\text{I}4,4',4'',4'''\text{-tetracyanotetraphenylmethane}]\text{BF}_4\cdot \text{C}_6\text{H}_5\text{NO}_2$. *J. Am. Chem. Soc.* 112, 1546–1554.

- Housty, J., Hospital, M., 1965. Localisation des atomes d'hydrogene dans l'acide suberique $\text{COOH}(\text{CH}_2)_6\text{COOH}$. *Acta Crystallogr.* 18, 753–755.
- Huang, J., Wang, X., Jacobson, A.J., 2003. Hydrothermal synthesis and structures of the new open-framework uranyl silicates $\text{Rb}_4(\text{UO}_2)_2(\text{Si}_8\text{O}_{20})$ (USH-2Rb), $\text{Rb}_2(\text{UO}_2)(\text{Si}_2\text{O}_6)\cdot\text{H}_2\text{O}$ (USH-4Rb) and $\text{A}_2(\text{UO}_2)(\text{Si}_2\text{O}_6)\cdot 0.5\text{H}_2\text{O}$ (USH-5A; A = Rb, Cs). *J. Mater. Chem.* 13, 191–196.
- Hughes Kubatko, K.-A., Burns, P.C., 2004. The Rb analogue of grimselite, $\text{Rb}_6\text{Na}_2[(\text{UO}_2)(\text{CO}_3)_3]_2(\text{H}_2\text{O})$. *Acta Crystallogr. C* 60, 25–26.
- Hughes, K.-A., Burns, P.C., 2003. A new uranyl carbonate sheet in the crystal structure of fontanite, $\text{Ca}[(\text{UO}_2)_3(\text{CO}_3)_2\text{O}_2](\text{H}_2\text{O})_6$. *Am. Mineral.* 88, 962–966.
- Ilyukhin, A., Dobrokhotova, Z., Petrosyants, S., Novotortsev, V., 2011. Yttrium thiocyanate-based supramolecular architectures: synthesis, crystal structures, and thermal properties. *Polyhedron* 30, 2654–2660.
- Immirzi, A., Bombieri, G., Degetto, S., Marangoni, G., 1975. The crystal and molecular structure of pyridine-2,6-dicarboxylatodioxouranium(VI) monohydrate. *Acta Crystallogr. B* 31, 1023–1028.
- Jiang, Y.-S., Yu, Z.-T., Liao, Z.-L., Li, G.-H., Chen, J.-S., 2006. Syntheses and photoluminescent properties of two uranyl-containing compounds with extended structures. *Polyhedron* 25, 1359–1366.
- Jouffret, L., Rivenet, M., Abraham, F., 2010. A new series of pillared uranyl-vanadates based on uranophane-type sheets in the uranium-vanadium-linear alkyl diamine systems. *J. Solid State Chem.* 183, 84–92.
- Kerr, A.T., Cahill, C.L., 2011. Crystal engineering with the uranyl cation III. Mixed aliphatic dicarboxylate/aromatic dipyrityl coordination polymers: synthesis, structures, and speciation. *Cryst. Growth Des.* 11, 5634–5641.
- Kerr, A.T., Cahill, C.L., 2014a. CuPYDC metalloligands and postsynthetic rearrangement/metalation as routes to bimetallic uranyl containing hybrid materials: syntheses, structures, and fluorescence. *Cryst. Growth Des.* 14, 4094–4103.
- Kerr, A.T., Cahill, C.L., 2014b. Postsynthetic rearrangement/metalation as a route to bimetallic uranyl coordination polymers: syntheses, structures, and luminescence. *Cryst. Growth Des.* 14, 1914–1921.
- Kerr, A., Kumalah, S., Holman, K.T., Butcher, R., Cahill, C., 2014. Uranyl coordination polymers incorporating $\eta 5$ -cyclopentadienyliron-functionalized $\eta 6$ -phthalate metalloligands: syntheses, structures and photophysical properties. *J. Inorg. Organ. Polym.* 24, 128–136.
- Kickelbick, G., 2007. Chapter 1: introduction to hybrid materials (pages 1–48). In: Kickelbick, G. (Ed.), *Hybrid Materials: Synthesis, Characterization, and Applications*. Wiley-VCH Verlag GmbH & Co, KGaA, Weinheim, p. 498. <http://dx.doi.org/10.1002/9783527610495>.
- Kim, J.-Y., Norquist, A.J., O'Hare, D., 2003. Incorporation of uranium(VI) into metal-organic framework solids, $[\text{UO}_2(\text{C}_4\text{H}_4\text{O}_4)]\cdot\text{H}_2\text{O}$, $[\text{UO}_2\text{F}(\text{C}_5\text{H}_6\text{O}_4)]\cdot 2\text{H}_2\text{O}$, and $[(\text{UO}_2)_{1.5}(\text{C}_8\text{H}_4\text{O}_4)_2]_2[(\text{CH}_3)_2\text{NCOH}_2]\cdot\text{H}_2\text{O}$. *Dalton Trans.* 14, 2813–2814.
- Knope, K.E., Cahill, C.L., 2007. Hydrothermal synthesis of a novel uranium oxalate/glycolate via in-situ ligand formation. *Inorg. Chem.* 46, 6607–6612.
- Knope, K.E., Cahill, C.L., 2008. Structural variation within homometallic uranium(VI) carboxyphosphonates: in situ ligand synthesis, directed assembly, metal–ligand coordination and hydrogen bonding. *Inorg. Chem.* 47, 7660–7672.
- Knope, K.E., Cahill, C.L., 2010a. Homometallic UO_2^{2+} diphosphonates assembled under ambient and hydrothermal conditions. *Dalton Trans.* 39, 8319–8324.
- Knope, K.E., Cahill, C.L., 2010b. Room temperature assembly of a uranyl carboxyphosphonate: synthesis, characterization and UO_2^{2+} hydrolysis. *Inorg. Chem. Commun.* 13, 1040–1042.

- Knope, K.E., Cahill, C.L., 2010c. Synthesis and characterization of 1-, 2-, and 3-dimensional bimetallic $\text{UO}_2^{2+}/\text{Zn}^{2+}$ phosphonoacetates. *Eur. J. Inorg. Chem.* 2010, 1177–1185.
- Knope, K.E., Cahill, C.L., 2012. Uranyl phosphonates: a structural survey. *Metal Phosphonate Chemistry: From Synthesis to Applications*. The Royal Society of Chemistry, Cambridge, UK.
- Knope, K.E., Soderholm, L., 2013. Solution and solid-state structural chemistry of actinide hydrates and their hydrolysis and condensation products. *Chem. Rev.* 113, 944–994.
- Knope, K.E., de Lill, D.T., Rowland, C.E., Cantos, P.M., de Bettencourt-Dias, A., Cahill, C.L., 2011. Uranyl sensitization of samarium(III) luminescence in a two-dimensional coordination polymer. *Inorg. Chem.* 51, 201–206.
- Kreno, L.E., Leong, K., Farha, O.K., Allendorf, M., Van Duyne, R.P., Hupp, J.T., 2011. Metal-organic framework materials as chemical sensors. *Chem. Rev.* 112, 1105–1125.
- Krivovichev, S.V., 2010. Actinyl compounds with hexavalent elements (S, Cr, Se, Mo)—structural diversity, nanoscale chemistry, and cellular automata modeling. *Eur. J. Inorg. Chem.* 2010, 2594–2603.
- Krivovichev Sergey, V., Burns Peter, C., 2003. Structural topology of potassium uranyl chromates: crystal structures of $\text{K}_8[(\text{UO}_2)(\text{CrO}_4)_4](\text{NO}_3)_2$, $\text{K}_5[(\text{UO}_2)(\text{CrO}_4)_3](\text{NO}_3)(\text{H}_2\text{O})_3$, $\text{K}_4[(\text{UO}_2)_3(\text{CrO}_4)_5](\text{H}_2\text{O})_8$ and $\text{K}_2[(\text{UO}_2)_2(\text{CrO}_4)_3(\text{H}_2\text{O})_2](\text{H}_2\text{O})_4$. *Z. Kristallogr.* 218 (11), 725–732. <http://dx.doi.org/10.1524/zkri.218.11.725.20298>.
- Krivovichev Sergey, V., Gurzhiy Vladislav, V., Tananaev Ivan, G., Myasoedov Boris, F., 2009. Amine-templated uranyl selenates with chiral $[(\text{UO}_2)_2(\text{SeO}_4)_3(\text{H}_2\text{O})]^{2-}$ layers: topology, isomerism, structural relationships. *Z. Kristallogr.* 224, 316–324.
- Krivovichev, S.V., Burns, P.C., 2003a. Combinatorial topology of uranyl molybdate sheets: syntheses and crystal structures of $(\text{C}_6\text{H}_{14}\text{N}_2)_3[(\text{UO}_2)_5(\text{MoO}_4)_8](\text{H}_2\text{O})_4$ and $(\text{C}_2\text{H}_{10}\text{N}_2)[(\text{UO}_2)(\text{MoO}_4)_2]$. *J. Solid State Chem.* 170, 106–117.
- Krivovichev, S.V., Burns, P.C., 2003b. The first sodium uranyl chromate, $\text{Na}_4[(\text{UO}_2)(\text{CrO}_4)_3]$: synthesis and crystal structure determination. *Z. Anorg. Allg. Chem.* 629, 1965–1968.
- Krivovichev, S.V., Gurzhiy, V.V., Tananaev, I.G., Myasoedov, B.F., 2009. Uranyl selenates with organic templates: principles of structure and characteristics of self-organization. *Russ. J. Gen. Chem.* 79, 2723–2730.
- Krivovichev, S.V., Menr e, O., Siidra, O.I., Colmont, M., Filatov, S.K., 2013. Anion-centered tetrahedra in inorganic compounds. *Chem. Rev.* 113, 6459–6535.
- Kubatko, K.-A., Helean, K.B., Navrotsky, A., Burns, P.C., 2005. Thermodynamics of uranyl minerals: enthalpies of formation of rutherfordine, UO_2CO_3 , andersonite, $\text{Na}_2\text{CaUO}_2(\text{CO}_3)_3(\text{H}_2\text{O})_5$, and grimselite, $\text{K}_3\text{NaUO}_2(\text{CO}_3)_3\text{H}_2\text{O}$. *Am. Mineral.* 90, 1284–1290.
- Leciejewicz, J., Alcock, N., Kemp, T., 1995. Carboxylato complexes of the uranyl ion: Effects of ligand size and coordination geometry upon molecular and crystal structure. In: Clarke, M.J., Goodenough, J.B., Ibers, J.A., Jorgensen, C.K., Mingos, D.M.P., Neilands, J.B., Palmer, G.A., Sadler, P.J., Weiss, R., Williams, R.J.P. (Eds.), *Coordination Chemistry*. Springer Berlin, Heidelberg. <http://dx.doi.org/10.1007/BFb0036823>. ISBN: 978-3-540-58761-3. Written with contributions from: Alcock, N.W., Chandrashekar, T.K., Deeth, R.J., Kemp, T.J., Leciejewicz, J., Lutz, H.D., Ravikanth, M.
- Lee, J., Farha, O.K., Roberts, J., Scheidt, K.A., Nguyen, S.T., Hupp, J.T., 2009. Metal-organic framework materials as catalysts. *Chem. Soc. Rev.* 38, 1450–1459.
- Li, Y., Burns, P.C., 2001. The crystal structure of synthetic grimselite, $\text{K}_3\text{Na}[(\text{UO}_2)(\text{CO}_3)_3](\text{H}_2\text{O})$. *Can. Mineral.* 39, 1147–1151.
- Li, J.-R., Kuppler, R.J., Zhou, H.-C., 2009. Selective gas adsorption and separation in metal-organic frameworks. *Chem. Soc. Rev.* 38, 1477–1504.

- Liao, Z.-L., Li, G.-D., Bi, M.-H., Chen, J.-S., 2008. Preparation, structures, and photocatalytic properties of three new uranyl-organic assembly compounds. *Inorg. Chem.* 47, 4844–4853.
- Liao, Z.-L., Li, G.-D., Wei, X., Yu, Y., Chen, J.-S., 2010. Construction of three-dimensional uranyl-organic frameworks with benzenetricarboxylate ligands. *Eur. J. Inorg. Chem.* 2010, 3780–3788.
- Liddle, S.T., 2015. The renaissance of non-aqueous uranium chemistry. *Angew. Chem. Int. Ed. Engl.* 54, 8604–8641.
- Lin, C.-H., Lii, K.-H., 2008. $A_3(U_2O_4)(Ge_2O_7)$ ($A=Rb, Cs$): mixed-valence uranium(V, VI) germanates. *Angew. Chem. Int. Ed. Engl.* 47, 8711–8713.
- Ling, J., Sigmon, G.E., Burns, P.C., 2009. Syntheses, structures, characterizations and charge-density matching of novel amino-templated uranyl selenates. *J. Solid State Chem.* 182, 402–408.
- Ling, J., Morrison, J.M., Ward, M., Poinssatte-Jones, K., Burns, P.C., 2010a. Syntheses, structures, and characterization of open-framework uranyl germanates. *Inorg. Chem.* 49, 7123–7128.
- Ling, J., Sigmon Ginger, E., Ward, M., Roback, N., Carman Burns, P., 2010b. Syntheses, structures, and IR spectroscopic characterization of new uranyl sulfate/selenate 1D-chain, 2D-sheet and 3D-framework. *Z. Kristallogr.* 225 (06), 230–239.
- Liu, S.-P., Chen, M.-L., Chang, B.-C., Lii, K.-H., 2013. Flux synthesis, crystal structure, and photoluminescence of a heterometallic uranyl-europium germanate with $UO-Eu$ linkage: $K_4[(UO_2)Eu_2(Ge_2O_7)_2]$. *Inorg. Chem.* 52, 3990–3994.
- Liu, H.-K., Ramachandran, E., Chen, Y.-H., Chang, W.-J., Lii, K.-H., 2014. High-temperature, high-pressure hydrothermal synthesis, characterization, and structural relationships of layered uranyl arsenates. *Inorg. Chem.* 53, 9065–9072.
- Locock, A.J., 2007. Chapter 6—crystal chemistry of actinide phosphates and arsenates. In: Tananaev, I.G., Krivovichev, S.V., Burns, P.C. (Eds.), *Structural Chemistry of Inorganic Actinide Compounds*. Amsterdam, Elsevier.
- Locock Andrew, J., Burns Peter, C., 2003. The crystal structure of synthetic autunite, $Ca[(UO_2)(PO_4)]_2(H_2O)_{11}$. *Am. Mineral.* 88, 240–244.
- Locock, A.J., Burns, P.C., 2002. The crystal structure of triuranyl diphosphate tetrahydrate. *J. Solid State Chem.* 163, 275–280.
- Locock, A.J., Burns, P.C., Duke, M.J.M., Flynn, T.M., 2004. Monovalent cations in structures of the meta-autunite group. *Can. Mineral.* 42, 973–996.
- Loiseau, T., Mihalcea, I., Henry, N., Volkringer, C., 2014. The crystal chemistry of uranium carboxylates. *Coord. Chem. Rev.*, 266–267, 69–109.
- Lommerse, J.P.M., Stone, A.J., Taylor, R., Allen, F.H., 1996. The nature and geometry of intermolecular interactions between halogens and oxygen or nitrogen. *J. Am. Chem. Soc.* 118, 3108–3116.
- Long, S., Zhou, P., Parkin, S., Li, T., 2013. From competition to commensuration by two major hydrogen-bonding motifs. *Cryst. Growth Des.* 14, 27–31.
- Mao, J.-G., 2007. Structures and luminescent properties of lanthanide phosphonates. *Coord. Chem. Rev.* 251, 1493–1520.
- Marangoni, G., Degetto, S., Graziani, R., Bombieri, G., Forsellini, E., 1974. Preparation, characterization, thermal analysis and crystal structure of bis(tetraphenylarsonium)uranyl bis(pyridine-2,6-dicarboxylate) hexahydrate. *J. Inorg. Nucl. Chem.* 36, 1787–1794.
- Masci, B., Thuéry, P., 2005. Uranyl complexes with the pyridine-2,6-dicarboxylate ligand: new dinuclear species with $\mu-\eta_2$, η_2 -peroxide, μ_2 -hydroxide or μ_2 -methoxide bridges. *Polyhedron* 24, 229–237.

- Mayer, H., Mereiter, K., 1986. Synthetic bayleyite, $\text{Mg}_2[\text{UO}_2(\text{CO}_3)_3] \cdot 18\text{H}_2\text{O}$: thermochemistry, crystallography and crystal structure. *TMPM Tschermarks Min. Petr. Mitt.* 35, 133–146.
- McNamara, B., Buck, E., Hanson, B., 2002. Observation of studtite and metastudtite on spent fuel. *MRS Online Proceedings Library* 757.
- Meek, S.T., Greathouse, J.A., Allendorf, M.D., 2011. Metal-organic frameworks: a rapidly growing class of versatile nanoporous materials. *Adv. Mater.* 23, 249–267.
- Mesa, J.L., Pizarro, J.L., Arriortua, M.I., 1998. Crystal structure and spectroscopic properties of the monoquoobis (N-thiocyanate) (2,2'-dipyridylamine)copper(II) complex. *Cryst. Res. Technol.* 33, 489–495.
- Metrangolo, P., Resnati, G., 2013. Metal-bound halogen atoms in crystal engineering. *Chem. Commun.* 49, 1783–1785.
- Metrangolo, P., Neukirch, H., Pilati, T., Resnati, G., 2005. Halogen bonding based recognition processes: a world parallel to hydrogen bonding. *Acc. Chem. Res.* 38, 386–395.
- Metrangolo, P., Pilati, T., Resnati, G., 2006. Halogen bonding and other noncovalent interactions involving halogens: a terminology issue. *CrystEngComm* 8, 946–947.
- Metrangolo, P., Meyer, F., Pilati, T., Resnati, G., Terraneo, G., 2008a. Halogen bonding in supramolecular chemistry. *Angew. Chem. Int. Ed. Engl.* 47, 6114–6127.
- Metrangolo, P., Resnati, G., Pilati, T., Biella, S., 2008b. Halogen bonding in crystal engineering. In: Metrangolo, P., Resnati, G. (Eds.), *Halogen Bonding*. Springer Berlin, Heidelberg.
- Mihalcea, I., Henry, N., Clavier, N., Dacheux, N., Loiseau, T., 2011a. Occurrence of an octanuclear motif of uranyl isophthalate with cation–cation interactions through edge-sharing connection mode. *Inorg. Chem.* 50, 6243–6249.
- Mihalcea, I., Henry, N., Loiseau, T., 2011b. Revisiting the uranyl-phthalate system: isolation and crystal structures of two types of uranyl–organic frameworks (UOF). *Cryst. Growth Des.* 11, 1940–1947.
- Mihalcea, I., Henry, N., Volklinger, C., Loiseau, T., 2011c. Uranyl–pyromellitate coordination polymers: toward three-dimensional open frameworks with large channel systems. *Cryst. Growth Des.* 12, 526–535.
- Mihalcea, I., Henry, N., Bousquet, T., Volklinger, C., Loiseau, T., 2012a. Six-fold coordinated uranyl cations in extended coordination polymers. *Cryst. Growth Des.* 12, 4641–4648.
- Mihalcea, I., Volklinger, C., Henry, N., Loiseau, T., 2012b. Series of mixed uranyl–lanthanide (Ce, Nd) organic coordination polymers with aromatic polycarboxylates linkers. *Inorg. Chem.* 51, 9610–9618.
- Mihalcea, I., Henry, N., Loiseau, T., 2014. Crystal chemistry of uranyl carboxylate coordination networks obtained in the presence of organic amine molecules. *Eur. J. Inorg. Chem.* 2014, 1322–1332.
- Minkin, V.I., 1999. Glossary of terms used in theoretical organic chemistry. *Pure Appl. Chem.* 71, 1919–1981.
- Mirzaei, M., Eshtiagh-Hosseini, H., Lippolis, V., Aghabozorg, H., Kordestani, D., Shokrollahi, A., Aghaei, R., Blake, A.J., 2011. Structural variation within uranium VI heterocyclic carboxylates: solid and solution states studies. *Inorg. Chim. Acta* 370, 141–149.
- Mishkevich, V.I., Grigoriev, M.S., Fedosseev, A.M., Moisy, P., 2012. Guanidinium dioxidobis(picolinato- $\kappa_2\text{N},\text{O}$)(picolinato- κO)uranate(VI). *Acta Crystallogr. C* 68, m1243.
- Mougel, V., Chatelain, L., Hermle, J., Caciuffo, R., Colineau, E., Tuna, F., Magnani, N., de Geyer, A., Pécaut, J., Mazzanti, M., 2014. A uranium-based $\text{UO}_2^+-\text{Mn}^{2+}$ single-chain magnet assembled through cation–cation interactions. *Angew. Chem. Int. Ed. Engl.* 53, 819–823.
- Muller, P., 1994. Glossary of terms used in physical organic chemistry (IUPAC Recommendations 1994). *Pure Appl. Chem.* 31 (8), 1260–1278.

- Murray-Rust, P., Motherwell, W.D.S., 1979. Computer retrieval and analysis of molecular geometry. 4. Intermolecular interactions. *J. Am. Chem. Soc.* 101, 4374–4376.
- Murray-Rust, P., Stallings, W.C., Monti, C.T., Preston, R.K., Glusker, J.P., 1983. Intermolecular interactions of the carbon-fluorine bond: the crystallographic environment of fluorinated carboxylic acids and related structures. *J. Am. Chem. Soc.* 105, 3206–3214.
- Nash, K.L., 1994. Actinide phosphonate complexes in aqueous solutions. *J. Alloys Compd.* 213–214, 300–304.
- Nash, K.L., 1997. F-Element complexation by diphosphonate ligands. *J. Alloys Compd.* 249, 33–40.
- Nash, K.L., Choppin, G.R., 1997. Separations chemistry for actinide elements: recent developments and historical perspective. *Sep. Sci. Technol.* 32, 255–274.
- Natrajan, L.S., 2012. Developments in the photophysics and photochemistry of actinide ions and their coordination compounds. *Coord. Chem. Rev.* 256, 1583–1603.
- Nazarchuk, E.V., Siidra, O.I., Krivovichev Sergey, V., 2011. Crystal chemistry of uranyl halides containing mixed $(\text{UO}_2)(\text{XmOn})_5$ bipyramids (X = Cl, Br): synthesis and crystal structure of $\text{Cs}_2(\text{UO}_2)(\text{NO}_3)\text{Cl}_3$. *Z. Kristallogr.* 66, 142–146.
- Nelson, A.-G.D., Bray, T.H., Zhan, W., Haire, R.G., Saylor, T.S., Albrecht-Schmitt, T.E., 2008. Further examples of the failure of surrogates to properly model the structural and hydrothermal chemistry of transuranium elements: insights provided by uranium and neptunium diphosphonates. *Inorg. Chem.* 47, 4945–4951.
- Nelson, A.-G.D., Alekseev, E.V., Ewing, R.C., Albrecht-Schmitt, T.E., 2012. Barium uranyl diphosphonates. *J. Solid State Chem.* 192, 153–160.
- Nelson, A.-G.D., Alekseev, E.V., Albrecht-Schmitt, T.E., Ewing, R.C., 2013. Uranium diphosphonates templated by interlayer organic amines. *J. Solid State Chem.* 198, 270–278.
- Nieweg, J.A., Lemma, K., Trewyn, B.G., Lin, V.S.Y., Bakac, A., 2005. Mesoporous silica-supported uranyl: synthesis and photoreactivity. *Inorg. Chem.* 44, 5641–5648.
- Norquist, A.J., Doran, M.B., Thomas, P.M., O'Hare, D., 2003. Controlled structural variations in templated uranium sulfates. *Inorg. Chem.* 42, 5949–5953.
- Norquist, A.J., Doran, M.B., O'Hare, D., 2005. The role of amine sulfates in hydrothermal uranium chemistry. *Inorg. Chem.* 44, 3837–3843.
- Novitchi, G., Costes, J.-P., Donnadieu, B., 2004. Synthesis and structure of 1-D heterometallic thiocyanato-bridged CuIIGdIII polymers with ferromagnetic properties. *Eur. J. Inorg. Chem.* 2004, 1808–1812.
- Nyman, M., Burns, P.C., 2012. A comprehensive comparison of transition-metal and actinyl polyoxometalates. *Chem. Soc. Rev.* 41, 7354–7367.
- Ok, K.M., Doran, M.B., O'Hare, D., 2006. $[\text{N}(\text{CH}_3)_4][(\text{UO}_2)_2\text{F}_5]$: a new organically templated open-framework uranium oxide fluoride (MUF-2). *J. Mater. Chem.* 16, 3366–3368.
- Olchowka, J., Falaise, C., Volkringer, C., Henry, N., Loiseau, T., 2013a. Structural observations of heterometallic uranyl copper(II) carboxylates and their solid-state topotactic transformation upon dehydration. *Chem. Eur. J.* 19, 2012–2022.
- Olchowka, J., Volkringer, C., Henry, N., Loiseau, T., 2013b. Synthesis, structural characterization, and dehydration analysis of uranyl zinc mellitate, $(\text{UO}_2)\text{Zn}(\text{H}_2\text{O})_4(\text{H}_2\text{mel})\cdot 2\text{H}_2\text{O}$. *Eur. J. Inorg. Chem.* 2013, 2109–2114.
- Paolucci, G., Marangoni, G., Bandoli, G., Clemente, D.A., 1980. Reactivity of uranyl ion with quinque-dentate chelating hydrazine derivatives. Part 2. 2,6-Diacetylpyridine bis(4-methoxybenzoyl-hydrazone). *J. Chem. Soc. Dalton*, (8), 1304–1311. <http://dx.doi.org/10.1039/DT9800001304>.
- Park, J.H., Lee, W.R., Kim, Y., Lee, H.J., Ryu, D.W., Phang, W.J., Hong, C.S., 2014. Interpenetration control, sorption behavior, and framework flexibility in $\text{Zn}(\text{II})$ metal–organic frameworks. *Cryst. Growth Des.* 14, 699–704.

- Parker, T.G., Cross, J.N., Polinski, M.J., Lin, J., Albrecht-Schmitt, T.E., 2013. Ionothermal and hydrothermal flux syntheses of five new uranyl phosphonates. *Cryst. Growth Des.* 14, 228–235.
- Piskula, Z., Manszewski, T., Kubicki, M., Lis, S., 2012. The structure and spectroscopic characterization of complexes with tetraethyl methylenediphosphonate in solution and in solid state. *J. Mol. Struct.* 1011, 145–148.
- Plášil, J., Mills, S.J., Fejfarová, K., Dušek, M., Novák, M., Škoda, R., Čejka, J., Sejkora, J., 2011. The crystal structure of natural zippeite, $K_{1.85}H^{+0.15}[(UO_2)_4O_2(SO_4)_2(OH)_2](H_2O)_4$, from Jáchymov, Czech Republic. *Can. Mineral.* 49, 1089–1103.
- Politzer, P., Lane, P., Concha, M., Ma, Y., Murray, J., 2007. An overview of halogen bonding. *J. Mol. Model.* 13, 305–311.
- Politzer, P., Murray, J.S., Clark, T., 2010. Halogen bonding: an electrostatically-driven highly directional noncovalent interaction. *Phys. Chem. Chem. Phys.* 12, 7748–7757.
- Politzer, P., Murray, J.S., Clark, T., 2013. Halogen bonding and other σ -hole interactions: a perspective. *Phys. Chem. Chem. Phys.* 15, 11178–11189.
- Poojary, D.M., Grohol, D., Clearfield, A., 1995a. Crystal structure of uranyl chloromethylphosphonate from X-ray powder diffraction data. *J. Phys. Chem. Solids* 56, 1383–1388.
- Poojary, D.M., Grohol, D., Clearfield, A., 1995b. Synthesis and X-ray powder structure of a novel porous uranyl phenylphosphonate containing unidimensional channels flanked by hydrophobic regions. *Angew. Chem. Int. Ed. Engl.* 34, 1508–1510.
- Poojary, D.M., Cabeza, A., Aranda, M.A.G., Bruque, S., Clearfield, A., 1996. Structure determination of a complex tubular uranyl phenylphosphonate, $(UO_2)_3(HO_3PC_6H_5)_2(O_3PC_6H_5)_2 \cdot H_2O$, from conventional X-ray powder diffraction data. *Inorg. Chem.* 35, 1468–1473.
- Qiu, J., Burns, P.C., 2012. Clusters of actinides with oxide, peroxide, or hydroxide bridges. *Chem. Rev.* 113, 1097–1120.
- Ramasubbu, N., Parthasarathy, R., Murray-Rust, P., 1986. Angular preferences of intermolecular forces around halogen centers: preferred directions of approach of electrophiles and nucleophiles around carbon-halogen bond. *J. Am. Chem. Soc.* 108, 4308–4314.
- Rankine, D., Avellaneda, A., Hill, M.R., Doonan, C.J., Sumbly, C.J., 2012. Control of framework interpenetration for in situ modified hydroxyl functionalised IRMOFs. *Chem. Commun.* 48, 10328–10330.
- Rivenet, M., Vigier, N., Roussel, P., Abraham, F., 2007. Hydrothermal synthesis, structure and thermal stability of diamine templated layered uranyl-vanadates. *J. Solid State Chem.* 180, 713–724.
- Rodriguez-Dieguez, A., Mota, A.J., Seco, J.M., Palacios, M.A., Romerosa, A., Colacio, E., 2009. Influence of metal ions, coligands and reaction conditions on the structural versatility and properties of 5-pyrimidyl-tetrazolate containing complexes. *Dalton Trans.* (48), 9578–9586.
- Rojas, R.M., Del Pra, A., Bombieri, G., Benetollo, F., 1979. Structural studies on actinides carboxylates—V[1]: crystal and molecular structure of ammonium uranyldimalonate monohydrate $(NH_4)_2[UO_2(C_3H_2O_4)_2] \cdot H_2O$. *J. Inorg. Nucl. Chem.* 41, 541–545.
- Rowland, C.E., Cahill, C.L., 2010a. Capturing hydrolysis products in the solid state: effects of pH on uranyl squarates under ambient conditions. *Inorg. Chem.* 49, 8668–8673.
- Rowland, C.E., Cahill, C.L., 2010b. Hydrothermal synthesis of uranyl squarates and squarate-oxalates: hydrolysis trends and in situ oxalate formation. *Inorg. Chem.* 49, 6716–6724.
- Rowland, C.E., Kanatzidis, M.G., Soderholm, L., 2012. Tetraalkylammonium uranyl isothiocyana-tes. *Inorg. Chem.* 51, 11798–11804.
- Sarkhel, S., Desiraju, G.R., 2004. N-H \cdots O, O-H \cdots O, and C-H \cdots O hydrogen bonds in protein–ligand complexes: strong and weak interactions in molecular recognition. *Proteins* 54, 247–259.

- Sarsfield, M.J., Helliwell, M., 2004. Extending the chemistry of the uranyl ion: Lewis acid coordination to a UO oxygen. *J. Am. Chem. Soc.* 126, 1036–1037.
- Schettini, M.F., Wu, G., Hayton, T.W., 2009. Coordination of N-donor ligands to a uranyl(V) β -diketiminato complex. *Inorg. Chem.* 48, 11799–11808.
- Schettini, M.F., Wu, G., Hayton, T.W., 2012. Synthesis and reactivity of a uranyl-imidazolyl complex. *Chem. Commun.* 48, 1484–1486.
- Serezhkina, L.B., Peresyphkina, E.V., Neklyudova, N.A., Virovets, A.V., 2010. Synthesis and an X-ray diffraction study of $\text{Rb}_2[(\text{UO}_2)_2(\text{C}_2\text{O}_4)_3]$. *Crystallogr. Rep.* 55, 769–772.
- Severance, R.C., Smith, M.D., zur Loye, H.-C., 2011a. Three-dimensional hybrid framework containing U_2O_{13} dimers connected via cation–cation interactions. *Inorg. Chem.* 50, 7931–7933.
- Severance, R.C., Vaughn, S.A., Smith, M.D., zur Loye, H.-C., 2011b. Structures and luminescent properties of new uranyl-based hybrid materials. *Solid State Sci.* 13, 1344–1353.
- Severance, R., Cortese, A., Smith, M., zur Loye, H.-C., 2013. Hydrothermal synthesis, structure, and luminescence of a U(VI) complex. *J. Chem. Crystallogr.* 43, 171–177.
- Shekhah, O., Liu, J., Fischer, R.A., Woll, C., 2011. MOF thin films: existing and future applications. *Chem. Soc. Rev.* 40, 1081–1106.
- Shimizu, G.K.H., Vaidhyanathan, R., Taylor, J.M., 2009. Phosphonate and sulfonate metal organic frameworks. *Chem. Soc. Rev.* 38, 1430–1449.
- Shu, Y.-B., Xu, C., Liu, W.-S., 2013. A uranyl hybrid compound designed from urea-bearing dipropionic acid. *Eur. J. Inorg. Chem.* 2013, 3592–3595.
- Siidra, O.I., Nazarchuk, E.V., Krivovichev, S.V., 2012. Isopropylammonium layered uranyl chromates: syntheses and crystal structures of $[(\text{CH}_3)_2\text{CHNH}_3]_3[(\text{UO}_2)_3(\text{CrO}_4)_2\text{O}(\text{OH})_3]$ and $[(\text{CH}_3)_2\text{CHNH}_3]_2[(\text{UO}_2)_2(\text{CrO}_4)_3(\text{H}_2\text{O})]$. *Z. Anorg. Allg. Chem.* 638, 976–981.
- Silverwood, P.R., Collison, D., Livens, F.R., Beddoes, R.L., Taylor, R.J., 1998. Uranyl monopicolinate complexes. *J. Alloys Compd.* 271–273, 180–183.
- Simard, M., Su, D., Wuest, J.D., 1991. Use of hydrogen bonds to control molecular aggregation. Self-assembly of three-dimensional networks with large chambers. *J. Am. Chem. Soc.* 113, 4696–4698.
- Smart, P., Bejarano-Villafuerte, A., Hendry, R.M., Brammer, L., 2013. Persistent C-I \cdots π halogen-bonded layer motifs involving 4-iodobenzoate paddlewheel units, $\text{Cu}_2(4\text{-Ibz})_4(\text{L})_2$. *CrystEngComm* 15, 3160–3167.
- Song, F., Zhang, T., Wang, C., Lin, W., 2012. Chiral porous metal-organic frameworks with dual active sites for sequential asymmetric catalysis. *Proc. R. Soc. Math. Phys. Eng. Sci.* 468 (2143), 2035–2052. <http://dx.doi.org/10.1098/rspa.2012.0100>.
- Spencer, E.C., Ross, N.L., Surbella III, R.G., Cahill, C.L., 2014. The influence of pressure on the structure of a 2D uranium(VI) carboxyphosphonate compound. *J. Solid State Chem.* 218, 1–5.
- Suh, M.P., Park, H.J., Prasad, T.K., Lim, D.-W., 2011. Hydrogen storage in metal–organic frameworks. *Chem. Rev.* 112, 782–835.
- Sumida, K., Rogow, D.L., Mason, J.A., McDonald, T.M., Bloch, E.D., Herm, Z.R., Bae, T.-H., Long, J.R., 2011. Carbon dioxide capture in metal–organic frameworks. *Chem. Rev.* 112, 724–781.
- Sun, D., Zhang, N., Xu, Q.-J., Huang, R.-B., Zheng, L.-S., 2010. A new clover-shaped trinuclear uranium(VI) complex: synthesis, structure and photoluminescence property. *Inorg. Chem. Commun.* 13, 859–862.
- Surbella III, R.G., Cahill, C.L., 2014. The exploration of supramolecular interactions stemming from the $[\text{UO}_2(\text{NCS})_4(\text{H}_2\text{O})]^{2-}$ tecton and substituted pyridinium cations. *CrystEngComm* 16, 2352–2364.

- Sureda, R., Casas, I., Giménez, J., de Pablo, J., Quiñones, J., Zhang, J., Ewing, R.C., 2011. Effects of ionizing radiation and temperature on uranyl silicates: soddyite $(\text{UO}_2)_2(\text{SiO}_4)(\text{H}_2\text{O})_2$ and uranophane $\text{Ca}(\text{UO}_2)_2(\text{SiO}_3\text{OH})_2 \cdot 5\text{H}_2\text{O}$. *Environ. Sci. Technol.* 45, 2510–2515.
- Surls Jr., J.P., Choppin, G.R., 1957. Ion-exchange study of thiocyanate complexes of the actinides and lanthanides. *J. Inorg. Nucl. Chem.* 4, 62–73.
- Takao, K., Ikeda, Y., 2007. Structural characterization and reactivity of $\text{UO}_2(\text{salophen})\text{L}$ and $[\text{UO}_2(\text{salophen})]_2$: dimerization of $\text{UO}_2(\text{salophen})$ fragments in noncoordinating solvents (salophen = N,N'-disalicylidene-o-phenylenediaminate, L = N,N-dimethylformamide, dimethyl sulfoxide). *Inorg. Chem.* 46, 1550–1562.
- Tanabe, K.K., Cohen, S.M., 2011. Postsynthetic modification of metal-organic frameworks—a progress report. *Chem. Soc. Rev.* 40, 498–519.
- Tanaka, D., Kitagawa, S., 2007. Template effects in porous coordination polymers. *Chem. Mater.* 20, 922–931.
- Thalladi, V.R., Nüsse, M., Boese, R., 2000. The melting point alternation in α,ω -alkanedicarboxylic acids. *J. Am. Chem. Soc.* 122, 9227–9236.
- Thangavelu, S.G., Cahill, C.L., 2015. Uranyl-promoted peroxide generation: synthesis and characterization of three uranyl peroxo $[(\text{UO}_2)_2(\text{O}_2)]$ complexes. *Inorg. Chem.* 54, 4208–4221.
- Thangavelu, S.G., Andrews, M.B., Pope, S.J.A., Cahill, C.L., 2013. Synthesis, structures, and luminescent properties of uranyl terpyridine aromatic carboxylate coordination polymers. *Inorg. Chem.* 52, 2060–2069.
- Thuéry, P., 2007a. Uranyl citrate dimers as guests in a copper-bipyridine framework: a novel heterometallic inorganic–organic hybrid compound. *CrystEngComm* 9, 358–360.
- Thuéry, P., 2007b. Uranyl ion complexation by citric and citramalic acids in the presence of diamines. *Inorg. Chem.* 46, 2307–2315.
- Thuéry, P., 2008a. Novel two-dimensional uranyl-organic assemblages in the citrate and d(–)-citramalate families. *CrystEngComm* 10, 79–85.
- Thuéry, P., 2008b. Uranyl ion complexes with cucurbit[n]urils (n = 6, 7, and 8): a new family of uranyl-organic frameworks. *Cryst. Growth Des.* 8, 4132–4143.
- Thuéry, P., 2009a. Structural variability in uranyl-lanthanide heterometallic complexes with DOTA and oxalato ligands. *CrystEngComm* 11, 2319–2325.
- Thuéry, P., 2009b. Two novel uranyl-organic frameworks with cyclohexane-1,3-dicarboxylate ligands. *CrystEngComm* 11, 232–234.
- Thuéry, P., 2009c. Two uranyl-organic frameworks with pyridinecarboxylate ligands. A novel heterometallic uranyl-copper(II) complex with a cation–cation interaction. *Inorg. Chem. Commun.* 12, 800–803.
- Thuéry, P., 2009d. Uranyl-lanthanide heterometallic complexes with cucurbit[6]uril and perchlorate ligands. *Inorg. Chem.* 48, 825–827.
- Thuéry, P., 2009e. Uranyl-organic bilayer assemblies with flexible aromatic di-, tri- and tetracarboxylic acids. *CrystEngComm* 11, 1081–1088.
- Thuéry, P., 2010. A lanthanide ion-decorated uranyl-organic two-dimensional assembly with all-cis 1,2,3,4,5,6-cyclohexanhexacarboxylic acid. *Cryst. Growth Des.* 10, 2061–2063.
- Thuéry, P., 2011a. Uranyl-alkali metal ion heterometallic complexes with cucurbit[6]uril and a sulfonated catechol. *Cryst. Growth Des.* 11, 3282–3294.
- Thuéry, P., 2011b. Uranyl ion complexation by aliphatic dicarboxylic acids in the presence of cucurbiturils as additional ligands or structure-directing agents. *Cryst. Growth Des.* 11, 2606–2620.
- Thuéry, P., 2011c. Coordination polymers and frameworks in uranyl ion complexes with sulfonates and cucurbit[6]uril. *Cryst Growth Des.* 11, 5702–5711.

- Thuéry, P., 2012a. Sulfonate complexes of actinide ions: structural diversity in uranyl complexes with 2-sulfobenzoate. *Inorg. Chem.* 52, 435–447.
- Thuéry, P., 2012b. Uranyl-lanthanide heterometallic assemblies with 1,2-ethanedisulfonate and cucurbit[6]uril ligands. *CrystEngComm* 14, 3363–3366.
- Thuéry, P., 2012c. Uranyl and mixed uranyl-lanthanide complexes with p-sulfonatocalix[4]arene. *CrystEngComm* 14, 6369–6373.
- Thuéry, P., 2013a. 2,2'-Bipyridine and 1,10-phenanthroline as coligands or structure-directing agents in uranyl-organic assemblies with polycarboxylic acids. *Eur. J. Inorg. Chem.* 2013, 4563–4573.
- Thuéry, P., 2013b. One- to three-dimensional uranyl-organic assemblies with 3-sulfophthalic and 5-sulfoisophthalic acids. *CrystEngComm* 15, 2401–2410.
- Thuéry, P., 2013c. Uranyl-3d block metal ion heterometallic carboxylate complexes including additional chelating nitrogen donors. *CrystEngComm* 15, 6533–6545.
- Thuéry, P., 2014. Molecular and polymeric uranyl and thorium complexes with sulfonate-containing ligands. *Eur. J. Inorg. Chem.* 2014, 58–68.
- Thuéry, P., Harrowfield, J., 2014. Uranyl ion complexes with trans-3-(3-pyridyl)acrylic acid including a uranyl-copper(II) heterometallic framework. *Eur. J. Inorg. Chem.* 2014, 4772–4778.
- Thuéry, P., Masci, B., 2009. Uranyl ion complexation by cucurbiturils in the presence of perhenic, phosphoric, or polycarboxylic acids. Novel mixed-ligand uranyl-organic frameworks. *Cryst. Growth Des.* 10, 716–725.
- Thuéry, P., Riviere, E., 2013. Uranyl-copper(II) heterometallic oxalate complexes: coordination polymers and frameworks. *Dalton Trans.* 42, 10551–10558.
- Tian, T., Yang, W., Pan, Q.-J., Sun, Z.-M., 2012. The first uranyl arsonates featuring heterometallic cation-cation interactions with U(VI)O—Zn(II) bonding. *Inorg. Chem.* 51, 11150–11154.
- Tian, T., Yang, W., Wang, H., Dang, S., Pan, Q.-J., Sun, Z.-M., 2013a. Syntheses and structures of uranyl ethylenediphosphonates: from layers to elliptical nanochannels. *Inorg. Chem.* 52, 7100–7106.
- Tian, T., Yang, W., Wang, H., Dang, S., Sun, Z.-M., 2013b. Flexible diphosphonic acids for the isolation of uranyl hybrids with heterometallic U(VI)O—Zn(II) cation-cation interactions. *Inorg. Chem.* 52, 8288–8290.
- Tian, W.-G., Yang, X.-Y., Li, Y.-H., Liu, X.-X., Yang, W., Tian, T., 2014. A new organically templated open-framework uranyl ethylenediphosphonate. *Inorg. Chem. Commun.* 46, 110–112.
- Troff, R.W., Mäkelä, T., Topić, F., Valkonen, A., Raatikainen, K., Rissanen, K., 2013. Alternative motifs for halogen bonding. *Eur. J. Org. Chem.* 2013, 1617–1637.
- Videnova-Adrabska, V., 2007. Coordination and supramolecular network entanglements of organodisulfonates. *Coord. Chem. Rev.* 251, 1987–2016.
- Villiers, C., Thuéry, P., Ephritikhine, M., 2008. The first cis-dioxido uranyl compound under scrutiny. *Angew. Chem. Int. Ed. Engl.* 47, 5892–5893.
- Volklinger, C., Henry, N., Grandjean, S., Loiseau, T., 2011. Uranyl and/or rare-earth mellitates in extended organic-inorganic networks: a unique case of heterometallic cation-cation interaction with U(VI)O—Ln(III) bonding (Ln=Ce, Nd). *J. Am. Chem. Soc.* 134, 1275–1283.
- Vrabel, V., Garaj, J., Sivy, J., Oktavec, D., 1999. Aquadiisothiocyanato(N,N,N',N'-tetramethylethylenediamine-N,N')copper(II). *Acta Crystallogr. C* 55, 551–553.
- Wang, K.-X., Chen, J.-S., 2011. Extended structures and physicochemical properties of uranyl-organic compounds. *Acc. Chem. Res.* 44, 531–540.
- Wang, Z., Cohen, S.M., 2009. Postsynthetic modification of metal-organic frameworks. *Chem. Soc. Rev.* 38, 1315–1329.

- Wang, W.-D., Bakac, A., Espenson, J.H., 1995. Uranium(VI)-catalyzed photooxidation of hydrocarbons with molecular oxygen. *Inorg. Chem.* 34, 6034–6039.
- Wang, S., Alekseev, E.V., Depmeier, W., Albrecht-Schmitt, T.E., 2011. Recent progress in actinide borate chemistry. *Chem. Commun.* 47, 10874–10885.
- Wang, J.-L., Wang, C., Lin, W., 2012. Metal–organic frameworks for light harvesting and photocatalysis. *ACS Catal.* 2, 2630–2640.
- Wang, C., Liu, D., Lin, W., 2013. Metal–organic frameworks as a tunable platform for designing functional molecular materials. *J. Am. Chem. Soc.* 135, 13222–13234.
- Weber, G., 1982. Versatility of the cyclic ligand 5,8,11-trioxa-2,14-dithia[15] (2,6)-pyridinophane: with copper(II) chloride. *Inorg. Chim. Acta* 58, 27–33.
- Wei, Y.Y., Tinant, B., Declercq, J.-P., Van Meerssche, M., Dale, J., 1987. Oligoether complexes of alkaline-earth metal ions. I. Structures of 2,5,8,11,14-pentaoxapentadecane ('tetraglyme') complexed with calcium, strontium and barium thiocyanates. *Acta Crystallogr. C* 43, 1076–1080.
- Wei, Y.Y., Tinant, B., Declercq, J.-P., Van Meerssche, M., Dale, J., 1988. Crown ether complexes of alkaline-earth metal ions. III. Structures of 1,4,7,10,13,16-hexaoxacyclooctadecane (18-crown-6) complexed with magnesium and barium thiocyanates. *Acta Crystallogr. C* 44, 77–80.
- Weng, Z., Zhang, Z.-h., Olds, T., Sterniczuk, M., Burns, P.C., 2014. Copper(I) and copper(II) uranyl heterometallic hybrid materials. *Inorg. Chem.* 53, 7993–7998.
- Wilkerson, M.P., Burns, C.J., Dewey, H.J., Martin, J.M., Morris, D.E., Paine, R.T., Scott, B.L., 2000. Basicity of uranyl oxo ligands upon coordination of alkoxides. *Inorg. Chem.* 39, 5277–5285.
- Willett, R.D., Awwadi, F., Butcher, R., Haddad, S., Twamley, B., 2003. The aryl bromine–halide ion synthon and its role in the control of the crystal structures of tetrahalocuprate(II) ions. *Cryst. Growth Des.* 3, 301–311.
- Wu, H.-Y., Wang, R.-X., Yang, W., Chen, J., Sun, Z.-M., Li, J., Zhang, H., 2012. 3-Fold-interpenetrated uranium–organic frameworks: new strategy for rationally constructing three-dimensional uranyl organic materials. *Inorg. Chem.* 51, 3103–3107.
- Wu, H.-Y., Ma, Y.-Q., Zhang, X., Zhang, H., Yang, X.-Y., Li, Y.-H., Wang, H., Yao, S., Yang, W., 2013. Syntheses, structures and luminescent properties of two organic templated uranyl phosphonates. *Inorg. Chem. Commun.* 34, 55–57.
- Wylie, E.M., Burns, P.C., 2012. Crystal structures of six new uranyl selenate and selenite compounds and their relationship with uranyl mineral structures. *Can. Mineral.* 50, 147–157.
- Xiao, C.-L., Wang, C.-Z., Yuan, L.-Y., Li, B., He, H., Wang, S., Zhao, Y.-L., Chai, Z.-F., Shi, W.-Q., 2014. Excellent selectivity for actinides with a tetradentate 2,9-diamide-1,10-phenanthroline ligand in highly acidic solution: a hard–soft donor combined strategy. *Inorg. Chem.* 53, 1712–1720.
- Xu, C., Tian, G., Teat, S.J., Rao, L., 2013. Complexation of U(VI) with dipicolinic acid: thermodynamics and coordination modes. *Inorg. Chem.* 52, 2750–2756.
- Yaghi, O.M., 2007. Metal-organic frameworks: a tale of two entanglements. *Nat. Mater.* 6, 92–93.
- Yang, W., Wu, H.-Y., Wang, R.-X., Pan, Q.-J., Sun, Z.-M., Zhang, H., 2012. From 1D chain to 3D framework uranyl diphosphonates: syntheses, crystal structures, and selective ion exchange. *Inorg. Chem.* 51, 11458–11465.
- Yang, W., Dang, S., Wang, H., Tian, T., Pan, Q.-J., Sun, Z.-M., 2013a. Synthesis, structures, and properties of uranyl hybrids constructed by a variety of mono- and polycarboxylic acids. *Inorg. Chem.* 52, 12394–12402.

- Yang, W., Tian, T., Wu, H.-Y., Pan, Q.-J., Dang, S., Sun, Z.-M., 2013b. Syntheses and structures of a series of uranyl phosphonates and sulfonates: an insight into their correlations and discrepancies. *Inorg. Chem.* 52, 2736–2743.
- Yang, W., Yi, F.-Y., Tian, T., Tian, W.-G., Sun, Z.-M., 2014. Structural variation within heterometallic uranyl hybrids based on flexible alkylidiphosphonate ligands. *Cryst. Growth Des.* 14, 1366–1374.
- Yin, P., Zheng, L.-M., Gao, S., Xin, X.-Q., 2001. $\text{Cu}_4\{\text{CH}_3\text{C}(\text{OH})(\text{PO}_3)_2\}_2(\text{C}_4\text{H}_4\text{N}_2)(\text{H}_2\text{O})_4$: a novel, three-dimensional copper diphosphonate with metamagnetism. *Chem. Commun.* (22), 2346–2347.
- Yoon, M., Srirambalaji, R., Kim, K., 2011. Homochiral metal–organic frameworks for asymmetric heterogeneous catalysis. *Chem. Rev.* 112, 1196–1231.
- Yu, Z.-T., Li, G.-H., Jiang, Y.-S., Xu, J.-J., Chen, J.-S., 2003. A uranium–zinc–organic molecular compound containing planar tetranuclear uranyl units. *Dalton Trans.* (22), 4219–4220.
- Yu, Z.-T., Liao, Z.-L., Jiang, Y.-S., Li, G.-H., Li, G.-D., Chen, J.-S., 2004. Construction of a microporous inorganic–organic hybrid compound with uranyl units. *Chem. Commun.* (16), 1814–1815.
- Zhang, J., Wojtas, L., Larsen, R.W., Eddaoudi, M., Zaworotko, M.J., 2009. Temperature and concentration control over interpenetration in a metal–organic material. *J. Am. Chem. Soc.* 131, 17040–17041.
- Zhao, D., Timmons, D.J., Yuan, D., Zhou, H.-C., 2010. Tuning the topology and functionality of metal–organic frameworks by ligand design. *Acc. Chem. Res.* 44, 123–133.
- Zheng, Y.-Z., Tong, M.-L., Chen, X.-M., 2005. Synthesis, structure and photoluminescent studies of two novel layered uranium coordination polymers constructed from $\text{UO}(\text{OH})$ polyhedra and pyridinedicarboxylates. *Eur. J. Inorg. Chem.* 2005, 4109–4117.
- Zordan, F., Brammer, L., 2006. $\text{M}-\text{X}\cdots\text{X}'-\text{C}$ halogen-bonded network formation in $\text{MX}_2(4\text{-halopyridine})_2$ complexes ($\text{M}=\text{Pd}, \text{Pt}$; $\text{X}=\text{Cl}, \text{I}$; $\text{X}'=\text{Cl}, \text{Br}, \text{I}$). *Cryst. Growth Des.* 6, 1374–1379.
- Zordan, F., Brammer, L., Sherwood, P., 2005a. Supramolecular chemistry of halogens: complementary features of inorganic ($\text{M}-\text{X}$) and organic ($\text{C}-\text{X}'$) halogens applied to $\text{M}-\text{X}\cdots\text{X}'-\text{C}$ halogen bond formation. *J. Am. Chem. Soc.* 127, 5979–5989.
- Zordan, F., Purver, S.L., Adams, H., Brammer, L., 2005b. Halometallate and halide ions: nucleophiles in competition for hydrogen bond and halogen bond formation in halopyridinium salts of mixed halide–halometallate anions. *Cryst. Growth Des.* 7, 350–354.

This page intentionally left blank

Chapter 277

Progress in the Separation Processes for Rare Earth Resources

Zhifeng Zhang*, Qiong Jia[†] and Wuping Liao^{*,1}

**State Key Laboratory of Rare Earth Resource Utilization, ERC for the Separation and Purification of REs and Thorium, Changchun Institute of Applied Chemistry, Chinese Academy of Sciences, Changchun, China*

[†]College of Chemistry, Jilin University, Changchun, China

¹Corresponding author: e-mail: wpliao@ciac.ac.cn

Chapter Outline

1 Introduction	288	4 Preparation of High-purity Rare Earths and the Associated Element Thorium	351
2 Progress in the Fundamental Research on Rare Earth Separation	289	4.1 High-purity Rare Earths	351
2.1 New Extractants and Extraction Systems	289	4.2 Ultrapure Thorium	353
2.2 Novel Extraction Equipment and Technology	301	5 Preparation of High-purity Rare Earth Metals	355
2.3 Optimizing Separation Processes by Theoretical Modeling	305	5.1 Vacuum Melting	356
3 Progress in Rare Earth Separation Processes	306	5.2 Vacuum Distillation/ Sublimation	356
3.1 Bastnäsite	306	5.3 CaF ₂ Fused-Salt Deoxidation	356
3.2 Monazite	320	5.4 Solid-State Electro-Transport	358
3.3 Mixed Bastnäsite and Monazite Ores	327	5.5 Plasma Melting	359
3.4 Ion-Adsorption Rare Earth Deposit	338	5.6 Electrolytic Refining	360
3.5 Associated Rare Earth Resources and Recycled Resources	346	5.7 Fused-Salt Extraction	360
		6 Summary and Perspective	360
		Acknowledgments	362
		References	362

1 INTRODUCTION

Due to their unique magnetic, luminescent, and electrochemical properties, rare earth elements (REs) are indispensable and nonreplaceable in high-tech and environmental applications. Especially in the past decades, their application has grown dramatically in diversity and importance. However, to satisfy their diverse application, REs should be mined, screened, leached, and separated into some proper feed materials. As a result, RE metallurgy is a very important facet before they are introduced into various products. As a major producer of rare earths in the world, China made important investments and progresses in the metallurgy of rare earths. China also became the major player worldwide in rare earth production, export, and manufacturing of rare earth-containing products. Presently, China contributes to about 90% of the world total rare earth production.

China is famous not only for its large rare earth reserves but also for its wide variety of minerals, especially the ion-adsorption ores rich in middle and heavy REs: elements such as terbium, dysprosium, europium, and yttrium are more than $10 \times$ more concentrated in the ion-adsorption ores than in bastnäsite and monazite. Middle and heavy rare earth reserves provide a powerful support for the development of rare earth industry in the world.

Research on the hydrometallurgy of rare earths in China began in the 1950s. A series of hydrometallurgical processes was specifically developed for exploiting different resources such as bastnäsite in Sichuan province, mixed ores in Baotou, and ion-adsorption deposits in South China. In particular, a popular extraction and separation processes with an acidic phosphoric extractant (named P507 in China) was established for the separation of individual rare earths. During the 1980s, a major breakthrough was obtained for the acid process (named an improved acid process) in the metallurgy of mixed rare earth ores in Baotou. The improved acid process involves roasting the ground ores with sulfuric acid to eliminate some impurities such as fluorides, resulting in purer rare earth solutions after leaching. Then, separation of individual rare earths requires a series of solvent extraction processes. This process has been widely applied for Baotou mixed ores that are the largest rare earth resource in China. Combined with solvent extraction with P507, this leads to an integral industrial production system. The production cost of rare earths is presently decreasing and the industrial status for rare earth production in the world is changing dramatically. In the last decades, many extraction and separation technologies were developed to reduce chemical consumption, comprehensively recover reactants, and control waste discharge during the rare earth hydrometallurgical processes.

In this review, we will mainly present progresses obtained in rare earth hydrometallurgy in China. Of course, progresses in the fundamental study and process exploit of the world will also be discussed. One should realize that Chinese RE industry is suffering from environmental problems because

a large amount of acid and base are consumed for the separation of rare earths, which lead to a huge discharge of salt-containing wastewater. Therefore, it is very urgent to develop greener separation technologies.

2 PROGRESS IN THE FUNDAMENTAL RESEARCH ON RARE EARTH SEPARATION

Due to their chemical similarity, REs usually coexist in minerals. However, in most cases, an individual RE shows unique intrinsic properties in optics, magnetism, or catalysis; it is therefore necessary to separate and purify individual REs for their use in functional materials. Since 1970s, scientists and engineers have carried out a lot of researches to further enhance the purity of RE products, decrease cost, and make the processes clean.

Solvent extraction having many advantages such as fast extraction reaction, high separation efficiency, and high extraction capacity, has become the main method for the separation and purification of REs, see the review by Xie et al. (2014). In 1970s, Chinese scientists achieved large-scale preparation of 2-ethylhexyl phosphoric acid mono-2-ethylhexyl ester (HEHEHP) (P507) and developed an extraction process for individual rare earth separation with ammoniated HEHEHP. In 1980s, three-outlet extraction or multioutlet extraction processes have been developed, in which three or more products can be obtained from one production line at the same time. So far, these processes have been widely applied in Chinese rare earth industry.

2.1 New Extractants and Extraction Systems

2.1.1 Acidic Phosphorous-Containing Extractants

From the late 1960s, di-(2-ethylhexyl)phosphoric acid (D_2 EHPA, Chinese brand P204) has become an important extractant and is widely used in rare earth industry (Wang et al., 2006c). Compared with the traditional extractant tributylphosphate (TBP), D_2 EHPA has many advantages such as low solubility in aqueous media and high separation factors. The average separation factor between adjacent REs for D_2 EHPA is 2.5 in hydrochloric acid medium (Sato, 1989) which is higher than that for TBP. D_2 EHPA can be used to prepare pure rare earth compounds. However, due to the lanthanide contraction, D_2 EHPA has strong binding capacity for heavy rare earths, such as Tm, Yb, and Lu. Thus, it is difficult to strip heavy rare earths from the loaded organic phases, which limits its industrial application.

In the last 1970s, HEHEHP (Chinese brand P507) was synthesized on industrial scale and studied systematically to separate rare earths. The extraction order is $La < Ce < Pr < Nd < Sm < Eu < Gd < Tb < Dy(Y) < Ho < Er < Tm < Yb < Lu$ (Sato, 1989). Li and collaborators systematically studied rare earth extraction mechanism with HEHEHP and found that in the low acidity

region, extraction mainly occurs with cation-exchange mechanism, while in the high acidity region, solvation extraction becomes predominant (Li et al., 1985, 1988a,b). In the transition region, both cation exchange and solvation extraction coexist in the system. Professor Deqian Li contributed substantially to the industrial application of this extractant in solvent extraction and separation of rare earths (Li et al., 1981, 1985, 1988a,b; Shen et al., 1986). His group successfully applied it to rare earth separation for Panxi bastnäsite, Baotou banyan obo ore, and ion-absorbed rare earth mineral (Wang et al., 2009, 2010a; Xiong et al., 2005; Zhao et al., 2004a). The technology based on HEHEHP significantly decreases the consumption of chemical reagents and reduces the waste discharge in industry. With the occurrence of HEHEHP, D₂EHPA is now usually used to separate light and medium rare earths, while HEHEHP is used to separate individual rare earths. HEHEHP is commonly used for the separation and purification of REs from chloride/nitrate medium, which can produce high recovery and high purity of rare earth products, such as La₂O₃ (99.97%) and Y₂O₃ (99.99%). HEHEHP saponified with ammonium was proposed to lower the extraction acidity and increase rare earth loading (Li et al., 1991; Shen et al., 1986). A problem is that this saponification method produces a large amount of ammonia-containing wastewater. Other technologies such as calcium saponification and nonsaponification extraction (Xiao et al., 2013) have been developed to solve this problem.

However, HEHEHP also has some shortcomings. For example, stripping of some heavy rare earths requires high acidity and it is difficult to strip these elements completely (Wang et al., 2011a). The separation factors of Nd/Pr, Gd/Eu, Er/Y, and Lu/Yb are low. Compared with light rare earths, heavy rare earths take longer time to reach equilibrium in hydrochloric acid and sulphuric acid media. To solve these problems, isooctanol was added into the HEHEHP system (Li et al., 2005; Wang et al., 2010a). Addition of isooctanol indeed improves the interfacial behavior of the extraction system, increases the separation factors between heavy REs, and decreases the stripping acidity.

Bis-2,4,4-trimethylpentyl phosphinic acid (Cyanex 272), a commercially available chemical developed by Cytech Industries Inc., is also an important extractant for rare earth extraction and separation. Compared with D₂EHPA and HEHEHP, Cyanex 272 has a higher pK_a value (Table 1). It also has larger steric hindrance due to the methyl groups, which leads to lower metal extraction efficiency and higher separation factors β between adjacent rare earths (Wang et al., 1995; Zhang and Li, 1993). The extraction behavior of rare earths in hydrochloric acid and nitric acid solutions with Cyanex 272 indicates that this extractant exhibits a higher selectivity for rare earth ions, lower extraction acidity and leads to easy stripping (Wang et al., 1995; Zhang and Li, 1993). Although Cyanex 272 is a commercial extractant, it has not been widely used in rare earth industry due to its lower extraction capacity, high price, easy emulsifying during extraction, and being unable to separate some rare earth couples effectively (e.g., Gd/Eu, Er/Y) (Wang et al., 1998). On the

TABLE 1 Structures and pK_a Values of Common Acidic Organophosphorus Extractants (Wang, 2013)

Brand Name	Full Name and Abbreviation	Chemical Structure	pK_a
P204	Di-(2-ethylhexyl) phosphoric acid (D ₂ EHPA)		3.24
P507	2-Ethylhexyl phosphoric acid mono-2-ethylhexyl ester (HEHEHP)		4.51
P229	Di(2-ethylhexyl) phosphinic acid (PIA-8)		4.98
Cyanex 272	Di-(2,4,4-trimethylpentyl) phosphinic acid (HBTMPPI)		6.37
Cyanex 302	Bis(2,4,4-trimethylpentyl) monothiophosphinic acid (HBTMPPI)		5.63
Cyanex 301	Bis(2,4,4-trimethylpentyl) dithiophosphinic acid (HBTMPDTP)		2.61

other hand, application of Cyanex 272 extraction resins in the separation of heavy rare earths in hydrochloric acid solution leads to high-purity (>99.8%) products and high recovery yields (>80%).

Synergistic extraction of rare earths with a mixture of Cyanex 272 and P507 was studied (Liu et al., 2000; Xiong et al., 2005; Zhang et al., 2014a) and high-purity Yb₂O₃ was obtained. Liao and collaborators also investigated the adsorption mechanism and kinetics of heavy rare earths by Cyanex 272–P507 impregnated resin which can be used to separate Tm, Yb, and Lu completely from heavy rare earth concentrates (Liao et al., 2007, 2010a,b).

Di(2-ethylhexyl) phosphinic acid (P229) and Cyanex 272 are isomers of a same molecular formula $C_{16}H_{35}PO$. Similar to Cyanex 272, P229 also has a high pK_a value, thus it has the advantage of lower extraction acidity and easier stripping. The extraction behavior and mechanism of Sc^{3+} , Th^{4+} , Ln^{3+} , and Fe^{3+} by P229 in hydrochloric and sulfuric acid solutions have been investigated in detail (Li, 1996; Xue and Li, 1991, 1992). P229 has higher separation factors than HEHEHP under the same experimental conditions: for instance, $\beta_{Lu/Yb}$ values are equal to 2.2 and 1.9 for P229 and HEHEHP, respectively. However, the extraction capacity of P229 is lower compared to HEHEHP. P229 is a good extractant for rare earths separation but unfortunately, its high price limits its industrial applications (Li and Yue, 1990; Yu et al., 2007). Recently, a novel synthesis route for dialkyl phosphonate compounds was invented, that starts from cheap and easily obtainable raw materials (Xiao et al., 2014). The procedures are simple, efficient, and suitable for industrial production. It was found that the synthesized compounds exhibit better properties than P507 and Cyanex 272 in the extraction and separation of heavy rare earths.

Recently, Cytech Industries Inc. has released a new product branded Cyanex 572 which is a mixture of phosphinic and phosphonic acids. Wang and collaborators studied the solvent extraction and separation of heavy REs from ion-adsorption deposits using Cyanex 572 and found that the extraction mechanism of heavy REEs is a typical cation-exchange reaction at lower acidity (Wang et al., 2015). Compared with the most commonly used industrial extractant P507, Cyanex 572 has the advantages of lower acid requirement and higher stripping efficiency.

In order to solve the problems of present acidic organophosphorus extractants and develop new extractants with excellent selectivity, higher extraction capacity, and lower stripping acidity for heavy rare earths, many kinds of novel extractants have been investigated. Examples are nonsymmetric dialkylphosphinic acid (Wang et al., 2015), sulfur-containing phosphinic acids, aminophosphonic acid (Jagodici and Tusek, 1972), ionic liquids, and calixarene derivatives. Among these extractants, dialkylphosphinic acids are considered as potential compounds due to their lower acidity. A series of dialkylphosphinic acid extractants were therefore synthesized and investigated with respect to their extraction and separation ability for heavy rare earths (Wang et al., 2013a). The authors found that dialkylphosphinic acids exhibit strong extraction ability when there is no branched chain in α -C or β -C. Furthermore, the nearer the branched chain moves to the P atom, the poorer extraction ability the extractant has. They pointed at di-(2,3-dimethylbutyl)-phosphinic acid as being a good extractant for the efficient separation of individual heavy rare earths. Later, the same authors synthesized some nonsymmetric dialkylphosphinic acid compounds and found that (2,3-dimethylbutyl)(2,4,4-trimethylpentyl) phosphinic acid has higher separation factors for heavy rare earths than Cyanex 272.

Some sulfur-containing extractants were also studied, for instance bis(2,4,4-trimethylpentyl) dithiophosphinic acid (Cyanex 301) and bis(2,4,4-trimethylpentyl) monothiophosphinic acid (Cyanex 302) (Nasab et al., 2011; Tong et al., 2009; Wu et al., 2004). However, their high price and low chemical stability limit further applications.

Table 1 gives the structures and pK_a values for the common acidic organophosphorus extractants.

2.1.2 Aminophosphonate Extractants

Both organophosphorus and amine extractants are regarded as important reagents for the extraction of rare earths. However, these two kinds of extractants exhibit different properties: the organophosphonates extract rare earths in the order of increasing atomic numbers while amines show a reverse trend. Thus, combining the functional groups of these two kinds of extractants may lead to unexpected properties. Various aminophosphonic acids and neutral aminophosphoryl compounds with low emulsifying ability, high thermal stability, and high solubility in organic phase were synthesized (Cherkasov et al., 2009b) and systematically studied (Jagodic and Tusek, 1972).

Compared with *N*-alkyl substituted mono-esters of aminophosphonic acid derivatives, *N*-aryl substituted phosphonates exhibit higher extractive properties. Jagodić and collaborators investigated the extraction of La and Eu by mono-octyl esters of *a*-anilinobenzylphosphonic acid (MOABP) and *ct*-(2-carboxyanilino)benzylphosphonic acid (MOCABP) and found that the extraction ability of MOCABP is higher compared to MOABP (Jagodić et al., 1971). Separation of Eu(III) and Tb(III) from U(VI) has also been achieved in different acidic media (Herak and Jagodic, 1964). Matveeva and collaborators investigated the extraction properties of a series of β -aminophosphoryl derivatives toward lanthanides (Matveeva et al., 2012). The results indicate that the extractants have higher efficiency when they bear more P=O functional groups. In addition, Cherkasov investigated the extraction of scandium (Cherkasov et al., 2009a) and rare earths (Cherkasov et al., 2012) by aminophosphinyl extractants.

2.1.3 Neutral Phosphorus-Containing Extractants

Cytec Industries Inc. synthesized a series of phosphine oxides extractants named Cyanex 921, Cyanex 923, and Cyanex 925. Table 2 shows the structures of these extractants and other neutral organophosphorus extractants. Among them, Cyanex 923 is the most studied. Cyanex 923 is a mixture of four trialkylphosphine oxides namely $R_3P=O$, $R'R_2P=O$, $R'_2RP=O$, and $R_3'P=O$ (R is *n*-octyl and R' is *n*-hexyl) that has average molecular weight of 348 and density of 880 kg/m^3 . Cyanex 923 has many excellent properties such as being a liquid at room temperature, hard to be hydrolyzed, sparingly soluble in aqueous solution, and having low extraction acidity, high extraction

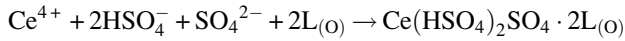
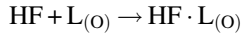
TABLE 2 Structures of Neutral Organophosphorus Extractants (Wang, 2013)

Brand Name	Full Name and Abbreviation	Chemical Structure
TBP	Tributylphosphate (TBP)	$\begin{array}{c} \text{O} \\ \parallel \\ \text{C}_4\text{H}_9-\text{O}-\text{P}-\text{O}-\text{C}_4\text{H}_9 \\ \diagup \quad \diagdown \\ \text{C}_4\text{H}_9-\text{O} \end{array}$
P350	Di-(1-methyl-heptyl) methyl phosphonate (DMHMP)	$\begin{array}{c} \text{CH}_3 \\ \\ \text{H}_3\text{C}-(\text{H}_2\text{C})_5-\text{C}-\text{O} \\ \\ \text{H} \\ \\ \text{H}_3\text{C}-(\text{H}_2\text{C})_5-\text{C}-\text{O} \\ \\ \text{CH}_3 \end{array} \begin{array}{c} \text{O} \\ \parallel \\ \text{P} \\ \diagup \quad \diagdown \\ \text{O}-\text{CH}_3 \end{array}$
P503	Di-(2-ethylhexyl) 2-ethylhexyl phosphonate (DEHEHP)	$\begin{array}{c} \text{C}_2\text{H}_5 \\ \\ \text{C}_4\text{H}_9-\text{C}-\text{C}-\text{O} \\ \quad \\ \text{H} \quad \text{H}_2 \\ \quad \\ \text{C}_4\text{H}_9-\text{C}-\text{C}-\text{O} \\ \quad \\ \text{C}_2\text{H}_5 \quad \text{C}_2\text{H}_5 \end{array} \begin{array}{c} \text{O} \\ \parallel \\ \text{P} \\ \diagup \quad \diagdown \\ \text{O}-\text{C}-\text{H} \\ \quad \\ \text{H}_2\text{C} \quad \text{C}_4\text{H}_9 \\ \\ \text{C}_2\text{H}_5 \end{array}$
Cyanex 921	Tri- <i>n</i> -octylphosphine oxide (TOPO)	$\begin{array}{c} \text{O} \\ \parallel \\ \text{C}_8\text{H}_{17}-\text{P} \\ \diagup \quad \diagdown \\ \text{C}_8\text{H}_{17} \quad \text{C}_8\text{H}_{17} \end{array}$
Cyanex 923	Trialkylphosphine oxides (TRPO)	$\begin{array}{cc} \begin{array}{c} \text{O} \\ \parallel \\ \text{C}_8\text{H}_{13}-\text{P}-\text{C}_8\text{H}_{17} \\ \diagup \quad \diagdown \\ \text{C}_8\text{H}_{13} \end{array} & \begin{array}{c} \text{O} \\ \parallel \\ \text{C}_8\text{H}_{13}-\text{P}-\text{C}_8\text{H}_{17} \\ \diagup \quad \diagdown \\ \text{C}_8\text{H}_{17} \end{array} \\ 31\% & 42\% \\ \\ \begin{array}{c} \text{O} \\ \parallel \\ \text{C}_8\text{H}_{13}-\text{P}-\text{C}_8\text{H}_{13} \\ \diagup \quad \diagdown \\ \text{C}_8\text{H}_{13} \end{array} & \begin{array}{c} \text{O} \\ \parallel \\ \text{C}_8\text{H}_{17}-\text{P}-\text{C}_8\text{H}_{17} \\ \diagup \quad \diagdown \\ \text{C}_8\text{H}_{17} \end{array} \\ 14\% & 8\% \end{array}$
Cyanex 925	Trialkylphosphine oxides (TRPO)	$\begin{array}{c} \text{CH}_3 \quad \text{H}_3\text{C} \\ \quad \\ \text{H}_3\text{C}-\text{C}-\text{C}-\text{H} \\ \quad \\ \text{CH}_3 \quad \text{H} \\ \quad \\ \text{H}_3\text{C}-\text{C}-\text{C}-\text{H} \\ \quad \\ \text{CH}_3 \quad \text{CH}_3 \end{array} \begin{array}{c} \text{O} \\ \parallel \\ \text{P} \\ \diagup \quad \diagdown \\ \text{O}-\text{C}-\text{H} \\ \quad \\ \text{H}_3\text{C} \quad \text{C}_8\text{H}_{17} \end{array} \begin{array}{c} \text{CH}_3 \\ \\ \text{C}_8\text{H}_{17} \end{array} \begin{array}{c} \text{O} \\ \parallel \\ \text{P} \\ \diagup \quad \diagdown \\ \text{O}-\text{C}-\text{H} \\ \quad \\ \text{H}_3\text{C} \quad \text{C}_8\text{H}_{17} \end{array} \begin{array}{c} \text{CH}_3 \\ \\ \text{C}_8\text{H}_{17} \end{array} \\ 85\% \end{array}$ $\begin{array}{c} \text{CH}_3 \quad \text{H}_3\text{C} \\ \quad \\ \text{H}_3\text{C}-\text{C}-\text{C}-\text{H} \\ \quad \\ \text{CH}_3 \quad \text{H} \\ \quad \\ \text{H}_3\text{C}-\text{C}-\text{C}-\text{H} \\ \quad \\ \text{CH}_3 \quad \text{CH}_3 \end{array} \begin{array}{c} \text{O} \\ \parallel \\ \text{P} \\ \diagup \quad \diagdown \\ \text{O}-\text{C}-\text{H} \\ \quad \\ \text{H}_3\text{C} \quad \text{C}_8\text{H}_{17} \end{array} \begin{array}{c} \text{CH}_3 \\ \\ \text{C}_8\text{H}_{17} \end{array} \begin{array}{c} \text{O} \\ \parallel \\ \text{P} \\ \diagup \quad \diagdown \\ \text{O}-\text{C}-\text{H} \\ \quad \\ \text{H}_3\text{C} \quad \text{C}_8\text{H}_{17} \end{array} \begin{array}{c} \text{CH}_3 \\ \\ \text{C}_8\text{H}_{17} \end{array} \\ 8\% \end{array}$

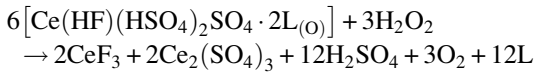
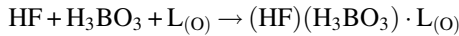
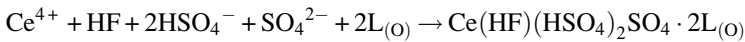
capacity, while being miscible in any common solvents and displaying strong surfactant properties (Liao and Jiao, 2005), which points to this extractant as being a serious candidate for commercial extraction processes. Cyanex 923 has indeed been used for the recovery of lanthanides and actinides (Shaibu et al., 2006) and extraction and separation of REs such as La, Ce, Pr, Nd, Sm (Lee et al., 2009), and Yb(III) (Wang et al., 2006a).

Our group has studied the extraction and separation of rare earths and related elements by Cyanex 923, since 1996. Examples are the studies on the extraction of Sc(III) (Li and Wang, 1998) and the extraction thermodynamic and kinetics of Ce(IV) from H_2SO_4 -HF medium (Liao et al., 2001,

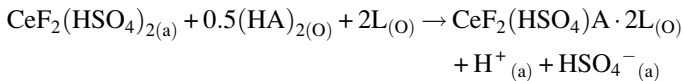
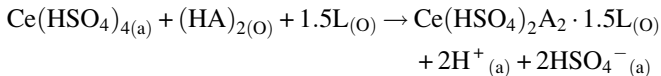
2002). The results indicate that the extraction of HF and Ce(IV) by Cyanex 923 can be expressed as follows:



Because fluorine coexists with cerium in the H_2SO_4 leachate of roasted bastnäsite and because boric acid is added to stabilize fluorine, the extraction of fluorine, and boric acid and the stripping of the loaded fluorine-containing chelates with H_2O_2 were also studied.



Due to high price of Cyanex 923, efforts were undertaken to cut its consumption by adding acidic organophosphorus extractants. Our group first studied the synergistic extraction and recovery of Ce(IV) and fluorine from sulfuric solutions by Cyanex 923 and di-2-ethylhexyl phosphoric acid (D_2EHPA) (Zhang et al., 2008) and then systematically investigated and compared the synergistic extraction of Ce(IV) and Th(IV) with mixtures of Cyanex 923 and other organophosphorous acids in sulfuric acid medium (Tong et al., 2013). The corresponding reaction equations could be written as:



where L stands for Cyanex 923 and HA means $\text{D}_2\text{EHPA/HEHEHP}$.

Cyanex 921 is composed of tri-*n*-octylphosphine oxide (TOPO). It has been tested for the extraction and separation of many elements such as non-metallic As(V) (Perez et al., 2007), transition metals Cu(II) (Choi et al., 2014; Mishra and Devi, 2011; Navarro et al., 2008), Zn(II) and Fe(II) (El Dessouky et al., 2008), rare and precious metals Rh, Pt, and Pd (Mhaske, and Dhadke, 2001), Au(III) (Martinez et al., 1997), and rare earth Nd(III) (Panda et al., 2012). However, Cyanex 921 is a solid at room temperature with a relatively low solubility in common solvents, which limits its use.

Cyanex 925 is a mixture of two compounds with formulae R_3PO and $\text{R}_2\text{R}'\text{PO}$, where $\text{R} = \text{CH}_3\text{C}(\text{CH}_3)_2\text{CH}_2\text{CH}(\text{CH}_3)\text{CH}_2$ (2,4,4-trimethyl pentyl)

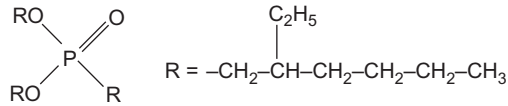
and $R' = \text{CH}_3(\text{CH}_2)_7$ (*n*-octyl). Because of the steric hindrance generated by the aliphatic chain, the extraction selectivity of Cyanex 925 is better compared to Cyanex 923 and Cyanex 921 (Yn et al., 2002). There are also some studies on the extraction and separation of 3d transition elements (Yadav et al., 1994) and rare and noble metals (Iyer and Dhadke, 2001; Martin and Alguacil, 1998) by Cyanex 925.

Another interesting reagent is di-(1-methyl-heptyl)methyl phosphonate (P350) that was first synthesized and applied in the extraction and separation of rare earth in China (Xu, 1995). P350 was also used in the extraction separation of protactinium (Chen et al., 1984), thorium (Qian et al., 1986; Xia, 1987; Zhu et al., 2015), uranium (Xia et al., 1985; Zhou, 1992; Zhu et al., 2015), iron (Zhou, 1992), and zirconium (Liu et al., 1983). Compared with TBP, P350 possesses higher extractability for REs in low acidity and the distribution ratio (*D*) of REs decreases after europium with increasing atomic numbers. Thus, the application of P350-HNO₃ is limited to the separation and purification of lanthanum from the mixed rare earths containing lower content of cerium, the separation of praseodymium and neodymium from enriched solutions, and the preparation of highly pure scandium oxide (Zhang et al., 1991). The extraction of heavy rare earths can be carried out in multicomponent system such as the P350-TTA-PMAP (Chen and Liu, 1992) and P350-PMAP-TTA-PMBP (Chen et al., 1997).

In the recent decades, P350 was primarily applied for the preparation of high-purity lanthanum. In the mixed HNO₃ and HSCN system, the distribution ratio of lanthanum, D_{La} , is the smallest one among those of the lanthanide series, thus lanthanum remains in aqueous phase while the other REs are extracted into the organic phase. China was the first country to adopt the P350 (kerosene)-RE(NO₃)₃-HNO₃ system for the preparation of high-purity lanthanum. With this extractant, the purity of La₂O₃ is increased from ~50% to 99–99.99% with a yield of 99% after a fractional extraction. Compared with the TBP system, the P350 system possesses many advantages such as low acidity of the extraction system, good operation environment, free from nitric acid recovery, improvement of distribution ratio, and separation coefficient by self-salting out of high concentrated feeds (Xu, 1995).

Moreover, it was reported that P350 could remove Th and part of Zr from scandium to obtain Sc₂O₃ with 99.9% purity and with a yield of 95% (Chen et al., 1981). Zhang and collaborators discussed the separation of scandium from a mixture of Ti(IV), Ca(II), RE_xO_y, and Fe(III) with Cl-P350 extraction-elution resin in chloride medium, and found that this resin has higher extraction capacity for scandium and prominent separation efficiency between scandium and Ti(IV), Ca(II), RE_xO_y, and Fe(III) at a given HCl concentration (Zhang et al., 1990). By taking 99% Sc₂O₃ as the raw material, the same authors studied the main factors that affect the extraction of scandium with P350 in HCl medium and designed a process for the preparation of high-purity scandium oxide, by which Sc₂O₃ (>99.99%) can be obtained with a yield >98% (Zhang et al., 1991).

Di-(2-ethylhexyl) 2-ethylhexyl phosphonate (DEHEHP) (P503), is a neutral organophosphorus extractant and boiling point of 210 °C. Its molecular structure is as follows:



P503 possesses many potential advantages such as: (1) it is easy to synthesize at low cost and with high purity; (2) it has good physico-chemical properties and resistance to hydrolysis; (3) its solubility in water is low, only 2.6×10^{-4} g/L at 25 °C; and (4) its viscosity is small and it can be dissolved in common solvents at room temperature.

It was found that P503 is an efficient and selective extractant for Ce(IV) in nitrate medium with fast kinetics and allowing easy stripping. Zhao et al. (2004b) investigated the separation of Ce(IV) from other commonly associate metals, such as La, Ce, Nd, Yb, and Th(IV), and found that P503 has selectivity for Ce(IV) and extractability varies in the order: Ce(IV) > Th(IV) \gg RE (III), namely Th(IV) does not interfere seriously and RE(III) show negligible extraction. After a 15-stage fractional extraction and stripping, CeO₂ is obtained with a purity of 99.95% and a yield of 84.9%; the content of thorium is less than 7×10^{-5} (ThO₂/CeO₂).

As a quadrivalent cation similar to Ce⁴⁺, Th⁴⁺ could also be extracted by P503 efficiently. Wang and collaborators studied thermodynamics and kinetics of thorium (IV) extraction by P503 in *n*-heptane from nitrate medium (Wang et al., 2013b,c). The factors influencing the process such as the concentration of HNO₃, the nature of salting-out reagents, temperature, the concentrations of metal ions, and P503 were investigated systematically. The extractant P503 showed a fast extraction rate in the P503-Th(NO₃)₄-HNO₃ system; Th(NO₃)₄·2(P503) was determined to be the extracted species and the rate equation could be deduced as follows:

$$-d[\text{Th}]/dt = k_0 \cdot [\text{Th}^{4+}]^{0.72} \cdot [\text{P503}]^{0.80} \cdot [\text{NO}_3^-]^{0.82}$$

The calculated extraction equilibrium constants (K_{ex}) and thermodynamic parameters (ΔG , ΔH , and ΔS) indicate that P503 has a high selectivity for thorium(IV) over rare earth(III). Stripping tests indicated that thorium could be completely stripped by distilled water from Th-loaded organic phase. Thorium product with a purity of 99.999% was then prepared with a yield of 98% from thorium concentrates with P503 as the extractant by a solvent extraction process comprising six extraction stages, six scrubbing stages, and six stripping stages. Compared with the known process for preparing highly pure thorium with TBP, the new protocol has the following advantages: low aqueous

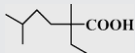
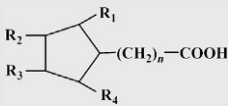
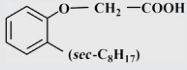
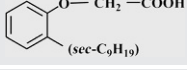
solubility of P503, simple process, and less reagent consumption. Thus, P503 is a potential replacement of TBP in thorium and cerium purification. It was also suggested that P503 is a good synergistic extractant for acidic chelating extractants for rare earths (Xiao et al., 2011; Zhao et al., 2006b).

Recently, our group synthesized a series of phosphoramidite and amino ethylphosphonate for the extraction and separation of Ce(IV) and fluorine from sulfuric acid leachates of bastnäsite (Liao et al., 2014c,d,e). It is found that these extractants can also extract Th(IV) cations from a sulfate medium (Liao et al., 2014a,b). Furthermore, Ce(IV) and Th(IV) can be separated by controlling the experimental conditions properly. These extractants are meant to replace Cyanex 923, which would make hydrometallurgy processes based on the pre-separation of Ce(IV) and Th(IV) for bastnäsite more efficient.

2.1.4 Carboxylic Acid Extractants

Several different carboxylic acid extractants such as naphthenic acid, *sec*-octylphenoxy acetic acid (CA-12), and *sec*-nonylphenoxy acetic acid (CA-100) (Table 3) are mainly used to separate yttrium from rare earths in the industry. The position of Y in the rare earth series with respect to extractability is different for each extractant. When the extractant is neodecanoic acid (Versatic 10), yttrium lies with the middle rare earths; however, when the extractant is naphthenic acid, yttrium appears in the light rare earths ($\text{La} < \text{Ce} < \text{Y} < \text{Nd} < \text{Gd} < \text{Ho} < \text{Yb}$), which indicates that high-purity yttrium can be separated from heavy rare earths. This behavior has been attributed to the acidity of the extractant (Zheng et al., 1991) but some authors explained that this phenomenon is caused by the structure and steric hindrance of the carboxylic acid (Preez and Preston, 1992).

TABLE 3 Structures and $\text{p}K_a$ of Carboxylic Acid Extractants

Brand Name	Full Name	Chemical Structure	$\text{p}K_a$
Versatic 10	Neodecanoic acid		7.33
HA	Naphthenic acid		6.91
CA-12	<i>sec</i> -octylphenoxy acetic acid		3.52
CA-100	<i>sec</i> -nonylphenoxy acetic acid		3.53

Naphthenic acid is a byproduct of petroleum industry and has the advantages of low cost and easy preparation. It is presently widely used for the preparation of high-purity yttrium. However, it has some disadvantages. For example, naphthenic acid has high solubility in aqueous phase which leads to extractant loss. The extraction of yttrium is usually carried out at high pH values, which result in unexpected emulsification. In addition, the composition of naphthenic acid changes during the extraction process.

In order to overcome the disadvantages of naphthenic acid, novel carboxylic acid extractants such as CA-12 and CA-100 have been developed for the preparation of high-purity yttrium. Compared with naphthenic acid, the novel extractants have the following advantages: stable composition, low solubility in water, low extraction acidity, and easy stripping from loaded organic phases. The extractant CA-12 was found to be useful for the separation of yttrium from light rare earth mixtures (Zhang et al., 2000). However, the separation factors between yttrium and heavy REs were not high (Li et al., 2007), which implied that it is difficult to obtain yttrium with high purity and high yield by sole CA-12 in industrial practice. Therefore, Wang et al. proposed a HAB extraction system containing mixed extractants of HA (CA-12) and HB (Cyanex 272) to improve the separation factor and prepare high-purity yttrium at industrial scale (Wang et al., 2011b). The process includes 15 stages of extraction and 10 stages of scrubbing. The yield and purity of the product were 95% and 99.94%, respectively.

Rare earth extraction by CA-100 gives the following order: yttrium < heavy lanthanides < light (middle) lanthanides (Wang et al., 2002), which indicates that CA-100 can be used for the extraction and separation of yttrium from light rare earths. Some CA-100 systems with the addition of complexing agents were studied to increase the separation factors between yttrium and heavy rare earths (Wang et al., 2004). The results suggest that the CA-100-EDTA system is more efficient than the other studied systems. Scientists also reported the synergistic effects of CA-100 and neutral organophosphorus extractants (Xiao et al., 2011) or acidic organophosphorus extractants (Sun et al., 2006) in the separation of yttrium from heavy rare earths.

2.1.5 Amine Extractants

Amine extractants, also called “liquid anion exchangers,” are highly effective extractants for radioactive elements, nonferrous metals, rare metals, and acids. As a consequence, primary amine extractants attracted a lot of attention. In 1975, domestic primary amine N1923 was used for the analysis of metal ions and acids in China. Its molecular formula is $R^1(R^2)CHNH_2$ (with the total number of carbon atoms being 19–23). Hydrometallurgy and rare earth separation are prominent aspects of the uses of the extractant N1923 and there are many reports on the extraction of transition metals, rare earth metals, and organic acids by N1923. Liu and collaborators studied the extraction kinetics of thorium with N1923 from a sulfate solution (Liu et al., 2007, 2008). The

TABLE 4 Structures of Amine Extractants (Wang, 2013)

Brand Name	Full Name and Abbreviation	Chemical Structure
N1923	Primary amine	$(C_nH_{2n+1})_2CHNH_2$ $n=9-11$
N235	Trialkylamine	$(C_nH_{2n+1})_3N$ $n=8-10$
N263	Methyltrioctylamine chloride Aliquat336	$[(C_8H_{17})_3N^+CH_3]Cl^-$

results indicated that N1923 is a highly effective extractant for this element, especially with respect to the recovery and enrichment of traces of thorium from massive iron and rare earths (Guo et al., 2009a; Liu et al., 2007).

N235 is a domestic amine extractant acting as an ionic exchanger. Its general formula is R_3N , and the alkyl chain is C_8-C_{10} . Its performance is similar to trioctylamine. N235 is widely used in rare earth industry (Zhuang, 1975). Quaternary ammonium salts such as methyltrioctylammonium chloride (Aliquat 336) have also proved promising for the separation of rare earths. In nitrate media, Aliquat 336 extracts light rare earths more readily than the heavier ones, which provides a means of removing light rare earths from process solutions (Xie et al., 2014). Table 4 shows the structures of amine extractants.

2.1.6 Ionic Liquids

Ionic liquids are commonly considered as being green solvents due to their low vapor pressure, high thermal stability, and low flammability. However, typical ionic liquids without functional groups are always considered not to extract metal cations in the absence of some extractant. For instance, in the past years, extraction systems with imidazolium ionic liquids as the solvents have been studied and higher extractability and selectivity than those with traditional solvents were found in some systems. Functionalized ionic liquids incorporating some functional groups in their cations and/or anions can behave as both the solvent and extractant. And some functionalized ionic liquids were also tested for rare earth separation; this field has recently been reviewed (Liu et al., 2012b; Sun et al., 2011). Some bifunctional ionic liquids obtained by the reaction of two traditional extractants such as P204 and N235 have also been used for rare earth separation (Liu et al., 2012b). Recently, Freiderich et al. presented one of the first uses of a pure ionic liquid system with acidic amide ionic liquid in an ionic liquid diluent to dissolve bastnäsite and found that heavy REs were enriched by nearly an order of magnitude (Freiderich et al., 2015).

2.2 Novel Extraction Equipment and Technology

In the extraction process of rare earths, the mixer–settler (Fig. 1) is the most common extraction equipment for the conventional extraction process. Although it has some obvious advantages such as high efficiency, high adaptation, easy application, and operation, it has some shortcoming such as long mixing time, low processing capacity, large factory area occupation, and high energy consumption. In order to overcome these problems, many equipments and methods have been developed, e.g., modified mixer–settler, hollow fiber membrane extractor, extraction column, liquid surfactant membrane extractor, microreactor, membrane dispersion microextractor, and three-liquid-phase extractor. Modification of the mixer–settler always aims at three goals, high mixing efficiency, low mixing velocity, and small occupation area. In order to improve the mixing efficiency, Wang and Huang proposed a mixer–settler with double mixer and shallow settler (Fig. 2, Wang and Huang, 2007). Yin

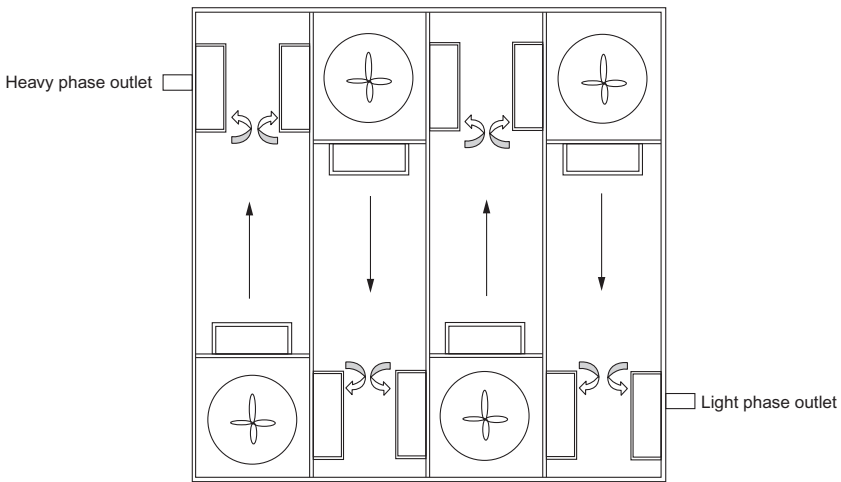


FIGURE 1 Schematic of mixer–settlers.

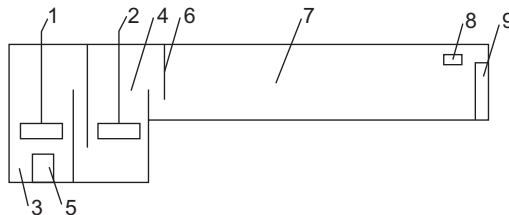


FIGURE 2 Structure of a mixer–settler with double mixer and shallow settler (Wang and Huang, 2007). (1) and (2) agitator. (3) and (4) mixer. (5) buffer chamber, (6) baffle plate, (7) shallow settler, (8) overflow weir for organic phase, and (9) overflow weir for the aqueous phase.

and collaborator employed microreactor (Fig. 3) for the extraction of lanthanum by P507 and found that the large specific surface area and short diffusion distance in these devices are beneficial for efficient extraction of La(III) (Yin et al., 2015). Other authors studied the extraction of La(III) by P507 by a membrane dispersion microextractor (Fig. 4, Hou et al., 2013). In order to improve the separation efficiency of mixer-settlers, Zhao and collaborators introduced another impeller into the settler (Fig. 5) and found that this

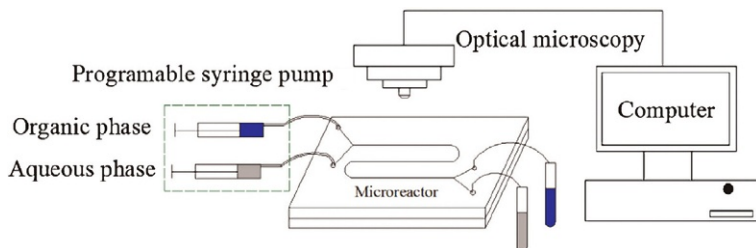


FIGURE 3 Schematic illustration of a microreactor system (Yin et al., 2015, © 2015 Elsevier B.V.).

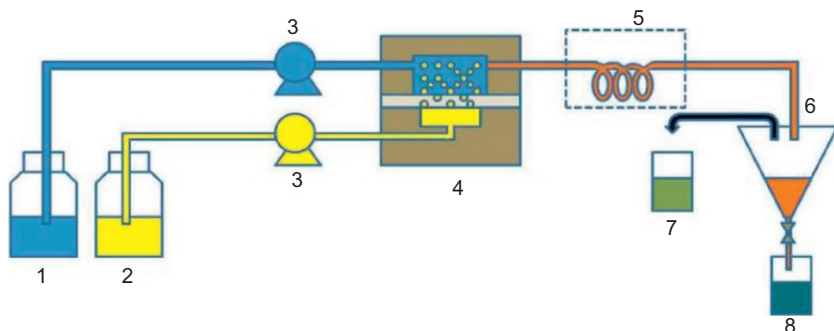


FIGURE 4 Sketch of membrane dispersion microextractor setup (Hou et al., 2013, © 2013 Elsevier B.V.). (1) Continuous phase tank, (2) dispersion phase, (3) metering pump, (4) membrane microdispersive module, (5) capillary tube, (6) phase separating funnel, (7) organic phase, and (8) aqueous phase.

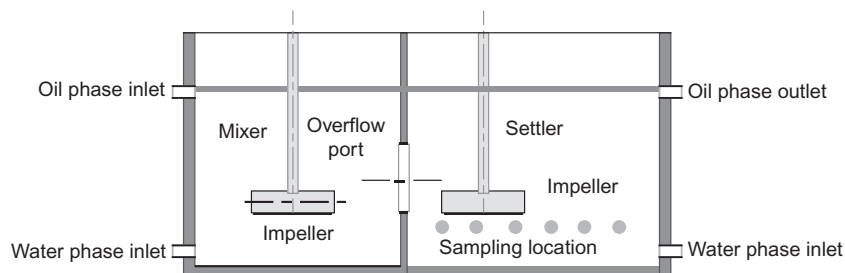


FIGURE 5 A schematic diagram of a mixer-settler with double agitation (Zhao et al., 2014).

addition improves the separation efficiency (Zhao et al., 2014). In order to improve the process capacity, Yu and Jiang proposed a nonbuffer chamber mixer–settler (Fig. 6) which mixes the feeds well while not leading to the formation of emulsion (Yu and Jiang, 2011). In order to decrease the occupation area, Paulo et al. proposed a new kind of mixer–settler named mixing-settler based on phase inversion (MSPI) (Fig. 7) in which a mixer is located on the top and a tubular settler is located under the mixer (Paulo and Hadjiev, 2006). So this mixer–settler needs less occupation area and the dead volume kept in the instrument is minimal. However, more energy is needed to lift the feeds to the mixer located at a higher level. Another modification is to

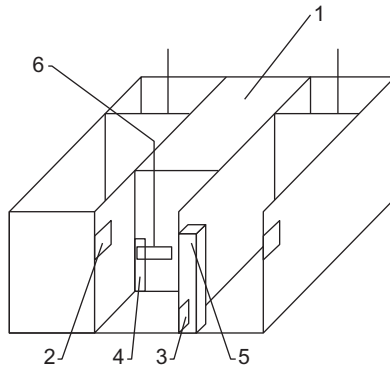


FIGURE 6 Structure of nonbuffer chamber mixer–settler (Yu and Jiang, 2011). (1) Settler, (2) overflow weir for organic phase, (3) aqueous phase inlet, (4) outlet on the mixer, (5) overflow weir for aqueous phase, and (6) agitator.

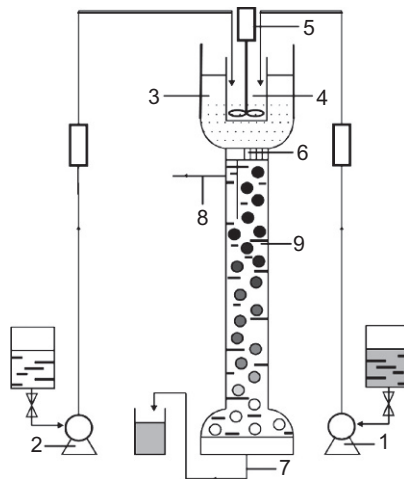


FIGURE 7 Process flowchart of MSPI mixer–settler (Paulo and Hadjiev, 2006, © 2006 ACS publications), (1) and (2) pumps, (3) mixer, (4) mixing zone, (5) driving motor with impeller, (6) scattering plate, (7) and (8) aqueous and organic phase outlets, and (9) organic layer.

stack every stage with mixer and settler vertically; this arrangement is named Hanson-type mixer–settler (Fig. 8, Hashtochahar et al., 2010). But it is difficult to design and not easy to operate. Sui et al. applied a novel mixer–settler–mixer three-chamber integrated extractor (Fig. 9) to three-liquid-phase extraction and separation of rare earths and/or non-REs (Sui et al., 2014). They found that REs were selectively extracted into the organic top phase

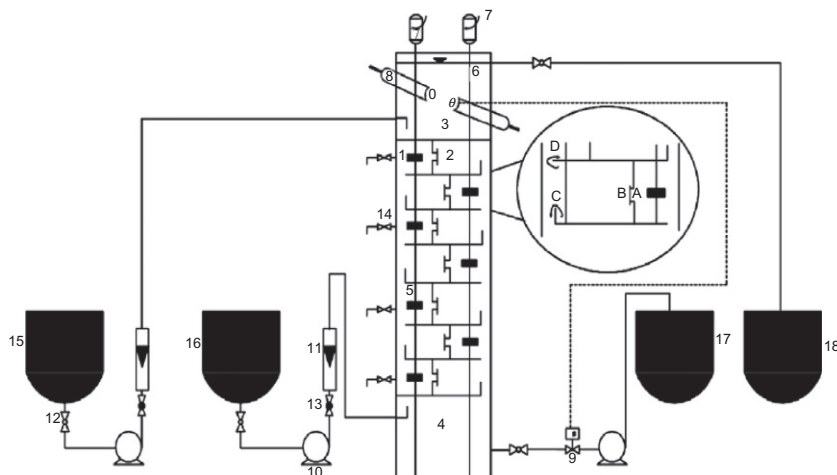


FIGURE 8 Flow diagram of the Hanson mixer–settler column (Hashtochahar et al., 2010, © 2010 John Wiley & Sons). (1) Mixer part, (2) settler part, (3) upper settler zone, (4) lower settler zone, (5) agitator, (6) shaft, (7) electromotor, (8) optical sensor, (9) solenoid valve, (10) pump, (11) rotameter, (12) ball valve, (13) globe valve, (14) sampling valve, (15) solvent vessel, (16) feed vessel, (17) extract vessel, and (18) raffinate vessel.

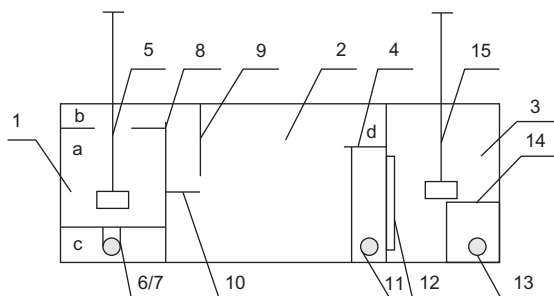


FIGURE 9 Principal schematic of the mixer–settler–mixer three-chamber integrated extractor (Sui et al., 2014, © 2014 American Chemical Society). (1) Three-phase mixer, (2) three-phase settler, (3) two-phase mixer, (4) liquid flow separator, (5) self-suction agitator, (6) and (7) liquid flow inlet (on the two sides of three-phase mixer), (8) liquid overflow gate, (9) longitudinal baffle, (10) transverse baffle, (11) liquid flow outlet, (12) baffle, (13) flow outlet, (14) overflow box, (15) self-suction agitator, (a) liquid mixing region, (b) liquid overflow region, (c) liquid inlet region, and (d) liquid flow control zone.

and salt-rich bottom phase, while most of non-REs such as Fe, Al, and Si were enriched into the PEG-rich middle phase. So REs and nonrare earth impurities can be separated. The application of three-liquid-phase extraction at industrial scale is feasible.

2.3 Optimizing Separation Processes by Theoretical Modeling

In the conventional RE separation process, a great amount of acid, base, and water are consumed as raw material in dissolution, extraction, separation, and precipitation operations. As environmental problems are receiving increased attention in recent years, novel extraction processes of rare earths are being designed with the aim of reducing chemical consumption and pollutant emission. To achieve this goal, hyperlink extraction technology was developed and widely used in Chinese RE separation industry in recent years. Supplying rare earth-containing extracting solvent or scrubbing agent solution between two separation units, indeed reduces the consumption of chemicals. The earlier theory of countercurrent extraction cannot determine the limits of chemical consumption of a hyperlink process in multicomponent separation. Recently, Cheng and collaborators expanded this theory and presented equations for calculating the minimum amounts of extracting solvent and scrubbing agent needed (Cheng et al., 2014c). They applied these equations to various systems such as nonbarren, aqueous feeding, organic feeding, and complex feeding systems, and provided an approach for estimating the theoretical limits of chemical consumptions of a given separation process in different feeding patterns. For an AB/BC countercurrent separation using aqueous feed, minimum amounts of both extraction solvent and scrubbing agent solution can be estimated only when the ratio between the flow rate of the central component B leaving the aqueous outlet to that leaving the organic outlet reaches an optimum value (Cheng et al., 2014a). This optimal flow rate ratio of the B component can be calculated with the known separation factors between the components, but it is independent of the feed composition. The minimum amount of extracting solvent can be calculated by the feed composition together with the separation factors, while that of scrubbing agent solution is only determined by the separation factor of the A/C pair and it is irrelevant to the feed composition and the separation factors of the other pairs as well. A different result was observed for an AB/BC countercurrent separation using organic feed (Cheng et al., 2014c). The minimum amount of extracting solvent was only related to the separation factors of the A/C pair and independent of the separation factors of the other pairs as well as of the feed composition. Finally, the minimum amount of scrubbing agent solution was determined by the separation factors between the components together with the feed composition. A complex feeding pattern named in-with-out feeding was also considered (Cheng et al., 2015). The authors derive the equations of minimum amounts of extracting solvent and scrubbing agent solution for

the separation and provide an approach for calculating the theoretical limits of chemical consumption for a given separation process with this feeding pattern. The influence of nonbarren extracting solvent and scrubbing agent solution on the minimum amounts of reactants was also investigated (Cheng et al., 2014b).

3 PROGRESS IN RARE EARTH SEPARATION PROCESSES

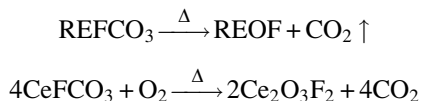
3.1 Bastnäsite

Bastnäsite (CeFCO_3) is one of main resources of rare earths in the world and it is found in many countries and areas such as China, Europe, America, and Africa. Commonly, the percentage of rare earth oxides (REO) in bastnäsite is about 60–70% by weight and Ce, La, Pr, and Nd oxides represent over 97% of the total REO in this mineral (Jordens et al., 2013). During the past 50 years, bastnäsite replaced monazite to become the main mineral source of light REs (Özbayoğlu and Atalay, 2000), which is mainly due to the discovery and development of the world's largest RE deposit, the Bayan Obo mine (a mixed-ore, about 80% of which is bastnäsite) in China, as well as of the Mountain Pass mine in the United States, which is the largest bastnäsite deposit in the world (Krishnamurthy and Gupta, 2004). The typical composition is listed in Table 5.

The processing methods for bastnäsite can be divided into two kinds: acid method and alkali method.

3.1.1 Acid Method

In order to obtain europium oxide for its wide usage in TV set from 1965 onward, American Molycorp, Inc. first applied a process with oxidizing roasting—selective leaching by HCl to recover Eu from bastnäsite, which has been one of the classical methods for exploiting bastnäsite (Xu, 1995). The reaction in the roasting process can be expressed as follows:



After roasting, most of RE_2O_3 in the ore are selectively leached by HCl into the aqueous phase and separated from REF_3 , CeO_2 , and CeOF_2 . The main process is sketched in Fig. 10. To recover cerium, the cerium concentrates are roasted with sulfuric acid and leached by water. Then cerium is recovered by solvent extraction using D_2EHPA as the extractant (Fig. 10).

A process named oxidizing roasting— H_2SO_4 leaching—double salt precipitation process was also developed for bastnäsite (Xu, 1995) (Fig. 11). Its advantages are less investment and fast factory construction so that it has been used widely in China. However, this process has some disadvantages such as

TABLE 5 Composition of Bastnäsite Concentrate (wt%) from Bayan Obo (Liu, 2007)

REO	CaO	BaO	Fe ₂ O ₃	F	ThO ₂	La ₂ O ₃	CeO ₂	Pr ₆ O ₁₁	Nd ₂ O ₃	Sm ₂ O ₃	Eu ₂ O ₃	Gd ₂ O ₃	Y ₂ O ₃
60.12	0.46	11.45	0.61	6.57	0.23	36	48	4	10	0.7	0.1	<0.3	<0.4

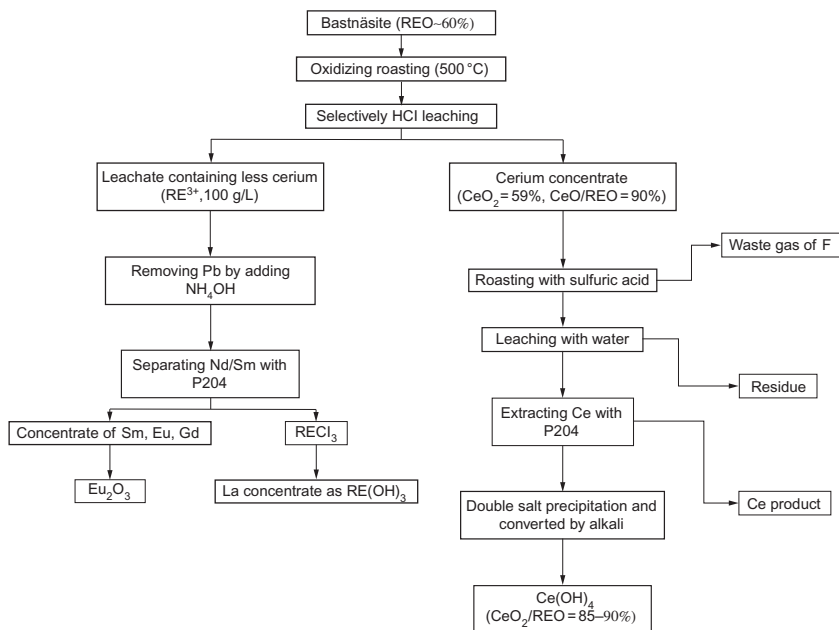
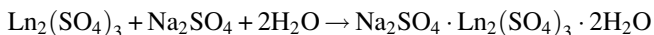
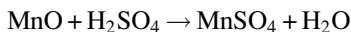
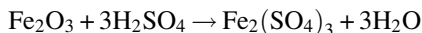
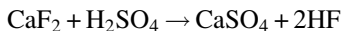
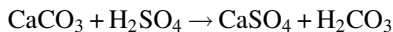
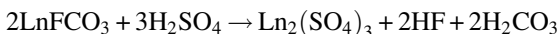


FIGURE 10 Oxidizing roasting—selective HCl-leaching process for bastnäsite.

long processing time, use of many filters, and low yield of rare earths (only 70–75%, with an especially serious loss of heavy rare earths). Kul et al. applied the double salt precipitation method to deal with low grade concentrates of Turkish bastnäsite (Kul et al., 2008) (Fig. 12). They found that the recovery of REs reaches 90% and fluorine can also be recuperated as hydrofluoric acid.

The reactions involved in this process can be expressed by the following equations:



Another method is named oxidizing roasting—selective HCl leaching—alkali conversion process (Fig. 13). The process usually involves the following steps: roasting under oxidation conditions to oxidize rare earths into their oxides, selective leaching by hydrochloric acid in which part of trivalent rare earths are leached into the aqueous phase while the quadrivalent elements

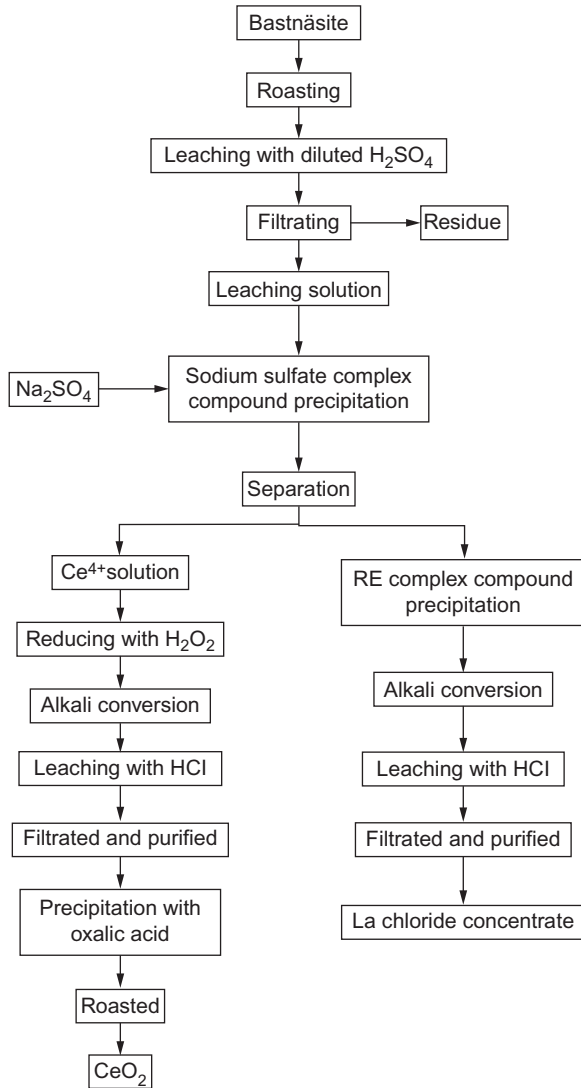


FIGURE 11 Process of separating cerium by double-sulfate salt method (Xu, 1995).

such as Ce(IV) and Th(IV) as well as fluorine remain in the slag. Then individual rare earths are extracted and separated from the aqueous solution and the slag is decomposed with caustic soda.

After removing fluorine by washing with water, cerium concentrates containing thorium are obtained which can be used for the production of ferrosilicon alloy. In this process, thorium and fluorine are removed as impurities from the chloride leachates by adding magnesium/calcium salts to precipitate

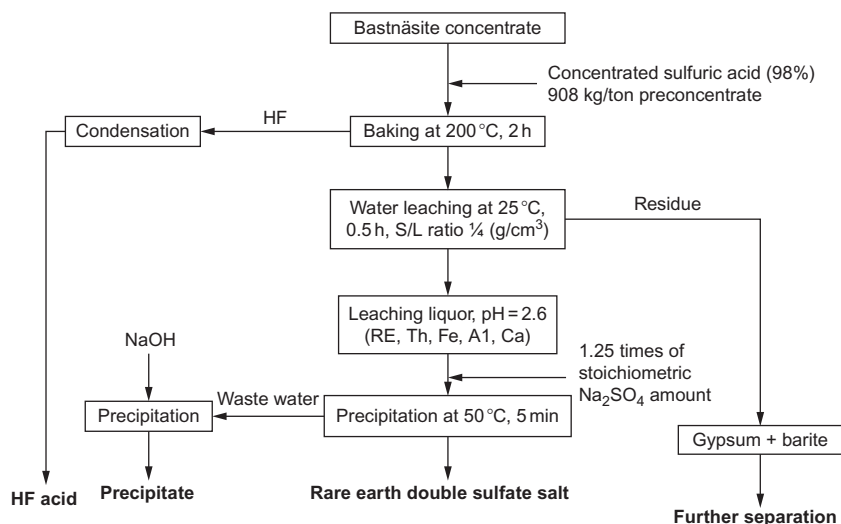


FIGURE 12 Working flowsheet for producing HF acid and rare earth double-sulfate salt. Reproduced from Kul et al. (2008), © 2007 Elsevier.

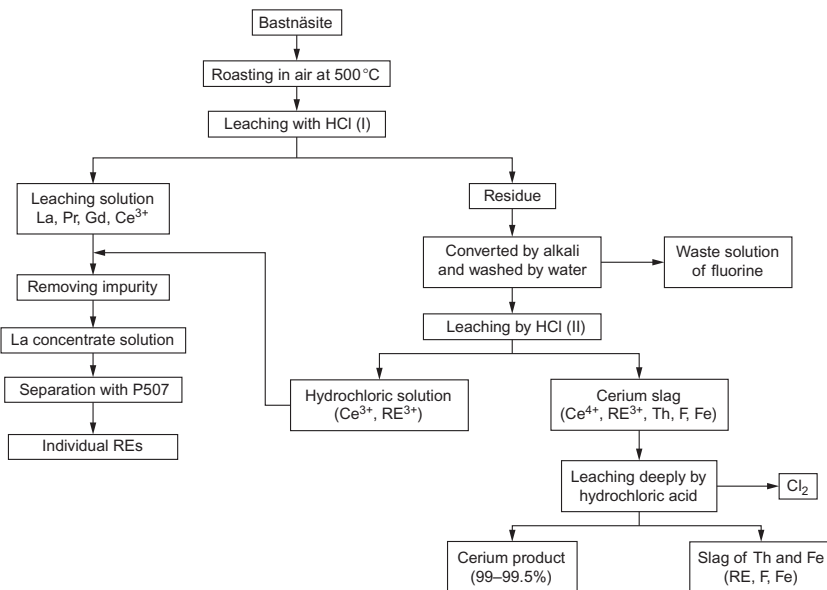


FIGURE 13 Oxidizing roasting—selective HCl leaching—alkali conversion process (Wang, 2013).

them. The advantages of the process is that various productions such as cerium-based polishing powders, lanthanum concentrates and the feeds for single rare earth separation can be obtained directly. However, there are also some problems such as low rare earth recovery, difficult disposal of the

TABLE 6 Element Contents Calculated as Their Oxides (Liu et al., 2004)

Oxides	La ₂ O ₃	CeO ₂	Pr ₆ O ₁₁	Nd ₂ O ₃	Sm ₂ O ₃
Content (%)	70.9	3.9	6.1	17.4	1.7
Oxides	MgO	Fe ₂ O ₃	CaO	PbO	Al ₂ O ₃
Content (ppm)	80	46	155	9.5	33.6
Oxides	SiO ₂	F		SO ₃	Na ₂ O
Content (ppm)	7.4	320		<200	<50

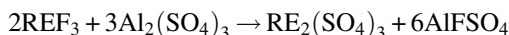
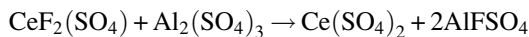
precipitated impurity, high pollution arising from radioactive precipitate, and the fluorine-containing wastewaters.

There are some other processes proposed for bastnäsité. Liu et al. invented a method that includes the following steps: roasting at 500 °C in air, leaching by water, precipitating trivalent rare earths by adding ammonia or alkali metal carbonates, reducing Ce(IV) to Ce(III) by adding reducing agents such as hydroxylamine hydrochloride or hydrazine dihydrate, and then precipitating Ce(III) by adding carbonate to form Ce₂(CO₃)₃ (Liu et al., 2004). Table 6 gives the typical composition of a REO product by this method.

Huang et al. invented another method to deal with bastnäsité (Huang et al., 2010) (Fig. 14). The main steps involve roasting in air, selective leaching rare earths with HCl, leaching the solid residue with H₂SO₄, extracting Ce(IV), Th(IV), fluorine in the solution by mixed D₂EHPA/HEHEHP extractants, washing fluorine in the organic solution with aluminum sulfate or boric acid, stripping Ce(IV) by 6 M HCl and H₂O₂, and finally stripping Th(IV) with 3 M H₂SO₄.

Direct extraction of Ce(IV) from bastnäsité leachates was also proposed (Guo and Guo, 1996). To eliminate emulsification of the organic phase, an aluminum salt was added to the leachates resulting in complexing fluoride with aluminum to form AlFSO₄ which cannot be extracted by the organic phase (Fig. 15). In this process, CeF₂(SO₄) and RE₂F₃ were dissolved into the sulfates and the concentration of free fluoride anions decreased substantially due to the presence of aluminum in solution. The addition of nitrate could increase the extraction rate.

The corresponding reactions can be expressed as follows:



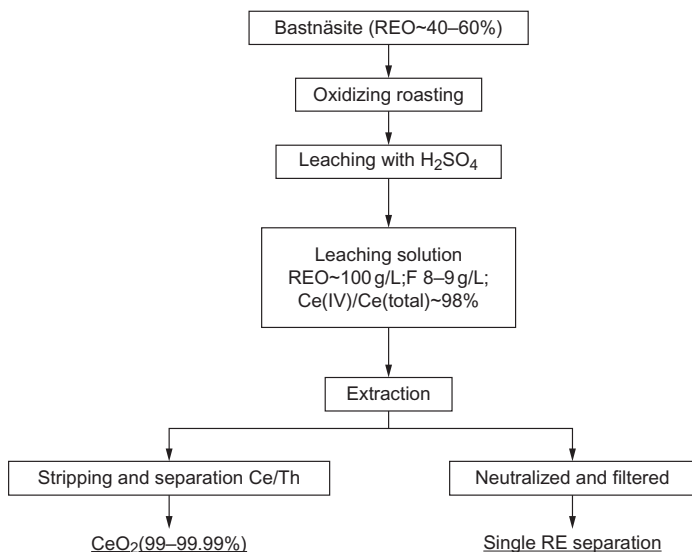


FIGURE 14 Flowchart of oxidizing roasting—sulfuric acid leaching—extraction treatment for bastnäsite (Huang et al., 2010).

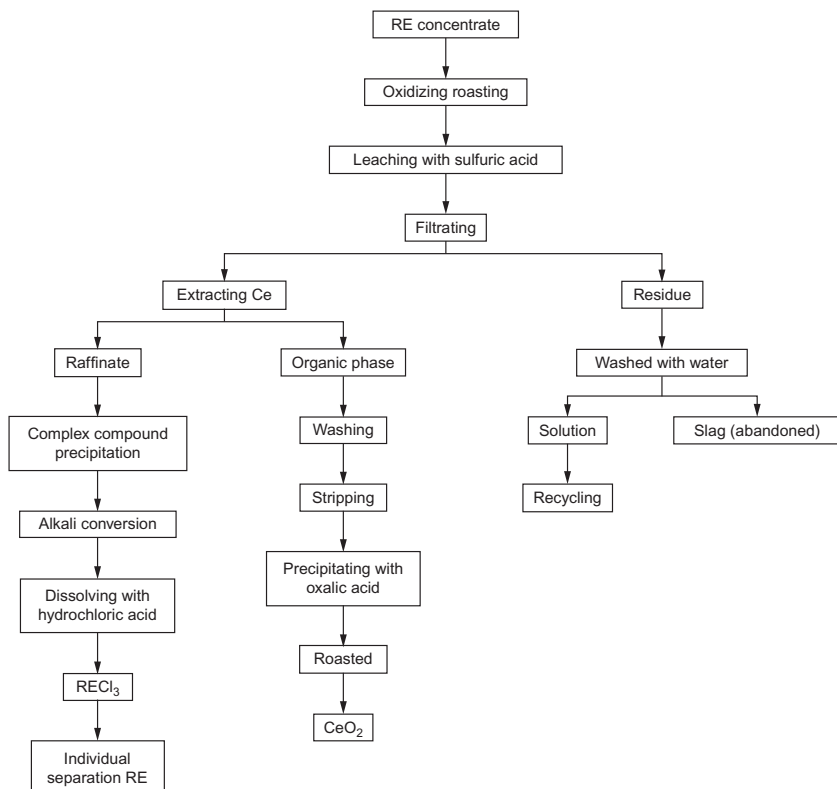


FIGURE 15 Flowchart of the direct extraction of Ce(IV) from leachate solution (Guo and Guo, 1996).

This process has been applied in industry in Shanxi Province. The total recovery of RE is more than 83% while the recovery of cerium is more than 70%. The purity of the cerium product can be modulated in the range 80–99.999%. This process is simpler, with just only a half of the steps of the conventional method.

However, it also has some disadvantages. For instance, in order to eliminate the unwanted effect of fluoride on the extraction process, much aluminum salt has to be added into the leachates, which then has to be removed by complex compound precipitation. Furthermore, impurities of radioactive thorium and iron cannot be extracted and separated from the leachate by this process.

Alternatively, in order to eliminate the effect of fluoride on the extraction procedure, alkali metal, or aluminum salts can be added directly into the bastnäs site ore to convert fluorine into water-soluble salts that can be washed off by water (Zhou, 1999). The residue is then leached with H_2SO_4 and the rare earth concentration in the leachate is 30–100g/L (REO). The process is showed in Fig. 16.

In all the above processes, fluorine is always thought as a harmful element for the extraction. However, in other processes, fluorine is just thought as an associated element which can be extracted together with REs. For instance, fluorine can be recovered by co-extraction of fluorine and tetravalent cerium in a process with Cyanex 923 as the extractant. Our group systematically studied the extraction of tetravalent cerium and thorium (Lu et al., 1998), fluorine (Liao et al., 2001), scandium (Li and Wang, 1998), manganese (Zhang et al., 2007c), rare earths (Tong et al., 2003) by Cyanex 923. Based on the results from fundamental research, an extraction process was developed to recover

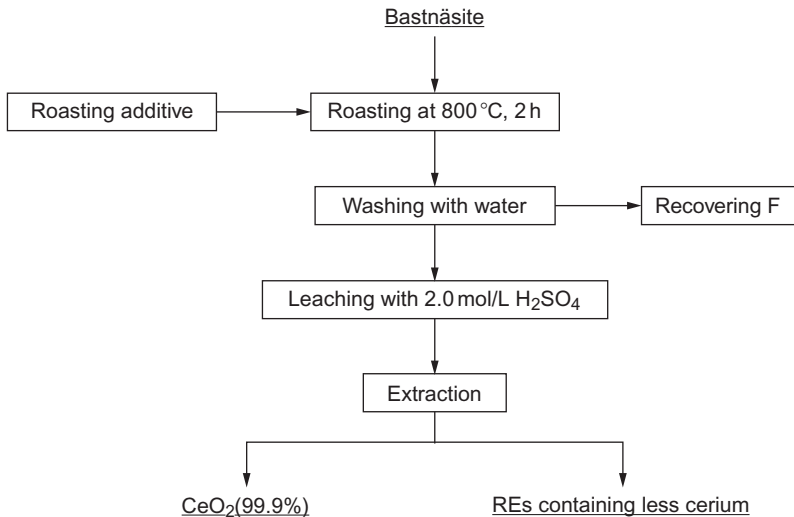


FIGURE 16 Flowchart of defluorination with the addition of alkali metal or aluminum salts and extraction of cerium (Zhou, 1999).

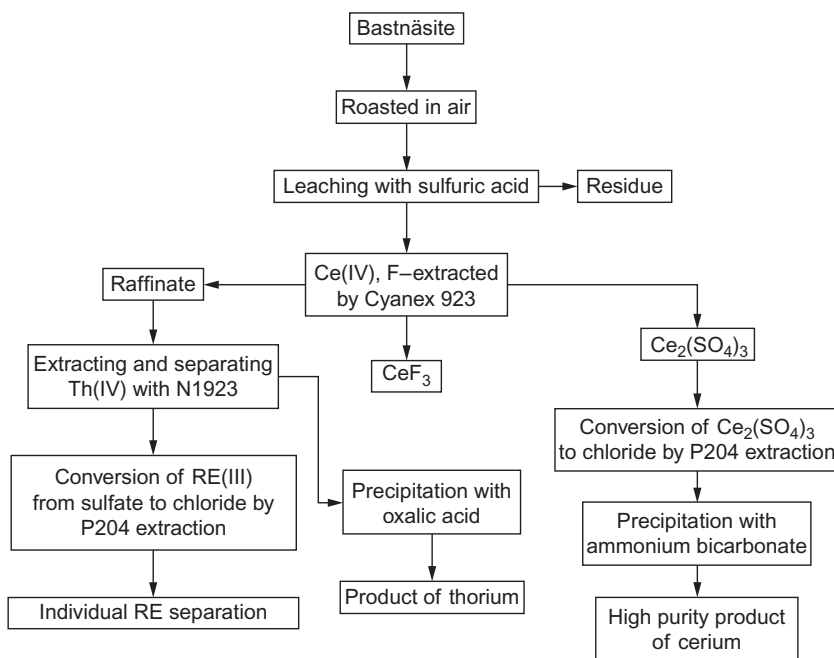


FIGURE 17 Recovery of cerium(IV) and fluoride from roasted bastnäsite sulfuric acid leachate extracted with Cyanex 923 (Li, 2005).

cerium(IV) and fluoride from sulfuric acid leachate of roasted bastnäsite with Cyanex 923 (Fig. 17) (Li et al., 1998), which has been applied in a factory in Sichuan Province, China to deal with 4000 tons of roasted bastnäsite per year. In this process, the majority of Ce(IV), Th(IV), F⁻, and RE(III) are converted into the leachate. Then Ce(IV) and F⁻ were extracted by Cyanex 923 into the organic phase and stripped by reducing agents such as H₂O₂. The reduced Ce(III) reacts with F⁻ to form a CeF₃ precipitate. Th(IV) in the raffinate is recovered by primary amine N1923 and RE(III) are transformed into a chloride solution by extraction with D₂EHPA and subsequent stripping with hydrochloric acid. The resulting RE(III) solution is then used as the feed for individual rare earth separation.

The yield of fluorine recovery is more than 90% and the total yield of cerium recovery reaches 86%. The purity of the cerium product is more than 99.99%, in which the content of the radioactive thorium is lower than 1×10^{-4} (ThO₂/CeO₂). More than 90% thorium in bastnäsite feed was recovered, the purity of which is more than 99%. The recovery yield of other rare earths is more than 90% with thorium content lower than 3×10^{-6} . This process has several advantages: (1) it is simple and provides a friendly operating environment; (2) the associated element fluorine can be recovered by co-extraction with cheap cerium to avoid environmental pollution; (3) thorium is recovered to avoid radioactive contamination; and (4) the acid and alkali

consumption in this process is less than that in the traditional processes. An obvious disadvantage of this process is that the extractant Cyanex 923 is expensive and separation costs for cerium are high. So the lower market price of cerium products makes it economically unviable.

In order to cut costs of cerium separation, Zhang and coworkers proposed a modified process to simultaneously recover cerium and fluorine from bastnäsité by a mixture of Cyanex 923 and P507/P204 (Zhang et al., 2008, 2010) (Fig. 18). In this process, part of Cyanex 923 is substituted by the cheaper P507 or P204 so that the cost of the extractant is reduced. At the same time,

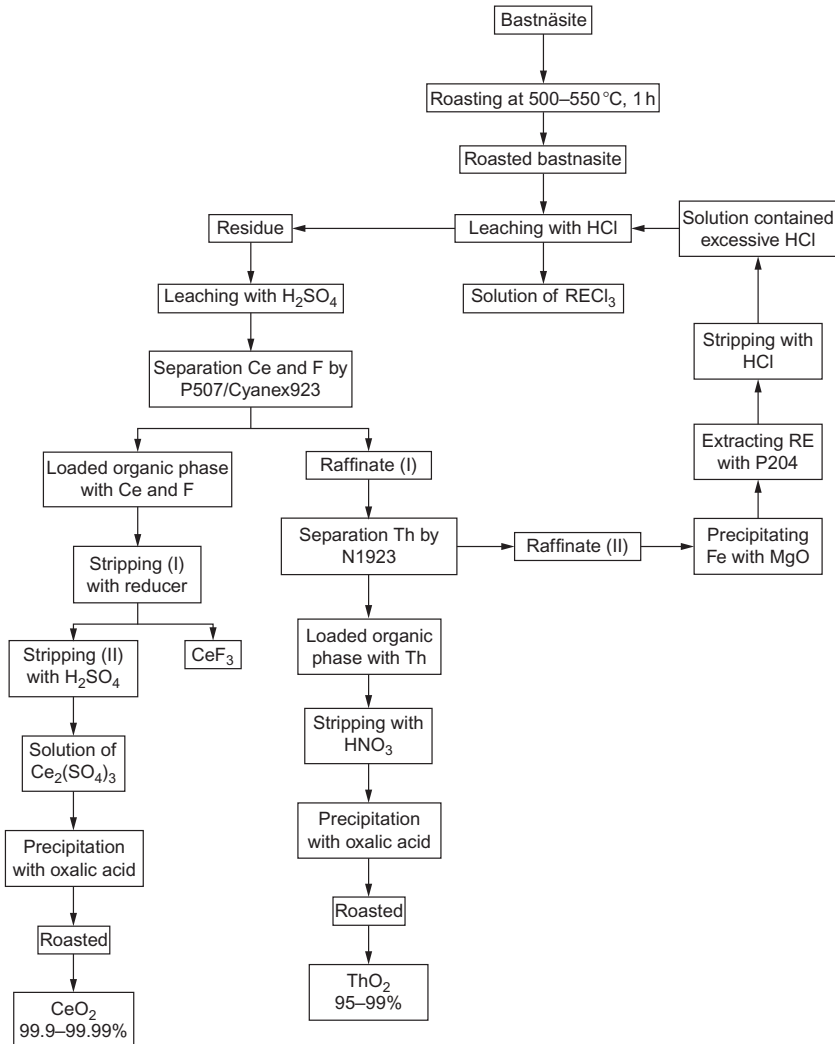


FIGURE 18 Scheme of recovery of cerium and fluorine from bastnäsité by a mixture of extractants (Zhang et al., 2010).

the extraction capacity of the organic phase increases by 30% so that this procedure becomes more economically feasible compared to the process solely based on Cyanex 923.

Considering the advantages of the selective HCl-leaching process, Wang and collaborators combined it with the Cyanex 923 process involving: oxidizing roasting—selective HCl-leaching— H_2SO_4 leaching—extraction with mixed Cyanex 923–P507 extractant—extraction with primary amine N1923 (Wang, 2013), see Fig. 19. In this process, about 35% of RE(III) is leached by HCl from roasted bastnäsite while most of cerium, fluorine, and thorium are left in the solid residue which can be leached by H_2SO_4 . The sulfate solution is then extracted by Cyanex 923 to recover cerium and fluorine and by N1923 to recover radioactive thorium. This process produces expensive trivalent REs rapidly and also recovers tetravalent cerium, fluoride, and tetravalent thorium. So it would make sound economic sense to implement it at industrial scale. However, the use of the expensive extractant Cyanex 923 has not been completely eliminated.

To make the process based on the initial extraction of tetravalent cerium more affordable, cheap and efficient extractants should be designed and developed. To reach this goal, our group designed and prepared a neutral

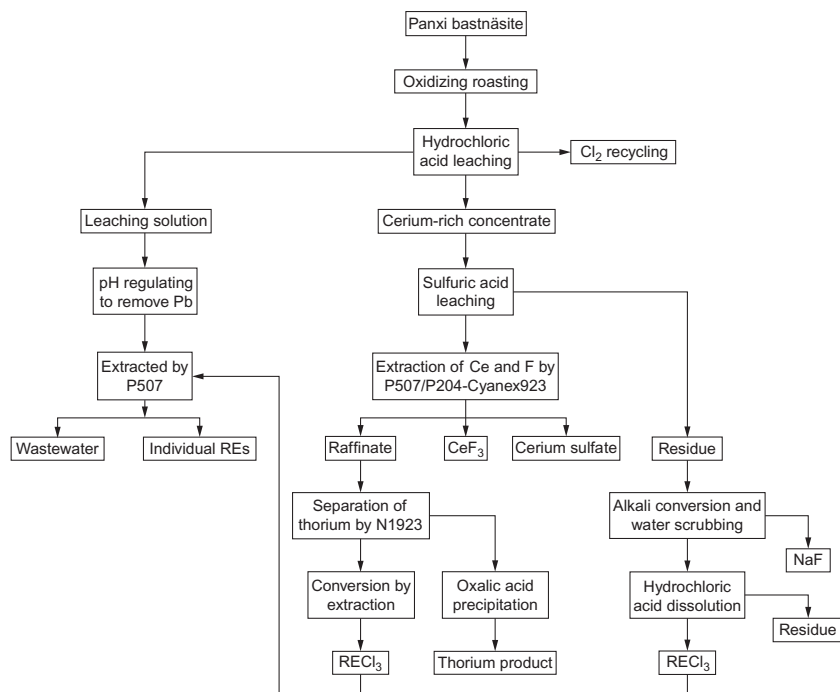


FIGURE 19 Oxidizing roasting—selective HCl leaching— H_2SO_4 leaching—alkali conversion solvent extraction process (Wang, 2013).

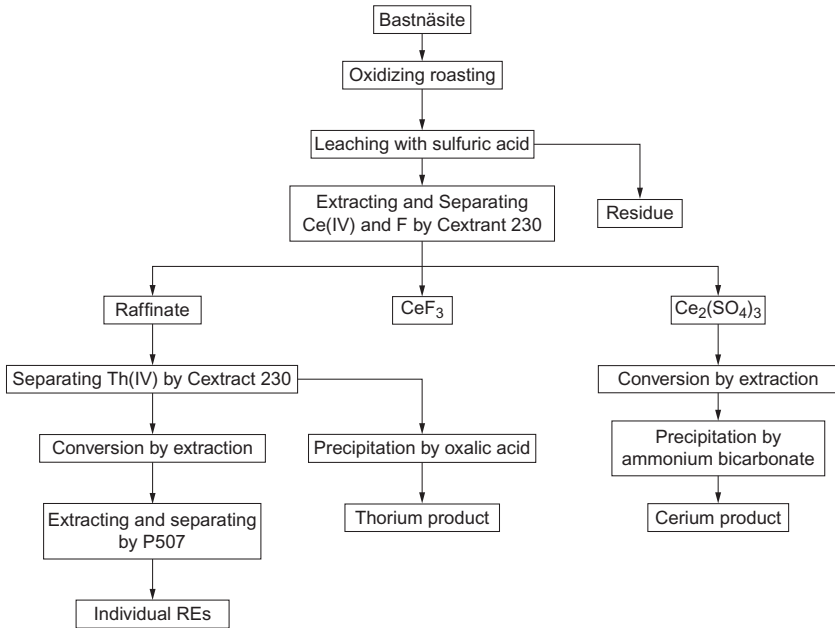


FIGURE 20 Extraction and separation of Ce(IV), F⁻, and Th(IV) from bastnäsite leaching solution by the novel extractant Cextrant 230 (Liao et al., 2014e).

nitrogen-containing phosphorus extractant named Cextrant 230 (Liao et al., 2014d). Compared to Cyanex 923, this reagent can extract both tetravalent cerium and thorium from low sulfuric acid solution while Cyanex 923 can only extract tetravalent cerium. The extraction capacity of 30% (v/v) Cextrant 230 for thorium is about 43 g/L, which means that less extractant is needed to recover the same amount of thorium. The extraction of cerium is more complete than that of thorium. So Cextrant 230 can separate these two elements under low acidity conditions. Furthermore, we developed a new process for the hydrometallurgy of bastnäsite in Sichuan province and had it tested at the pilot-plant level. The results indicate that Cextrant 230 effectively extracts not only tetravalent cerium and fluorine but also the radioactive element thorium. Thorium contents in the cerium products and raffinate are both less than 5×10^{-5} . Compared with the previous process with Cyanex 923, the new procedure is simpler since it extracts cerium and thorium by a same extractant. Importantly, the price of the new extractant is much lower compared to Cyanex 923. The flowchart is given in Fig. 20.

3.1.2 Alkali Method

There are two alkali methods for bastnäsite, i.e., caustic soda method and sodium carbonate method. The purpose of alkali methods is to remove

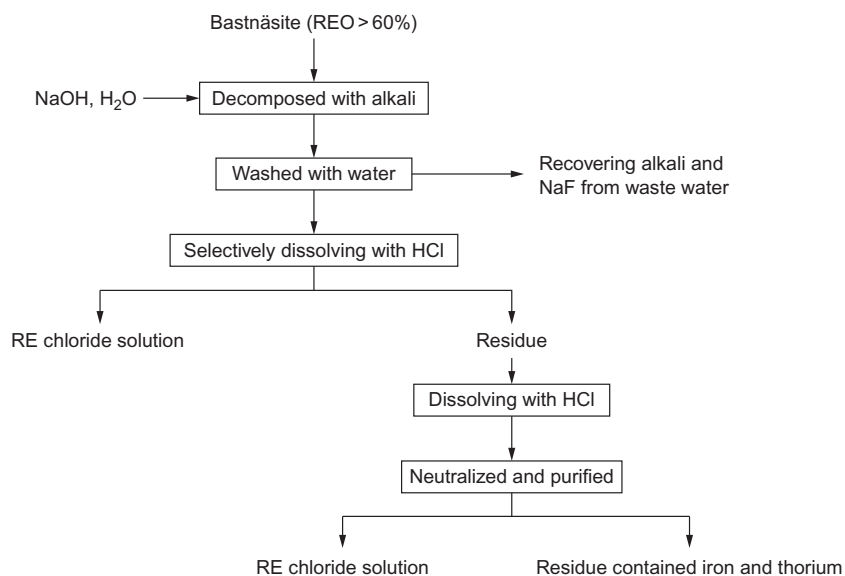


FIGURE 21 Flowchart of the caustic soda process for bastnäsite (Xu, 1995).

fluorine from the ores by completely decomposing the ores and then treating by water. Fluorine is washed away and some neat rare earth compounds are obtained for further separation. The main process of the caustic soda method includes the following steps: mixing bastnäsite with caustic soda solution; heating the mixture to a given temperature for decomposing the ore; washing fluorine with water, filtering, and selectively dissolving the rare earth hydroxide slag with HCl; and finally, separating individual rare earths by known solvent extraction processes. The undissolvable residue contains iron and thorium. The yield of rare earths reaches 95%. This process is sketched in Fig. 21.

Because Na_2CO_3 is cheaper than NaOH, it was chosen as a decomposer for bastnäsite (Zheng et al., 1993). The resulting method is similar to that of caustic soda and the yield of rare earths reaches 97.5%. The typical flow is shown in Fig. 22. However, the main disadvantage of both alkali methods is to generate too much wastewater when washing fluoride. In addition, these processes consume large amounts of chemical reagents due to multiple washing and filtering, which increase the cost and make the operations discontinuous.

Another alkali method uses ammonium chloride as the additive (Zhu et al., 2000) (Fig. 23). First, bastnäsite is roasted in air with reagents to fix fluorine. Fluorine is then washed away by water and the slag is mixed with ammonium chloride to decompose the rare earth ores. Finally, the roasted ore is leached by water to get the rare earth-containing solution. This process can be adapted

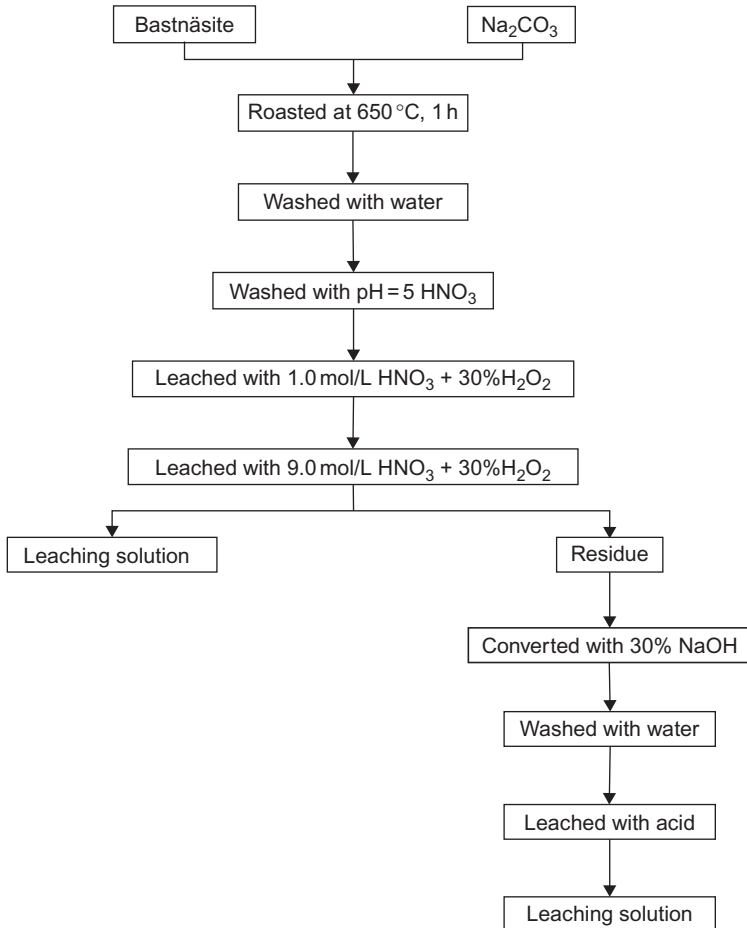


FIGURE 22 Flowchart of the sodium carbonate process for bastnäsite (Zheng et al., 1993).

to other minerals with different rare earth contents. Its principle should be that HCl produced by the decomposition of NH_4Cl at high temperature reacts with rare earths in the roasted bastnäsite devoid of fluorine. There are some problems for this process, that is, NH_3 produced by the decomposition of NH_4Cl is not easy to deal with and substantial quantity of energy is consumed because of repeated roasting.

Yang et al. studied in detail the transformation of bastnäsite in this process when it is calcined in saturated steam and found that mixed $\text{REF}_3\text{-RE}_2(\text{CO}_3)_3$ ores decompose into REF_3 and RE_2O_3 while REOF forms at the same time (Yang et al., 2015). Then, the defluorination reactions of REF_3 and REOF occur if there is enough water around them. The reactions can be written as follows:

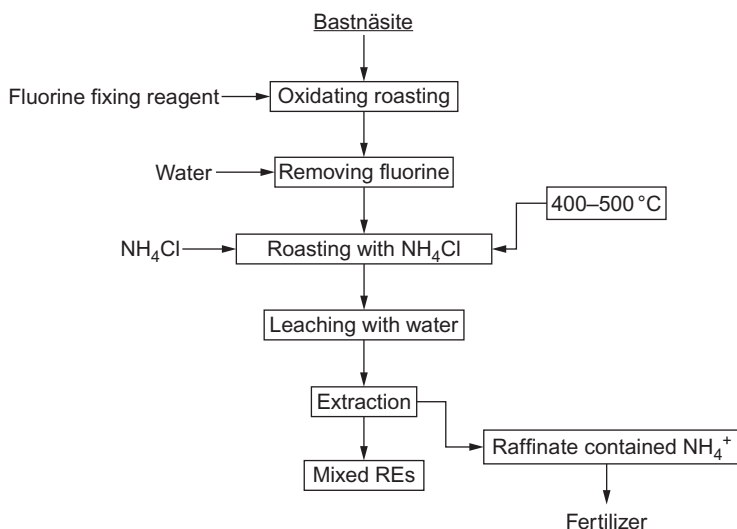
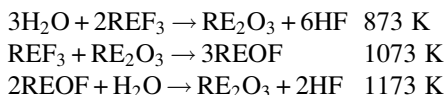


FIGURE 23 Flowchart of ammonium chloride decomposing bastnäsite (Zhu et al., 2000).



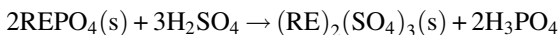
3.1.3 Direct Usage of Bastnäsite

Another way to deal with bastnäsite is its direct usage as polishing powder. Indeed, the polishing powders mainly contain CeO_2 and CeOF and the best way to make polishing powders from bastnäsite is to grind it with $(\text{NH}_4)_2\text{SO}_4$ as an additive (He et al., 1998). A Chinese patent (Ma et al., 1999) introduced a method of preparing mixed rare earth metals from bastnäsite by direct electrolysis. The process does not produce harmful gas and the yield of rare earth metals reaches 88–95%, with an efficiency of electric current use reaching 48–62%.

3.2 Monazite

3.2.1 Sulfuric Acid Method

Sulfuric acid has been used extensively for monazite leaching, where H_2SO_4 reacts with the ores at a temperature ranging from 200 to 220 °C (Fig. 24). Decomposition products exist in the form of $\text{RE}_2(\text{SO}_4)_3$, $\text{Th}(\text{SO}_4)_2$, and UO_2SO_4 . The process can be described as follows (Barghusen and Smutz, 1958):



However, decomposing monazite with alkali or acid wastes a large amount of water and raw materials. To remedy these problems, mechanical ball-milling

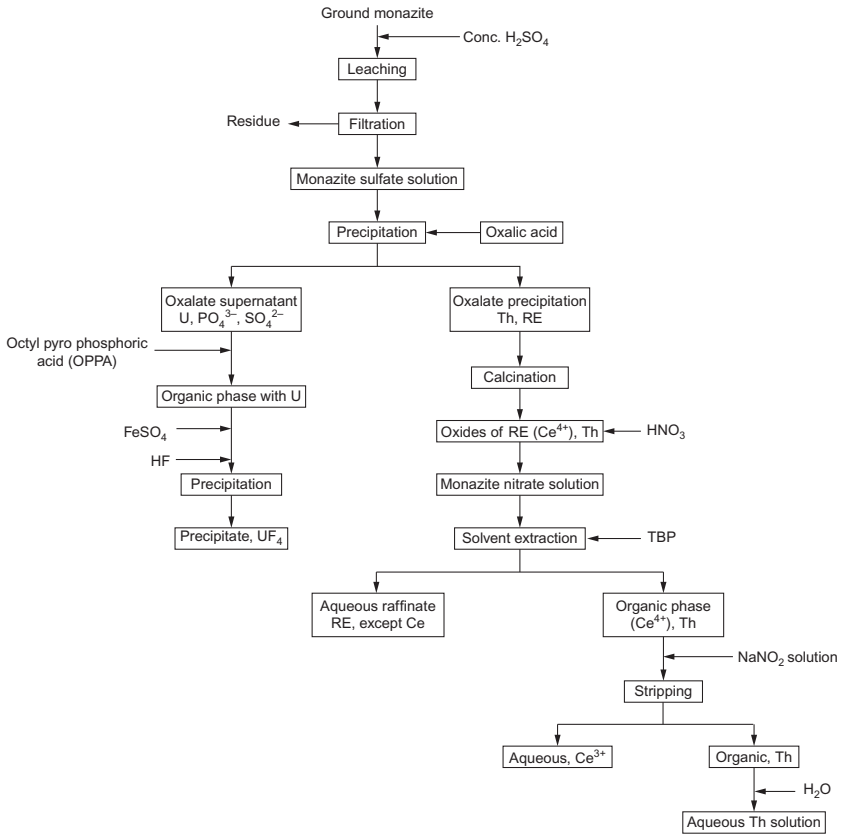
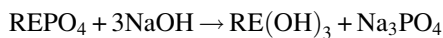


FIGURE 24 Flow sheet for the processing of monazite sand by digesting in sulfuric acid (Smutz, 1958).

method emerged in recent years. The treatment of monazite by various processes has been reviewed (Gupta and Krishnamurthy, 1992), see Fig. 25. Kim et al. reported in 2009, sulfuric acid leaching after mechanochemical treatment of beneficiated monazite (212 μm size) obtained from a beach sand deposit in Malaysia with sodium hydroxide at room temperature (Kim et al., 2009). The formation of RE hydroxides and sodium phosphate was found to be complete within 120 min of grinding according to the reaction below:



About 92.3% of P element was removed by washing. Subsequent leaching with 0.05 N sulfuric acid enabled to improve the yield of La, Nd, and Sm to more than 85%. The yields of both Ce and Pr were around 20%; and 70% remains undissolved since they are transformed into the oxides according to the reaction given below:

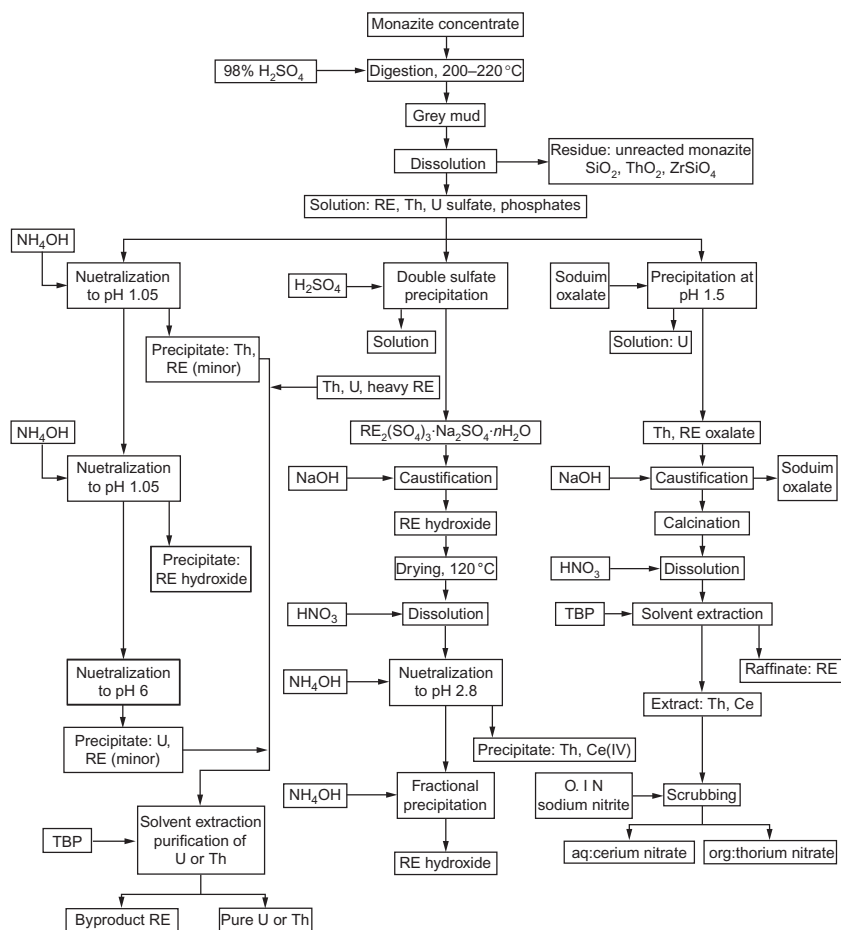
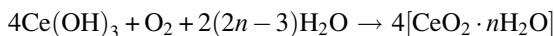


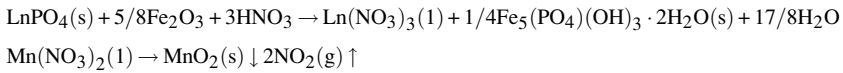
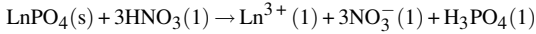
FIGURE 25 Flowchart of monazite processing by acid treatment. *Reproduced from Gupta and Krishnamurthy (1992), © 1992 W. S. Maney & Son Ltd.*



Thus, mechanochemical milling plays a significant role in achieving high recovery of REs (Kim et al., 2009).

Nitric acid was used for the dissolution of monazite and other associated metals from apatites (phosphorites) containing monazite (Aly and Mohammed, 1999; Jorjani et al., 2011). Nitric acid is more effective for leaching REs from phosphorites than sulfuric acid (Bunuş and Dumitrescu, 1992). In 2002, Gupta et al. reported the dissolution of monazite sand in concentrated HNO_3 with HF and HClO_4 in ratio 3:1.5:0.5 in a Teflon vessel for 24 h at 80 °C (Gupta et al., 2002).

Recently, [Kuzmin et al. \(2012\)](#) used nitric acid to leach the metals from ground RE ore (74 μm size) from Chuktukon deposit in East Siberia in a rotating autoclave. The ore contains 3–7% REO in phosphate form (monazite, turnerite, and florensite), Fe–Mn oxides, and 0.5–1% niobium oxide (chalcoclamprite). The leaching reactions of monazite and florensite with nitric acid are as follows:



Iron and phosphorus remain in the residue during the leaching process because of the formation of complex hydroxy ferric phosphates which are poorly soluble in nitric acid. In the temperature ranging from 180 to 220 $^\circ\text{C}$, RE recovery can reach 87–90%. The slurry is filtered to separate the cake containing the niobium concentrate for subsequent processing and the filtrate is treated with sodium carbonate to precipitate the RE concentrate for subsequent production of rare earth salts. Additionally, manganese is also recovered as pyrolusite ([Kuzmin et al., 2012](#)), see [Fig. 26](#).

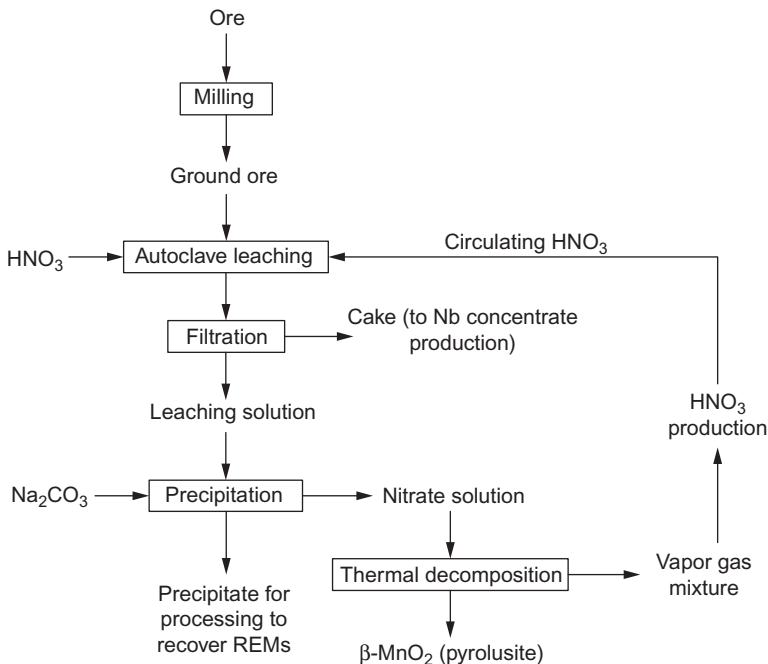
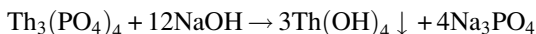


FIGURE 26 Schematic flow sheet for the breakdown of the Chuktukon rare earth ore. *Reproduced from Kuzmin et al. (2012), © 2012 Elsevier B.V.*

3.2.2 Alkali Method

Alkali treatment is also used for monazite dissolution. The phosphate in the ore is recovered as a marketable by-product, trisodium phosphate, by using caustic soda. The decomposition of the phosphates from monazite with caustic soda at high temperature and high pressure was elucidated and can be summarized with the following equations (da Costa Lauria and Rochedo, 2005; El-Nadi et al., 2005; Mirson, 1957):



The decomposition of monazite using caustic soda solution was processed in a heated ball mill by Mirson (1957). The decomposition of monazite at temperatures ranging from 140 to 200 °C as processed in Brazil includes the following sequence of operations: magnetic field separation, milling, alkaline treatment, trisodium phosphate filtration, and Th-U cake filtration (Ney et al., 1992). The alkali decomposition of monazite with hot concentrated 50–75% NaOH was also carried out at 150 °C in an autoclave (Fathi, 1997). In the 1980s, several authors treated monazite using 70% NaOH under pressure for 2 h at 150 °C to produce insoluble REs and Th hydroxides for subsequent processing (Hart and Levins, 1988; Mackey, 1986).

There are also many reports about alkali treatment of monazite obtained from different mines, for instance from Santo Amaro (Usina de Santo Amaro, USAM) in Brazil, see Fig. 27 (da Costa Lauria and Rochedo, 2005).

Da Costa and Rochedo also developed an economic method for the separation and purification of thorium and uranium from the hydroxide cake concentrate obtained from Egyptian monazite sands by alkali treatment (da Costa Lauria and Rochedo, 2005). Hydrometallurgical process of monazite for RE recovery by optimizing leaching conditions was achieved by a hot digestion method using NaOH (El-Nadi et al., 2005; Kim and Osseo-Asare, 2012). A modified flowchart of the alkaline digestion, leaching, and extraction of uranium from Egyptian monazite is presented in Fig. 28 (El-Nadi et al., 2005). Similarly, thorium was recovered from Egyptian monazite sand after alkaline treatment and leaching with alkaline carbonate solution (Ali et al., 2007). This process was further studied to accommodate various complex ores/concentrates. The treatment of Korean monazite concentrate using 50% NaOH (w/v) at 170 °C is also reported (Panda et al., 2014). In an alkaline treatment of Egyptian monazite in ball mill autoclaves, grinding, and decomposing of monazite take place simultaneously (Abdel-Rehim, 2002).

In 2006, de Vasconcellos et al. enriched yttrium from the RE concentrate produced industrially by chemical treatment of monazite sand in Sao Paulo, Brazil (de Vasconcellos et al., 2006). The yttrium concentrate was treated with 200 g/L ammonium carbonate for 10–30 min at room temperature to

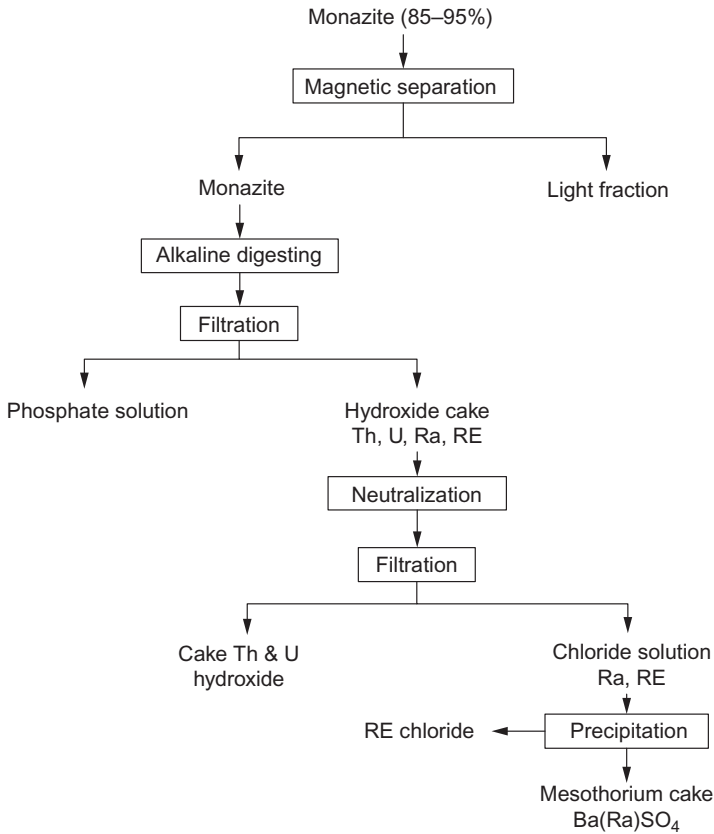


FIGURE 27 Basic steps for chemical processing of monazite at USAM. Reproduced from *da Costa Lauria and Rochedo (2005)*, © 2005 Oxford University Press.

dissolve yttrium along with other REs. Subsequently, cerium, praseodymium, and neodymium were selectively precipitated from the leachate by using hydrogen peroxide. Yttrium remained in the carbonate solution and was then recovered as the oxalate.

3.2.3 Recovery and Separation of the Metals from Leaching by Solvent Extraction

Solvent extraction is commonly used to recover the valuable elements from the monazite leachates. In 1959, Crouse and Brown reported the recovery of thorium, uranium, and rare earths from monazite sulfate liquors by an amine extractant (Crouse and Brown, 1959). Borrowman and Rosenbaum decomposed the monazite concentrate from the Wyoming ore by the sulfuric acid-curing method and separated Th and REEs by solvent extraction

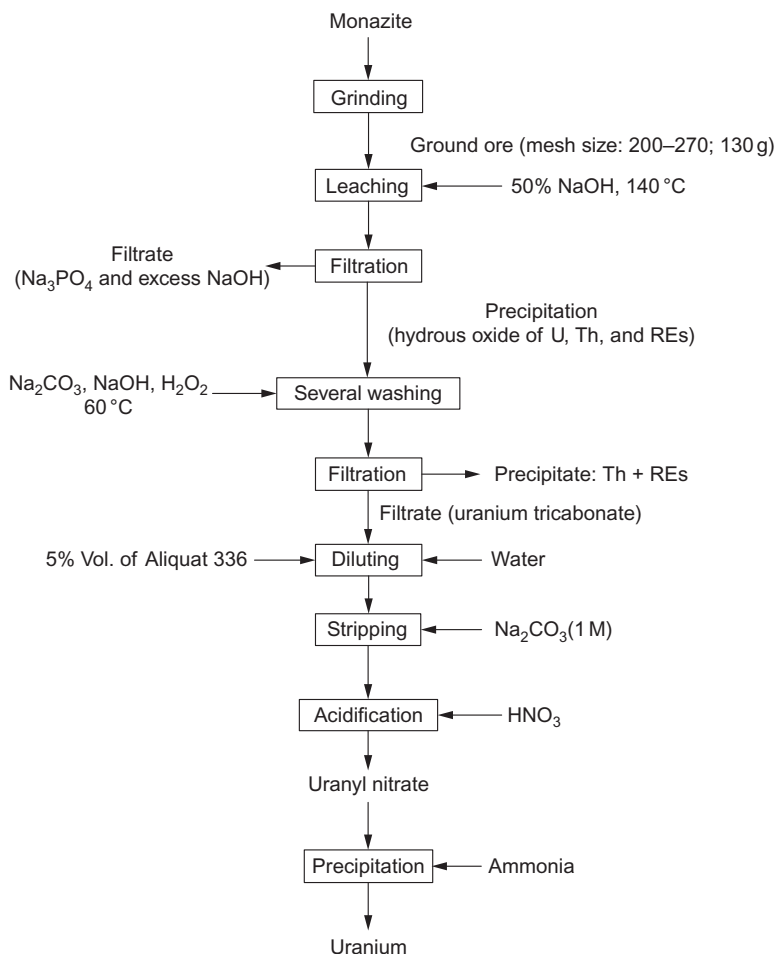


FIGURE 28 Modified flow sheet of alkaline digestion, leaching, and extraction of uranium from Egyptian monazite. Reproduced from *El-Nadi et al. (2005)*, © 2004 Elsevier B.V.

([Borrowman and Rosenbaum, 1961](#)). Barghusen and Smutz used tributylamine and di-*n*-octylamine (DOA) for the recovery of uranium and thorium from the sulfuric acid leachate of Egyptian monazite ([Barghusen and Smutz, 1958](#)). In 2002, Gupta et al. studied the separation of uranium, thorium, cerium, and yttrium by Cyanex 923 from the digested monazite leachate with a mixture of HNO₃, HF, and HClO₄ ([Gupta et al., 2002](#)). In 2007, Rabie applied di-2-ethylhexylphosphoric acid in kerosene for the separation of Sm, Eu, and Gd in mixed nitric acid–hydrochloric acid solution obtained by leaching the lanthanide hydroxide cake produced from monazite of the Egyptian beach black sand deposits after Ce-separation ([Rabie, 2007](#)).

3.3 Mixed Bastnäsite and Monazite Ores

3.3.1 Acidic Process

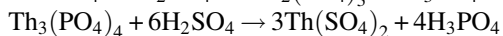
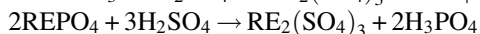
Baotou mixed rare earth ore is a peculiar and important resource in China; it consists in bastnäsite and monazite in ratios ranging from 9:1 to 1:1 and it is rich in light rare earths. The content of radioactive elements is much lower than in pure monazite and xenotime while the thorium content is slightly higher than that in pure bastnäsite (see Table 7).

The sulfate roasting process dealing with Baotou mixed rare earth concentrates and bastnäsite was developed in the 1970s. In this process, rare earth compounds in the ores are transformed into soluble sulfates while most non-rare earth compounds are insoluble in water, so that relatively pure rare earth

TABLE 7 Content of Rare Earth Elements in Various Ores (wt%) (Xu, 1995)

Single Rare Earth	Mixed Concentrate (Baotou, China)	Bastnäsite (Mountain Pass, USA)	Monazite (Mount Weld, Australia)	Xenotime (Malaysia)	Apatite (Soviet Union)
La ₂ O ₃	27.2169	32.2460	23.8980	1.2577	23.4949
CeO ₂	48.7302	49.1681	46.0259	3.1748	50.9055
Pr ₆ O ₁₁	5.1332	4.3461	5.0451	0.5001	5.3842
Nd ₂ O ₃	16.6303	12.0166	17.3836	1.6128	13.7053
Sm ₂ O ₃	1.2408	0.7901	2.5315	1.1563	2.4474
Eu ₂ O ₃	0.2071	0.1182	0.0531	0.0122	0.4895
Gd ₂ O ₃	0.4002	0.1662	1.4870	3.5197	1.3705
Tb ₄ O ₇	0.0290	0.0159	0.0354	0.9190	0.1468
Dy ₂ O ₃	0.0941	0.0312	0.6904	8.4391	0.2447
Ho ₂ O ₃	0.0200	0.0051	0.0531	2.0083	0.0490
Er ₂ O ₃	0.0260	0.0035	0.2124	6.5220	0.1468
Tm ₂ O ₃	0.0009	0.0009	0.0177	1.1360	0.0490
Yb ₂ O ₃	0.0021	0.0006	0.1239	6.8669	0.0490
Lu ₂ O ₃	0.0010	0.0001	0.0354	1.0021	0.0490
Y ₂ O ₃	0.2682	0.0914	2.4075	64.8730	1.4684
Total	100.0000	100.0000	100.0000	100.0000	100.0000

solutions are obtained after solid–liquid separation. The reaction mechanism can be expressed as follows:



There are three generations of acidic processes which were developed successively and widely applied for Baotou rare earth concentrates (Du et al., 2010; Huang et al., 2006). The first generation includes roasting with concentrated sulfuric acid at lower temperature, double salt precipitation, transformation with alkali, water washing, and selective hydrochloric acid leaching. Finally, rare earth chloride mixtures are obtained. The relationship between ore grade, acid/ore ratio, and decomposition rate is given in Table 8. The analysis results of rare earth double salt and aqueous leachates are given in Table 9. The flowchart of this process is shown in Fig. 29. The advantages, such as ease to control and operate and steady quality of the products, made this process more popular in the 1970s. However, there are many disadvantages for this process such as a long flow-sheet, too many solid–liquid

TABLE 8 Relationship Between Concentrate Grades, Acid/Ore Ratio and Decomposition Rate (Xu, 1995)

Name	Values				
Content of REO in concentrate (%)	22.16			33.28	
H ₂ SO ₄ /REO ratio	1.35	1.5	1.7	1.45	1.55
Decomposition rate (%)	85.8	93.1	96.7	89.2	96.7

TABLE 9 Analysis of Rare Earth Double Salts and Aqueous Leachates (Xu, 1995)

Name	REO	ThO ₂	Fe	CaO	Mn	P ₂ O ₅	F	H ₂ O	[H ⁺] (mol/L)
Double salts (%)	42.5	0.09	0.15			0.31		15	
	45.4	0.23	0.20	1.6		0.33		22	
Leachates (g/L)	0.13	0.021	21.4	0.55	2.28	11.2	0.23		1.45
	0.13	0.046	22.4		2.14	10.9	0.22		1.62

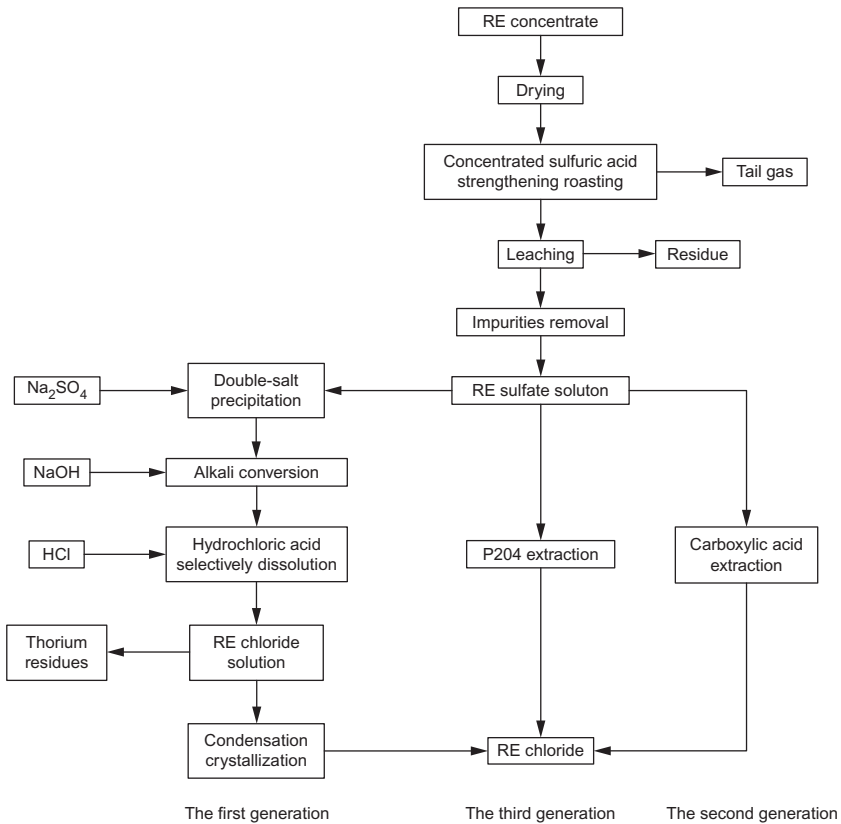


FIGURE 29 Flowchart of sulfuric acid roasting technology (Liu, 2010).

transfers, tedious removal of impurities, intensive labor, large amount of industrial wastewater, and tail gas. Importantly, the rare earth yield was too low.

In contrast to the first generation of the acidic process, the second generation used high temperature (800–900 °C) roasting with concentrated sulfuric acid, lime neutralization and purification, and extraction transformation by naphthenic acid. Chloride solutions of mixed rare earths were obtained for further separation of individual rare earths. The flowchart of this process is shown in Fig. 29. Because the impurity sulfates are gradually decomposed into insoluble substances at high temperature, the amount of the impurities in the leachate was greatly reduced. Compared with the first generation, this procedure has many advantages such as shorter processing time, only one solid–liquid separation, less damage to the equipment, higher recovery of rare earths, strong continuity, and adaptability for different grade of rare earth concentrates. The main impurities, including Fe, P, Th, and Ca, were concentrated into the leaching residue, easily amenable to further treatment and

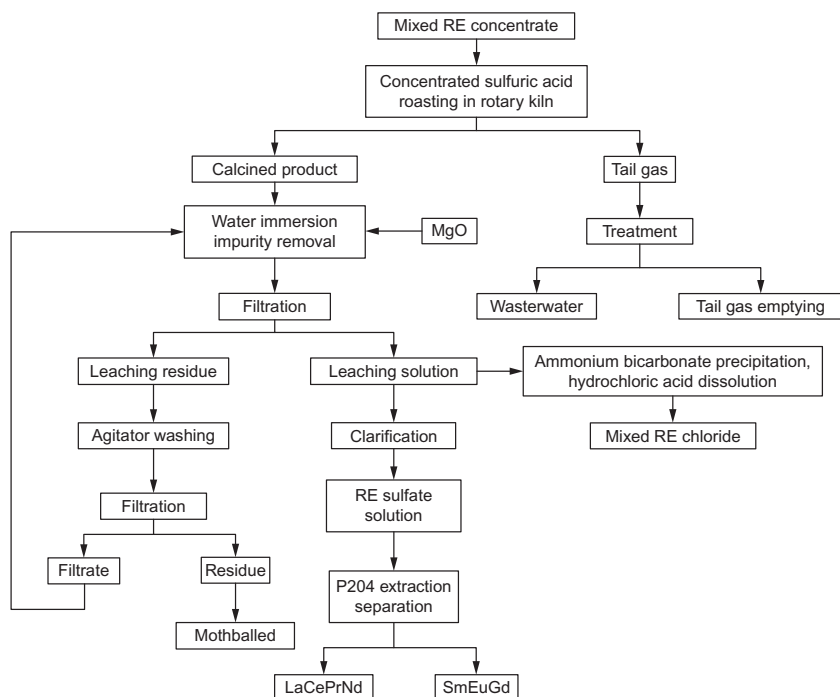


FIGURE 30 Flowchart of higher temperature strengthening roasting with concentrated sulfuric acid technology (the third generation) (Liu et al., 2012a).

radioactivity protection. But this method has also some shortcomings, for instance it needs large tail-gas treatment capacity and it requires of many different devices. In addition, recycling of the mixed acid is difficult.

The third generation of sulfuric acid process (Fig. 30) (Liu et al., 2012a) comprises the roasting with concentrated sulfuric acid in rotary kilns, water leaching, neutralizing, ammonium bicarbonate precipitation, removing impurities by acid dissolution, and finally preparing mixed rare earth chlorides (Wang et al., 2006b). The effect of acid/ore ratio and temperature on the ore decomposition is given in Table 10. This method has many advantages such as low requirement for the concentrate grade, continuous, and easy control of the industrial procedure, ease to produce in large scale, less reagent consumption, and reduced operation cost. On the other hand, the technology has also some disadvantages. For instance, it may cause radioactivity pollution because thorium in the mine is transformed into thorium pyrophosphate and is kept in the residue when leached, leading to huge volume of waste and unrecoverable thorium. Moreover, tail gasses and wastewater-containing sulfur and fluorine lead to environmental pollution. The roasting temperature reaches up to 800–900 °C and a large amount of sulfur dioxide, hydrogen fluoride, fluorosilicic acid gasses are given off. Fortunately, these compounds

TABLE 10 Effect of Acid/Ore Ratio and Temperature on the Ore Decomposition Rate (Xu, 1995)

Roasting Condition		Leachates							Decomposition Rate (%)
<i>Acid/Ore Ratio</i>	<i>Temperature (°C)</i>	<i>Fe (mg/L)</i>	<i>Fe/REO (%)</i>	<i>P (mg/L)</i>	<i>P/REO (%)</i>	<i>Th (mg/L)</i>	<i>Th/REO (%)</i>	<i>[H⁺] (mol/L)</i>	
1.5:1	450	490	0.72	340	0.50	53	0.078	0.31	98.64
1.5:1	500	48	0.057	38	0.045	7	0.0085	0.041	95.25
1.5:1	550	30	0.035	18	0.021	6	0.0071	0.019	94.4
1.5:1	600	41	0.057	15	0.021	6	0.0084	0.014	91.34
1.4:1	450	220	0.28	114	0.14	28	0.035	0.11	97.72
1.4:1	500	30	0.051	4	0.006	6	0.01	pH ₃	93.80

can be absorbed by water spray of the tail gasses, but it is costly and difficult to treat the mixed solution-containing sulfuric acid, hydrofluoric acid, and fluorosilicic acid. Currently, 90% of Baotou rare earth concentrates are treated by this concentrated sulfuric acid roasting process (Du et al., 2010). The comparison of the rare earth recovery rate between high temperature roasting process and low temperature roasting process is given in Table 11. Since then, many systematic works have been performed about mineral processing (Abreu and Morais, 2010; Alex et al., 1998; Goyne et al., 2010; Khanchi et al., 2014; Kuzmin et al., 2012; Moldoveanu and Papangelakis, 2013; Sapsford et al., 2012; Tassinari et al., 2001) and rare earth recovery (Preston et al., 1996a,b,c). Separation techniques that are currently employed for rare earth minerals have been recently reviewed (Binnemans et al., 2013; Jordens et al., 2013).

In order to solve the shortcoming of high temperature sulfuric acid roasting process and to avoid radioactive pollution to the environment and waste of thorium resource, a lot of new clean metallurgical separation technologies, such as low temperature sulfuric acid roasting combining thorium extraction by primary amine, fluorine fixing by magnesium oxide, chloride roasting, and calcium oxide roasting have been developed (Liao et al., 2013).

Baotou Rare Earth High-tech and Changchun Institute of Applied Chemistry (CIAC) from the Chinese Academy of Sciences have worked out a technique for the production of mixed rare earth chlorides by means of concentrate sulfuric acid static roasting at low temperature, extraction of thorium by primary amine N1923, and extraction transformation by P204 or saponified P507 (Fig. 31) (Huang et al., 2006).

In this technological process, concentrated sulfuric acid roasting is conducted at low temperature ($<300\text{ }^{\circ}\text{C}$), which not only leads to much higher decomposition yield of rare earth ores, but also keeps thorium under an easy-to-leach phosphate form. Moreover, concentrated sulfuric acid is stable at low temperature. The tail gas has a low temperature and it contains only hydrogen fluoride which is recovered by water spray or ammonia absorption to form ammonium fluoride or kryocide. The volume of ammonia-containing wastewater is greatly reduced if solvent extraction is used for rare earth transformation. However, there remain some problems. One lies in the difficulty of achieving continuous dynamic large-scale industrial production. Moreover, the P204 extractant has strong extractability for middle and heavy rare earth, which is adverse to the metal stripping and it causes the composition of rare earth chloride product to fluctuate.

Baotou Research Institute of Rare Earths further studied and modified this low temperature roasting process (Ma et al., 2003). Concentrated ores are roasted for 2 h with an ore/acid ratio ranging from 1:1.1 to 1:1.7 and roasting temperature ranging $150\text{--}330\text{ }^{\circ}\text{C}$ (with the optimum temperature being $180\text{--}220\text{ }^{\circ}\text{C}$). The leaching rate of rare earths and thorium is greater than 95%. The total specific radioactivity of the residue is not more than

TABLE 11 Comparison of the Rare Earth Recovery Rates Between High Temperature Roasting Process and Low Temperature Roasting Process, % (Xu, 1995)

Roasting Technology		Drying	H ₂ SO ₄ Roasting	Decomposition Rate of Ores	Subtotal	Leaching and Purification	Extraction Transformation	Iron Removal	Subtotal	Total
Strengthening roasting-extraction transformation		99	99	94	92.1	96	99	99.5	94.6	87
Roasting Technology	Drying	H ₂ SO ₄ Roasting	Decomposition Rate of Ores	Subtotal	Leaching	Double Salt Precipitation	Alkali Transformation	HCl Selective Dissolution	Subtotal	Total
Low temperature roasting	99	99	95–97	93.1–95	96–98	98	95	95–96	84.9–87.6	79–83

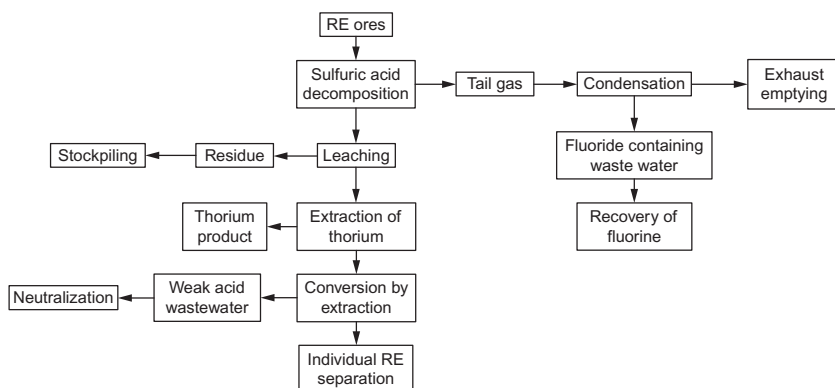


FIGURE 31 Flowchart of low temperature roasting with concentrated sulfuric acid technology (Wang and Wang, 2006).

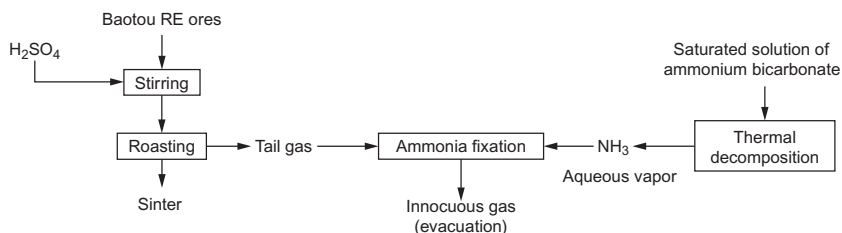


FIGURE 32 Flowchart of hydrogen fluoride recovery with ammonium bicarbonate decomposition in low temperature sulfuric acid roasting process (Hu, 2000).

7.4×10^4 Bq kg⁻¹. Rare earth and thorium products could be obtained by extracting the leachates.

China Nonferrous Engineering Design & Research Institute and Baoding Rare Earth Materials Factory also adopted this low temperature roasting process and introduced low temperature aging technology (Li et al., 2004a). The acidic concentrated ores are aged at 40–150 °C with an ore/acid ratio ranging from 1:1.1 to 1:1.7 and then roasted at 150–330 °C. The leaching yield of rare earth and thorium is greater than 95% and the total specific radioactivity of the residue does not exceed 1×10^3 Bq kg⁻¹. The recovery of fluorine reaches 95%. This method increases the dispersity and decomposition yield of the concentrated rare earth ores, prevents the attachment of roasted ore on kiln walls, reduces the acid consumption, and reaches continuum dynamic calcination successfully at low temperature. By adopting low temperature roasting process, the decomposition of sulfuric acid is suppressed. In order to meet the requirements of the national tail-gas emission standard, Baoding Rare Earth Materials Factory developed a technology for the absorption of hydrogen fluoride with ammonia obtained from the decomposition of ammonium bicarbonate (Hu, 1998). The main process flowchart is shown in Fig. 32.

Recently, YouYan Rare Earth New Materials Co., Ltd and Beijing General Research Institute for Nonferrous Metals investigated the effects of auxiliaries on the leaching of thorium during the concentrated sulfuric acid roasting process (Huang et al., 2005c). By adding appropriate auxiliaries containing iron and by roasting the ore at lower temperature, between 250 and 300 °C, most thorium is leached out and low radioactivity residues are produced. The leached thorium, iron, and phosphorus are precipitated by neutralizing the leachate and are therefore separated from rare earths. Thorium can be extracted after dissolving the precipitated residues. The leaching yield of rare earth may reach over 90%. This process recovers thorium and does not require changes to the current separation operations. The main process flowchart is shown in Fig. 33. They also developed an extraction and separation process for rare earth using mixed nonsaponified extractants from sulfuric acid and hydrochloric acid mixture media. This method applies the ore leachate as the feed and uses mixed nonsaponified extractants to conduct the extraction grouping and transformation of Nd/Sm or the extraction and separation of Ce/Pr–Nd/Sm in three distinct outlets. The sought products are obtained by one-step extraction, which greatly simplifies the technological process, eliminates the production of ammonia-nitrogen wastewater, and reduces the

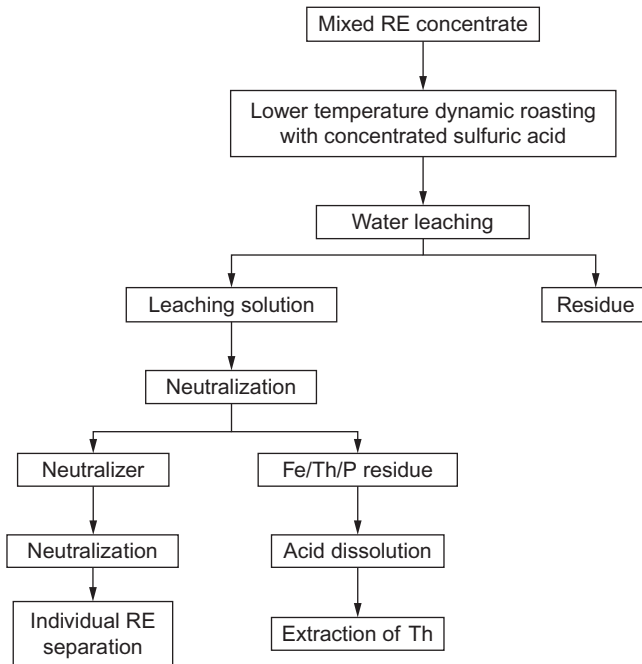


FIGURE 33 Flowchart of lower temperature dynamic roasting with concentrated sulfuric acid technology (Liu et al., 2012a,b).

consumption of chemicals by more than 20%. In addition, it overcomes many shortcomings such as easy emulsification of P204 extractant in low acidity, middle and heavy rare earth stripping difficulty, low concentration of rare earth in the loaded organic phase, and high acidity of the stripped solution. It is presently successfully applied in the improvement of Baotou rare earth concentrate technological process with ammonium bicarbonate decomposition (Huang et al., 2005a,b).

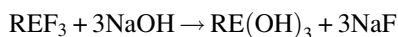
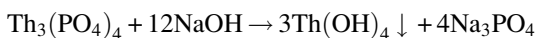
3.3.2 Alkaline Process

Caustic soda technology started in India. A factory was established in 1952 in Alwaye, which decomposed monazite with caustic soda and possessed a capability of treating 1500 t/a. After this successful operation, America, Brazil, Malaysia, and China adopted the same method to process monazite. In the 1970s, China began to use caustic soda method to deal with Baotou mixed monazite–bastnäsite concentrate (Du et al., 2010).

The caustic soda technology is simple, rapid and generates minimum amounts of three classical wastes: gasses, wastewater, and slag. The production of rare earth mixed concentrates using caustic soda method went through three phases: liquid caustic soda decomposition at atmospheric pressure, solid caustic soda electric field decomposition, and finally, concentrated alkali electric field heating decomposition.

3.3.2.1 Liquid Caustic Soda Decomposition at Atmospheric Pressure

This process is shown in Fig. 34. The concentrate containing about 70% REO is decomposed at 140 °C with 50% caustic soda according to the following reactions:



This method has the advantages of higher RE recovery yield, simple devices, and little pollution and it is still used as a traditional decomposing method. At present, many countries still use this method for dealing with monazite and other minerals. The shortcomings of this process are great energy consumption, great consuming of caustic soda, and the need for high-grade ore.

3.3.2.2 Solid Caustic Soda-Electric Field Decomposition

Traditional caustic soda decomposition of Baotou ore is commonly processed using a steam jacket to boil alkali. However, because Baotou ore contains fluorine, the tank wall becomes deeply corroded so that the service lifetime of the

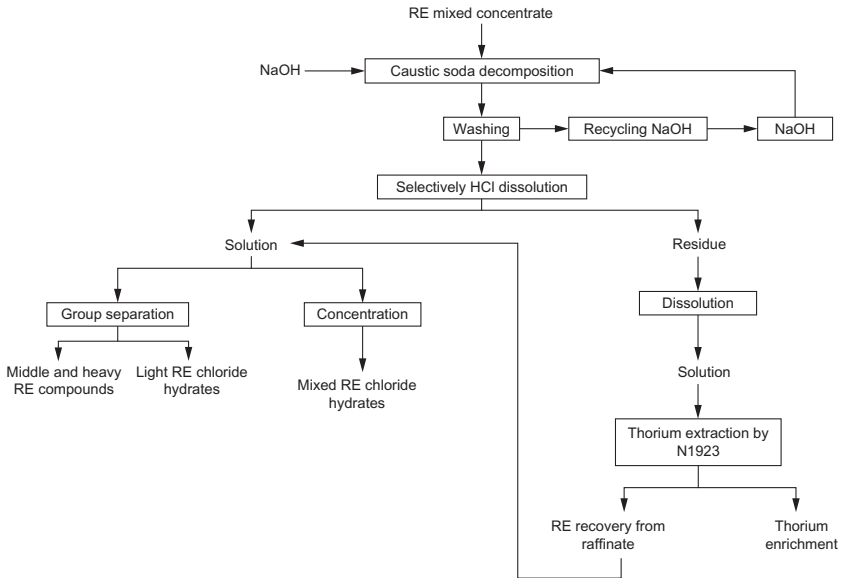


FIGURE 34 Flowchart of alkali decomposition of Baotou rare earth concentrates at atmospheric pressure (Liu, 2005).

equipment is short and the overall operation is quite insecure. The electric field decomposition method consists in mixing the concentrated ore containing 12–14% water with solid flake caustic soda in a given ratio and passing an electric charge after 10 min of stirring. Caustic soda plays the role of dispersant and electrolyte. This method uses ac power supply and the decomposing temperature is 200 °C. The equipment works for 15–20 min and the chemicals become orange, after which the decomposition reaction terminates.

Baotou Research Institute of Rare Earths studied the decomposition of rare earth concentrates by this method. Powdery solid caustic soda was mixed with the concentrates and then the ore was decomposed by resistors. The features of the method are shorter decomposition time (about 20 min) and less caustic soda consumption (80–90% of the concentrates). As a result of the inhomogeneous mixture of two solid phases and of local overheating decomposition, rare earths are however difficult to solubilize in acids and the process is labor intensive.

3.3.2.3 Concentrated Alkali-Electric Fields Decomposition

This technology is an improved NaOH digestion process realized in 1984, in which higher concentration of caustic soda solution is adopted. Due to higher boiling point of the caustic soda solution, the decomposing temperature can be raised and then the decomposition reactions are accelerated. Compared with liquid caustic soda decomposition at atmospheric pressure, this process has

the advantages of lower caustic soda consumption, shorter decomposition time, and lower energy consumption.

Han et al. found that the NaOH concentration, the ratio of the ore to the alkali, reaction time, and temperature have a great effect on the decomposition of rare earth minerals (Han et al., 1985). Firstly, the acid leaching yield of rare earths increases with increasing NaOH concentration while that of iron decreases. However, high concentration of NaOH leads to some problems so that the NaOH concentration is kept to a maximum of 80%. Secondly, the acid leaching rate of rare earths increases with the increasing decomposing temperature while the rate of residual phosphate and fluoride decreases. Thirdly, the acid leaching rate of rare earths increases with lengthening of the decomposing time while the rate of residual phosphate and fluoride decreases. Fourthly, the acid leaching rate of rare earths increases with increasing NaOH amount while the rate of residual phosphate and fluoride decreases. When the amount of NaOH reaches 80% of the ore, rare earths minerals can be decomposed completely. The optimum technological conditions for the decomposition of mixed rare earth minerals with concentrated NaOH solution are as follows: the amount of NaOH equal to 80–90% of the ores, concentration of NaOH equal to 70%, decomposing time of 30 min, and decomposition temperature higher than 160 °C.

3.3.2.4 Technological Innovation for the Caustic Soda Process

The high price of caustic soda decreases the economic benefits of this process when dealing with Baotou ore. So some innovations were made. The features of the improved process (Fig. 35) are as follows:

Firstly, a hydrochloric acid leaching operation was added to dissolve REFCO₃ as much as possible. Consequently, the amount of the concentrate for alkaline decomposition is greatly decreased. At the same time, acid leaching results in the reduction of particle size and in increasing the surface area, which benefits alkali decomposition and allows the consumption of caustic soda to decrease by 20%.

Secondly, the method dissolving the base cake in acid and neutralizing the resulting solution was adopted to prepare RECl₃ solutions. There are several advantages to this procedure. First of all, the process completely recovers rapidly the soluble part of the base cake. Then, the major ingredient of the residue insoluble in acid, i.e., mixed rare earth ores and monazite, can be recycled back to the alkali decomposition process. In addition, during each pass in the circulation, iron and thorium are discharged from the process, which make them not be accumulated and ensure smooth and environmental-friendly operation.

3.4 Ion-Adsorption Rare Earth Deposit

Unlike many rare earth minerals which appear in solid-state mineral phases, ion-adsorption rare earth deposits just exist as trivalent cations which are

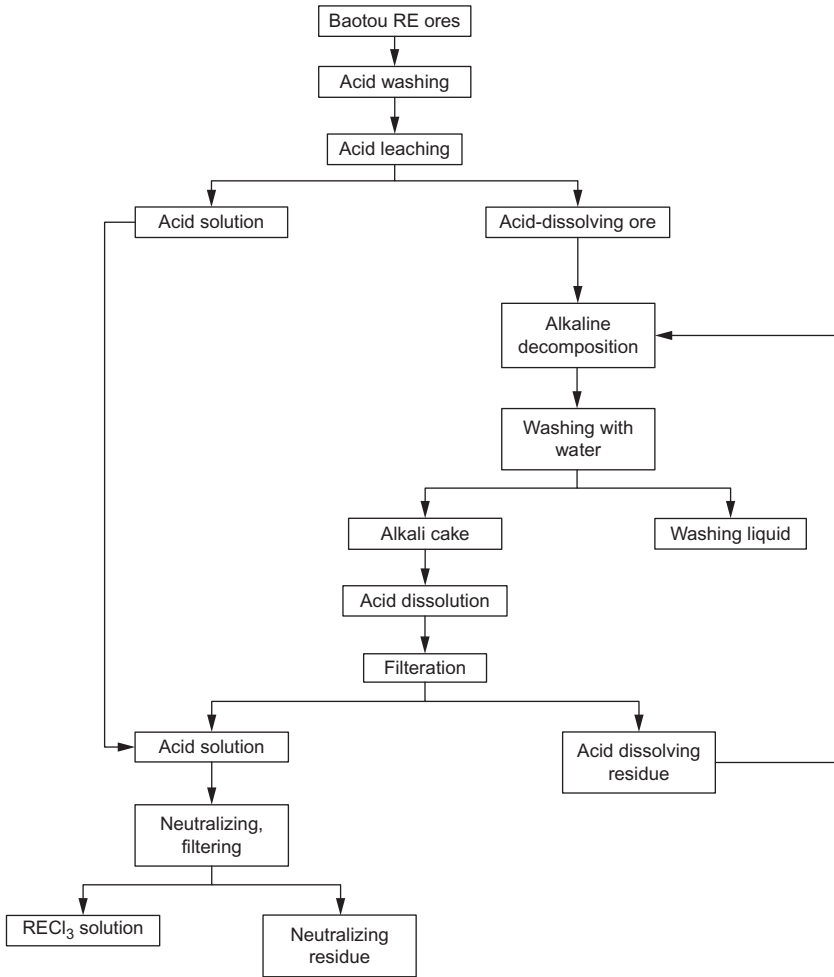
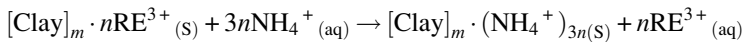


FIGURE 35 Flowchart of the upgraded technology of alkali decomposition of Baotou rare earth concentrates (Liu, 2010).

simply adsorbed onto clays. They cannot be enriched and recovered by the conventional methods such as gravity, magnetic separation, and flotation. However, REs in the ion-adsorption ore can be exchanged with other cations such as Na^+ , K^+ , H^+ , and NH_4^+ . The leaching equation can be written as:



where [Clay] means clay minerals, S indicates solid state, and aq refers to liquid solution. Based on the characteristics of ion-adsorption ores, three generations of leaching processes have been developed.

3.4.1 Indoor Barrel-Leaching Process (First Generation)

Ion-adsorption rare earth deposits were first discovered in China in 1970. It was found that trivalent rare earths in the ore can be leached by a solution of NaCl. The first leaching method that has been set up was based on this discovery. The main steps include removing the trees and vegetation, removing the topsoil, carrying ore to the plant, leaching with NaCl solution, precipitating the leached solution with oxalic acid, and obtaining oxalate precipitates (Fig. 36).

However, the process had several disadvantages: firstly, large amounts and high concentration (over 6%) of the leaching agent used and large amounts of waste solution-containing NaCl brought out which render the soil salty and compacted. Secondly, some impurities are leached out, which decreases the purity of REO obtained by calcination of the oxalates. Thirdly, the method is labor intensive with low production efficiency so that production costs are high (Luo et al., 2002; Zhou et al., 2012).

3.4.2 Pool-Leaching Process (Second Generation)

To solve these problems, Chinese researcher developed an improved leaching process for ion-adsorption ore (second generation), by which the ion-adsorption ores are put into an outdoor pond whose volume is about 10–20 m³ and to which the leaching agent is added. The leachate is then collected for further separation. The main process is shown in Fig. 37 (Tian et al., 2006). The

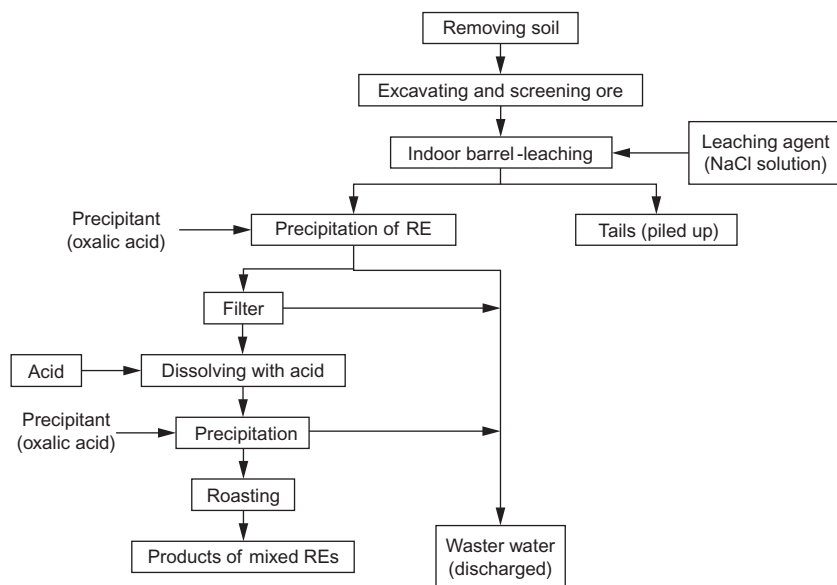


FIGURE 36 Indoor barrel-leaching process for ion-adsorption rare earth ores (Luo et al., 2002).

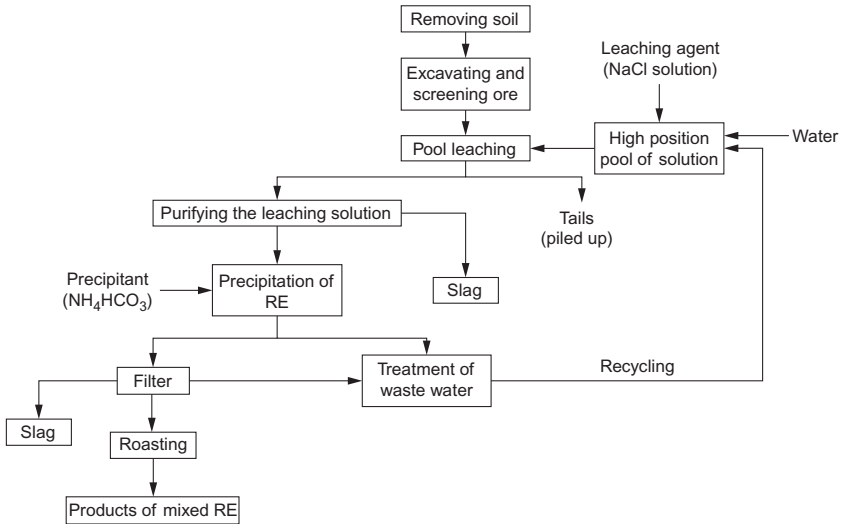


FIGURE 37 Pool-leaching process for ion-adsorption rare earth ores (Luo et al., 2002).

second-generation process uses $(\text{NH}_4)_2\text{SO}_4$ as the leaching agent to increase production efficiency. In addition, $(\text{NH}_4)_2\text{SO}_4$ is more environmentally friendly especially that its concentration is much smaller than in the first-generation process ($[(\text{NH}_4)_2\text{SO}_4] = 1\text{--}4\%$), which reduces soil pollution. Moreover, this leaching agent increases the selectivity for RE(III) ions and decreases the amount of impurities such as Ca^{2+} , Ba^{2+} in the leachate (Chi and Tian, 2008). However, there are still two shortcomings in this process (Chi and Tian, 2006). One is environmental in that 200–800 m² surface area of the mountain would be destroyed and 1200–1500 m³ of solid waste would be generated per each ton of rare earth produced. The second one lies in low resource utilization. Furthermore, the leaching agent may flow to one side of the ore only because of difficult permeability so that all the ore is not in contact with it (Luo et al., 2002). A solution is to use higher concentration of $(\text{NH}_4)_2\text{SO}_4$, low liquid/solid ratio and to add the leaching agent slowly to the ion-adsorption ore (Lu and Tian, 1994; Lu et al., 1997). With these improvements, the peak and average concentrations of RE(III) in the leached solution become higher than in classical process. Rao et al. adopted adding *Sesbania cannabina* into the leaching agent to decrease the resistance to permeation (Rao et al., 1995).

3.4.3 In Situ Leaching Process (Third Generation)

The *in situ* leaching process was developed in the mid-1980s and the first plant began operating in 1997. It does not require clearing of vegetation and forests or removal of the topsoil. Instead, leaching holes with diameter of ~0.8 m are drilled to a depth of 1.5–3 m and at distances of 2–3 m. The

leaching solution is generally 3–5% ammonium sulfate and the leaching takes 150–400 days. Obviously, removal of all the topsoil and vegetation above the ore deposits and subsequent filling of valleys with the tailings are avoided in this *in situ* process. The implementation of such operation requires comprehensive geological and geotechnical surveys to obtain information on the hydrogeological structure of the mining areas, ore characteristics, occurrence, composition, and grade, surrounding rock infiltration properties and to estimate the amount of ore. As a consequence, each mine requires a dedicated *in situ* leaching program based on the geological survey. Otherwise, the recovery of resources could be as low as 5% only (Fig. 38) (Zhao, 2000).

However, the practice of *in situ* leaching also generates some environmental concerns including groundwater contamination, mine collapses, and landslides. Ammonium sulfate contaminations of 3.5–4.0 g/L in groundwater, as well as elevated pH and increased concentrations of ammonium, sulfate, and rare earths (e.g., 80–160 mg/L of ammonium and 20 mg/L REs) in the surface water have been reported (Liu, 2002). The pH of the surface and ground waters near the *in situ* leaching sites of Longnan and Xunwu of Ganzhou region increased by 11% and 17.8% (Du, 2001). Water contamination owing to increased pH, electrical conductivity, total dissolved solids, sulfate, and other pollutants directly cause environmental degradation, including disruption of water and ion balances and stream biodiversity decline (Palmer et al., 2010). Sulfate pollution persists long after mining ceases through exacerbated nutrient pollution of downstream rivers and reservoirs and increased

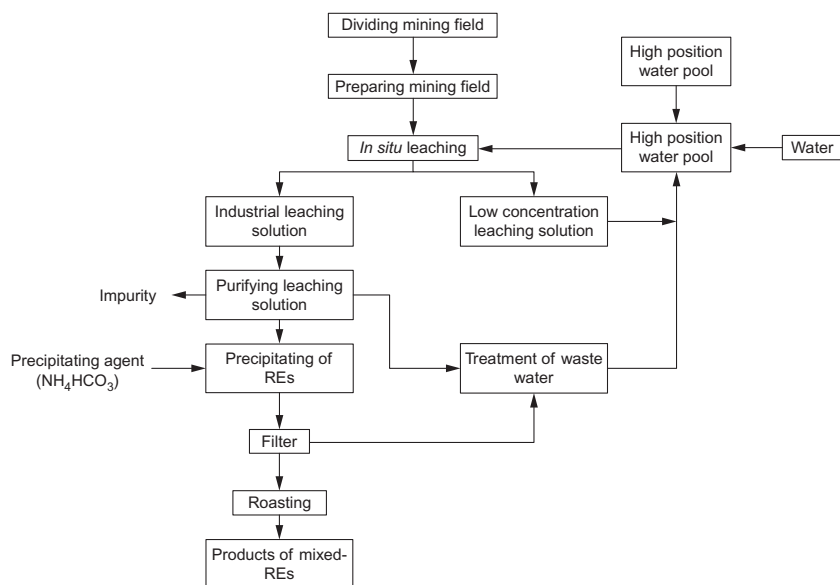


FIGURE 38 *In situ* leaching process for ion-adsorption ores (Zhao, 2000).

microbial production of hydrogen sulfide, an extremely toxic substance for many aquatic organisms and plants (Palmer et al., 2010). In addition, capillary forces surrounding the leaching holes attract high concentrations of leaching solution back to topsoil layer, destroying surface vegetation and plants, and making rehabilitation more difficult. More than 100 landslides reported in Ganzhou region were attributed to *in situ* mining and leaching practices, at significant human costs and losses of ion-adsorption rare earth resources. The reclamation of finished *in situ* leaching mines is conducted on a case-by-case basis and could be more costly than that of surface mining/heap leaching mines (Qiu et al., 2002).

Moldoveanu and Papangelakis studied the mechanism of *in situ* leaching and found that it is a complex heterogeneous process (Moldoveanu and Papangelakis, 2013). They also found that the exchange process was fast between NH_4^+ of the leaching agent and rare earth ions. Xunzhong et al. optimized the parameters of *in situ* leaching process through indoor simulation and confirmed the characteristics of the leaching poles which are affected by the leakage rate and the porosity of ore (Xunzhong et al., 1999). Increasing the quantity of leaching poles can increase the recovery yield of rare earths. Qiu et al. found that magnetic fields could change the physical and chemical properties of the leaching agent (such as the concentration of dissolved oxygen, surface tension, and penetration ability), which could decrease the amount of leaching agent needed and increase the leaching yield of rare earths (Qiu et al., 2002).

3.4.3.1 Purifying the Leachates

The main impurity elements in ion-adsorption rare earth ores are calcium, iron, and silicon. When the leaching agent is added into the ore, part of Ca^{2+} , Fe^{3+} , and Si^{4+} ions enter into the solution along with rare earth cations and co-precipitate with them; in turn, this decreases the crystallinity of the rare earth carbonates, renders the filtration more difficult, and affects the quality of the rare earth products.

Presently, the main method for purifying the leachate is neutralization hydrolysis, that is, adjusting the acidity of the solution to pH 4–5 by adding a neutralizer such as ammonia or ammonium bicarbonate. Most of the impurity ions are then precipitated in the form of hydroxides; aluminum and iron precipitate quantitatively, about 60% of calcium and silicon ions precipitate along with about 2–3% of rare earth ions (Luo et al., 2012; Qiu et al., 2012). Alternatively, sulfur-containing compounds can be used as precipitants (Li and Chi, 2000) or the impurity ions can be extracted with naphthenic acid (Han et al., 2013). Both methods remove impurity ions well and decrease the loss of rare earths.

3.4.3.2 Precipitation of Rare Earths

The concentration of rare earth ions in the purified solution is low (about 1–4 g/L); in addition, the leachate contains large amounts of ammonium ions

and a small amount of impurity ions. It is necessary therefore to separate rare earths by precipitation under the form of oxalate (Chi and Xu, 1999; Qiu et al., 2008). Although this process has many advantages such as good crystallinity and high purity of the oxalates, it is hampered by the high price of oxalic acid and its toxicity. In order to overcome these disadvantages, ammonium bicarbonate has been proposed as precipitation agent (Chi and Tian, 2006). Ammonium bicarbonate is cheap with its price being about $10\times$ less than oxalic acid and it is nontoxic. However, it is difficult to obtain crystalline precipitates and large amounts of water contained in the precipitates render it gelatinous. In order to obtain crystalline precipitates, crystal seeds, or surfactants have been added (Luo et al., 2013). The various factors governing rare earth precipitation have been investigated and it was found that crystalline precipitates of good quality can be obtained by carefully adjusting the concentration of rare earths, the amount of ammonium bicarbonate, the stirring, and aging times (Yu and Li, 1993). In addition, controlling the acidity of the solution improves the crystallinity of the precipitate (Chi et al., 2003).

Other methods were used as well, such as the resin slurry method (Wang and Ouyang, 1983). In this method, 732# resin was chosen as adsorbent and a $(\text{NH}_4)_2\text{SO}_4$ solution is used as leaching reagent. By adding rare earth ores and the 732# resin into the leaching reagent, the REs are leached and then adsorbed by the resin. Alternatively, a liquid membrane separation method (Wen et al., 1997) or precipitation with NaOH followed by flotation (Liu et al., 1992) were also used. All these methods yielded good rare earth separation efficiency. However, in terms of economy and environmental protection, they are not as suitable as ammonium bicarbonate precipitation. So, ammonium bicarbonate precipitation will continue to be the main method for separating rare earth from the leachate in the long run.

3.4.4 Separation of Individual Rare Earths from Mixed-Rare Earth Products

Solvent extraction has become the main method for obtaining pure individual rare earths. Figure 39 shows the classical extraction and separation process, which features three separation modules: countercurrent extraction (a), countercurrent washing (b), and countercurrent stripping (c) (Han, 2010).

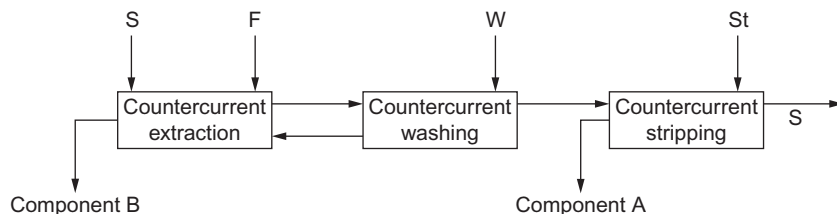


FIGURE 39 Traditional modules for rare earth extraction and separation. S, organic phase; F, feed; W, washing solution; St, stripping agent (Han, 2010).

Classical saponification of the organic phase usually uses $\text{NH}_3 \cdot \text{H}_2\text{O}$ or NaOH . However, the waste solution-containing high concentration of NH_4^+ is difficult to handle. On the other hand, NaOH is expensive and Na^+ creates difficulties in the separation of rare earths. Wang invented a new method of saponification using BaS as reagent (Wang, 2006), but the evolved H_2S gas is difficult to collect. Sun et al. used electrolysis extraction method for saponification, which generates H_2 gas also difficult to be collected (Sun et al., 1994). Hu proposed Ca^{2+} as saponification reagent (Hu, 2004) and this method is used in some factories. Calcium is a cheap saponification reagent which could cut the costs and also decrease the concentration of NH_4^+ in wastewater. But, there are some disadvantages such as large loss of organic phase and decreased purity of the rare earth products. Another method was processed with saponifying the organic phase by rare earths (Huang, 2003). Saponification of the organic phase with the raffinate of the separation tank has also been proposed (Zang and Qi, 1995). The main steps include saponification of the organic phase in 2–3 flow steps to reach a loading of the organic phase in the range 85–95%. The technology decreases the difficulty caused by extracting ions such as Na^+ , NH_4^+ , Ca^{2+} , and Al^{3+} ; it also decreases the quantity of interfering impurity ions; and increases the overall quality of the product.

Han introduced an organic phase continuous saponification technology which had been adopted by many separation factories (Han, 2010). The main steps include adding saponification agents into the outlet of the extraction tank or of the lower receiving slot of the organic phase. Practice has been proven that the saponification degree is stable and accurate, if the flows of alkali and organic phases are stable. After extraction, the loaded organic phase can be scrubbed with the rare earth solution (Huang, 2003). In a classical extraction and separation process, washing and stripping agents are added into the scrubbing and stripping sections, respectively. Presently, a new technology used in the industry relies on the same solution functioning as both washing and stripping solution; it is added into the stripping section at once. Part of the stripping solution is siphoned and used as washing liquid. The excess stripping solution is then used as the feed for the next stage. The technology has many advantages such as decreasing the consumption of acid and alkali (being only 3–5% of classical process), saving production costs, improving the rare earth concentration in the outgoing organic phase, increasing the distribution ratio of rare earths, and decreasing the volume of feed. Because part of the stripping liquor-containing components easy to be extracted is used as the washing solution, the easily extractable elements in the aqueous phase exchange with those difficult to be extracted in the organic phase in the scrubbing section so that separation is improved. In order to improve the stripping effect, the acid of the washing solution can be added into the stripping solution so that the acid concentration of this solution increases and the quantity of rare earths and iron in the organic phase decreases.

Furthermore, Long et al. came up with a new nonsaponification technology for the extraction and separation of REs from sulfate medium (Long et al., 2006). In this method, the organic phase is not saponified and heavier REs are extracted first. Individual rare earth separation is also processed with nonsaponified extractants such as P204 or P507.

3.5 Associated Rare Earth Resources and Recycled Resources

Xenotime, a phosphate ore, is one of the valuable mineral deposits of rare earths similar to monazite. The main characteristics of xenotime are listed below: (1) The content of yttrium is high while that of the light rare earths is low (Table 12). (2) The content of thorium is lower than that in monazite (Table 13). (3) The composition of tungsten-containing xenotime is very complicated. The content of tungsten is higher than that of rare earths and there are more impurities such as iron and silicon. But the contents of niobium, tantalum, beryllium, and niobium are lower. Consequently, the screening process is harder. (4) Generally, xenotime is more difficult to decompose than monazite. Several methods have been used, i.e., concentrated sulfuric acid, alkaline solution at elevated pressure, fusing with molten caustic soda, and mixing with sodium carbonate and roasting. The flow-sheets of these three typical processes are shown in Fig. 40 (Gupta and Krishnamurthy, 1992).

Because rare earths belong to strategic elements in view of their wide applications in high-technology products, their recycling either from industrial scrap (Tanaka et al., 2013) or from consumer products is an increasingly important issue for the engineers. Many technologies such as precipitation, filtration, liquid–liquid extraction, solid–liquid extraction, ion exchange, super critical extraction, biosorption (Das and Das, 2013), and electrowinning have been applied for the recycling of rare earths from the spent rare earth products such as luminescent materials and permanent magnetic materials.

Generally, a fluorescent lamp is covered with a thin layer of tricolor phosphors. To recover rare earths from end-of-life fluorescent lamps, they are commonly dismantled, crushed, leached with acid, and extracted and separated by solvent extraction methods (Fig. 41) (Wu et al., 2014). Such a procedure has been developed by Rabah (2008) (Fig. 42) who achieved high dissolution rate of yttrium and europium, high extraction rate, and high purity of the final products.

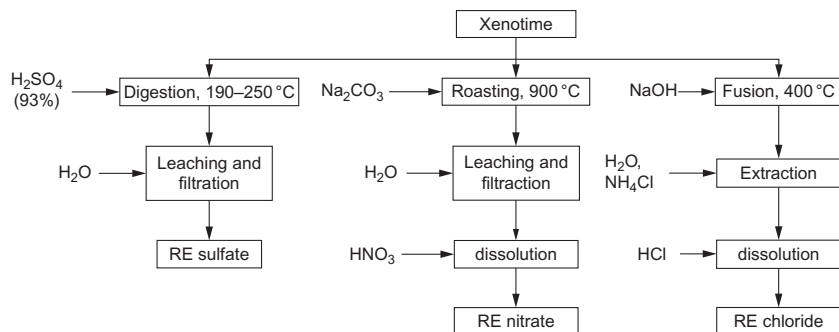
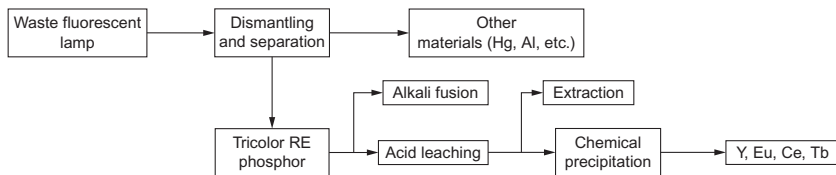
Other authors rely on a scheme implying liquid crushing—leaching by hydrochloric acid—precipitation of ammonia—solid–liquid separation by precipitation of oxalates to recycle yttrium from end-of-life fluorescent lamps as shown in the corresponding flow-sheet in Fig. 43 (Mei et al., 2009; Rao et al., 2009). Yang et al. investigated a recycling progress for the recovery of rare earths from phosphor powders by a two-step process, acid leaching and solvent extraction with ionic liquids (Yang et al., 2013) (Fig. 44). Alternatively, Wu et al. developed a “dry-wet” combining method of two hydrometallurgy steps as shown in Fig. 45 (Wu et al., 2014).

TABLE 12 Content of Rare Earth Elements in Xenotime, wt% (Xu, 1995)

Category of Ores	Y ₂ O ₃	La ₂ O ₃	CeO ₂	Pr ₆ O ₇	Nd ₂ O ₃	Sm ₂ O ₃	Eu ₂ O ₃	Gd ₂ O ₃
Xenotime	57.7	1.2	2.9	0.6	3.4	2.0	<0.2	4.9
Tungsten-containing xenotime	53.0	1.5	4.2	1.5	3.6	3.0	<0.1	5.8
Category of ores	Tb ₄ O ₇	Dy ₂ O ₃	Ho ₂ O ₃	Er ₂ O ₃	Tm ₂ O ₃	Yb ₂ O ₃	Lu ₂ O ₃	Total
Xenotime	1.2	8.8	2.5	5.4	1.7	5.8	1.7	100.0
Tungsten-containing xenotime	1.7	8.9	1.7	6.6	1.2	5.8	1.4	100.0

TABLE 13 Chemical Composition of Xenotime, wt% (Xu, 1995)

Category of Ores	REO	ThO ₂	U ₃ O ₈	P ₂ O ₅	Sc ₂ O ₃	WO ₃	BeO
Xenotime	55	1–2	0.8	26–30	0.05	15–25	0.2
Tungsten-containing xenotime	10–20	0.5–1	0.1	5–8			
Category of ores	Fe	Mn	CaO	SiO ₂	Al ₂ O ₃	Nb(Ta) ₂ O ₅	
Xenotime	0.5	1–4	1	3	0.2	0.5	
Tungsten-containing xenotime	10–20		1	3–30			

**FIGURE 40** Flow sheet of three typical processes dealing with xenotime. *Reproduced from Gupta and Krishnamurthy (1992), © 2015 W. S. Maney & Son Ltd.***FIGURE 41** Flow sheet of a typical recycling process for fluorescent lamps. *Reproduced from Wu et al. (2014), © 2014 Elsevier B.V.*

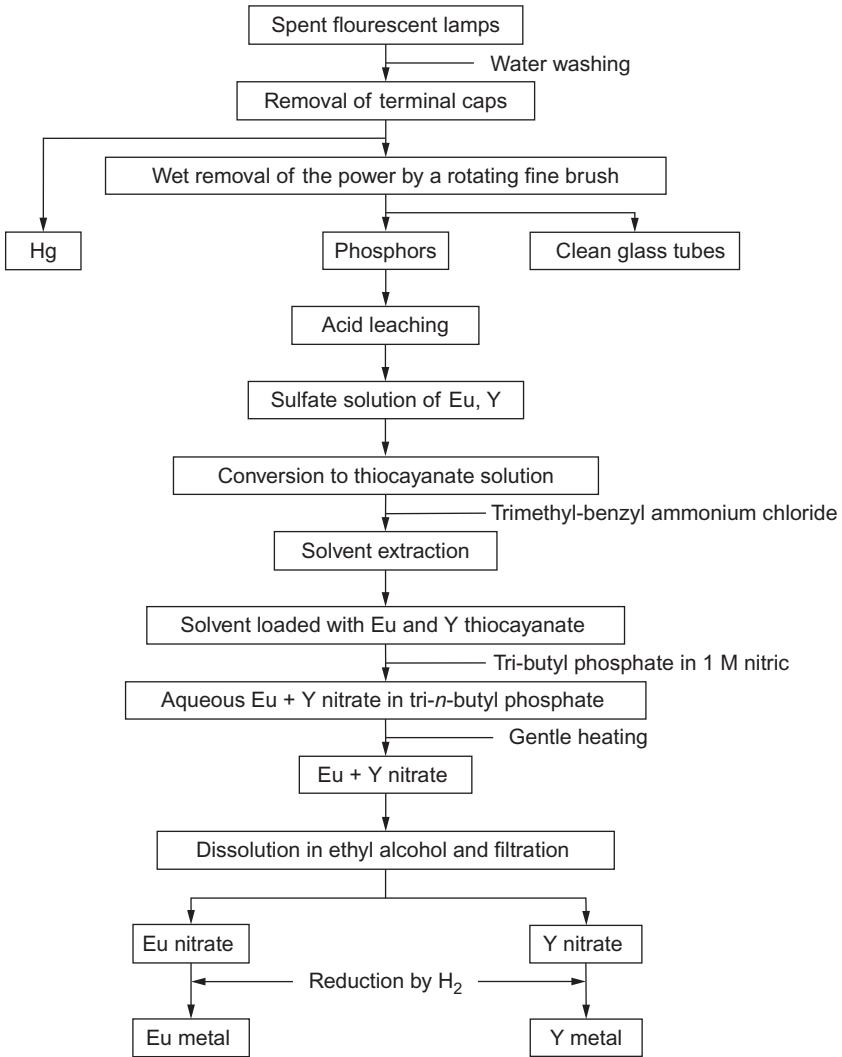


FIGURE 42 Flow sheet for the recovery of Y and Eu from end-of-life fluorescent lamps (Rabah, 2008).

Binnemans and Jones put forward three main options for recycling rare earths from end-of-life fluorescent lamps (Binnemans and Jones, 2014): (1) direct-use of lamp phosphor mixture; (2) separation of phosphor mixture into different phosphor components; and (3) recovery of the rare earth content to get pure products.

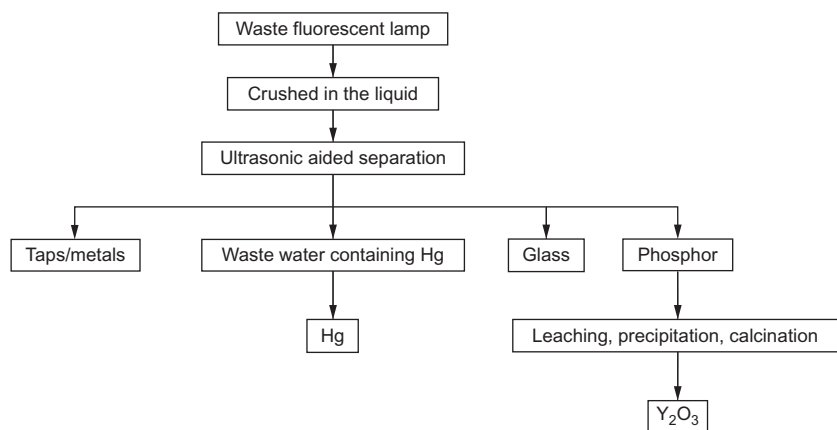


FIGURE 43 Recycling and innocuous process of end-of-life fluorescent lamps (Mei et al., 2009; Rao et al., 2009).

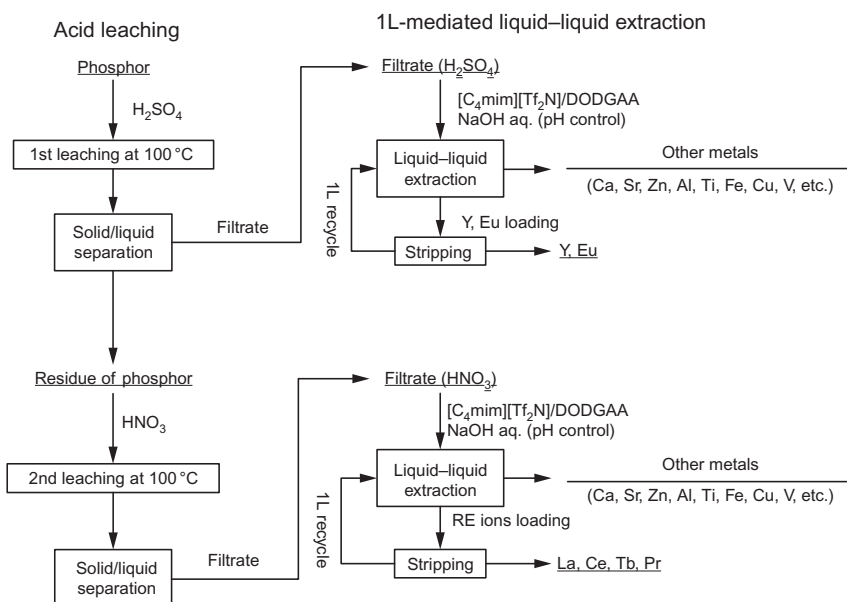


FIGURE 44 Conceptual flow sheet for recovery of rare earths from waste phosphor powders in spent fluorescent lamps by ionic liquid extraction. Reproduced from Yang et al. (2013), © 2013 Elsevier B.V.

The recycling of rare earths from spent NdFeB magnets is also attracting attention. As an example, a method was developed based on the selective extraction of REs from NdFeB scrap by molten chlorides (Fig. 46) (Zhong et al., 2014).

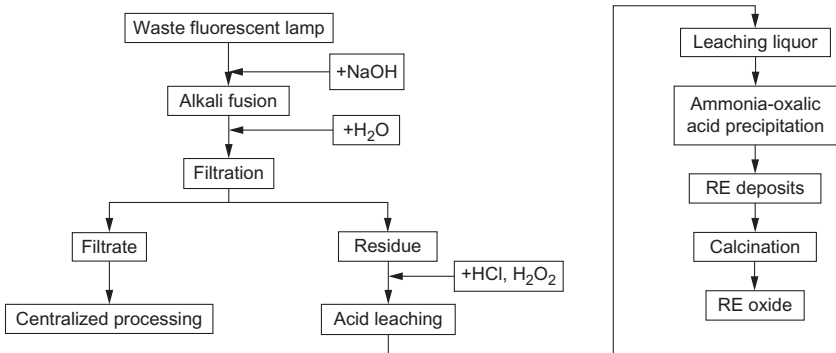


FIGURE 45 Flow sheet of “dry-wet” combining process. *Reproduced from Wu et al. (2014), © 2014 Elsevier B.V.*

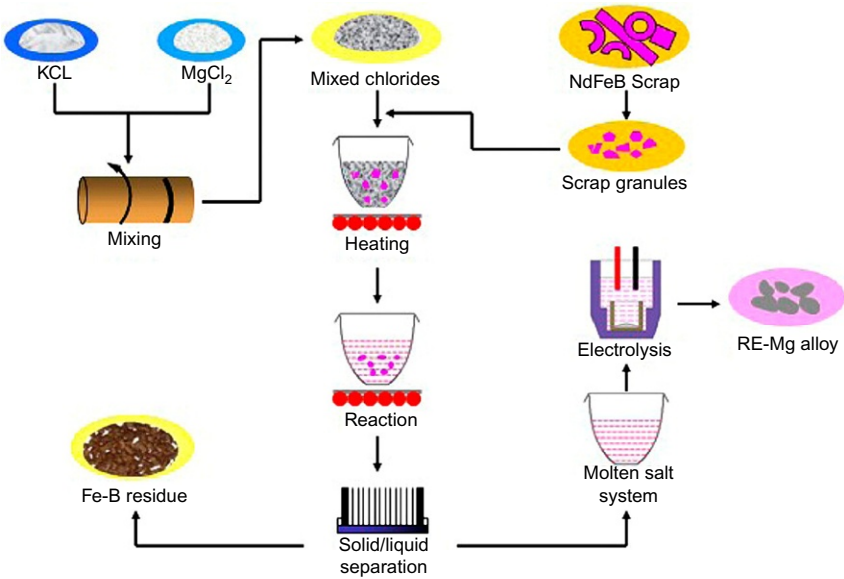


FIGURE 46 Illustration of flow sheet of RE recovery from NdFeB scraps using molten chlorides. *Reproduced from Zhong et al. (2014), © 2014 American Chemical Society.*

4 PREPARATION OF HIGH-PURITY RARE EARTHS AND THE ASSOCIATED ELEMENT THORIUM

4.1 High-purity Rare Earths

Currently, the dominant methods for the enrichment and recovery of lanthanides from acid leachates include fractional crystallization, precipitation (Quill and Salutsky, 1952), ion exchange (Zheng et al., 1995), and solvent

extraction (Huang, 2003; Kumari et al., 2015; Liao et al., 2006; Rollat et al., 1988; Xie et al., 2014). China first adopted the P350 (in kerosene)-RE(NO₃)₃-HNO₃ system to prepare high-purity lanthanum oxide, which increases the purity of La₂O₃ from ~50% to 99–99.99% with a yield of 99% after fractional extraction. After decades of industry practice, P507 proved to be superior for La₂O₃ preparation, with good extractability, high distribution ratio and recovery, and low cost. Li et al. presented a method of preparing high-purity lanthanum oxide containing low calcium by one-step extraction (Li et al., 2013a). Raw materials containing 99–99.5 wt% lanthanum are dissolved in hydrochloric acid and then extracted by saponified P507 in an 80-stage cascade extraction tank. The obtained lanthanum chloride (>99.9995% in purity) solution contains <30 ppm of calcium and <10 ppm of iron after 3 saponification stages, 18 calcium-washing stages, 31 extraction stages, 20 scrubbing stages, and 8 stripping and water-washing stages.

Although other methods, especially solvent extraction, can yield high-purity rare earth products, up to of 99.99–99.999%, ion exchange is still the main method for the preparation of high purity or ultra-pure rare earth products. Spedding and collaborators reported a series of works on the purification of rare earths by this method (Spedding and Powell, 1954a,b; Spedding et al., 1947a,b,c, 1950a,b, 1951). Cerium and yttrium with spectroscopy purity were obtained in macro quantities by adsorption on Amberlite IR-1 columns and elution with 5% citric acid-ammonium citrate solutions (Spedding et al., 1947b). The principles established for the separation and purification of cerium and yttrium have been applied to relatively large-scale separation of adjacent rare earths Pr and Nd in spectroscopically pure form. A series of columns can be used to further purify the rich fractions and higher yield of pure product can be obtained (Spedding et al., 1947a,c). The method has been further developed by several authors (Freiling and Bunney, 1954; Harris and Tompkins, 1947; Mayer and Freiling, 1953; Mayer and Tompkins, 1947; Tompkins and Mayer, 1947; Tompkins et al., 1947; Wish et al., 1954). By a process of elution from ion-exchange columns with complex-forming reagents, macroscopic amounts of cationic species can be separated from those in trace amounts (Tompkins et al., 1947). It is possible to get essentially complete separations between several REs of the cerium group (lanthanum, cerium, praseodymium, and neodymium) in a single adsorption–elution cycle and impurities represent less than 0.1% in content (Harris and Tompkins, 1947). Cation-exchange (Fitch and Russell, 1951) and anion-exchange methods (Faris and Warton, 1962; Fritz and Greene, 1964) have been widely applied in the separation of rare earths over the past century. More recently, Zheng et al. reported a novel industrial technology for producing REO of high purity (>99.99%) by temperature-pressurized ion-exchange displacement chromatography (Zheng et al., 1995) and found that the concentration of the complexing agent in the eluent can be several times higher than that used in the classical ion-exchange method if a given amount of buffer is present.

In the past decade, studies on the separation and purification of rare earths by ion-exchange chromatography have made great progress. Ludek et al. carried out separation of Ce (IV) from La (III) and Y (III) from 6 M nitric acid with PVP-based anion exchanger and gained Ce solutions of high purity (>99.97%) (Ludek et al., 2006). Wu presented a process for the preparation of laser crystal REO Ho_2O_3 , Er_2O_3 , Tm_2O_3 , Yb_2O_3 , and Lu_2O_3 with a purity >99.999% via microlevel exchange resin warming compression ion exchange (Wu, 2008). Other researchers studied the separation of holmium and lutetium by cation-exchange chromatography with *N*-hydroxyethylenediaminetriacetic acid (HEDTA)–citric acid system (Guo et al., 2009b; He et al., 2010). The separation efficiency increases with increasing acidity and column ratio (but it should not be more than 1:6); but this protocol requires a long separation time. The optimal processing conditions were determined as HEDTA concentration of 0.024 M, pH of 6.00 and a flow rate of 0.6 mL/min, column ratio of 1:6. Compared with the HEDTA system, the mixed HEDTA and citric acid (H_3Cit) system yields much higher separation degree and the elution rate decreases; separation of ytterbium (III) and lutetium (III) was carried out with this method for an equimolar mixture 0.02 M in HEDTA and H_3Cit . The progress of the separation and purification of heavy REs has been recently reviewed (Jiao et al., 2013).

4.2 Ultrapure Thorium

Thorium is an important associated element in rare earth ores and also an important nuclear fuel. The most efficient method to recover it from the rare earth sulfuric acid solutions is by solvent extraction with a primary amine extractant N1923. TBP is a traditional extractant for further purification of the extracted thorium. There are however some problems with TBP such as its high water-solubility and intricate extraction mechanism. Several extraction systems have been developed to overcome these difficulties.

Christensen and Prater invented a process to recover and purify thorium oxide from a thorium-loaded aqueous solution by liquid–liquid extraction (Christensen and Prater, 1960). The procedure includes: (1) leaching the ore material with hydrochloric acid; (2) extracting thorium with an organophosphate selected from the group consisting of mono-heptadecyl-orthophosphoric acid, 2,6,8-trimethylnonyl-orthophosphoric acid, 2-monotridecyl-orthophosphoric acid, and 5-ethylnonyl-orthophosphoric acid; (3) scrubbing the impurities by hydrochloric acid; (4) partially stripping thorium by sulfuric acid and complete stripping of thorium by an alkali carbonate solution; and (5) precipitating thorium with oxalic acid and calcinating it to thorium oxide. High-purity thorium (99.99%) is obtained. The main operating process flow path is shown in Fig. 47.

Our group has been studied the extraction behavior of thorium (IV) by DEHEHP from nitric acid medium and systematically investigated the key

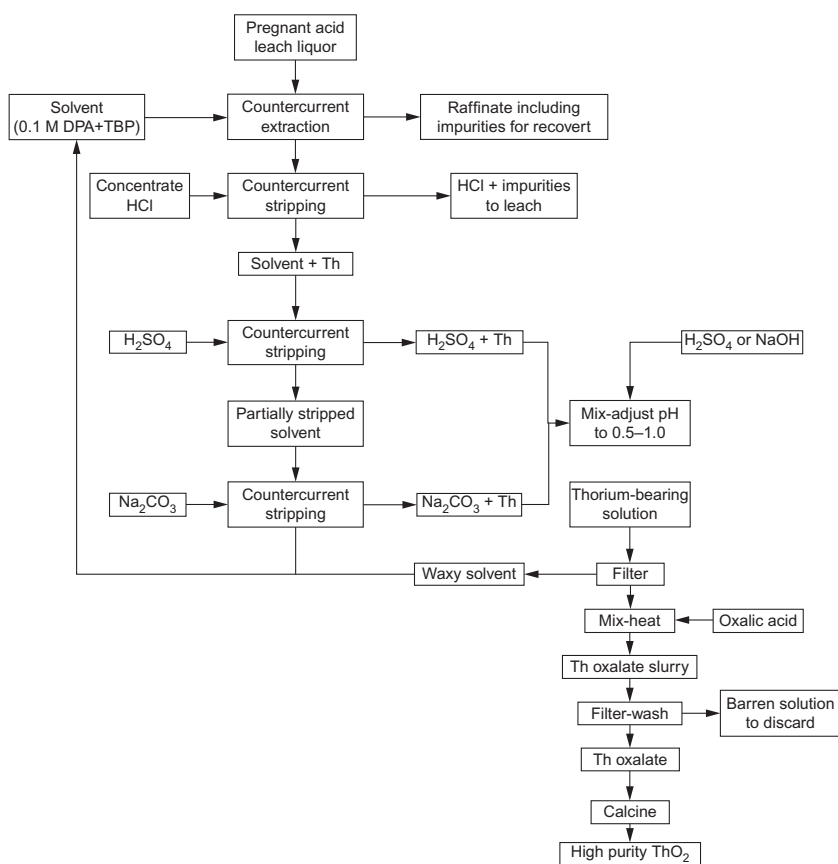


FIGURE 47 Flowchart of the liquid-liquid extraction process for the recovery of high-purity thorium oxide (Christensen and Prater, 1960).

parameters (Wang et al., 2013c), which allowed us to propose a possible extraction mechanism, confirm the nature of the extracted species, and calculate the extraction equilibrium constants and associated thermodynamic parameters. DEHEHP shows a high selectivity for tetravalent thorium over trivalent rare earths. Stripping tests indicate that thorium can be completely stripped by distilled water from the thorium-loaded organic phase. Furthermore, highly pure thorium (>99.999%) in 98% yield was obtained from thorium concentrates by designing a solvent extraction process with DEHEHP (Li et al., 2011, 2012, 2013b). The concentration and extractability of organic phases were stable during the fractional extraction process. This process is simple and consumes few reagents. Importantly, DEHEHP possesses lower aqueous solubility than TBP. In addition, trace impurities such as rare earths, iron, and aluminum present in the starting materials can be removed effectively. The flow-sheet is shown in Fig. 48.

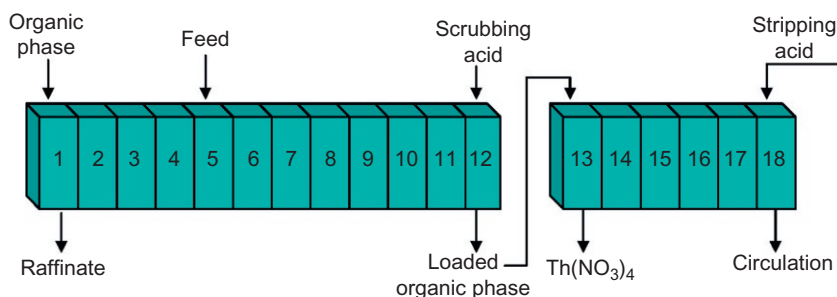


FIGURE 48 Flowchart of the process for thorium purification by DEHEHP. Reproduced from Wang et al. (2013c), © Springer International Publishing AG.

Liao et al. reported the separation and purification of thorium using calixarene derivatives as the extractants (Liao et al., 2012). These macrocycles have high separation coefficients for thorium and rare earths. They also overcome the shortcoming that extraction of thorium has to be processed at high acidity when a traditional extractant such as TBP is used. Thorium can be selectively recovered with 99.99% purity in hydrochloric acid, sulfuric acid, nitric acid, or mixed acid media.

Liao et al. have also described the preparation of high-purity thorium by using levestrel resin with DEHEHP (Liao et al., 2013). That is, the acidic solution-containing thorium flows through a separation column to obtain a thorium-loaded column which is then eluted with washing acid and desorbed with a stripping solution. The extraction resin is the effective constituent of the separation column, prepared with a phenylethylene–divinylbenzene macroporous copolymer and the neutral organophosphorus extractant DEHEHP combined *in situ*. The extraction resin is prepared in one step by using the emulsion *in situ* suspension polymerization method to treat the phenylethylene, divinylbenzene, and the neutral organophosphorus extractant; this prevents detachment of the neutral organophosphorus chelating agent from the phenylethylene–divinylbenzene copolymer. The extraction resin can be repeatedly used after desorption, which reduces the cost of separation and purification.

5 PREPARATION OF HIGH-PURITY RARE EARTH METALS

The methods for the preparation of high-purity rare earth metals include vacuum melting (VM) (Attia, 1990; Shi, 1987), vacuum distillation/sublimation (VD/SUB) (Ionov et al., 1996; Wu et al., 2013; Zhang et al., 2007a), fused-salt reduction (Alexis et al., 1975; Daane and Spedding, 1953; Spedding et al., 1952), solid-state electro-transport (Isshiki, 1996; Tian et al., 2014), plasma melting (PM) (Li et al., 2013c), electrolytic refining (ER) (Edward, 1970; Nagai et al., 1978), and fused-salt extraction (FE) (Li et al., 2004b).

5.1 Vacuum Melting

This method mainly targets at the purification of rare earth metals with low vapor pressure, such as Y, Sc, La, Ce, Pr, Nd, Gd, Tb, and Lu. Generally, the sample is heated with vacuum arc or electron beam and the volatile impurities are removed under the conditions of pressure $<1.33 \times 10^{-4}$ Pa and temperature in the range of 1450–1900 °C. The impurities, especially the volatile ones, having high vapor pressure such as alkali metals, alkaline-earth metals, have an excellent purifying effect.

5.2 Vacuum Distillation/Sublimation

This method purifies rare earth metals under high vacuum on the basis of different vapor pressure for each element. Heavy rare earth metals (Sm, Eu, Dy, Ho, Er, Tm, and Yb) and Sc have enough high vapor pressure and a large difference of vapor pressure with impurities, so it is suitable to use VD to purify these metals. This purification method has some advantages, such as high throughput capacity and it is widely applied in industrial production. Many researchers employed VD to purify La, Ce, Pr, Nd, Gd, Tb, Dy, Ho, Er, Lu, Sc, and Y; and discussed the factors affecting the purification of rare earth metals by VD (Cheng et al., 2011; Ionov et al., 1996; Jiang et al., 2003; Lei and Liu, 2000, 2001; Li and Liu, 2000; Li et al., 2002; Pang et al., 2008, 2013; Wang et al., 2010b; Yang et al., 2005; Zhang et al., 2007b, 2014b,c). The purity of the rare earth metals is greater than 99.9%, among which the purity of praseodymium achieved 99.995% or more under a vacuum of $\sim 2.0 \times 10^{-4}$ Pa. The contents of main impurities in the starting material and in vacuum-distilled praseodymium are given in Table 14 (Zhang et al., 2014b).

5.3 CaF₂ Fused-Salt Deoxidation

This technology utilizes Ca/CaO equilibrium in the fused calcium halide salt system to obtain a lower oxygen potential than that in simply sealed system, thus provides a lower deoxidation limitation. CaO generated at the surface of the metals dissolves in CaF₂ fused salt continuously during deoxidation, and its activity is less than unity before reaching its solubility. Thus, this technology can only remove small amounts of oxygen, because the effectiveness of deoxidation decreases with the increase of O²⁻ ions in the flux. Deoxidation of Dy₂O₃ in CaF₂ fused salt can be conducted in a CaF₂ flux (Liu et al., 2003; Yun et al., 2006). Direct reaction of Dy₂O₃ with anhydrous HF was carried out in a nickel boat inside a fluorination furnace. The crude Dy was made by Ca thermal reduction of anhydrous DyF₃ and then was purified by FE. The obtained dysprosium metal has purity larger than 99.9%, in which the contents of O and F are lower than 0.02%. Other halogens (Daane and Spedding, 1953; Spedding et al., 1952) and alkaline metals (Yu, 2001) have also been used in this technology.

TABLE 14 Content (ppm Weight) of Impurities in Pr Before and After Vacuum Distillation

Impurity Element in Pr	Before Vacuum Distillation (ppm w)	After Vacuum Distillation (ppm w)
C	83	15
N	50	<10
O	1600	370
S	<10	<10
Mg	670	<0.05
Al	34	1.7
Si	5.7	<0.05
Ca	8200	1.1
Ti	14	0.05
Cr	0.32	0.36
Mn	26	2.1
Fe	6.5	14
Co	0.03	0.02
Ni	12	0.71
Cu	0.8	1.3
Zn	4.7	<0.05
Nb	<0.05	<0.05
Mo	1.9	<0.1
Cd	<0.5	<0.05
Sn	<0.1	<0.05
Ta	84	<5
W	1600	<0.05
Pb	0.8	0.1
Pt	84	<0.1
La	2.8	<0.5
Ce	0.22	<0.5
Nd	0.21	<0.5
Sm	0.07	0.17

Continued

TABLE 14 Content (ppm Weight) of Impurities in Pr Before and After Vacuum Distillation—cont'd

Impurity Element in Pr	Before Vacuum Distillation (ppm w)	After Vacuum Distillation (ppm w)
Eu	<0.05	<0.01
Gd	0.12	2.4
Tb	0.89	<1
Dy	1.2	0.62
Ho	3.3	0.63
Er	1.5	0.29
Tm	0.5	0.84
Yb	<0.05	<0.01
Lu	0.08	<0.01
Y	5.3	0.26
Sc	0.07	<0.01
Total	<12504.76	<439.74

Reproduced from Zhang et al. (2014b), © 2013 Elsevier Ltd.

5.4 Solid-State Electro-Transport

This method passes direct current into solid-state rare earth metals to transport the impurities. Gerardin observed the electro-transport phenomenon during his work on Pb–Sn liquid alloy in 1861, while the solid-state electro-transport phenomenon was not discovered until 1930s. Fort et al. carried out an experiment by using solid-state electro-transport (SSE) to purify dysprosium from a feed with 99.9% purity and found that a high temperature, short-time run gives enhanced purification when compared with a low temperature, long-time run (Fort et al., 1995). Two major impurities, i.e., O and C, were more remarkable. The analysis results for the starting metal and the anode and cathode position of both runs after SSE is given in Table 15. Interstitial impurities such as H, C, N, and O embedded within the lattice of rare earth metals can be significantly removed by SSE leading to purities >99.99%. But SSE has shortcomings, such as costly equipment, complicated operation, high requirements for the material purity, long refining time, and low production efficiency.

TABLE 15 Analysis Results for the Start Metal and for the Anode and Cathode Position of Both Runs After SSE (Fort et al., 1995)

Impurity	Start Metal	Low Temperature Run		High Temperature Run	
		Cathode	Anode	Cathode	Anode
H	242 (1.5)	48 (0.3)	226 (1.4)	145 (0.9)	129 (0.8)
C	44 (3.3)	62 (4.6)	70 (5.2)	43 (3.2)	130 (9.6)
N	3 (0.3)	4.8 (0.4)	9.1 (0.8)	3.8 (0.3)	14 (1.2)
O	330 (33)	250 (25)	180 (18)	130 (13)	730 (72)
F	42 (4.9)	2.8 (0.3)	11 (1.3)	2.4 (0.3)	15 (1.8)
Al	9.1 (1.5)	15 (2.5)	11 (1.8)	14 (2.3)	13 (2.2)
Si	6.4 (1.1)	8.4 (1.5)	7.6 (1.3)	14 (2.4)	7.6 (1.3)
Cl	2.3 (0.5)	4.7 (1)	1.1 (0.2)	8.1 (1.8)	5.4 (1.2)
Sc	1.7 (0.5)	2.2 (0.6)	1.1 (0.3)	2.2 (0.6)	1.4 (0.4)
Ti	0.2 (0.1)	0.6 (0.2)	0.6 (0.2)	2.3 (0.7)	0.8 (0.2)
Cr	5.8 (1.9)	0.4 (0.1)	7.6 (2.4)	0.8 (0.2)	5.3 (1.7)
Fe	4.2 (1.5)	0.4 (0.1)	7.6 (2.6)	0.1 (0.04)	11 (3.8)
Ni	0.5 (0.2)	0.2 (0.1)	6.1 (2.2)	0.3 (0.1)	6.1 (2.2)
Cu	26 (10)	63 (25)	1.4 (0.6)	49 (19)	2.5 (1)
Ho	2.3 (2.3)	2.9 (2.9)	2.3 (2.3)	2.3 (2.3)	2.2 (2.2)
Total	732 (63)	478 (65)	556 (41)	425 (47)	1079 (102)
Overall	99.93 at.%	99.95 at.%	99.94 at.%	99.96 at.%	99.89 at.%
Purity	99.993 wt%	99.993 wt%	99.996 wt%	99.995 wt%	99.989 wt%

Values are in ppm with ppm weight in parentheses. Only elements with concentrations greater than 1 ppm are given.

Reproduced from Fort et al. (1995), © 1995 Published by Elsevier B.V.

5.5 Plasma Melting

This method takes advantage of the ultra-high temperature of the plasma (usually 2000–5000 K) and the effective control of the atmosphere inside the furnace. Carbon, nitrogen, and oxygen can be removed from crude metals by adopting (H₂+Ar) mixture as the plasma gas. Li et al. presented a method to prepare high-purity gadolinium by hydrogen plasma electric arc melting

technology (Li et al., 2013c). The procedure includes (1) introducing Gd, Ti (both >99.7% in purity) in the high-vacuum ($<10^{-5}$ Torr) arc melting furnace and vacuum pumping; (2) introducing high-purity argon (>99.999%) into the vacuum chamber where titanium melts first while gadolinium melts gradually; (3) introducing a mixture of hydrogen (>99.999%) and argon (>99.999%) in a volume ratio <1:10) into the vacuum chamber; (4) moving slowly the electrode about 2–4 mm above the sample; (5) overturning the sample several times to ensure uniform melting; and (6) introducing again high-purity argon (>99.999%) to replace the furnace inside atmosphere and overturning the sample several times. This technique removes oxygen lowering its initial content of 162.5–55 ppm.

5.6 Electrolytic Refining

ER is conducted in the selected electrolytic molten salt system; the anode is the rare earth metal or alloy to be purified, and the cathode is a simple rare earth metal or tungsten. During the purification process anodic rare earth metals fused into the molten salt under ionic form and then deposited on the cathode (Nagai et al., 1978). For instance, electro-purification of crude gadolinium was realized by using a LiCl-LiF-GdF₃ electrolyte and the best conditions include a molten salt composition of 77.6 wt.% LiCl, 11.2 wt% LiF, 11.2 wt% GdF₃, 700 °C, and an electrolysis current of 600 mA. Deposition on the cathode must be performed with great attention and the electrolyte salts must be pure. The removal of any adhering salt is a crucial condition. Complete separation of the cathodic metals and the molten salts adhering to it is rather difficult. The temperature of the electro-refining process, the amount of the deposit, and the purity of the molten salts represent crucial parameters.

5.7 Fused-Salt Extraction

Low content of oxygen in rare earth metals can be removed effectively by FE method with rare earth fluoride as extracted agent (Li et al., 2004b). An appropriate amount of rare earth fluoride is added according to the desired product quality. The oxygen existing in crude metals, whether under free state or combined such as in REO, rare earth oxyfluorides or calcium oxide, is well extracted by the rare earth fluorides and rare earth metals with low oxygen content can be obtained.

6 SUMMARY AND PERSPECTIVE

In this chapter, the progress on extraction and separation technologies for rare earths is reviewed with respect to bastnäsite, monazite, mixed rare earth ores, and other rare earth resources. The present technology and hydrometallurgical

processes for rare earths satisfy the technical needs for the recovery and separation of rare earths at industrial scale. However, for meeting increasingly stringent environmental regulations, key research directions in rare earth separation, purification, and recovery should be as follows.

Firstly, novel extractants for the extraction and separation of rare earths should be exploited. The P=O bond of organophosphorus extractants has strong polarity, which allows one to design extractants with better suited steric and electronic effects. At present, the nonpolar groups of the organophosphorus extractants are mostly two or three identical, unsubstituted alkyl groups. These structural characteristics prevent to dramatically change the nature of the molecular structure and to adjust electronic effect and steric effects of presently available organophosphorus extractants. For example, due to similar ionic radii of rare earths, the commercial currently available organophosphorus extractants such as D₂EHPA, HEHEHP, and Cyanex 272 do not generate large separation coefficient for these elements. Therefore, the design and synthesis of organophosphorus extractants with novel structural features, such as asymmetry (the molecule has different nonpolar groups), cyclic structure (cyclic substituent or two substituents on the phosphorus forming a ring), and bearing alkyl chains decorated with other substituents (hydroxyl, halogen-, nitrogen-, and sulfur-containing groups), may become the main direction of future research. For example, in our group, a new organophosphorus extractant containing a nitrogen substituent (named Cextrant 230) has been synthesized and successfully used for the extraction and separation of Ce(IV), F, and Th(IV) from sulfuric leachates of Bastnäsite.

A second emphasis would be to develop high-efficiency prepreparation technology for rare earth ores. A good technology should comprehensively recover all of the valuable elements from rare earth ores. It would give out less emission of noxious gasses, liquid, and solid wastes, decrease the extraction and separation costs, and improve resource utilization. Some new technologies have already emerged for the separation of rare earths, such as molecular recognition technology (MRT). Ucore Rare Metals Inc. applied MRT to generate heavy rare earth concentrates with purity >99%. One of the significant advantages of MRT is that the separation process does not use any solvent or hazardous chemicals. The other is the highly selective recovery of high-purity rare earths.

Finally, it is also important to combine the study on the separation of rare earths and the preparation of rare earth compounds with specific properties. The continuous development of high technology requires increasing demands for high-purity rare earth products. This translates in higher requirements with respect to the impurity content of rare earth products and to their physical and/or chemical properties. Therefore, integrating studies on the separation of rare earths and the preparation of targeted rare earth compounds will be beneficial to both fields; in particular this would decrease the cost of the whole process from mining to the consumer products. Furthermore, improving the level of automatic control of rare earth separation processes as well as

ensuring a constant quality of rare earth products is also important. Much attention should be put on the preparation of target compounds for the manufacture of phosphors, laser crystals, functional ceramics, cocatalysts, and among others.

ACKNOWLEDGMENTS

We thank Mr. Shengting Kuang, Ms. Youcai Lu, Ms. Meixuan Cao, Mr. Jun Miao, Ms. Haiqin Wei, Ms. Yanling Li, and other group members for the reference collection. This work was supported by 973 program (2012CBA01206), the National Natural Science Foundation of China (No. 21221061, 51222404), and the strategic priority research program of CAS (XDA02030100).

REFERENCES

- Abdel-Rehim, A.M., 2002. An innovative method for processing Egyptian monazite. *Hydrometallurgy* 67, 9–17.
- Abreu, R.D., Morais, C.A., 2010. Purification of rare earth elements from monazite sulphuric acid leach liquor and the production of high-purity ceric oxide. *Miner. Eng.* 23, 536–540.
- Alex, P., Suri, A.K., Gupta, C.K., 1998. Processing of xenotime concentrate. *Hydrometallurgy* 50, 331–338.
- Alexis, A.P., Antoine, P.R., Claude, R.A., 1975. Production of metals and metal alloys of high purity. US Patent 3909247.
- Ali, A., El-Nadi, Y., Daoud, J., Aly, H., 2007. Recovery of thorium (IV) from leached monazite solutions using counter-current extraction. *Int. J. Miner. Process.* 81, 217–223.
- Aly, M.M., Mohammed, N.A., 1999. Recovery of lanthanides from Abu Tartur phosphate rock, Egypt. *Hydrometallurgy* 52, 199–206.
- Attia, Y.A., 1990. Extraction and refining of high purity terbium metal from rare earth resources. *Miner. Process. Extr. Metall. Rev.* 7, 95–114.
- Barghusen, J., Smutz, M., 1958. Processing of monazite sands. *Ind. Eng. Chem.* 50, 1754–1755.
- Binnemans, K., Jones, P.T., 2014. Perspectives for the recovery of rare earths from end-of-life fluorescent lamps. *J. Rare Earths* 32, 195–200.
- Binnemans, K., Jones, P.T., Blanpain, B., Van Gerven, T., Yang, Y., Walton, A., Buchert, M., 2013. Recycling of rare earths: a critical review. *J. Clean. Prod.* 51, 1–22.
- Borrowman, S.R., Rosenbaum, J., 1961. Recovery of Thorium from a Wyoming Ore. Bureau of Mines. Salt Lake City Metallurgy Research Center, Washington.
- Bunuş, F., Dumitrescu, R., 1992. Simultaneous extraction of rare earth elements and uranium from phosphoric acid. *Hydrometallurgy* 28, 331–338.
- Chen, J., Liu, J., 1992. Synergistic extraction of Lutetium(III) by the ternary system of PMAP-TTA-DMHMP. (*Xitu Chin. Rare Earths*), 13, 1–6.
- Chen, Y., Li, R., Chen, G., 1981. Separation of Sc and Th by solvent extraction. *Chin. J. Rare Met.*, 6, 82–83.
- Chen, L., Bao, B., Qian, H., Li, Y., 1984. Separation of Th, Pa and U by DMHMP column extraction chromatography. *J. Nucl. Radiochem.* 4, 010.
- Chen, H., Zhao, H., Chen, J., Liu, J., 1997. Studies of synergistic extraction of Lutetium(III) by the quaternary system of PMAP-TTA-PMBP-DMHMP. *J. Inner Mongolia Teachers' College for Nationalities*, 12, 57–60.

- Cheng, W., Li, Z., Chen, D., Pang, S., Wang, Z., Wang, X., 2011. Preparation of high purity lanthanum by combined method of lithium-thermal reduction and vacuum distillation. *Xiyou Jinshu (Chin. J. Rare Met.)*, 35, 781–785.
- Cheng, F., Wu, S., Liu, Y., Wang, S., Zhang, B., Liao, C., Yan, C., 2014a. Minimum amount of extracting solvent for AB/BC countercurrent separation using aqueous feed. *Sep. Purif. Technol.* 131, 8–13.
- Cheng, F., Wu, S., Wang, S., Zhang, B., Liu, Y., Liao, C., Yan, C., 2014b. Minimum amount of extracting solvent of (A1A2... At-1)/(A2A3... At) separation when using non-barren extracting solvent. *Chin. J. Chem.* 32, 1022–1028.
- Cheng, F., Wu, S., Zhang, B., Liu, Y., Wang, S., Liao, C., Yan, C., 2014c. Minimum amount of extracting solvent of AB/BC countercurrent extraction separation using organic feed. *J. Rare Earths* 32, 439–444.
- Cheng, F., Wu, S., Zhang, B., Liu, Y., Wang, S., Liao, C., Yan, C., 2015. Minimum amount of extracting solvent of two-component extraction separation in a complex feeding pattern. *Sep. Purif. Technol.* 142, 162–167.
- Cherkasov, R., Garifzyanov, A., Leont'ev, S., Davletshin, R., Koshkin, S., 2009a. Extraction of scandium ions by new aminophosphinyl extractants. *Russ. J. Gen. Chem.* 79, 2599–2605.
- Cherkasov, R., Garifzyanov, A., Talan, A., Davletshin, R., Kurnosova, N., 2009b. Synthesis of new liophilic functionalized aminomethylphosphine oxides and their acid–base and membrane transport properties toward acidic substrates. *Russ. J. Gen. Chem.* 79, 1835–1849.
- Cherkasov, R., Garifzyanov, A., Bazanova, E., Davletshin, R., Leont'eva, S., 2012. Liquid extraction of some rare earth elements with aminomethylphosphine oxides. *Russ. J. Gen. Chem.* 82, 33–42.
- Chi, R., Tian, J., 2006. *Chemical and Metallurgy of Weathered Crust Elution-Deposited Rare Earth Ore*. Science Press, Beijing.
- Chi, R., Tian, J., 2008. *Weathered Crust Elution Deposited Rare Earth Ores*. Nova Science Publishers, New York.
- Chi, R.A., Xu, Z., 1999. A solution chemistry approach to the study of rare earth element precipitation by oxalic acid. *Metall. Mater. Trans. B* 30, 189–195.
- Chi, R., Zhou, Z., Xu, Z., Hu, Y., Zhu, G., Xu, S., 2003. Solution-chemistry analysis of ammonium bicarbonate consumption in rare-earth-element precipitation. *Metall. Mater. Trans. B* 34, 611–617.
- Choi, S.Y., Nguyen, V.T., Lee, J.C., Kang, H., Pandey, B., 2014. Liquid–liquid extraction of Cd (II) from pure and Ni/Cd acidic chloride media using Cyanex 921: a selective treatment of hazardous leachate of spent Ni–Cd batteries. *J. Hazard. Mater.* 278, 258–266.
- Christensen, C.C., Prater, J.D., 1960. Liquid–liquid extraction process for the recovery of high purity thorium oxide. US Patent 2945742.
- Crouse, D.J., Brown, K.B., 1959. The amex process for extracting thorium ores with alkyl amines. *Ind. Eng. Chem.* 51, 1461–1464.
- Daane, A., Spedding, F., 1953. Preparation of yttrium and some heavy rare earth metals. *J. Electrochem. Soc.* 100, 442–444.
- da Costa Lauria, D., Rochedo, E.R., 2005. The legacy of monazite processing in Brazil. *Radiat. Prot. Dosimetry* 114, 546–550.
- Das, N., Das, D., 2013. Recovery of rare earth metals through biosorption: an overview. *J. Rare Earths* 31, 933–943.
- de Vasconcellos, M.E., da Rocha, S.M.R., Pedreira, W.R., da S. Queiroz, C.A., Abrão, A., 2006. Enrichment of yttrium from rare earth concentrate by ammonium carbonate leaching and peroxide precipitation. *J. Alloys Compd.* 418, 200–203.

- Du, W., 2001. The impact of in-situ leaching on natural environment of ion-type rare earth mine. *Jiangxi Nonferrous Met.* 15, 41–44 (in Chinese).
- Du, C., Li, M., Liu, Z., Chang, H., Hu, Y., 2010. Present situation and suggestions for treatment of Baotou's rare earth concentrate. *Hydrometall. China* 1, 002.
- Edward Jr, M., 1970. Method for the production of samarium alloys. US Patent 3524800.
- El Dessouky, S., El-Nadi, Y., Ahmed, I., Saad, E., Daoud, J., 2008. Solvent extraction separation of Zn(II), Fe(II), Fe(III) and Cd(II) using tributylphosphate and Cyanex 921 in kerosene from chloride medium. *Chem. Eng. Process. Process Intensif.* 47, 177–183.
- El-Nadi, Y., Daoud, J., Aly, H., 2005. Modified leaching and extraction of uranium from hydrous oxide cake of Egyptian monazite. *Int. J. Miner. Process.* 76, 101–110.
- Faris, J.P., Warton, J.W., 1962. Anion exchange resin separation of the rare earths, yttrium, and scandium in nitric acid–methanol mixtures. *Anal. Chem.* 34, 1077–1080.
- Fathi, H., 1997. *Handbook of Extractive Metallurgy*. Wiley-VCH, Weinheim.
- Fitch, F., Russell, D., 1951. The separation of the rare earths by ion-exchange procedures. *Can. J. Chem.* 29, 363–371.
- Fort, D., Pecharsky, V.K., Gschneidner, K.A., 1995. Solid state electrotransport purification of dysprosium. *J. Alloys Compd.* 226, 190–196.
- Freiderich, J.W., Stankovich, J.J., Luo, H., Dai, S., Moyer, B.A., 2015. Dissolution of the rare-earth mineral bastnaesite by acidic amide ionic liquid for recovery of critical materials. *Eur. J. Inorg. Chem.* 2015, 4354–4361.
- Freiling, E.C., Bunney, L.R., 1954. Ion exchange as a separations method. VII. Near optimum conditions for the separation of fission product rare earths with lactic acid eluant at 87°. *J. Am. Chem. Soc.* 76, 1021–1022.
- Fritz, J.S., Greene, R.G., 1964. Separation of rare earths from other metal ions by anion exchange. *Anal. Chem.* 36, 1095–1097.
- Goyne, K.W., Brantley, S.L., Chorover, J., 2010. Rare earth element release from phosphate minerals in the presence of organic acids. *Chem. Geol.* 278, 1–14.
- Guo, X.L., Guo, Q., 1996. A method of extraction Ce(IV) from leaching solution directly. CN Patent 1114365.
- Guo, G., Luo, M., Xu, J., 2009a. Recent progress of primary amine N1923 research. *Fujian Anal. Test.* 18, 31–34.
- Guo, W., He, H., Jia, S., Wu, B., 2009b. Separation of holmium and lutecium by ion exchange chromatography with HEDTA system. *Mater. Sci. Eng. Powder Metall.* 3, 014.
- Gupta, C., Krishnamurthy, N., 1992. Extractive metallurgy of rare earths. *Int. Mater. Rev.* 37, 197–248.
- Gupta, B., Malik, P., Deep, A., 2002. Extraction of uranium, thorium and lanthanides using Cyanex 923: their separations and recovery from monazite. *J. Radioanal. Nucl. Chem.* 251, 451–456.
- Han, Q., 2010. The present situation analysis of rare earth extraction separation technology. *Hunan Nonferrous Met.* 26, 24–27.
- Han, X., Li, L., Chang, S., Liu, X., Xu, B., 1985. Study on the rare earth ore decomposition with concentrated NaOH. *Xitu (Chin. Rare Earths)*, 3, 39–44.
- Han, Q., Liu, Z., Yang, J., Li, J., 2013. A new technology for aluminum removal from rare earth feed liquid with naphthenic acid. *Chin. Rare Earths* 3, 017.
- Harris, D.H., Tompkins, E.R., 1947. Ion-exchange as a separations method. II. Separations of several rare earths of the cerium group (La, Ce, Pr and Nd). *J. Am. Chem. Soc.* 69, 2792–2800.
- Hart, K., Levins, D., 1988. Management of wastes from the processing of rare earth minerals. In: *Chemeca 88: Australia's Bicentennial International Conference for the Process Industries*. National Conference Publication (Institution of Engineers, Australia). Sydney, vol. 88, pp. 82–88.

- Hashtochahar, E., Safdari, S.J., Haghghi-As, A., Torab-Mostaedi, M., 2010. Prediction of slip velocity in a Hanson mixer-settler extraction column. *Can. J. Chem. Eng.* 88, 808–817.
- He, S., Gao, Y., Zeng, Q.H., 1998. Study on property comparison of bastnasite rare earth polishing powder and fluoro-carbonate rare earth polishing powder. *Chin. J. Rare Met.* 22, 304–307.
- He, H., Jia, S., Guo, W., 2010. Separation of ytterbium (III) and lutetium (III) by cation exchange chromatography with HEDTA-H₃Cit system. *J. Chin. Rare Earth Soc.* 1, 010.
- Herak, M., Jagodic, V., 1964. Solvent extraction and separation of europium (III) and terbium (III) from uranium (VI) by mono-octyl anilinobenzylphosphonate. *Croat. Chem. Acta (Yugoslavia)* 36, 51–58.
- Hou, H., Wang, Y., Xu, J., Chen, J., 2013. Solvent extraction of La (III) with 2-ethylhexyl phosphoric acid-2-ethylhexyl ester (EHEHPA) by membrane dispersion micro-extractor. *J. Rare Earths* 31, 1114–1118.
- Hu, K., 1998. Technological process of Baotou rare earth ores acid decomposition. CN Patent 98118153.8.
- Hu, K., 2000. Non-tail gas pollution decomposition of Baotou ore by acid method. In: *Progress of Chinese Rare Earth Science and Technology*, Beijing, pp. 725–728.
- Hu, J., 2004. Method of preparing saponified acidic extractant of organic phase in the rare earth separation process. CN Patent 200410050948.4.
- Huang, G., 2003. Development tendency and present situation of rare earth extraction separation technology in China. *Jiangxi Metall.* 6, 62–68.
- Huang, X., Li, J., Peng, X., Long, Z., Zhu, Z., Cui, D., Zhao, N., Liu, Y., Li, H., Zhang, G., 2005a. A technological process of extracting and separating rare earth by using non-saponified extractants. CN Patent 200510098261.2.
- Huang, X., Li, J., Peng, X., Long, Z., Zhu, Z., Cui, D., Zhao, N., Liu, Y., Li, H., Zhang, G., 2005b. A technological process of extracting and separating rare earth by using non-saponified mixed extractants. CN Patent 200510137231.8.
- Huang, X., Zhang, G., Long, Z., Zhu, Z., Li, H., Peng, X., Li, J., Cui, D., Zhao, N., 2005c. Technological method of comprehensive recovery of rare earth and thorium from rare earth ore. CN Patent 200510085230.3.
- Huang, X., Li, H., Xue, X., Zhang, G., 2006. Development status and research progress in rare earth hydrometallurgy in China. *J. Chin. Rare Earth Soc.* 24, 129 (Chinese Edition).
- Huang, X.W., Cui, D.L., Long, Z.Q., Q, Z.Y., Wang, C.M., Yu, Y., Zhao, N., Li, H.W., Liu, Y., Wang, L.S., 2010. A method of smelting and separation process of bastnasite. CN Patent 201010109290.5.
- Ionov, A.M., Nikiforova, T.V., Rytus, N.N., 1996. Aspects of the purification of volatile rare earth metals by UHV sublimation: Sm, Eu, Tm, Yb. *Vacuum* 47, 879–883.
- Isshiki, M., 1996. Purification of rare earth metals. *Vacuum* 47, 885–887.
- Iyer, J., Dhadke, P., 2001. Liquid-liquid extraction and separation of gallium (III), indium (III), and thallium (III) by Cyanex-925. *Sep. Sci. Technol.* 36, 2773–2784.
- Jagodic, V., Tusek, L., 1972. Synthesis of some benzene azo derivatives of phosphonic acid monoesters. *J. Org. Chem.* 37, 1222–1223.
- Jagodić, V., Herak, M., Šipalo, B., Radošević, J., 1971. Solvent extraction study of lanthanum and europium by acidic esters of aminophosphonic acids. *J. Inorg. Nucl. Chem.* 33, 2651–2659.
- Jiang, Y., Hao, Z., Zhang, X., Dai, Q., 2003. Discussion on the factors affecting purification of rare earth metals by vacuum distillation. *Chin. Rare Earths* 24, 60.
- Jiao, Y., He, X., Liao, C., Jiang, P., 2013. Progress of research on separation and purification of heavy rare earth elements in recent decade. *Chin. Rare Earths* 4, 21.
- Jordens, A., Cheng, Y.P., Waters, K.E., 2013. A review of the beneficiation of rare earth element bearing minerals. *Miner. Eng.* 41, 97–114.

- Jorjani, E., Bagherieh, A.H., Chelgani, S.C., 2011. Rare earth elements leaching from Chadormalu apatite concentrate: laboratory studies and regression predictions. *Korean J. Chem. Eng.* 28, 557–562.
- Khanchi, A.R., Sedighi, H., Ansari, S., Fasihi, J., 2014. Preconcentration of rare earth elements from Iranian monazite ore by spiral separator using multi-response optimization method. *Int. J. Min. Sci. Technol.* 24, 117–121.
- Kim, E., Osseo-Asare, K., 2012. Aqueous stability of thorium and rare earth metals in monazite hydrometallurgy: Eh-pH diagrams for the systems Th-, Ce-, La-, Nd-(PO₄)-(SO₄)-H₂O at 25 °C. *Hydrometallurgy* 113, 67–78.
- Kim, W., Bae, I., Chae, S., Shin, H., 2009. Mechanochemical decomposition of monazite to assist the extraction of rare earth elements. *J. Alloys Compd.* 486, 610–614.
- Krishnamurthy, N., Gupta, C.K., 2004. *Extractive Metallurgy of Rare Earths*. CRC Press, Florida.
- Kul, M., Topkaya, Y., Karakaya, İ., 2008. Rare earth double sulfates from pre-concentrated bastnäsite. *Hydrometallurgy* 93, 129–135.
- Kumari, A., Panda, R., Jha, M.K., Kumar, J.R., Lee, J.Y., 2015. Process development to recover rare earth metals from monazite mineral: a review. *Miner. Eng.* 79, 102–115.
- Kuzmin, V.I., Pashkov, G.L., Lomaev, V.G., Voskresenskaya, E.N., Kuzmina, V.N., 2012. Combined approaches for comprehensive processing of rare earth metal ores. *Hydrometallurgy* 129–130, 1–6.
- Lee, G.S., Uchikoshi, M., Mimura, K., Isshiki, M., 2009. Distribution coefficients of La, Ce, Pr, Nd, and Sm on Cyanex 923-, D2EHPA-, and PC88A-impregnated resins. *Sep. Purif. Technol.* 67, 79–85.
- Lei, B., Liu, B., 2000. Technology investigation of making high-pure metal terbium. *Sichuan Nonferrous Met.* 2, 009.
- Lei, B., Liu, B., 2001. Study and commercial operation of high-purity Dy metal. *Rare Met. Cemented Carbides*, 20–34.
- Li, D., 1996. Extraction of rare earth(III), Th(IV), and Fe(III) with dialkylphosphinic acid. *Jiangxi Nonferrous Met.*, 01, 29–32.
- Li, H., 2005. *Chemical Problems in the Separation Process of Bastnäsite*. Changchun Institute of Applied Chemistry, Chinese Academy of Sciences, Changchun.
- Li, X., Chi, R., 2000. Using sodium sulfide to remove heavy metal ions from rare earth ore leachates. *Multipurpose Util. Miner. Resour.*, 3, 46–47.
- Li, G., Liu, Y., 2000. Study on technology and optimization of purifying scandium metal by vacuum distillation method. *J. Chin. Soc. Rare Earths* 18, 183.
- Li, D., Wang, C., 1998. Solvent extraction of Scandium (III) by Cyanex 923 and Cyanex 925. *Hydrometallurgy* 48, 301–312.
- Li, D., Yue, S., 1990. Kinetics and mechanism of Er (III) extraction from hydrochloric acid solutions with H (DEHP). *J. Nucl. Radiochem.* 4, 007.
- Li, D., Wu, Z., Guo, X., Ji, E., 1981. Extraction and separation of light and heavy rare earth elements by using P507 from nitric acid solution. (*Xitu Chin. Rare Earths*), 01, 23–27.
- Li, D., Zhang, J., Xu, X., 1985. Studies of extraction mechanism of rare earth compounds with mono (2-ethylhexyl) 2-ethylhexylphosphonate (HEH [EHP]). *Chin. J. Appl. Chem.* 2, 17–23.
- Li, D., Wang, Z., Chen, Z., 1988a. Studies of extraction mechanism of rare earth elements with 2-ethylhexylphosphonic acid mono-2-ethylhexyl ester II: equilibrium reaction for extraction of erbium (III) from sulphuric acid solution by HEH (EHP). *Acta Chim. Sin.* 46, 492–495.
- Li, D., Wang, Z., Zhang, C., Le, S., 1988b. Studies of extraction mechanism of rare earth elements with 2-ethylhexylphosphonic acid mono-2-ethylhexyl ester III: the distribution of high

- aqueous Ln(III) concentrations in the system $H^+(HNO_3, HCl)-H_2O-HEH(EHP)$ -kerosene and extraction reaction. *Acta Chim. Sin.* 46, 586–589.
- Li, D., Wang, H., Xu, W., 1991. Separation of dysprosium by liquid–liquid extraction. CN Patent 8610813.
- Li, D., Lu, J., Wei, Z., Wang, Z., Meng, S., Ma, G., 1998. Process of extraction and separation of cerium and thorium from bastnäsite leachate. CN Patent 98122348.6.
- Li, Z., Zhang, W., Xu, J., Zhao, B., Xiao, F., Zhang, Y., 2002. Study on the preparing process of high purity terbium metal. *Chin. Rare Earths* 23, 36.
- Li, G., Hu, K., Liu, J., Wang, G., Xu, Q., Wang, W., Guo, L., Yu, J., Hu, T., Chen, P., Zen, T., Xiao, R., 2004a. Method of the decomposition of mixed rare earth concentrate. CN Patent 200410006443.8.
- Li, G., Li, G., Liu, Y., 2004b. Study on preparation of hypoxia rare metal by fused-salt extraction method. *Sci. Technol. Eng.* 2, 106–107.
- Li, D., Wang, X., Meng, S., Li, W., 2005. Method of separation of rare earth by adding phase modifier. CN Patent 200510016682.6.
- Li, W., Wang, X., Meng, S., Li, D., Xiong, Y., 2007. Extraction and separation of yttrium from the rare earths with sec-octyl phenoxy acetic acid in chloride media. *Sep. Purif. Technol.* 54, 164–169.
- Li, D., Wang, Y., Liao, W., 2011. Method of purification of thorium. CN Patent 201110074345.8.
- Li, D., Wang, Y., Liao, W., 2012. Method of separation and purification of thorium. CN Patent 201210552752.X.
- Li, B., Pang, Z., Wu, J., Xu, W., 2013a. Method of prepare high purity lanthanum oxide by one step extraction. CN Patent 201310686894.X.
- Li, D., Wang, Y., Liao, W., 2013b. Process of separating and purifying thorium. US Patent 20140170039A1.
- Li, G., Li, L., Li, X., Tian, F., 2013c. Preparation of high purity gadolinium element by hydrogen plasma electric arc melting technology. CN Patent 201310317555.4.
- Liao, C.F., Jiao, Y.F., 2005. Review on research and application of Cyanex phosphinic extractants in extractive separation of nonferrous metals. *Nonferrous Met. (China)* 57, 76–80.
- Liao, W., Yu, G., Li, D., 2001. Solvent extraction of cerium (IV) and fluorine (I) from sulphuric acid leaching of bastnäsite by Cyanex 923. *Solvent Extr. Ion Exch.* 19, 243–259.
- Liao, W., Yu, G., Yue, S., Li, D., 2002. Kinetics of cerium (IV) extraction from H_2SO_4 -HF medium with Cyanex 923. *Talanta* 56, 613–618.
- Liao, C., Nie, H., Jiao, Y., Liang, Y., 2006. Progress and prospect in separation and purification of rare earth metals with extraction-chromatography. *Chin. J. Process Eng.* 6, 128.
- Liao, C., Jiao, Y., Qiu, D., Xue, J., 2007. Separating of thulium, ytterbium, lutetium by cooperative extraction chromatography with Cyanex272-P507 impregnated resin. *J. Chin. Rare Earth Soc.* 25, 249 (Chinese Edition).
- Liao, C., Jiao, Y., Liang, Y., Jiang, P., Nie, H., 2010a. Adsorption–extraction mechanism of heavy rare earth by Cyanex 272-P507 impregnated resin. *Trans. Nonferrous Met. Soc. China* 20, 1511–1516.
- Liao, C., Nie, H., Jiao, Y., Yong, L., Yang, S., 2010b. Study on the diffusion kinetics of adsorption of heavy rare earth with Cyanex272-P507 impregnated resin. *J. Rare Earths* 28, 120–124.
- Liao, W., Wang, X., Sun, Y., Lu, Y., Li, Y., 2012. Method of separation and purification of thorium with calixarene. CN Patent 201210453853.1.
- Liao, C., Wu, S., Cheng, F., Wang, S., Liu, Y., Zhang, B., Yan, C., 2013. Clean separation technologies of rare earth resources in China. *J. Rare Earths* 31, 331–336.

- Liao, W., Li, Y., Zhang, Z., Lu, Y., 2014a. Extraction and separation Th^{4+} by neutral phosphoramidite extractants. CN Patent 201410409451.0.
- Liao, W., Li, Y., Zhang, Z., Wu, G., Lu, Y., 2014b. Extraction and separation Th^{4+} by neutral amino group-containing phosphorus extractants. PCT application PCT/CN2015/077208.
- Liao, W., Lu, Y., Zhang, Z., 2014c. Extraction and separation Ce^{4+} by neutral phosphoramidite extractants. CN Patent 201410040023.5.
- Liao, W., Lu, Y., Zhang, Z., Li, Y., Wu, G., 2014d. Extraction and separation Ce^{4+} by neutral amino group-containing phosphorus extractants. PCT application PCT/CN2015/077212.
- Liao, W., Zhang, Z., Li, Y., Wu, G., Lu, Y., 2014e. A method of extraction and separation of cerium, fluorine and thorium. CN Patent 201410764960.5.
- Liu, Y., 2002. Soil erosion and conservation strategies of rare earth mining. *Water Resour. Dev. Res.* 2, 30–32 (in Chinese).
- Liu, G., 2005. *Rare Earth Materials and Its Application Technology*. Chemical Industry Press, Beijing.
- Liu, J., 2007. *Clean Hydrometallurgy and Extraction Kinetics of Rare Earths*. Changchun Institute of Applied Chemistry, Chinese Academy of Sciences, Changchun.
- Liu, H., 2010. Study of the Technology for the Decomposition of Baotou Rare Earth Concentrate by Concentrated NaOH Solution. Inner Mongolia University, Inner Mongolia.
- Liu, B., Qian, H., Li, Y., 1983. The mechanism of extraction of $\text{Zr}(\text{NO}_3)_4$ with DMHMP. *J. Nucl. Radiochem.* 3, 000.
- Liu, G., Liu, J., Liu, L., Cheng, J., 1992. Precipitate flotation of rare earth elements. *Anal. Lab.* 1, 010.
- Liu, Y., Deng, Z., Xu, T., 2000. Solvent extraction and separation of heavy rare earths with mixed Cyanex 272 and HEHEHP. *Chin. J. Rare Met.* 5, 394–397.
- Liu, W., Yun, Y., Li, G., 2003. Preparation of high purity dysprosium metal using anhydrofluorination. *Chin. J. Rare Met.* 1, 037.
- Liu, Y., Liao, C., Zhang, B., Jia, J., Wang, S., Yan, C., 2004. Method of separating and purifying cerium by sulfuric acid treatment of bastnaesite. CN Patent 200410031179.3.
- Liu, J., Wang, W., Li, D., 2007. Interfacial behavior of primary amine N1923 and the kinetics of thorium (IV) extraction in sulfate media. *Colloids Surf. A Physicochem. Eng. Asp.* 311, 124–130.
- Liu, J., Wang, W., Li, D., 2008. Extraction kinetics of thorium (IV) with primary amine N1923 in sulfate media using a constant interfacial cell with laminar flow. *Sep. Sci. Technol.* 43, 431–445.
- Liu, J., Luo, M., Ping, A., Jiang, X., Yuan, Z., 2012a. Progress in extraction technology of thorium from rare earth concentrate. *Xiyou Jinshu (Chin. J. Rare Met.)*, 36, 651–658.
- Liu, Y., Chen, J., Li, D., 2012b. Application and perspective of ionic liquids on rare earths green separation. *Sep. Sci. Technol.* 47, 223–232.
- Long, Z., Huang, X., Peng, X., Li, J., Zhu, Z., Zhao, N., Cui, D., Zhang, S., 2006. Technological process of extracting and separating rare earth in non-saponified system. CN Patent 200610072668.2.
- Lu, S., Tian, J., 1994. Speed controlling trickle leaching process on ion-absorbed rare earth ore passed the min-term evaluation. *China Rare Earth Inf.* 21, 6.
- Lu, S., Lu, C., Wu, N., 1997. Study on speed controlling trickle leaching process of ion type rare earth ore. *Chin. Hydrometall.*, 3, 34–39.
- Lu, J., Wei, Z., Li, D., Ma, G., Jiang, Z., 1998. Recovery of $\text{Ce}(\text{IV})$ and $\text{Th}(\text{IV})$ from rare earths (III) with Cyanex 923. *Hydrometallurgy* 50, 77–87.
- Ludek, J., Wei, Y., Mikio, K., 2006. Adsorption of $\text{Ce}(\text{IV})$ anionic nitrate complexes onto anion exchangers and its application for $\text{Ce}(\text{IV})$ separation from rare earths (III). *J. Rare Earths* 24, 385–391.

- Luo, X., Qiu, T., Yan, Q., 2002. Research progress and developing orientation of chemical extraction technology of weathering crust strain amass-type rare earth. *J. South. Inst. Metall.* 23, 2–6.
- Luo, X., Qian, Y., Liang, C., 2012. Research progress and developing trend of rare earth extraction from ionic rare earth leach solution. *Nonferrous Metals Science and Engineering* 3, 50–53.
- Ma, P.Q., Luo, H., Ma, X.K., 1999. A method of preparation mixture rare earth metals from bastnasite by electrolysis directly. CN Patent 99117868.8.
- Ma, Y., Zhang, L., Xu, Y., Wang, X., Qiao, J., Bai, Y., Chang, S., Zhang, J., 2003. Low temperature roasting and decomposing process of rare earth heading concentrated sulfuric acid. CN Patent 02144405.
- Mackey, T.S., 1985. Recent developments in USA rare earth technology. In: Xu, G., Xiao, J. (Eds.), *New Frontiers in Rare Earth Science and Applications*, vol. 2. Science Press, Beijing, p. 1131.
- Martin, M., Alguacil, F.J., 1998. Synergism in gold-cyanide extraction with Primene JMT-Cyanex 925 mixed extractant system. *Hydrometallurgy* 49, 309–322.
- Martinez, S., Sastre, A., Alguacil, F.J., 1997. Gold extraction equilibrium in the system Cyanex 921-HCl-Au (III). *Hydrometallurgy* 46, 205–214.
- Matveeva, E., Sharova, E., Turanov, A., Karandashev, V., Odinets, I., 2012. Extraction properties of β -aminophosphine oxides towards lanthanides and alkaline earth metals. *Open Chem.* 10, 1933–1941.
- Mayer, S., Freiling, E., 1953. Ion exchange as a separation method. VI. Column studies of the relative efficiencies of various complexing agents for the separation of lighter rare earths. *J. Am. Chem. Soc.* 75, 5647–5649.
- Mayer, S.W., Tompkins, E.R., 1947. Ion exchange as a separations method. IV. A theoretical analysis of the column separations process. *J. Am. Chem. Soc.* 69, 2866–2874.
- Mei, G., Lei, Y., Xie, K., 2009. Study on the recovery of Y_2O_3 from waste fluorescent powder. In: *The First Academic Conference Proceedings of Chinese Comprehensive Utilization of Rare Earth Resources Conference and the Fifth Chinese Rare Earth Society of Selective Professional Committee*.
- Mhaske, A.A., Dhadke, P.M., 2001. Extraction separation studies of Rh, Pt and Pd using Cyanex 921 in toluene: a possible application to recovery from spent catalysts. *Hydrometallurgy* 61, 143–150.
- Mirson, G., 1957. Alkaline leaching of monazite. *At. Energ. (Moscow)* 3, 259–264.
- Mishra, S., Devi, N., 2011. Extraction of copper (II) from hydrochloric acid solution by Cyanex 921. *Hydrometallurgy* 107, 29–33.
- Moldoveanu, G.A., Papangelakis, V.G., 2013. Recovery of rare earth elements adsorbed on clay minerals: II. Leaching with ammonium sulfate. *Hydrometallurgy* 131–132, 158–166.
- Nagai, H., Beaudry, B., Gschneider, K., 1978. Purification of gadolinium by electrorefining. *Metall. Trans. B* 9, 25–28.
- Nasab, M.E., Sam, A., Milani, S.A., 2011. Determination of optimum process conditions for the separation of thorium and rare earth elements by solvent extraction. *Hydrometallurgy* 106, 141–147.
- Navarro, R., Saucedo, I., Núñez, A., Ávila, M., Guibal, E., 2008. Cadmium extraction from hydrochloric acid solutions using Amberlite XAD-7 impregnated with Cyanex 921 (tri-octyl phosphine oxide). *React. Funct. Polym.* 68, 557–571.
- Ney, C., Tauhata, L., Oliveira Filho, D., 1992. Dose equivalent estimate of works in a Brazilian monazite sand plant. In: *International congress of the International Radiation Protection Association (IRPA8)*.

- Özbayoğlu, G., Atalay, M.Ü., 2000. Beneficiation of bastnaesite by a multi-gravity separator. *J. Alloys Compd.* 303, 520–523.
- Palmer, M.A., Bernhardt, E., Schlesinger, W., Eshleman, K., Foufoula-Georgiou, E., Hendryx, M., Lemly, A., Likens, G., Loucks, O., Power, M., 2010. Mountaintop mining consequences. *Science* 327, 148–149.
- Panda, N., Devi, N., Mishra, S., 2012. Solvent extraction of neodymium (III) from acidic nitrate medium using Cyanex 921 in kerosene. *J. Rare Earths* 30, 794–797.
- Panda, R., Kumari, A., Jha, M.K., Hait, J., Kumar, V., Kumar, J.R., Lee, J.Y., 2014. Leaching of rare earth metals (REMs) from Korean monazite concentrate. *J. Ind. Eng. Chem.* 20, 2035–2042.
- Pang, S., Wang, Z., Zhou, L., Chen, B., Xu, L., Zhao, B., Yan, S., Li, Z., 2008. Study on preparation of high-purified terbium and dysprosium metals used for rare earth giant magnetostrictive materials. *Chin. Rare Earths* 6, 009.
- Pang, S., Chen, D., Li, Z., Yan, S., Zhou, L., Xu, L., Wang, Z., Xu, J., 2013. Theory and technology of vacuum distillation method for preparing high-purity metal neodymium. *J. Chin. Soc. Rare Earths* 1, 14–19.
- Paulo, J.B., Hadjiev, D.E., 2006. Mixer–settler based on phase inversion: design of the mixing zone. *Ind. Eng. Chem. Res.* 45, 3821–3829.
- Perez, M.M., Reyes-Aguilera, J., Saucedo, T., Gonzalez, M., Navarro, R., Avila-Rodriguez, M., 2007. Study of As (V) transfer through a supported liquid membrane impregnated with triocetylphosphine oxide (Cyanex 921). *J. Membr. Sci.* 302, 119–126.
- Preez, A.D., Preston, J.S., 1992. The solvent extraction of rare-earth metals by carboxylic acids. *Solvent Extr. Ion Exch.* 10, 207–230.
- Preston, J.S., Cole, P.M., Craig, W.M., Feather, A.M., 1996a. The recovery of rare earth oxides from a phosphoric acid by-product. Part 1: leaching of rare earth values and recovery of a mixed rare earth oxide by solvent extraction. *Hydrometallurgy* 41, 1–19.
- Preston, J.S., Cole, P.M., du Preez, A.C., Fox, M.H., Fleming, A.M., 1996b. The recovery of rare earth oxides from a phosphoric acid by-product. Part 2: the preparation of high-purity cerium dioxide and recovery of a heavy rare earth oxide concentrate. *Hydrometallurgy* 41, 21–44.
- Preston, J.S., du Preez, A.C., Cole, P.M., Fox, M.H., 1996c. The recovery of rare earth oxides from a phosphoric acid by-product. Part 3. The separation of the middle and light rare earth fractions and the preparation of pure europium oxide. *Hydrometallurgy* 42, 131–149.
- Qian, H., Bao, B., Xia, Y., 1986. Investigation of synergistic extraction I. Synergistic extraction of thorium by DMHMP and HEHEHP. *J. Nucl. Radiochem.* 3, 004.
- Qiu, T., Luo, X., Fang, X., 2002. A new technology intensified by magnetic field for leaching of granitoid weathering crust strain amass-type rare earth ores. *Multipurpose Util. Miner. Resour.* 5, 14–16.
- Qiu, T., Fang, X., Cui, L., Fang, Y., 2008. Behavior of leaching and precipitation of weathering crust ion-absorbed type by magnetic field. *J. Rare Earths* 26, 274–278.
- Qiu, T., Wu, H., Fang, X., Li, X., 2012. The current situation and trends of the technology for impurity removal of weathering crust ion-absorbed type rare earth ores. *Xitu (Chin. Rare Earths)* 33, 81–85.
- Quill, L.L., Salutsky, M.L., 1952. Separation of praseodymium from lanthanum. *Anal. Chem.* 24, 1453–1455.
- Rabah, M.A., 2008. Recyclables recovery of europium and yttrium metals and some salts from spent fluorescent lamps. *Waste Manag.* 28, 318–325.
- Rabie, K., 2007. A group separation and purification of Sm, Eu and Gd from Egyptian beach monazite mineral using solvent extraction. *Hydrometallurgy* 85, 81–86.

- Rao, G., Mao, Y., Wu, N., 1995. Effect of sesbanina gum and its derivative on leaching process of weathered crust elution deposited rare earth ore. *Hydrometall. China* 54, 10–14.
- Rao, P., Mitsuaki, M., Toyohisa, F., 2009. Separation of red (Y_2O_3 : Eu^{3+}), blue (Sr, Ca, Ba) $_{10}(PO_4)_6C_{12}$: Eu^{2+} and green ($LaPO_4$: Tb^{3+} , Ce^{3+}) rare earth phosphors by liquid/liquid extraction. *J. Wuhan Univ. Technol. Mater. Sci. Ed.* 24, 418–423.
- Rollat, A., Sabot, J.L., Burgard, M., Delloye, T., 1988. Production of rare-earth oxides of high purity. US Patent 4726938.
- Sapsford, D.J., Bowell, R.J., Geroni, J.N., Penman, K.M., Dey, M., 2012. Factors influencing the release rate of uranium, thorium, yttrium and rare earth elements from a low grade ore. *Miner. Eng.* 39, 165–172.
- Sato, T., 1989. Liquid–liquid extraction of rare-earth elements from aqueous acid solutions by acid organophosphorus compounds. *Hydrometallurgy* 22, 121–140.
- Shaibu, B., Reddy, M., Bhattacharyya, A., Manchanda, V., 2006. Evaluation of Cyanex 923-coated magnetic particles for the extraction and separation of lanthanides and actinides from nuclear waste streams. *J. Magn. Magn. Mater.* 301, 312–318.
- Shen, C., Xie, Y., Li, D., 1986. Technological process of solvent extracting and separating for mixed rare earth with aminated P507. CN Patent 85102210B.
- Shi, N., 1987. Preparation of high purity rare earth metals and crystals. *Chin. J. Mater. Res.* 2, 002.
- Smutz, M., 1958. Method of processing monazite sand. US Patent 2849286 A.
- Spedding, F., Powell, J., 1954a. The separation of rare earths by ion exchange. VII. Quantitative data for the elution of neodymium. *J. Am. Chem. Soc.* 76, 2545–2550.
- Spedding, F., Powell, J., 1954b. The separation of rare earths by ion exchange VIII. Quantitative theory of the mechanism involved in elution by dilute citrate solutions. *J. Am. Chem. Soc.* 76, 2550–2557.
- Spedding, F., Fulmer, E., Butler, T., Gladrow, E., Gobush, M., Porter, P., Powell, J., Wright, J., 1947a. The separation of rare earths by ion exchange. III. Pilot plant scale separations. *J. Am. Chem. Soc.* 69, 2812–2818.
- Spedding, F., Voigt, A., Gladrow, E., Sleight, N., 1947b. The separation of rare earths by ion exchange I. Cerium and yttrium. *J. Am. Chem. Soc.* 69, 2777–2781.
- Spedding, F., Voigt, A., Gladrow, E., Sleight, N., Powell, J., Wright, J., Butler, T., Figard, P., 1947c. The separation of rare earths by ion exchange II. Neodymium and praseodymium. *J. Am. Chem. Soc.* 69, 2786–2792.
- Spedding, F., Fulmer, E., Butler, T., Powell, J., 1950a. The separation of rare earths by ion exchange IV. Further investigations concerning variables involved in the separation of samarium, neodymium and praseodymium. *J. Am. Chem. Soc.* 72, 2349–2354.
- Spedding, F., Fulmer, E., Powell, J., Butler, T., 1950b. The separation of rare earths by ion exchange V. Investigations with one-tenth percent citric acid-ammonium citrate solutions. *J. Am. Chem. Soc.* 72, 2354–2361.
- Spedding, F., Fulmer, E., Powell, J., Butler, T., Yaffe, I., 1951. The separation of rare earths by ion exchange VI. Conditions for effecting separations with nalcite HCR and one-tenth percent citric acid-ammonium citrate solutions. *J. Am. Chem. Soc.* 73, 4840–4847.
- Spedding, F.H., Wilhelm, H.A., Keller, W.H., Ahmann, D.H., Daane, A.H., Hach, C.C., Ericson, R.P., 1952. Production of pure rare earth metals. *Ind. Eng. Chem.* 44, 553–556.
- Sui, N., Huang, K., Zheng, H., Lin, J., Wang, X., Xiao, C., Liu, H., 2014. Three-liquid-phase extraction and separation of rare earths and Fe, Al, and Si by a novel mixer–settler–mixer three-chamber integrated extractor. *Ind. Eng. Chem. Res.* 53, 16033–16043.
- Sun, D., Xia, X., Lu, W., Yu, Y., 1994. Method of rare earth electrolysis. CN Patent 1095111.

- Sun, X., Wang, J., Li, D., Li, H., 2006. Synergistic extraction of rare earths by mixture of bis(2,4,4-trimethylpentyl) phosphinic acid and Sec-nonylphenoxy acetic acid. *Sep. Purif. Technol.* 50, 30–34.
- Sun, X., Luo, H., Dai, S., 2011. Ionic liquids-based extraction: a promising strategy for the advanced nuclear fuel cycle. *Chem. Rev.* 112, 2100–2128.
- Tanaka, M., Oki, T., Koyama, K., Narita, H., Oishi, T., 2013. Recycling of rare earths from scrap. In: Bünzli, J.-C.G., Pechasky, V.K. (Eds.), *Handbook on the Physics and Chemistry of Rare Earths*, vol. 43. Elsevier Science B.V., Amsterdam, p. 159ff (Ch. 255).
- Tassinari, M.M.L., Kahn, H., Ratti, G., 2001. Process mineralogy studies of Corrego do Garimpo REE ore, catalao-I alkaline complex, Goias, Brazil. *Miner. Eng.* 14, 1609–1617.
- Tian, J., Yin, J., Ouyang, K., Chi, R., 2006. Development progress and research connotation of green chemistry of extraction process of rare earth from weathering crust elution-deposited rare earth ores in China. (*Xitu Chin. Rare Earths*) 27, 70–72.
- Tian, F., Li, G., Li, L., Wang, Z., Yan, S., Li, X., 2014. Advance in solid-state purification technology for metals. *J. Alloys Compd.* 592, 176–184.
- Tompkins, E.R., Mayer, S.W., 1947. Ion exchange as a separations method. III. Equilibrium studies of the reactions of rare earth complexes with synthetic ion exchange resins. *J. Am. Chem. Soc.* 69, 2859–2865.
- Tompkins, E.R., Khym, J.X., Cohn, W.E., 1947. Ion-exchange as a separations method I. The separation of fission-produced radioisotopes, including individual rare earths, by complexing elution from amberlite resin. *J. Am. Chem. Soc.* 69, 2769–2777.
- Tong, H., Lei, J., Li, D., 2003. Mass transfer kinetics of extraction of RE (III) with Cyanex 923. *J. Wuhan Univ. Technol.* 6, 2.
- Tong, S., Zhao, X., Song, N., Jia, Q., Zhou, W., Liao, W., 2009. Solvent extraction study of rare earth elements from chloride medium by mixtures of sec-nonylphenoxy acetic acid with Cyanex301 or Cyanex302. *Hydrometallurgy* 100, 15–19.
- Tong, H., Wang, Y., Liao, W., Li, D., 2013. Synergistic extraction of Ce (IV) and Th (IV) with mixtures of Cyanex 923 and organophosphorus acids in sulfuric acid media. *Sep. Purif. Technol.* 118, 487–491.
- Wang, Z., 2006. Method of preparing rare earth saponifier by using barium sulfate. CN Patent 200610047115.1.
- Wang, Y., 2013. *Clean Hydrometallurgy Process of Rare Earths & Purification Technology of Thorium*. Changchun Institute of Applied Chemistry, Chinese Academy of Sciences, Changchun.
- Wang, C.H., Huang, G.W., 2007. A mixer–settler with double mixer and shallow settler. *Rare Earth* 28, 60–64.
- Wang, J., Ouyang, H., 1983. The study of extraction rare earth with resin slurry. *Jiangxi Metall.* 3, 31–32.
- Wang, J., Wang, X., 2006. Comprehensive utilization and cleaner production process of Bayan Obo rare earth resource. *Chin. Rare Earths* 27, 103–105.
- Wang, Z., Meng, S., Li, D., 1995. Extraction separation of rare earth elements (III) with bis(2,4,4-trimethylpentyl) phosphinic acid. *Chin. J. Anal. Chem.* 23, 391–394.
- Wang, Z., Ma, G., Li, D., 1998. Extraction and separation of heavy rare earth (III) with extraction resin containing di(2,4,4-trimethyl pentyl) phosphinic acid (Cyanex 272). *Solvent Extr. Ion Exch.* 16, 813–828.
- Wang, Y., Yue, S., Li, D., Jin, M., Li, C., 2002. Solvent extraction of scandium(III), yttrium(III), lanthanides(III), and divalent metal ions with sec-nonylphenoxy acetic acid. *Solvent Extr. Ion Exch.* 20, 701–716.

- Wang, Y., Xiong, Y., Meng, S., Li, D., 2004. Separation of yttrium from heavy lanthanide by CA-100 using the complexing agent. *Talanta* 63, 239–243.
- Wang, W., Wang, X., Meng, S., Li, H., Li, D., 2006a. Extraction and stripping of ytterbium (III) from H₂SO₄ medium by Cyanex 923. *J. Rare Earths* 24, 685–689.
- Wang, W., Wang, G., Jia, J., Zhang, Z., 2006b. Economical and technical indices of decomposition processes of typical rare earth minerals in China. *J. Chin. Rare Earth Soc.* 24, 385 (Chinese Edition).
- Wang, X., Li, W., Meng, S., Li, D., 2006c. The extraction of rare earths using mixtures of acidic phosphorus-based reagents or their thio-analogues. *J. Chem. Technol. Biotechnol.* 81, 761–766.
- Wang, X., Li, W., Wang, W., Meng, S., Li, D., 2009. Influence of isooctanol on the interfacial activity and mass transfer of ytterbium (III) using 2-ethylhexylphosphonic acid mono-2-ethylhexyl ester as an acidic extractant. *J. Chem. Technol. Biotechnol.* 84, 269–274.
- Wang, X., Meng, S., Li, D., 2010a. Extraction kinetics of ytterbium (III) by 2-ethylhexylphosphonic acid mono-(2-ethylhexyl) ester in the presence of isooctanol using a constant interfacial cell with laminar flow. *Sep. Purif. Technol.* 71, 50–55.
- Wang, Z., Li, Z., Yan, S., Wang, X., Pang, S., Chen, D., Zhou, L., Xu, L., Chen, B., 2010b. Method of preparing high purity rare earth metals and its device. CN Patent 201010534284.4.
- Wang, X., Li, W., Li, D., 2011a. Extraction and stripping of rare earths using mixtures of acidic phosphorus-based reagents. *J. Rare Earths* 29, 413–415.
- Wang, Y., Liao, W., Li, D., 2011b. A solvent extraction process with mixture of CA12 and Cyanex272 for the preparation of high purity yttrium oxide from rare earth ores. *Sep. Purif. Technol.* 82, 197–201.
- Wang, J., Xu, S., Li, L., Li, J., 2013a. Synthesis of organic phosphinic acids and studies on the relationship between their structure and extraction–separation performance of heavy rare earths from HNO₃ solutions. *Hydrometallurgy* 137, 108–114.
- Wang, Y., Li, Y., Li, D., Liao, W., 2013b. Kinetics of thorium extraction with di-(2-ethylhexyl) 2-ethylhexyl phosphonate from nitric acid medium. *Hydrometallurgy* 140, 66–70.
- Wang, Y., Li, Y., Liao, W., Li, D., 2013c. Preparation of high-purity thorium by solvent extraction with di-(2-ethylhexyl) 2-ethylhexyl phosphonate. *J. Radioanal. Nucl. Chem.* 298, 1651–1657.
- Wang, J., Chen, G., Xu, S., Li, L., 2015. Synthesis of novel nonsymmetric dialkylphosphinic acid extractants and studies on their extraction–separation performance for heavy rare earths. *Hydrometallurgy* 154, 129–136.
- Wen, X., Yu, Q., Ma, R., 1997. Liquid membrane extraction of rare earths from simulated leaching solution. *Min. Metall. Eng. (China)* 17, 47–50.
- Wish, L., Freiling, E.C., Bunney, L.R., 1954. Ion exchange as a separations method. VIII. Relative elution positions of lanthanide and actinide elements with lactic acid eluant at 87°. *J. Am. Chem. Soc.* 76, 3444–3445.
- Wu, Y., 2008. On the process of preparing laser crystals by warming compressing ion-exchange method. *Jiangxi Nonferrous Met.* 22, 26–28.
- Wu, D., Niu, C., Li, D., Bai, Y., 2004. Solvent extraction of scandium (III), yttrium (III), lanthanum (III) and gadolinium (III) using Cyanex 302 in heptane from hydrochloric acid solutions. *J. Alloys Compd.* 374, 442–446.
- Wu, S., Wang, T., Xu, F., Liu, H., 2013. Current research of preparation processes of high-purity rare-earth metals. *Rare Met. Cemented Carbides* 4, 005.
- Wu, Y., Yin, X., Zhang, Q., Wang, W., Mu, X., 2014. The recycling of rare earths from waste tricolor phosphors in fluorescent lamps: a review of processes and technologies. *Resour. Conserv. Recycl.* 88, 21–31.

- Xia, Y., 1987. Investigation of the synergistic extraction of thorium nitrate with DMHMP and HTTA. *J. Nucl. Radiochem.* 3, 011.
- Xia, Y., Chen, L., Qian, H., 1985. Study on the extraction mechanisms of uranyl nitrate and thorium nitrate by DMHMP. *J. Nucl. Radiochem.* 3, 003.
- Xiao, P., Bao, C., Song, N., Li, C., Jia, Q., 2011. Liquid-liquid solvent extraction of rare earths from chloride medium with sec-nonylphenoxy acetic acid and its mixtures with neutral organophosphorus extractants. *Russ. J. Inorg. Chem.* 56, 1157–1161.
- Xiao, Y., Long, Z., Huang, X., Feng, Z., Cui, D., Wang, L., 2013. Study on non-saponification extraction process for rare earth separation. *J. Rare Earths* 31, 512–516.
- Xiao, J., Du, R., Wang, Z., Zhang, Y., Zhang, T., 2014. Preparation method and usage of dialkylphosphinic acid compound or its salt. CN Patent 201410010389.8.
- Xie, F., Zhang, T.A., Dreisinger, D., Doyle, F., 2014. A critical review on solvent extraction of rare earths from aqueous solutions. *Miner. Eng.* 56, 10–28.
- Xiong, Y., Wang, X., Li, D., 2005. Synergistic extraction and separation of heavy lanthanide by mixtures of bis(2,4,4-trimethylpentyl) phosphinic acid and 2-ethylhexyl phosphinic acid mono-2-ethylhexyl ester. *Sep. Sci. Technol.* 40, 2325–2336.
- Xu, G., 1995. Rare earths, second ed. Metallurgical Industry Press, Beijing, pp. 364–466.
- Xue, L., Li, D., 1991. Extraction mechanism of scandium from sulphuric acid solution by di-(2-ethylhexyl) phosphonic acid. *J. Nucl. Radiochem.* 13, 163–168. +175.
- Xue, L., Li, D., 1992. Extraction of scandium (III), yttrium (III), lanthanides (III) and iron (III) from hydrochloric acid solutions with di-(2-ethylhexyl)phosphonic acid. *Chin. J. Appl. Chem.*, 4, 21–25.
- Xunzhong, T., Maonan, L., Dian, Y., 1999. The research of indoor simulation experiments of the ion absorbed rare earth mineral in situ leach mining. *J. Cent. South Univ. Technol. (Natural Science)* 30 (2), 133–136.
- Yadav, S., Singh, O., Tandon, S., 1994. Extraction and separation of some 3d transition elements using Cyanex 925: application to zinc ores. *Hydrometallurgy* 36, 53–59.
- Yang, Q., Liu, S., Ouyang, Y., Liu, S.Z., Su, Z.F., 2005. Study on production technology of high-purity terbium metal. *Jiangxi Nonferrous Met.* 1, 008.
- Yang, F., Kubota, F., Baba, Y., Kamiya, N., Goto, M., 2013. Selective extraction and recovery of rare earth metals from phosphor powders in waste fluorescent lamps using an ionic liquid system. *J. Hazard. Mater.* 254, 79–88.
- Yang, Y., Sun, S.C., Zhu, X.P., Jia, W., Tu, G.F., 2015. Defluorination mechanism in bastnaesite calcining process. *J. Chin. Soc. Rare Earths* 33, 95–100.
- Yin, S., Zhang, L., Peng, J., Li, S., Ju, S., Zhang, L., 2015. Microfluidic solvent extraction of La (III) with 2-ethylhexyl phosphoric acid-2-ethylhexyl ester (P507) by a microreactor. *Chem. Eng. Process. Process Intensif.* 91, 1–6.
- Yn, J., Tian, J., Ouyang, K., Chen, K., 2002. Development and application of Cyanex extractants in solvent extraction of noble metals. *Hydrometall. China* 21, 1–4.
- Yu, Q., 2001. Production of high-purity Dy metal by magnesium reduction. *Rare Met. Cemented Carbides*, 145, 14–18.
- Yu, Z.C., Jiang, X., 2011. A non-buffer-chamber mixer-settler. CN Patent 202061414U.
- Yu, Q.H., Li, X.B., 1993. The forming and its influence factors of crystal rare earth carbonate. *J. Chin. Rare Earth Soc.* 11, 171–173.
- Yu, X., Yao, B., Nagaosa, Y., 2007. Study on solvent extraction of Pr^{3+} from different medium by bis(2-ethylhexyl)phosphonic acid in heptane. *Rare Metal Mater. Eng.* 36, 1099–1101.
- Yun, Y., Huang, J., Liu, W., Tai, X., Li, G., 2006. One time to produce low oxygen and low fluorine dysprosium metal by the combining method of calcium reducing agent and fused-salt extraction. *Xitu (Chin. Rare Earths)* 27, 91–93.

- Zang, L., Qi, W., 1995. The new application of re's saponification technique in the separation of LRE. *Chin. Rare Earths* 3, 28–30.
- Zhang, X., Li, D., 1993. Extraction of rare-earth ions (III) with bis(2,4,4-trimethylpentyl) phosphinic acid. *Chin. J. Appl. Chem.* 10, 72.
- Zhang, P., Jiang, Y., Zhang, L., Hou, S., 1990. Cl-P350 extraction resin and its extracting for scandium. *Xitu (Chin. Rare Earths)*, 2, 12–16.
- Zhang, P., Zhang, L., You, S., Feng, S., Hou, S., 1991. Investigation of the purification of high pure scandium oxide in P350-HCl system. *Xitu (Chin. Rare Earths)*, 4, 18–21.
- Zhang, X., Bo, Q., Lu, J., Li, D., Ye, W., 2000. Extraction of rare earth elements with sec-octylphenoxy acetic acid in n-heptane. *Chin. J. Appl. Chem.* 17, 200–201.
- Zhang, W., Yang, Q., Chen, J., 2007a. Preparation method and development trend of high purity RE materials. *Met. Mater. Metall. Eng.* 3, 015.
- Zhang, X., Jiang, Y., Dai, Q., 2007b. Preparation of high purity metallic gadolinium by the vacuum distillation method. *Sci. Technol. Baotou Steel (Group) Corp.* 33, 17.
- Zhang, Z., Li, H., Guo, F., Zhang, H., Li, D., Meng, S., 2007c. Thermodynamic behavior and applications of KMnO_4 in cerium separation process using Cyanex 923. *Ind. Eng. Chem. Res.* 46, 901–906.
- Zhang, Z., Li, H., Guo, F., Meng, S., Li, D., 2008. Synergistic extraction and recovery of Cerium (IV) and Fluorine from sulfuric solutions with Cyanex 923 and di-2-ethylhexyl phosphoric acid. *Sep. Purif. Technol.* 63, 348–352.
- Zhang, Z., Guo, F., Meng, S., Jia, Q., Li, H., Li, D., 2010. Simultaneous recovery of cerium and fluorine from bastnaesite leach liquor by mixtures of Cyanex 923 and HEH (EHP). *Ind. Eng. Chem. Res.* 49, 6184–6188.
- Zhang, C., Wang, L., Huang, X., Dong, J., Long, Z., Zhang, Y., 2014a. Yttrium extraction from chloride solution with a synergistic system of 2-ethylhexyl phosphonic acid mono-(2-ethylhexyl) ester and bis(2,4,4-trimethylpentyl) phosphinic acid. *Hydrometallurgy* 147, 7–12.
- Zhang, Z., Wang, Z., Chen, D., Miao, R., Zhu, Q., Zhang, X., Zhou, L., Li, Z.A., 2014b. Purification of praseodymium to 4N5+ purity. *Vacuum* 102, 67–71.
- Zhang, Z., Wang, Z., Miao, R., Zhu, Q., Chen, D., Zhang, X., Zhou, L., Li, Z., Yan, S., 2014c. Purification of yttrium to 4N5+ purity. *Vacuum* 107, 77–82.
- Zhao, Z., 2000. In-situ leach mining of ion-absorbed rare-earth mineral and some problems in application and dissemination. *J. South. Inst. Metall.* 3, 179–183.
- Zhao, J., Meng, S., Li, D., 2004a. Liquid-liquid extraction of cerium (IV) from nitric acid media by di-(2-ethylhexyl) 2-ethylhexyl phosphonate (DEHEHP). *Solvent Extr. Ion Exch.* 22, 429–447.
- Zhao, J., Zuo, Y., Li, D., Liu, S., 2004b. Extraction and separation of cerium(IV) from nitric acid solutions containing thorium(IV) and rare earths(III) by DEHEHP. *J. Alloys Compd.* 374, 438–441.
- Zhao, J., Meng, S., Li, D., 2006b. Synergistic extraction of rare earths (III) from chloride medium with mixtures of 1-phenyl-3-methyl-4-benzoyl-pyrazalone-5 and di-(2-ethylhexyl)-2-ethylhexylphosphonate. *J. Chem. Technol. Biotechnol.* 81, 1384–1390.
- Zhao, Q., Zhang, T., Liu, Y., Wang, S., Xie, C., 2014. Effect of stirring on liquid-liquid separation in modified mixer-settlers. *J. Chem. Eng. Chin. Univ.* 28, 530–534.
- Zheng, D., Gray, N., Stevens, G., 1991. Comparison of naphthenic acid, versatic acid and D2EHPA for the separation of rare earths. *Solvent Extr. Ion Exch.* 9, 85–102.
- Zheng, W., Wang, S., Fan, Y., Xu, Y., Li, S., Ying, T., 1993. Preparation of rare earth feed with bastnasite. CN Patent 93114910.X.
- Zheng, Z., Ling, D., Sun, Y., 1995. Production of rare-earth oxides of high purity. *J. Chromatogr. A* 707, 131–135.

- Zhong, S., Wang, J., Wang, L., Zhao, Z., Li, X., Xiao, Y., Yang, Y., 2014. Selective extraction of rare earth elements from NdFeB scrap by molten chlorides. *ACS Sustain. Chem. Eng.* 2, 2536–2543.
- Zhou, D., 1992. Extraction separation process for U, Fe, Th and rare earth elements in monazite. *Guang Dong Nonferrous Met.* 2, 16–22 (in Chinese).
- Zhou, J., 1999. Method of elimination of fluorine from bastnäsite to prepare cerium. CN Patent 99117381.3.
- Zhou, X., Wen, D., Luo, X., 2012. The status quo and development trend of the extraction technology of ion-absorbed rare earth in southern China. *Nonferrous Met. Sci. Eng.* 6, 017.
- Zhu, G., Chi, R.A., Zhou, J., Tian, J., 2000. Recovering RE by NH_4Cl roasting method from bastnasite. *Nonferrous Met. (Beijing)* 52, 66–68.
- Zhu, Z., Pranolo, Y., Cheng, C., 2015. Separation of uranium and thorium from rare earths for rare earth production: a review. *Miner. Eng.* 77, 185–196.
- Zhuang, W., 1975. The application of extractant N-235 in analytical chemistry. *Chin. J. Anal. Chem.* 3, 343–350.

Index

Note: Page numbers followed by “*f*” indicate figures, and “*t*” indicate tables.

A

Afterglow intensity of persistent phosphors
excitation conditions, 12, 35, 65–66
fitting of decay curves, 12, 81
radiometric units, 64
threshold value, 35
visibility index, 27–31

Applications of persistent phosphors

energy storage, 66–70, 83
in vivo imaging, 71–79, 83–84
luminous paints, 4
night vision surveillance, 36
road markings, 82
safety signage, 2, 32–34, 65–68, 80–83
solar cells, 83
white afterglow, 75–76

Associated resources (in rare earth separations),
346–350, 347–348*t*, 348–351*f*

B

Barrel-leaching, 340, 340*f*
Bastnäsite, 306–320
acid method, 306–317, 308–310*f*, 311*t*,
312–317*f*
alkali method, 317–320, 318–320*f*
Bologna stone, 3–4, 36–58
Building unit, 251–252

C

Capping ligand, 209, 211–215, 233
Coordination polymers, 164, 170–171
Crystallographic relationships in chalcogenides
Dy₃Ge_{1.25}S₇, 156, 157*t*
Eu₃As₂S₈, 145, 156, 156*t*
Eu₃Sn₂S₇, 155*f*, 157
Eu₅Sn₃S₁₂, 153, 154*f*, 157
La₂PbSi₂S₈, 145, 156, 156*t*
La₂SnS₅, 153–154, 155*f*, 157
lattice parameters, 152, 153*f*
R₃Ge_{1+x}Se₇, 152, 153*f*
R_{1.32}Pb_{1.68}Ge_{1.67}Se₇, 152, 153*f*

Sm₃Ge_{1.48}Se₇, 150–152, 151*f*
Sm_{1.32}Pb_{1.68}Ge_{1.67}Se₇, 150–152, 151*f*
substitution, 150–154, 151*f*, 154–155*f*,
156–157, 156–157*t*
superstructure, 155*f*, 157
Y_{1.32}Pb_{1.68}Ge_{1.67}Se₇, 156, 157*t*
Y₂Pb₃Sn₃S₁₂, 153, 154*f*, 157

D

Disordered structure

La₂PbSi₂S₈, 134–137, 146*f*, 147*t*, 156
Pb_{0.2}Ge_{0.8}Se, 115–117, 117*t*
Pb_{0.9}Ge_{0.1}Se, 117–118, 118*t*
R₃Ge_{1+x}Se₇, 152, 153*f*
R_{1.32}Pb_{1.68}Ge_{1.67}Se₇, 152, 153*f*
Sm₃Ge_{1.48}Se₇, 150–152, 151*f*
Y_{1.32}Pb_{1.68}Ge_{1.67}Se₇, 137–138, 147*f*, 148*t*,
150–152, 151*f*, 156

E

Electrolytic refining, 360
Electro-transport, 358, 359*t*
Extractants
acidic, 289–293, 291*t*
amines, 299–300, 300*t*
aminophosphonate, 293
carboxylic acids, 298–299, 298*t*
ionic liquids, 300
neutral, 293–298, 294*t*
Extraction equipment, 301–305, 301–304*f*

F

Fused-salt deoxidation, 356–357
Fused-salt extraction, 360

H

Halogen bond, 239, 244, 251–252
Heterofunctional, 199–200, 203, 222,
225–226, 231–233, 235, 248
Heterometallic, 192, 205, 222–223, 231–234
High-purity rare earths, 351–355

Homofunctional, 222–223
 Hybrid material, 170–171
 Hydrogen bonding interactions, 188–189,
 192–193, 235–237, 240–243, 241*f*,
 249–250, 250*f*, 254, 254*f*, 258*f*, 260–261,
 260*f*, 265
 Hydrolysis, 165–166, 167*f*, 169–170, 174,
 183–184, 193–194, 213–214, 223,
 233–235, 251–252, 259–260, 265

I

In situ leaching, 341–344, 342*f*
 In vivo imaging, 71–79, 83–84
 Ion-adsorption deposit, 338–346, 339–342*f*,
 344*f*
 Isothermal section
 Er₂Se₃–PbSe–GeSe₂, 121*t*, 127–130,
 135–136*f*, 137–139*t*
 Er₂S₃–PbS–SiS₂, 124, 124–125*f*, 126–128*t*
 Ho₂S₃–PbS–SnS₂, 130–133, 140–142*f*,
 142–146*t*
 La₂Se₃–PbSe–GeSe₂, 121*t*, 127–130,
 135–136*f*, 137–139*t*
 La₂Se₃–PbSe–SiSe₂, 124, 128–129*f*,
 129–130*t*
 La₂S₃–PbS–GeS₂, 124, 124–125*f*, 126,
 126–128*t*, 131–132*f*, 132–134*t*
 La₂S₃–PbS–SiS₂, 124, 124–125*f*, 126–128*t*
 La₂S₃–PbS–SnS₂, 130–133, 140–142*f*,
 142–146*t*
 PbSedSnSe₂, 110–112
 PbX–ZX₂, 110–112
 Pr₂S₃–PbS–GeS₂, 124, 124–125*f*, 126–128*t*
 Pr₂S₃–PbS–SnS₂, 130–133, 140–142*f*,
 142–146*t*
 R₂Se₃–PbSe–GeSe₂, 121*t*, 127
 R₂Se₃–PbSe–GeSe₂, 121*t*, 127, 137–138
 R₂Se₃–PbSe–SiSe₂, 121*t*, 124
 R₂S₃–PbS–GeS₂, 121*t*, 126
 R₂S₃–PbS–SiS₂, 119–124, 121*t*
 R₂S₃–PbS–SnS₂, 121*t*, 130, 138–144
 R₂X₃–PbX, 110
 R₂X₃–PbX–ZX₂, 110, 119, 120–121*t*,
 134–137, 144, 146*f*, 147*t*, 154–158
 R₂X₃–ZX₂, 110
 Sm₂Se₃–PbSe–GeSe₂, 127–130, 135–136*f*,
 137–139*t*
 Sm₂S₃–PbS–SnS₂, 130–133, 140–142*f*,
 142–146*t*
 Y₂Se₃–PbSe–GeSe₂, 127–130, 135–136*f*,
 137–139*t*
 Y₂Se₃–PbSe–SiSe₂, 121*t*, 124, 128–129*f*,
 129–130*t*

Y₂S₃–PbS–GeS₂, 121*t*, 124, 124–125*f*, 126,
 126–128*t*
 Y₂S₃–PbS–SiS₂, 124, 124–125*f*, 126–128*t*
 Y₂S₃–PbS–SnS₂, 130–133, 140–142*f*,
 142–146*t*

L

Luminescence, 222, 232–233, 235, 238
 Luminous paint, 4

M

Magnetic properties
 Curie–Weiss law, 158–159, 158*t*
 La₂PbSi₂S₈, 158–159, 158*t*
 La₂PbSi₂Se₈, 158–159, 158*t*
 modified Curie–Weiss law, 158–159, 158*t*
 R₂PbSi²X₈, 158–159, 158*t*
 Sm₂PbSi₂S₈, 158–159, 158*t*
 Sm₂PbSi₂Se₈, 158–159, 158*t*
 Mechanisms of luminescence
 Ce³⁺, 16, 18, 34, 37*t*, 43*t*
 Cr³⁺, 77–79, 77*t*
 Eu²⁺, R³⁺, 2–3, 2*f*, 5–7, 6*f*, 16
 hole trapping, 5, 18
 Mn²⁺, 34–36, 37*t*, 56*t*, 75–76
 R³⁺, 18
 thermal barrier for trapping, 2–3, 2*f*, 13–14,
 61, 61*f*
 Mechanoluminescence (ML), 3, 70–71, 83–84
 Mesopic vision, 25, 31
 Metalloligand, 233–235
 Metal organic frameworks, 171
 Microextractors, 301–305, 302*f*
 Microreactors, 301–305, 302*f*
 Mixed ore, 327–338
 acid method, 327–328*t*, 329–330*f*, 331*t*,
 334–335*f*
 alkali method, 336–338, 337*f*
 Mixer-settler, 301–305, 301–304*f*
 Monazite, 320–326
 acid method, 320–323, 321–323*f*
 alkali method, 324–325, 325–326*f*

N

N-donor chelating ligands, 208, 212–213
 Non-covalent interactions, 170–171, 239–240,
 251–252

O

Optical characterization
 afterglow, 11–12
 optically stimulated luminescence (OSL), 14

- steady state excitation spectra, 10–11, 11*f*
 thermoluminescence emission spectroscopy, 12–14
 thermoluminescence excitation spectroscopy, 10, 12–13
 Optically stimulated luminescence (OSL), 14, 14*f*
- P**
- Persistent phosphors, see Afterglow intensity, Applications, Phosphors, Synthesis
 Phosphors (selected)
 CaAl₂O₄:Eu, 6–7, 12–13, 17, 63–64, 67*f*
 Ca₂Si₅N₈:Eu, 32–34, 81
 SrAl₂O₄:Eu, 5–7, 6*f*
 Sr₂MgSi₂O₇:Eu, 35–36
 Y₂O₂S:Eu, 18, 36–58, 74
 ZnGa₂O₄, 46*t*, 77–79, 77*t*, 81
 ZnS:Cu, 4–5
 Photoconductivity, 5, 17
 Photopic vision, 24, 30
 Plasma melting, 359–360
 Pool-leaching, 340–341, 341*f*
 Primary building units, 165
- R**
- Rare earth metals, 355–360, 357*t*, 359*t*
 Recycled resources, 346, 348–351*f*
 Restricted speciation, 251–252, 259–260
- S**
- Scotopic vision, 24–25
 Secondary building units, 165–166
 Self-assembly, 243, 252–253
 Structural characterization
 electron spin resonance (ESR), 17–19
 precipitation of dopants, 15–16, 15*f*
 Structure type
 Dy₃Ge_{1.25}S₇, 150–152, 151*f*
 GeS, 115–117, 117*t*
 La₂PbSi₂S₈, 119–124, 121*t*, 126–127, 134–137, 145, 146*f*, 147*t*
 NaCl, 117–118, 118*t*, 118*f*
 [NH₄]CdCl₃, 118, 119*f*, 119*t*
 Pb₂GeS₄, 114, 114*f*, 115*t*
 PbGeS₃, 115, 116*f*, 117*t*
 Pb₂GeS₄–high temperature phase, 115, 116*f*, 116*t*
 Pb₂SiS₄, 112–113, 112*t*, 112*f*
 Pb₂SiSe₄, 113–114, 113*f*, 113*t*
 PbSnS₃, 118, 119*t*
 R₂S₃–PbS–SnS₂ isothermal section, 121*t*, 137–138
 Sm₃Ge_{1.48}Se₇, 150–152, 151*f*
 Sm_{1.32}Pb_{1.68}Ge_{1.67}Se₇, 150–152, 151*f*
 Y_{1.32}Pb_{1.68}Ge_{1.67}Se₇, 121*t*, 127, 137–138, 147*f*, 148*t*, 150–152, 151*f*
 Y₂Pb₃Sn₃S₁₂, 121*t*, 130, 138–144, 148*f*, 149*t*, 153
- Supramolecular interactions, 243–244, 248–253, 261*t*
- Synthesis
 chalcogenides, 110
 phosphors, 10, 70
- T**
- Template, 216, 218, 220–221
 Ternary system
 Pb–Z–X, 110–112, 111*t*
 Sm–Ge–Se, 150–152, 151*f*
 Theoretical modeling of separation, 305–306
 Thermoluminescence (TL)
 emission spectroscopy, 12–14, 61
 excitation spectroscopy, 5, 10, 12–13
 fading, 66
 guidelines, 12, 58–61
 retrapping, 12, 58, 62–63
 trap depths, 58–59, 62–64
 Thorium, ultrapure, 353–355, 354–355*f*
 Trap depths
 distribution of, 2*f*, 65–66
 frequency factor, 59, 62
 Hoogenstraaten, 6–7, 60, 63
 initial rise, 62–64
 peak shape method, 62–63
 thermal barrier for trapping, 2–3, 14, 61, 61*f*
- V**
- Vacuum distillation, 356
 Vacuum melting, 356
 Vacuum sublimation, 356, 357*t*
 Valence state of (co)dopants
 synthesis conditions, 16
 XANES, 16–17
 Vision
 scotopic, 24–25
 mesopic, 25, 31

Handbook on the Physics and Chemistry of Rare Earths, Volume 48

Including Actinides

Edited by **Jean-Claude G. Bünzli**, *Swiss Federal Institute of Technology, Lausanne, Switzerland*

Vitalij K. Pecharsky, *Iowa State University, Ames, Iowa, USA*

This volume of the *Handbook on the Physics and Chemistry of Rare Earths* series features four chapters spanning broadly different, but timely, subjects ranging from luminescent materials to properties of chalcogenides, uranyl hybrid materials, and rare-earth separation processes.

The first chapter (Chapter 274) is devoted to persistent luminescence, a phenomenon whereby a material keeps emitting light for a long time after excitation is switched off. The review covers all aspects of lanthanide persistent luminescence along with a critical evaluation of potential applications in markings and signage, solar energy conversion, and biosciences.

Chapter 275 sheds light on the quaternary rare-earth chalcogenide systems $R_2X_3\text{-PbX-ZX}_2$ ($X = \text{S, Se}$; $Z = \text{Si, Ge, Sn}$) that are of potential importance due to their intriguing thermal, optical, electrical, and magnetic properties. Synthetic conditions are detailed, followed by a systematic presentation of known phase diagrams, crystal structures, and magnetism.

Chapter 276 deals with crystalline hybrid materials of uranyl, $[\text{UO}_2]^{2+}$. These materials combine a substrate (organic or inorganic) with uranyl ion or its complexes that are blended on the molecular scale. The review explores covalent bonding with O- and N-donor ligands, ways of programming targeted coordination geometries and connectivities, supramolecular systems, as well as their luminescent properties.

The final chapter (Chapter 277) describes historical aspects and recent progress in separation processes of rare earths, with a special focus on Chinese industrial operations. Extractants, methods, and equipment developed for achieving efficient extraction methodologies are reviewed, including preparation of high-purity rare-earth elements and thorium.



North-Holland

An imprint of Elsevier
store.elsevier.com

ISBN 978-0-444-63483-2



9 780444 634832